

# **Active Stimuli-Responsive Polymer Surfaces and Thin Films: Design, Properties and Applications**

**Habilitationsschrift**

vorgelegt

der Fakultät Mathematik und Naturwissenschaften

der Technischen Universität Dresden

von

Dr. rer. nat. Leonid Ionov

geboren am 13.11.1977 in Obninsk

Eingereicht am:

Die Habilitationsschrift wurde in der Zeit von 04 / 2007 bis 04 / 2013 an der Professur für Physikalische Chemie polymerer Materialien angefertigt.

## Table of Contents

1. LIST OF ABBREVIATIONS .....	3
2. INTRODUCTION .....	4
3. 2D MICROSTRUCTURING BY THIN RESPONSIVE POLYMER FILMS.....	6
3.1 STATE OF THE ART IN 2D MICROFABRICATION USING THIN POLYMER FILMS..	6
3.2 NANOPATTERNED STIMULI-RESPONSIVE SURFACES BY BIOTEMPLATING .....	7
3.3 PATTERNED SURFACES WITH FIXED SWITCHABLE PATTERNS.....	9
3.4 PATTERNED SURFACES WITH SWITCHABLE PATTERN SIZE.....	13
3.5 "IN-SITU" PHOTOPATTERNING USING STIMULI-RESPONSIVE PHOTORESISTS	19
3.6 "IN-SITU" PATTERNING USING VISIBLE LIGHT .....	22
4. 3D MICROSTRUCTURING USING SELF-FOLDING POLYMER FILMS.....	23
4.1 STATE OF THE ART IN SELF-FOLDING FILMS.....	23
4.2 POLYMER-BASED SELF-FOLDING FILMS WITH SPECIAL PROPERTIES .....	27
4.3 PROPERTIES OF SELF-FOLDING FILMS .....	29
4.4 PROPERTIES AND APPLICATIONS OF SELF-FOLDING FILMS.....	38
5. CONCLUSIONS .....	45
6. OUTLOOK.....	48
7. ACKNOWLEDGEMENTS.....	50
8. PUBLICATIONS .....	51
9. REFERENCES.....	53
10. APPENDIX .....	60

## 1. LIST OF ABBREVIATIONS

AA	acrylic acid
AFM	atomic force microscopy
ATRP	atom-transfer radical-polymerization
BA	4-acryloylbenzophenone
BRB80	80 mM Brinkley Reassembly Buffer
CVD	chemical vapor deposition
FITC	fluorescein isothiocyanate
FLIC	fluorescence interference contrast
IEP	isoelectric point
LHC	light-to-heat conversion
MMA	methyl methacrylate
NBA	2-nitrobenzyl acrylate
NIPAM	N-isopropylacrylamide
P2VP	poly-(2-vinylpyridine)
PAA	poly (acrylic acid)
PBS	phosphate buffered saline
PCL	polycaprolactone
PDMAEMA	poly(dimethylaminoethyl methacrylate)
PGMA	poly(glycidyl methacrylate)
PMMA	poly(methyl methacrylate)
PNIPAM	poly-(N-isopropylacrylamide)
PSI	polysuccinimide
PtBA	poly( <i>tert</i> butylacrylate)
tBA	tert butylacrylate

## 2. INTRODUCTION

Design of 2D and 3D micropatterned materials is highly important for printing technology, microfluidics, microanalytics, information storage, microelectronics and biotechnology. Biotechnology deserves particular interest among the diversity of possible applications because it opens perspectives for regeneration of tissues and organs that can considerably improve our life. In fact, biotechnology is in constant need for development of microstructured materials with controlled architecture. Such materials can serve either as scaffolds or as microanalytical platforms, where cells are able to self-organize in a programmed manner. Microstructured materials, for example, allow *in vitro* investigation of complex cell-cell interactions, interactions between cells and engineered materials. With the help of patterned surfaces it was demonstrated that cell adhesion and viability as well as differentiation of stem cells<sup>1</sup> depend on the character of nano- and micro- structures<sup>2</sup> as well as their size.

There are number of methods based on optical lithography, atomic force microscopy, printing techniques, chemical vapor deposition, which have been developed and successfully applied for 2D patterning. While each of these methods provides particular advantages, a general trade-off between spatial resolution, throughput, “biocompatibility of method” and usability of fabricated patterned surfaces exists. For example, AFM-based techniques allow very high nanometer resolution and can be used to place small numbers of functional proteins with nanometer lateral resolution, but are limited to low writing speeds and small pattern sizes. Albeit, the resolution of photolithography is lower, while it is much faster and cheaper.

Therefore, it is highly desirable to develop methods for high-resolution patterning at reasonably low cost and high throughput. Although many approaches to fabricate sophisticated surface patterns exist, they are almost entirely limited to producing fixed patterns that cannot be intentionally modified or switched on the fly in physiologic environment. This limits the usability of a patterned surface to a single specific application and new microstructures have to be fabricated for new applications. Therefore, it is desirable to develop methods for design of switchable and rewritable patterns. Next, the high-energy of the ultraviolet radiation, which is typically used for photolithography, can be harmful for biological species. It is also highly important to develop an approach for photopatterning where visible light is used instead of UV light. **Therefore, it is very important for biotechnological applications to achieve good resolution at low costs, create surface with switchable and reconfigurable patterns, perform patterning in mild physiologic conditions and avoid use of harmful UV light.**

3D patterning is experimentally more complicated than 2D one and the applicability of available techniques is substantially limited. For example, interference photolithography allows fabrication of 3D structures with limited thickness. Two-photon photolithography, which allows nanoscale resolution, is very slow and highly expensive. Assembling of 3D structures by stacking of 2D ones is time consuming and does not allow fabrication of fine hollow structures. At the same time, nature offers an enormous arsenal of ideas for the design of novel materials with superior properties. In particular, self-assembly and self-organization being the driving principles of structure formation in nature attract significant interest as promising concepts for the design of intelligent materials<sup>3</sup>. Self-folding films are the examples of biomimetic materials<sup>4</sup>. Such films mimic movement mechanisms of plants<sup>5-7</sup> and are able to self-organize and form complex 3D structures. The self-folding films consist of two materials with different properties. At least one of these materials, active one, can change its volume. Because of non-equal expansion of the materials, the self-folding films are able to form a tubes, capsules or more complex structure. Similar to origami, the self-folding films provide unique possibilities for the straightforward fabrication of highly complex 3D micro-structures with patterned inner and outer walls that cannot be achieved using other currently available technologies. The self-folded micro-objects can be assembled into sophisticated, hierarchically-organized 3D super-constructs with structural anisotropy and highly complex surface patterns.



Till now most of the research in the field of self-folding films was focused on inorganic materials. Due to their rigidity, limited biocompatibility and non-biodegradability, application of inorganic self-folding materials for biomedical purposes is limited. Polymers are more suitable for these purposes. There are many factors, which make polymer-based self-folding films particularly attractive. There is a variety of polymers sensitive to different stimuli that allows design of self-folding films, which are able to fold in response to various external signals. There are many polymers changing their properties in physiological ranges of pH and temperature as well as polymers sensitive to biochemical processes. There is a variety of biocompatible and biodegradable polymers. These properties make self-folding polymer highly attractive for biological applications. Polymers undergo considerable and reversible changes of volume that allows design of systems with reversible folding. Fabrication of 3D structures with the size ranging from hundreds of nanometers to centimeters is possible. In spite of their attractive properties, the polymer-based systems remained almost out of focus – ca 15 papers including own ones were published on this topic (see own review <sup>8</sup>, state October 2011).

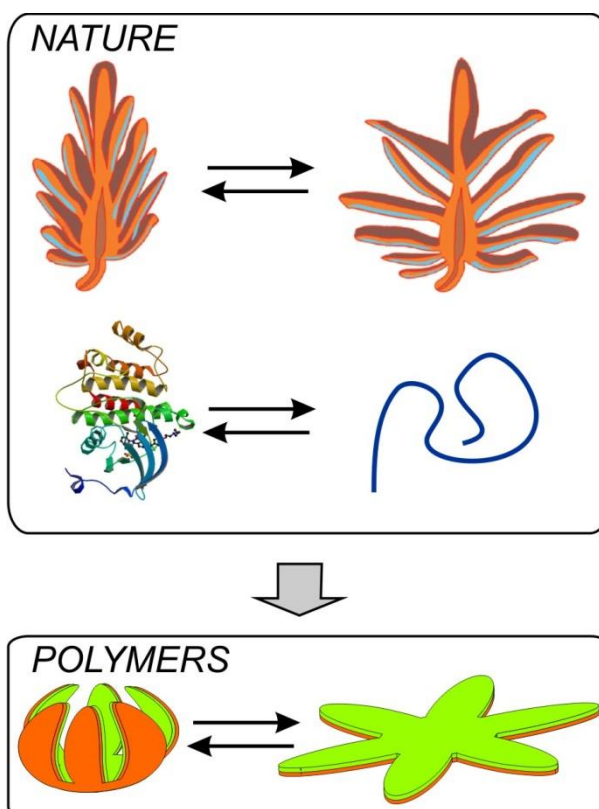


**Figure 1.** Examples of self-folding in nature (pine cone and protein) and synthetic self-folding polymeric films. (Ref <sup>6</sup>, Copyright (2011) by Elsevier).

**Thereby the development of biomimetic materials based on self-folding polymer films is highly desired and can open new horizons for the design of unique 3D materials with advanced properties for lab-on-chip applications, smart materials for everyday life and regenerative medicine.**

### 3. 2D MICROSTRUCTURING BY THIN RESPONSIVE POLYMER FILMS

#### 3.1 STATE OF THE ART IN 2D MICROFABRICATION USING THIN POLYMER FILMS

Microstructuring is highly important technology for design of microelectronic devices<sup>9, 10</sup>, sensor<sup>11-17</sup>, printing, microfluidics<sup>18, 19</sup>, information storage<sup>20</sup>, photonic applications<sup>21</sup>, biotechnology<sup>22-25</sup>, bioanalytics<sup>26, 27</sup>, and tissue engineering<sup>1, 2, 24, 28-33</sup> as well as design of smart materials<sup>34</sup>. Typically, topographical relief and/or a contrast of physico-chemical properties - such as wettability, charge, and fluorescence - are the results of microstructuring. All microstructuring approaches can be divided in two groups: top-down and bottom-up ones.

##### Top-down approaches

There are a number of top-down techniques including photolithography<sup>35, 36</sup>, microcontact printing<sup>16</sup>, chemical vapor deposition (CVD)<sup>37, 38</sup>, atomic force microscopy (AFM)<sup>39, 40</sup>, electron beam lithography and dip-pen technology<sup>13, 16, 29-33, 41, 42</sup>, which were used for surface structuring. While each of these methods provides particular advantages, a general trade-off between spatial resolution, throughput and maximum pattern size exists. For example, AFM-based techniques can be used to place small numbers of functional proteins with nanometer lateral resolution, but are limited to low writing speeds and small pattern sizes. Optical methods, such as the light-based activation of functional groups or ligands on the surface<sup>43</sup>, deserve particular interest because these techniques often offer sufficient resolution combined with the potential for high throughput production. However, when based on conventional lithography, expensive metal masks are needed and only predefined patterns can be created. Moreover, the high-energy of the ultraviolet radiation ( $\lambda < 350$  nm) is often needed to trigger the photoactivation of proteins or protein-binding molecules and can be harmful for biological species such as proteins, DNAs, cells etc<sup>44</sup>. Continuous illumination with light can also lead to the photogeneration of highly reactive radicals causing undesirable effects including protein conformational changes and loss of biological function.

##### Photolithography remain

ns the cheapest and most efficient method for large scale fabrication of structured surfaces. The essential steps of photolithography are photocrosslinking or photodegradation. Therefore, different compounds undergoing photoinduced degradation<sup>45</sup> or crosslinking<sup>46</sup> are implemented as photoresists for the fabrication of structured surfaces. In fact, the design of photosensitive compounds determines the applicability of any particular sort of photolithography. For example, water-soluble photoresists<sup>45, 47</sup> are of particular interest for the *in situ* patterning of proteins and cells<sup>48-50</sup> under biologically-relevant conditions. Recently, various photoresists that are water-soluble and can be developed in aqueous environment were designed. However, most of them undergo immediate development upon illumination. This causes an undesired contamination of the surrounding media due to the uncontrolled release of dissolved photoresist.

Other methods employ a variety of photoactive moieties, which can link specific molecule of interest to the surface. For example, aryl azides and aryldiazirine moieties were used to capture proteins in patterns via light activation to highly reactive nitrenes<sup>51-53</sup> and carbenes.<sup>54-59</sup> Benzophenone groups were employed to create reactive benzhydrol radicals<sup>60-63</sup>. Various forms of deprotection chemistry using nitrobenzene as a caging moiety have also been used to pattern active surfaces<sup>64-68</sup>. Two particularly popular strategies employ caged biotin<sup>69, 70</sup> and photobiotin<sup>71, 72</sup>, which exploit the ubiquitous biotinavidin/streptavidin interaction.

Most of current surface structuring approaches are almost entirely limited to producing fixed patterns that cannot be intentionally modified under physiological conditions. However, patterns that can be generated or modified on demand in aqueous environment would tremendously extend the applicability of structured surfaces. In order to achieve such *in-situ* treatment in a localized manner a number of optical<sup>73-76</sup> and electrochemical techniques have been proposed<sup>77-80</sup>. For example, structured illumination of a surface containing light-sensitive groups was used to irreversibly add and to remove pattern elements<sup>75, 81</sup>. Reconfigurable optical patterning was shown based on reversibly-isomerizable chemical groups<sup>74, 76</sup> and application of such surfaces was demonstrated for light-programmed cell adsorption<sup>73, 74</sup>. However, most of the optical strategies use UV illumination, which is often harmful to biological species.

### Bottom-up approaches

The use of self-assembling biological objects as templates (bottom-up approach) for the design of the nanostructures offers a range of advantages<sup>82</sup>. In particular, selective molecular recognition and proof-reading during the build-up of biomolecules can provide a high degree of uniformity in the possible structures. Different biomacromolecules and their assemblies including DNA, viral capsids, cytoskeleton filaments and protein crystals were successfully applied as templates for the fabrication of inorganic nanostructured materials (see recent review<sup>82</sup>). In fact, design of functional organic nanostructures<sup>83-85</sup> using biotemplating is highly important research direction.

There are many examples of use of natural self-assembling molecules for design of nanostructured materials. Oligo and polynucleotides are the most studied and widely applied for the fabrication of 2D and 3D structures. Due to very specific recognition, oligonucleotide chains are able to form very stable origami like structures with various chemical functionality and shape<sup>86</sup>. Microtubules, which are cylindrical protein filaments with outer diameter of about 24 nm and length up to tens of micrometers, deserve a particular interest as templates<sup>87-90</sup>. First, microtubules can easily be formed by self-assembly of tubulin dimers. Second, microtubules are able to form segmented structures with different functionality in a controlled manner<sup>91</sup>. Third, a number of approaches to control position as well as orientation of microtubules on artificial substrates are available<sup>92-96</sup>. This makes microtubules highly promising for templated synthesis of complex materials.

## 3.2 NANOPATTERNED STIMULI-RESPONSIVE SURFACES BY BIOTEMPLATING

In this chapter the possibilities of use of microtubules as templates for the fabrication of nanopatterned surfaces are discussed. The rhodamine- modified red-fluorescent microtubules, which are obtained by self-assembly of tubulin dimers, were first adsorbed on a silane-modified surface. The adsorbed microtubules were crosslinked in order to provide chemical stability and the reactive bromoisobutyryl groups capable of initiating atom transfer radical polymerisation were immobilized. The initiator-modified microtubules were the used to initiate growth of thermoresponsive PNIPAM – brushes from surface-adsorbed microtubules (Figure 2).

Structural changes of the microtubule were imaged by AFM before and after the polymerisation (Figure 3). These measurements revealed that the contour length of the microtubules increased by up to 100 %. On the other hand, the end-to-end distance of the surface-attached microtubules remained almost unchanged. The increase of the contour length is attributed to stretching within and between the tubulin-dimers caused by steric repulsions between the grafted polymer chains.

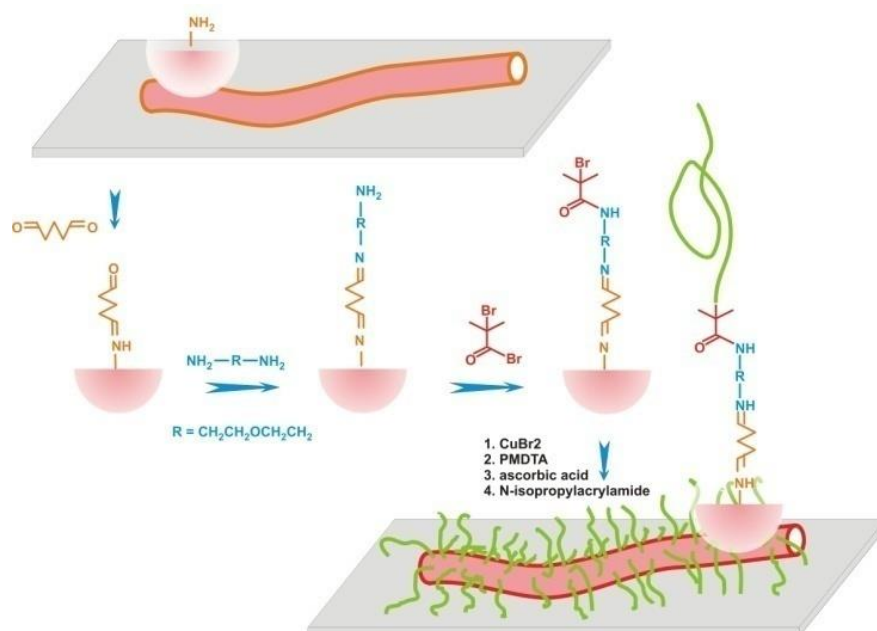


**Figure 2.** Schematic diagram of microtubule modification and polymer grafting. The polymer chains were grown from microtubules that were adsorbed on a hydrophobic glass substrate and sequentially crosslinked and modified by initiator for ATRP<sup>97</sup>.

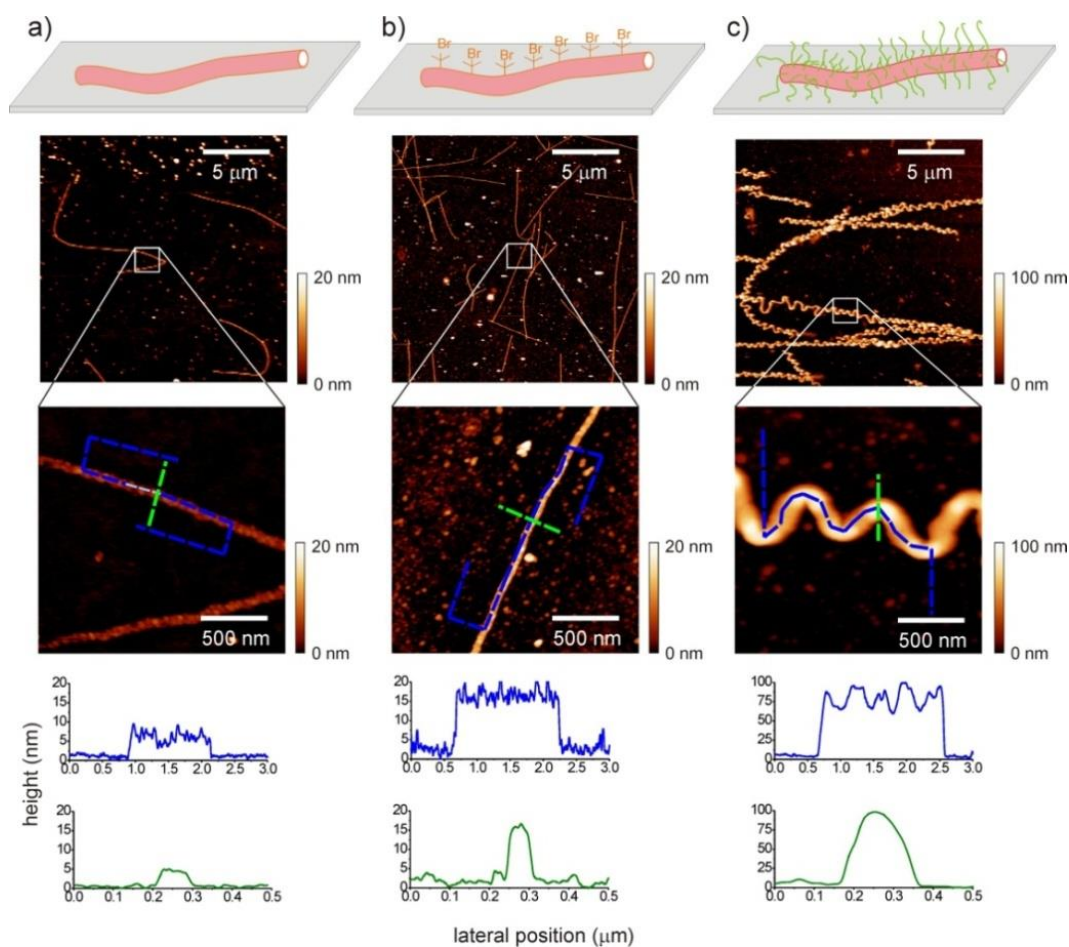


**Figure 3.** Morphology of microtubules at different stages of the modification procedure. AFM images (middle panel) of microtubules (a) after crosslinking, (b) after immobilisation of initiator, and (c) after grafting of poly-(N-isopropylacrylamide - fluorescein o-acrylate). Cross-

sections (bottom panel) are given along the paths indicated with the corresponding colour on the AFM images. No tip-deconvolution was performed<sup>97</sup>.

Grafting density was found to be  $\Gamma_{\text{length}} \approx 40$  chains/nm ( $\Gamma_{\text{area}} \approx 0.3$  chains/nm<sup>2</sup>). The average distance  $D$  between grafting sites can then be calculated by  $D = \Gamma_{\text{area}}^{-1/2} \approx 1.8$  nm. This value is substantially smaller than the gyration radius of PNIPAM chains with molecular weight around  $M_n = 69000$  g/mol in the collapsed state ( $R_g \approx 20$  nm). Consequently, the polymer-grafted shell can be considered as a brush-like. The apparent density of potential grafting sites  $N_{\text{POL}}$  was found to be in the range  $N_{\text{POL}} = 100 \text{ nm}^{-1} - 130 \text{ nm}^{-1}$  meaning that about  $\Gamma_{\text{length}} / N_{\text{POL}} = 30\% - 40\%$  reactive amino acid residues initiated growth of polymer chains<sup>23</sup>.

It was found that biotemplated PNIPAM brushes demonstrate pronounced switching properties. In particular, the fluorescence intensity of the polymer chains gradually decreased with increasing temperature (Figure 4), reaching almost zero above the low critical solution temperature of PNIPAM ( $T = 33^\circ\text{C}$ ). The reason of this effect was, most probably, fluorophore quenching by the collapsed polymer chains<sup>98</sup>, indicating that the polymer chains were capable of switching. Given the optical resolution of the imaging system, no morphological changes of the PNIPAM-decorated microtubules resulting from temperature-induced swelling and collapse of the polymer were detected.

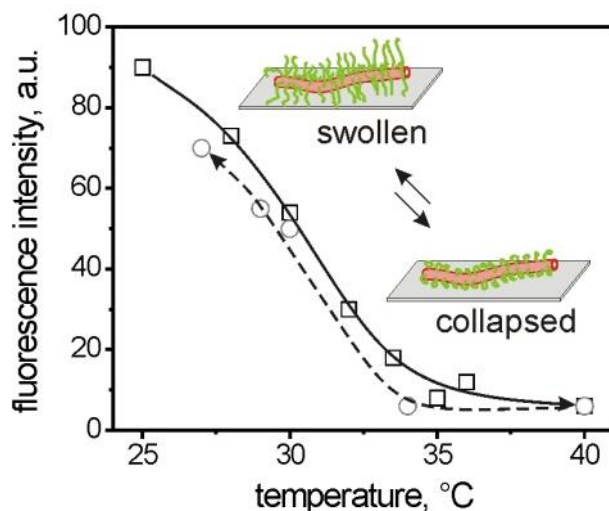


**Figure 4.** Switching of PNIPAM grafted on protein microtubules. Dependence of fluorescence intensity of poly-(N-isopropylacrylamide - fluorescein o-acrylate) brushes on temperature upon heating (open squares, solid line) and cooling (open circles, dashed line).<sup>97</sup>

In conclusion, a novel approach for the design of nanopatterned polymer brushes based on the use of microtubules as biological templates was developed. The formed structures have the width of around 100 nm that is smaller than the resolution of optical microscopy. The fabricated thermoresponsive nanopatterned PNIPAM brushes can be further used for design of responsive material systems<sup>99</sup> as well as biomolecular switches<sup>100</sup> and will be of interest for a variety of nanotechnological and microelectronic applications.

### 3.3 PATTERNED SURFACES WITH FIXED SWITCHABLE PATTERNS

Another very important task is to develop simple methods for the fabrication of switchable patterned surfaces when the surface pattern can be switchable by external signal. One approach towards this goal is based on the site-selective deposition of stimuli-responsive materials forming self-assembled monolayers (SAM) or polymer brushes. On such surfaces, the topographical and physico-chemical properties can be locally triggered by external control over the environmental conditions. Novel surface properties are expected when two or more kinds of polymer chains are grafted onto the same substrate. However, the



fabrication of patterned two- and multi- component switchable surfaces is still not a trivial task <sup>101</sup>. Commonly, for the fabrication of patterned surfaces, researchers use surface-initiated polymerisation <sup>101-107</sup>, which requires high purification of the monomers and special conditions for polymerisation procedure. **The goal is, therefore, to develop simple and robust method of patterning of two kinds of stimuli-responsive polymers on the surface.**

To fabricate micropatterned polymer surfaces that are switchable in aqueous environments, poly-(2-vinylpyridine) (P2VP) and polyacrylic acid (PAA) were used. These polymers reversibly change their conformation and charge depending on pH. The PAA chains are negatively charged and extended at pH > 5.5, while the P2VP chains are positively charged and extended at pH < 2.3. Both polymers are uncharged and collapsed at all other pH values. Surface grafted films of PAA and P2VP demonstrate reversible switching from moderately hydrophobic to hydrophilic behavior after treatment with alkali and acidic water, respectively.

Micropatterning was performed by a combination of photolithography, lift-off, and grafting-to techniques (Figure 5). In brief, silicon wafers were coated with a thin film of poly(glycidyl methacrylate) (PGMA), which served as a coupling agent for carboxyl-terminated polymers <sup>108</sup>. Next, photoresist was spin-coated, illuminated through a mask, and developed. Afterwards, a thick film of carboxy-terminated poly(*tert*butylacrylate) (PtBA-COOH) was deposited and the leftover photoresist was removed leaving the patches of PtBA film. The resulting PtBA-COOH was grafted by annealing at elevated temperature. Next, P2VP-COOH has been spincoated on the top of PtBA patterned surface and grafted at elevated temperature. Finally, PtBA was hydrolyzed yielding PAA <sup>109</sup>. The typical thicknesses of the PAA and P2VP grafted areas were found to be about 7 nm and 5 nm, respectively. Generally, the advantage of the technique is the combination of (i) high chemical stability of the obtained polymer layer (polymer chains are chemically anchored to the substrate), (ii) easy control over the molecular weight as well as the grafting density of the polymer and (iii) simplicity of the fabrication procedure.

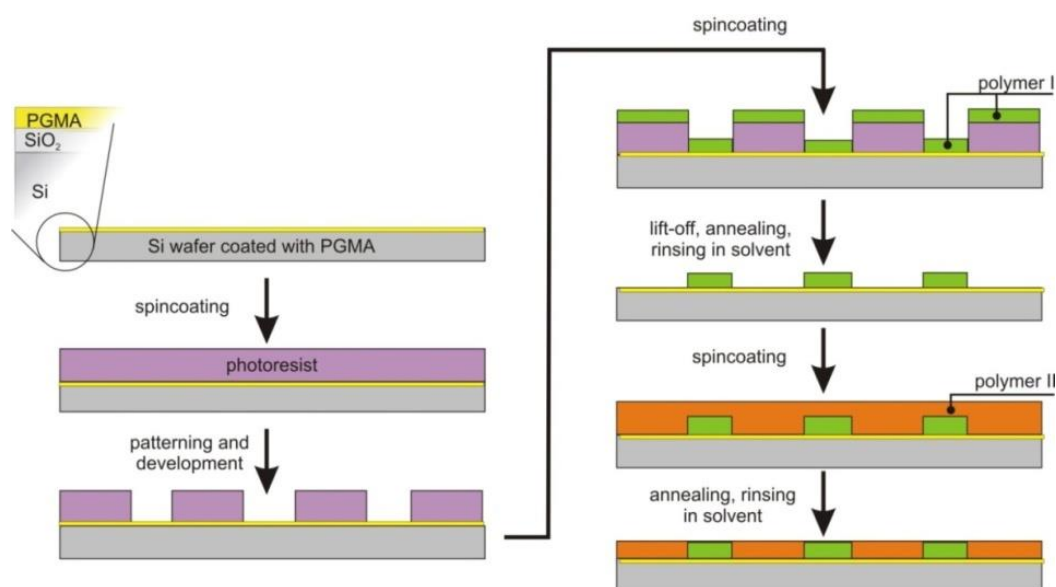


**Figure 5.** Preparation of micropatterned bicomponent polymer grafted layers using a combination of photolithography, “lift-off” and “grafting to” techniques. Polymer I – poly(*tert*-butyl acrylate) - PtBA, polymer II – poly(2-vinylpyridine) – P2VP <sup>12</sup>.

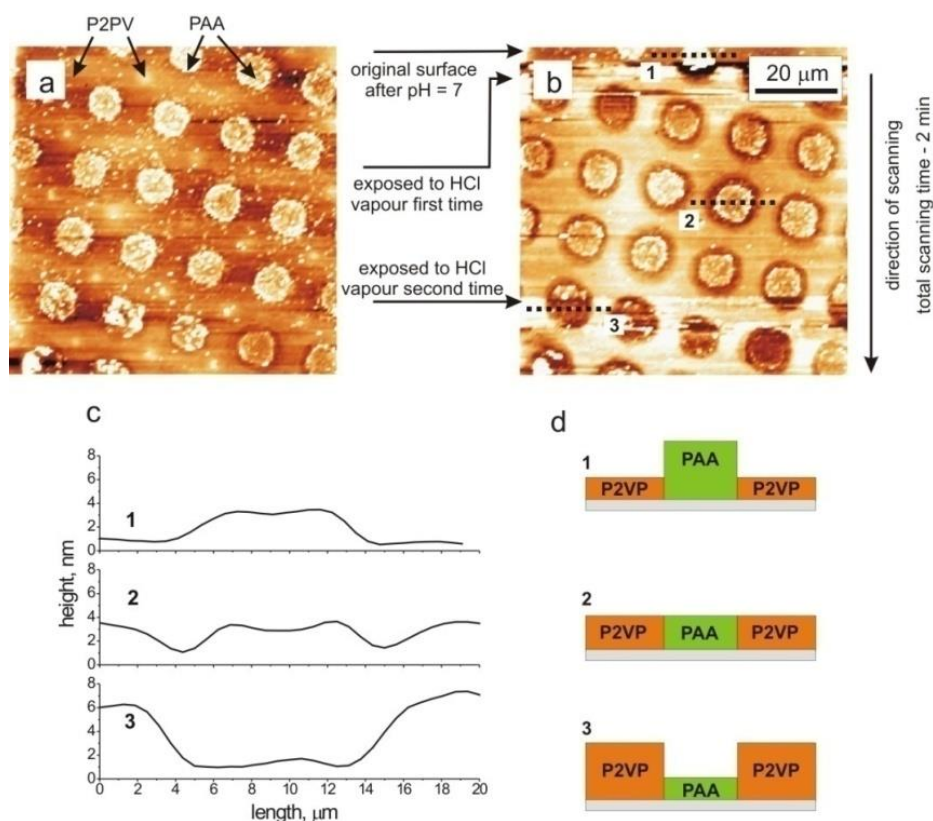


**Figure 6.** Surface topography of patterned PAA/P2VP under various conditions. (a) - AFM image after exposure to pure water ( $\text{pH} = 6.7$ ); (b) - In-situ observation of topography switching upon exposure to HCl vapor. First, the surface was treated with pure water (cross-section 1) and then exposed to HCl vapor twice (cross-sections 2 and 3); (c) - Quantification of the topographical profiles from (b); (d) - Schematic diagram of the switching. The PAA islands are swollen after exposure to pure water (cross-section 1). Exposure to HCl vapor leads to the depression of PAA while P2VP becomes protonated and swollen (cross-sections 2 and 3). AFM scanning was performed in air at room temperature.

The fabricated patterned P2VP/PAA brushes demonstrate pronounced responsive behavior. In particular, topography, charge and wetting can be switched by exposure to water with different pH. For example, the PAA-islands are elevated above the P2VP-area after treating the surfaces with pure water ( $\text{pH} = 6.7$ ) and drying with nitrogen (Figure 6a and c cross-section 1). However, exposure of the surface to HCl vapor inverted the surface topography: the collapsed PAA islands were lower than the now elevated P2VP structures (Figure 6b, c, d cross-section 3). This inverse switching results from electrostatic interactions within the polymer layer. Repulsion between the charged groups (carboxyl groups in alkalic medium and protonated pyridine rings in acidic medium) causes the swelling of the respective polymer incorporating water molecules from the moderately humid air atmosphere (Figure 6d).

Importantly, the switching of the surface topography was accompanied by the switching of the surface properties with regard to hydrophobicity. Local condensation of water droplets revealed a distinct contrast between P2VP and PAA areas (Figure 7a). After exposure to pure water ( $\text{pH} = 6.7$ ), very small water droplets wetted the hydrophobic P2VP area, whereas larger drops occurred on the hydrophilic PAA islands. The inverse scenario was observed after exposure of the patterned surface to acidic water ( $\text{pH} = 2$ ). The observed switching between hydrophobic and hydrophilic surface properties was applied to the generation of various liquid patterns (Figure 7b).

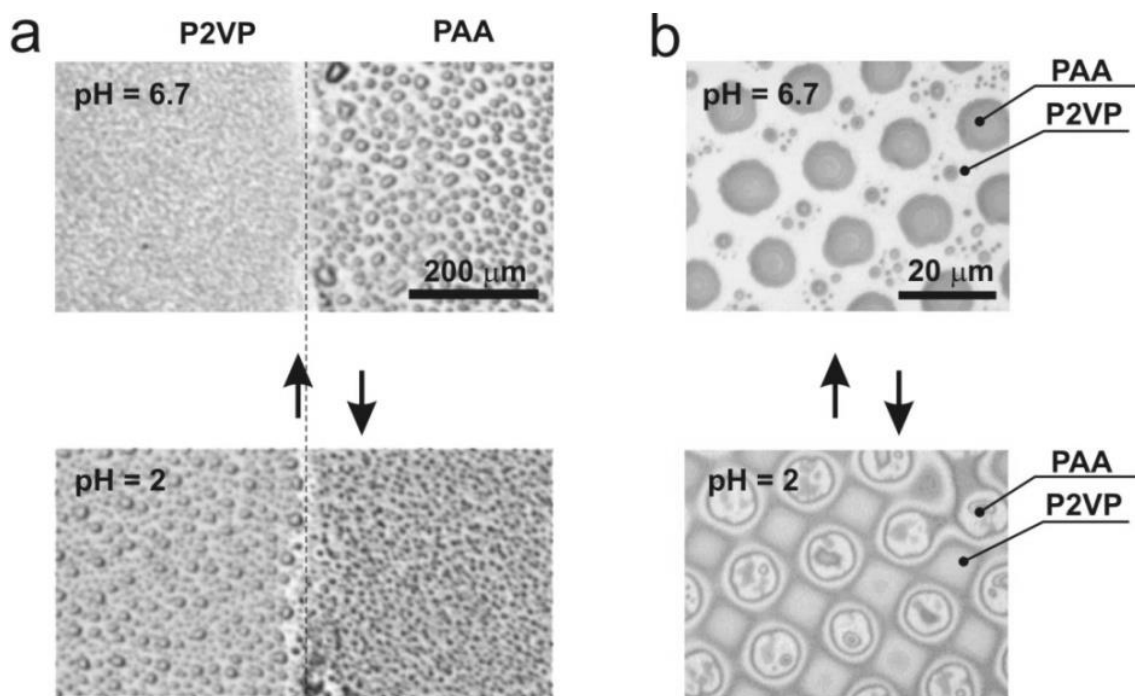


**Figure 7.** Adsorption of water droplets on structured PAA/P2VP brushes. Optical bright-field microscopy of water droplets on a PAA/P2VP boundary (a) and microstructure (b) at different pH. Water selectively wetted the P2VP or PAA areas at low or high pH, respectively <sup>12</sup>.

To test the usability of the switchable surface for programmed protein adsorption, fluorescently labeled protein (FITC-casein) was adsorbed on the micropatterned PAA/P2VP surfaces at different pH. It was observed that FITC-casein selectively adsorbed onto the PAA islands at pH = 1.2 and onto the P2VP areas at pH = 8.6 (Figure 8). The selective adsorption of FITC-casein (IEP = 7.63) onto the areas occupied by one of the polymers can be readily explained by considering electrostatic interactions. As stated earlier, P2VP is charged positively at pH < 2.3 and PAA is negatively charged at pH > 5.5. Therefore, FITC-casein is repelled from the P2VP features at low pH and from the PAA features at high pH. On the other hand, FITC-casein – similarly to most other proteins - can adsorb on polymer surfaces due to hydrophobic interactions or hydrogen bonds in the absence of electrostatic repulsion.

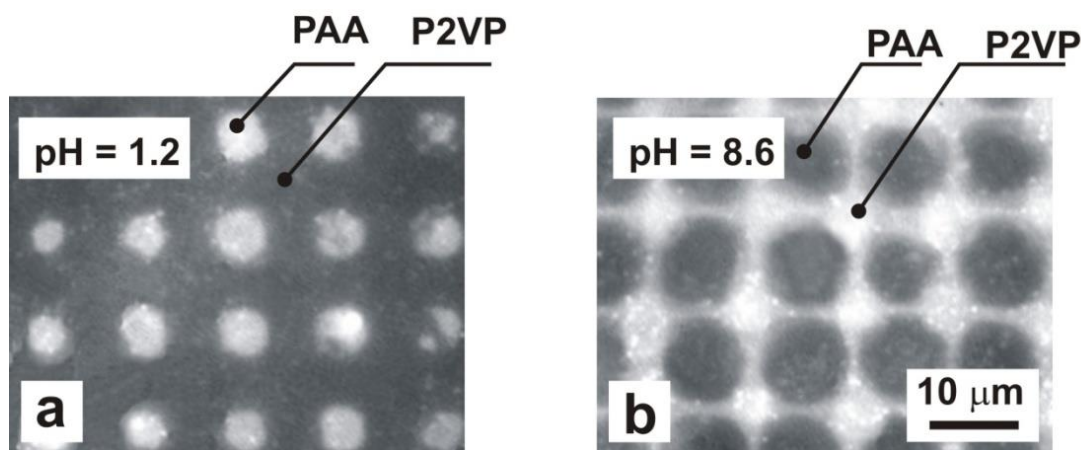


**Figure 8.** Fluorescence micrographs of FITC-casein adsorbed onto PAA/P2VP micropatterned surfaces. Adsorption of FITC-casein was performed at pH = 1.2 (a) and pH = 8.6 (b) <sup>12</sup>.

In summary, a straightforward method for the preparation of switchable micro-patterned polymer surfaces based on bicomponent polyelectrolyte brushes was developed. This method utilizes “grafting to” approach instead of widely used surface initiated polymerization.



It makes preparation of bicomponent patterned polymer grafted layers simple and quick. It was demonstrated that the approach allows the inverse and reversible switching of surface topography, wettability, and charge. This approach can be easily extended for the fabrication of multicomponent ( $n > 2$ ) micropatterned polymer surfaces by repeating the structuring cycle multiple times. One foresees a large potential of inversely switchable micropatterned surfaces for (i) microprinting where the topographical features of polymer layer can be used as a microstamp that is switchable via external stimuli, (ii) microfluidic devices where liquid movement (direction, speed, etc) can be easily manipulated by pH, and (iii) microanalytical purposes where chemicals and proteins can be deposited in a switchable site-selective manner (programmed protein adsorption).

### 3.4 PATTERNED SURFACES WITH SWITCHABLE PATTERN SIZE

While the switchable patterned polymer brushes discussed in previous chapter demonstrate switching of surface topography, charge and wetting, the surface pattern is fixed and cannot be altered. The next step towards the freely reconfigurable patterns is to develop methods for the fabrication of patterns, whose lateral size can be reversibly changed.

The design is based on the patterned surface-immobilization of thermoresponsive PNIPAM polymer chains. In aqueous environments, PNIPAM (homopolymer) chains undergo reversible collapse or swelling above or below the cloud point  $T = 33\text{ }^{\circ}\text{C}$ , respectively. However, the cloud point can be gradually increased or decreased by incorporation of additional hydrophilic or hydrophobic comonomers, respectively. Likewise, the cloud point can be tuned by varying the ratio of both added comonomer types. Using this principle, a surface containing lateral cloud point gradients by laying down opposing gradients of hydrophilic and hydrophobic PNIPAM-copolymers was fabricated (Figure 9 a,b,c). Across this surface, polymers whose cloud point is above or below the actual temperature of the surrounding are collapsed or swollen, respectively. The changes in ambient temperature can alter the size of the area in which a particular polymer was collapsed or swollen (Figure 9d). Thus, the method allows design of surfaces with patterns whose size can be changed in response to variation of the environmental conditions, rather than local treatment.

To demonstrate that the cloud point of thermoresponsive copolymers gradually changes with the ratio of hydrophilic to hydrophobic components, series of (poly(N-isopropylacrylamide-*tert* butyl acrylate - acrylic acid) (poly-(NIPAM-tBA-AA)) copolymers containing different *tert* butyl acrylate(tBA) to acrylic acid (AA) ratios were prepared. As expected, the cloud point decreased gradually as the tBA to AA ratio increased (Figure 10). Moreover, the cloud point depends on the ionic strength of the aqueous solution. Attributable to changing the balance between intramolecular hydrogen bonds and hydrogen bonds with water<sup>110</sup> an increase in ionic strength leads to (i) a pronounced increase in the cloud point of PNIPAM copolymers that have AA as the predominant co-monomer and to (ii) a decrease in the cloud point for PNIPAM copolymers that have tBA as the predominant co-monomer.

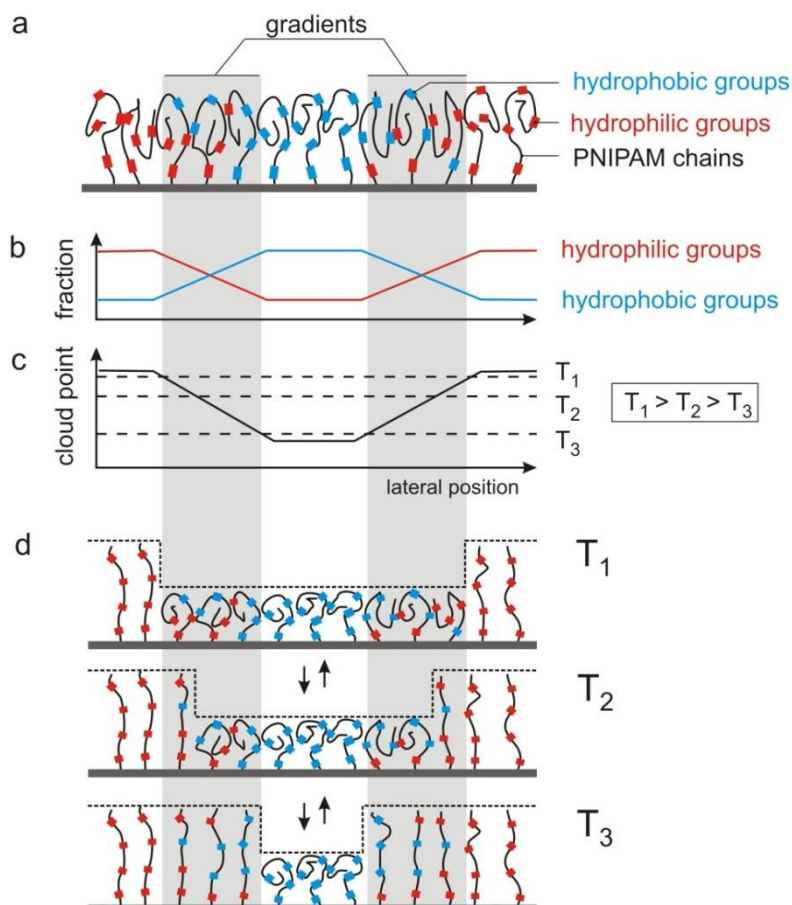


**Figure 9.** Concept of surfaces with size-controlled patterns: (a,b) Lateral gradients of thermoresponsive PNIPAM copolymers with hydrophobic or hydrophilic groups are formed on the surface; (c) cloud point of PNIPAM copolymers changes gradually with the ratio of hydrophobic to hydrophilic groups. The dashed lines indicate three examples of ambient temperatures  $T_1$ ,  $T_2$  and  $T_3$ ; (d) Polymer chains with an cloud point below and above ambient temperatures  $T_1$ ,  $T_2$  and  $T_3$  are collapsed and swollen, respectively. As a result, the size of the area containing the collapsed polymer depends on the ambient temperature and can be reversibly tuned<sup>23</sup>.

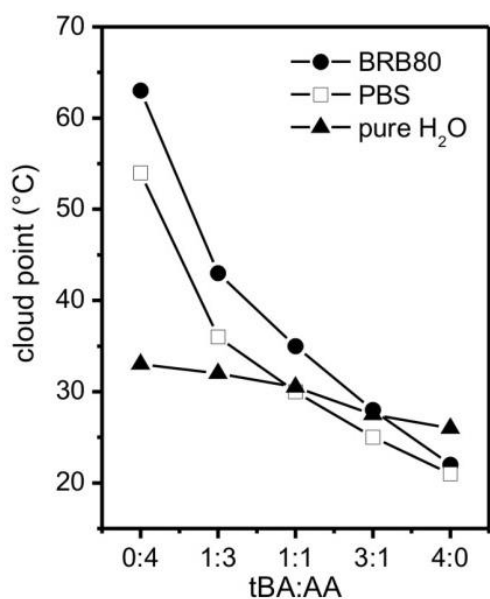


**Figure 10.** The cloud point of poly-(NIPAM-tBA-AA) copolymers (%tBA + %AA in monomer mixture is 6 mol %) in different aqueous environments: 80 mM Brinkley Reassembly Buffer (BRB80, pH = 6.9), 100 mM Phosphate Buffered Saline (PBS, pH = 7.5) and pure water<sup>23</sup>.

Next, surface-immobilized PNIPAM copolymer layers were fabricated and their swelling behavior was investigated. A poly-(NIPAM-tBA) layer grafted to the surface of the silicon wafer was prepared using surface-initiated atom-transfer radical polymerization. The thickness of the polymer layer in the dry state was  $h_{\text{DRY}} = 33$  nm. A poly-(NIPAM-AA) layer was obtained by hydrolysis of the poly-(NIPAM-tBA) layer in methanesulfonic acid<sup>12</sup>. Ellipsometric investigations revealed that the poly-(NIPAM-AA) layer was thicker than the poly-(NIPAM-tBA) layer at both high and low temperatures as a result of electrostatic repulsions between negatively charged carboxylic groups (Table 1).

Polymer	T (°C)	$h$ (nm)	$n$	$h \times n$ (nm)
poly-(NIPAM-tBA)	16	86.2	1.39	120
	55	27.2	1.52	42
poly-(NIPAM-AA)	16	118.7	1.37	163
	55	46.9	1.44	67

**Table 1.** Height  $h$  and refractive indexes  $n$  of poly-(NIPAM-tBA) and poly-(NIPAM-AA) grafted layers obtained by ellipsometry in BRB80 at different temperatures. The initial thickness of the poly-(NIPAM-tBA) layer in the dry state was  $h_{\text{DRY}} = 33$  nm<sup>23</sup>.

Swelling properties of poly-(NIPAM-tBA) and poly-(NIPAM-AA) layers were investigated using fluorescence interference contrast (FLIC) microscopy in a spatially resolved manner. For this fluorescent protein was adsorbed onto the polymer layers<sup>111</sup>. FLIC microscopy is based on interference effects between the direct excitation and emission light with reflected light from the surface leading to a periodic modulation of the detected emission intensity as a function of height above the surface (Figure 11a)<sup>111</sup>. Due to a half wavelength phase shift upon reflection on the reflecting surface (silica-silicon interface), fluorescent molecules are almost invisible if located directly on the reflecting surface. The intensity increases as the distance between the fluorescent molecules and the reflecting surface grows, and it passes through the maximum at a distance of about a quarter of a wavelength. FLIC microscopy thus allows obtaining information about the vertical position of fluorescent objects in the vicinity to a reflecting surface with high spatial accuracy<sup>112, 113</sup>. The intensity ( $I$ ) can be expressed by the following equation<sup>114</sup>:

$$I(h) = I_0 \left( 2 \cdot (1 - r_f)^2 + 8r_f \sin^2 \left( \frac{2\pi}{\lambda_{\text{EX}}} (n_{\text{SiO}_2} \cdot h_{\text{SiO}_2} + n_{\text{PGMA}} \cdot h_{\text{PGMA}} + n_{\text{PNIPAM}} \cdot h) \right) \right) \times \left( 2 \cdot (1 - r_f)^2 + 8r_f \sin^2 \left( \frac{2\pi}{\lambda_{\text{EM}}} (n_{\text{SiO}_2} \cdot h_{\text{SiO}_2} + n_{\text{PGMA}} \cdot h_{\text{PGMA}} + n_{\text{PNIPAM}} \cdot h) \right) \right) \quad (1)$$

where,  $I_0$  serves as a proportionality factor. Refractive indexes for the PNIPAM layer, PGMA with initiator and  $\text{SiO}_2$  are represented by  $n_{\text{PNIPAM}}$ ,  $n_{\text{PGMA}} = 1.5$  and  $n_{\text{SiO}_2} = 1.46$ .  $h_{\text{SiO}_2} = 1.4$  nm is the oxide thickness,  $h_{\text{PGMA}} = 2.2$  nm is the height of PGMA layer, and  $h$  is the height of the fluorophores above the oxide surface. The reflection coefficient is represented by  $r_f$ . A set of optical filters defining the excitation and emission wavelengths,  $\lambda_{\text{EX}} = 565$  nm and  $\lambda_{\text{EM}} = 610$  nm, has been used.

Rhodamine-labelled tubulin was adsorbed on polymer layer at  $T = 65$  °C when it is collapsed. It was found that the poly-(NIPAM-tBA) area was brighter than the poly-(NIPAM-AA) area (Figure 11b) when the surface was imaged by FLIC microscopy at low temperature ( $T < 20$  °C, when both polymers were swollen). The opposite behavior was observed when the polymers were collapsed at high temperature ( $T = 55$  °C). Notably, this change in fluorescence intensity mainly originated from the changed distance of the fluorescent

proteins from the surface rather than from desorption or temperature induced changes in the quantum yield of the fluorophores. To clarify the differences in the fluorescence intensities of poly-(NIPAM-tBA) and poly-(NIPAM-AA) areas, the thicknesses and refractive index of the polymer layer were considered (Table 1). Considering the ellipsometric results, one can expect that the intensity of the collapsed poly-(NIPAM-AA) and collapsed poly-(NIPAM-tBA) areas must be relatively low because the  $h \times n$  values correspond to a position close to the first minimum on the FLIC curve (Table 1, Figure 11c). The  $h \times n$  values of the swollen poly-(NIPAM-tBA) and swollen poly-(NIPAM-AA) areas correspond to the positions right before and after the first maximum, respectively, and the apparent fluorescence is predicted to be strong. Thus, the observed degree of fluorescence in poly-(NIPAM-tBA) area is consistent with the expectation (Figure 11c,d). The difference between the expected and observed behavior in the collapsed and swollen states of the poly-(NIPAM-AA) area was likely caused by a larger thickness of the poly-(NIPAM-AA) layer than detected by ellipsometry.

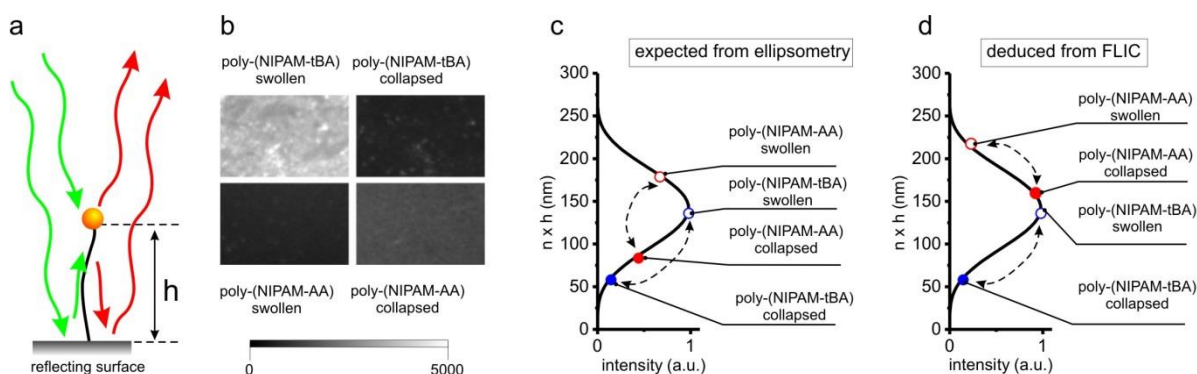


**Figure 11.** Fluorescent Interference Contrast (FLIC) microscopy of poly-(NIPAM-tBA) and poly-(NIPAM-AA) surfaces; (a) Interference of exciting (green) and emitted (red) light near a reflecting surface; (b) Observed fluorescence of rhodamine-labelled tubulin adsorbed onto poly-(NIPAM-tBA) and poly-(NIPAM-tBA) layers in swollen ( $T < 20^\circ\text{C}$ ) and collapsed ( $T = 55^\circ\text{C}$ ) states; (c) and (d)  $h \times n$  values for poly-(NIPAM-tBA) (blue symbols) and poly-(NIPAM-AA) (red symbols) layers in swollen (open symbols) and collapsed (solid symbols) states as measured by ellipsometry (measured height values are projected onto the theoretical FLIC curve, c) and deduced from FLIC (measured intensity values are projected onto the theoretical FLIC curve, d)<sup>23</sup>.

To directly investigate the switching of the polymer layers by FLIC microscopy, a gradient poly-(NIPAM-tBA-AA) layer with gradually changing ratio between tBA and AA was formed. FLIC images of adsorbed fluorescent tubulin (same preparation as described above) revealed a strong fluorescent signal on the poly-(NIPAM-tBA) area and a weak signal at the poly-(NIPAM-AA) area at low temperature ( $T < 20^\circ\text{C}$ ) (Figure 12a). At high temperature ( $T > 50^\circ\text{C}$ ) the poly-(NIPAM-AA) appeared brighter than the poly-(NIPAM-tBA) area. This behavior was expected from the results shown in Figure 11. However, most interestingly, a bright, spatially confined band in the poly-(NIPAM-tBA-AA) gradient area was detected at temperatures between  $21^\circ\text{C}$  and  $50^\circ\text{C}$ .

Considering equation 1, this bright band represents the maximum of the FLIC curve at  $n \times h \approx 140$  nm (see also Figure 11c, d). The lateral coordinate of this band shifted towards the poly-(NIPAM-AA) areas when the temperature increased (Figure 12b). This directly indicates that the height and/or refractive index profile of the polymer layer changes with temperature. Since the difference in the refractive indices in the swollen versus the collapsed polymers is rather small - namely  $100\% \times n_{\text{collapsed}} - n_{\text{swollen}} / n_{\text{collapsed}} \approx 10\%$  (Table 1) - the change in the intensity profile along the sample was mainly caused by changes in the height of the polymer layer. A qualitative reconstruction of the height profile of the polymer layer at different temperatures is shown in Figure 12 c. Here, one can see an obvious gradual shift of the border between the swollen and the collapsed areas. This border was not completely step-like due to the unsharp transition between the collapsed and the swollen polymer chain

conformations. In this particular experiment, the border between the collapsed and the swollen areas was reversibly shifted by about 50  $\mu\text{m}$ , but shifts up to 120  $\mu\text{m}$  were obtained in additional experiments. Importantly, the changes in the size of the collapsed and the swollen areas were fully reversible.

In order to fabricate circular patterns whose diameter can be controlled by temperature, a thermoresponsive polymer layer based on random copolymerization of NIPAM with hydrophobic photoliable 2-nitrobenzyl acrylate (NBA) was synthesized. The cloud point of the poly-(NIPAM-NBA) copolymer was about 7  $^{\circ}\text{C}$  in BRB80 (80 mM Brinkley Reassembly Buffer). Then a part of the poly-(NIPAM-NBA) layer was illuminated with narrow UV beam ( $\lambda = 360\text{ nm}$ ). This resulted in the localized cleavage (deprotection) of the hydrophobic 2-nitrobenzyl groups and the formation of hydrophilic carboxylic groups (Figure 13) in a circular area. The cloud point of the fully deprotected polymer was more than 90  $^{\circ}\text{C}$ . Because, in this case, the degree of deprotection gradually decreased from the center of the illuminated area towards the edges, a two-dimensional poly-(NIPAM-NBA-AA) gradient was obtained.

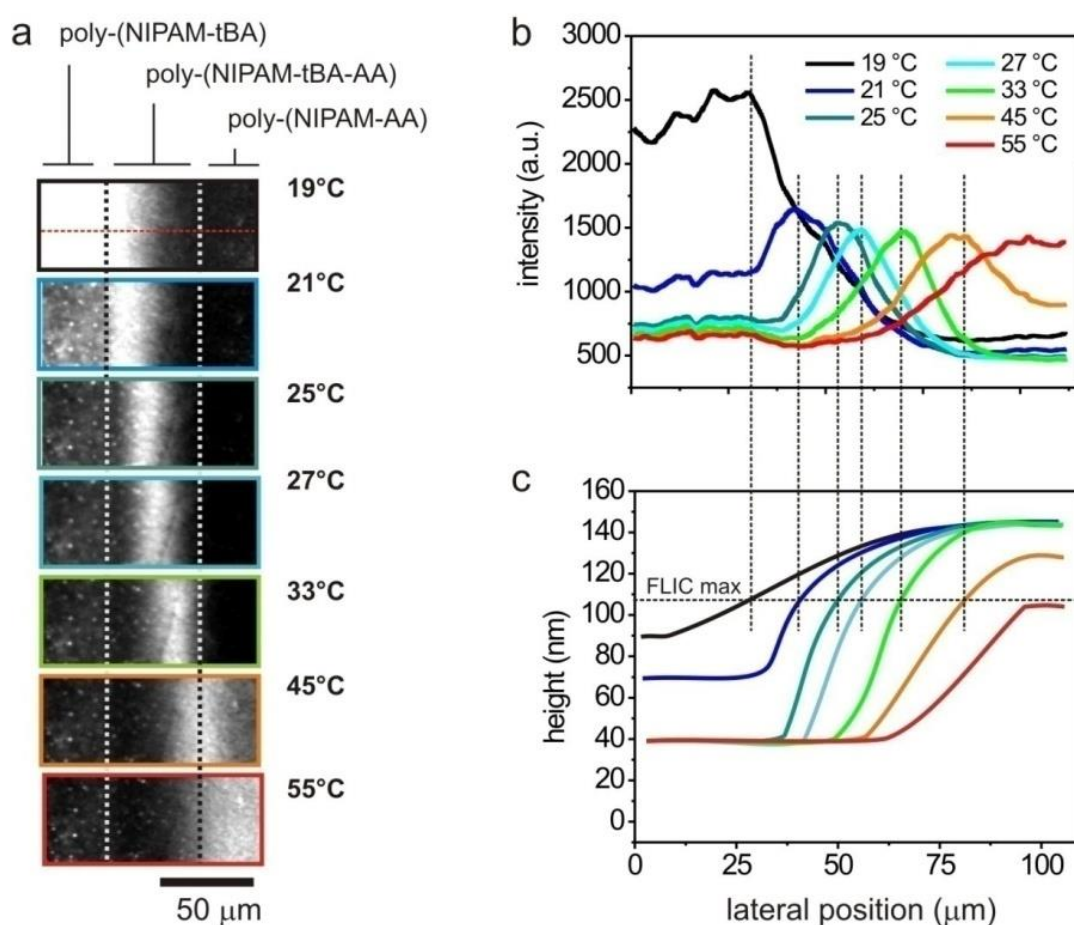


**Figure 12.** Switching of the height profile of the poly-(NIPAM-tBA-AA) gradient layer. (a) FLIC images of the poly-(NIPAM-tBA-AA) layer with adsorbed rhodamine-labeled tubulin at different temperatures. Intensity profile (b) and qualitatively reconstructed height profile (c) along red dotted line in (a) of the polymer layer at different temperatures. The initial thickness of the poly-(NIPAM-tBA) layer in the dry state was  $h_{\text{DRY}} = 33\text{ nm}$ .<sup>23</sup>



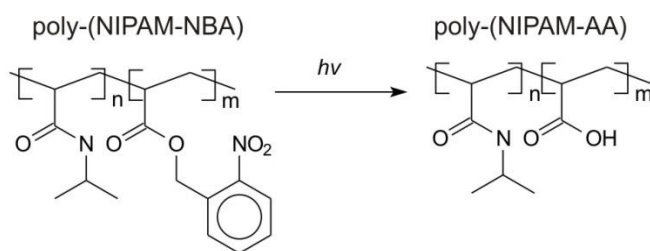


**Figure 13.** Conversion of poly-(NIPAM-NBA) copolymer into poly-(NIPAM-AA) upon UV illumination.<sup>23</sup>

Using FLIC microscopy (with fluorescent tubulin, as described above) a decrease in the fluorescence intensity in the center of the deprotected area as well as a decrease in the size of the bright area was observed upon raising the temperature (Figure 14a, b). This behavior is attributed to the collapse of the polymer chains and thus a decrease in the detected fluorescence intensity in a spatially varying manner. Remarkably, when the temperature was lowered back to the initial value the size of the swollen area was fully recovered (Figure 14a, lower right image). This observation indicates the reversibility of the switching process. Note, that smaller patterns can be fabricated on demand by UV-illumination through a mask<sup>115</sup>.

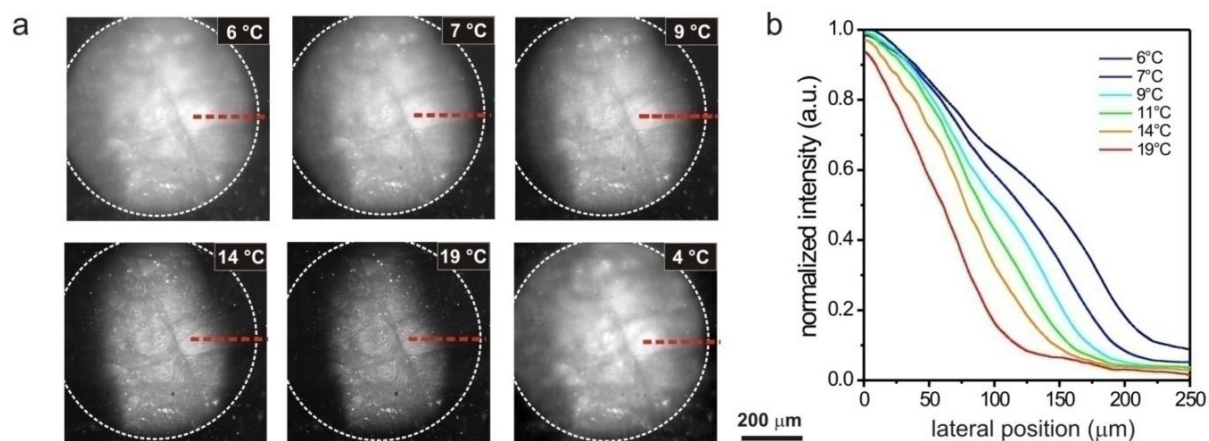


**Figure 14.** Switching the size of a circular poly-(NIPAM-NBA-AA) pattern. (a) FLIC images of rhodamine-labelled tubulin on poly-(NIPAM-NBA-AA) pattern at different temperatures. The size of the swollen (bright) area changes with temperature. (b) Normalized fluorescence intensity profiles of the polymer layer at different temperatures along the red dashed line in (a). The initial thickness of the poly-(NIPAM-NBA) layer in the dry state was  $h_{\text{DRY}} = 15.7$  nm.<sup>23</sup>

In summary, a new concept to design bioactive patterned surfaces, whose size can be controlled by altering the ambient conditions, was developed. In one set of experiment, lateral gradients composed of thermoresponsive poly-(N-isopropylacryl amide – *tert* butyl acrylate – acrylic acid) copolymers was generated. It was shown that the border between the collapsed and the swollen polymer areas could be reversibly shifted by up to 120 μm when raising or lowering the temperature between 21 °C and 50 °C. Circular gradients of poly-(N-isopropylacryl amide - 2-nitrobenzyl acrylate - acrylic acid) by UV irradiation was generated in a second set of experiments. It is possible to use photolithography to produce switchable polymer gradients with customized layouts. Notably, the temperature range over which switching occurs can be precisely tuned by selecting the appropriate copolymer composition. This novel strategy to produce surface patterns, whose size and shape can be reversibly switched *in-situ*, will be of interest for a variety of biotechnological applications, such as programmed cell adhesion, viability and differentiation.

### 3.5 “IN-SITU” PHOTOPATTERNING USING STIMULI-RESPONSIVE PHOTORESISTS

The methods discussed in the previous chapters allow design of patterns whose lateral and vertical dimensions can be switched by an external signal. While switching occurs under physiological conditions, the pattern cannot be really modified but remains within the borders, which are defined during preparation.

A step towards development of patterns, which can be reconfigured on the fly under physiological conditions, is smart water-processable photoresists which development is triggered by temperature. The design is based on random copolymers of PNIPAM with photocleavable groups. In aqueous environment, PNIPAM homopolymer reversibly changes its solubility at the cloud point  $T = 33\text{ }^{\circ}\text{C}$ . It was found that the incorporation of photosensitive nitrobenzyl acrylate reduced the cloud point by more than  $20\text{ }^{\circ}\text{C}$  (poly-(2-nitrobenzyl acrylate-co-*N*-isopropylacrylamide) copolymers (poly-(NIPAM-NBA)), Figure 15). The conversion of hydrophobic nitrobenzyl acrylate groups into carboxylic acid occurred upon irradiation with UV light (poly-(acrylic acid-co-*N*-isopropylacrylamide) (poly-(NIPAM-AA), Figure 15a). The cloud point of the polymer thereby significantly increased due to the formation of hydrophilic groups. This remarkable change in the thermoresponsive behavior of PNIPAM-based copolymers after UV irradiation - in combination with the possibility to deposit it onto substrates from aqueous solutions - allows their use as photoresist with thermo-triggered development.

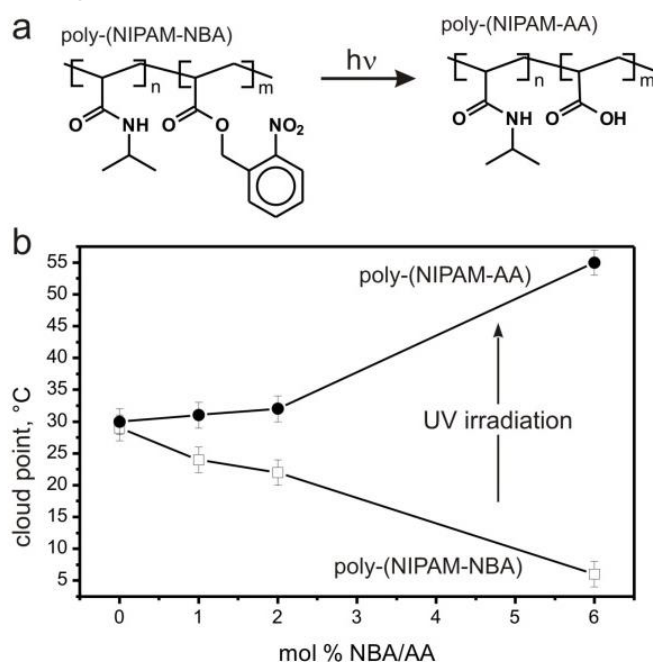


**Figure 15.** Properties of photocleavable PNIPAM-copolymers: (a) Schematic conversion of poly-(NIPAM-NBA) into poly-(NIPAM-AA) upon UV irradiation; (b) Thermoresponsive behavior (cloud point) of poly-(NIPAM-NBA) (open squares) and poly-(NIPAM-AA) (solid circles) in PBS 100 mM buffer (pH = 7) as a function of copolymer composition<sup>116</sup>.

The general concept of this novel type of photolithography using PNIPAM-based photoresists is illustrated in Figure 16. A thin film of poly-(NIPAM-NBA) (Figure 16a) is deposited on a substrate and irradiated with UV light through a mask at elevated temperature (Figure 16b). Reducing the temperature slightly below the cloud point of the poly-(NIPAM-AA) leads to pattern development in biological buffer (Figure 16c). While proteins can bind to the patterned surface everywhere (Figure 16d), proteins adsorbed to the top of the photoresist are removed by lowering the temperature below the cloud point of the poly-(NIPAM-NBA) (Figure 16e).

To experimentally demonstrate the thermo-triggered development of PNIPAM-based photoresist, films of poly(NIPAM-NBA) (cloud point =  $6\text{ }^{\circ}\text{C}$ ) with admixed small amount of fluorescent nanoparticles were spincoated on a glass substrate. Illumination with the UV light through a mask caused the photocleavage of nitrobenzyl groups and changed the optical

properties of the photoresist. As a result, the contrast between illuminated and non-illuminated areas can be detected using fluorescence microscopy (Figure 17a). The illuminated polymer was removed by rinsing in PBS buffer at 25°C leading to pattern development (Figure 17b). The photoresist pattern was completely removed by rinsing in cold PBS buffer at 4°C (below cloud point of poly-(NIPAM-NBA) which is 6 °C) (Figure 17c).

Finally, the applicability of the developed method for protein patterning was demonstrated. Poly-(NIPAM-NBA) with admixed red-fluorescent CdSeS nanoparticles was used as photoresist. After illumination through a mask and development at moderate temperature ( $T = 30^{\circ}\text{C}$ ), fluorescent casein was adsorbed to the patterned surface. The unbound casein was then washed out by rinsing in warm PBS buffer ( $T = 30^{\circ}\text{C}$ )<sup>117</sup> and the residual photoresist was removed by rinsing in cold PBS buffer ( $T = 4^{\circ}\text{C}$ ). A clear pattern of fluorescent casein (green) on the surface was observed (Figure 18a) and a minor residual red signal in the areas, which were covered by photoresist (Figure 18b).

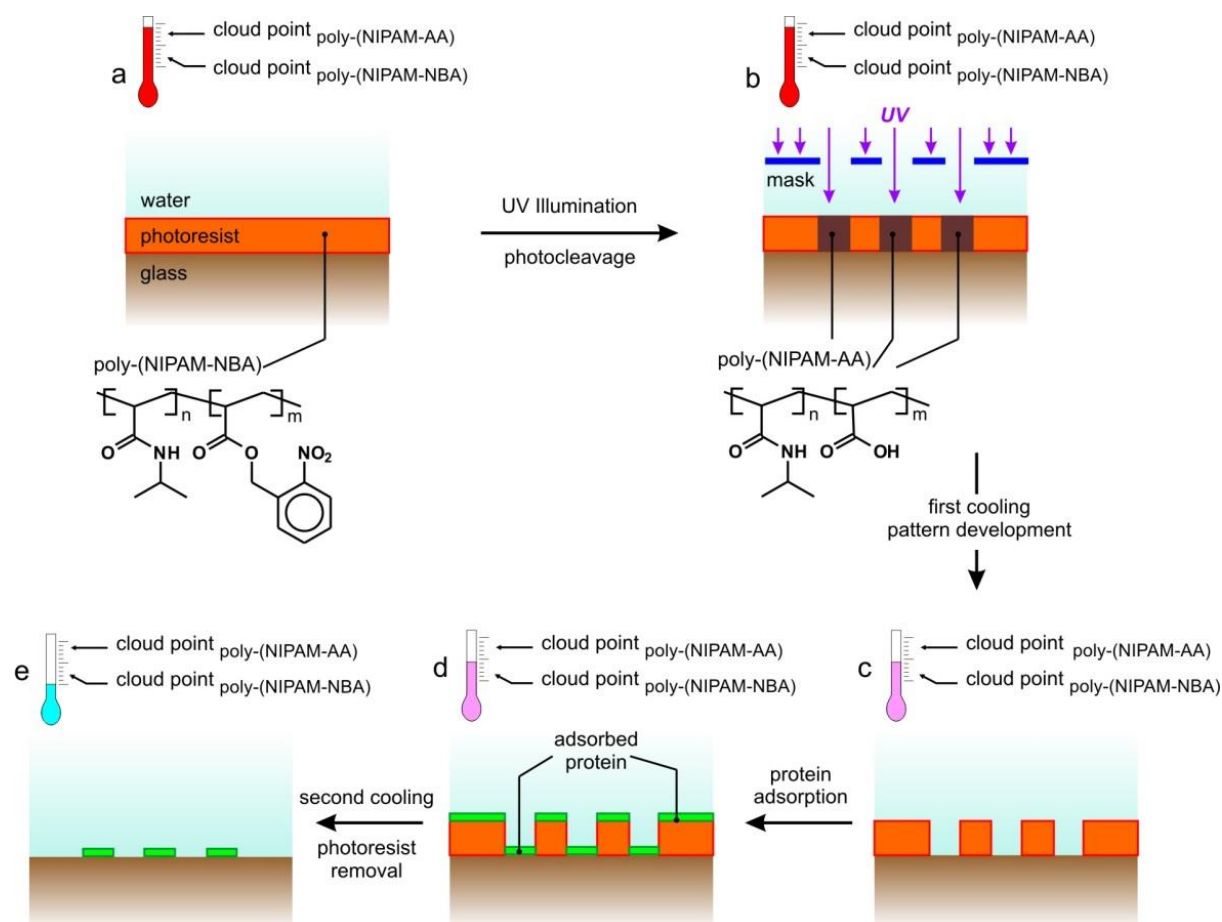


**Figure 16.** Scheme of photopatterning using PNIPAM-based photoresists with temperature-triggered development. Thermoresponsive poly-(NIPAM-NBA) is deposited as photoresist onto a substrate (a). Illumination of the photoresist (b) results in photo-cleavage of nitrobenzyl acrylate groups and formation of poly-(NIPAM-AA), increasing the cloud point. After the photoresist pattern is developed at slightly lower temperature (c), proteins are adsorbed (d). The photoresist (together with the proteins on top) can be completely removed in aqueous environment at low temperatures (e)<sup>116</sup>.



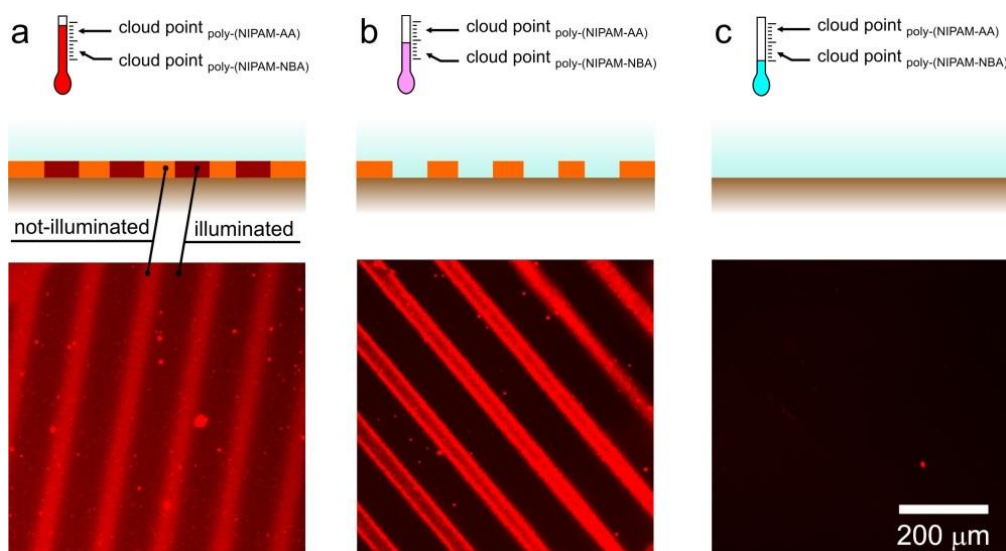


**Figure 17.** Fluorescence micrographs of poly-(NIPAM-NBA) photoresist with admixed fluorescent CdSeSnanocrystals<sup>16</sup> at different stages of processing: (a) after illumination; (b) after development at 25°C; and (c) after cooling to 4 °C<sup>116</sup>.

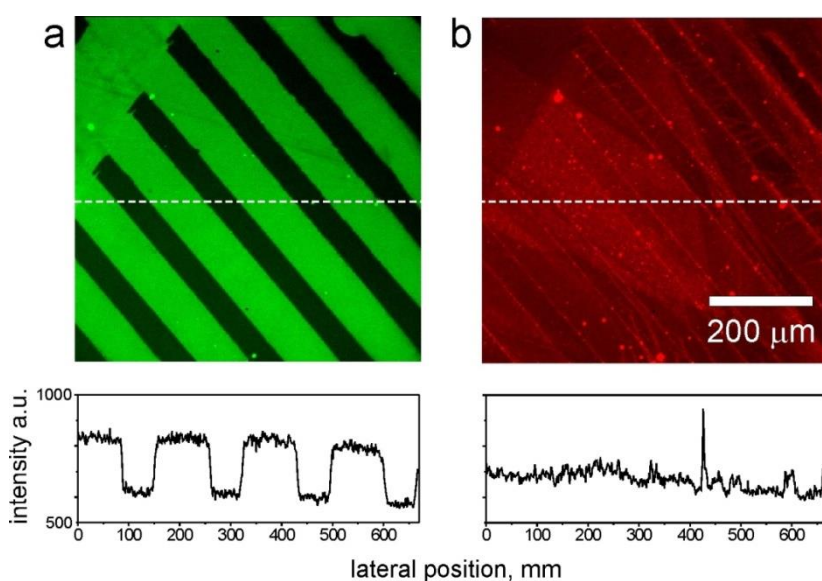


**Figure 18.** Fluorescence micrographs of a FITC-casein pattern obtained by photolithography using poly(NIPAM-NBA) photoresist with added CdSeS fluorescent nanocrystals. (a) Signal of FITC-casein (green) and (b) signal from the FITC-casein and from precipitated fluorescent nanocrystals (red)<sup>116</sup>.

In conclusion, a novel approach for the design of an environment-friendly (water-soluble/water-developing) photoresists with stimuli-triggered development based on photocleavable copolymers of PNIPAM was developed. The proposed photoresists possess a unique combination of advantages: (i) they are soluble in PBS, (ii) their photocleaved products are soluble in aqueous environment as well, and (iii) their development is triggered by temperature in physiological buffer in a controllable way and no change of pH is required. The applicability of the presented method for *in situ* patterning inside microfluidic channels and for protein patterning on surfaces was demonstrated. There is a strong potential of the developed method for patterning and harvesting proteins, particles, and cells in microfluidic devices, where all procedures have to be performed in biological buffers.

### 3.6 “IN-SITU” PATTERNING USING VISIBLE LIGHT

The approaches described in the previous chapters allow fabrication of patterns with switchable topography, size and *in situ* patterning. All these approaches utilized UV irradiation at least in one of the steps. UV irradiation is able to generate free radicals that can affect bioactivity of proteins and viability of cells. Therefore, the development of an approach for optical patterning using visible light is the next goal.

The new approach allows pattern proteins onto a surface using visible light. The method is based on localized light-to-heat conversion (LHC) combined with a thermoresponsive polymer surface capable of binding proteins and maintaining their functionality. Previously it was shown that PNIPAM can be used to control the binding of proteins onto surfaces<sup>116, 118, 119</sup>. There, the conformation of PNIPAM molecules in aqueous solution was switched in a spatially unstructured manner between the collapsed state at  $T > 33^{\circ}\text{C}$  (protein-binding conformation) and the swollen state at  $T < 30^{\circ}\text{C}$  (protein-repelling conformation). This approach was extended by using optical signals to generate heat in a highly-localized manner (Figure 19). In order to efficiently convert light to heat, glass-bound carbon layers with grafted PNIPAM chains were used. Illumination with a light beam causes local collapse of the surface-grafted PNIPAM molecules and allowed proteins in solution to bind to the surface in the illuminated areas exclusively. When the illumination was turned off, the heat quickly dissipated. The PNIPAM molecules resumed their extended conformation and either blocked the surface against further protein binding or led to release of proteins. The swollen polymer chains also protected the patterned proteins during consequent fluid exchanges.

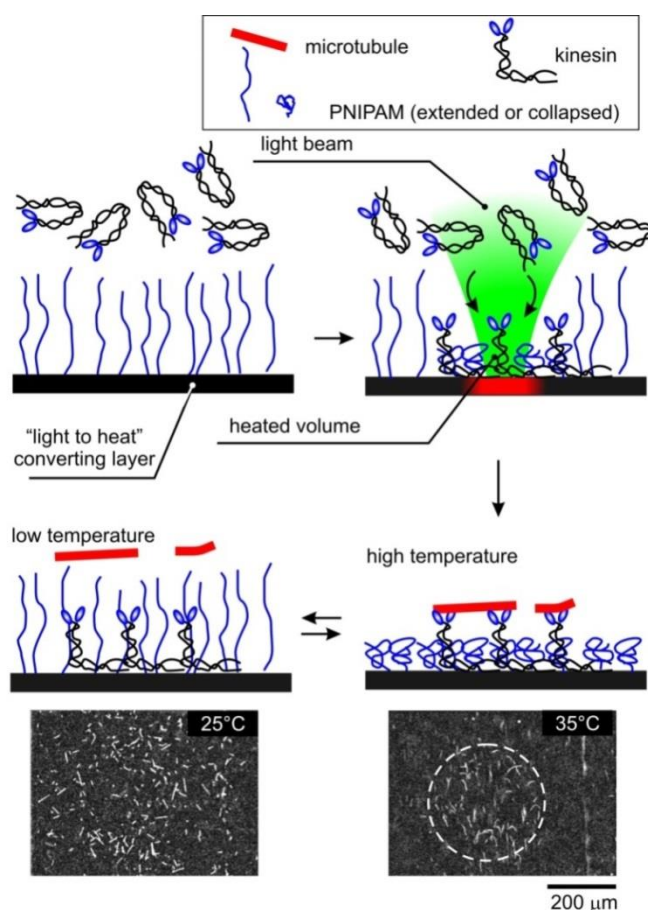


**Figure 19.** LHC photopatterning of biomolecular motors on PNIPAM surfaces. Kinesin was photopatterned onto the immobilized PNIPAM layer which was grafted onto the LHC layer. After the patterning, the kinesin retained its biological functionality and provided continuous gliding of microtubules over the patterned surface at high temperature (35°C). Cooling down

*to room temperature (25°C) led to the release of microtubules due to steric repulsion of the swollen polymer chains.*

Patterning experiments were performed by incubating kinesin-casein solutions onto PNIPAM-coated carbon-glass samples. The samples were kept at low temperature, e.g. 22°C, so that the PNIPAM was swollen and therefore protein-repelling. For illuminating the surface a collimated green laser beam was employed. The surface was illuminated for 2 min in order to allow the kinesin molecules to bind out of solution (Figure 19). After turning off the illumination, unbound protein was washed out. Successful patterning and functionality of patterned proteins were then confirmed by microtubule-based gliding motility assays. For this, the temperature of the sample was raised to 35°C to collapse the PNIPAM chains on the entire surface and allow microtubules to bind to the patterned kinesin molecules. Indeed, it was observed that microtubules adsorb on the substrate and glide continuously solely in the preliminary illuminated areas (Figure 19). Though microtubule binding and motility was mainly confined to the illuminated areas, few microtubules were also observed in non-illuminated surface parts. However, these microtubules were, in contrast to the ones moving in the patterned area, loosely bound to single motor molecules, often swiveled and mostly moved only short distances. These experiments proved that kinesin molecules could be patterned reproducibly onto PNIPAM-coated carbon-glass samples via photo-thermal patterning and they keep their biological activity and do not denature on the surface.

In conclusion, the approach for irreversible photopatterning functional proteins using thermoresponsive polymer locally heated by light-to-heat conversion was developed. The approach was experimentally demonstrated on the example of irreversible sequential patterning of kinesin motor proteins on poly-(*N* isopropylacrylamide) surface. The suggested approach has distinct advantages that make it very promising: (1) any wavelength of light (VIS and IR) can be used under physiological conditions; (2) although the pattern resolution is lower than AFM or CVD techniques, one can potentially achieve sub-micron resolution based on heat diffusion calculations; (3) because the technique is maskless, arbitrary pattern sizes and shapes can be created. It is expected that this technique can find wide application as a method of simple and quick fabrication of protein microarrays for bio- and nanotechnological applications in lab-on-chip systems.

## **4. 3D MICROSTRUCTURING USING SELF-FOLDING POLYMER FILMS**

### **4.1 STATE OF THE ART IN SELF-FOLDING FILMS**

Self-folding films are particularly attractive building elements for 3D fabrication. The self-folding films consist of two materials with different properties. At least one of these materials can change its volume in response to change of temperature, pH or light illumination. Because of non-equal expansion of materials, the film bends and can form a tube, capsule or more complex structure. Similar to origami, the self-folding films provide unique possibilities for straightforward fabrication of highly complex 3D micro-structures with patterned inner and outer walls that cannot be achieved using other currently available technologies. The self-folded objects can further be assembled in sophisticated 3D super-constructs with the structural anisotropy and highly complex surface patterns. The goals are to develop polymer-based self-folding polymer films, investigate folding and unfolding and apply them for controlled encapsulation and release.

Bending is essentially required for design of self-folding materials and allows conversion of semi one-dimensional (rods) and semi two-dimensional (sheets) objects into 2D and 3D ones, respectively. Typically bending is the result of either expansion or contraction of a material caused by change of environmental conditions. In most cases change of conditions, however, results in homogenous expansion or contraction in all directions and does not lead to increase of dimensionality. Bending is produced as a result of inhomogeneous expansion/shrinking, which occurs with different magnitudes in different

directions. Bending can be achieved either (i) by applying gradients of field to homogenous materials or (ii) by applying non-gradient stimuli to inhomogeneous materials. The example of first case is the bending of polyelectrolyte hydrogel during electrolysis<sup>120</sup>. The examples of the second group are the bending of liquid crystalline films<sup>121</sup>, hydrogel with the lateral gradient monomer concentration<sup>122</sup>, cantilever sensors<sup>123</sup> and shape-memory polymers<sup>124</sup>.

### Bending of films

In 1925 Timoshenko<sup>125</sup> published a paper, which considers bending of a metal bilayer consisting of two metals with different thermal expansion coefficients. He assumed that the bilayer can bend in only one direction and results in a bilayer with uniform curvature (Figure 20a):

$$\frac{1}{\rho} = \frac{6(\varepsilon_2 - \varepsilon_1)(1+m)^2}{h \left( 3(1+m)^2 + (1+mn) \left( m^2 + \frac{1}{mn} \right) \right)} \quad (2)$$

$$\frac{E_1}{E_2} = n \quad (3)$$

$$\frac{a_1}{a_2} = m \quad (4)$$

where  $E_1$ ,  $E_2$  are the elasticity modulus;  $\alpha_1$ ,  $\alpha_2$  are the thickness of the layers;  $h$  is the total thickness ( $h = \alpha_1 + \alpha_2$ );  $\varepsilon_1$ ,  $\varepsilon_2$  are the stress of the films,  $\rho$  is the radius of curvature. As it comes from the equations (2-4), the radius of curvature is inversely proportional to the film stress. The Timoshenko equation applies to a beam bending in only one direction, does not predict the folding direction and is applicable for reversible elastic deformations.

More recent models have considered complex bending of a bilayer in two dimensions. Mansfield found analytical solutions for large deflections of circular<sup>126</sup> and elliptical<sup>127</sup> plates having lens-shape cross sections with a temperature gradient through the thickness. For small gradients, the plates formed spherical caps, curved equally in all directions. At a critical gradient, a configuration with greater curvature in one direction became more favorable. Because of the lens-shaped thickness profile, even though the elliptical plate had a major axis, it showed no preferred direction for bending even for large deflections. Freund determined the strain at which a spherical cap, formed by circular bilayer of uniform thickness, becomes unstable using low order polynomial solutions and finite element simulations.<sup>128</sup> Later Smela *et al.* showed that short-side bending of inorganic bilayer was preferred in the case of free homogeneous actuation (volume change) and that this preference increased with aspect ratio (ratio of length to width of a rectangular pattern)<sup>129</sup>. Li<sup>130</sup> et al and Schimd<sup>131</sup> experimentally demonstrated the opposite scenario, namely a preference for long-side bending, in the case where bilayers are progressively etched from a substrate.

Hydrogel-based bilayers, consisting of two kinds of hydrogel rods, behave similar to inorganic materials and are able to bend in different directions depending on the swelling properties of polymers<sup>132-135</sup>. First report of bending of a hydrogel bilayer rods, consisting of thermoresponsive part and non-thermoresponsive one, was published by Hu et al in 1985<sup>136</sup>. It was demonstrated that rods bend due to shrinking of thermoresponsive hydrogel when the temperature changes. Similar to rods, bilayer hydrogel-based films are also able to bend<sup>137</sup>. It was found that when the radius of curvature is small, bending of the films leads to their folding and formation of 3D structures, such as tubes<sup>138</sup>.

Thermoresponsive hydrogels with radial gradients of swelling properties are able to deform and form complex figures with Gaussian curvature <sup>122</sup>. Similar to this work, Hayward and Santangelo investigated folding of patterned rectangular strips divided into one high- and one low-swelling region, which can be characterized as thick but narrow bilayer <sup>139</sup>. When swollen in an aqueous medium, it does not bend to the side of the less swelling component that is the case of “classical” bilayer discussed by Timoshenko (Figure 20a), but rolls into a three-dimensional shape consisting of two nearly cylindrical regions connected by a transitional neck (Figure 20b).

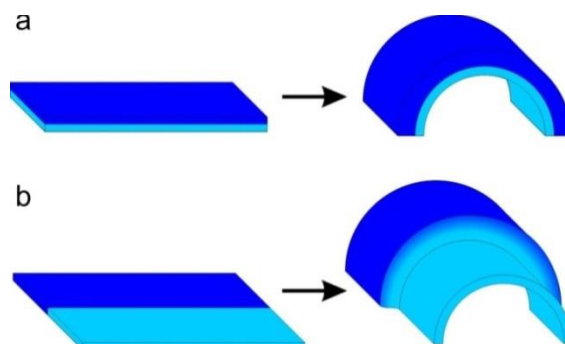


**Figure 20.** Bending of a “classical” bilayer (a) and rectangular strips divided into one high- and one low-swelling regions.

### Complex shapes by bending

There are many parameters that determine the folded shape. For example, the shape of a formed 3D object depends on the 2D shape of the polymer films. The simplest bending is observed when the thickness of each layer is constant over the sample. For example, tubes are formed from rectangle bilayers <sup>137, 138, 140-144</sup>. Envelope-like capsules with rounded corners or nearly spherical ones are formed from the homogeneous star-like polymer bilayers with four and six arms, respectively <sup>143-145</sup>. By making a sloped bilayer structure, the planar structure can be twisted when one of the layers is asymmetrically expanded in a specifically selected solvent. When the bilayer actuating device with triangular layers with respect to the y-axis is swollen, a helical-type actuating sensor can be formed. A double twisted helical structure can also be formed. <sup>146</sup> In these examples, rounded figures are formed (Figure 21, left). Objects with sharp edges are formed by patterned bilayer where the active component is deposited locally. The active component can either swell/shrink or change its shape due to melting. In this way cubes and pyramids are formed by patterned bilayer with active junction elements (Figure 21, right) <sup>146-148</sup>.

Importantly, in many cases folding runs in one step. Step-by-step folding of different elements of self-folding films can be achieved by local activation of selected areas of self-folding films by light <sup>149</sup>. Another possibility is to use two or more kinds of active material which are sensitive to different signals. Gracias *et al.* demonstrated two-step deformation of patterned films where the active elements are two kinds of biodegradable polymers <sup>150</sup>. Each of these polymers is degraded by specific enzyme. As a result, the film folds when the first enzyme is added and unfolds when the second one is added. <sup>150</sup>



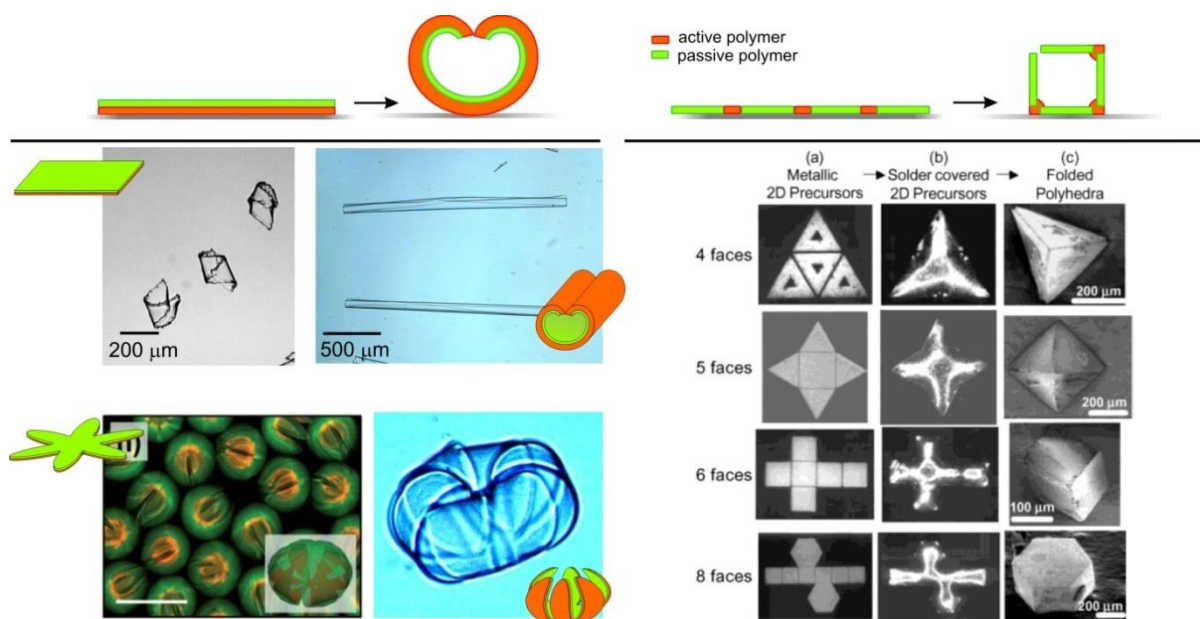


**Figure 21.** Two main approaches for the fabrication of self-folding structures: (left) bilayers (Reprinted with permission of refs<sup>180, 156</sup> Copyright (2011) by Wiley-VCH Verlag GmbH & Co. KGaA and American Chemical Society) and (right) patterned films (Reprinted with permission of ref<sup>152</sup>, Copyright (2002) by Wiley-VCH Verlag GmbH & Co. KGaA).

### Properties & applications of folding films

There are several reports describing fabrication of self-folding films with different responsive properties. For example, there are pH-responsive systems based on polyelectrolytes<sup>138, 142, 144, 148, 153-158</sup>, thermoresponsive systems based on gradient of thermal expansion<sup>140, 141</sup>, fusible polymers<sup>159, 160-162</sup>, solvent-responsive systems<sup>144, 146, 155, 163</sup>, electric field responsive systems<sup>164, 165, 166</sup>, enzyme-responsive systems<sup>150</sup>, light responsive systems based on light-to-heat conversion<sup>167, 168</sup>.

One field of application of self-folding polymer thin films is the controlled encapsulation and release of drugs, particles and cells. Kalaitzidou *et al.* demonstrated reversible adsorption-desorption of fluorescently labeled polyethylene glycol, which is considered as a model drug, inside PDMS-gold tubes at 60-70°C<sup>140</sup>. Gracias *et al.* demonstrated irreversible encapsulation of yeast cells inside self-folding SU8 photoresist - polycaprolactone films upon heating above at 60°C<sup>159</sup> (Figure 22a). Self-folded objects with nanoporous walls and encapsulated cells were suggested as prototype of artificial pancreas. The small molecules such as glucose and dissolved oxygen are able to pass through the pores, while larger ones such as antibodies are unable to do it. This size-selective permeability of self-folded capsules allows avoiding immune response that is highly demanded during transplantation of pancreas cells (Figure 22b)<sup>169</sup>. Gracias *et al.* used rigid metal-made self-folding microgrippers for capturing pieces of tissues and their controlled transport (Figure 22c). Such systems are particularly attractive for non-invasive biopsy<sup>162</sup>. Self-folded objects were used as scaffolds for fabrication of 3D cellular constructs (Figure 22d)<sup>170, 171</sup>.

Controlled release of small molecules through the pores of self-folded microconstructs was used to spontaneously organize cells in 3D environment<sup>172</sup>. Self-folding films can also be used as smart plasters (Figure 22e). Lee *et al.* demonstrated this concept on the example of millimeter size poly(methyl methacrylate) - poly(2-hydroxyethyl methacrylate) (PHEMA) bilayer with attached mucoadhesive drug layer. The non-swelling PHEMA layer serves as a diffusion barrier, minimizing any drug leakage in the intestine. The resulting unidirectional release provides improved drug transport through the mucosal epithelium. The functionality of this device is successfully demonstrated *in vitro* using a porcine small

intestine<sup>142</sup>. There are several non-biorelated examples of application of self-folding polymer films. Deposition of patterned metal on the polymer bilayer allowed fabrication of self-rolled tubes with patterned conductive inner wall<sup>138</sup>. In another example, pyrolysis of polystyrene-poly(4 vinyl pyridine)-polydimethylsiloxane trilayer<sup>153</sup> was used for fabrication of silica tubes. Gracias *et al.* used self-folding polymers films to fabricate self-assembled curved microfluidic networks (Figure 22f)<sup>173</sup>.

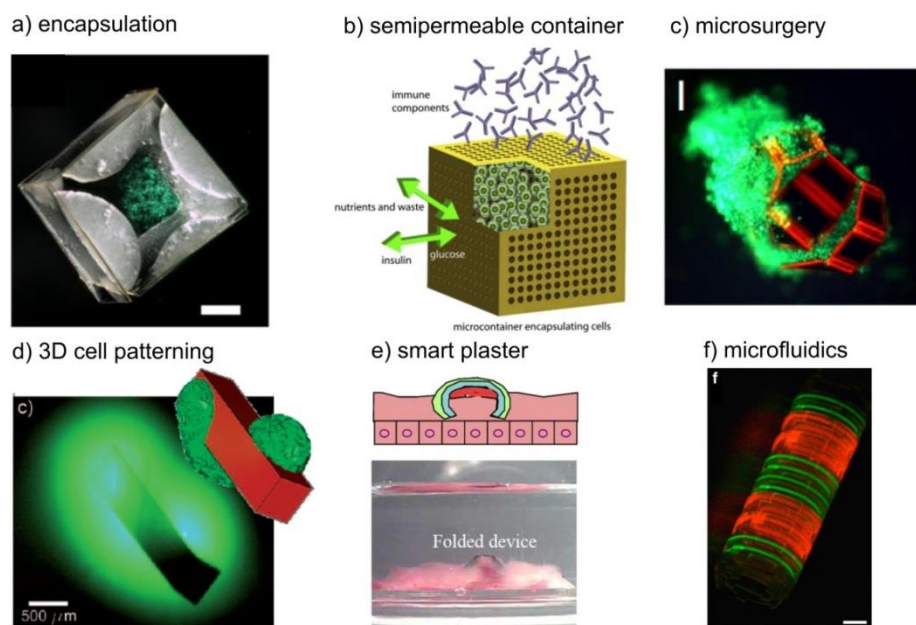


**Figure 22.** Examples of applications of self-folding films: (a) - stained fibroblast cells encapsulated within a non-porous polymeric container (right, Reprinted with kind permission from Springer Science+Business Media permission, Copyright 2010<sup>174</sup>); (b) - scheme of artificial pancreas based on nanoporous self-folded devices: glucose and oxygen can penetrate through the pores of the folded device with encapsulated pancreas cell while immune components are unable to penetrate (Reprinted with permission of ref<sup>169</sup>, Copyright (2011) by Elsevier); (c) - self-folding microgripper with tissue (Reprinted with permission of ref<sup>162</sup>, copyright 2009 PNAS); (d) - 3D cellular pattern produced by controlled diffusion of chemical through pores of self-folded object (Reprinted with permission of ref<sup>172</sup>, Copyright (2002) by Wiley-VCH Verlag GmbH & Co. KGaA); (e) - smart plasters which direct diffusion of drugs and prevent their leakage (Reprinted with permission of ref<sup>142</sup>, Copyright (2006) by Elsevier); (f) - 3D microfluidic device obtained by folding (Reprinted with permission of ref<sup>173</sup>, Copyright (2011) by Nature Publishing Group).

## 4.2 POLYMER-BASED SELF-FOLDING FILMS WITH SPECIAL PROPERTIES

The non-biodegradability and non-biocompatibility of developed self-folding films as well as the difficulty to locally control such low pH values and the high temperature hamper the use of these systems for biotechnological applications. Therefore, the goals were to design (i) self-folding films which can undergo folding within physiological ranges of different stimuli and (ii) self-folding films from fully biodegradable and biocompatible materials.

### Thermoresponsive self-folding films

The thermoresponsive self-folding films were designed by using polymer bilayers where active component is PNIPAM (Figure 23a). Second polymer, which is non-active one, was either biodegradable polycaprolactone (PCL) or non-biodegradable PMMA. In aqueous media, PNIPAM homopolymer reversibly changes its solubility at the cloud point  $T = 33\text{ }^{\circ}\text{C}$ . Photocrosslinkable polymers were prepared by copolymerizing of respective monomer with 4-acryloylbenzophenone (BA). The polymers containing acryloyl benzophenone can be

crosslinked by UV light (260 nm). Photocrosslinked PNIPAM thus undergoes reversible swelling and shrinking which is induced by change of temperature.

The bilayers were prepared by sequential dipcoating of PNIPAM and PMMA containing photoactive groups. The bilayer was irradiated through photomask with UV light (250 nm). Non crosslinked polymers were removed by washing in chloroform leading to formation of patterned bilayers. The two-layer film made of these polymers is able to self-roll and unroll due to swelling and collapse of PNIPAM at low and elevated temperatures, respectively.

It was found that bilayer films remain undeformed at  $T > 28\text{ }^{\circ}\text{C}$  and start to roll and form tubes when the temperature decreases below the cloud point of thermoresponsive polymer. The following heating affects the morphology of the formed microtube. In particular, the microtubes produced by single revolution are able to unroll almost completely at elevated temperatures when the thermoresponsive hydrogel is shrunk. Contrary, tubes formed by multiple revolutions shrink at elevated temperature and are unable to unroll.

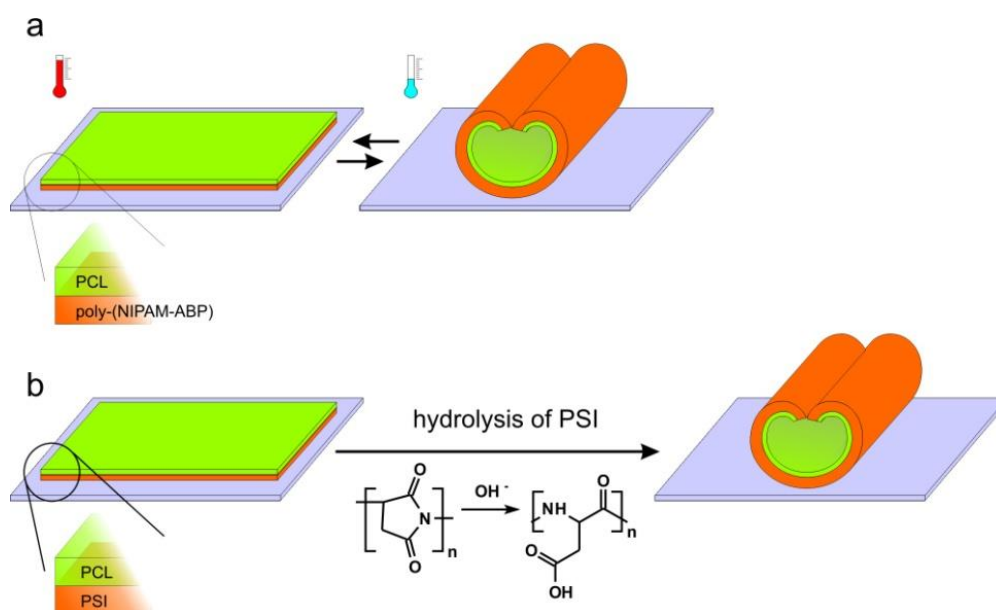


**Figure 23.** Scheme of folding of thermoresponsive PNIPAM-based and fully biodegradable PCL-PSI polymer bilayers<sup>137, 175</sup>.

### Fully biodegradable self-folding films

The fully biodegradable self-folding films were designed by using crosslinked polysuccinimide (PSI)/polycaprolactone (PCL) bilayer, which contain benzophenone as photocrosslinker (Figure 23b). These polymers are biocompatible, biodegradable<sup>176, 177</sup>, produced industrially and were already approved for biomedical purposes. Both polycaprolactone and polysuccinimide are hydrophobic and intrinsically water insoluble. Polysuccinimide, however, is able to hydrolyze in physiological buffer environment yielding water-swellaible polyaspartic acid, which is also biodegradable (Figure 23b)<sup>178</sup>.

First, the swelling of photocrosslinked PSI thin film in physiological buffer (PBS 0.15 M, pH = 7.4) at  $T = 25^{\circ}\text{C}$  was investigated. The swelling of the PSI film had a step-like character (Figure 24a). The thickness of PSI increased slightly during the first period (0 – 9 h) and strong swelling started after 8 - 9 hours of incubation in buffer. The swelling was nearly completed after 24 h. The observed step-like characters of the swelling is most probably due to diffusion-limited penetration of water in hydrophobic PSI layer hydrolyzing it. In the beginning, water starts to diffuse slowly in the hydrophobic PSI layer hydrolyzing it. As soon as a threshold amount of succinimide groups is hydrolyzed, the PSI layer starts to swell to a higher degree due to repulsion between the formed negatively charged carboxylic groups. As a result, the



diffusion of water in the polymer layer increases that leads to a faster hydrolysis of the remaining succinimide groups.

The folding PSI/PCL bilayers follows step-like swelling scenario of PSI layer. The bilayers remain unchanged during the first 9 hours at  $T = 25^{\circ}\text{C}$  (Figure 24b). The rolling started after 9 h of incubation and incompletely-rolled tubes ( $d = 55\ \mu\text{m}$ , Figure 24c) were formed. Further incubation led to a shrinkage of the tubes and a decrease of their diameter ( $d = 25\ \mu\text{m}$ , Figure 24d). The formed tubes can be easily detached from the silicon substrate due to the swelling of the polyaspartic acid (hydrolyzed PSI).

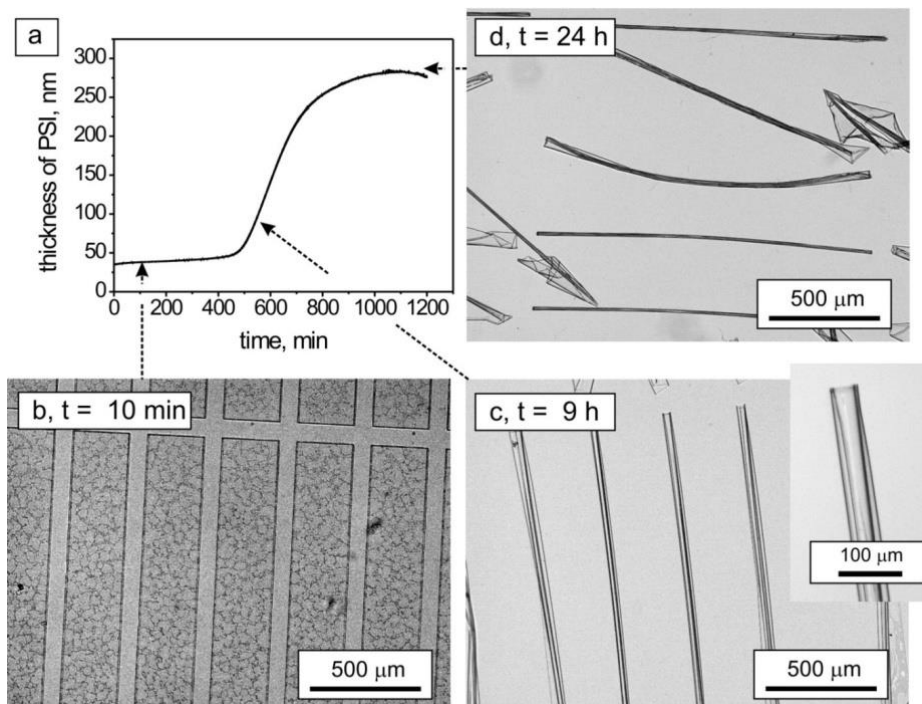


**Figure 24.** Swelling of photo-crosslinked polysuccinimide films: (a) and morphologies of self-rolling tubes ( $H_{\text{PSI}} = 200\ \text{nm}$ ;  $H_{\text{PCL}} = 86\ \text{nm}$ ) on different stages of rolling; (b) – after 10 min of incubation; (c) after 9 h of incubation,  $d = 55\ \mu\text{m}$ ; (d) after 24 h of incubation, diameter of tubes ( $d$ ) =  $25\ \mu\text{m}$ <sup>175</sup>.

In conclusion, approaches for design of thermoresponsive self-folding films which can be reversibly folded at the physiological temperature and fully biodegradable self-folding films, which spontaneously fold due to hydrolysis of the components, were developed.

### 4.3 PROPERTIES OF SELF-FOLDING FILMS

Any practical application of self-folding films requires understanding of mechanisms of folding and of the ways how to control the folding. Previously, self-rolling systems, where the active component undergoes relatively small volume changes or actuation strains were investigated, which are nearly homogenous over the whole sample.

Hydrogels, however, demonstrate considerably different properties. First, hydrogels undergo large volume changes (more than 10 times) upon swelling and contraction. Second, the swelling of a hydrogel is often kinetically limited: due to slow diffusion of water through hydrogel, the parts which are closer to the edges swell first while the parts which are closer to the center of the films swell later. Thus, the actuation profile inside the active layer is heterogeneous. The goal is, therefore, to investigate the effects of shape, size and rolling

curvature on the direction of folding of rectangular polymer bilayers placed on a substrate, where the bottom component is a stimuli-responsive hydrogel.

### **Folding of rectangular polymer bilayers**

First, folding of rectangular films was investigated. Such films, as it was demonstrated earlier, form typically tubes<sup>179</sup>. The goal was to find conditions which allow the most efficient fabrication of the tubes. It was found that the direction of rolling strongly depends on the size and shape of the films as well as on the relative thickness of the active and passive layer (Figure 25, Figure 26). Four general types of rolling were distinguished: long-side rolling, diagonal rolling, short-side rolling as well as mixed all-side rolling, which is a combination of the three first types. For example, all-side rolling is observed when both length ( $L$ ) and width ( $W$ ) considerably exceed the circumference. Diagonal rolling is observed when  $L = W$  and both are comparable to the circumference. In this case, short diagonally-rolled tubes are formed. Mixtures of diagonal rolling and the formation of “tick or check mark-like” structures is observed when  $L > W$  and both  $L$  and  $W$  are comparable to the circumference ( $C$ ). The long-side rolling takes place when the length considerably exceeds the deformed circumference ( $L/C > 4$ ) and aspect ratio is larger than 4. Short-side rolling was observed very rarely in a combination with diagonal rolling when  $L/C$  and  $W/C$  were small.

In order to clarify the variety of observed rolling scenarios, the time evolution of swelling and rolling of the bilayers was experimentally investigated. Diagonal rolling started from corners in a dog-ear manner and stopped, when two rolling fronts met each other (Figure 27a). Long-side rolling started later (Figure 27b) but eventually dominated leading to a switching of the diagonally-rolled corners to long-side rolled (Figure 27c,d). The formed double tubes were unrolled at elevated temperature. The subsequent rolling proceeded similar to the first one: rolling started from the corners and then switched to long-side rolling. This shows that the adhesion forces between the bilayer and the substrate are restored during unrolling. In order to explain the fact that rolling starts from the corners, swelling process was experimentally investigated (Figure 27e). It is observed that color of the films start to change at the corners first, which confirms the assumption that the inhomogeneous activation profile in the active layer due to slow water diffusion into the hydrogels. This can be at the origin of the experimentally observed fact that rolling starts at the corners.

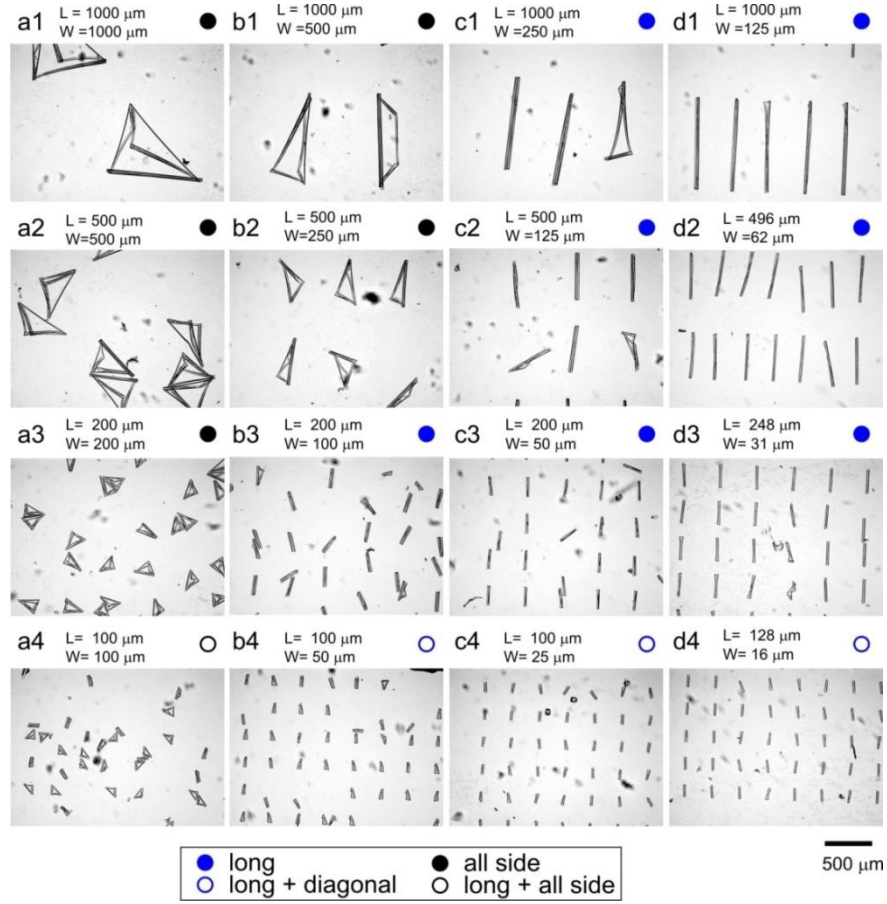


**Figure 25.** Microscopy snapshots of folded poly(*N* isopropylacrylamide – co- acrylic acid-co- benzophenone acrylate) (*P*(NIPAM-AA-BA)) – poly(methyl methacrylate – co – benzophenone acrylate) (*P*(MMA-BA)) bilayers of different length (*L*) and width (*W*) which form narrow tubes of diameter  $d = 20 \mu\text{m}$ ,  $H_{P(\text{MMA-BA})} = 500 \text{ nm}$ ;  $H_{P(\text{NIPAM-AA-BA})} = 1200 \text{ nm}$ <sup>180</sup>.

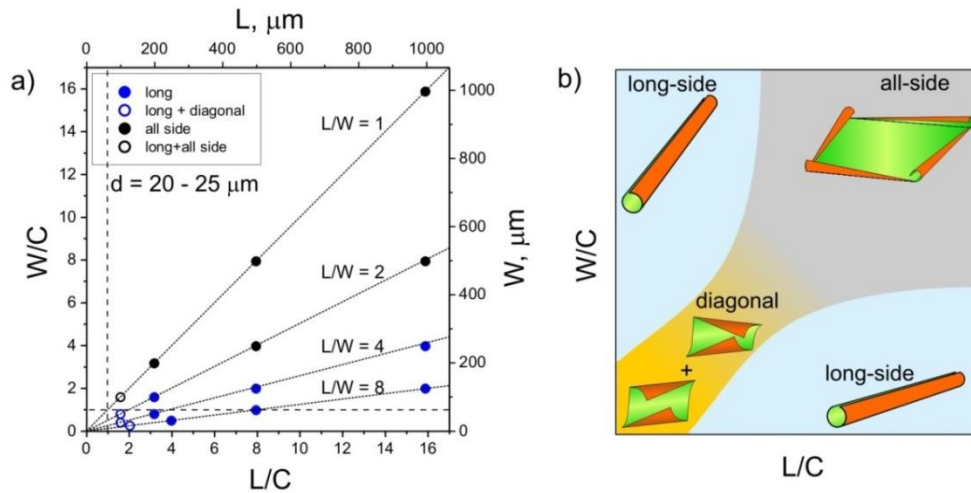


**Figure 26.** Dependence of preferential rolling direction of *P*(NIPAM-AA-BA) - *P*(MMA-BA) bilayers on the size and shape of the films (a) ( $d = 20 \mu\text{m}$ ,  $H_{P(\text{MMA-BA})} = 500 \text{ nm}$ ;  $H_{P(\text{NIPAM-AA-BA})} = 1200 \text{ nm}$ ). Dashed lines correspond to  $L/C = 1$  and  $W/C = 1$ ; Schematic diagram of rolling scenario as a function of normalized length and width (b)<sup>180</sup>.

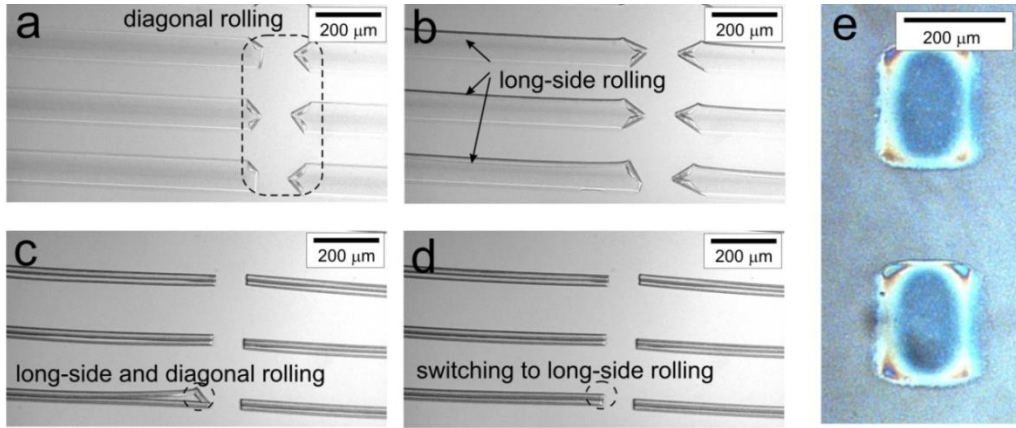


**Figure 27.** Time-resolved rolling of  $P(\text{NIPAM-BA})$  -  $\text{PCL}$  bilayer ( $H_{\text{PCL}} = 300 \text{ nm}$ ,  $H_{P(\text{NIPAM-BA})} = 750 \text{ nm}$ ,  $930\mu\text{m} \times 90\mu\text{m}$ ), diameter of the tube  $d = 41 \mu\text{m}$ ; (a-d) experimentally obtained microscopy snap-shot of swollen  $P(\text{NIPAM-BA})$  -  $\text{PMMA}$  bilayer ( $H_{P(\text{MMA-BA})} = 400 \text{ nm}$ ;  $H_{P(\text{NIPAM-AA-BA})} = 35 \text{ nm}$ ); (e) after few seconds of swelling<sup>180</sup>.

The following scenario of rolling of hydrogel-based polymer bilayer laying on a substrate is assigned by considering experimental results. The rolling starts from the edges due to faster diffusion of water from the lateral surfaces, which then are able to detach from the substrate and to bend. Rolling can start either from two adjacent or opposite edges or from all corners simultaneously, which is less probable if the bilayer is small due to the presence of imperfections and becomes energetically unfavorable once a sufficient actuation strain is reached. Rolling is almost immediately finished if the films are small and if the deformed circumference is comparable to the size of the bilayer (Figure 28a). As a result, diagonally-rolled tubes are formed if rolling starts from two opposite corners or “tick or check mark-like” structures are formed if rolling starts from two adjacent corners.

A more complicated scenario is observed when the width of the films is small and the length is considerably larger than the deformed circumference. Rolling starts at the corners first like before, but long-side rolling starts later (Figure 28b) and is energetically favored. Rolling along the short side is unfavorable because it implies more stored stretching energy along the long side. Further long-side rolling makes diagonally rolled corners unfavorable and leads to the switching of bent corners to a “long-side rolling” scenario. Depending on the width of the film compared to the deformed circumference, either an incompletely rolled tube is formed, or the two long-side rolling fronts collide into a completely rolled or doubled tube.

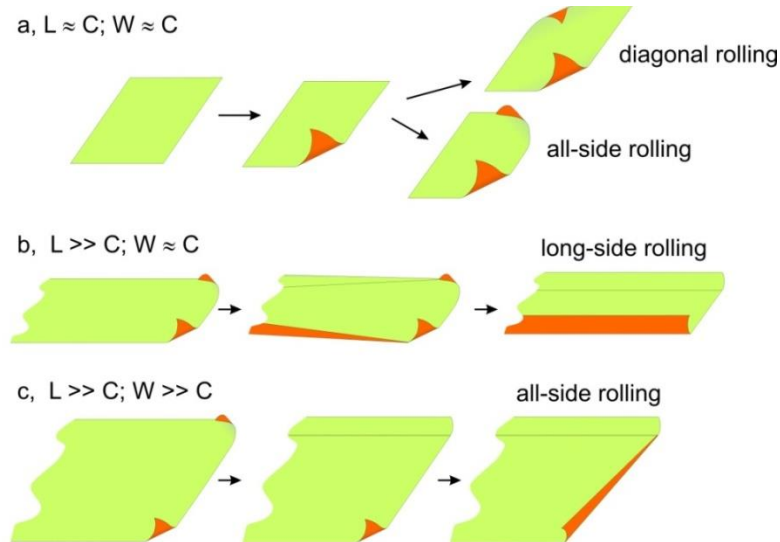


**Figure 28.** Schematics of rolling leading to diagonal rolling, long-side rolling and all-side rolling<sup>180</sup>.

If the deformed circumference is considerably smaller than the width and length of the films (which implies a high activation strain), then rolling starts first from corners and then continues along all sides (Figure 28c). The rolling fronts do not collide until several revolutions are made, which were shown to be almost irreversible. As a result, already rolled fronts are unable to unroll and irreversible all-side rolling is observed.

### Folding of complex shapes

In the next step, folding of complex shapes such as four and six-ray stars was investigated. It was assumed that stars must be able to fold and form capsule-like structures (Figure 29). In the experiments three types of folding behavior were observed depending on the ratio between radius of curvature of the folding film and size of the film. Multiple folds along the perimeter of star are formed, when the radius of curvature of bending films is small (Figure 30a). Increase of the curvature radius leads to the decrease of number of the folds ( $n$ ) until two half-rolled tubes along shoulders of each arm are formed (Figure 30b). Further increase of the curvature radius results in bending of arms in the direction to the center of star (Figure 30c). The tubes are formed when the arms are considerably smaller than the curvature radius (Figure 30d).

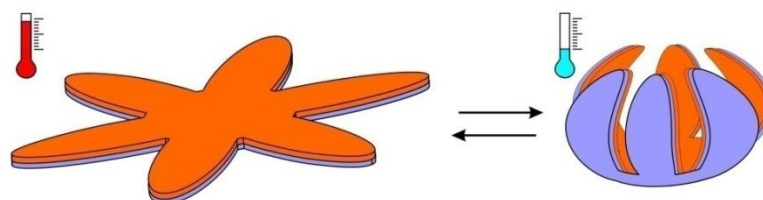


**Figure 29.** Scheme of folding of star-shaped polymer bilayer. Swelling of thermoresponsive hydrogel layer at lower temperature increases stress in the film that results in bending of the star arms and folding<sup>145</sup>.

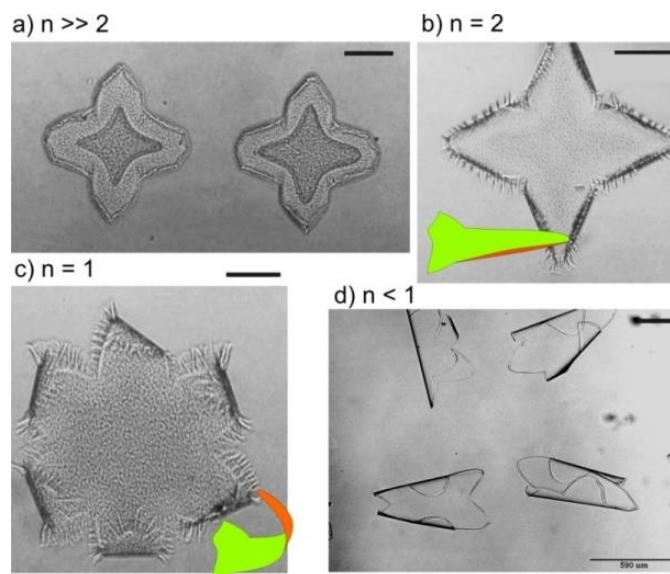


**Figure 30.** Folding of star-like films with different radius of curvature:  $n$  is the number of folds per star arm. Insets are illustrations of the shape of the bent rays.

### Multistep folding of complex shapes

Important, in all reported cases the folding runs in one step: the active polymer changes its volume that results in simple bending. Complex folding is achieved by site-selective deposition of active polymer and by the shape of the folding film. Rectangular bilayers, for example, form tubes while star-like films form capsules reminding flower buds, which are



formed by semi-tube-like folded star arms. In both these examples, simple rounded figures based on different combinations of fully or semi-folded tubes are formed. Moreover, because of the isotropy of mechanical properties of the bilayer, formation of hinges during folding of bilayers was considered to be impossible. Here, it is demonstrated that shape of isotropic polymer bilayer is able to direct its folding in a highly sophisticated manner leading to highly complex hierarchical folding. In particular, films can undergo sequential steps of folding by forming various 3D shapes with sharp hinges. By analyzing the folding of bilayer empirical rules, which allow programming of folding and design 3D shapes in a predicted manner, were elucidated.

We experimentally investigated the folding of circular/elliptical and star-like films. Swelling of the polymer layer leads to the formation of wrinkles along the perimeter. The spatial wavelength of the wrinkles is proportional to the activation depth ( $AD$ ) as observed in the wrinkles of leafs. As the activation depth increases, the number of wrinkles decreases as  $P/AD$ , where  $P$  is the perimeter of the shape (Figure 31e). The fact that there is both a gradient in radial- (edge-activation) and transversal direction (bilayer), results in a combination of wrinkling and bending respectively. Due to the transversal bending effect, the wrinkles actually evolve into local partial tubes as the activation depth increases. We observed that, at some point, the wrinkles stop to merge and their number remains constant. The probability of merging of two tubes depends on the angle between them ( $\beta$ , Figure 31e). Experimentally, we found that the critical value of  $\beta$  below which merging of folded tubes was not observed is ca.  $120-150^\circ$ . This corresponds to 6 – 8 wrinkles when starting with a circular shape (inset in Figure 31e). Based on these experimental observations we can derive the first folding rule, which is **“Bilayer polymer films placed on a substrate start to fold from their periphery and the number of formed wrinkles/tubes decreases until the angle between adjacent wrinkles/tubes approaches  $150^\circ$ ”**.

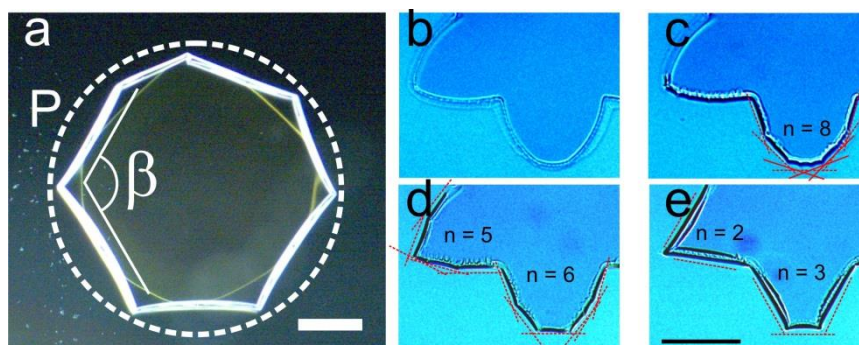


**Figure 31.** First step of folding of circular (a) and star-like (b-e) bilayer polymer films. The experimental observation of heptahedrons (a) when folding is typically stopped in the case of circular shapes; (b-e) two rays of six-ray star during wrinkling, decrease of number of wrinkles is observed. Scale bar is  $200\ \mu\text{m}$ <sup>181</sup>.

After the number of wrinkles/tubes along the perimeter of the bilayer film stopped to change the bilayers are locked for some time until the subsequent folding step occurs. For example, the wrinkled semi-ellipse bends towards its base (Figure 32a). To explain the origin of the second step of folding we considered the geometry of the film after the first folding step. As mentioned, wrinkling of a bilayer leads to the formation of tubes along the perimeter of the film. Considering the fact that the rigidity of tubes is higher than that of the undeformed films, the polygonal shapes are stiffened by this tube formation, and therefore possess a number of weak points located at the intersection of the tubes, i.e. at the vertices. These points act like hinges and folding is only observed along the lines connecting them (dashed line in Figure 32a). The formation of hinges during folding of isotropic bilayers, which to our knowledge has not been reported in the literature, is induced by the progressive activation from the lateral sides and the folded shapes are controlled by the initial shapes of the bilayers. This leads to the second rule of the folding, which states: **“After the wrinkles along the perimeter of the**

**film form tubes, further folding proceeds along the lines connecting the vertexes of the folded film”.**

In case there are more than two hinges in the film, a question arises upon which connecting line will the folding occur? The number of hinges is substantially determined by the shape of the semi-ellipses. The regular semi-ellipse, which has a triangular shape after the first step of folding, simply bends towards the base along the line connecting the two bottom vertexes (dashed line in Figure 32a). If the semi-ellipse is more rounded, it forms a trapezoid after the first-step of folding (Figure 32b). In the second step of folding, the trapezoid bends along one of the lines connecting the opposite top and bottom vertexes (dashed line in second image from left in Figure 32b). Next, the formed triangle bends towards its base along the line connecting the two bottom vertexes. The elongated semi-ellipse forms four folds after the first step of folding (Figure 32c). Interestingly, the semi-ellipse folds further along the lines connecting the vertexes at the base and the top vertex and no folding along the lines connecting neither the vertexes of the middle nor the ones at the base is observed. Looking at the evolution of the activation pattern through time, we observe that the lines connecting the hinges can only be used if they are within the activated pattern (red). Thus, the third rule of the folding states: **“the folding goes along the lines which are closer to the periphery of the films”**.

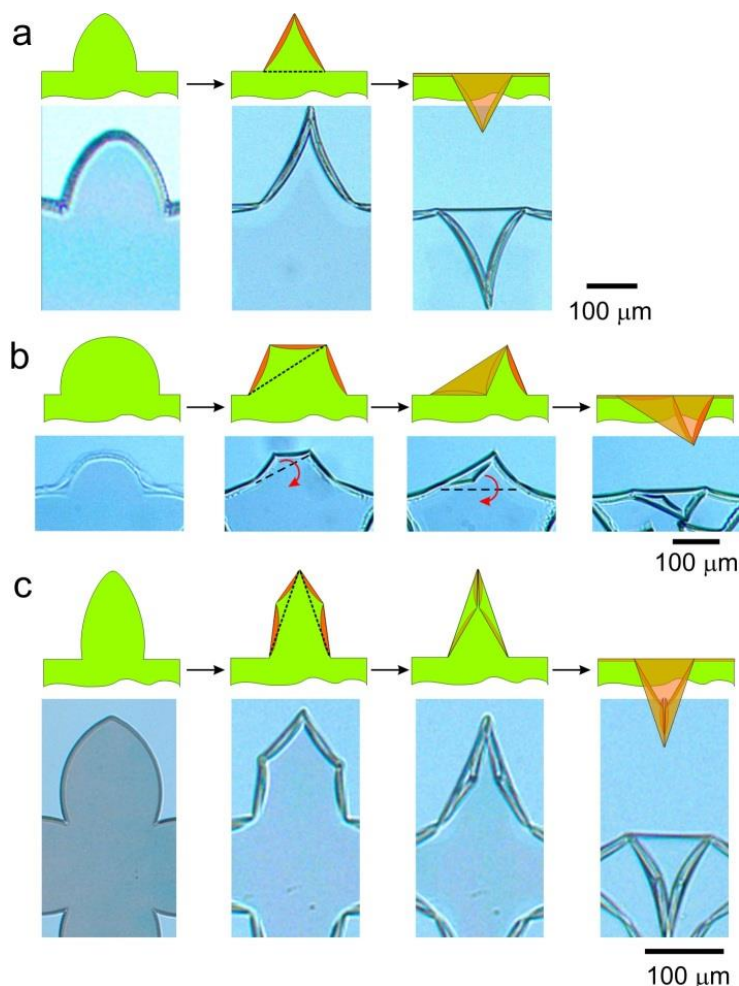


**Figure 32.** Scheme and experimental observation of second step of folding of elliptical arms depending on their shape: (a)  $H_{(PNIPAM-AA)} = 1200 \text{ nm}$ ,  $H_{PMMA} = 170 \text{ nm}$ ; (b)  $(H_{(PNIPAM-AA)} = 1200 \text{ nm}$ ,  $H_{PMMA} = 400 \text{ nm}$ ; (c)  $H_{(PNIPAM-AA)} = 900 \text{ nm}$ ,  $H_{PMMA} = 170 \text{ nm}$ <sup>181</sup>.

Six-ray stars demonstrate the formation of very complex structures (Figure 33). Notably simultaneous folding of all rays is observed very rarely and in most cases triangles (Figure 33g) were formed. We investigated the folding in a time resolved manner in order to explain

the formation of the triangles (Figure 34). Similar to the experiment demonstrated in Figure 31, wrinkles get longer and bend transversally into tubes (Figure 34b) thus increasing the rigidity of the ray. Next, one of the rays folds towards the center of the star (II in Figure 34c). Folding of this ray leads to the formation of a rigid semi-rolled tube, which is formed by the folded ray and the tubular shoulders of the adjacent rays (Figure 34c). The angle between the base of the folded ray and the shoulders of the neighboring arms is close to  $180^\circ$  (Figure 34c). In this configuration, the weak points located at the intersection between I- II and II- III has disappeared and rays I and III (Figure 34c) cannot bend anymore. As a result, only three remaining rays (IV, V, VI) can bend. If ray V folds, no additional rays can bend (Figure 4l). If ray IV folds (Figure 34d) ray V is blocked. Finally, ray VI can fold leading to the formation of a triangle (Figure 34e). The discussed principle can be easily applied to understand the formation of the other observed figures (Figure 33c-l). In fact, several factors can be held responsible for the observed symmetry breaking (rays do not fold at the same time) such as inhomogeneities in the films and shape imperfections resulting in small deviations from the symmetric diffusion profile. Based on these experimental observations, one can derive the fourth folding rule: ***“Folding of the rays may result in blocking of the neighboring rays if the angle between the base of the folded ray and the shoulders of the neighboring rays is close to  $180^\circ$ ”.***

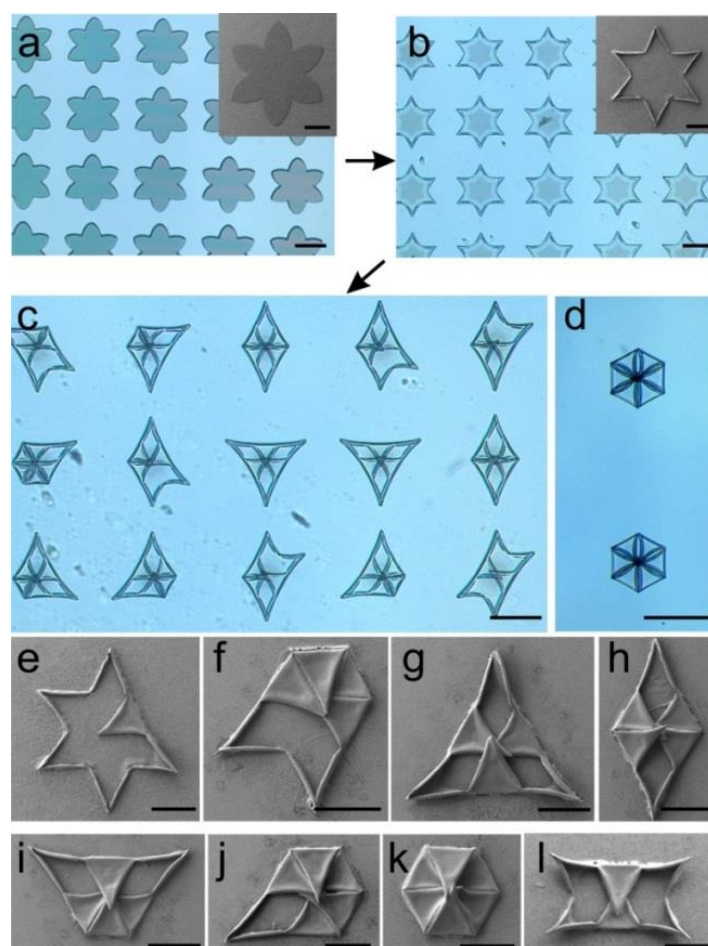


**Figure 33.** Examples of structures obtained by progressive edge-activation of six-ray star-like bilayers: (a) – patterned bilayers; (b) – First step of actuation: wrinkles collapse into tubes; (c-l) – Second step of actuation: rays fold leading to several configurations depending on the order of folding. Scale bars are  $200\ \mu\text{m}$ ,  $H_{(\text{PNIPAM-AA})} = 1200\ \text{nm}$ ,  $H_{\text{PMMA}} = 260\ \text{nm}$ <sup>181</sup>.



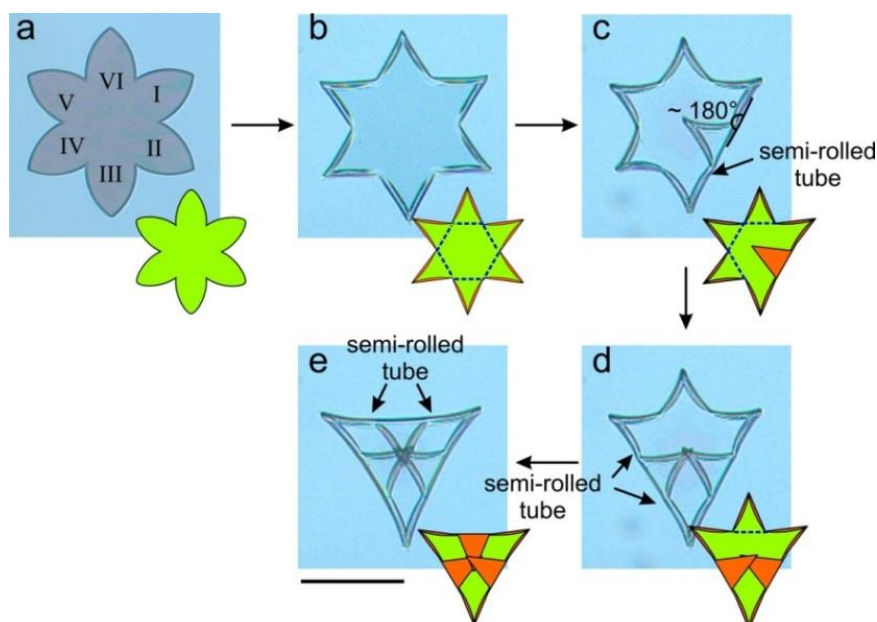


**Figure 34.** Microscopy snap-shots illustrating the mechanism of formation of triangles during actuation of a six-ray stars. Scale bar is 200  $\mu\text{m}$ ,  $H_{(\text{PNIPAM-AA})} = 1200 \text{ nm}$ ,  $H_{\text{PMMA}} = 170 \text{ nm}$ <sup>181</sup>.

Finally, the derived rules were applied for the design of truly 3D structures – pyramids. In fact, the reason why six-ray star formed flattened folded structures is their short arms and the hindering of the folding. Therefore, in order to fabricate pyramids we increased the relative length of the rays and changed the angle between them by decreasing their number (Figure 35a, b). The rays of the fabricated four-ray stars first wrinkle along their perimeter (Figure 35c, d). Four tubes are formed along the perimeter of each ray (first rule, Figure 35c), which then collapse two by two and form triangles (second rule, Figure 35d). Since the angle between the folds located on the shoulders of each ray is considerably smaller than 180°, the folding of rays is not self-interfering (forth rule) and all rays fold in the direction of the center of the star (third rule) thus forming a hollow pyramid (Figure 35e, f, g). In fact these rules are also applicable to other shapes such as rectangles. As an example we included two-step folding of rectangles.

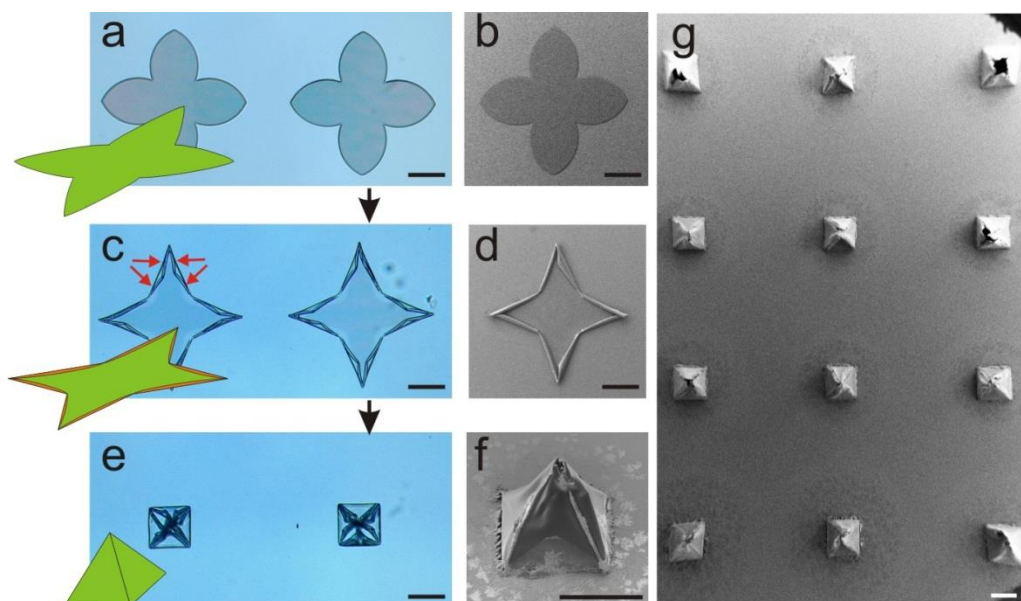


**Figure 35.** Sequential actuation of four-ray stars leads to the formation of pyramids: (a, b) – unactivated film; (c, d) – after wrinkling of the ray periphery into tubes, red arrows indicate

four wrinkles formed on each arm during first step of folding ; (e, f, g) after folding of rays leading to the formation of pyramids. Scale bar is 200  $\mu\text{m}$ ,  $H_{(\text{PNIPAM-AA})} = 1200 \text{ nm}$ ;  $H_{\text{PMMA}} = 260 \text{ nm}$ <sup>181</sup>.

In conclusion, folding of bilayers was investigated. It was demonstrated that the shape of folded 3D object is determined by the shape and size of the 2D film. For example tubes are formed by rectangular films and capsules are formed by star-like films. It was also demonstrated that folding depends strongly on the presence of the substrate, where the bilayer is located. In fact, folding starts from periphery due to restricted diffusion of solvent inside the active polymer. For the first time it was demonstrated that the bilayer can undergo multi-step complex folding that resulted in a variety of shapes. Empirical rules which allow programming of the folding of polymer films were derived basing on the experimental observations. In particular, one can introduce hinges into the folded structure by proper design of the bilayer shape of the bilayer. The advantage is that no site selective deposition of active polymers is required. It is expected that derived algorithm will allow very simple (one step photolithography) design of highly complex self-folding 3D folding objects and will open new horizons for 3D patterning which is highly important for design of microfluidic device, biomaterials, electronics, etc.

#### 4.4 PROPERTIES AND APPLICATIONS OF SELF-FOLDING FILMS

##### Controlled encapsulation and release

The developed self-folding films are very promising for different kinds of applications. The main focus is, however, controlled encapsulation and release of particles and cells. In particular, we demonstrated that colloidal particles and cells can be both reversibly and irreversibly encapsulated inside thermoresponsive self-folding films. For the demonstration of the approach, 10  $\mu\text{m}$  large  $\text{SiO}_2$  microparticles were adsorbed from their aqueous dispersion on PNIPAM-PCL bilayer film at elevated temperature, when PNIPAM is collapsed and the film is unfolded. Decrease of the temperature resulted in swelling of the PNIPAM and led to the formation of microtubes with encapsulated microparticles (Figure 36). Two mechanisms of particle encapsulation were observed – microparticles were either encapsulated inside rolls or entrapped between the rolls. The microparticles encapsulated inside the rolls produced by multiple rolling cannot be released at elevated temperature due to inability of microtubes to unroll. These particles remain entrapped inside the microtubes. On the other hand, microparticles encapsulated inside one-revolution rolls and between the rolls are able to leave the microtubes at elevated temperatures when thermoresponsive polymer is collapsed. These experiments demonstrated the possibilities to encapsulate, trap and release particles using self-rolling tubes.

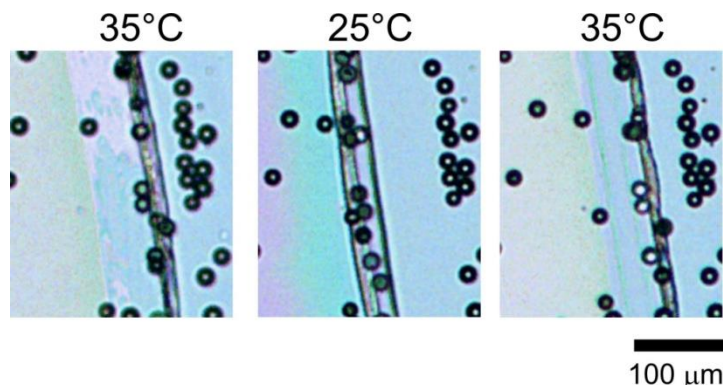


**Figure 36.** Encapsulation and release of microparticles from microtube at different temperatures. The one-revolution microtubes unroll at elevated temperature and release the particles<sup>137</sup>.

Cells can also be irreversibly encapsulated and grown inside fully biodegradable self-rolled tubes. For the demonstration, the bakery yeast cells were adsorbed on patterned PSI/PCL bilayer from PBS pH = 7.4 buffer. After 27 h of incubation, the PSI/PCL bilayer formed tubes with diameter 80-100  $\mu\text{m}$  with encapsulated yeast cells (Figure 37a). The number of cells remained approximately constant in PBS. One microtube with encapsulated yeast cells was transferred into the nutrition media (Figure 37b) and further incubated for 14 hours. Incubation in nutrition media led to proliferation and division of the yeast cells that increased their number.

The advantage of the thermoresponsive microtubes is the possibility of both encapsulation and release, which occurs due to folding and unfolding, respectively. The disadvantage is non-biodegradability that limits *in vivo* applications. On the other hand, due to possibility of reversible encapsulation, PNIPAM-based systems can be readily applied for micro-analytical investigation of cell behavior in confinement. The PSI-PCL systems are more suitable for biomedical applications since both polymers are biodegradable and were already approved for biomedical applications.

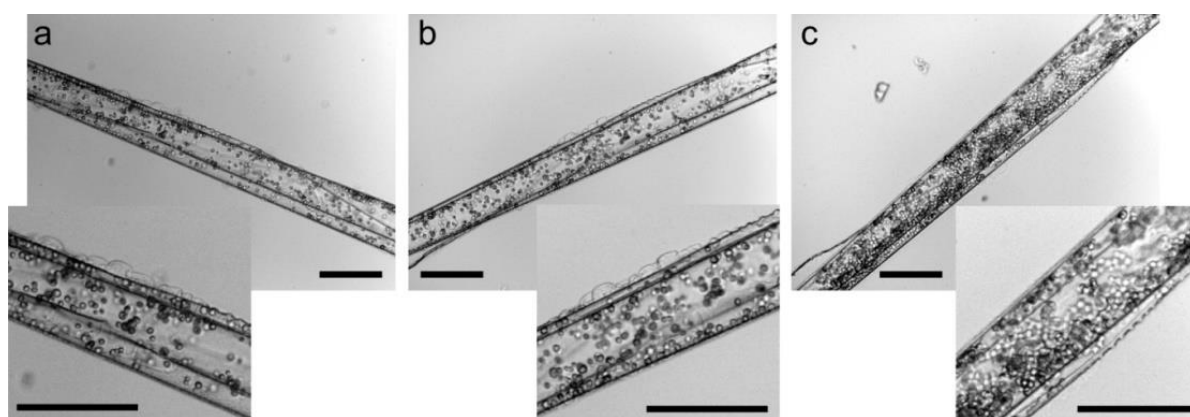


**Figure 37.** The PSI/PCL self-rolled tubes: (a) after encapsulation of yeast cells in PBS buffer, (b) directly after the transfer to the nutrition media and (c) after 14 hr of incubation in the nutrition media. Scale bar is 100  $\mu\text{m}$ <sup>175</sup>.

### Manipulation with self-folded objects

Micro-analytical application of self-folding films will definitely require development of the ways to control their position and orientation in 3D space. Toward this goal, the possibility to manipulate particle-loaded microtubes using magnetic field was tested. For this, microtubes containing  $\text{Fe}_3\text{O}_4$  supermagnetic nanoparticles in the thermoresponsive layer were first prepared and then loaded with microparticles. It was found that the freely flowing particle-loaded microtubes start to move in the direction of the magnet (Figure 38). The direction of the microtubes flow can be immediately switched by changing the position of the magnet, thus demonstrating the possibility to manipulate the position of microtubes using magnetic field.



**Figure 38.** Magneto-sensitive properties of microtubes. Microcopy snapshots of microtubes containing magnetic nanoparticles flowing in the applied magnetic field. Arrows show the direction of flowing <sup>137</sup>.

### Self-assembly of self-folded objects

Many kinds of tissues such as bones<sup>182</sup>, vascular tissue<sup>183, 184</sup>, cardiac tissue<sup>185-187</sup>, nerves<sup>188, 189</sup> have either tubular or uniaxially aligned porous structures. In order to mimic the tubular structural environment, phase separation techniques<sup>183, 184, 190</sup>, polymer fiber templating<sup>185, 188, 189</sup>, directed foaming<sup>191</sup>, directional freezing<sup>183, 192-195</sup>, prototyping<sup>186</sup>, uniaxial stretching of porous materials<sup>196</sup>, or using of natural porous materials such as wood<sup>197</sup> were used. In these approaches the separate tubes or scaffold with tubular structure are first fabricated and then filled with a material. This “post-filling” strategy suffers, however, often from non-homogenous filling of porous scaffold.

Self-folding films offer a very elegant solution to the problem of non-homogenous distribution inside the pores<sup>4, 8, 198</sup>. The main advantage of self-folding films is that they can be filled during formation and then assembled that provides desired homogeneity of filling<sup>8, 137, 145</sup>. Moreover, self-rolled tubes are able to provide structural anisotropy. Our approach consists of the fabrication of homogeneously filled self-rolled tubes and their self-assembly in complex 3D constructs with uniaxially aligned pores.

In order to demonstrate this approach, pH-responsive self-rolling polymer bilayer films were used. The bilayer consists of hydrophilic stimuli-responsive poly(N-isopropylacrylamide-co-acrylic acid-co-benzophenoneacrylate) (p(NIPAM-AA-BA)) bottom layer and hydrophobic poly(methylmethacrylate-co-benzophenoneacrylate) (p(MMA-BA)) top layer.

In order to assemble the tubes, they were transferred into pure water and a small amount<sup>199</sup> of water dispersion of SiO<sub>2</sub> particles with grafted polycation poly((2-dimethylamino)ethyl methacrylate) (PDMAEMA) brush layer was added (Figure 39a). This led to fast aggregation of the tubes due to formation of a polyelectrolyte complex between the charged groups on the particles (amino, PDMAEMA) and the tubes (carboxylic, PAA) surfaces (Figure 39b-e). The formed aggregates are mechanically stable in pure water. Upon intensive shaking they can break apart into smaller aggregates, which however, re-assemble again (Figure 39f-h). The aggregates are less stable in a saline buffer environment (Figure 39i). In fact, an increase of ionic strength leads to screening of the charges of the carboxylic and amino groups that results in weakening of the bonds between the tubes and disassembly. Transfer of the tubes obtained by disassembly of aggregates back into pure water leads to restoration of the electrostatic interactions and re-agglomeration of the tubes (not shown). The self-rolled tubes, thus, demonstrate the ability to undergo reversible stimuli-controlled assembly-disassembly.



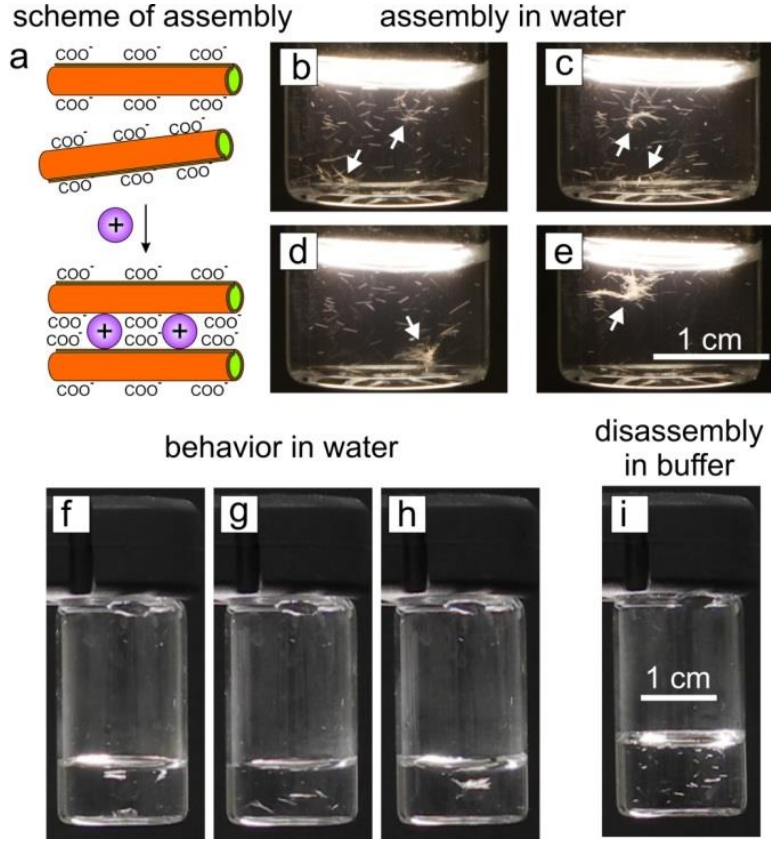


**Figure 39.** Self-assembly of self-rolled tubes: (a) – scheme of physical crosslinking of tubes by oppositely charged particles; (b-e) optical photographs of microtubes during self-assembly (concentration 180 tubes/ml); (f-g) optical photographs of microtube aggregates in water after shaking (concentration 90 tubes/ml); (i) optical photographs of the disassembly of microtube aggregates in PBS buffer<sup>200</sup>.

The tubes strongly align in one direction when a force is applied. This, for example, occurs when the aggregates are pulled out from the water with a needle (Figure 40). Moreover, aggregates where tubes are aligned are more stable compared to ones where the tubes are disordered – the aligned aggregates do not break apart in the PBS buffer. The character of tube orientation corresponds to orientation in nematic liquid crystals – tubes are oriented in one direction while their centers of mass are unordered. We estimated a two-dimensional degree of tube orientation ( $S$ ) using equation 5<sup>201</sup>. It was found that the orientation degree in the sample illustrated in Figure 40f-h (50 tubes/ml) is extremely high  $S = 0.98$ . Tubes in the sample illustrated in Figure 40c-e, which was obtained by assembly at higher concentration of microtubes (250 tubes/ml), have an apparently lower orientation degree.

$$S = \frac{\langle 3(\cos \theta)^2 - 1 \rangle}{2} \quad (5)$$

where  $\theta$  is deviation angle of each individual tube with respect to the average direction of orientation of the tubes in the aggregate.

We estimated porosity of the formed agglomerates by considering the inner diameter of the tubes, wall thickness as well as packing density of the tubes. The inner diameter ( $d_{inn}$ ) varies in the range of 10 – 100  $\mu\text{m}$ , the thickness ( $d_{wall}$ ) of swollen wall is ca 1 - 5  $\mu\text{m}$  depending on the thickness of polymer layers. The maximal packing density of cylinders is ca 0.91. The porosity ( $P$ , ratio of pore volume to total volume), which was estimated



using equation 6, varies in the range  $P = 76\% - 90\%$ .

$$S = \frac{(0.5d_{inn})^2}{0.91(0.5d_{inn} + d_{wall})^2} \quad (6)$$

where  $d_{inn}$  and  $d_{wall}$  are internal and external diameters of the tubes.

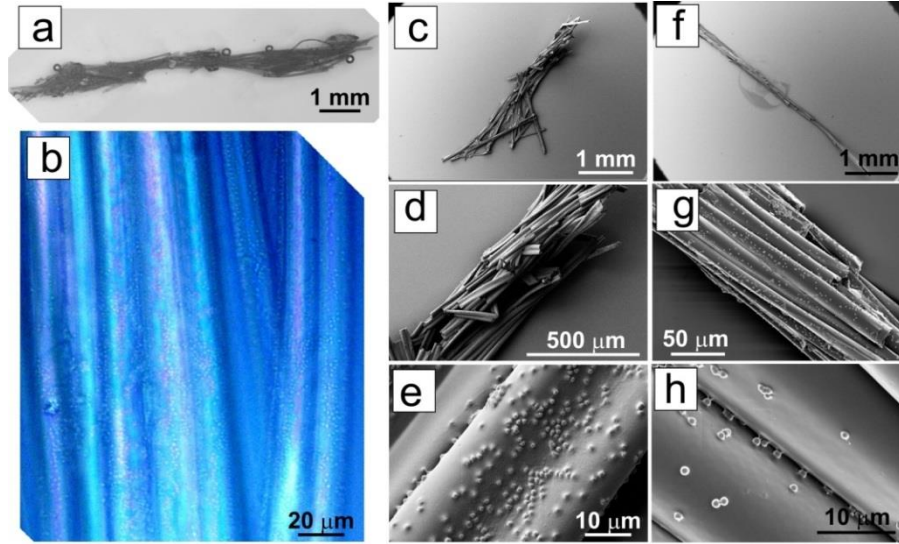


**Figure 40.** Aligned self-assembled self-rolled tubes. (a, b) – optical microscopy (c-h) scanning electron microscopy images of two aggregated (c-e and f-h) formed by self-rolled tubes crosslinked by positively charged particles and aligned by pulling out from the water with a needle<sup>200</sup>.

Next, the possibilities for the fabrication of complex porous architectures consisting of microtubes with different properties was demonstrated. In particular, two types of porous structures formed by tubes of two sorts, which are labeled with green and red fluorescent quantum dots admixed to PMMA layer, were fabricated. In one experiment, tubes of one sort (red ones) were assembled by crosslinking with colloidal particles and stretched by pulling with a needle. The formed aggregate of uniaxially aligned tubes was immersed in dispersions of tubes of the second sort (green ones). The negatively charged green tubes stuck to the positively charged particles patches presented on the aggregate of red tubes (Figure 41a, b), starting to form a “core-shell” structure. In the second experiment, green tubes were mixed with an excess of PDMAEMA-coated particles in PBS buffer that terminates aggregation, and incubated together for 30 min. The particle-coated but not agglomerated green tubes were added to a dispersion of red ones in water and as a result agglomerate (Figure 41c, d) consisting of randomly distributed red and green tubes was formed (cross-sections in Figure 41e, f).

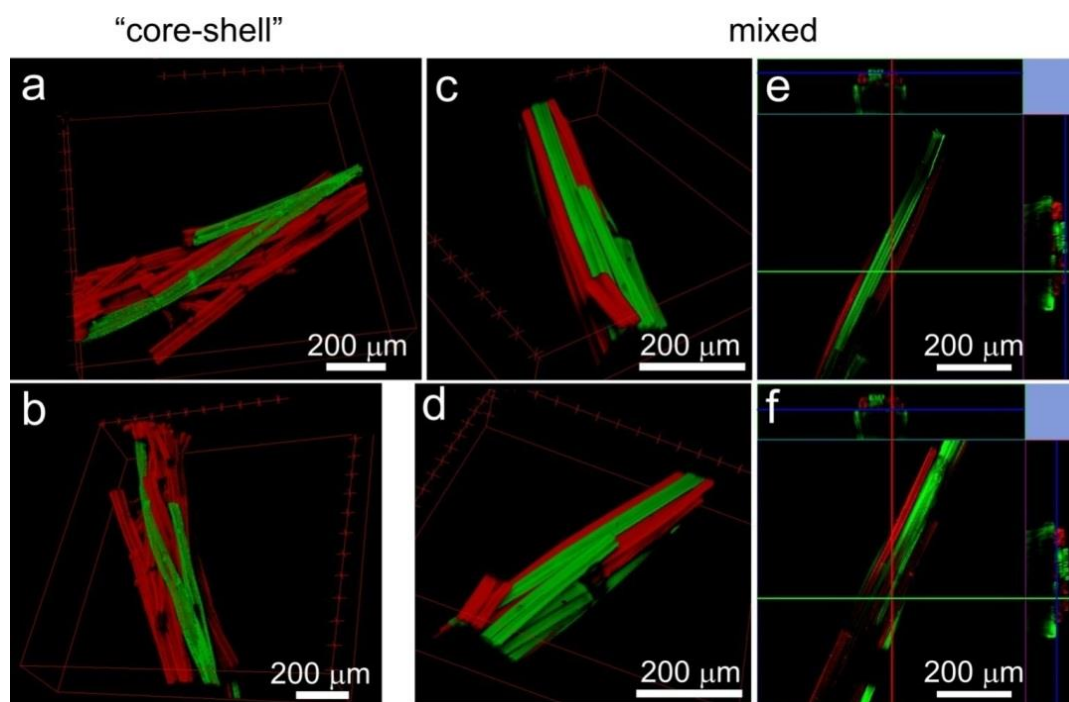


**Figure 41.** Confocal microscopy images of assemblies of microtubes with different colors: (a,b) – 3D reconstruction of a “core-shell” porous scaffold, where green tubes are immobilized on an assembly of red ones; (c,d) – 3D reconstruction of a “mixed” porous scaffold, where green tubes are first coated by PDMAEMA particles and then assembled together with red ones; (e,f) – cross-section of a mixed scaffold (c,d) in different planes. Due to low penetration depth of light beam imaging of whole aggregate was not possible<sup>200</sup>.

Finally, the possibility to fabricate a porous self-assembled construct where tubular pores are filled with cells was explored (Figure 42). For this, we adsorbed yeast cells from a water dispersion on the top of a patterned unfolded p(NIPAM-AA-BA)/p(MMA-BA) bilayer. After the yeast cells had settled down from their aqueous dispersion, the tubes were rolled that resulted in encapsulation of the yeast cells. The tubes filled with cells were washed off from the substrate with several milliliters of water into a glass vial. Afterwards, the tubes were assembled, aligned and transferred into the culture medium and incubating them for 24 h at room temperature. The number of cells in the tubes increased significantly that indicates viability of yeast cells as well as on free diffusion of nutrition molecules into the tubes (Figure 42b). In this experiment, we fabricated tubes with a small diameter ( $d = 20 \mu\text{m}$ ), which is very close to the size of the yeast cells ( $d = 5 \mu\text{m}$ ) in order to demonstrate the advantage of our method. Obviously, post filling of narrow tubes, which is disconnected from tubular network, with cells is almost impossible due to slow migration of cells into the narrow tubes. Indeed, some tubes, which were occasionally not filled with cells during tube formation, remained empty after incubation in cell culture medium. For example tube 1 (Figure 42a) was empty after cell encapsulation and it remained empty after 24 h of incubation in cell culture medium. In contrast, tube 2, which was initially partly filled with yeast cells, become completely filled with yeast cells after incubation. In this experiment yeast cells were used for demonstration of the proof of the concept. In fact it was demonstrated that number of yeast cells increases with time and cells receive enough nutrition, which might be the issue in the narrow tubes. Previous research demonstrated that mammalian cells can also be encapsulated inside tubes<sup>202</sup> that potentially allows fabrication of 3D scaffolds for tissue engineering.

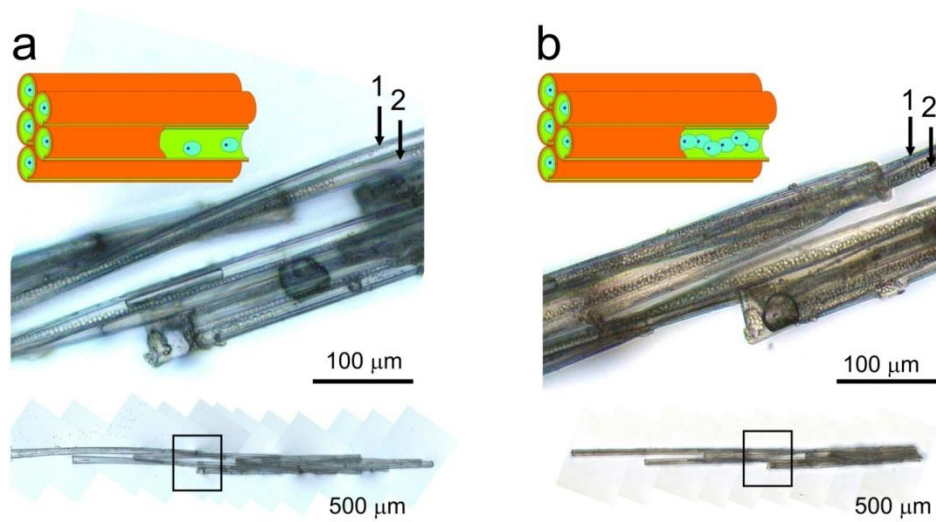


**Figure 42.** Porous 3D construct obtained by self-assembly of self-rolled tubes filled with yeast cells: (a) – directly after self-assembly; (b) – after 1 day of incubation in the cell culture medium. The images in the lower panel are the microscopy snap shots of the whole cell-filled agglomerate. The images in the middle panel are the magnifications of the areas restricted by rectangles. Tubes 1 and 2 are empty and partially filled with yeast cells, respectively right after assembly. Tube 1 remains empty after incubation in the cell culture medium. Tube 2 is completely filled with cells after incubation in the cell culture medium<sup>200</sup>.

In conclusion of this section, it was demonstrated that self-folding approach can be used for controlled reversible/irreversible encapsulation of particles and cells. Moreover, self-folded objects can be manipulated by magnetic field and assembled in porous 3D constructs.

## 5. CONCLUSIONS

This work aimed to develop novel approaches for 2D and 3D micro and nanostructuring, which allow design of patterned surfaces with switchable and reconfigurable patterns, as well as to develop methods for patterning in physiologic conditions without using of harmful UV light. The second goal was development of approach for design of complex 3D structures using self-folding polymer films. The main achievements are summarized below:

1. It was demonstrated that protein assemblies can be used to fabricate nanopatterned stimuli-responsive surfaces. The approach was demonstrated on the example of the synthesis of nanostructured stimuli-responsive polymer brushes using atom transfer radical polymerization initiated on protein filaments of the cytoskeleton. In particular, microtubules were used as template for the synthesis of nanostructured thermoresponsive PNIPAM brushes with incorporated fluorescent groups.

2. Novel approach for the fabrication of switchable patterned surfaces where two kinds of stimuli-responsive polymers are grafted in site-selective manner was developed. Micropatterned surfaces were prepared by grafting two oppositely charged polyelectrolytes (polyacrylic acid and poly(2-vinylpyridine)) using a combination of photolithography, “lift-off” and “grafting to” techniques. This method utilizes “grafting to” approach instead of widely used surface initiated polymerization. That makes preparation of bicomponent patterned polymer grafted layers simple and quick. The patterned surfaces demonstrate switching of surface topography, wetting and character of adsorption of proteins. This approach can be easily extended for the fabrication of multicomponent ( $n > 2$ ) micropatterned polymer surfaces by repeating the structuring cycle multiple times.

3. Novel method to fabricate patterned stimuli-responsive surfaces with the pattern whose lateral size can be controlled by external stimuli was developed. In one set of experiment, lateral gradients composed of thermoresponsive poly-(N-isopropylacryl amide – *tert* butyl acrylate – acrylic acid) copolymers were generated by local hydrolysis using methanesulfonic acid. It was shown that the border between the collapsed and the swollen polymer areas on these gradients could be reversibly shifted by up to 120  $\mu\text{m}$  when raising or lowering the temperature between 21  $^{\circ}\text{C}$  and 50  $^{\circ}\text{C}$ . Utilizing kinesin-driven motility of microtubules, we demonstrated the applicability of these gradients for the temperature-induced size-control of bioactive surface patterns. In a second set of experiments circular gradients of poly-(N-isopropylacryl amide – 2-nitrobenzyl acrylate – acrylic acid) were generated by UV irradiation. It is thus possible to use photolithography to produce switchable polymer gradients with customized layouts. Notably, the temperature range over which switching occurs can be precisely tuned by selecting the appropriate copolymer composition. It was demonstrated that the area where protein molecules are active, which are adsorbed on the patterned surface, can be reversibly switched by temperature.

4. A novel approach to design of an environment-friendly (water-soluble/water-developing) photoresists with stimuli-triggered development based on photocleavable copolymers of PNIPAM was established. The proposed photoresists possess a unique combination of advantages: (i) they are soluble in biological buffers, (ii) their photocleaved products are soluble in aqueous environment as well, and (iii) their development is triggered by temperature in physiological buffer in a controllable way and no change of pH is required. The applicability of the presented method for *in situ* patterning inside microfluidic channels and for protein patterning on surfaces was demonstrated. The method has a strong potential for patterning and harvesting proteins, particles, and cells in microfluidic devices, where all procedures have to be performed in biological buffers.

5. Two approaches for irreversible and reversible photopatterning functional proteins using thermoresponsive polymer locally heated by light-to-heat conversion were developed. The approaches were experimentally demonstrated on the example of

irreversible sequential patterning of kinesin motor proteins on poly-(N isopropylacrylamide) surface as well as on the example of reversible activation of kinesin adsorbed on substrate between grafted poly-(N isopropylacrylamide) chains. The suggested approaches have distinct advantages that make them very promising: (1) any wavelength of light (UV to VIS) can be used under physiological conditions; (2) although the pattern resolution is lower than AFM or CVD techniques, sub-micron resolution could be achieved basing on heat diffusion calculations; (3) because the technique is maskless, arbitrary pattern sizes and shapes can be created. We expect that this technique can find wide application as a method of simple and quick fabrication of protein microarrays for bio- and nanotechnological applications in lab-on-chip systems.

6. Novel approach for design of complex 3D polymer structures using self-folding polymer films was developed. The self-folding polymer films are polymer bilayer, which consists of one layer of hydrophobic polymer and a layer of hydrophilic stimuli-responsive hydrogel. The hydrogel is able to undergo reversible volume changes stimulated by change of environmental conditions. The bilayer folds, that leads to the formation of tubes and unfolds upon swelling and shrinking of hydrogel layer.

7. Approaches for design of thermoresponsive and fully biodegradable self-folding polymer films were developed. The developed self-folding systems demonstrate folding within physiological ranges of temperature and pH. Thermoresponsive self-folding films were fabricated using poly(N isopropylacrylamide) as active layer. The advantage of this approach is that folding/unfolding is reversible and occurs in physiological buffer at temperature close to body temperature. The fully biodegradable self-folding films were fabricated using polycaprolactone and polysuccinimide. Polysuccinimide is active component and is able to slowly hydrolyze and swell in a physiological buffer environment leading to self-rolling of the polymer bilayer and the formation of microtubes. It was also demonstrated that the self-rolled tubes can be used for encapsulation of cells, which proliferate and divide inside the tube. Since the used polymers are biocompatible, biodegradable, produced industrially and are approved for biomedical purposes, the proposed approach is of practical interest for controlled cell delivery and the design of scaffolds for tissue engineering.

8. Folding of polymer bilayers with different lengths, widths and thicknesses was investigated. It was found that long-side rolling dominates at high aspect ratios (ratio of length to width) when the width is comparable to the circumference of the formed tubes. Rolling from all sides occurs when the width and length considerably exceed this circumference. Diagonal or all-side rolling is observed when the width and length are comparable to the circumference. Short-side rolling was observed very rarely and in combination with diagonal rolling. Based on both experimental observations, we argued that bilayers placed on a substrate start to roll from corners due to quicker diffusion of water. Rolling from long-side starts later but dominates at high aspect ratio due to energetic considerations. It was shown experimentally that the main reasons causing a variety of rolling scenarios are (i) non-homogenous swelling due to slow diffusion of water in hydrogels and (ii) adhesion of polymer to a substrate until a certain threshold. Moreover, non-homogenous swelling determines folding in first moments while adhesion plays decisive role at later stages of folding.

9. Folding of bilayers with complex shape was also investigated. It was found that films can demonstrate several kinds of actuation behaviors such as wrinkling, bending and folding that result in a variety of shapes. It was also demonstrated that one can introduce hinges into the folded structure by proper design of the bilayer's external shape through diffusion without having to use site selective deposition of active polymers. Experimental observations allowed deriving of four empirical rules. It was then demonstrated how those rules can be used to direct the folding of edge-activated polymer bilayers through a concrete example – the design of a 3D pyramid.



10. It was demonstrated that self-folding films are very promising for controlled encapsulation and release of cells. The folded objects can be controlled by magnetic field and can be assembled in complex 3D constructions mimicking structure of bones and muscles.

11. A novel approach for the fabrication of self-assembled porous scaffolds with uniaxial tubular pores was developed. The approach is based on the use of microtubes formed by the stimuli-induced rolling of rectangular bilayers consisting of hydrophobic and stimuli-responsive hydrophilic polymers. Any micrometer objects, for example yeast cells, can be encapsulated inside the tubes during their rolling. The self-rolled tubes filled with yeast cells can be easily assembled into a uniaxial tubular scaffold homogeneously filled with the cells. The main advantage of this approach is the possibility to homogeneously fill the pores with any kind of matter – inorganic, organic or living. Moreover, the approach allows design of porous materials with complex architectures formed by tubes of different sorts.

## 6. OUTLOOK

Nowadays methods for the 2D surface structuring are already very strongly developed. The best illustration of this is the fact that 16 nm and 22 nm lithographic technologies are already applied for the large-scale manufacturing of computer chips. This clearly illustrates that current top-down technologies allow achievement of resolution, which is comparable with that which can be achieved using bottom-up approaches. **Nevertheless, development of methods for freely reconfigurable patterning, which can be applied for biotechnology and microelectronics is still a big challenge.** Development of such method is expected to allow appearing of dynamically smart substrates where cells can change their shape, orientation, connection with other cells that may be used for development of reconfigurable neural networks.

Current approaches for 3D structuring are less developed. The 3D structures are typically fabricated by multistep deposition of one structured layer on another that is performed by printing of lithography. Interference and two photon lithography can be used for 3D structuring but they are expensive and relatively slow. Use of self-folding films can be a good alternative to these methods. The self-folding films are potentially very promising for microelectronics as well as for biotechnology (controlled encapsulation and release of drugs and cells). In the case of self-folding films, cells are not locked inside amorphous and densely crosslinked matrix, as it happens in the case of hydrogels, but are free to move. This is particularly important for design of tissue engineering scaffolds. The limited applicability of self-folding films for design of scaffolds is, on one hand, caused by their folding at non-physiological conditions. On the other hand, pH is not favorable signal to trigger folding for encapsulation of cells. Use of temperature as stimuli is more suitable, since cells readily withstand temperature variation. On the other hand, most of the reported systems are non-biodegradable. There is only one own report about fully-biodegradable self-folding polymer film. In future, these two problems must become the focus of research in this field.

One of the recent trends is the development of approaches which allows design of complex 3D structures. One approach to design complex structures, which is inspired by nature, is to use inhomogeneity of swelling path that allows very complex folding in the way that star-arm bilayers build pyramids with sharp hinges. **Further development in understanding of basic principles of folding is expected to allow design of 3D shapes with the complexity close to origami.**

One of the factors limiting broad applicability of self-folding polymer films is the manufacturing cost. In fact, because polymer can be deposited by using spin and dip coating at ambient conditions, the fabrication of polymer self-folding films is substantially cheaper than fabrication of inorganic ones, which are produced by vacuum deposition. **Therefore, I believe, development of the route for cheap and fast manufacturing of large quantity of self-folding films will boost their broad application.**

Due to their softness, better biocompatibility, possible biodegradability and easy manufacturing polymer self-folding films can compete with inorganic ones in the field of microelectronics and bio-microelectronics for *in vivo* applications. **I believe that self-assembled polymer 3D constructs formed by uniaxially alighted tubes remind morphologies of bones and cardiac tissue and may be used to their regeneration. Self-rolling tubes can be also potentially used to assist with regeneration of neurons and to replace blood vessels.**

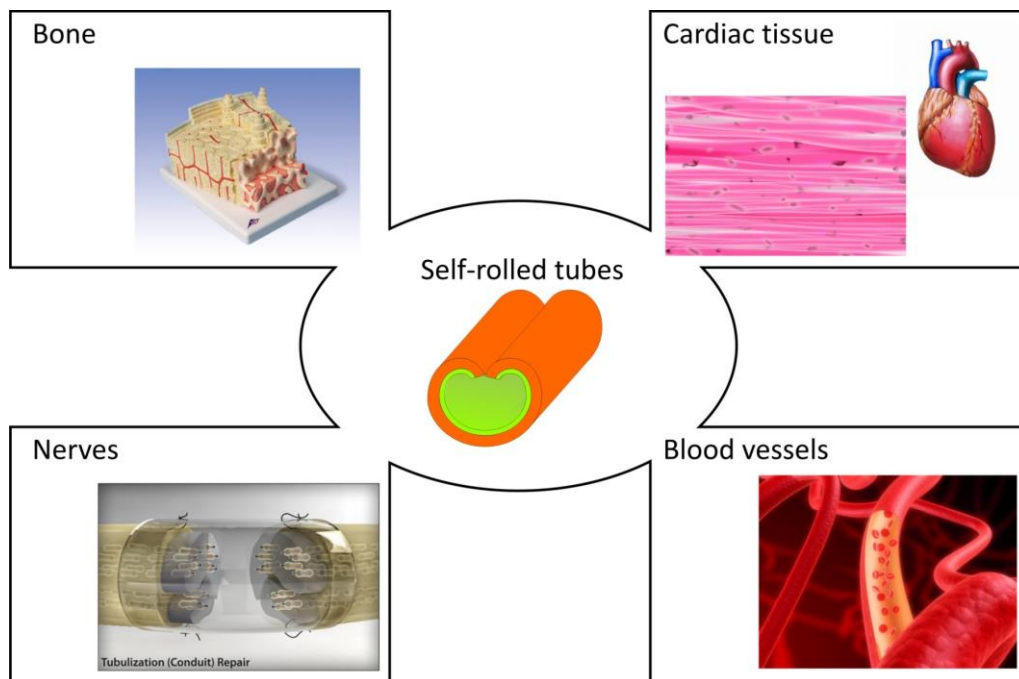


**Figure 43.** Potential biomedical applications of self-folding polymer films.

## 7. ACKNOWLEDGEMENTS

The results presented in this habilitation were obtained during my work at the Max-Planck Institute of Molecular Cell Biology and Genetics as well as at the Leibniz Institute of Polymer Research.

I would like to specially thank Professor Manfred Stamm for his support and advice that made this habilitation possible. I am incredibly thankful to Professor Stefan Diez for introducing me into fascinating world of biophysics and supporting my first steps in independent research. I am grateful to Professor Sergiy Minko for his long-year support and many fruitful discussions.

Further, I would like to express my deep gratitude to my colleagues and taught students from my group with whom I have worked the past years: Nikolay Puretskiy, Georgi Stoychev, Svetlana Zakharchenko, Ivan Raguzin, Soumyadip Choudhury, Elisabeth Kaul, Kathrin Müller, Mukesh Agrawal, Evgeni Sperling, and Nidhi Chandrama Dubey.

I am very thankful to my dear colleagues and collaborators Dr. Cordula Reuther, Dr. Rob Tucker, Prof. Henry Hess, Prof. Andrey Rogach, Prof. Sameer Sapra, Dr. Christian Waurisch, Dr. Stephen Hickey, Prof. Alexander Eychmüller, Prof. Jens Uwe Sommer, Sébastien Turcaud, Dr. John Dunlop, Prof. Peter Fratzl and Dr. Vera Bocharova for their advises, interesting ideas and help with experiments.

I would like specially thank Dr. Marina Grenzer and Dr. Alben Lederer for their helpful comments on this habilitation.

I am very grateful to my wife, Dr. Alla Synytska, my son Pavlo and daughter Sophia for their continuous support, believing in me and permanent inspiration.

This work has been supported over the years by IPF, MPI-CBG and several funding bodies in the frameworks of the following projects: DFG (Project IO 68/1-1) and VW Stiftung.

## 8. PUBLICATIONS

The following articles on 2D and 3D microstructured materials have been published / submitted during the Habilitation period.

### Invited review papers during Habilitation period:

Ionov, L.\* Biomimetic hydrogel-based actuating systems, **Advanced Functional Materials** 2013 (23), 4555-4570.

Ionov, L.\* Bioinspired microorigami by self-folding polymer films, **Macromolecular Chemistry and Physics** 2013, 214, 1178 – 1183.

Ionov, L.\* 3D Microfabrication using stimuli-responsive self-folding polymer films, **Polymer Reviews** 2013, 53, 92 - 107.

Ionov, L.\* Biomimetic 3D self-assembling biomicroconstructs by spontaneous deformation of thin polymer films, **Journal of Materials Chemistry** 2012, 22, 19366 – 19375.

Luchnikov, V.\*; Ionov, L.\*; Stamm, M. Self-rolled polymer tubes: novel tools for microfluidics, microbiology and drug-delivery systems, **Macromolecular Rapid Communications** 2011, 32(24), 1943 - 1952.

Ionov, L.\* Soft microorigami: self-folding polymer films, **Soft Matter** 2011, 7, 6786-6791.

Ionov, L.\* Actively-moving materials based on stimuli-responsive polymers **Journal of Materials Chemistry** 2010, 20, 3382-3390.

### Original per-reviewed papers:

Reuther, C.; Ionov, L.\*; Tucker, R.; Diez, S\* Freely programmable patterning of protein bioactivity on surfaces using visible light – “green” photopatterning, submitted.

Stoychev, G.; Turcaud, S.; Dunlop, J.; and Ionov, L.\* Hierarchical multi-step folding of polymer bilayers, **Advanced Functional Materials** 2013, 23(18), 2295-2300.

Zakharchenko, S.; Puretskiy, N.; Stoychev, G.; Waurisch, C.; Hickey, S.G.; Eychmüller, A.; Sommer, J.U.; and Ionov, L.\* Stimuli-responsive hierarchically self-assembled 3D porous polymer-based structures with aligned pores, **Journal of Materials Chemistry B**, 2013, 1, 1786-1793.

Stoychev, G.; Zakharchenko, S.; Turcaud, S.; Dunlop, J.; and Ionov, L.\* Shape programmed folding of stimuli-responsive polymer bilayers, **ACS Nano** 2012, 6 (5), 3925-3934.

Zakharchenko, S.; Sperling, E.; Ionov, L.\* Fully biodegradable self-rolled polymer tubes: a candidate for tissue engineering scaffolds, **Biomacromolecules** 2011, 12 (6), 2211-2215.

Stoychev, G.; Puretskiy, N.; Ionov, L.\* Self-folding all-polymer thermoresponsive microcapsules, **Soft Matter** 2011, 7, 3277-3279.

Zakharchenko, S.; Puretskiy, S.; Stoychev, G.; Stamm, M.; and Ionov, L.\* Temperature controlled encapsulation and release using partially biodegradable thermo-magneto-sensitive self-rolling tubes, **Soft Matter** 2010, 12, 2633-2636.



Ionov, L.\*; Synytska, A.; Kaul, E.; Diez S. Protein-resistant polymer coatings based on surface-adsorbed poly(aminoethyl methacrylate)/poly(ethylene glycol) copolymers, **Biomacromolecules** 2010, 11 (1), 233-237.

Ionov, L.\*; Diez S. Environment-friendly photolithography using poly-(N-isopropylacrylamide)-based thermoresponsive photoresist, **Journal of American Chemical Society**, 2009 131(37), 13315-13319.

Ionov\*, L.; Bocharova, V.; Diez, S. Biotemplated synthesis of stimuli-responsive nanopatterned polymer brushes on microtubules, **Soft Matter** 2009, 5, 67 - 71.

Ionov\*, L.; Synytska A.; Diez S. Temperature-induced size-control of bioactive surface patterns, **Advanced Functional Materials** 2008, 18, 1501-1507.

Synytska, A; Stamm, M.; Diez, S.; Ionov, L.\* Simple and fast method for the fabrication of switchable bicomponent micro-patterned polymer surfaces, **Langmuir** 2007, 23(9), 5205-5209.

Ionov, L.; Stamm, M.; Diez, S.\* Reversible switching of microtubule motility using thermoresponsive polymer surfaces, **Nano Letters** 2006, 6(9), 1982 - 1987.

Ionov, L.\*; Sapra, S.; Synytska, A; Rogach, A. L.; Stamm, M.; Diez, S.\* Fast and spatially resolved environmental sensing using grafted composite layers of stimuli-responsive polymers and semiconductor nanocrystals, **Advanced Materials** 2006, 18(11), 1453-1457.

Ionov, L.; Stamm, M.; Diez, S.\* Size sorting of protein assemblies using polymeric gradient surfaces, **Nano Letters** 2005, 5(10), 1910-1914.

\* - Corresponding author

## 9. REFERENCES

1. R. McBeath, D. M. Pirone, C. M. Nelson, K. Bhadriraju and C. S. Chen, *Dev Cell*, 2004, **6**, 483-495.
2. C. S. Chen, M. Mrksich, S. Huang, G. M. Whitesides and D. E. Ingber, *Science*, 1997, **276**, 1425-1428.
3. G. M. Whitesides and B. Grzybowski, *Science*, 2002, **295**, 2418-2421.
4. T. G. Leong, A. M. Zarafshar and D. H. Gracias, *Small*, 2010, **6**, 792-806.
5. M. J. Harrington, K. Razghandi, F. Ditsch, L. Guiducci, M. Rueggeberg, J. W. C. Dunlop, P. Fratzl, C. Neinhuis and I. Burgert, *Nat Commun*, 2011, **2**, 337.
6. J. W. C. Dunlop, R. Weinkamer and P. Fratzl, *Mater Today*, 2011, **14**, 70-78.
7. J. M. Skotheim and L. Mahadevan, *Science*, 2005, **308**, 1308-1310.
8. L. Ionov, *Soft Matter*, 2011, **7**, 6786-6791.
9. E. Menard, M. A. Meitl, Y. Sun, J. U. Park, D. J. L. Shir, Y. S. Nam, S. Jeon and J. A. Rogers, *Chem. Rev.*, 2007, **107**, 1117-1160.
10. W. S. Beh, I. T. Kim, D. Qin, Y. N. Xia and G. M. Whitesides, *Adv. Mater.*, 1999, **11**, 1038-1041.
11. L. Ionov, S. Minko, M. Stamm, J. F. Gohy, R. Jerome and A. Scholl, *J. Am. Chem. Soc.*, 2003, **125**, 8302-8306.
12. A. Synytska, M. Stamm, S. Diez and L. Ionov, *Langmuir*, 2007, **23**, 5205-5209.
13. M. Geissler and Y. N. Xia, *Adv. Mater.*, 2004, **16**, 1249-1269.
14. R. K. Smith, P. A. Lewis and P. S. Weiss, *Progress in Surface Science*, 2004, **75**, 1-68.
15. A. Ulman, *Chem. Rev.*, 1996, **96**, 1533-1554.
16. Y. N. Xia and G. M. Whitesides, *Angew Chem Int Edit*, 1998, **37**, 551-575.
17. B. Zhao and W. J. Brittain, *Progress in Polymer Science*, 2000, **25**, 677-710.
18. L. Ionov, N. Houbenov, A. Sidorenko, M. Stamm and S. Minko, *Advanced Functional Materials*, 2006, **16**, 1153-1160.
19. B. Zhao, J. S. Moore and D. J. Beebe, *Science*, 2001, **291**, 1023-1026.
20. H. Sato and T. Homma, *Journal of Nanoscience and Nanotechnology*, 2007, **7**, 225-231.
21. A. Boker, J. He, T. Emrick and T. P. Russell, *Soft Matter*, 2007, **3**, 1231-1248.
22. A. Revzin, R. J. Russell, V. K. Yadavalli, W. G. Koh, C. Deister, D. D. Hile, M. B. Mellott and M. V. Pishko, *Langmuir*, 2001, **17**, 5440-5447.
23. L. Ionov, A. Synytska and S. Diez, *Adv. Funct. Mater.*, 2008, **18**, 1501-1508.
24. D. Falconnet, G. Csucs, H. M. Grandin and M. Textor, *Biomaterials*, 2006, **27**, 3044-3063.
25. M. J. Dalby, N. Gadegaard, R. Tare, A. Andar, M. O. Riehle, P. Herzyk, C. D. W. Wilkinson and R. O. C. Oreffo, *Nature Materials*, 2007, **6**, 997-1003.
26. D. C. Duffy, J. C. McDonald, O. J. A. Schueller and G. M. Whitesides, *Analytical Chemistry*, 1998, **70**, 4974-4984.
27. A. S. Blawas and W. M. Reichert, *Biomaterials*, 1998, **19**, 595-609.
28. S. Kaihara, J. Borenstein, R. Koka, S. Lalan, E. R. Ochoa, M. Ravens, H. Pien, B. Cunningham and J. P. Vacanti, *Tissue Eng*, 2000, **6**, 105-117.
29. A. Khademhosseini, R. Langer, J. Borenstein and J. P. Vacanti, *Proc. Natl. Acad. Sci. U. S. A.*, 2006, **103**, 2480-2487.
30. A. Folch and M. Toner, *Annual Review of Biomedical Engineering*, 2000, **2**, 227-+.
31. N. Li, A. Tourovskaia and A. Folch, *Critical Reviews™ in Biomedical Engineering*, 2003, **31**, 423-488.
32. S. Raghavan and C. S. Chen, *Advanced Materials*, 2004, **16**, 1303-1313.
33. N. Sniadecki, R. A. Desai, S. A. Ruiz and C. S. Chen, *Annals of Biomedical Engineering*, 2006, **34**, 59-74.
34. A. Sidorenko, T. Krupenkin, A. Taylor, P. Fratzl and J. Aizenberg, *Science*, 2007, **315**, 487-490.
35. R. D. Allen, *Journal of Photopolymer Science and Technology*, 2007, **20**, 453-455.

36. M. Yamaguchi, O. Nishimura, S. H. Lim, K. Shimokawa, T. Tamura and M. Suzuki, *Colloids and Surfaces a-Physicochemical and Engineering Aspects*, 2006, **284**, 532-534.
37. J. M. Slocik, E. R. Beckel, H. Jiang, J. O. Enlow, J. S. Zabinski, T. J. Bunning and R. R. Naik, *Advanced Materials*, 2006, **18**, 2095-+.
38. J. M. Jung, K. Y. Kwon, T. H. Ha, B. H. Chung and H. T. Jung, *Small*, 2006, **2**, 1010-1015.
39. A. Tinazli, J. Piehler, M. Beuttler, R. Guckenberger and R. Tampe, *Nat Nano*, 2007, **2**, 220-225.
40. H. Z. C. A. M. David S. Ginger, *Angewandte Chemie International Edition*, 2004, **43**, 30-45.
41. R. D. Piner, J. Zhu, F. Xu, S. H. Hong and C. A. Mirkin, *Science*, 1999, **283**, 661-663.
42. Y. N. Xia, J. A. Rogers, K. E. Paul and G. M. Whitesides, *Chem. Rev.*, 1999, **99**, 1823-1848.
43. M. A. Holden and P. S. Cremer, *J. Am. Chem. Soc.*, 2003, **2003**, 8074-8075.
44. K. E. Gerhardt, M. I. Wilson and B. M. Greenberg, *Photochemistry and photobiology*, 2005, **81**, 1061-1068.
45. S. Yamada, T. Mrozek, T. Rager, J. Owens, J. Rangel, C. G. Willson and J. Byers, *Macromolecules*, 2004, **37**, 377-384.
46. S. Trakhtenberg, J. C. Warner, R. Nagarajan, F. F. Bruno, L. A. Samuelson and J. Kumar, *Chemistry of Materials*, 2006, **18**, 2873-2878.
47. Q. H. Lin, T. Steinhausler, L. Simpson, M. Wilder, D. R. Medeiros, C. G. Willson, J. Havard and J. M. J. Frechet, *Chemistry of Materials*, 1997, **9**, 1725-1730.
48. J. Doh and D. J. Irvine, *J. Am. Chem. Soc.*, 2004, **126**, 9170-9171.
49. J. Doh and D. J. Irvine, *Proc. Natl. Acad. Sci. U. S. A.*, 2006, **103**, 5700-5705.
50. J. S. Katz, J. Doh and D. J. Irvine, *Langmuir*, 2006, **22**, 353-359.
51. G. P. Chen, Y. Ito, Y. Imanishi, A. Magnani, S. Lamponi and R. Barbucci, *Bioconjugate Chem.*, 1997, **8**, 730-734.
52. Y. Ito, G. P. Chen and Y. Imanishi, *Biotechnol. Prog.*, 1996, **12**, 700-702.
53. M. D. Yan, S. X. Cai, M. N. Wybourne and J. F. W. Keana, *J. Am. Chem. Soc.*, 1993, **115**, 814-816.
54. I. Caelen, H. Gao and H. Sigrist, *Langmuir*, 2002, **18**, 2463-2467.
55. T. Wessa, M. Rapp and H. Sigrist, *Colloids and Surfaces B-Biointerfaces*, 1999, **15**, 139-146.
56. Y. Chevolot, O. Bucher, D. Leonard, H. J. Mathieu and H. Sigrist, *Bioconjugate Chem.*, 1999, **10**, 169-175.
57. M. Sanger and H. Sigrist, *Sens. Actuator A-Phys.*, 1995, **51**, 83-88.
58. J. F. Clemence, J. P. Ranieri, P. Aebischer and H. Sigrist, *Bioconjugate Chem.*, 1995, **6**, 411-417.
59. G. Sundarababu, H. Gao and H. Sigrist, *Photochem. Photobiol.*, 1995, **61**, 540-544.
60. E. Delamarche, G. Sundarababu, H. Biebuyck, B. Michel, C. Gerber, H. Sigrist, H. Wolf, H. Ringsdorf, N. Xanthopoulos and H. J. Mathieu, *Langmuir*, 1996, **12**, 1997-2006.
61. G. Dorman and G. D. Prestwich, *Biochemistry*, 1994, **33**, 5661-5673.
62. G. Dorman and G. D. Prestwich, *Trends in Biotechnology*, 2000, **18**, 64-77.
63. X. H. Liu, H. K. Wang, J. N. Herron and G. D. Prestwich, *Bioconjugate Chem.*, 2000, **11**, 755-761.
64. L. F. Rozsnyai, D. R. Benson, S. P. A. Fodor and P. G. Schultz, *Angew. Chem.-Int. Edit. Engl.*, 1992, **31**, 759-761.
65. M. Nakagawa and K. Ichimura, *Colloid Surface A*, 2002, **204**, 1-7.
66. D. Leipert, P. Heiduschka, J. Mack, H. J. Egelhaaf, D. Oelkrug and G. Jung, *Angew Chem Int Edit*, 1998, **37**, 2338-2340.
67. S. P. A. Fodor, J. L. Read, M. C. Pirrung, L. Stryer, A. T. Lu and D. Solas, *Science*, 1991, **251**, 767-773.
68. S. P. A. Fodor, *Science*, 1997, **278**, 1551-1551.

69. A. S. Blawas, T. F. Oliver, M. C. Pirrung and W. M. Reichert, *Langmuir*, 1998, **14**, 4243-4250.
70. Z. P. Yang, W. Frey, T. Oliver and A. Chilkoti, *Langmuir*, 2000, **16**, 1751-1758.
71. D. J. Pritchard, H. Morgan and J. M. Cooper, *Analytical Chemistry*, 1995, **67**, 3605-3607.
72. M. Hengsakul and A. E. G. Cass, *Bioconjugate Chem.*, 1996, **7**, 249-254.
73. J. Edahiro, K. Sumaru, Y. Tada, K. Ohi, T. Takagi, M. Kameda, T. Shinbo, T. Kanamori and Y. Yoshimi, *Biomacromolecules*, 2005, **6**, 970-974.
74. A. Higuchi, A. Hamamura, Y. Shindo, H. Kitamura, B. O. Yoon, T. Mori, T. Uyama and A. Umezawa, *Biomacromolecules*, 2004, **5**, 1770-1774.
75. J. Nakanishi, Y. Kikuchi, T. Takarada, H. Nakayama, K. Yamaguchi and M. Maeda, *Journal of the American Chemical Society*, 2004, **126**, 16314-16315.
76. H. S. Lim, J. T. Han, D. Kwak, M. H. Jin and K. Cho, *Journal of the American Chemical Society*, 2006, **128**, 14458-14459.
77. C. Zhao, I. Witte and G. Wittstock, *Angewandte Chemie-International Edition*, 2006, **45**, 5469-5471.
78. H. Kaji, M. Kanada, D. Oyamatsu, T. Matsue and M. Nishizawa, *Langmuir*, 2004, **20**, 16-19.
79. H. Kaji, K. Tsukidate, T. Matsue and M. Nishizawa, *Journal of the American Chemical Society*, 2004, **126**, 15026-15027.
80. X. Y. Jiang, R. Ferrigno, M. Mrksich and G. M. Whitesides, *Journal of the American Chemical Society*, 2003, **125**, 2366-2367.
81. B. Zhao, J. S. Moore and D. J. Beebe, *Science*, 2001, **291**, 1023-1026.
82. S. Sotiropoulou, Y. Sierra-Sastre, S. S. Mark and C. A. Batt, *Chemistry of Materials*, 2008, **20**, 821-834.
83. C. Reuther, L. Hajdo, R. Tucker, A. A. Kasprzak and S. Diez, *Nano Letters*, 2006, **6**, 2177-2183.
84. Z. Niu, J. Liu, L. A. Lee, M. A. Bruckman, D. Zhao, G. Koley and Q. Wang, *Nano Letters*, 2007, **7**, 3729-3733.
85. M. Young, D. Willits, M. Uchida and T. Douglas, *Annual Review of Phytopathology*, 2008, **46**, 361-384.
86. P. W. K. Rothmund, *Nature*, 2006, **440**, 297-302.
87. C. Brunner, C. Wahnes and V. Vogel, *Lab Chip*, 2007, **7**, 1263-1271.
88. S. Behrens, K. Rahn, W. Habicht, K. J. Bohm, H. Rosner, E. Dinjus and E. Unger, *Advanced Materials*, 2002, **14**, 1621-1625.
89. S. Hiyama, T. Inoue, T. Shima, Y. Moritani, T. Suda and K. Sutoh, *Small*, 2008, **4**, 410-415.
90. M. Platt, G. Muthukrishnan, W. O. Hancock and M. E. Williams, *Journal of the American Chemical Society*, 2005, **127**, 15686-15687.
91. G. D. Bachand, S. B. Rivera, A. K. Boal, J. Gaudioso, J. Liu and B. C. Bunker, *Nano Letters*, 2004, **4**, 817-821.
92. L. Ionov, M. Stamm and S. Diez, *Nano Lett.*, 2006, **6**, 1982-1987.
93. F.-U. Gast, P. S. Dittrich, P. Schwill, M. Weigel, M. Mertig, J. Opitz, U. Queitsch, S. Diez, B. Lincoln, F. Wottawah, S. Schinkinger, J. Guck, J. Käs, J. Smolinski, K. Salchert, C. Werner, C. Duschl, M. S. Jäger, K. Uhlig, P. Geggier and S. Howitz, *Microfluid Nanofluid*, 2006, **2**, 21-36.
94. M. G. L. van den Heuvel, M. P. De Graaff and C. Dekker, *Science*, 2006, **312**, 910-914.
95. B. M. Hutchins, M. Platt, W. O. Hancock and M. E. Williams, *Small*, 2007, **3**, 126-131.
96. R. Tucker, P. Katira and H. Hess, *Nano Letters*, 2008, **8**, 221-226.
97. L. Ionov, V. Bocharova and S. Diez, *Soft Matter*, 2009, **5**, 67-71.
98. S. Morita, F. Tsunomori and H. Ushiki, *European Polymer Journal*, 2002, **38**, 1863.
99. M. Kaholek, W. K. Lee, S. J. Ahn, H. W. Ma, K. C. Caster, B. LaMattina and S. Zauscher, *Chemistry of Materials*, 2004, **16**, 3688-3696.

100. J. Hyun, W. K. Lee, N. Nath, A. Chilkoti and S. Zauscher, *Journal of the American Chemical Society*, 2004, **126**, 7330-7335.
101. F. Zhou, Z. Zheng, B. Yu, W. Liu and W. T. S. Huck, *J. Am. Chem. Soc.*, 2006, **128**, 16253-16258.
102. F. J. Xu, Y. Song, Z. P. Cheng, X. L. Zhu, C. X. Zhu, E. T. Kang and K. G. Neoh, *Macromolecules*, 2005, **38**, 6254-6258.
103. Y. Liu, V. Klep and I. Luzinov, *J. Am. Chem. Soc.*, 2006, **128**, 8106-8107.
104. K. Yu, Y. Cong, J. Fu, R. B. Xing, N. Zhao and Y. C. Han, *Surf Sci*, 2004, **572**, 490-496.
105. L. Ionov, S. Minko, M. Stamm, J. F. Gohy, R. Jerome and A. Scholl, *J. Am. Chem. Soc.*, 2003, **125**, 8302-8306.
106. L. J. Feng Zhou, Weimin Liu, Qunji Xue, *Macromol Rapid Comm*, 2004, **25**, 1979-1983.
107. O. Prucker, J. Habicht, I. J. Park and J. Ruhe, *Mat Sci Eng C-Bio S*, 1999, **8-9**, 291-297.
108. K. S. Iyer, B. Zdyrko, H. Malz, J. Pionteck and I. Luzinov, *Macromolecules*, 2003, **36**, 6519-6526.
109. G. Tao, A. Gong, J. Lu, H.-J. Sue and D. E. Bergbreiter, *Macromolecules*, 2001, **34**, 7672-7679.
110. J. D. Debord and L. A. Lyon, *Langmuir*, 2003, **19**, 7662-7664.
111. A. Lambacher and P. Fromherz, *Appl. Phys. A.*, 1996, **63**, 207-216.
112. J. Kerssemakers, J. Howard, H. Hess and S. Diez, *Proceedings of the National Academy of Sciences of the United States of America*, 2006, **103**, 15812-15817.
113. L. Ionov, S. Sapra, A. Synytska, A. L. Rogach, M. Stamm and S. Diez, *Adv. Mater.*, 2006, **18**, 1453-+.
114. Y. Kaizuka and J. T. Groves, *Biophysical Journal*, 2004, **86**, 905-912.
115. J. Opitz, F. Braun, R. Seidel, W. Pompe, B. Voit and M. Mertig, *Nanotechnology*, 2004, **15**, 717-723.
116. L. Ionov and S. Diez, *J. Am. Chem. Soc.*, 2009, **131**, 13315-13319.
117. Warm buffer was used to prevent further pattern development.
118. L. Ionov, M. Stamm and S. Diez, *Nano letters*, 2006, **6**, 1982-1987.
119. D. L. Huber, R. P. Manginell, M. A. Samara, B.-I. Kim and B. C. Bunker, *Science*, 2003, **301**, 352-354.
120. G. H. Kwon, Y. Y. Choi, J. Y. Park, D. H. Woo, K. B. Lee, J. H. Kim and S.-H. Lee, *Lab Chip*, 2010, **10**, 1604-1610.
121. C. Ohm, M. Brehmer and R. Zentel, *Adv. Mater.*, 2010, **22**, 3366-3387.
122. Y. Klein, E. Efrati and E. Sharon, *Science*, 2007, **315**, 1116-1120.
123. F. Zhou, P. M. Biesheuvel, E. Y. Chol, W. Shu, R. Poetes, U. Steiner and W. T. S. Huck, *Nano Lett.*, 2008, **8**, 725-730.
124. M. Behl, M. Y. Razzaq and A. Lendlein, *Adv. Mater.*, 2010, **22**, 3388-3410.
125. S. Timoshenko, *J. Opt. Soc. Am. Rev. Sci. Instrum.*, 1925, **11**, 233-255.
126. E. H. Mansfield, *Proc. R. Soc. A*, 1962, **268**, 316-237.
127. E. H. Mansfield, *Proc. R. Soc. A*, 1965, **288**, 396-417.
128. L. B. Freund, *J Mech Phys Solids*, 2000, **48**, 1159-1174.
129. S. Alben, B. Balakrisnan and E. Smela, *Nano Lett.*, 2011, **11**, 2280-2285.
130. I. S. Chun, A. Challa, B. Derickson, K. J. Hsia and X. Li, *Nano Lett.*, 2010, **10**, 3927-3932.
131. P. Cendula, S. Kiravittaya, I. Monch, J. Schumann and O. G. Schmidt, *Nano Lett.*, 2011, **11**, 236-240.
132. P. D. Topham, J. R. Howse, C. J. Crook, S. P. Armes, R. A. L. Jones and A. J. Ryan, *Macromolecules*, 2007, **40**, 4393.
133. S. Saha, D. Copic, S. Bhaskar, N. Clay, A. Donini, A. J. Hart and J. Lahann, *Angew Chem Int Edit*, 2012, **51**, 660-665.
134. K. J. Lee, J. Yoon, S. Rahmani, S. Hwang, S. Bhaskar, S. Mitragotri and J. Lahann, *Proc. Natl. Acad. Sci. U. S. A.*, 2012, **109**, 16057-16062.



135. K. K. Westbrook and H. J. Qi, *J. Intell. Mater. Syst. Struct.*, 2008, **19**, 597-607.
136. Z. B. Hu, X. M. Zhang and Y. Li, *Science*, 1995, **269**, 525-527.
137. S. Zakharchenko, N. Pureskiy, G. Stoychev, M. Stamm and L. Ionov, *Soft Matter*, 2010, **6**, 2633-2636.
138. V. Luchnikov, O. Sydorenko and M. Stamm, *Adv. Mater.*, 2005, **17**, 1177-1182.
139. J. Kim, J. A. Hanna, R. C. Hayward and C. D. Santangelo, *Soft Matter*, 2012, **8**, 2375-2381.
140. K. Kalaitzidou and A. J. Crosby, *Appl Phys Lett*, 2008, **93**, 041910
141. B. Simpson, G. Nunnery, R. Tannenbaum and K. Kalaitzidou, *J. Mater. Chem.*, 2010, **20**, 3496-3501.
142. H. Y. He, J. J. Guan and J. L. Lee, *J. Control. Release*, 2006, **110**, 339-346.
143. J. J. Guan, H. Y. He, L. J. Lee and D. J. Hansford, *Small*, 2007, **3**, 412-418.
144. J. J. Guan, H. Y. He, D. J. Hansford and L. J. Lee, *J Phys Chem B*, 2005, **109**, 23134-23137.
145. G. Stoychev, N. Pureskiy and L. Ionov, *Soft Matter*, 2011, **7**, 3277-3279
146. K.-U. Jeong, J.-H. Jang, D.-Y. Kim, C. Nah, J. H. Lee, M.-H. Lee, H.-J. Sun, C.-L. Wang, S. Z. D. Cheng and E. L. Thomas, *J. Mater. Chem.*, 2011, **21**, 6824-6830.
147. A. Azam, K. E. Laflin, M. Jamal, R. Fernandes and D. H. Gracias, *Biomed. Microdevices*, 2011, **13**, 51-58.
148. N. Bassik, B. T. Abebe, K. E. Laflin and D. H. Gracias, *Polymer*, 2010, **51**, 6093-6098.
149. K. E. Laflin, C. J. Morris, T. Muqem and D. H. Gracias, *Appl Phys Lett*, 2012, **101**, 131901
150. N. Bassik, A. Brafman, A. M. Zarafshar, M. Jamal, D. Luvsanjav, F. M. Selaru and D. H. Gracias, *J. Am. Chem. Soc.*, 2010, **132**, 16314-16317.
151. G. Stoychev, S. Zakharcheko, S. Turcaud, J. W. C. Dunlop and L. Ionov, *submitted*.
152. D. H. Gracias, V. Kavthekar, J. C. Love, K. E. Paul and G. M. Whitesides, *Adv. Mater.*, 2002, **14**, 235-238.
153. K. Kumar, B. Nandan, V. Luchnikov, F. Simon, A. Vyalikh, U. Scheler and M. Stamm, *Chem. Mat.*, 2009, **21**, 4282-4287.
154. K. Kumar, V. Luchnikov, B. Nandan, V. Senkovskyy and M. Stamm, *Eur. Polym. J.*, 2008, **44**, 4115-4121.
155. T. S. Kelby, M. Wang and W. T. S. Huck, *Adv. Funct. Mater.*, 2011, **21**, 652-657.
156. T. S. Shim, S.-H. Kim, C.-J. Heo, H. C. Jeon and S.-M. Yang, *Angewandte Chemie International Edition*, 2011, **51**, 1420..
157. S. Singamaneni, M. E. McConney and V. V. Tsukruk, *Adv. Mater.*, 2010, **22**, 1263-1268.
158. S. Singamaneni, M. E. McConney and V. V. Tsukruk, *ACS Nano*, 2010, **4**, 2327-2337.
159. T. Tanaka, M. Okayama, Y. Kitayama, Y. Kagawa and M. Okubo, *Langmuir*, 2010, **26**, 7843-7847.
160. T. G. Leong, B. R. Benson, E. K. Call and D. H. Gracias, *Small*, 2008, **4**, 1605-1609.
161. T. G. Leong, C. L. Randall, B. R. Benson, A. M. Zarafshar and D. H. Gracias, *Lab Chip*, 2008, **8**, 1621-1624.
162. T. G. Leong, C. L. Randall, B. R. Benson, N. Bassik, G. M. Stern and D. H. Gracias, *Proc. Natl. Acad. Sci. U. S. A.*, 2009, **106**, 703-708.
163. D. P. Holmes, M. Roche, T. Sinha and H. A. Stone, *Soft Matter*, 2011, **7**, 5188-5193.
164. E. Smela, O. Inganas and I. Lundstrom, *Science*, 1995, **268**, 1735-1738.
165. E. W. H. Jager, O. Inganas and I. Lundstrom, *Science*, 2000, **288**, 2335-2338.
166. A. W. Feinberg, A. Feigel, S. S. Shevkoplyas, S. Sheehy, G. M. Whitesides and K. K. Parker, *Science*, 2007, **317**, 1366-1370.
167. X. Zhang, C. L. Pint, M. H. Lee, B. E. Schubert, A. Jamshidi, K. Takei, H. Ko, A. Gillies, R. Bardhan, J. J. Urban, M. Wu, R. Fearing and A. Javey, *Nano Lett.*, 2011, **11**, 3239-3244.
168. Y. Liu, J. K. Boyles, J. Genzer and M. D. Dickey, *Soft Matter*, 2012, **8**, 1764-1769.

169. C. L. Randall, Y. V. Kalinin, M. Jamal, A. Shah and D. H. Gracias, *Nanomed-Nanotechnol*, 2011, **7**, 686-689.
170. C. L. Randall, Y. V. Kalinin, M. Jamal, T. Manohar and D. H. Gracias, *Lab Chip*, 2011, **11**, 127-131.
171. M. Jamal, N. Bassik, J. H. Cho, C. L. Randall and D. H. Gracias, *Biomaterials*, 2010, **31**, 1683-1690.
172. Y. V. Kalinin, J. S. Randhawa and D. H. Gracias, *Angew Chem Int Edit*, 2011, **50**, 2549-2553.
173. M. Jamal, A. M. Zarafshar and D. H. Gracias, *Nature Communications*, 2011, **2**.
174. A. Azam, K. Laflin, M. Jamal, R. Fernandes and D. Gracias, *Biomedical Microdevices*, 2010, 1-8.
175. S. Zakharchenko, E. Sperling and L. Ionov, *Biomacromolecules*, 2011, **12**, 2211–2215.
176. C. Low Kim, A. P. Wheeler and P. Koskan Larry, in *Hydrophilic Polymers*, American Chemical Society, 1996, pp. 99-111.
177. T. Klein, R.-J. Moritz and R. Graupner, *Polyaspartates and Polysuccinimide*, Wiley-VCH Verlag GmbH & Co. KGaA, 2000.
178. S. M. Thombre and B. D. Sarwade, *Journal of Macromolecular Science, Part A: Pure and Applied Chemistry*, 2005, **42**, 1299 - 1315.
179. V. Luchnikov and M. Stamm, *Physica E-Low-Dimensional Systems & Nanostructures*, 2007, **37**, 236-240.
180. G. Stoychev, S. Zakharchenko, S. Turcaud, J. W. C. Dunlop and L. Ionov, *ACS Nano*, 2012, **6**, 3925–3934.
181. G. Stoychev, S. Turcaud, J. W. C. Dunlop and L. Ionov, *Adv. Funct. Mater.*, **10.1002/adfm.201203245**.
182. M. J. Yaszemski, R. G. Payne, W. C. Hayes, R. Langer and A. G. Mikos, *Biomaterials*, 1996, **17**, 175-185.
183. H. Ma, J. Hu and P. X. Ma, *Adv. Funct. Mater.*, 2010, **20**, 2833-2841.
184. X. Hu, H. Shen, F. Yang, J. Bei and S. Wang, *Biomaterials*, 2008, **29**, 3128-3136.
185. L. R. Madden, D. J. Mortisen, E. M. Sussman, S. K. Dupras, J. A. Fugate, J. L. Cuy, K. D. Hauch, M. A. Laflamme, C. E. Murry and B. D. Ratner, *Proc. Natl. Acad. Sci. U. S. A.*, 2010.
186. G. C. Engelmayer, M. Y. Cheng, C. J. Bettinger, J. T. Borenstein, R. Langer and L. E. Freed, *Nat. Mater.*, 2008, **7**, 1003-1010.
187. H. Kenar, G. T. Kose, M. Toner, D. L. Kaplan and V. Hasirci, *Biomaterials*, 2011, **32**, 5320-5329.
188. D. Yucel, G. T. Kose and V. Hasirci, *Biomacromolecules*, 2010, **11**, 3584-3591.
189. J. Li, T. A. Rickett and R. Shi, *Langmuir*, 2008, **25**, 1813-1817.
190. P. X. Ma and R. Zhang, *J. Biomed. Mater. Res.*, 2001, **56**, 469-477.
191. L. M. Mathieu, T. L. Mueller, P. E. Bourban, D. P. Pioletti, R. Muller and J. A. E. Manson, *Biomaterials*, 2006, **27**, 905-916.
192. H. F. Zhang, I. Hussain, M. Brust, M. F. Butler, S. P. Rannard and A. I. Cooper, *Nat Mater*, 2005, **4**, 787-793.
193. H. Zhang and A. I. Cooper, *Adv. Mater.*, 2007, **19**, 1529-1533.
194. H. F. Zhang, J. Long and A. I. Cooper, *J. Am. Chem. Soc.*, 2005, **127**, 13482-13483.
195. S. Stokols and M. H. Tuszynski, *Biomaterials*, 2004, **25**, 5839-5846.
196. Y. Nakamichi, Y. Hirai, H. Yabu and M. Shimomura, *J. Mater. Chem.*, 2011, **21**, 3884-3889.
197. P. Greil, T. Lifka and A. Kaindl, *J. Eur. Ceram. Soc.*, 1998, **18**, 1961-1973.
198. B. Yuan, Y. Jin, Y. Sun, D. Wang, J. Sun, Z. Wang, W. Zhang and X. Jiang, *Adv. Mater.*, 2012, **24**, 890-896.
199. The amount of particles was taken with respect to cover 25-30% of outer surface of tubes.
200. S. Zakharchenko, N. Puretskiy, G. Stoychev, C. Waurisch, S. G. Hickey, A. Eychmuller, J.-U. Sommer and L. Ionov, *Journal of Materials Chemistry B*, 2013.

201. L. Onsager, *Ann. NY Acad. Sci.*, 1949, **51**, 627-659.
202. S. Pedron, S. van Lierop, P. Horstman, R. Penterman, D. J. Broer and E. Peeters, *Adv. Funct. Mater.*, 2011, **21**, 1624-1630.

## 10. APPENDIX

Ionov, L.

Biomimetic hydrogel-based actuating systems

***Advanced Functional Materials***, 2013, 23 (36), 4555–4570.



# Biomimetic Hydrogel-Based Actuating Systems

Leonid Ionov\*

Active motion is intrinsic to all kinds of living organisms from unicellular ones to humans and inspires development of synthetic actively moving materials. Hydrogels, which are three dimensional polymer networks imbibed with aqueous solutions, mimic the swelling/shrinking behavior of plant cells and produce macroscopic actuation upon swelling and shrinking. This Feature Article covers basic principles of design as well as recent advances in the development of hydrogel based actuating systems. It is discussed how simply swelling can be used to generate very complex multistep motion, which can be used to develop new optical devices, sensors, biomaterials, smart surface, etc.

hydrogels have found broad applications in the design of micromechanical and drug delivery systems, as well as for microfluidic devices and sensors (see recent reviews).<sup>[4b,6]</sup>

In the first part of the Feature Article (Section 2), a brief description of reversible mechanisms of movement in plants is given. Design and applications of hydrogel actuators based on principles of movement in plants and other more complex mechanisms of movement is discussed in the second part (Section 3).

## 1. Introduction

Active motion is intrinsic to all kinds of living organisms from unicellular ones to humans. In nature motion occurs on every scale of organization of organisms: from individual animals or their groups down to a single molecule. For example, motor proteins convert chemical energy directly into mechanical work and allow cell migration, division, sensing and adaptation.<sup>[1]</sup> Contrary to animals, where macroscopic movement is provided by cooperative nanoscale movement of motor proteins,<sup>[1a]</sup> motion in plants is provided by microscopic swelling of cells<sup>[2]</sup> (Figure 1a). In different schemes relatively slow swelling/shrinking can result in slow shape changes such as elongation, contraction, bending, twisting or fast snap-buckling and fracture-dominated movement that allow their rotation toward the sun, growth and dissemination of seeds.<sup>[2,3]</sup> Nature has many actuators, such as jellyfish, sea cucumbers, sea anemones, Venus flytraps, touch-me-nots, etc.

Hydrogels, which are three dimensional polymer networks imbibed with aqueous solutions, mimic the swelling/shrinking behavior of plant cells and produce macroscopic actuation upon swelling and shrinking (Figure 1b).<sup>[4]</sup> There are also many reports describing the design of hydrogels, which can swell and shrink in response to a change in light intensity, pH, temperature, biochemical processes, and electric and magnetic fields.<sup>[5]</sup> Exposure to one or multiple stimuli causes reversible contraction/swelling of hydrogels that is due to a change of interactions of the polymer molecules with water. The reversible changes in size and shape of

## 2. Reversible Movement of Plants

This section aims to give brief overview of mechanism of reversible movement in plants. The more detailed overviews of different mechanisms of movement of plants are given in recent reviews.<sup>[2,3,8]</sup> The irreversible movement due to growth of cells and disruption of tissues is not discussed.

Uptake and release of water is the main driving force of movement in plants. One aspect of this phenomenon is turgor pressure caused by osmotic flow of water in cells, which is due to concentration gradients (Figure 2a). In many cases, a whole organ is actuated by the changes in turgor pressure. Two prominent examples of rapid movements are the leaf folding of mimosa (*Mimosa pudica*) and of the Venus flytrap (*Dionaea muscipula*). Another aspect of swelling-driven deformation of plant tissues is swelling and shrinking of cell walls (Figure 2b). In this case, the directionality of deformation is controlled by orientation of cellulose fibers. The principle is based on the fact that the length of cellulose fibrils remains unchanged and swelling occurs preferentially in the direction perpendicular to the fibrils. A well-known example is the release of ripe seeds from conifer cones. The cones are formed by two kinds of tissues with different orientation of cellulose fibrils. As a result, length of one kind of the tissue and the width of another one increases in humid environments. This inhomogeneous increase in the volume results in opening of the cone.<sup>[9]</sup>

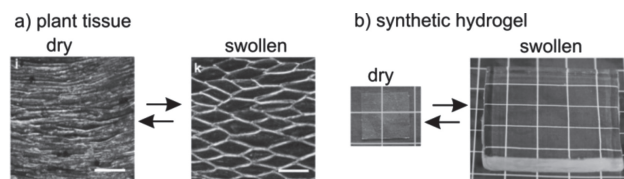


**Figure 1.** a) Reversible swelling of natural plant tissue of ice plant seed capsules. Reproduced with permission.<sup>[2a]</sup> Copyright 2011, Nature Publishing Group. b) Synthetic polymer hydrogel. Reproduced with permission.<sup>[7]</sup> Copyright 2011, American Chemical Society.

Dr. L. Ionov  
Leibniz Institute of Polymer Research Dresden  
Hohe Str. 6, D-01069 Dresden, Germany  
E-mail: ionov@ipfdd.de



DOI: 10.1002/adfm.201203692

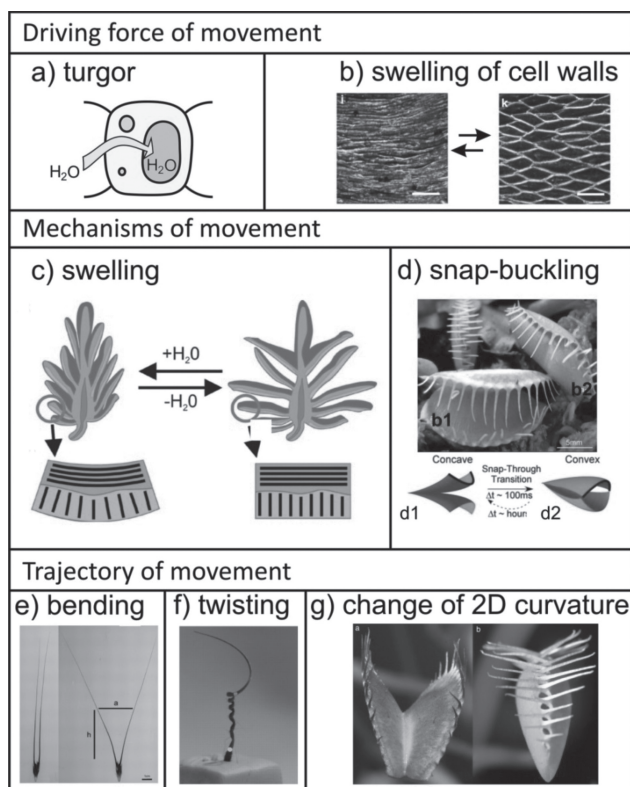


**Figure 2.** Summary of examples of reversible movement in plants with respect to driving force: a) turgor, b) swelling of cell walls; mechanism: c) swelling, d) snap-buckling; and trajectory: e) bending, f) twisting, g) change of 2D curvature of movement. b) Reproduced with permission.<sup>[2a]</sup> Copyright 2011, Nature Publishing Group; c) Reproduced with permission.<sup>[13]</sup> Copyright 2011, Elsevier; d) Reproduced with permission.<sup>[14]</sup> Copyright 2007, Wiley-VCH; e) Reproduced with permission.<sup>[3b]</sup> Copyright 2007, AAAS; f) Reproduced with permission.<sup>[12]</sup> Copyright 2011, The Company of Biologists Ltd; g) Reproduced with permission.<sup>[15]</sup> Copyright 2012, Elsevier.

It was observed that a change in the amount of water in plant tissues can result in relatively slow movement, such as in the case of cone, or can lead to extremely fast movement, such as in the case of Venus flytrap. The origin of the difference in the speed of actuation is the mechanism of the movement.<sup>[8]</sup> In the case of the cone, tissues with different orientation of cellulose fibrils act as classical bilayers, as described by Timoshenko:<sup>[10]</sup> an increase of the volume of one of the components results in bending (Figure 2c).<sup>[9]</sup> The geometry of the Venus flytrap is far more complex. The leaf has a doubly curved shape and a bistable configuration. Swelling of the cells results in snap-buckling transition from one stable state to another (Figure 2d).<sup>[11]</sup>

It was found that change of the amount of water in plant tissues can result in various shape changes. Wheat awn and pine cone bend when humidity changes that is used for burying itself and dissemination of seeds, respectively (Figure 2e).<sup>[3b,9]</sup> The filaree (*Erodium cicutarium*) seeds can bury themselves by drilling into the ground, twisting and untwisting in response to changes in humidity (Figure 2f).<sup>[12]</sup> The Venus flytrap changes its shape from double curved to another one that is used to trap insects (Figure 2g).<sup>[11]</sup>



**Leonid Ionov** came to Leibniz Institute of Polymer Research Dresden in 2009 as a group leader for stimuli-responsive interactive polymeric materials. After studying polymer chemistry at the Lomonosov Moscow State University/Russia and graduation at the Technical University Dresden he spent his post-doc at the Max Planck Institute of Molecular Cell and Biology

with Prof. S. Diez, working on biomolecular motors on responsive thin polymer films. He completed a research stay at the Clarkson University/USA with Prof. S. Minko working on biotechnology approaches. 2012 he was awarded with the Georg Meier Award of the GDCh (German Chemical Society). The research of Leonid Ionov is multi-disciplinary and exploratory positioned at the interface between synthetic polymer chemistry, physics and cell biology. His current focus lies on the design and self-assembly of functional stimuli-responsive polymeric materials and bio-active hydrogels.

### 3. Hydrogel-Based Moving Systems

This part of the article aims to discuss principles of design of actuating structures, based on reversible swelling/shrinking of stimuli-responsive hydrogels. Typically change of conditions such as temperature, pH, light, results in homogeneous expansion or contraction of hydrogels in all directions that is similar to swelling/shrinking of cells (Figure 3a). Complex deformation such as bending and twisting as well as even more complex folding is produced as a result of inhomogeneous expansion/shrinking, which occurs with different magnitudes in different directions<sup>[16]</sup> and can be achieved either (i) by applying inhomogeneous field, for example gradient of temperature or concentration, to homogeneous materials (Figure 3b) or (ii) by applying homogeneous field to inhomogeneous materials (Figure 3c). There is no known example in the plants,

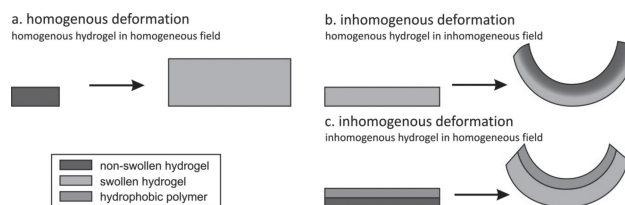


**Figure 3.** Different scenario of swelling of hydrogels: a) homogeneous deformation of homogeneous hydrogel; b) inhomogeneous deformation of homogeneous hydrogel; c) inhomogeneous deformation of inhomogeneous hydrogel

where applying an inhomogeneous field to homogeneous materials (Figure 3b) was used, because it is rather difficult to keep the concentration or temperature gradient constant. Nevertheless, this approach is included in the present article, since it is very important part of the field of hydrogel-based actuators. The plants typically form tissues with inhomogeneous properties (Figure 3c), which are used to produce complex movements such as bending or twisting.

### 3.1. Homogeneous Deformation of Hydrogels

#### 3.1.1. Microgels

In most cases swelling/shrinking results in a change of volume of the hydrogel object while the shape remains nearly the same; this is similar to the behavior of plant cells.<sup>[17]</sup> Homogeneous swelling, for example, is demonstrated by thermoresponsive poly(*N*-isopropylacrylamide)-based hydrogel micro- and nanoparticles. The microgel particles swell above the lower critical solution temperature (LCST) and shrink below the LCST. Homogeneous swelling of hydrogel microparticles can be used for a variety of applications. For example, reversible swelling and shrinking of thermoresponsive and pH-sensitive hydrogels was used as a mean for smart release of drugs.<sup>[18]</sup> The microgel particles, which have transition temperature of around 40 °C, are imbibed with water-soluble drug. The microgel particles are swollen at normal body temperature and the drug is not released. Since the inflammation induces a local increase in temperature, the drug-loaded microgel particles shrink at the point of inflammation which leads to the release of drugs.<sup>[19]</sup> Stimuli-responsive hydrogel microparticles can also be used as microlenses with tunable by external stimuli focal length.<sup>[20]</sup> Incorporation of gold or semiconductor nanoparticles in hydrogel particles, which are able to reversibly change their volume, can be used for design of hydrogel-based materials with tunable optical properties.<sup>[21]</sup> In this case, swelling and shrinking of hydrogel particles results in the change of aggregation/disaggregation of the incorporated nanoparticles that change their plasma resonance properties or fluorescence. Closely-packed homogeneous swelling hydrogel microparticles can also be used for design of photonic crystals with switchable optical properties.<sup>[22]</sup> Spherical particles form densely packed arrays, their periodicity being defined by the size of the particles and their reversible swelling/shrinking being responsible for changes in the periodicity of the lattice that results in the change of the wavelength of transmitted and reflected light. Different signals, such as mechanical treatment,<sup>[23]</sup> temperature,<sup>[22d]</sup> light, magnetic<sup>[24]</sup> and electric<sup>[25]</sup> fields were used as stimuli to switch optical properties. Notably, this mechanism of switching of periodicity is similar to the natural mechanism of the change in coloration of squid.<sup>[1e]</sup>

#### 3.1.2. Macroscopic Hydrogels

Large pieces of hydrogels demonstrate similar homogeneous swelling;<sup>[17a]</sup> the size of sample changes while the shape remains unchanged. The homogeneous swelling/shrinking

of macroscopic hydrogels was used to control the flow inside microfluidic devices.<sup>[26]</sup> The hydrogel acts as a smart valve, which allows the liquid to flow when the hydrogel is shrunk and closes the channel when swollen. There are many examples of such smart microfluidic valves sensitive to various signals, such as pH, temperature, enzyme, light and electric field.<sup>[27]</sup> For lab-on-a-chip applications, the use of light and electric field as stimuli hold the promise, since they allow switching with both high spatial and temporal resolution. For example, Richter and co-workers explored possibilities to control the liquid flow by stimuli-responsive hydrogels. In particular, they used hydrogels as pumps and gates, which control liquid flow in microfluidic devices.<sup>[28]</sup>

Swelling/shrinking of hydrogels can be used not only to affect optical properties that are perceived by visual sense but also to change topography that can be felt by touching. Very recently, Richer and co-workers reported design of palpable displays based on thermoresponsive hydrogels.<sup>[29]</sup> They integrated 4000 temperature-sensitive controlled actuators, each of them being heated by an individual electro-heating element. The designed hydrogel array was able to form a visual and palpable artificial imaging system.

Homogeneous swelling of macroscopic layers was also applied for the design of sensors.<sup>[30]</sup> One approach is based on the direct detection of changes in the hydrogel volume or mass. This, for example, can be done by ellipsometry, quartz microbalance (for hydrogel thin films) or scattering techniques (for hydrogel particles).<sup>[30,31]</sup> Another approach for design of hydrogel-based sensors is the incorporation of semiconductor or metal nanoparticles into the hydrogel matrix. In this case, particles serve as optically active probes. Contraction/swelling of hydrogels switches interactions between nanoparticles that results in the change of optical properties<sup>[17a,32]</sup>

Macroscopic hydrogels have been utilized for design of smart lenses with switchable focal length as well. In particular, adjustment of focal length by changing the curvature of the meniscus between water and oil by switching of the swelling of hydrogel was used to tune focal length of the optical lens.<sup>[33]</sup> The basic design (Figure 4) consists of a stimuli-responsive hydrogel ring placed within a microfluidic channel system and sandwiched between a glass plate and an aperture slit, the latter with an opening centered over the ring. The microchannels are filled with water and oil is placed on top of this structure and capped with a glass cover slip. The sidewall and bottom surface of the aperture are hydrophilic and the top surface is hydrophobic, which ensures that the water–oil meniscus is pinned along the hydrophobic–hydrophilic contact line. When exposed to an appropriate stimulus, the hydrogel ring underneath the aperture responds by expanding or shrinking. This leads to a change in the volume of the water droplet located in the middle of the ring. The net volume change—the change in the volume enclosed by the ring and the change in water droplet volume—causes a change in the pressure difference across the water/oil interface that directly determines the geometry of the liquid meniscus.

Homogeneous swelling/shrinking of macroscopic hydrogels can be used to change the shape of mammalian cells. For example, Pelah and co-workers have developed an approach to



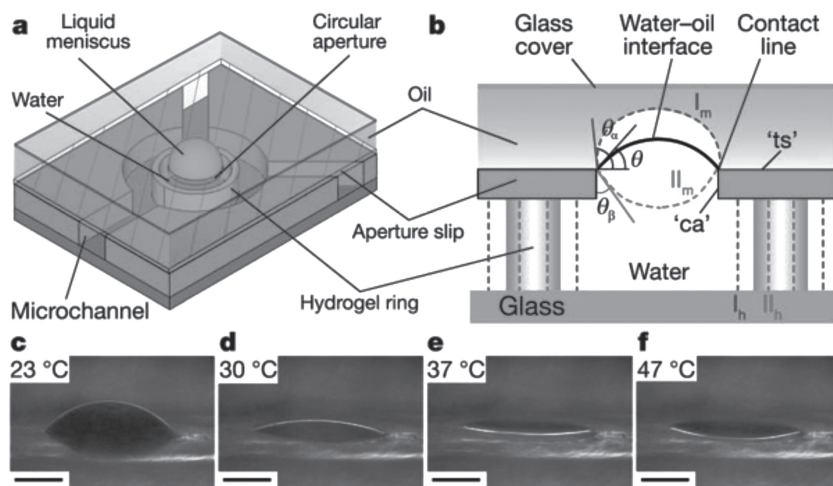


**Figure 4.** Design of smart lenses with switchable focal length using reversible swelling/shrinking of hydrogels. a) water/oil interface forms liquid microlens. Microchannels allow the flow of fluids to the microlens structure. b) Smart variable-focus mechanism. The hydrophilic sidewall and bottom surface ('ca') and hydrophobic top surface ('ts') of the aperture pin the water–oil meniscus along the contact line 'ca-ts'. The expansion and contraction of the hydrogel regulates the shape of the liquid meniscus by changing the angle  $\theta$  of the pinned water/oil interface. The blue dashed lines show the expanded state of the hydrogel ring ('l<sub>h</sub>') and the corresponding divergent microlens ('l<sub>m</sub>') at  $\theta = \theta_a$ . The red dashed lines show the contracted state of the hydrogel ring ('l<sub>h</sub>') and the corresponding convergent microlens ('l<sub>m</sub>') at  $\theta = -(90^\circ - \theta_b)$ . c–f) The shape of the liquid microlens varies with local environmental temperature. Scale bars: 1.0 mm. Reproduced with permission.<sup>[33]</sup> Copyright 2006, Nature Publishing Group.

reversibly deform cells using a thermoresponsive polymeric actuator,<sup>[34]</sup> which squeezes the cell from two sides. Since the behavior of cells (differentiation, growth, apoptosis) depends on geometrical constraints, one can expect that this actuator can be used to study cell responses on mechanical treatment. Langer and Khademhosseini used a similar approach for the

normal orientation of the bristles (**Figure 5**).<sup>[37]</sup> These hydrogel films were, in particular, used for the design of surfaces with “conventional” and “reverse” switching behavior. These surfaces revealed conventional switching—hydrophilic after exposure to water and hydrophobic after drying if the rods are fixed on the surfaces. They could achieve reverse switching—hydrophobic

after exposure to water and hydrophilic after drying—by using hydrogel films with non-fixed rods. The hydrogel-actuated hairs can further be used to control flow of reaction and to design really self-regulating systems. The idea is to fix a catalyst, which catalyzes certain chemical reactions, on the top of the hairs. Bending of the hairs changes the accessibility of the catalyst to the reagent in solution that affects the rate of chemical reactions. Use of thermoresponsive hydrogel coupled with the catalyst which catalyzes exothermic reaction allows for the design of self-regulating oscillating systems.<sup>[38]</sup>

**Summary:** The homogenous expansion/shrinking of hydrogels can be used for (i) controlled release of drugs, (ii) design of smart lenses with switchable focal length, (iii) design of materials with switchable coloration, (iv) control of flow in microfluidic devices, (v) design of sensors, (vi) control shape of cells and design complex 3D structures from cells, (vii) design of surfaces with switchable topography.

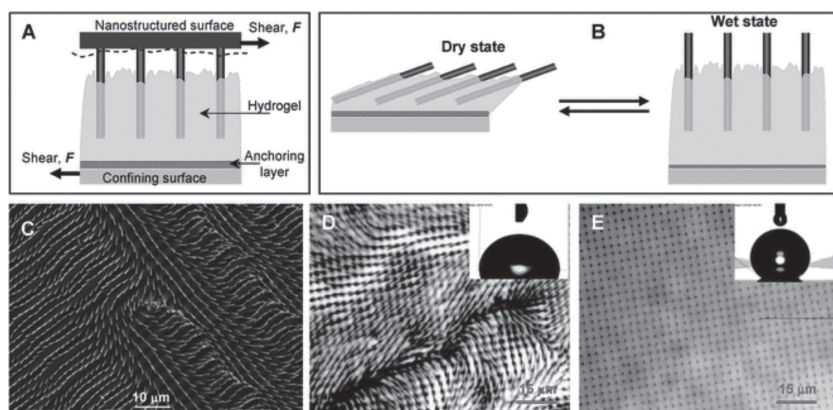


**Figure 5.** Gel-embedded array of rigid setae (GEARS) designed to provide a reverse response to exposure to water. a) Schematic of the setae transfer into the hydrogel layer attached to the confining solid surface modified with the PGMA anchoring layer upon in situ synthesis. b) Schematic illustration of the dynamic rearrangement of the GEARS in the dry and wet states. c) Representative SEM image of the GEARS bristle in the dry state. d) Optical microscopy analysis of the dry GEARS surface reveals highly tilted setae. The surface is relatively hydrophilic (d, inset). e) Optical microscopy analysis of the same region as in (d) in a humid atmosphere reveals setae standing perpendicular to the surface and its hydrophobic character (e, inset). Reproduced with permission.<sup>[37]</sup> Copyright 2008, Royal Society of Chemistry.

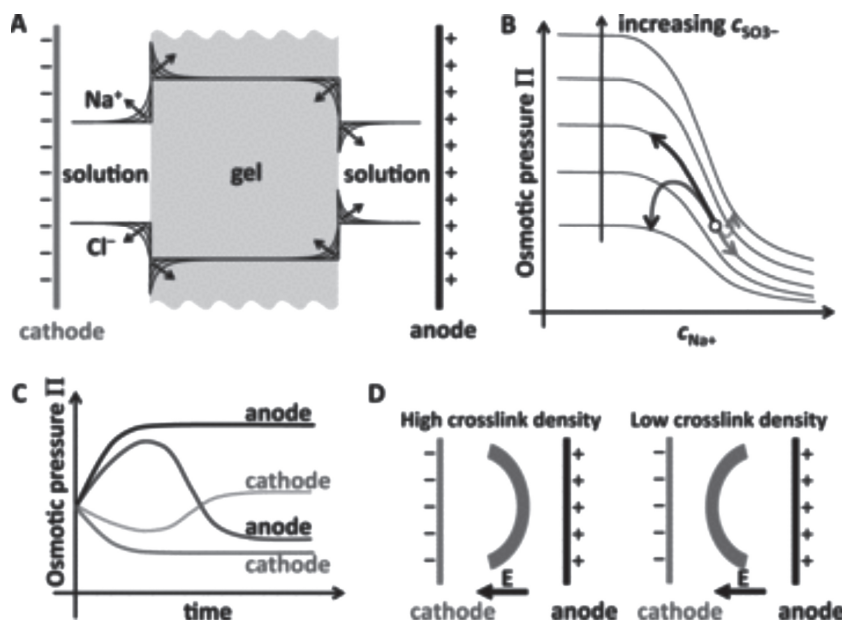


**Figure 6.** Theoretical concept behind unidirectional and bidirectional bending hydrogels. a) Expected accumulation of  $\text{Na}^+$  and depletion of  $\text{Cl}^-$  ions at the cathode-side hydrogel boundary and depletion of  $\text{Na}^+$  and accumulation of  $\text{Cl}^-$  ions at the anode-side hydrogel boundary with time. b) Variation of osmotic pressure with solution  $\text{Na}^+$  concentration for different concentrations of anionic groups ( $\text{SO}_3^-$ ) within the gel. Solid arrows indicate the anticipated (from Doi theory) monotonic swelling and shrinkage of a high crosslink density hydrogel at the anode (black) and cathode (gray) sides, respectively. Dashed arrows indicate the non-monotonic swelling behavior (from modification of Doi theory) expected from a low crosslink density hydrogel as a result of swelling and shrinkage of the gel causing large changes in the concentration of anionic groups within the gel. c) Time evolution of the osmotic pressure of a high and low crosslink hydrogels at the anode and cathode sides. Solid and dashed lines correspond to trajectories for high and low crosslink density hydrogels, respectively. d) Steady-state bent conformation of high and low-crosslink hydrogels predicted by our modified theory. Reproduced with permission.<sup>[46]</sup> Copyright 2011, Wiley-VCH.

### 3.2. Non-Homogeneous Deformation of Hydrogels

Non-homogeneous deformation (bending, twisting) could be achieved by applying either (i) an inhomogeneous field to homogeneous materials or (ii) homogeneous stimuli to inhomogeneous materials. An example of the first case is the bending of polyelectrolyte hydrogel in solution with lateral gradient of pH, which is formed during electrolysis<sup>[39]</sup> or PDMS strips with locally deposited solvent droplets.<sup>[40]</sup> Examples of the second group include bending of a liquid crystalline film,<sup>[41]</sup> hydrogel with a lateral gradient monomer concentration,<sup>[42]</sup> and cantilever sensors.<sup>[43]</sup>

#### 3.2.1. Homogeneous Hydrogels in an Inhomogeneous Field

There are no known examples of the use this principle of movement in plants. The main reason is that it is rather difficult to generate and maintain continuous gradients (gradient of pH, salt concentration or temperature). On the other hand, this approach for the design of actuators is discussed in this paper since this is widely used for design of synthetic actuators.

It is well known that a strip of an anionic hydrogel bends towards the cathode in an electric field.<sup>[44]</sup> Doi and co-workers have provided a comprehensive theory to explain this

behavior.<sup>[45]</sup> They predicted that the swelling behavior is governed by the concentration of the dominant ions and that the swelling speed is proportional to the square of the electric current.

Varghese and Arya have extended this theory in conceptual terms by relaxing one of its assumptions that the concentration of gel anionic groups remains constant during the bending process, which leads to a new scenario that the same anionic hydrogel can be made to bend in two different directions by changing its crosslink density.<sup>[46]</sup> They considered an anionic hydrogel poly (2-acryloylamido-2-methyl propane sulfonic acid) (PAMPS) containing  $\text{SO}_3^-$  within the electrolyte:  $\text{NaCl}$  solution. When an electric field is applied across the hydrogel,  $\text{Na}^+$  and  $\text{Cl}^-$  ions travel towards the cathode and the anode, respectively. The Doi theory shows that with time the interfacial concentration of  $\text{Na}^+$  will increase and decrease at the cathode and anode sides, respectively (Figure 6a). At the same time, the interfacial concentration of  $\text{Cl}^-$  will decrease and increase at the cathode and anode sides, respectively (Figure 6a). The theory also shows that for hydrogels with a fixed concentration of anionic groups ( $c_{\text{SO}_3^-}$ ) that are fully dissociated, the osmotic pressure ( $\Pi$ ) within the hydrogel decreases monotonically with increasing  $\text{Na}^+$  concentration ( $c_{\text{Na}^+}$ ) on the solution side, and that each  $\Pi$ - $c_{\text{Na}^+}$  plot (at fixed  $c_{\text{SO}_3^-}$ ) shifts upward with increasing  $c_{\text{SO}_3^-}$  (Figure 6b).

This implies that  $\Pi$  will increase at the anode side (due to decreasing  $c_{\text{Na}^+}$ ) and decrease at the cathode side (due to increasing  $c_{\text{Na}^+}$ ). The solid black and gray arrows in Figure 6b schematically depict one such trajectory of  $\Pi$  vs.  $c_{\text{Na}^+}$  at the two hydrogel interfaces, and the solid black and gray lines in Figure 6c show the corresponding  $\Pi$  vs. time behavior. Thus, the model explains how anionic hydrogels swell at the anode side and shrink at the cathode side causing it to bend towards the cathode (Figure 6d left).

Varghese and Arya showed that an anionic hydrogel could be designed to swell on the cathode side and shrink at the anode side such that it bends towards the anode, exactly opposite to the behavior described by the Doi theory. Indeed, such a hydrogel could be achieved if one realizes that hydrogel swelling at the anode side is also accompanied by a decrease in the effective concentration of anionic groups ( $c_{\text{SO}_3^-}$ ). Similarly, as the hydrogel shrinks at the cathode side, the effective concentration of anionic groups increases. This implies that the osmotic pressure trajectory at the anode side does not follow a single  $\Pi$ - $c_{\text{Na}^+}$  curve but instead moves downwards to lower  $\Pi$ - $c_{\text{Na}^+}$  curves corresponding to a smaller  $c_{\text{SO}_3^-}$  while climbing up each  $\Pi$ - $c_{\text{Na}^+}$  curve. Therefore, it is envisioned that if the change in  $c_{\text{SO}_3^-}$  is sufficiently large, the trajectory will exhibit a maximum in the  $\Pi$ - $c_{\text{Na}^+}$  plot and then dip downwards, as indicated by the black dashed arrow in Figure 6b and by the black dashed



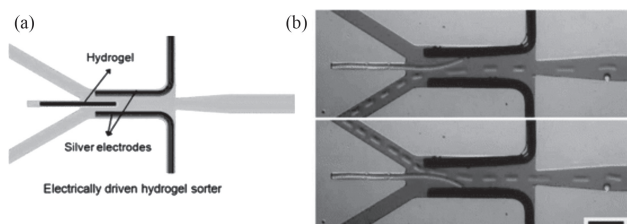


**Figure 7.** a) Schematic of the sorting device composed of three parts: an electrically-driven hydrogel sorter, a droplet generation channel, and a focused mEBs channel; b) Examples of droplet sorting (oil phase flow rate =  $2 \mu\text{L min}^{-1}$  and water phase flow rate =  $6 \mu\text{L min}^{-1}$ ). The scale bar indicates 1 mm. Reproduced with permission.<sup>[39]</sup> Copyright 2010, Royal Society of Chemistry.

line in Figure 6c. At the cathode side, the osmotic pressure trajectory will hop to higher  $\Pi$ - $c_{\text{Na}^+}$  curves due to the increase in  $c_{\text{SO}_3}$ . While climbing down each  $\Pi$ - $c_{\text{Na}^+}$  curve, allowing for the possibility of a reversal in the direction of  $\Pi$ , as indicated by the gray dashed arrow in Figure 5b and gray dashed line in Figure 6c. Depending on the conditions, the final location of the osmotic pressure at the anode side could end up lower than that at the cathode (Figure 6b,c), causing the gel to eventually bend towards the anode after transiently bending towards the cathode (Figure 6d, right).

Thus, it is expected lightly-crosslinked hydrogels to initially bend towards the cathode, then straighten out and eventually bend towards the anode (Figure 6d right). On the other hand, a highly crosslinked hydrogel that is relatively stiffer possesses little capacity to further swell or shrink in an electric field. The osmotic pressure of such a hydrogel would therefore be expected to exhibit the conventional monotonically increasing and decreasing osmotic pressure trajectory at the anode and cathode respectively, making the gel bend towards the cathode (Figure 6d left).

Bending of electroactive hydrogel strips in a microfluidic channel was applied to control flow as well as to sort particles and cells.<sup>[39]</sup> The hydrogel strip is integrated in a Y-junction and is able to bend either to one side or to another depending on the polarity of the applied voltage (Figure 7). It was demonstrated that the device is suitable for sorting mouse embryoid bodies (mEBs). The sorted and collected mEBs maintained pluripotency and selected mEBs successfully differentiated into three germ layers: endoderm, mesoderm, and ectoderm, thereby indicating the “biocompatibility” of the sorting device.

Non-homogenous swelling of polypyrrole-based films in humid air was used to make actuator which reversibly bends folds and form the tubes.<sup>[47]</sup> The actuator generates a contractile stress up to 27 MPa, lift objects 380 times heavier than itself, and transports cargo 10 times heavier than itself.

In these examples, bending occurred when an electric field was applied and repeatable changes in shape require applying of alternating electric field. Alternatively, cyclical changes in shape of a homogeneous hydrogel<sup>[48]</sup> can be achieved by using the Belousov–Zhabotinsky (BZ) reaction.<sup>[49]</sup> The BZ reaction is well known as a non-equilibrium dissipative reaction and generates autonomous oscillations in the redox potential that

changes the swelling properties of a hydrogel.<sup>[50]</sup> For example, Yoshida fabricated gels exhibiting autonomous peristaltic motion without external stimuli, prepared by copolymerizing temperature-responsive N-isopropylacrylamide with ruthenium tris(2,2'-bipyridine) ( $\text{Ru}(\text{bpy})_3$ ) as a catalyst for the BZ reaction and were used for directed particle transport.<sup>[51]</sup> BZ reaction results in local swelling of the hydrogel that changes with time. As a result, a moving wave of swollen hydrogel is formed. The wave provides peristaltic motion of the adsorbed microparticles. In another approach, Maeda fabricated a self-oscillating gel actuator without external stimuli by producing a gradient structure, which generates a pendulum motion by fixing one edge of the gel (Figure 8).<sup>[52]</sup>

**Summary:** It was observed that homogeneous hydrogels typical undergo simple bending, which is caused by a 1D gradient of fields (concentration or temperature). The reason for such relatively simple behavior is that it is rather difficult to form complex spatial gradient of concentration, which can, for example, cause twisting. More complex behavior can, in principle, be achieved using oscillating reactions.

### 3.2.2. Inhomogeneous Hydrogels in a Homogeneous Field

This principle of hydrogel-based actuators is inspired by the actuating behavior of pine cones, wheat awn and the Venus flytrap, which are built by materials with different swelling properties.

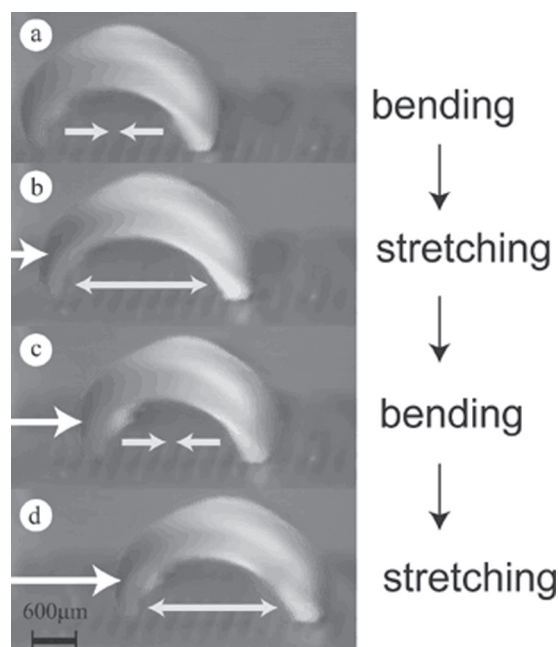


**Figure 8.** A gel actuator that can generate autonomous motility with a wormlike motion without external driving stimuli. The autonomous motion is produced by dissipating the chemical energy of an oscillating reaction occurring inside the gel. Even though the gel is completely composed of synthetic polymer, it shows an autonomous motion as if it were “alive”. By coupling this with a ratchet mechanism, the gel walks by repeatedly bending and stretching itself like a loop. Reproduced with permission.<sup>[52]</sup> Copyright 2007, Wiley-VCH.

**Rods:** The deformation of inhomogeneous materials has been known for a very long time and in 1925, Timoshenko<sup>[10]</sup> published a paper, which considered bending of a metal bilayer consisting of two metals with different thermal expansion coefficients. The deformation of non-hydrogel-based inhomogeneous inorganic materials is considered because the effects, which are produced by them, are similar to effects that can be achieved using hydrogels. Timoshenko assumed that the bilayer can bend in only one direction and results in a bilayer with uniform curvature:

$$\frac{1}{\rho} = \frac{6(\varepsilon_2 - \varepsilon_1)(1+m)^2}{h(3(1+m)^2 + (1+mn)(m^2 + \frac{1}{mn}))} \quad (1)$$

$$\frac{E_1}{E_2} = n \quad (2)$$

$$\frac{a_1}{a_2} = m \quad (3)$$

where  $E_x$  are the elasticity modulus,  $a_x$  are the thickness of the layers,  $h$  is the total thickness ( $h = a_1 + a_2$ ),  $\varepsilon$  is the stress of the films,  $\rho$  is the radius of curvature. From Equations (1–3), the radius of curvature is inversely proportional to the film stress. Moreover, the radius of curvature first decreases and then increases with the increase in  $m$ . The resultant curvature is not very sensitive to the difference in stiffness between the two layers and is mainly controlled by the actuation strain and the layer thickness.

Similar to bimetal strips, hydrogel-based ones consisting of two kinds of hydrogel rods are able to bend in different direction depending on the swelling properties of polymers (Figure 9).<sup>[53]</sup>

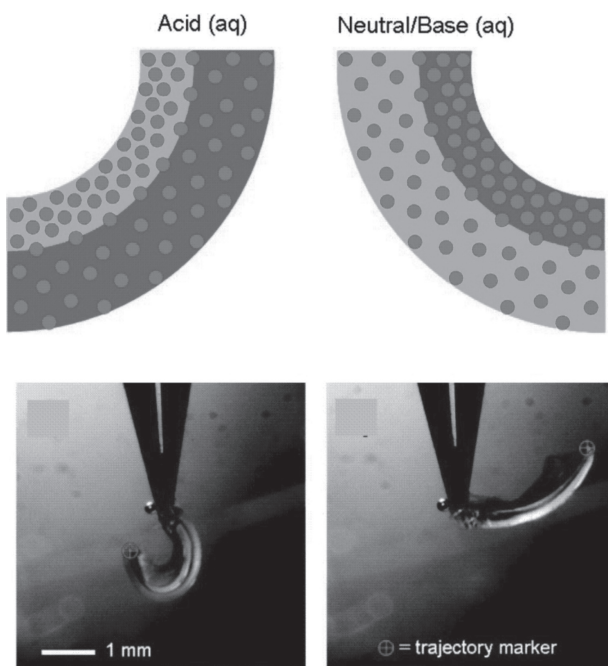


**Figure 9.** Bending of a biopolymer strip by positively and negatively charged polyelectrolytes. Reproduced with permission.<sup>[53a]</sup> Copyright 2007, American Chemical Society.

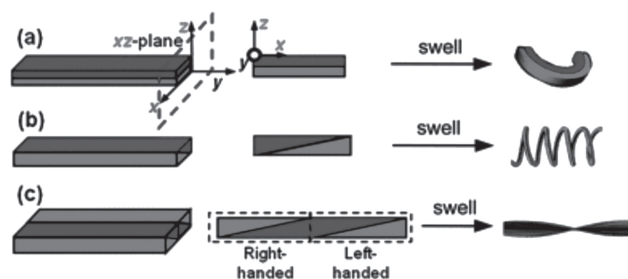


**Figure 10.** Schematic illustrations of a) bending, b) polypeptide -type twisting, c) DNA-type twisting actuators and d) formation of sharp hinges. Reproduced with permission.<sup>[55]</sup> Copyright 2011, Royal Society of Chemistry.

The first report of bending of a hydrogel bilayer rod, consisting of thermoresponsive part and non-thermoresponsive one, was published by Hu and co-workers in 1985.<sup>[54]</sup> They demonstrated that rods bend due to shrinking of thermoresponsive hydrogels when the temperature changes.

The bilayer rod with constant ratio between thicknesses of each layer along the sample bends in one direction (Figure 10a). By making a sloped bilayer structure, the planar structure described in Figure 10b can be bent along the  $y$ -axis as well as be twisted around this axis when one of the layers is asymmetrically expanded in a specifically selected solvent. When the bilayer actuating device with triangular layers with respect to the  $y$ -axis is swollen, a helical-type actuating sensor can be formed. A double twisted helical photonic actuator can be formed as shown in Figure 10c. The double twist actuating behavior is due to the competition of the twisting powers between the right-handed and the left-handed polypeptide-like helical structures.<sup>[55]</sup>

Turcaud and co-workers simulated deformation of rods with different geometry and asymmetry.<sup>[56]</sup> For constant cross-sections, it is possible to achieve planar bending (Figure 11a) or twisting when the material distribution breaks some of symmetry elements of the initial shape, preserving one mirror

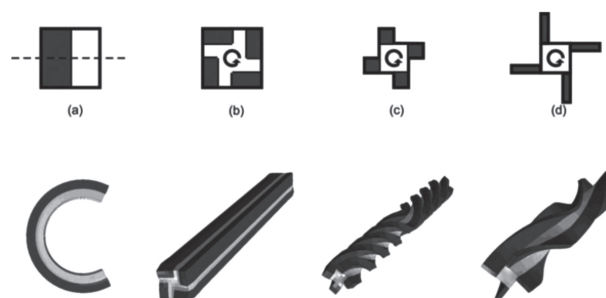


**Figure 11.** Simulated actuation for several cross-sections with passive/active areas ratio of 50:50: (from left to right). a) classical bilayer bending in its mirror plane; b) closed fourfold cross-section with bilayer repetitive unit cell remains straight; c) opened fourfold cross-section with bilayer repetitive unit cell shows huge twisting; d) opened fourfold cross-section with bigger moment of inertial shows less twisting than (c). Reproduced with permission.<sup>[56]</sup> Copyright 2011, Carl Hanser Verlag.

plane or one rotational axis. Twisting is more sensitive to other geometrical factors. In the case of compact cross-section (Figure 11b), no actual twisting is observed despite the fourfold rotational symmetry axis. However, the augmentation of free-border with the volume ratio of the two phases staying equal triggers twisting (Figure 11c). The moment of inertia of the cross-section relates inversely to the amount of twisting (Figure 11d). The eccentricity of the expanding region relative to the geometric centre of the cross-section is proportional to the degree of twisting.

**Bending of Hydrogel Films With Vertical Swelling Gradients:** Deformation of films is more complex than the deformation of rods. The Timoshenko equation applies to a beam bending in only one direction, does not predict the bending direction and is applicable for reversible elastic deformations. More recent models have considered complex bending of a bilayer in two dimensions. Mansfield found analytical solutions for large deflections of circular<sup>[57]</sup> and elliptical<sup>[58]</sup> plates having lenticular cross sections with a temperature gradient through the thickness. For small gradients, the plates formed spherical caps, curved equally in all directions. At a critical gradient, a configuration with greater curvature in one direction became more favorable. Because of the lens-shaped thickness profile, even though the elliptical plate had a major axis, it showed no preferred direction for bending even for large deflections. Freund determined the strain at which a spherical cap, formed by circular bilayer of uniform thickness, becomes unstable using low order polynomial solutions and finite element simulations.<sup>[59]</sup> Later Smela and co-workers showed that short-side bending of inorganic bilayer was preferred in the case of free homogeneous actuation and that this preference increased with aspect ratio (ratio of length to width of a rectangular pattern)<sup>[60]</sup> (Figure 12). Li and co-workers<sup>[61]</sup> and Schimdt<sup>[62]</sup> experimentally demonstrated the opposite scenario, namely a preference for long-side bending, in the case where bilayers are progressively etched from a substrate.

In inorganic bilayer systems, the active component undergoes relatively small volume changes or actuation strains, which are nearly homogeneous over the whole sample. Hydrogels, however, demonstrate considerably different properties. First, hydrogels undergo large volume changes (up to 10 times) upon swelling and contraction. Second, the swelling of a hydrogel is often kinetically limited: due to slow diffusion of water through a hydrogel, the parts which are closer to the edges swell first while the parts which are closer to the center of the films swell later.

It was found that when the radius of curvature is small, bending of the films leads to their folding and formation of 3D structures, such as tubes.<sup>[63]</sup> We investigated the bending/folding of rectangular stimuli-responsive hydrogel-based polymer bilayers with different aspect ratios and relative thicknesses placed on a substrate (Figure 13).<sup>[64]</sup> It was found that long-side folding dominates at high aspect ratios (ratio of length to width) when the width is comparable to the circumference of the formed tubes, which corresponds to a small actuation strain. Folding from all sides occurs for a higher actuation strain, namely when the width and length considerably exceed the deformed circumference. In the case of moderate actuation, when the width and length are comparable to the deformed

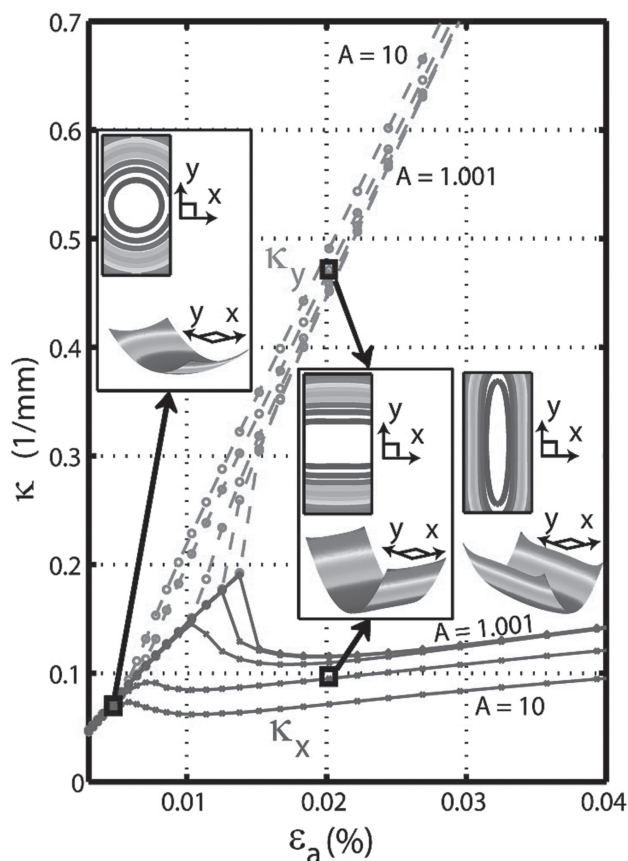


**Figure 12.** Simulations of curvature of free-standing inorganic bilayer as a function of actuation strain  $\epsilon_a$ . The insets show shapes for  $A$  (ratio of length to width of the film) = 2 at the indicated  $\epsilon_a$ ; the out-of-plane  $z$  axis is greatly exaggerated for illustration. The colors go from blue to red as the  $z$  displacement increases. Simulation show that above threshold strain short side rolling dominates. Reproduced with permission.<sup>[60]</sup> Copyright 2011, American Chemical Society.

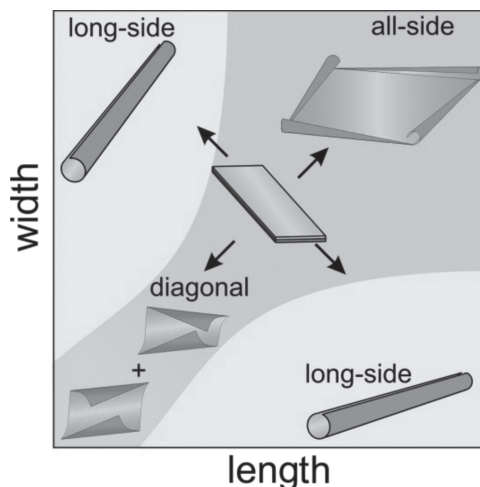


**Figure 13.** Different scenarios of deformation of polymer bilayers on a substrate depending of the width and length. Adapted with permission.<sup>[64b]</sup> Copyright 2012, American Chemical Society.



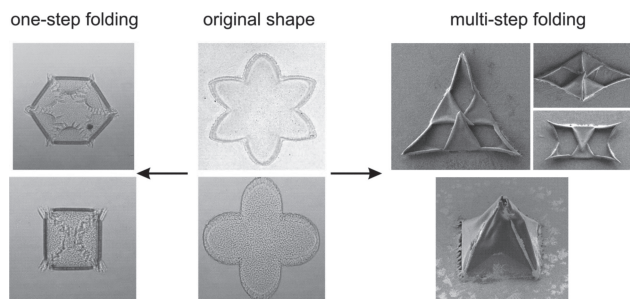


**Figure 14.** Results of one- and multi-step folding of four- and six-arm stars. Reproduced with permission.<sup>[66,70]</sup> Copyright 2011, Royal Society of Chemistry; Copyright 2013, Wiley-VCH.

circumference, diagonal rolling is observed. Short-side folding was observed very rarely and in combination with diagonal bending. In fact it was observed that bilayers placed on a substrate start to roll from corners due to quicker diffusion of water. Folding from the long-side starts later but dominates at high aspect ratios in agreement with energetic considerations. It was showed experimentally and by modeling that the main reasons causing a variety of rolling scenarios are (i) non-homogeneous swelling due to the presence of the substrate and (ii) adhesion of the polymer to the substrate. On the other hand, films, which are floating in solution, bend along their short side and formed scrolls.

One of the parameters, which determines the shape of a formed 3D object is the 2D shape of the polymer films. For example, tubes are formed from rectangle bilayers<sup>[63–65]</sup> (Figure 13). Envelope-like capsules with rounded corners or nearly spherical ones are formed the homogeneous star-like polymer bilayers with four and six arms, respectively (Figure 14, left).<sup>[65d,65e,66]</sup> Importantly, in many cases folding runs in one step. Step-by-step folding of different elements of self-folding films can be achieved by local activation of selected areas of self-folding films by light.<sup>[67]</sup> Another possibility is to use two or more kinds of active material which are sensitive to different signals. Gracias and co-workers demonstrated two-step deformation of patterned films where the active elements are two kinds of biodegradable polymers. Each of these polymers is degraded by specific enzyme. As a result, the film folds when the first enzyme is added and unfolds when the second one is added.<sup>[68]</sup> On the other hand, there are reports that folding in nature can have a very complex character, which strongly depends on the geometry and swelling path<sup>[69]</sup> and may result in multi-step folding (development of curvature in different directions).<sup>[2a]</sup> Recently, we demonstrated that the shape of isotropic polymer bilayers is able to direct folding in a sophisticated manner, leading to even more complex hierarchical folding than in nature. In particular, homogeneous bilayer films can undergo sequential steps of folding by forming various 3D shapes with sharp hinges (Figure 14, right). Experimental observations lead us to derive four empirical rules backed up by theoretical understanding as well as simulations. It was demonstrated how those rules can be used to direct the folding of edge-activated polymer bilayers through a concrete example: the design of a pyramid.<sup>[70]</sup>

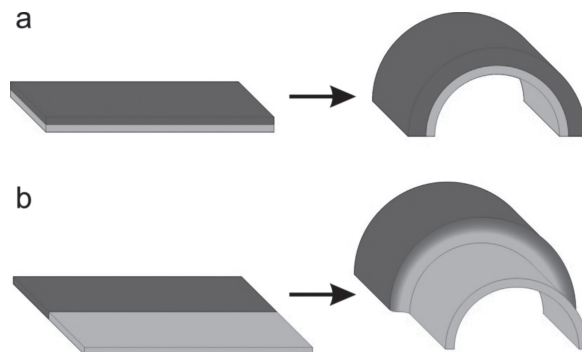


**Figure 15.** a) Bending of a “classical” bilayer and b) rectangular strips divided into one high- and one low-swelling regions. Dark blue is swelling hydrogel, light blue does not swell. Reproduced with permission.<sup>[72]</sup> Copyright 2013, Taylor & Francis.

*Bending of Hydrogels Films with Lateral Swelling Gradients:* Similar to bilayers, hydrogels with lateral gradients of swelling properties are also able to deform. They form complex figures with Gaussian curvature.<sup>[42]</sup> Similar to this work, Hayward and Santangelo investigated folding of patterned rectangular strips divided into one high- and one low-swelling region, which can be characterized as a thick but narrow bilayer.<sup>[71]</sup> When swollen in an aqueous medium, it does not bent to the side of the less swelling component that is the case of “classical” bilayer discussed by Timoshenko (Figure 15a), but rolls into a three-dimensional shape consisting of two nearly cylindrical regions connected by a transitional neck (Figure 15b).

Santangelo and Hayward further extended investigation of hydrogel films which consist of multiple areas with different swelling properties. The hydrogel was patterned using so-called halftone gel lithography using only two photomasks, wherein highly cross-linked dots embedded in a lightly cross-linked matrix provide access to nearly continuous and fully two-dimensional patterns of swelling. This method is used to fabricate surfaces with constant Gaussian curvature (spherical caps, saddles, and cones) or zero mean curvature (Enneper's surfaces), as well as more complex and nearly closed shapes (Figure 16)

Similar to the work of Hayward and Santangelo, Kumacheva and co-workers investigated deformation of hydrogel films formed by multiple regions with different swelling properties.<sup>[74]</sup> They demonstrated that the films are able to undergo multiple shape transitions when different polymers are swollen and shrunk. Thus, the polyelectrolyte film can be unfolded when there is no salt in solution, moderate increase of the ionic strength leads to folding and formation of tube, further increase of ionic strength results in unfolding of the film.

*Snap-Buckling Deformation:* In all these examples of hydrogels with vertical and later swelling gradients and in most plants movement occurs relatively slowly. Some plants such as the Venus flytrap, however, are able to move very quickly, which is due to a swelling-induced snap-buckling between two stable shapes. For snap-buckling instability, it is essential for the device to have directional swelling capability in addition to a doubly curved shape. The Venus flytrap, for instance, actively regulates the internal hydraulic pressure to bend its leaves in

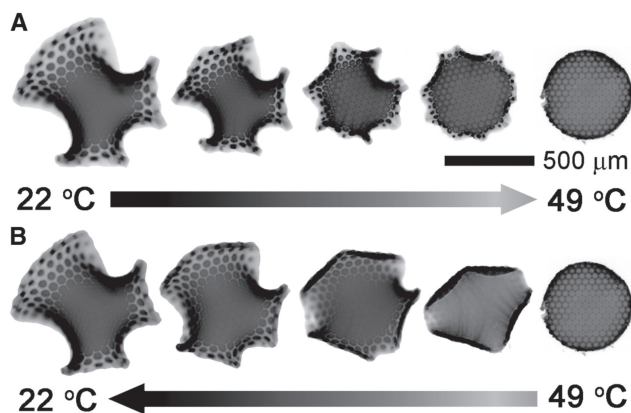


**Figure 16.** Thermal actuation of patterned sheets. a) When the temperature of the aqueous medium is increased, the hybrid Enneper's surface deswells and recovers its flat shape by 49 °C. b) Upon lowering the temperature to 22 °C the disk swells back to the initial hybrid shape through a different pathway. Initial thickness and disk diameter are 7 and 390  $\mu\text{m}$ , respectively. Reproduced with permission.<sup>[73]</sup> Copyright 2012, AAAS.

a direction perpendicular to the midline. From a mechanical point of view, the leaf is an elastic shell with a doubly curved shape. When bent along one axis only, an elastic body becomes stretched as a result of bending-stretching coupling of a doubly curved plate, thereby storing elastic energy. As the leaf further deforms and passes through the energy barrier, this stored elastic energy is instantaneously released and converted into kinetic energy, creating a rapid trap closure. Fang and co-workers [75] designed and fabricated a hydrogel device with a doubly curved shape to incorporate elastic instability. Unlike other hydrogel systems where the entire device needs to be immersed in solvent for actuation, swelling in this device takes place locally around the channels by direct solvent delivery. Therefore, a desired motion can be obtained by embedding channels where swelling is needed. The swelling of the device needs to be controlled in such a way that the curvature

is actively manipulated only in one direction while the curvature in the other direction remains passive. To achieve directional swelling of a doubly curved hydrogel device, microfluidic channels were aligned vertically with spacing in between. Once supplied to the channels, the solvent diffuses out in all directions around it. Swelling in lateral direction is negligible within a short period of actuation time since the solvent diffusion speed is finite. On the contrary, swelling along the channels can quickly cause significant amount of bending in the vertical direction as the diffusion length in thickness direction is relatively short. Therefore, local swelling around the aligned channels makes the doubly curved device bend only along the vertical axis and, as a result, snap-buckling occurs. Similarly, the device snaps back to the original shape during de-swelling (Figure 17).

**Summary:** It was shown that inhomogeneous films with lateral and vertical gradients of swelling properties are able to fold and form various 2D and 3D objects. The shape of the formed objects is determined by the character of the gradient of swelling properties, size of the film, and its shape. The folding may occur in one step or in multiple steps. It was also demonstrated that folding can be relatively slow and, thus, mimics actuation mechanism in pine cones or can be very fast, mimicking actuation mechanism in the Venus flytrap.

### 3.2.3. Application of Inhomogeneous Deformation of Hydrogels

**Actuators:** One possible kind of application of inhomogeneous hydrogels is bending actuators.<sup>[76]</sup> For example, AFM cantilevers coated on one side with hydrogel bend depending on the swelling state of the hydrogel and can be used for design of sensors.<sup>[77]</sup> In this way, pH-,<sup>[77a]</sup> temperature-, ion-<sup>[78]</sup> and biosensors<sup>[77b]</sup> were developed. Bashir and co-workers fabricated bending cantilever using PEG-based hydrogel with seeded cardiomyocytes, which were derived from neonatal rats.<sup>[79]</sup> These cantilevers were used as a mechanical sensor to measure the contractile forces of cardiomyocyte cell sheets and as an early prototype for the design of optimal cell-based biohybrid actuators.

Yu and co-workers used bending of bilayers for design of biomimetic check valve that allows for the directional control of fluid (Figure 18).<sup>[80]</sup> The valve consists of a bistrap formed by pH sensitive poly(HEMA-AA) hydrogel and a pH-indifferent poly(HEMA) hydrogel. Back pressure closes the leaflets, thereby restricting backflow, whereas forward pressure opens the leaflets and allows fluid to pass. The valve activates and deactivates in response to solution pH due to the use of a pH-responsive hydrogel in the leaflets. At high pH, the valve is functional and at low pH the leaflets contract to close the valve. Therefore, the valve not only functions as a one-way check valve, but also provides the ability to call the valve into service when desired. Similar check valves were found in mammalian veins.

In fact, bending can easily be transformed in walking or swimming by applying cyclical

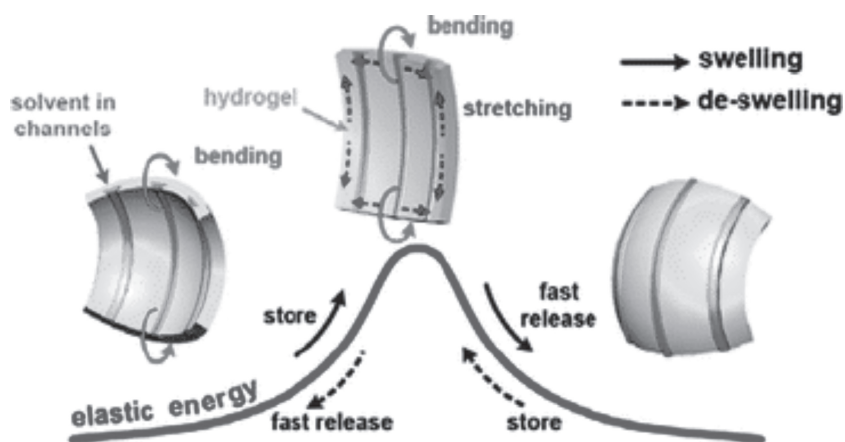


**Figure 17.** Swelling-induced snap-buckling in a doubly curved hydrogel device with embedded microfluidic channels. Scale bar indicates 100  $\mu\text{m}$ . Reproduced with permission.<sup>[75]</sup> Copyright 2010, Royal Society of Chemistry.



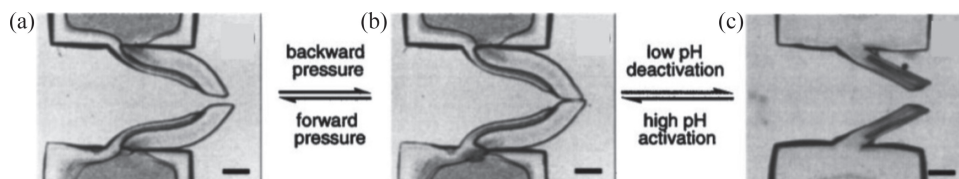


**Figure 18.** Smart biomimetic hydrogel valve based on hydrogel bistrup. When exposed to pH = 8 phosphate buffer, the bistrup hydrogel changes its size and shape to form a normally closed check valve (b); when exposed to pH = 3 buffer, the valve is deactivated due to shrinking (c). The activated valve allows forward fluid flow when forward pressure reaches a threshold value (a) while resisting backward flow (b). Scale bars are 500  $\mu\text{m}$ . Reproduced with permission.<sup>[80]</sup> Copyright 2001, American Institute of Physics.

stimuli. In 1992 Osada and co-workers reported deformation of polyelectrolyte hydrogel immersed in surfactant solution causing swelling of the hydrogel.<sup>[81]</sup> The deformation of the hydrogel was due to complexing of the surfactant with the charged groups in the gel. Swelling occurred due to osmotic pressure changes and ions freely moving in the gel and solution. The hydrogel bends towards the cathode that allows to control direction of bending by polarity of applied voltage. Positive ions in the surfactant solution moved to the cathode and complex there. Switching of the polarity led to release of the surfactant. On the other hand, surfactant molecules complexed with charged group on the other side of the hydrogel that resulted in change of the bending direction. Thus, the gel demonstrated bending and stretching upon cyclic change in the polarity of the applied voltage. The specific deformation of hydrogel allowed its walking at a speed of 15 mm/min. Similar to this work, Sun and co-workers developed macroscopical hydrogel-based actuating system, which is able to walk on ratchet substrate. The system is based on bending of a hydrophobic (Norland Optical Adhesive 63)–hydrophilic (thermally crosslinked poly(acrylic acid)/PAA)/poly(allylamine hydrochloride)) bilayer in response to a change in humidity (Figure 19).<sup>[82]</sup> This bilayer actuator could drive a walking device carrying a load 120 times heavier than the actuator and to walk

steadily on a ratchet substrate under periodic alternation of the relative humidity (RH) between 11 and 40%.

Hydrogel-based actuators are also able to swim when their shape changes cyclically. Lee and co-workers used inhomogeneous deformation of hydrogels and fabricated pH-sensitive hydrogel actuators mimicking the shape and the swimming motion of octopus and sperm (homogeneous hydrogel in electric field).<sup>[83]</sup> Such aquabots are able to produce directional motion in response to change of electrochemical potential and can be potentially used for biomedical applications to sense and destroy certain microorganism. Jager and co-workers demonstrated more complex actuation on the example of conjugated polymer actuators formed by bilayer consisting of polypyrrole and metal.<sup>[84]</sup> They showed that such bilayer actuators are able to operate in aqueous media, which is highly desirable for bio-analytical applications or to capture and release particles.<sup>[85]</sup> Whitesides, Parker and co-workers designed swimming biohybrid materials from engineered tissue and synthetic polymer thin film. The construct was built by culturing neonatal rat ventricular cardiomyocytes on PDMS film micropatterned with ECM (what's ECM) to promote spatially ordered, two-dimensional myogenesis. The centimeter-scale constructs performed diverse gripping, pumping, walking and swimming with good spatial and temporal control and were able to generate forces as high as 4 millinewtons per square millimeter.<sup>[86]</sup> Later on, Parker and Dabiri reported construction of a freely swimming jellyfish from chemically dissociated rat tissue and silicone polymer as a proof of concept (Figure 20).<sup>[87]</sup> The constructs, termed 'medusoids', were designed with computer simulations and experiments to match key determinants of jellyfish propulsion and feeding performance by quantitatively mimicking structural design, stroke kinematics and animal-fluid interactions. The combination of the engineering design algorithm with quantitative benchmarks of physiological performance suggests that this strategy is broadly applicable to reverse engineering of muscular organs or simple life forms that pump to survive. Similar approach was recently used by Bashir and co-workers to fabricate walking biological machines consisting of polymer layer with attached cardiac cell sheet.<sup>[88]</sup>

**Self-Folding Films:** In examples given above, the deformation of a hydrogels was used to generate mechanical force that allows development of moving systems. Deformation of hydrogel can also lead to considerable change of their shape this is used for design complex 2D and 3D systems in an origami-inspired self-folding concept. Utilization of hydromorphic folding of hydrogels for design of structured materials is highly attractive: it allows very simple, template-free fabrication of very

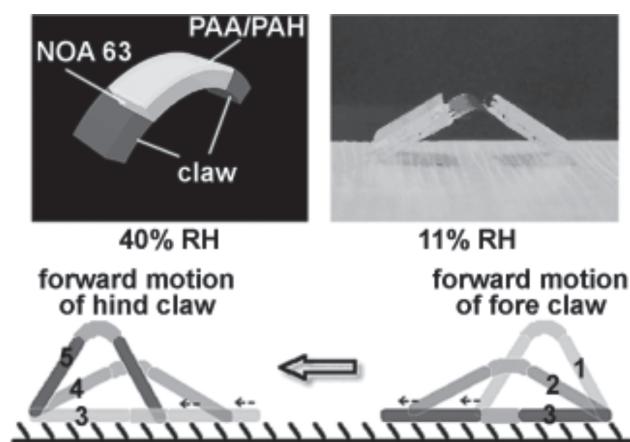


**Figure 19.** Walking device based on a polyelectrolyte multilayer film that can drive a walking device carrying a load 120 times heavier than the actuator and can walk steadily on a ratchet substrate under periodic alternation of the relative humidity (RH) between 11 and 40% (see picture). NOA 63: Norland Optical Adhesive 63, PAA: poly(acrylic acid), PAH: poly(allylamine hydrochloride). Reproduced with permission.<sup>[82]</sup> Copyright 2011, Wiley-VCH.

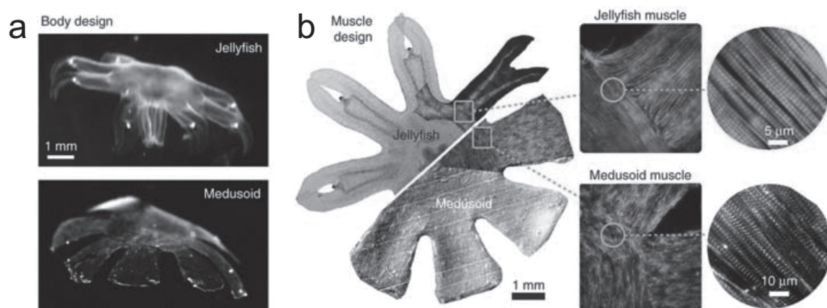


**Figure 20.** a) Body design of jellyfish (top) and free-swimming medusoid construct (bottom). Comparison demonstrates similar geometry and dimensions but also illustrates that the medusoid constitutes a simplified version of a jellyfish, reduced to elements necessary for propulsive function. b) Jellyfish 2D muscle architecture (top) was reverse-engineered in medusoids (bottom). Left: Composite brightfield image overlaid with F-actin stain (green) of muscle cell monolayer. Square inset: Close-up on muscle organization at lobe-body junction; F-actin stain (green). Reproduced with permission.<sup>[87]</sup> Copyright 2011, Nature Publishing Group.

complex repetitive 2D and 3D patterns,<sup>[89]</sup> which can hardly be prepared using other very sophisticated methods, such as two-photon and interference photolithography (Figure 21). One of the advantages of self-folding hydrogels is the possibility of quick, reversible and reproducible fabrication of 3D hollow objects with controlled chemical properties and morphology of both the exterior and interior. Most of the efforts until now were focused on inorganic self-folding materials.<sup>[16a,62,90]</sup> On the other hand, there are many factors, which make polymer-based self-folding films particularly attractive:<sup>[16b,91]</sup> i) there is a variety of polymers sensitive to different stimuli that allow design of self-folding films, which are able to fold in response to various external signals; ii) there are many polymers changing their properties in physiological ranges of pH and temperature, as

well as polymers sensitive to biochemical signals; iii) there is a variety of biocompatible and biodegradable polymers. These properties make polymer-based self-folding films very attractive for biotechnological applications; iv) polymers undergo considerable and reversible changes of volume that allow design of systems with reversible folding; v) fabrication of 3D structures with sizes ranging from hundreds of nanometers to centimeters is possible.

There are numerous reports describing fabrication of self-folding films with different responsive properties. For example, there are pH-responsive systems based on polyelectrolytes,<sup>[63,65c,65e,92,94]</sup> thermoresponsive based on gradient of thermal expansion,<sup>[65a,65b]</sup> melting of polymer,<sup>[95,96]</sup> thermoresponsive polymers,<sup>[64a,66]</sup> polymers responsive to sol electric signal,<sup>[85a,86,97]</sup> enzymes,<sup>[68]</sup> and light (based on light-to-heat conversion)<sup>[98]</sup>

One field of application of self-folding polymer thin films is controlled encapsulation and release of drugs, particles, and cells. Kalaitzidou demonstrated reversible adsorption-desorption of fluorescently labeled polyethyleneglycol, which was considered as model drug, inside PDMS-gold tubes at 60–70 °C.<sup>[65a]</sup> Similar, Gracias and co-workers showed irreversible encapsulation of yeast cells inside self-folding SU8-PCL films upon heating above 60 °C.<sup>[95]</sup> Poly-(N-isopropylacrylamide)-based self-folding films were also suitable for reversible encapsulation of particles and yeast cells.<sup>[64a,66]</sup> Cells were encapsulated upon cooling below 30 °C and could be released from the film, which is unfolded above 30 °C (Figure 22a). This encapsulation

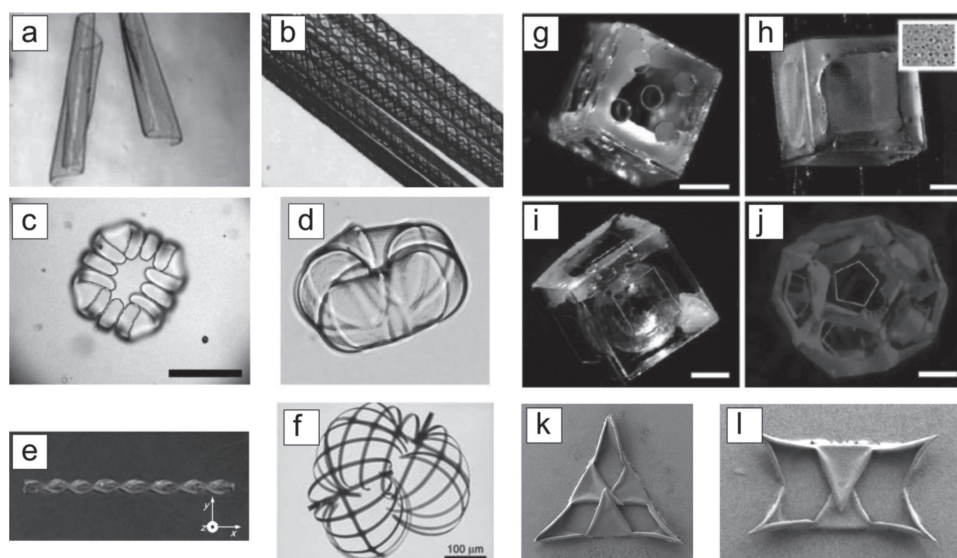


**Figure 21.** Examples of self-folding polymer films with different shapes: a,b) tubes. Reproduced with permission.<sup>[63,65b]</sup> Copyright 2005, Wiley-VCH Verlag; c,d) capsules. Reproduced with permission.<sup>[65d,66]</sup> Copyright 2007, Wiley-VCH, Copyright 2013, Taylor & Francis; e) helix. Reproduced with permission.<sup>[55]</sup> Copyright 2011, Royal Society of Chemistry; f) hierarchically-shaped tube. Reproduced with permission.<sup>[92]</sup> Copyright 2011, Wiley-VCH; g–i) cubes with porous walls. Reproduced with permission.<sup>[93]</sup> Copyright 2011, Springer; j) dodecahedron. Reproduced with permission.<sup>[93]</sup> Copyright 2011, Springer; k,l) complex structures obtained by folding of six-armed stars. Reproduced with permission.<sup>[70]</sup> Copyright 2013, Wiley-VCH.

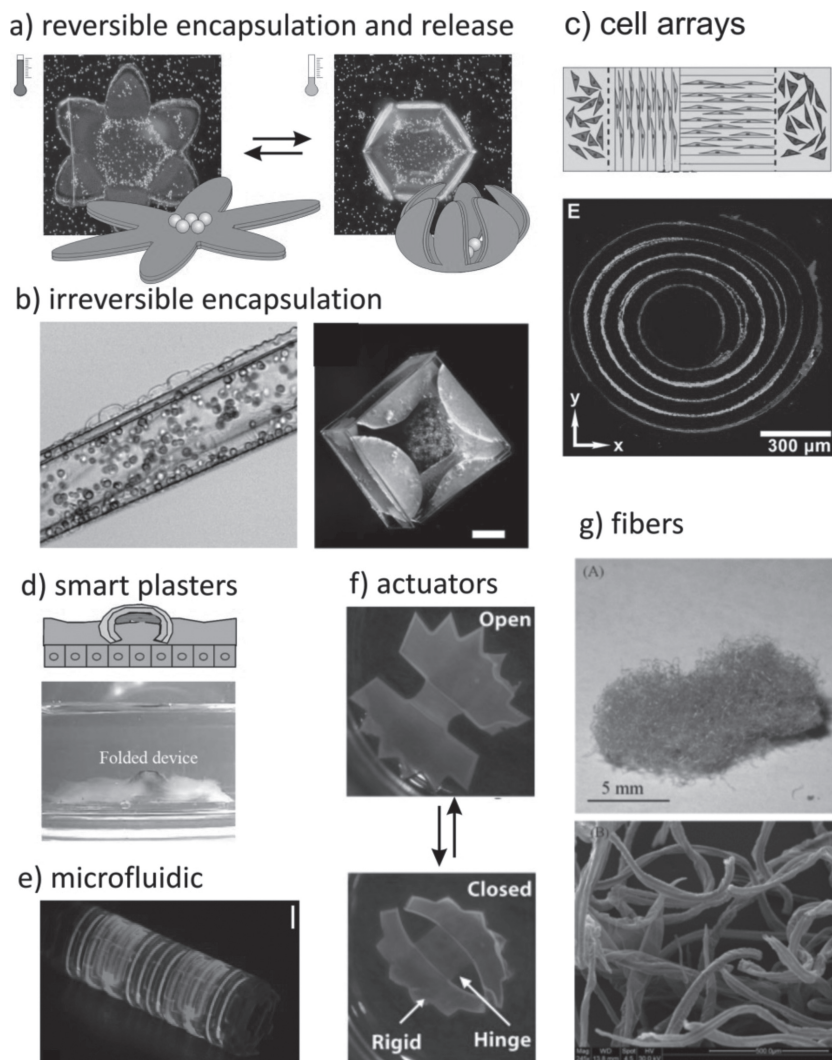


**Figure 22.** Examples of applications of self-folding polymer films: a) reversible encapsulation and release of yeast cells inside thermoresponsive self-folding capsules. Reproduced with permission.<sup>[66]</sup> Copyright 2010, Royal Society of Chemistry; b) irreversible encapsulation of cells—yeast cells encapsulation inside fully biodegradable self-rolled film (left: Reproduced with permission.<sup>[99]</sup> Copyright 2011, American Chemical Society) and stained fibroblast cells encapsulated within a non-porous polymeric container (right: Reproduced with permission.<sup>[110]</sup> Copyright 2010, Springer; c) array of multiple cells inside self-rolled prestressed PDMS film (Reproduced with permission.<sup>[106]</sup> Copyright 2012, Wiley-VCH; d) smart plasters which direct diffusion of drugs and prevent their leakage (Reproduced with permission.<sup>[65c]</sup> Copyright 2006, Elsevier; e) 3D microfluidic device obtained by folding (Reproduced with permission.<sup>[108]</sup> Copyright 2011, Nature Publishing Group; f) actuator with hinges folding in changing pH and ionic strength (Reproduced with permission.<sup>[94c]</sup> Copyright 2010, Elsevier; g) optical (top) and electron microscopy (bottom) images of fibrous material obtained from self-folding polymer films (Reproduced with permission.<sup>[109]</sup> Copyright 2012, Wiley-VCH).

and release is completely reversible and could be repeated many times. Very recently, fully biodegradable self-folding films, which consist of commercially available biodegradable polymers, were also used to encapsulate cells (Figure 22b).<sup>[99]</sup> It was also found out that cells are able to stimulate folding of patterned film.<sup>[100]</sup> In fact, there are many approaches which can be used for encapsulation of cells including LbL, microfluidic technique and controlled precipitation. The advantage of the self-folding approach is the possibility of reversible

encapsulation and release. Self-folded objects with nanoporous walls and encapsulated cells were suggested as prototype for artificial pancreas. Small molecules, such as glucose and dissolved oxygen, are able to pass through the pores, while larger ones, such as antibodies, are unable to do so. This size-selective permeability of self-folded capsules makes it possible to avoid the immune response what is highly demanded during transplantation of pancreas cells.<sup>[101]</sup> Gracias and co-workers used rigid metal-made self-folding microgrippers for capturing pieces of tissues and their controlled transport. Such systems are particularly attractive for non-invasive biopsy.<sup>[96c,102]</sup> Self-folded objects were used as scaffolds for the fabrication of 3D cellular constructs.<sup>[103]</sup> Controlled release of small molecules through the pores of self-folded microconstructs was used to spontaneously organize cells in a 3D environment<sup>[104]</sup> that potentially allows fabrication of 3D scaffolds for tissue engineering.<sup>[105]</sup> For example, self-rolling prestressed PDMS films with adsorbed cells of different kinds were used to make tubular structures mimicking the structure of blood vessels (Figure 22c).<sup>[106]</sup>

Self-folding films can also be used as smart plasters (Figure 22d). Lee demonstrated this concept with the example of a millimeter size poly(methyl methacrylate)–poly(2-hydroxyethyl methacrylate) bilayer with attached mucoadhesive drug layer. The non-swelling PHEMA layer serves as a diffusion barrier minimizing any drug leakage in the intestine. The resulting unidirectional release provides improved drug transport through the mucosal epithelium. The functionality of this device was successfully proven in vitro using a porcine small intestine.<sup>[65c]</sup>

There are several non-biorelated examples of applications of self-folding polymer films. Deposition of patterned metal on the polymer bilayer allowed fabrication of self-rolled tubes with patterned conductive inner wall.<sup>[63]</sup> In another examples, pyrolysis of polystyrene-poly(4-vinyl pyridine)-polydimethylsiloxane trilayer<sup>[94a]</sup> and polystyrene-poly(4-vinyl pyridine)/resorcinol bilayer<sup>[107]</sup>

was used for the fabrication of silica and carbon tubes, respectively. Gracias used self-folding polymers films to fabricate self-assembled curved microfluidic networks (Figure 22e)<sup>[108]</sup> and designed smart actuating systems mimicking opening and closing of the Venus flytrap by using pH responsive polymer, which form a hinge between two polymer films (Figure 22f).<sup>[94c]</sup> Very recently, Luchnikov and co-workers fabricated fibers with hollow interiors using scratched self-folding polymer films (Figure 22g).<sup>[109]</sup>



## 4. Conclusions and Outlook

Nature offers myriads of ideas for the design of advanced materials with novel properties. The principles of movement in plants have been successfully transferred in the design of actively-moving hydrogel-based materials. In different applications, swelling/shrinking of stimuli-responsive hydrogels is used to generate forces, and to change their volume and shape. Experiments show that hydrogel actuators can produce simple motion, such as homogeneous increase of volume, more complex bending and twisting as well as highly complex origami-like folding.

One can distinguish: (i) homogenous hydrogels with homogenous in all directions deformation; (ii) homogenous hydrogels with inhomogeneous in deformation and (iii) inhomogeneous hydrogels with inhomogeneous in deformation. Behavior of the first type is similar to swelling of cells. Behavior of the second type has no examples in nature. Behavior of third type mimics movements of pine cones, wheat awn, Venus flytrap etc. The third type of hydrogel actuator demonstrates the most complex scenarios of deformation such as bending, twisting, one- and multi-step folding leading to formation of complex 2D and 3D structures. In particular, one of the recent trends is to develop approaches for multi-step hierarchical actuation. One way to achieve multi-step actuation is to use several hydrogels sensitive to several stimuli or site-selective activation of different elements of self-folding films. In these cases either manufacturing or folding becomes more time-consuming. Another approach, which is inspired by nature, is to use inhomogeneity of the swelling path that allows very complex folding in a way that star-arm bilayers build pyramids with sharp hinges. One can even imagine the use of complex deformation of hydrogels for folding of printed origami structures<sup>[11]</sup> in order to achieve higher degree of complexity.

The complex movement/deformation of hydrogels has been successfully applied for the design of active elements for microfluidic devices, materials and devices with tunable optical properties, switchable surface, engineering of biomaterials, cell encapsulation, 3D microfluidic systems. There are also very interesting examples of “cyborg” devices build from living cells and synthetic materials. These first experiments give hope for the development of biomimetic polymer materials, which can be completely integrated into living organisms and be controlled by them. It was also demonstrated that self-folding hydrogel-based films are very promising for the design of biomaterials, controlled encapsulation and release of drugs and cells. In particular, due to their softness, better biocompatibility, possible biodegradability and easy manufacturing, hydrogel actuators can be applied in the fields of microelectronics and bio-microelectronics for in vivo applications.

## Acknowledgements

The author is grateful to DFG (Grant IO 68/1-1) for financial support. Georgi Stoychev is acknowledged for helpful comments on the manuscript.

Received: December 13, 2012

Revised: March 27, 2013

Published online: June 5, 2013

- [1] a) F. Tama, C. L. Brooks, *Annu. Rev. Biophys. Biomol. Struct.* **35**, 2006, 115–133; b) A.-L. Barabasi, Z. N. Oltvai, *Nat. Rev. Genet.* **2004**, 5, 101–113; c) J. Bath, A. J. Turberfield, *Nat. Nanotechnol.* **2007**, 2, 275–284; d) P. Schwill, S. Diez, *Crit. Rev. Biochem. Mol. Biol.* **2009**, 44, 223–242; e) W. J. Crookes, L. L. Ding, Q. L. Huang, J. R. Kimbell, J. Horwitz, M. J. McFall-Ngai, *Science* **2004**, 303, 235–238; f) R. Vaia, J. Baur, *Science* **2008**, 319, 420–421.
- [2] a) M. J. Harrington, K. Razghandi, F. Ditsch, L. Guiducci, M. Rueggeberg, J. W. C. Dunlop, P. Fratzl, C. Neinhuis, I. Burgert, *Nat. Commun.* **2011**, 2, 337; b) P. Fratzl, F. G. Barth, *Nature* **2009**, 462, 442–448.
- [3] a) I. Burgert, P. Fratzl, *Philos. Trans. R. Soc. A* **2009**, 367, 1541–1557; b) R. Elbaum, L. Zaltzman, I. Burgert, P. Fratzl, *Science* **2007**, 316, 884–886; c) E. Reyssat, L. Mahadevan, J. R. Soc., *Interface* **2009**, 6, 951–957.
- [4] a) L. Ionov, *J. Mater. Chem.* **2010**, 20, 3382–3390; b) I. Tokarev, S. Minko, *Soft Matter* **2009**, 5, 511–524; c) Y. Qiu, K. Park, *Adv. Drug Delivery Rev.* **2001**, 53, 321–339; d) W. T. S. Huck, *Mater Today* **2008**, 11, 24–32; e) Z. Liu, P. Calvert, *Adv. Mater.* **2000**, 12, 288–291; f) B. Kaehr, J. B. Shear, *Proc. Natl. Acad. Sci. USA* **2008**, 105, 8850–8854.
- [5] a) C. D. Jones, L. A. Lyon, *J. Am. Chem. Soc.* **2003**, 125, 460–465; b) Z. Y. Meng, M. H. Smith, L. A. Lyon, *Colloid Polym. Sci.* **2009**, 287, 277–285; c) S. Bhattacharya, F. Eckert, V. Boyko, A. Pich, *Small* **2007**, 3, 650–657.
- [6] a) S. K. Ahn, R. M. Kasi, S. C. Kim, N. Sharma, Y. X. Zhou, *Soft Matter* **2008**, 4, 1151–1157; b) D. Buenger, F. Topuz, J. Groll, *Prog. Polym. Sci.* **2012**, 37, 1678–1719.
- [7] K. Haraguchi, K. Murata, T. Takehisa, *Macromolecules* **2011**, 45, 385–391.
- [8] J. M. Skotheim, L. Mahadevan, *Science* **2005**, 308, 1308–1310.
- [9] C. Dawson, J. F. V. Vincent, A.-M. Rocca, *Nature* **1997**, 390, 668–668.
- [10] S. Timoshenko, *J. Opt. Soc. Am. Rev. Sci. Instrum.* **1925**, 11, 233–255.
- [11] Y. Forterre, J. M. Skotheim, J. Dumais, L. Mahadevan, *Nature* **2005**, 433, 421–425.
- [12] D. Evangelista, S. Hotton, J. Dumais, *J. Exp. Biol.* **2011**, 214, 521–529.
- [13] J. W. C. Dunlop, R. Weinkamer, P. Fratzl, *Mater Today* **2011**, 14, 70–78.
- [14] D. P. Holmes, A. J. Crosby, *Adv. Mater.* **2007**, 19, 3589–3593.
- [15] A. G. Volkov, V. A. Murphy, J. I. Clemmons, M. J. Curley, V. S. Markin, *J. Plant Physiol.* **2012**, 169, 55–64.
- [16] a) T. G. Leong, A. M. Zarafshar, D. H. Gracias, *Small* **2010**, 6, 792–806; b) L. Ionov, *Soft Matter* **2011**, 7, 6786–6791.
- [17] a) Y. Gong, M. Gao, D. Wang, H. Möhwald, *Chem. Mat.* **2005**, 17, 2648–2653; b) C. Chang, B. Duan, J. Cai, L. Zhang, *Eur. Polym. J.* **2010**, 46, 92–100; c) D. J. Gan, L. A. Lyon, *J. Am. Chem. Soc.* **2001**, 123, 7511–7517.
- [18] J. K. Oh, R. Drumright, D. J. Siegwart, K. Matyjaszewski, *Prog. Polym. Sci.* **2008**, 33, 448–477.
- [19] J. Rubio-Retama, N. E. Zafeiropoulos, C. Serafinelli, R. Rojas-Reyna, B. Voit, E. L. Cabarcos, M. Stamm, *Langmuir* **2007**, 23, 10280–10285.
- [20] a) J. S. Kim, N. Singh, L. A. Lyon, *Angew. Chem. Int. Ed.* **2006**, 45, 1446–1449; b) J. Kim, M. J. Serpe, L. A. Lyon, *J. Am. Chem. Soc.* **2004**, 126, 9512–9513.
- [21] a) I. Gorelikov, L. M. Field, E. Kumacheva, *J. Am. Chem. Soc.* **2004**, 126, 15938–15939; b) M. Agrawal, J. Rubio-Retama, N. E. Zafeiropoulos, N. Gaponik, S. Gupta, V. Cimrova, V. Lesnyak, E. Lopez-Cabarcos, S. Tzavalas, R. Rojas-Reyna, A. Eychemuller, M. Stamm, *Langmuir* **2008**, 24, 9820–9824.
- [22] a) K.-U. Jeong, J.-H. Jang, C. Y. Koh, M. J. Graham, K.-Y. Jin, S.-J. Park, C. Nah, M.-H. Lee, S. Z. D. Cheng, E. L. Thomas, J.

- Mater. Chem.* **2009**, 19, 1956–1959; b) K. Ueno, K. Matsubara, M. Watanabe, Y. Takeoka, *Adv. Mater.* **2007**, 19, 2807–2812; c) H. Fudouzi, Y. Xia, *Adv. Mater.* **2003**, 15, 892–896; d) K. Matsubara, M. Watanabe, Y. Takeoka, *Angew. Chem. Int. Ed.* **2007**, 46, 1688–1692.
- [23] J. R. Lawrence, G. H. Shim, P. Jiang, M. G. Han, Y. Ying, S. H. Foulger, *Adv. Mater.* **2005**, 17, 2344–2349.
- [24] J. P. Ge, Y. X. Hu, Y. D. Yin, *Angew. Chem. Int. Ed.* **2007**, 46, 7428–7431.
- [25] K. Ueno, J. Sakamoto, Y. Takeoka, M. Watanabe, *J. Mater. Chem.* **2009**, 19, 4778–4783.
- [26] a) K.-F. Arndt, D. Kuckling, A. Richter, *Polym. Adv. Technol.* **2000**, 11, 496–505; b) L. Dong, H. Jiang, *Soft Matter* **2007**, 3, 1223–1230; c) D. J. Beebe, J. S. Moore, Q. Yu, R. H. Liu, M. L. Kraft, B.-H. Jo, C. Devadoss, *Proc. Natl. Acad. Sci. USA* **2000**, 97, 13488–13493; d) D. T. Eddington, D. J. Beebe, *Adv. Drug Delivery Rev.* **2004**, 56, 199–210.
- [27] a) D. T. Eddington, R. H. Liu, J. S. Moore, D. J. Beebe, *Lab Chip* **2001**, 1, 96–99; b) D. J. Beebe, J. S. Moore, J. M. Bauer, Q. Yu, R. H. Liu, C. Devadoss, B. H. Jo, *Nature* **2000**, 404, 588–590; c) Z. Xuefeng, J. Hongrui, *Appl. Phys. Lett.* **2008**, 93, 151101.
- [28] a) A. Richter, D. Kuckling, S. Howitz, T. Gehring, K. F. Arndt, *J. Microelectromech. Syst.* **2003**, 12, 748–753; b) A. Richter, S. Klatt, G. Paschew, C. Klenke, *Lab Chip* **2009**, 9, 613–618.
- [29] A. Richter, G. Paschew, *Adv. Mater.* **2009**, 21, 979–983.
- [30] A. Richter, G. Paschew, S. Klatt, J. Lienig, K. F. Arndt, H. J. P. Adler, *Sensors* **2008**, 8, 561–581.
- [31] L. J. Millet, E. A. Corbin, R. Free, K. Park, H. Kong, W. P. King, R. Bashir, *Small* **2012**, 8, 2450–2450.
- [32] a) I. Tokarev, I. Tokareva, S. Minko, *Adv. Mater.* **2008**, 20, 2730–2734; b) V. Kozlovskaya, E. Kharlampieva, B. P. Khanal, P. Manna, E. R. Zubarev, V. V. Tsukruk, *Chem. Mat.* **2008**, 20, 7474–7485; c) J. Li, X. Hong, Y. Liu, D. Li, Y. W. Wang, J. H. Li, Y. B. Bai, T. J. Li, *Adv. Mater.* **2005**, 17, 163–166; d) M. Kuang, D. Wang, H. Möhwald, *Adv. Funct. Mater.* **2005**, 15, 1611–1616.
- [33] L. Dong, A. K. Agarwal, D. J. Beebe, H. Jiang, *Nature* **2006**, 442, 551.
- [34] A. Pelah, R. Seemann, T. M. Jovin, *J. Am. Chem. Soc.* **2006**, 129, 468–469.
- [35] H. Tekin, J. G. Sanchez, C. Landeros, K. Dubbin, R. Langer, A. Khademhosseini, *Adv. Mater.* **2012**, 24, 5543–5547.
- [36] a) B. Pokroy, A. K. Epstein, M. C. M. Persson-Gulda, J. Aizenberg, *Adv. Mater.* **2009**, 21, 463–469; b) A. Sidorenko, T. Krupenkin, A. Taylor, P. Fratzl, J. Aizenberg, *Science* **2007**, 315, 487–490; c) L. D. Zarzar, P. Kim, J. Aizenberg, *Adv. Mater.* **2011**, 23, 1442–1446.
- [37] A. Sidorenko, T. Krupenkin, J. Aizenberg, *J. Mater. Chem.* **2008**, 18, 3841–3846.
- [38] X. He, M. Aizenberg, O. Kuksenok, L. D. Zarzar, A. Shastri, A. C. Balazs, J. Aizenberg, *Nature* **2012**, 487, 214–218.
- [39] G. H. Kwon, Y. Y. Choi, J. Y. Park, D. H. Woo, K. B. Lee, J. H. Kim, S.-H. Lee, *Lab Chip* **2010**, 10, 1604–1610.
- [40] D. P. Holmes, M. Roche, T. Sinha, H. A. Stone, *Soft Matter* **2011**, 7, 5188–5193.
- [41] C. Ohm, M. Brehmer, R. Zentel, *Adv. Mater.* **2010**, 22, 3366–3387.
- [42] Y. Klein, E. Efrati, E. Sharon, *Science* **2007**, 315, 1116–1120.
- [43] a) F. Zhou, P. M. Biesheuvel, E. Y. Chol, W. Shu, R. Poetes, U. Steiner, W. T. S. Huck, *Nano Lett.* **2008**, 8, 725–730; b) M. C. LeMieux, M. E. McConney, Y.-H. Lin, S. Singamaneni, H. Jiang, T. J. Bunning, V. V. Tsukruk, *Nano Lett.* **2006**, 6, 730–734.
- [44] T. Tanaka, I. Nishio, S. T. Sun, S. Uenonishio, *Science* **1982**, 218, 467–469.
- [45] M. Doi, M. Matsumoto, Y. Hirose, *Macromolecules* **1992**, 25, 5504–5511.
- [46] H. L. Lim, J. C. Chuang, T. Tran, A. Aung, G. Arya, S. Varghese, *Adv. Funct. Mater.* **2011**, 21, 55–63.
- [47] M. Ma, L. Guo, D. G. Anderson, R. Langer, *Science* **2013**, 339, 186–189.
- [48] D. Suzuki, T. Kobayashi, R. Yoshida, T. Hirai, *Soft Matter* **2012**.
- [49] A. N. Zaikin, A. M. Zhabotinsky, *Nature* **1970**, 225, 535–537.
- [50] S. Maeda, Y. Hara, R. Yoshida, S. Hashimoto, *Int. J. Mol. Sci.* **2010**, 11, 52–66.
- [51] Y. Murase, S. Maeda, S. Hashimoto, R. Yoshida, *Langmuir* **2008**, 25, 483.
- [52] a) S. Maeda, Y. Hara, R. Yoshida, S. Hashimoto, *Macromol. Rapid. Commun.* **2008**, 29, 401–405; b) S. Maeda, Y. Hara, T. Sakai, R. Yoshida, S. Hashimoto, *Adv. Mater.* **2007**, 19, 3480–3484.
- [53] a) P. D. Topham, J. R. Howse, C. J. Crook, S. P. Armes, R. A. L. Jones, A. J. Ryan, *Macromolecules* **2007**, 40, 4393; b) S. Saha, D. Copic, S. Bhaskar, N. Clay, A. Donini, A. J. Hart, J. Lahann, *Angew. Chem. Int. Ed.* **2012**, 51, 660–665; c) K. J. Lee, J. Yoon, S. Rahmani, S. Hwang, S. Bhaskar, S. Mitragotri, J. Lahann, *Proc. Natl. Acad. Sci. USA* **2012**, 109, 16057–16062; d) K. K. Westbrook, H. J. Qi, *J. Intell. Mater. Syst. Struct.* **2008**, 19, 597–607.
- [54] Z. B. Hu, X. M. Zhang, Y. Li, *Science* **1995**, 269, 525–527.
- [55] K.-U. Jeong, J.-H. Jang, D.-Y. Kim, C. Nah, J. H. Lee, M.-H. Lee, H.-J. Sun, C.-L. Wang, S. Z. D. Cheng, E. L. Thomas, *J. Mater. Chem.* **2011**, 21, 6824–6830.
- [56] S. Turcaud, L. Guiducci, P. Fratzl, Y. J. M. Brechet, J. W. C. Dunlop, *Int. J. Mater. Res.* **2011**, 102, 607–612.
- [57] E. H. Mansfield, *Proc. R. Soc. A* **1962**, 268, 316–237.
- [58] E. H. Mansfield, *Proc. R. Soc. A* **1965**, 288, 396–417.
- [59] L. B. Freund, *J. Mech. Phys. Solids* **2000**, 48, 1159–1174.
- [60] S. Alben, B. Balakrishnan, E. Smela, *Nano Lett.* **2011**, 11, 2280–2285.
- [61] I. S. Chun, A. Challa, B. Derickson, K. J. Hsia, X. Li, *Nano Lett.* **2010**, 10, 3927–3932.
- [62] P. Cendula, S. Kiravittaya, I. Monch, J. Schumann, O. G. Schmidt, *Nano Lett.* **2011**, 11, 236–240.
- [63] V. Luchnikov, O. Sydorenko, M. Stamm, *Adv. Mater.* **2005**, 17, 1177–1182.
- [64] a) S. Zakharchenko, N. Pureskiy, G. Stoychev, M. Stamm, L. Ionov, *Soft Matter* **2010**, 6, 2633–2636; b) G. Stoychev, S. Zakharchenko, S. Turcaud, J. W. C. Dunlop, L. Ionov, *ACS Nano* **2012**, 6, 3925–3934.
- [65] a) K. Kalaitzidou, A. J. Crosby, *Appl. Phys. Lett.* **2008**, 93, 041910; b) B. Simpson, G. Nunnery, R. Tannenbaum, K. Kalaitzidou, *J. Mater. Chem.* **2010**, 20, 3496–3501; c) H. Y. He, J. J. Guan, J. L. Lee, *J. Controlled Release* **2006**, 110, 339–346; d) J. J. Guan, H. Y. He, L. J. Lee, D. J. Hansford, *Small* **2007**, 3, 412–418; e) J. J. Guan, H. Y. He, D. J. Hansford, L. J. Lee, *J. Phys. Chem. B* **2005**, 109, 23134–23137.
- [66] G. Stoychev, N. Pureskiy, L. Ionov, *Soft Matter* **2011**, 7, 3277–3279.
- [67] K. E. Laflin, C. J. Morris, T. Muqem, D. H. Gracias, *Appl. Phys. Lett.* **2012**, 101, 131901.
- [68] N. Bassik, A. Brafman, A. M. Zarafshar, M. Jamal, D. Luvsanjav, F. M. Selaru, D. H. Gracias, *J. Am. Chem. Soc.* **2010**, 132, 16314–16317.
- [69] a) H. Y. Liang, L. Mahadevan, *Proc. Natl. Acad. Sci. USA* **2011**, 108, 5516–5521; b) H. Liang, L. Mahadevan, *Proc. Natl. Acad. Sci. USA* **2009**, 106, 22049–22054.
- [70] G. Stoychev, S. Turcaud, J. W. C. Dunlop, L. Ionov, *Adv. Funct. Mater.* DOI: 10.1002/adfm.201203245.
- [71] J. Kim, J. A. Hanna, R. C. Hayward, C. D. Santangelo, *Soft Matter* **2012**, 8, 2375–2381.
- [72] L. Ionov, *Polym. Rev.* **2013**, 53, 92–107.
- [73] J. Kim, J. A. Hanna, M. Byun, C. D. Santangelo, R. C. Hayward, *Science* **2012**, 335, 1201–1205.

- [74] a) H. Thérien-Aubin, Z. L. Wu, Z. Nie, E. Kumacheva, *J. Am. Chem. Soc.* **2013**; b) Z. L. Wu, M. Moshe, J. Greener, H. Thérien-Aubin, Z. Nie, E. Sharon, E. Kumacheva, *Nat. Commun.* **2013**, *4*, 1586.
- [75] H. Lee, C. Xia, N. X. Fang, *Soft Matter* **2010**, *6*, 4342–4345.
- [76] J. S. Randhawa, K. E. Laflin, N. Seelam, D. H. Gracias, *Adv. Funct. Mater.* **2011**, *21*, 2395–2410.
- [77] a) R. Bashir, J. Z. Hilt, O. Elibol, A. Gupta, N. A. Peppas, *Appl. Phys. Lett.* **2002**, *81*, 3091–3093; b) J. Z. Hilt, A. K. Gupta, R. Bashir, N. A. Peppas, *Biomed. Microdevices* **2003**, *5*, 177–184.
- [78] a) K. Liu, H. F. Ji, *Anal. Sci.* **2004**, *20*, 9–11; b) Y. Zhang, H.-F. Ji, G. M. Brown, T. Thundat, *Anal. Chem.* **2003**, *75*, 4773–4777.
- [79] V. Chan, J. H. Jeong, P. Bajaj, M. Collens, T. Saif, H. Kong, R. Bashir, *Lab Chip* **2012**, *12*, 88–98.
- [80] Q. Yu, J. M. Bauer, J. S. Moore, D. J. Beebe, *Appl. Phys. Lett.* **2001**, *78*, 2589–2591.
- [81] Y. Osada, H. Okuzaki, H. Hori, *Nature* **1992**, *355*, 242–244.
- [82] Y. Ma, Y. Zhang, B. Wu, W. Sun, Z. Li, J. Sun, *Angew. Chem. Int. Ed.* **2011**, *50*, 6254–6257.
- [83] G. H. Kwon, J. Y. Park, J. Y. Kim, M. L. Frisk, D. J. Beebe, S. H. Lee, *Small* **2008**, *4*, 2148–2153.
- [84] E. Smela, *Adv. Mater.* **2003**, *15*, 481–494.
- [85] a) E. Smela, O. Inganas, I. Lundstrom, *Science* **1995**, *268*, 1735–1738; b) E. W. H. Jager, E. Smela, O. Inganas, *Science* **2000**, *290*, 1540–1545.
- [86] A. W. Feinberg, A. Feigel, S. S. Shevkoplyas, S. Sheehy, G. M. Whitesides, K. K. Parker, *Science* **2007**, *317*, 1366–1370.
- [87] J. C. Nawroth, H. Lee, A. W. Feinberg, C. M. Ripplinger, M. L. McCain, A. Grosberg, J. O. Dabiri, K. K. Parker, *Nat. Biotechnol.* **2012**, *30*, 792–797.
- [88] V. Chan, K. Park, M. B. Collens, H. Kong, T. A. Saif, R. Bashir, *Sci. Rep.* **2012**, *2*, 857.
- [89] a) S. Yang, K. Khare, P. C. Lin, *Adv. Funct. Mater.* **2010**, *20*, 2550–2564; b) T. R. Hendricks, W. Wang, I. Lee, *Soft Matter* **2010**, *6*, 3701–3706; c) X. Chen, J. Yin, *Soft Matter* **2010**, *6*, 5667–5680; d) A. Schweikart, N. Pazos-Perez, R. A. Alvarez-Puebla, A. Fery, *Soft Matter* **2011**, *7*, 4093–4100; e) A. Schweikart, A. Fery, *Microchim. Acta* **2009**, *165*, 249–263; f) J. Genzer, J. Groenewold, *Soft Matter* **2006**, *2*, 310–323.
- [90] G. Huang, Y. Mei, *Adv. Mater.* **2012**, *24*, 2517–2546.
- [91] a) D. H. Gracias, *Curr. Opin. Chem. Eng.* **2013**, *2*, 112–119; b) C. L. Randall, E. Gultepe, D. H. Gracias, *Trends Biotechnol.* **2012**, *30*, 138–146.
- [92] T. S. Kelby, M. Wang, W. T. S. Huck, *Adv. Funct. Mater.* **2011**, *21*, 652–657.
- [93] A. Azam, K. E. Laflin, M. Jamal, R. Fernandes, D. H. Gracias, *Biomed. Microdevices* **2011**, *13*, 51–58.
- [94] a) K. Kumar, B. Nandan, V. Luchnikov, F. Simon, A. Vyalikh, U. Scheler, M. Stamm, *Chem. Mat.* **2009**, *21*, 4282–4287; b) K. Kumar, V. Luchnikov, B. Nandan, V. Senkovskyy, M. Stamm, *Eur. Polym. J.* **2008**, *44*, 4115–4121; c) N. Bassik, B. T. Abebe, K. E. Laflin, D. H. Gracias, *Polymer* **2010**, *51*, 6093–6098; d) S. Singamaneni, M. E. McConney, V. V. Tsukruk, *Adv. Mater.* **2010**, *22*, 1263–1268; e) S. Singamaneni, M. E. McConney, V. V. Tsukruk, *ACS Nano* **2010**, *4*, 2327–2337; f) T. S. Shim, S.-H. Kim, C.-J. Heo, H. C. Jeon, S.-M. Yang, *Angew. Chem. Int. Ed.* **2012**, *51*, 1420–1423.
- [95] T. Tanaka, M. Okayama, Y. Kitayama, Y. Kagawa, M. Okubo, *Langmuir* **2010**, *26*, 7843–7847.
- [96] a) T. G. Leong, B. R. Benson, E. K. Call, D. H. Gracias, *Small* **2008**, *4*, 1605–1609; b) T. G. Leong, C. L. Randall, B. R. Benson, A. M. Zarafshar, D. H. Gracias, *Lab Chip* **2008**, *8*, 1621–1624; c) T. G. Leong, C. L. Randall, B. R. Benson, N. Bassik, G. M. Stern, D. H. Gracias, *Proc. Natl. Acad. Sci. USA* **2009**, *106*, 703–708.
- [97] E. W. H. Jager, O. Inganas, I. Lundstrom, *Science* **2000**, *288*, 2335–2338.
- [98] a) X. Zhang, C. L. Pint, M. H. Lee, B. E. Schubert, A. Jamshidi, K. Takei, H. Ko, A. Gillies, R. Bardhan, J. J. Urban, M. Wu, R. Fearing, A. Javey, *Nano Lett.* **2011**, *11*, 3239–3244; b) Y. Liu, J. K. Boyles, J. Genzer, M. D. Dickey, *Soft Matter* **2012**, *8*, 1764–1769; c) J. Ryu, M. D'Amato, X. Cui, K. N. Long, H. J. Qi, M. L. Dunn, *Appl. Phys. Lett.* **2012**, *100*, 161908.
- [99] S. Zakharchenko, E. Sperling, L. Ionov, *Biomacromolecules* **2011**, *12*, 2211–2215.
- [100] a) K. Kuribayashi-Shigetomi, H. Onoe, S. Takeuchi, in IEEE 25th International Conference, *Micro Electro Mechanical Systems (MEMS)*, **2012**, pp. 72–75; b) K. Kuribayashi-Shigetomi, H. Onoe, S. Takeuchi, *Plos One* **2012**, *7*, e51085.
- [101] C. L. Randall, Y. V. Kalinin, M. Jamal, A. Shah, D. H. Gracias, *Nanomed. Nanotechnol.* **2011**, *7*, 686–689.
- [102] E. Gultepe, J. S. Randhawa, S. Kadam, S. Yamanaka, F. M. Selaru, E. J. Shin, A. N. Kalloo, D. H. Gracias, *Adv. Mater.* **2012**, *25*, 514–519.
- [103] a) C. L. Randall, Y. V. Kalinin, M. Jamal, T. Manohar, D. H. Gracias, *Lab Chip* **2011**, *11*, 127–131; b) M. Jamal, N. Bassik, J. H. Cho, C. L. Randall, D. H. Gracias, *Biomaterials* **2010**, *31*, 1683–1690.
- [104] a) Y. V. Kalinin, J. S. Randhawa, D. H. Gracias, *Angew. Chem. Int. Ed.* **2011**, *50*, 2549–2553; b) S. Pedron, S. van Lierop, P. Horstman, R. Penterman, D. J. Broer, E. Peeters, *Adv. Funct. Mater.* **2011**, *21*, 1624–1630.
- [105] M. Jamal, S. S. Kadam, R. Xiao, F. Jivan, T.-M. Onn, R. Fernandes, T. D. Nguyen, D. H. Gracias, *Adv. Healthcare Mater.* **2013**, *10*, 1002/adhm.201200458.
- [106] B. Yuan, Y. Jin, Y. Sun, D. Wang, J. Sun, Z. Wang, W. Zhang, X. Jiang, *Adv. Mater.* **2012**, *24*, 890–896.
- [107] K. Kumar, B. Nandan, P. Formanek, M. Stamm, *J. Mater. Chem.* **2011**, *21*, 10813–10817.
- [108] M. Jamal, A. M. Zarafshar, D. H. Gracias, *Nat. Commun.* **2011**, *2*, 527.
- [109] V. A. Luchnikov, Y. Saito, L. Tzanis, *Macromol. Rapid Commun.* **2012**, *33*, 1404–1408.
- [110] A. Azam, K. Laflin, M. Jamal, R. Fernandes, D. Gracias, *Biomed. Microdevices* **2011**, *13*, 51–58.
- [111] B. Y. Ahn, D. Shoji, C. J. Hansen, E. Hong, D. C. Dunand, J. A. Lewis, *Adv. Mater.* **2010**, *22*, 2251–2254.



Ionov, L.

Bioinspired microorigami by self-folding polymer films

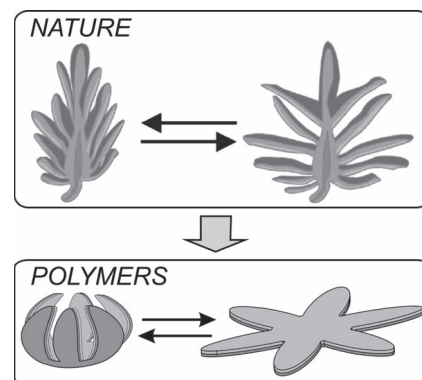
***Macromolecular Chemistry and Physics***, 2013, 214, 1178-1183.

## Trends in Polymer Science

# Bioinspired Microorigami by Self-Folding Polymer Films

Leonid Ionov\*

Investigation of self-folding thin films, which mimic natural mechanisms of movement and form complex 3D structures, is a novel and very promising research direction. This manuscript summarizes recent advances in the development and application of biomimetic self-folding polymer films.



## Introduction

Nature offers enormous arsenal of ideas for the design of novel materials with superior properties. For example, evolution led to development of highly sophisticated and efficient movement mechanisms of plants, which allow their rotation to sun, growth, and dissemination of seeds.<sup>[1]</sup> Contrary to animals where a macroscopic movement is provided by nanoscale movement of motor proteins,<sup>[2]</sup> motion in plants is provided by microscopic swelling of cells<sup>[1a]</sup> (Figure 1). In different schemes, relatively slow swelling/shrinking results in either slow shape changes such

as elongation, contraction, bending, twisting, or fast snap-buckling and fracture-dominated movement. Stimuli-responsive hydrogels mimic swelling/shrinking behavior of plant cells and produce macroscopic actuation in response to small variations of environmental conditions.<sup>[3]</sup> In most cases, change of conditions, however, results in homogeneous expansion or contraction in all directions. More complex behavior such as bending, twisting, and folding is produced as a result of inhomogeneous expansion/shrinking, which occurs with different magnitudes in different directions<sup>[4]</sup> and, thus, mimic mechanisms of development of animal organs, fruit growth, and plant movement. Utilization of these phenomena for design of structured materials is highly attractive—they allow very simple, template-free fabrication of very complex repetitive 2D, and 3D patterns,<sup>[5]</sup>


which can hardly be prepared using other very sophisticated methods such as two-photon and interference photolithography. Moreover, there are many factors, which make polymer-based self-folding films particularly attractive. First, there is a variety of polymers sensitive to different stimuli that allow design of self-folding films, which are able to fold in response to the various external signals. Second, there are many polymers changing their properties in physiological ranges of pH and temperature as well as polymers sensitive to biochemical processes. Third, there are a variety of biocompatible and biodegradable polymers. These properties make polymer-based self-folding films very attractive for biotechnological applications. Fourth, polymers undergo considerable and reversible changes of volume that allows design of systems with reversible folding. Fifth,

Dr. L. Ionov  
Leibniz Institute of Polymer Research  
Dresden, Hohe Str. 6, D-01069  
Dresden, Germany  
E-mail: ionov@ipfdd.de

fabrication of 3D structures with the size ranging from hundreds of nanometers to centimeters is possible. The focus of this review is to summarize the recent developments in the field of self-folding polymer films.

## Folding in Nature

Nonuniform swelling different part of tissues is the main principle of movement in plant. The pine cone is the natural example of actively moving folding system (Figure 1a).<sup>[6]</sup> In pine cone, the dead tissue makes up the scales moves upon changes in humidity and allows the seeds inside the pine cone to be released. Each scale consists of two types of tissues, one if formed by cells in which the cellulose microfibrils are aligned along the length of the scale and the other in which they are perpendicular. Upon drying, the interfacial matrix between the fibers shrinks on the lower half of the scales. The presence of the fibers leads to anisotropic contraction, which is hindered by the stiffer surrounding tissue, thus leading to a bending of the scales. The similar mechanism, which is based on a bilayer structure, is used by *Aizoaceae* to protect seeds against drought and to release when it is wet.<sup>[1a]</sup> The folding and unfolding in both cases are relatively slow and occur typically on the scale from several minutes to hours.<sup>[7]</sup> Folding in Venus Flytrap (Figure 1b) is much



Leonid Ionov is a group leader at the Leibniz Institute of Polymer Research Dresden, Germany. He graduated from Lomonosov Moscow State University (Russia) and received a Ph.D. in Polymer Chemistry in 2005 from Dresden University of Technology (Germany). He has worked as a guest and postdoctoral researcher at the Eindhoven University Technology (the Netherlands), Max Planck Institute of Molecular Cell Biology and Genetics (Germany), and at the Clarkson University (USA). He is the author of more than 40 publications, several patent applications, and book chapters. His research interests lie in the fields of stimuli-responsive and self-assembling materials.

quicker—is one of the fastest movements in the plant kingdom and it is able to close “jaws” in about 100 ms.<sup>[7,8]</sup> In the “open” state, the leaves are doubly curved. Upon stimulation, the plant “actively” changes one of its principal natural curvatures by hydration that results in snapping and closing of the “jaws.”

## Design of Self-Folding Films

There are two general approaches for the design of self-folding films. First approach is based on homogeneous bilayer films (Figure 2, a–e). The approach is very simple and patterned bilayers are prepared by using one-step photolithography. The formed structures are, however, hinge-free and have rounded shapes such as tubes<sup>[10]</sup> and capsules.<sup>[10f,10g,11]</sup> Complexly patterned films where locally deposited active materials form hinges are used in the second approach (Figure 2, f–g).

Active material can undergo either reversible swelling/shrinking or irreversible change of shape, which is caused by melting. In this way, objects with sharp edges such as cubes and pyramids are formed by patterned bilayer with the active junction elements.<sup>[12]</sup> Important, in all reported cases, folding runs in one step—active polymer changes its volume that results in simple bending.

Experimentally, the polymer films with different shapes can be obtained either by cutting,<sup>[10a–c]</sup> using microwell-like substrates<sup>[10e–g]</sup> or photolithography.<sup>[10d,11,12]</sup> Cutting allows fabrication of millimeter relatively large objects with the rectangular shape, which form the tubes. The main advantage of this method is simplicity and applicability to almost all combinations of cross-linkable polymers. Use of microwell-like substrates is technically more complicated while allows fabrication of polymer layers with different shapes such as rectangles or stars. Photolithography of bilayers allows large scale fabrication of self-folding objects of different shape and size starting from several microns. The formed self-folding objects have rounded corners. The main disadvantage of this approach is necessity to choose proper solvents for polymer deposition in the way that first polymer is not dissolved during deposition of the second polymer. Fabrication of patterned polymer films (Figure 2 right) is the technically most complicated procedure

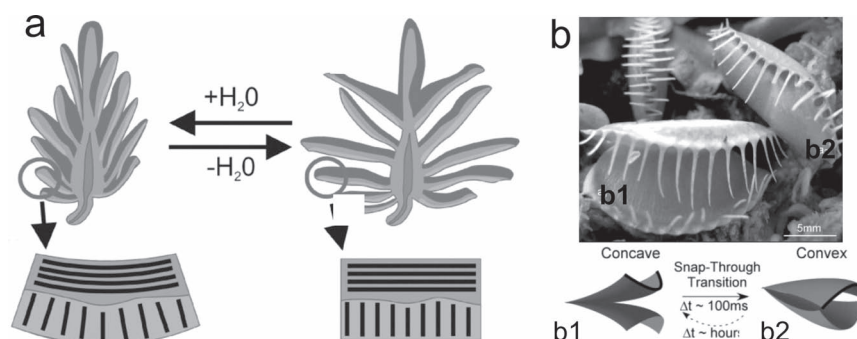


**Figure 1.** Two examples of natural self-folding systems. (d) A sketch of actuation of scales in a pine cone upon drying and wetting. Reproduced with permission,<sup>[6]</sup> Copyright 2011, Elsevier. (e) Snap-through of the Venus flytrap leaves from concave to convex occurs through the onset of an elastic instability films. Reproduced.<sup>[9]</sup>

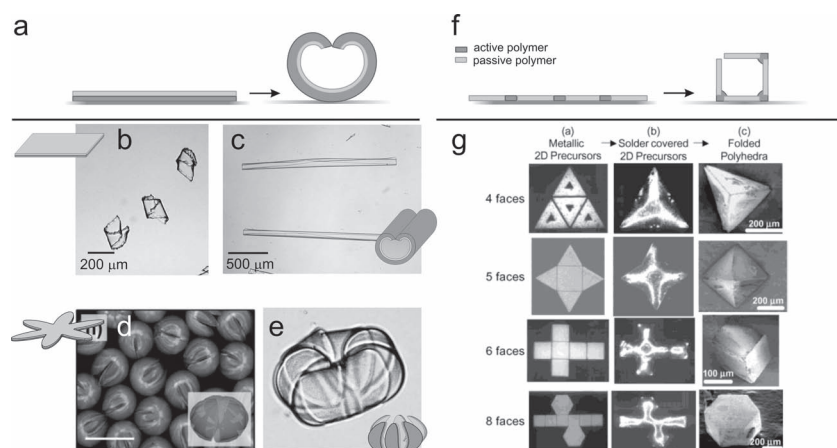


**Figure 2.** Two main approaches for fabrication of self-folding structures: (a) bilayers, and (f) patterned films. Panels (b) and (c) are reproduced with permission.<sup>[13a]</sup> Panels (d) and (e) are reproduced with permission.<sup>[13b]</sup> Copyright 2011, American Chemical Society. Panels (f) and (g) are reproduced with permission.<sup>[14]</sup>

and requires mask alignment during several steps of photolithography. On the other hand, it allows fabrication of the broadest range of shapes of self-folding objects.

### Folding of Polymer Films and Their Properties

Folding or rolling is macroscopic deformation of thin films having different expansion coefficient in different locations. The most primitive example of self-folding film is a bilayer consisting of two kinds of materials with different properties. One of them can be, for example, stimuli-responsive hydrogel, which considerably changes volume in response to small changes of environment, that is, active polymer. Second polymer can be hydrophobic, that is, passive.

Timoshenko<sup>[15]</sup> was the first who addressed the problem of bending investigated bending of bilayer, which consist of two materials with different expansion coefficients. He assumed that the bilayer can bend in only one direction and results in a bilayer with uniform curvature

$$\frac{1}{\rho} = \frac{6(\epsilon_2 - \epsilon_1)(1+m)^2}{h(3(1+m)^2 + (1+mn)(m^2 + \frac{1}{mn}))} \quad (1)$$

$$\frac{E_1}{E_2} = n \quad (2)$$

$$\frac{a_1}{a_2} = m \quad (3)$$

where  $E$  is the elasticity modulus,  $a$  is the thickness of the layers,  $h$  is the total thickness ( $h = a_1 + a_2$ ),  $\epsilon$  is the stress of the films, and  $\rho$  is the radius of curvature. Timoshenko equation predicts that the radius of curvature is inversely proportional to film stress. Moreover, radius of curvature first decreases and then increases with the increase of  $m$ . The resultant curvature is not very sensitive to the difference in stiffness between the two layers and is mainly controlled by the actuation strain and the layer thickness. The Timoshenko equation applies to a beam bending in only one direction and does not predict the folding direction. Moreover, Timoshenko equation considers elastic deformations, the polymers and hydrogels often demonstrate viscoelastic properties.

More recent models have considered complex bending of bilayer in two dimensions. Mansfield found analytical solutions for large deflections of circular<sup>[16]</sup> and elliptical<sup>[17]</sup> plates having lenticular cross-sections with a temperature gradient through the thickness. For small

gradients, the plates formed spherical caps, curved equally in all directions. At a critical gradient, a configuration with greater curvature in one direction became more favorable. Because of the lens-shaped thickness profile, even though the elliptical plate had a major axis, it showed no preferred direction for bending even for large deflections. Freund<sup>[18]</sup> determined the strain at which the spherical cap, formed by circular bilayer of uniform thickness, becomes unstable using low-order polynomial solutions and finite element simulations.

Later Smela and co-workers<sup>[19]</sup> showed that short-side rolling was preferred in the case of free homogeneous actuation and that this preference increased with aspect ratio (ratio of length to width of rectangular pattern). Li and co-workers<sup>[20]</sup> and Schmid<sup>[21]</sup> experimentally demonstrated the opposite scenario, namely a preference for long-side rolling, in the case where bilayers are progressively etched from a substrate. They observed that when the tube circumference was much larger than the width or the aspect ratio of the rectangle was high, rolling always occurred from the long side. When the tube circumference was much smaller than the width and the aspect ratio of the membrane pattern was not very high, the rolling resulted in a mixed yield of long- and short-side rolling, as well as a “dead-locked turnover” shape. Short-side rolling occurred at small aspect ratios when the deformed circumference is close to the width. In these self-rolling systems, the active component undergoes relatively small volume changes or actuation strains, which are nearly homogeneous over the whole sample. Hydrogels, however, demonstrate considerably different properties. First, hydrogels undergo large volume changes (up to 10 times) upon swelling and contraction. Second, the swelling of a hydrogel is often kinetically limited: due to slow diffusion of water through hydrogel, the parts



which are closer to the edges swell first while the parts which are closer to the center of the films swell later. Stoychev et al.<sup>[13b]</sup> investigated the folding of rectangular stimuli-responsive hydrogel-based polymer bilayers with different aspect ratios and relative thicknesses placed on a substrate. It was found that long-side rolling dominates at high aspect ratios (ratio of length to width) when the width is comparable to the circumference of the formed tubes, which corresponds to a small actuation strain. Rolling from all sides occurs for a higher actuation strain, namely when the width and length considerably exceed the deformed circumference. In the case of moderate actuation, when the width and length are comparable to the deformed circumference, diagonal rolling is observed. Short-side rolling was observed very rarely and in combination with diagonal rolling. Based on experimental observations, finite-element modeling as well as energetic considerations, it was argued that bilayers placed on a substrate start to roll from corners due to quicker diffusion of water. Rolling from the long-side starts later but dominates at high aspect ratios in agreement with energetic considerations. It was shown experimentally and by modeling that the main reasons causing a variety of rolling scenarios are (i) nonhomogeneous swelling due to the presence of the substrate and (ii) adhesion of the polymer to the substrate.

Gracias and co-workers<sup>[22]</sup> investigated folding of complexly patterned inorganic films where fusible material (solder) is deposited between plates of passive one (green material in Figure 2, right). They demonstrated that fold angle between adjacent plates is linearly decreased with the increase of the solder amount. Insufficient amount and excess of solder result in overfolding and underfolding, respectively. They also demonstrated that shape of patterned film determines the probability to form any particular

shape and derived algorithms to program folding.<sup>[23]</sup>

Very recently, Hayward and co-workers<sup>[24]</sup> demonstrated design of self-folding hydrogel films using half-tone photolithography. They patterned thermoresponsive hydrogel film and generated patches with different cross-linking densities and swelling degree. They demonstrated that film undergoes bending when the distance between regions with higher cross-linking density is larger than threshold value, which is linearly proportional to the film thickness. The 3D structure formed by the films depends on its 2D shape and swelling degree.

### Applications of Self-Folding Films

There are plenty reports describing fabrication of self-folding films with different responsive properties. For example, there are pH-responsive systems based on polyelectrolytes,<sup>[10c,10e,10g,12a,13a,25]</sup>

thermoresponsive based on gradient of thermal expansion,<sup>[10a,10b]</sup> melting of polymer,<sup>[12b,26]</sup> thermoresponsive polymers,<sup>[10d,11]</sup> solvent,<sup>[10g,12c,25c,27]</sup> electric signal,<sup>[28–30]</sup> enzymes,<sup>[31]</sup> light based on light-to-heat conversion.<sup>[32]</sup>

Self-folding polymer thin films are particular suitable for controlled encapsulation and release of drugs, particles, and cells (Figure 3 a,b). Kalaitzidou<sup>[10a]</sup> demonstrated reversible adsorption-desorption of fluorescently labeled polyethyleneglycol, which is considered as a model drug, inside PDMS-gold tubes at 60–70 °C. Gracias et al.<sup>[12b]</sup> demonstrated irreversible encapsulation of yeast cells inside self-folding SU8-PCL films upon heating above at 60 °C. Poly(*N*-isopropylacrylamide)-based self-folding films were also demonstrated to be suitable for reversible encapsulation of particles and yeast cells (Figure 3b).<sup>[10d,11]</sup> Cells were encapsulated upon cooling below 30 °C and could be released from the film, which

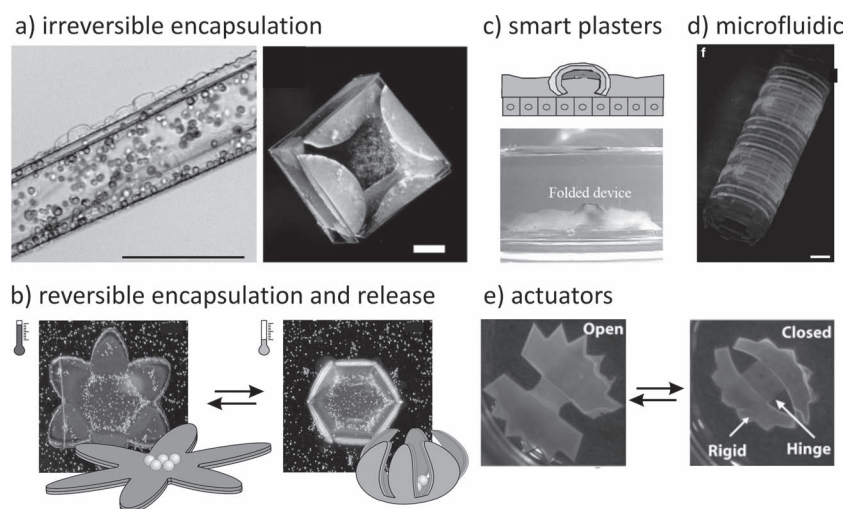


**Figure 3.** Examples of applications of self-folding polymer films: (a) irreversible encapsulation of cells-yeast cells encapsulation inside fully biodegradable self-rolled film (left, reproduced with permission,<sup>[33]</sup> Copyright 2011, American Chemical Society) and stained fibroblast cells encapsulated within a non-porous polymeric container (right, reproduced with permission,<sup>[12b]</sup> Copyright 2010, Springer); (b) reversible encapsulation and release of yeast cells inside thermoresponsive self-folding capsules (reproduced with permission,<sup>[11]</sup> Copyright 2010, Royal Society of Chemistry); (c) smart plasters, which direct diffusion of drugs and prevent their leakage (reproduced with permission,<sup>[10e]</sup> Copyright 2006, Elsevier); (d) 3D microfluidic device obtained by folding (reproduced with permission,<sup>[37]</sup> Copyright 2011, Nature Publishing Group); (e) Actuator with hinges folding in changing pH and ionic strength (reproduced with permission,<sup>[12a]</sup> Copyright 2010, Elsevier).

is unfolded above 30 °C. This encapsulation and release are completely reversible and could be repeated many times. Very recently, fully biodegradable self-folding films, which consist of commercially available biodegradable polymers, were also used to encapsulate cells (Figure 3a).<sup>[33]</sup> Self-folded objects with nanoporous walls and encapsulated cells were suggested as prototype of artificial pancreas. The small molecules such as glucose and dissolved oxygen are able to pass through the pores while larger ones such as antibody are unable to do it. This size-selective permeability of self-folded capsules allows avoiding immune response that is highly demanded during transplantation of pancreas cells.<sup>[34]</sup> Gracias et al.<sup>[26c]</sup> used rigid inorganic responsive microgrippers for capturing parts of tissues and their controlled transport to unloading station. Such systems are particularly attractive for low-invasive biopsy. Self-folded objects were suggested as scaffolds for fabrication of 3D cellular constructs.<sup>[35]</sup> Controlled release of small molecules through the pores of self-folded microconstructs was used to spontaneously organize cells in 3D environment.<sup>[36]</sup> In this approach, the unfolded film with pores is put in the solution of certain chemicals, folded to encapsulate it inside. Afterward, living cells were allowed to spontaneously organize. Cells, as it was observed, migrate to the pores where the chemical is released.

Self-folding films can also be used as smart plasters. Lee demonstrated this concept on the example of millimeter size poly(methyl methacrylate)–poly(2-hydroxyethyl methacrylate) bilayer with attached mucoadhesive drug layer (Figure 3c). The non-swelling PHEMA layer serves as a diffusion barrier, minimizing any drug leakage in the intestine. The resulting unidirectional release provides improved drug transport through the mucosal epithelium (Figure 3c). The functionality of this device is successfully demonstrated in

vitro using a porcine small intestine.<sup>[10e]</sup> Gracias and co-workers<sup>[37]</sup> used self-folding polymers films were used to fabricate self-assembled curved microfluidic networks (Figure 3d). Very recently, they designed smart actuating systems mimicking opening and closing of Venus flytrap by using a pH-responsive polymer, which forms a hinge between two polymer films (Figure 3e).<sup>[12a]</sup>

## Conclusions and Outlook

Self-folding polymeric thin films are emerging, but this is a rapidly developing field. There are many examples of the polymer thin films folding due to immersion in an aqueous environment, change of pH, temperature, light, electric signal, or presence of enzymes. The self-folding films are particularly promising for design of biomaterials, controlled encapsulation, and release of drugs, and cells. Here, cells are not locked inside amorphous and densely cross-linked matrix, as it happens in the case of hydrogels, but are free to move. Moreover, self-folding films are highly promising for design of smart actuating systems for in vivo application and elements of organic electronics. In future, the efforts may be focused on development of biomimetic polymer materials, which can be completely integrated into living organisms and be controlled by them. Moreover, elucidation of algorithms, which allow design of highly complex 3D architectures in controlled way using film shape or structural inhomogeneities as a “programming code” would tremendously advance field of self-folding films.

**Acknowledgements:** The author is grateful to DFG (Grant IO 68/1-1) for financial support.

Received: May 4, 2012; Revised: June 26, 2012; Published online: August 31, 2012;  
DOI: 10.1002/macp.201200246

**Keywords:** actuator; biomimetic; folding; hydrogels

- [1] a) M. J. Harrington, K. Razghandi, F. Ditsch, L. Guiducci, M. Rueggeberg, J. W. C. Dunlop, P. Fratzl, C. Neinhuis, I. Burgert, *Nat. Commun.* **2011**, *2*, 337; b) I. Burgert, P. Fratzl, *Phil. Trans. R. Soc. A* **2009**, *367*, 1541; c) P. Fratzl, F. G. Barth, *Nature* **2009**, *462*, 442; d) R. Elbaum, L. Zaltzman, I. Burgert, P. Fratzl, *Science* **2007**, *316*, 884; e) E. Reyssat, L. Mahadevan, *J. R. Soc. Interface* **2009**, *6*, 951.
- [2] F. Tama, C. L. Brooks, *Annu. Rev. Biophys. Biomol. Struct.* **2006**, *35*, 115.
- [3] a) L. Ionov, *J. Mater. Chem.* **2010**, *20*, 3382; b) I. Tokarev, S. Minko, *Soft Matter* **2009**, *5*, 511; c) Y. Qiu, K. Park, *Adv. Drug Deliv. Rev.* **2001**, *53*, 321.
- [4] a) T. G. Leong, A. M. Zarafshar, D. H. Gracias, *Small* **2010**, *6*, 792; b) L. Ionov, *Soft Matter* **2011**, *7*, 6786.
- [5] a) S. Yang, K. Khare, P. C. Lin, *Adv. Funct. Mater.* **2010**, *20*, 2550; b) T. R. Hendricks, W. Wang, I. Lee, *Soft Matter* **2010**, *6*, 3701; c) X. Chen, J. Yin, *Soft Matter* **2010**, *6*, 5667; d) A. Schweikart, N. Pazos-Perez, R. A. Alvarez-Puebla, A. Fery, *Soft Matter* **2011**, *7*, 4093; e) A. Schweikart, A. Fery, *Microchim. Acta* **2009**, *165*, 249; f) J. Genzer, J. Groenewold, *Soft Matter* **2006**, *2*, 310.
- [6] J. W. C. Dunlop, R. Weinkamer, P. Fratzl, *Mater. Today* **2011**, *14*, 70.
- [7] J. M. Skotheim, L. Mahadevan, *Science* **2005**, *308*, 1308.
- [8] Y. Forterre, J. M. Skotheim, J. Dumais, L. Mahadevan, *Nature* **2005**, *433*, 421.
- [9] D. P. Holmes, A. J. Crosby, *Adv. Mater.* **2007**, *19*, 3589.
- [10] a) K. Kalaitzidou, A. J. Crosby, *Appl. Phys. Lett.* **2008**, *93*; b) B. Simpson, G. Nunnery, R. Tannenbaum, K. Kalaitzidou, *J. Mater. Chem.* **2010**, *20*, 3496; c) V. Luchnikov, O. Sydorenko, M. Stamm, *Adv. Mater.* **2005**, *17*, 1177; d) S. Zakharchenko, N. Pureskiy, G. Stoychev, M. Stamm, L. Ionov, *Soft Matter* **2010**, *6*, 2633; e) H. Y. He, J. J. Guan, J. L. Lee, *J. Controlled Release* **2006**, *110*, 339; f) J. J. Guan, H. Y. He, L. J. Lee, D. J. Hansford, *Small* **2007**, *3*, 412; g) J. J. Guan, H. Y. He, D. J. Hansford, L. J. Lee, *J. Phys. Chem. B* **2005**, *109*, 23134.
- [11] G. Stoychev, N. Pureskiy, L. Ionov, *Soft Matter* **2011**, *7*, 3277.
- [12] a) N. Bassik, B. T. Abebe, K. E. Laflin, D. H. Gracias, *Polymer* **2010**, *51*, 6093; b) A. Azam, K. Laflin, M. Jamal, R. Fernandes, D. Gracias, *Biomed. Microdevices* **2010**, *13*, 51; c) K.-U. Jeong, J.-H. Jang, D.-Y. Kim,



- C. Nah, J. H. Lee, M.-H. Lee, H.-J. Sun, C.-L. Wang, S. Z. D. Cheng, E. L. Thomas, *J. Mater. Chem.* **2011**, *21*, 6824.
- [13] a) T. S. Shim, S.-H. Kim, C.-J. Heo, H. C. Jeon, S.-M. Yang, *Angew. Chem., Int. Ed.* **2011**, *51*, 1420; b) G. Stoychev, S. Zakharchenko, S. Turcaud, J. W. C. Dunlop, L. Ionov, *ACS Nano* **2012**, *6*, 3925.
- [14] D. H. Gracias, V. Kavthekar, J. C. Love, K. E. Paul, G. M. Whitesides, *Adv. Mater.* **2002**, *14*, 235.
- [15] S. Timoshenko, *J. Opt. Soc. Am.* **1925**, *11*, 233.
- [16] E. H. Mansfield, *Proc. R. Soc. London, Ser. A* **1962**, *268*, 316.
- [17] E. H. Mansfield, *Proc. R. Soc. London, Ser. A* **1965**, *288*, 396.
- [18] L. B. Freund, *J. Mech. Phys. Solids* **2000**, *48*, 1159.
- [19] S. Alben, B. Balakrishnan, E. Smela, *Nano Lett.* **2011**, *11*, 2280.
- [20] I. S. Chun, A. Challa, B. Derickson, K. J. Hsia, X. Li, *Nano Lett.* **2010**, *10*, 3927.
- [21] P. Cendula, S. Kiravittaya, I. Monch, J. Schumann, O. G. Schmidt, *Nano Lett.* **2011**, *11*, 236.
- [22] T. G. Leong, P. A. Lester, T. L. Koh, E. K. Call, D. H. Gracias, *Langmuir* **2007**, *23*, 8747.
- [23] a) S. Pandey, M. Ewing, A. Kunas, N. Nguyen, D. H. Gracias, G. Menon, *Proc. Natl. Acad. Sci. U. S. A.* **2011**, *108*, 19885; b) A. Azam, T. G. Leong, A. M. Zarafshar, D. H. Gracias, *Plos One* **2009**, *4*, e4451.
- [24] J. Kim, J. A. Hanna, M. Byun, C. D. Santangelo, R. C. Hayward, *Science* **2012**, *335*, 1201.
- [25] a) K. Kumar, B. Nandan, V. Luchnikov, F. Simon, A. Vyalikh, U. Scheler, M. Stamm, *Chem. Mater.* **2009**, *21*, 4282; b) K. Kumar, V. Luchnikov, B. Nandan, V. Senkovskyy, M. Stamm, *Eur. Polym. J.* **2008**, *44*, 4115; c) T. S. Kelby, M. Wang, W. T. S. Huck, *Adv. Funct. Mater.* **2011**, *21*, 652; d) S. Singamaneni, M. E. McConney, V. V. Tsukruk, *Adv. Mater.* **2010**, *22*, 1263; e) S. Singamaneni, M. E. McConney, V. V. Tsukruk, *ACS Nano* **2010**, *4*, 2327.
- [26] a) T. G. Leong, B. R. Benson, E. K. Call, D. H. Gracias, *Small* **2008**, *4*, 1605; b) T. G. Leong, C. L. Randall, B. R. Benson, A. M. Zarafshar, D. H. Gracias, *Lab Chip* **2008**, *8*, 1621; c) T. G. Leong, C. L. Randall, B. R. Benson, N. Bassik, G. M. Stern, D. H. Gracias, *Proc. Natl. Acad. Sci. U. S. A.* **2009**, *106*, 703.
- [27] D. P. Holmes, M. Roche, T. Sinha, H. A. Stone, *Soft Matter* **2011**, *7*, 5188.
- [28] E. Smela, O. Inganas, I. Lundstrom, *Science* **1995**, *268*, 1735.
- [29] E. W. H. Jager, O. Inganas, I. Lundstrom, *Science* **2000**, *288*, 2335.
- [30] A. W. Feinberg, A. Feigel, S. S. Shevkoplyas, S. Sheehy, G. M. Whitesides, K. K. Parker, *Science* **2007**, *317*, 1366.
- [31] N. Bassik, A. Brafman, A. M. Zarafshar, M. Jamal, D. Luvsanjav, F. M. Selaru, D. H. Gracias, *J. Am. Chem. Soc.* **2010**, *132*, 16314.
- [32] a) X. Zhang, C. L. Pint, M. H. Lee, B. E. Schubert, A. Jamshidi, K. Takei, H. Ko, A. Gillies, R. Bardhan, J. J. Urban, M. Wu, R. Fearing, A. Javey, *Nano Lett.* **2011**, *11*, 3239; b) Y. Liu, J. K. Boyles, J. Genzer, M. D. Dickey, *Soft Matter* **2012**, *8*, 1764; c) J. Ryu, M. D'Amato, X. Cui, K. N. Long, H. J. Qi, M. L. Dunn, *Appl. Phys. Lett.* **2012**, *100*, 161908.
- [33] S. Zakharchenko, E. Sperling, L. Ionov, *Biomacromolecules* **2011**, *12*, 2211.
- [34] C. L. Randall, Y. V. Kalinin, M. Jamal, A. Shah, D. H. Gracias, *Nanomed.: Nanotechnol., Biol. Med.* **2011**, *7*, 686.
- [35] a) C. L. Randall, Y. V. Kalinin, M. Jamal, T. Manohar, D. H. Gracias, *Lab Chip* **2011**, *11*, 127; b) M. Jamal, N. Bassik, J. H. Cho, C. L. Randall, D. H. Gracias, *Biomaterials* **2010**, *31*, 1683.
- [36] Y. V. Kalinin, J. S. Randhawa, D. H. Gracias, *Angew. Chem., Int. Ed.* **2011**, *50*, 2549.
- [37] M. Jamal, A. M. Zarafshar, D. H. Gracias, *Nat. Commun.* **2011**, *2*, 527.

Ionov, L.

3D Microfabrication using stimuli-responsive self-folding polymer films

***Polymer Reviews*** 2013, 53, 92-107

# 3D Microfabrication using Stimuli-Responsive Self-Folding Polymer Films

LEONID IONOV

Leibniz Institute of Polymer Research Dresden, Dresden, Germany

*Fabrication of complex 3D objects using folding of thin films is a novel and very attractive research field. This manuscript overviews recent progress in development, investigation, and application of self-folding polymer films which are able to fold and form various 3D structures. The review discusses the basic principles of design of self-folding films, fabrication of self-folding films, possibilities to build complex 3D shapes, their responsive properties, and applications.*

**Keywords** polymer, stimuli-responsive, hydrogel, actuator, self-folding

## 1. Introduction

The design of complex 3D microstructures is a highly challenging task for the development of novel materials for optics, biotechnology, lab-on-chips, as well as for micro and nanoelectronics. Three-dimensional materials can be fabricated using a variety of methods including two-photon photolithography, interference lithography, and molding;<sup>1</sup> however, 3D structuring using these techniques is very experimentally complicated, which limits their upscaling and broad applicability. For example, interference photolithography allows fabrication of 3D structures with limited thickness. Two-photon photolithography, which allows nanoscale resolution, is very slow and highly expensive. Assembling of 3D structures by stacking of 2D ones is time consuming and does not allow fabrication of fine hollow structures.

On the other hand, nature offers a huge number of ideas for the design of novel materials with superior properties. In particular, self-assembly and self-organization being the main principles of structure formation in nature attract significant interest as promising concepts for the design of intelligent materials.<sup>2</sup> For example, evolution led to the development of highly sophisticated and efficient movement mechanisms of plants, which allow their rotation to sun, growth, and dissemination of seeds<sup>3–7</sup> that is provided by microscopic swelling of cells.<sup>3</sup> In different schemes relatively slow swelling/shrinking results in either slow shape changes such as elongation, contraction, bending, twisting, or fast snap-buckling and fracture-dominated movement.

Stimuli-responsive hydrogels mimic swelling/shrinking behavior of plant cells and produce macroscopic actuation in response to small variations of environmental conditions.<sup>8–10</sup> In most cases, a change of conditions results in homogeneous expansion or contraction in

Received October 3, 2012; accepted November 16, 2012.

Address correspondence to Leonid Ionov, Leibniz Institute of Polymer Research Dresden, Hohe Str. 6, D-01069 Dresden, Germany. E-mail: ionov@ipfdd.de

all directions. More complex behavior such as bending, twisting, and folding is produced as a result of inhomogeneous expansion/shrinking, which occurs with different magnitudes in different directions.<sup>1,11</sup> As a result, complex behavior such as plant movement can be mimicked. Utilization of these phenomena for the design of structured materials is highly attractive—they allow very simple, template-free fabrication of very complex repetitive 2D and 3D patterns,<sup>12–16</sup> which however, cannot be prepared using sophisticated fabrication methods such as two-photon and interference photolithography. One of the advantages of the self-folding approach is the possibility of quick, reversible, and reproducible fabrication of 3D hollow objects with controlled chemical properties and morphology of both the exterior and the interior.

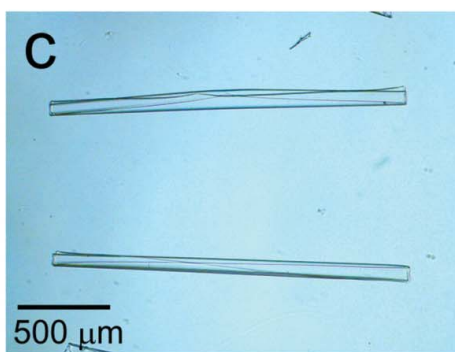
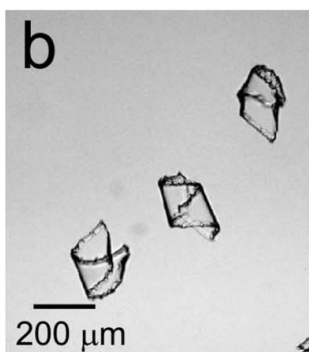
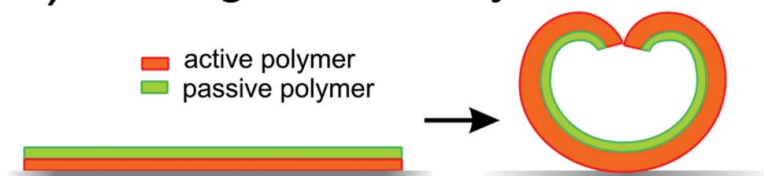
Most of the efforts till now have been focused on inorganic self-folding materials.<sup>1,17–19</sup> On the other hand, there are many factors, which make polymer-based self-folding films particularly attractive. First, there are a variety of polymers sensitive to different stimuli<sup>20</sup> that allow the design of actuators<sup>21,22</sup> and self-folding films, which are able to fold in response to the various external signals. Second, many polymers can change their properties in physiological ranges of pH and temperature as well as polymers sensitive to biochemical processes. Third, there are a variety of biocompatible and biodegradable polymers. These properties make polymer-based self-folding films very attractive for biotechnological applications. Fourth, polymers undergo considerable and reversible changes of volume that allows design of systems with reversible folding. Fifth, fabrication of 3D structures with the size ranging from hundreds of nanometers to centimeters is possible. The focus of this review is to summarize the recent developments in the field of self-folding polymer films.

## 2. Bending vs. Expansion

Bending is essential for the conversion of two-dimensional objects (films, layers) into 3D ones. Typically bending results from either expansion or contraction of a material caused by change of environmental conditions. Homogeneous expansion or contraction in all directions does not lead to change of geometry. Bending/folding/buckling are produced as a result of inhomogeneous expansion/shrinking, which occurs with different magnitudes in different directions. Similar to buckling, which is the deformation of a films resulting in appearance of regular wrinkles or irregular creases,<sup>15,23–26</sup> bending could be achieved either (i) by applying gradients of field to homogeneous materials or (ii) by applying non-gradient stimuli to inhomogeneous materials. The example of the first case is the bending of polyelectrolyte hydrogel in solution with lateral gradient of pH, which is formed during electrolysis.<sup>27</sup> The examples of the second group are the bending of liquid crystalline films,<sup>28</sup> hydrogel with the lateral gradient monomer concentration,<sup>29</sup> cantilever sensors.<sup>30</sup>

In fact, the design of self-folding objects using homogeneous materials is technically very complicated because a very complex spatial force gradient must be formed and kept continuously. The folded film typically unfolds when the gradient disappears. This, for example, is observed when a water droplet is deposited on thin film.<sup>31</sup> The film folds immediately after the droplet is deposited. The formed 3D object changes its shape during drying of the droplet and unfolds when water is completely evaporated. In an aqueous environment, the effects of surface tension are weak and bending can be observed when the swelling of hydrogel film is restricted from one side by, for example, substrate. On the other hand, fabrication of self-folding objects using inhomogeneous films is more straightforward. The inhomogeneous films fold due to the difference in the properties on constituting materials in a pre-programmed manner, which is defined by the film structure/pattern.

## a) homogenous bilayer



## d) patterned bilayer

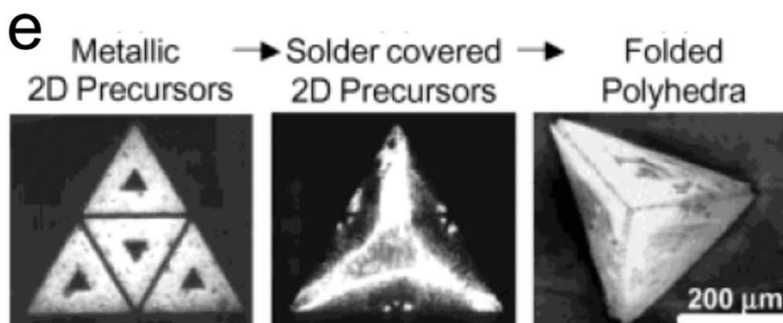


**Figure 1.** Approaches for design and examples of self-folding polymer objects prepared using (a) homogeneous polymer bilayer (d) patterned bilayer. Examples of folded homogenous bilayers (b,c) and patterned bilayer (e) are reproduced from Stoychev et al.<sup>37</sup> with permission from American Chemical Society. (e) is reproduced from Gracias et al.<sup>35</sup> with permission from Wiley-VCH Verlag GmbH & Co. KGaA. (Color figure available online).

There are two approaches for the design of inhomogeneous polymer films that are capable of folding (Figure 1). In both approaches at least two polymers are used. One of the polymers is active and its volume or shape is changed when stimulus is applied. The second polymer can also be active or it can be passive, in which its properties will



remain unchanged. In the first approach, a homogeneous bilayer, whose working principle is similar to bimetals, is used (Figure 1a).<sup>32,33</sup> When exposed to a stimulus, the active polymer will swell or shrink; however, the swelling will be restricted in one direction by the passive polymer. As a result, the bilayer does not uniformly expands/shrinks but folds and unfolds. The second approach is based on use of a patterned bilayer film (Figure 1b).<sup>34,35</sup> In this approach, the active polymer undergoes a shape transition, which could be due to swelling or melting that results in local bending of the film. The areas with the bilayer thus form hinges of the 3D object and other areas form facets. Very recently, Hayward and Santangelo reported a new way of preparation of self-folding films using hydrogels films with photopatterned crosslinking density.<sup>36</sup> These films undergo non-uniform swelling that leads to the deformation and formation of complex 3D shapes.

### 3. Folding of Bilayers

In 1925, Timoshenko<sup>38</sup> considered the bending of metal bilayers consisting of two metals with different thermal expansion coefficients. He assumed that the bilayer could bend in only one direction and results in a bilayer with uniform curvature

$$\frac{1}{\rho} = \frac{6(\varepsilon_2 - \varepsilon_1)(1 + m)^2}{h(3(1 + m)^2 + (1 + mn)(m^2 + \frac{1}{mn}))} \quad (1)$$

$$\frac{E_1}{E_2} = n \quad (2)$$

$$\frac{a_1}{a_2} = m \quad (3)$$

where  $E$  are the elasticity modulus,  $a$  are the thickness of the layers,  $h$  is the total thickness ( $h = a_1 + a_2$ ),  $\varepsilon$  is the stress of the films, and  $\rho$  is the radius of curvature. As it comes from Eqs. (1–3), the radius of curvature is inversely proportional to film stress. Moreover, the radius of curvature first decreases and then increases with the increase of  $m$ . The resultant curvature is not very sensitive to the difference in stiffness between the two layers, and is mainly controlled by the actuation strain and the layer thickness. The Timoshenko equation applies to a beam bending in only one direction and does not predict the folding direction. Moreover, the Timoshenko equation is only applicable for elastic deformations.

More recent models have considered a complex bending of the bilayer in two dimensions. Mansfield found analytical solutions for large deflections of circular<sup>39</sup> and elliptical<sup>40</sup> plates having lenticular cross sections with a temperature gradient through the thickness. For small gradients, the plates formed spherical caps, curved equally in all directions. At a critical gradient, a configuration with greater curvature in one direction became more favorable. Because of the lens-shaped thickness profile, even though the elliptical plate had a major axis it showed no preferred direction for bending even for large deflections. Freund determined the strain at which the spherical cap, formed by the circular bilayer of uniform thickness, becomes unstable using a low order polynomial solutions and finite element simulations.<sup>41</sup>

Later Smela et al. showed that short-side rolling was preferred in the case of free homogeneous actuation and that this preference increased with aspect ratio (ratio of length to width of rectangular pattern).<sup>42</sup> Li et al.<sup>43</sup> and Schmidt<sup>18</sup> experimentally demonstrated the opposite scenario, namely a preference for long-side rolling, in the case where bilayers are

progressively etched from a substrate. They observed that when the tube circumference was much larger than the width (incomplete rolling) or the aspect ratio of the rectangle was high (long stripes), rolling always occurred from the long side. When the tube circumference was much smaller than the width (formation of tubes rolled several times) and the aspect ratio of the membrane pattern was not very high (nearly square film), the rolling resulted in a mixed yield of long- and short-side rolling, as well as a “dead-locked turnover” shape. Short-side rolling occurred at small aspect ratios when the deformed circumference is close to the width. In these self-rolling systems, the active component undergoes relatively small volume changes, which are nearly homogeneous over the whole sample.

In inorganic self-rolling systems, the active component undergoes a relatively small volume changes or actuation strains, which are nearly homogeneous over the whole sample. Hydrogels, however, demonstrate considerably different properties. First, hydrogels undergo large volume changes (up to 10 times) upon swelling and contraction. Second, the swelling of a hydrogel is often kinetically limited: due to slow diffusion of water through hydrogel, the parts which are closer to the edges swell first while the parts which are closer to the center of the films swell later. Stoychev et al. investigated the folding of rectangular stimuli-responsive hydrogel-based polymer bilayers with different aspect ratios and relative thicknesses placed on a substrate.<sup>44</sup> It was found that long-side rolling dominates at high aspect ratios (ratio of length to width) when the width is comparable to the circumference of the formed tubes, which corresponds to a small actuation strain. Rolling from all sides occurs for a higher actuation strain, namely when the width and length considerably exceed the deformed circumference. In the case of moderate actuation, when the width and length are comparable to the deformed circumference, diagonal rolling is observed. Short-side rolling was observed very rarely and in combination with diagonal rolling. In fact it was observed that bilayers placed on a substrate start to roll from corners due to quicker diffusion of water. Rolling from the long side starts later but dominates at high aspect ratios in agreement with energetic considerations. It was shown experimentally and by modeling that the main reasons causing a variety of rolling scenarios are (i) non-homogeneous swelling due to the presence of the substrate and (ii) adhesion of the polymer to the substrate.

Recently Hayward and Santangelo investigated folding of patterned rectangular strips divided into one high- and one low-swelling region, which can be characterized as a thick but narrow bilayer.<sup>45</sup> When swelled in an aqueous medium, it does not bend to the side of the less swelling component as it is observed is the case of the “classical” bilayer discussed by Timoshenko (Figure 2a) but rolls into a three-dimensional shape consisting of two nearly cylindrical regions connected by a transitional neck (Figure 2b).

Swelling of hydrogels is usually a relatively slow process, which is limited by diffusion of water inside the polymer network, and the folding/bending of bilayers occurs of the timescale of seconds and minutes. Recently Bunning et al. demonstrated on the example of liquid crystalline polymer films possibility of very fast deformation (ca 1/300 s).<sup>46</sup>

#### 4. Complex Shapes

The shape of a formed 3D object depends on the 2D shape of the polymer films. The simplest case of a self-folding object is a tube, which is formed by rectangular bilayers (Figure 3a,b).<sup>32,33,47–51</sup> Envelop-like capsules with rounded corners or nearly spherical ones are formed the star-like polymer bilayers with four and six arms, respectively (Figure 3c,d).<sup>50–52</sup> Helixes of different kinds are formed by polymer stripes with the gradually changing ratio between polymers (Figure 3e).<sup>53</sup> In these examples, simple rounded figures based on different combinations of fully or semi-folded tubes are formed. Moreover,

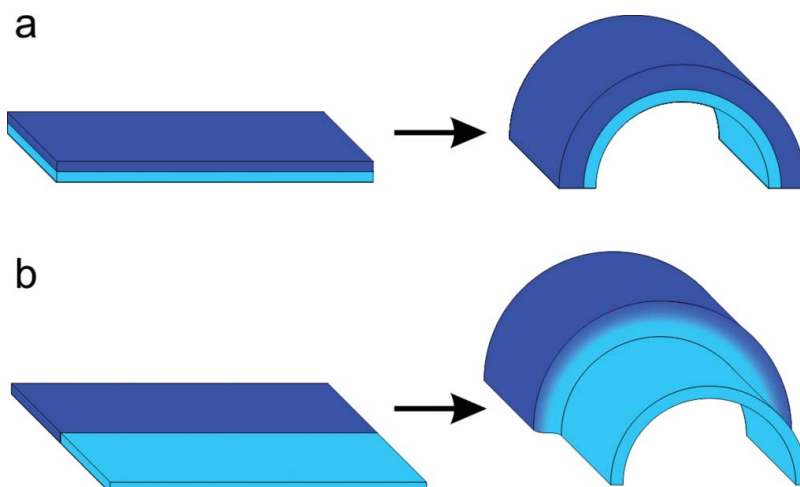


**Figure 2.** Bending of “classical” bilayer (a) and rectangular strips divided into one high- and one low-swelling regions. (Color figure available online).

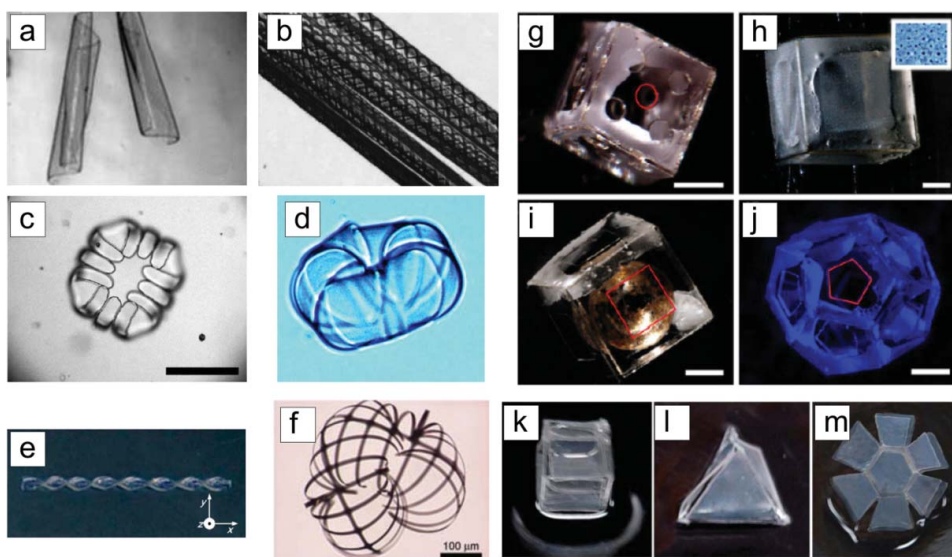


**Figure 3.** (a, b) Examples of self-folding polymer films with different shapes: tubes;<sup>32,48</sup> (c, d) capsules;<sup>50,52</sup> (e) helix;<sup>53</sup> (f) hierarchically-shaped tube;<sup>56</sup> (g, h, i, k) cubes with porous walls;<sup>53,54</sup> (j) dodecahedron;<sup>53</sup> (l) pyramid;<sup>53</sup> (m) phlat ball.<sup>53</sup> (a, b) reproduced from Luchnikov et al.<sup>32</sup> with permission from Wiley-VCH Verlag GmbH & Co. KGaA; (c) reproduced from Guan et al.<sup>50</sup> with permission from Wiley-VCH Verlag GmbH & Co. KGaA; (d) reproduced from Stoychev et al.<sup>52</sup> with permission from Royal Society of Chemistry; (f) reproduced from Kelby et al.<sup>56</sup> with permission from Wiley-VCH Verlag GmbH & Co. KGaA; (g, h, i, j) reproduced from Azam et al.<sup>54</sup> with permission from Springer Science + Business Media; (k, l, m) reproduced from Jeong et al.<sup>53</sup> with permission from Royal Society of Chemistry. (Color figure available online).

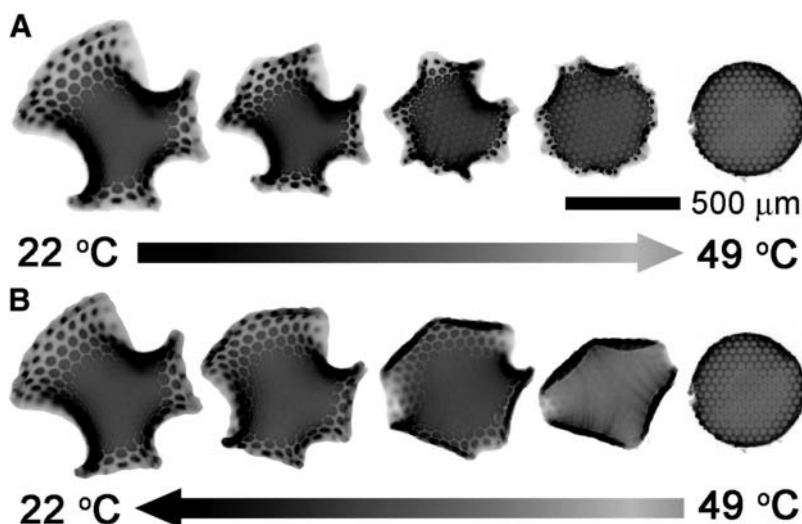


**Figure 4.** Thermal actuation of patterned sheets. (a) When the temperature of the aqueous medium is increased, the hybrid Enneper's surface deswells and recovers its flat shape by 49°C. (b) Upon lowering the temperature to 22°C, the disk swells back to the initial hybrid shape through a different pathway. Reproduced from Kim et al.<sup>36</sup> with permission from AAAS.

because of the isotropy of mechanical properties of the bilayer, the formation of hinges during the folding of bilayers is considered to be impossible. Objects with sharp edges are formed in a patterned bilayer where the active component is deposited locally (Figure 3g-m). The active component can either swell/shrink or change its shape due to melting. In this way, cubes and pyramids are formed by a patterned bilayer with active junction elements.<sup>53–55</sup> It is important to note that in all reported cases folding occurs in one step, that is, the active polymer changes its volume and results in simple bending.

Santangelo and Hayward reported on photopatterned hydrogel films that yield temperature-responsive gel sheets and can transform between a flat state and a prescribed three-dimensional shape. The hydrogel was patterned using so-called halftone gel lithography using only two photomasks, wherein highly cross-linked dots embedded in a lightly cross-linked matrix provide access to nearly continuous, and fully two-dimensional, patterns of swelling. This method is used to fabricate surfaces with constant Gaussian curvature (spherical caps, saddles, and cones) or zero mean curvature (Enneper's surfaces), as well as more complex and nearly closed shapes (Figure 4)

Importantly, in most cases folding runs in one step. Step-by-step folding of different elements of self-folding films can be achieved by local activation of selected areas by light.<sup>57</sup> Another possibility is to use two or more kinds of active material which are sensitive to different stimulus. Gracias et al. demonstrated a two-step deformation of patterned films where active elements are two kinds of biodegradable polymers. Each of these polymers is degraded by a specific enzyme. As a result the films fold when the first enzyme is added and unfold when the second one is added.<sup>58</sup> On the other hand, there are reports that folding in nature can have a very complex character, which strongly depends on the swelling path<sup>59,60</sup> that may result in multi-step folding (development of curvature in different directions).<sup>3</sup> Recently, we demonstrated that the shape of isotropic polymer bilayers determines swelling path and is able to direct folding in a sophisticated manner leading to even more complex

hierarchical folding than in nature. In particular, films can undergo sequential steps of folding by forming various 3D shapes with sharp hinges. Experimental observations lead us to derive four empirical rules backed up by theoretical understanding as well as simulations. We then demonstrated how those rules can be used to direct the folding of edge-activated polymer bilayers through a concrete example—the design of a 3D pyramid.<sup>44</sup>

## 5. Fabrication of Self-Folding Films

Experimentally, polymer films with different shapes can be obtained either by cutting,<sup>32,47,48</sup> using microwell-like substrates<sup>49–51</sup> or photolithography.<sup>33,52,54,55</sup> Cutting allows fabrication of millimeter-sized species with the rectangular shape, which form the tubes. The main advantage of this method is simplicity and applicability to almost all combinations of crosslinkable polymers. Use of microwell-like substrates is technically more complicated, while allowing the fabrication of polymer layers with different shapes such as rectangles or stars. Photolithography of bilayers allows for large-scale fabrication of self-folding objects of different shape and size starting from several microns. The formed self-folding objects have rounded corners. The main limitation of this approach is the careful choice of the solvents used for dissolving the polymers in the way that first polymer is not dissolved during deposition of the second polymer. Fabrication of patterned polymer films is technically the most complicated procedure and requires mask alignment during several steps of photolithography. On the other hand, it allows for fabrication of the broadest range of shapes of self-folding objects. Very recently Luchnikov et al. demonstrated a method for upscaling of fabrication of self-folding films by merely scratching folding polymer film with an array of metallic blade.<sup>61</sup>

## 6. Stimuli-Responsive Self-Folding Films

The use of polymers that are sensitive to different signals allows for the design of self-folding films upon immersion in solvent, change of pH, temperature, and electric or biochemical signals.

### 6.1 pH-Responsive

Self-folding films sensitive to pH are commonly designed using weak polyelectrolytes as active polymers.<sup>25,32,49,51,55,56,62–64</sup> It was demonstrated that polystyrene-poly(4 vinyl pyridine) bilayer<sup>32</sup> as well as polystyrene-poly(4-vinylpyridine)-polydimethylsiloxane tri-layer<sup>62</sup> are able to roll at low pH when poly(4-vinylpyridine) is protonated and swells in water. The use of layers with a two-dimensional gradient of thickness allows for a thorough investigation of folding.<sup>63</sup> It was found that the rate of rolling increased with the acidity of the solution. The tube diameter and rate of rolling decreased with the increase of the UV exposure time. Moreover, the increase of thickness of PS resulted in an increase of the diameter of tube.

Lee et al. used pH sensitive poly(methacrylic acid) - poly(2-hydroxyethyl methacrylate)<sup>49</sup> and poly(methacrylic acid) (PMAA)/ polyEGDMA<sup>51</sup> patterned the bilayer which folds when in contact with biological fluids. It was not shown that the folding depended on pH; however, the systems were expected to respond to the pH signal since a weak polyelectrolyte poly(methacrylic acid) was used. Gracias et al. fabricated millimeter large polyethylene glycol/ poly-(N-isopropylacrylamide-acrylic acid) bilayers which were able to snap in response to the pH signal.<sup>55</sup> One can also expect that this system is thermoresponsive. Huck



et al. reported pH responsive gold-poly(methacryloxyethyl trimethylammonium chloride) brush patterned films which fold in response to the change of pH and salt concentration.<sup>56</sup> Very recently, Yang et al. demonstrated the folding of pH responsive poly(2-hydroxyethyl methacrylate-co-acrylic acid)/ poly(2-hydroxyethyl methacrylate) bilayers.<sup>65</sup>

## 6.2 Thermoresponsive

Thermoresponsive self-folding films can be designed using continuous thermal expansion, melting, shape-memory transition, or polymers which demonstrate LCST (Low Critical Solution Temperature) behavior in solutions. Kalaitzidou et al. used continuous volume expansion with temperature and demonstrated thermoresponsive rolling-unrolling of polydimethylsiloxane-gold bilayers tubes at 60°C–70°C<sup>47,48</sup> which is due to coefficients of different temperature expansion.

Gracias et al. used melting of polymer, which form a droplet and forces patterned polymer films to fold. This was demonstrated on the example of patterned SU-8 photoresist-polycaprolactone film, which irreversibly folds at 60°C<sup>66</sup> due to the melting of polycaprolactone. In order to reduce the transition temperature and make film more suitable bio-related applications, Gracias et al. used photoresist hinges which are sensitive to temperature around 40°C.<sup>67–69</sup> The metal-polymer grippers irreversibly fold in response to temperature as well.

Lendlein et al. demonstrated the possibilities of designing thermoresponsive macroscopic self-folding objects using shape-memory polymers based on different poly( $\epsilon$ -caprolactone).<sup>70</sup> At low temperatures, the materials are in a temporary shape. The films recover to their permanent shape and irreversibly fold by heating, which could be accompanied by a change of transparency. The exact size of the self-folding film as well as transition temperature was not given.

Polymer bilayers, where the active component is thermoresponsive poly-(N-isopropylacrylamide)-based copolymers, are more suitable for encapsulation of cells. In aqueous media, poly-(N-isopropylacrylamide)-based hydrogels reversibly swell and shrink below and above 33°C. Moreover, the temperature of transition between swollen and shrunk states can be tuned by proper selection of composition of copolymer. As a result, poly-(N-isopropylacrylamide)-polycaprolactone patterned bilayers fold and unfold forming tubes of capsules below and above this temperature, respectively (Figure 5a).<sup>33,52</sup>

## 6.3 Solvent Responsive

Most examples of solvent-responsive self-folding films fold upon immersion in aqueous media. Such films contain water-swellaable uncharged polymers. Lee fabricated partially biodegradable polyvinyl alcohol-chitosan<sup>50</sup> and chitosan-poly(PEGMA-co-PEGDMA) bilayers<sup>51</sup> which folds in water due to the swelling of polyvinyl alcohol and polyethyleneglycol, respectively. Jeong and Jang et al. developed the approach for fabrication of millimeter size self-folding objects that are able to fold and form different 3D objects such as tube, cube, pyramids, and helices.<sup>53</sup> Water-swellaable polydimethylsiloxane-polyurethane/2-hydroxyethyl methacrylate complex bilayers and patterned films were used. Since poly(vinyl alcohol), polyethyleneglycol and poly(2-hydroxyethyl methacrylate) are not polyelectrolytes, the swelling is expected to be independent of pH of aqueous media. These systems immediately fold upon immersion in aqueous media that hampers loading of cells. Huck reported an example system that folds in methanol. This system was based on poly(glycidyl methacrylate) brush layer grafted to gold patterned films.<sup>56</sup>

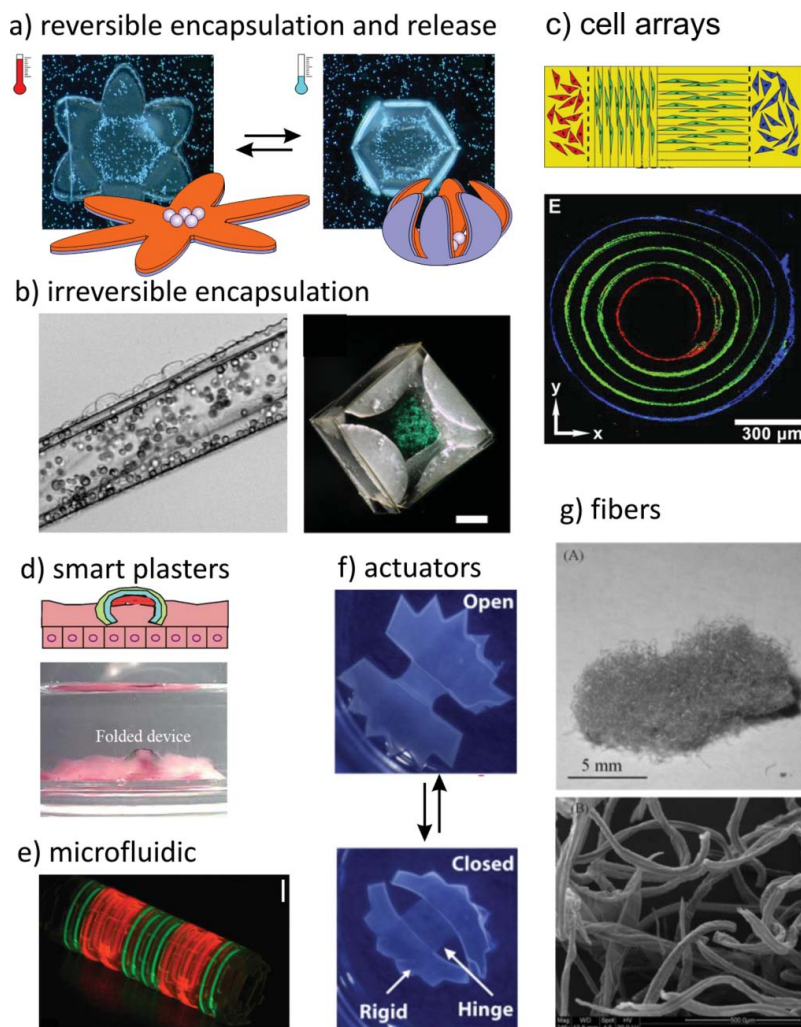


**Figure 5.** Examples of applications of self-folding polymer films: (a) reversible encapsulation and release of yeast cells inside the thermoresponsive self-folding capsules; (b) irreversible encapsulation of cells – yeast cells encapsulation inside fully biodegradable self-rolled film and stained fibroblast cells encapsulated within a non-porous polymeric container; (c) array of multiple cells inside selfrolled prestressed PDMS film; (d) smart plasters which direct diffusion of drugs and prevent their leakage; (e) 3D microfluidic device obtained by folding; (f) actuator with hinges folding in changing pH and ionic strength; (g) optical (top) and electron microscopy (bottom) images of fibrous material obtained from self-folding polymer films. (a) reproduced from Stoychev et al.<sup>52</sup> with permission from Royal Society of Chemistry; (b, left) reproduced from Zakharchenko et al.<sup>75</sup> with permission from American Chemical Society; (b, right) reproduced from Azam et al.<sup>54</sup> with permission from Springer Science + Business Media; (c) reproduced from Yuan et al.<sup>81</sup> with permission from Wiley-VCH Verlag GmbH & Co. KGaA; (d) reproduced from He et al.<sup>49</sup> with permission from Elsevier; (e) reproduced from Jamal et al.<sup>83</sup> with permission from Nature Publishing Group; (f) reproduced from Bassik et al.<sup>55</sup> with permission from Elsevier; (g) reproduced from Luchnikov et al.<sup>61</sup> with permission from Wiley-VCH Verlag GmbH & Co. KGaA. (Color figure available online).

#### 6.4 Light-Responsive

Light-responsive self-folding polymer films have been designed from thermoresponsive polymers with incorporated particles, which convert light into heat.<sup>71,72</sup> Light-to-heat converting substance could be carbon nanotubes or any other black material. Poly(N-isopropylacrylamide) hydrogel and pre-stressed polystyrene sheets (Shrinky-Dinks) were used as thermoresponsive components. The first system is active in aqueous medium, while the second one is capable of folding in both air and water.

#### 6.5 Other Systems

Except for pH-, thermo-, and solvent-responsive systems, there are also several examples of systems, which fold in response to other stimuli such as presence of enzymes or applied electric field. Smella<sup>34</sup> and Jager et al.,<sup>73</sup> who introduced the self-folding films, demonstrated folding and unfolding of patterned gold film with polypyrrole hinges in the response to electric signal. Whilesides et al. fabricated electro-responsive self-folding bilayer, which consists of polydimethylsiloxane with the aligned cardiomyocytes.<sup>74</sup> The polymer-cell film adopted functional three-dimensional conformations when an electric signal was applied. These centimeter-scale constructs can perform functions as diverse as gripping, pumping, walking, and swimming with fine spatial and temporal control.

Enzyme-sensitive self-folding films were developed for the first time by Gracias et al. The approach is based on the use of self-folding metallic grippers with active polymer hinges, which are sensitive to presence of enzymes.<sup>58</sup> Two kinds of biodegradable polymers were used. The gripper, which is unfolded in its initial state, folds when the first polymer is degraded due to the addition of the first enzyme. The gripper unfolds when the second enzyme is added and the second polymer is degraded. As a result one circle of folding and unfolding is achieved.

### 7. Properties and Applications of Folding

One field of application for self-folding polymer thin films is the controlled encapsulation and release of drugs, particles, and cells. Kalaitzidou demonstrated reversible adsorption-desorption of fluorescently labeled polyethyleneglycol, which is considered as model drug, inside PDMS-gold tubes at 60–70°C.<sup>47</sup> Gracias et al. demonstrated irreversible encapsulation of yeast cells inside self-folding SU8-PCL films upon heating above at 60°C.<sup>66</sup> Poly(N-isopropylacrylamide)-based self-folding films were also demonstrated to be suitable for reversible encapsulation of particles and yeast cells.<sup>33,52</sup> Cells were encapsulated upon cooling below 30°C and could be released from the film, which is unfolded above 30°C (Figure 5a). This encapsulation and release is completely reversible and could be repeated many times. Very recently, fully biodegradable self-folding films, which consist of commercially available biodegradable polymers, were also used to encapsulate cells (Figure 5b).<sup>75</sup> In fact, there are many approaches that can be used for encapsulation of cells including LbL, microfluidic technique, and controlled precipitation. The advantage of self-folding approach is possibility of reversible encapsulation and release. Self-folded objects with nanoporous walls and encapsulated cells were suggested as prototype of artificial pancreas. The small molecules such as glucose and dissolved oxygen are able to pass through the pores while larger ones such as antibody are blocked. This size-selective permeability of self-folded capsules allows avoiding immune response that is highly demanded during transplantation of pancreas cells.<sup>76</sup> Gracias et al. used rigid metal-made

self-folding microgrippers for capturing pieces of tissues and their controlled transport. Such systems are particularly attractive for non-invasive biopsy.<sup>69</sup> Self-folded objects were used as scaffolds for fabrication of 3D cellular constructs.<sup>77,78</sup> Controlled release of small molecules through the pores of self-folded microconstructs was used to spontaneously organize cells in 3D environment,<sup>79,80</sup> which potentially allows fabrication of 3D scaffolds for tissue engineering. For example, self-rolling prestressed PDMS films with adsorbed cells of different kinds were used to make tubular structures mimicking the structure of blood vessels (Figure 5c).<sup>81</sup>

Self-folding films can also be used as smart plasters (Figure 5d). Lee demonstrated this concept on the example of millimeter size poly(methyl methacrylate)-poly(2-hydroxyethyl methacrylate) bilayer with an attached muco-adhesive drug layer. The non-swelling PHEMA layer serves as a diffusion barrier, minimizing any drug leakage in the intestine. The resulting unidirectional release provides improved drug transport through the mucosal epithelium. The functionality of this device is successfully demonstrated *in vitro* using a porcine small intestine.<sup>49</sup>

There are also several non-biorelated examples of application of self-folding polymer films. Deposition of patterned metal on the polymer bilayer allowed fabrication of self-rolled tubes with patterned conductive inner wall.<sup>32</sup> In another example, pyrolysis of polystyrene-poly(4 vinyl pyridine)-polydimethylsiloxane trilayer<sup>62</sup> and polystyrene- poly(4 vinyl pyridine)/resorcinol bilayer<sup>82</sup> was used for fabrication of silica and carbon tubes, respectively. Gracias used self-folding polymers films which were used to fabricate self-assembled curved microfluidic networks (Figure 5e)<sup>83</sup> and designed smart actuating systems mimicking opening and closing of the Venus flytrap by using a pH responsive polymer, which forms a hinge between two polymer films (Figure 5f).<sup>55</sup> Very recently Luchnikov et al. fabricated fibers with hollow interior using scratched self-folding polymer films (Figure 5g).<sup>61</sup>

## 8. Conclusions and Outlook

Nature offers a myriad of ideas for the design of novel materials with advanced properties. Very recently, the principle of movement in plants was successfully transferred for the design of special sort of actively moving materials: self-folding polymer films. Till now many examples of polymer thin films folding due to immersion in the aqueous environment, change of pH, temperature, light, electric signal, or the presence of enzymes were demonstrated. These experiments showed that one step-folding can be used for fabrication of both simple shapes such as tubes or flower-like capsules and more complex ones such as cubes or tetrahedron. One of the recent trends is to develop approaches for multi-step hierarchical folding. One way to achieve multi-step folding is to use several polymers sensitive to several stimuli or site-selective activation of different elements of self-folding films. In these cases either manufacturing or folding become more time consuming. Another approach, which is inspired by nature, is to use inhomogeneity of swelling path that allows very complex folding in the way that star-arm bilayers build pyramids with sharp hinges.

It was also demonstrated that self-folding films are very promising for the design of biomaterials, controlled encapsulation, and release of drugs and cells. In particular, due to their softness, better biocompatibility, possible biodegradability, and easy manufacturing polymer self-folding films can compete with inorganic ones in the field of microelectronics and bio-microelectronics for *in vivo* applications.

One of the factors limiting broad applicability of self-folding polymer films is the manufacturing cost. In fact, because polymer can be deposited by using spin and dip

coating at ambient conditions, the fabrication of polymer self-folding films is substantially cheaper than fabrication of inorganic ones, which are produced by vacuum deposition. On the other hand, there is still no method for very cheap and large-scale production of self-folding polymer films that substantially limits their applications.

In order to address these issues, future research in self-folding films must be focused on deeper investigation of folding to allow design of complex 3D structures using very simple 2D shapes. Moreover, development of the way for cheap and fast manufacturing of large quantity of self-folding films will boost their broad application.

## Acknowledgement

The author is grateful to DFG (Grant IO 68/1-1) for financial support.

## References

1. Leong, T.G.; Zarafshar, A.M.; Gracias, D.H. "Three-Dimensional Fabrication at Small Size Scales," *Small* **2010**, 6(7), 792–806.
2. Whitesides, G.M.; Grzybowski, B. "Self-Assembly at All Scales," *Science* **2002**, 295(5564), 2418–2421.
3. Harrington, M.J.; Razghandi, K.; Ditsch, F.; Guiducci, L.; Rueggeberg, M.; Dunlop, J.W.C.; Fratzl, P.; Neinhuis, C.; Burgert, I. "Origami-like unfolding of hydro-actuated ice plant seed capsules," *Nat. Commun.* **2011**, 2, 337.
4. Burgert, I.; Fratzl, P. "Actuation systems in plants as prototypes for bioinspired devices," *Philos. T. R. Soc. A* **2009**, 367(1893), 1541–1557.
5. Fratzl, P.; Barth, F.G. "Biomaterial systems for mechanosensing and actuation," *Nature* **2009**, 462(7272), 442–448.
6. Elbaum, R.; Zaltzman, L.; Burgert, I.; Fratzl, P. "The role of wheat awns in the seed dispersal unit," *Science* **2007**, 316(5826), 884–886.
7. Reyssat, E.; Mahadevan, L. "Hygromorphs: from pine cones to biomimetic bilayers," *J. R. Soc. Interface* **2009**, 6(39), 951–957.
8. Ionov, L. "Actively-moving materials based on stimuli-responsive polymers," *J. Mater. Chem.* **2010**, 20(17), 3382–3390.
9. Tokarev, I.; Minko, S. "Stimuli-responsive hydrogel thin films," *Soft. Matter* **2009**, 5(3), 511–524.
10. Qiu, Y.; Park, K. "Environment-sensitive hydrogels for drug delivery," *Adv. Drug. Deliver. Rev.* **2001**, 53(3), 321–339.
11. Ionov, L. "Soft microorigami: self-folding polymer films," *Soft. Matter* **2011**, 7, 6786–6791.
12. Yang, S.; Khare, K.; Lin, P.C. "Harnessing Surface Wrinkle Patterns in Soft Matter," *Adv. Funct. Mater.* **2010**, 20(16), 2550–2564.
13. Hendricks, T.R.; Wang, W.; Lee, I. "Buckling in nanomechanical films," *Soft. Matter* **2010**, 6(16), 3701–3706.
14. Chen, X.; Yin, J. "Buckling patterns of thin films on curved compliant substrates with applications to morphogenesis and three-dimensional micro-fabrication," *Soft. Matter* **2010**, 6(22), 5667–5680.
15. Schweikart, A.; Pazos-Perez, N.; Alvarez-Puebla, R.A.; Fery, A. "Controlling inter-nanoparticle coupling by wrinkle-assisted assembly," *Soft. Matter* **2011**, 7(9), 4093–4100.
16. Schweikart, A.; Fery, A. "Controlled wrinkling as a novel method for the fabrication of patterned surfaces," *Microchim. Acta* **2009**, 165(3–4), 249–263.
17. Huang, G.; Mei, Y. "Thinning and Shaping Solid Films into Functional and Integrative Nanomembranes," *Adv. Mater.* **2012**, 24(19), 2517–2546.
18. Cendula, P.; Kiravittaya, S.; Monch, I.; Schumann, J.; Schmidt, O.G. "Directional Roll-up of Nanomembranes Mediated by Wrinkling," *Nano. Lett.* **2011**, 11(1), 236–240.
19. Genzer, J.; Groenewold, J. "Soft matter with hard skin: From skin wrinkles to templating and material characterization," *Soft. Matter* **2006**, 2(4), 310–323.



20. Stuart, M.A.C.; Huck, W.T.S.; Genzer, J.; Muller, M.; Ober, C.; Stamm, M.; Sukhorukov, G.B.; Szleifer, I.; Tsukruk, V.V.; Urban, M.; Winnik, F.; Zauscher, S.; Luzinov, I.; Minko, S. "Emerging applications of stimuli-responsive polymer materials," *Nat. Mater.* **2010**, 9(2), 101–113.
21. Sidorenko, A.; Krupenkin, T.; Taylor, A.; Fratzl, P.; Aizenberg, J. "Reversible switching of hydrogel-actuated nanostructures into complex micropatterns," *Science* **2007**, 315(5811), 487–490.
22. Zarzar, L.D.; Kim, P.; Aizenberg, J. "Bio-inspired Design of Submerged Hydrogel-Actuated Polymer Microstructures Operating in Response to pH," *Adv. Mater.* **2011**, 23(12), 1442–1446.
23. Schweikart, A.; Horn, A.; Boker, A.; Fery, A. "Controlled Wrinkling as a Novel Method for the Fabrication of Patterned Surfaces," *Adv. Polym. Sci.* **2010**, 227, 75–99.
24. Huang, J.; Juskiewicz, M.; de Jeu, W.H.; Cerda, E.; Emrick, T.; Menon, N.; Russell, T.P. "Capillary wrinkling of floating thin polymer films," *Science* **2007**, 317(5838), 650–653.
25. Singamaneni, S.; McConney, M.E.; Tsukruk, V.V. "Spontaneous Self-Folding in Confined Ultrathin Polymer Gels," *Adv. Mater.* **2010**, 22(11), 1263–1268.
26. Horn, A.; Schoberth, H.G.; Hiltl, S.; Chiche, A.; Wang, Q.; Schweikart, A.; Fery, A.; Boker, A. "Nanostructured wrinkled surfaces for templating bionanoparticles-controlling and quantifying the degree of order," *Faraday Discussions* **2009**, 143, 143–150.
27. Kwon, G.H.; Choi, Y.Y.; Park, J.Y.; Woo, D.H.; Lee, K.B.; Kim, J.H.; Lee, S.-H. "Electrically-driven hydrogel actuators in microfluidic channels: fabrication, characterization, and biological application," *Lab. Chip.* **2010**, 10(12), 1604–1610.
28. Ohm, C.; Brehmer, M.; Zentel, R. "Liquid Crystalline Elastomers as Actuators and Sensors," *Adv. Mater.* **2010**, 22(31), 3366–3387.
29. Klein, Y.; Efrati, E.; Sharon, E. "Shaping of Elastic Sheets by Prescription of Non-Euclidean Metrics," *Science* **2007**, 315(5815), 1116–1120.
30. Zhou, F.; Biesheuvel, P.M.; Chol, E.Y.; Shu, W.; Poetes, R.; Steiner, U.; Huck, W.T.S. "Poly-electrolyte brush amplified electroactuation of microcantilevers," *Nano. Lett.* **2008**, 8(2), 725–730.
31. Py, C.; Reverdy, P.; Doppler, L.; Bico, J.; eacute; Roman, B.; icirc; Baroud, C.N. "Capillary Origami: Spontaneous Wrapping of a Droplet with an Elastic Sheet," *Phys. Rev. Lett.* **2007**, 98(15), 156103.
32. Luchnikov, V.; Sydorenko, O.; Stamm, M. "Self-rolled polymer and composite polymer/metal micro- and nanotubes with patterned inner walls," *Adv. Mater.* **2005**, 17(9), 1177–1182.
33. Zakharchenko, S.; Pureskiy, N.; Stoychev, G.; Stamm, M.; Ionov, L. "Temperature controlled encapsulation and release using partially biodegradable thermo-magneto-sensitive self-rolling tubes," *Soft. Matter* **2010**, 6(12), 2633–2636.
34. Smela, E.; Inganas, O.; Lundstrom, I. "Controlled Folding of Micrometer-Size Structures," *Science* **1995**, 268(5218), 1735–1738.
35. Gracias, D.H.; Kavthekar, V.; Love, J.C.; Paul, K.E.; Whitesides, G.M. "Fabrication of Micrometer-Scale, Patterned Polyhedra by Self-Assembly," *Adv. Mater.* **2002**, 14(3), 235–238.
36. Kim, J.; Hanna, J.A.; Byun, M.; Santangelo, C.D.; Hayward, R.C. "Designing Responsive Buckled Surfaces by Halftone Gel Lithography," *Science* **2012**, 335(6073), 1201–1205.
37. Stoychev, G.; Zakharchenko, S.; Turcaud, S.; Dunlop, J.W.C.; Ionov, L. "Shape programmed folding of stimuli-responsive polymer bilayers ACS Nano **2012**, 6(5), 3925–3934.
38. Timoshenko, S. "Analysis of bi-metal thermostats," *J. Opt. Soc. Am. Rev. Sci. Instrum.* **1925**, 11(3), 233–255.
39. Mansfield, E.H. "Bending, buckling and curling of a heated thin plate," *Proc. R. Soc. A.* **1962**, 268(1334), 316–237.
40. Mansfield, E.H. "Bending buckling and curling of a heated elliptical plate," *Proc. R. Soc. A.* **1965**, 288(1414), 396–417.
41. Freund, L.B. "Substrate curvature due to thin film mismatch strain in the nonlinear deformation range," *J. Mech. Phys. Solids.* **2000**, 48(6-7), 1159–1174.
42. Alben, S.; Balakrishnan, B.; Smela, E. "Edge Effects Determine the Direction of Bilayer Bending," *Nano. Lett.* **2011**, 11(6), 2280–2285.

43. Chun, I.S.; Challa, A.; Derickson, B.; Hsia, K.J.; Li, X. "Geometry Effect on the Strain-Induced Self-Rolling of Semiconductor Membranes," *Nano. Lett.* **2010**, 10(10), 3927–3932.
44. Stoychev, G.; Turcaud, S.; Dunlop, J.W.C.; Ionov, L. "Hierarchical multi-step folding of polymer bilayers Adv," *Funct. Mater.* 10.1002/adfm.201203245.
45. Kim, J.; Hanna, J.A.; Hayward, R.C.; Santangelo, C.D. "Thermally responsive rolling of thin gel strips with discrete variations in swelling," *Soft. Matter* **2012**, 8(8), 2375–2381.
46. Serak, S.; Tabiryan, N.; Vergara, R.; White, T.J.; Vaia, R.A.; Bunning, T.J. "Liquid crystalline polymer cantilever oscillators fueled by light," *Soft. Matter* **2010**, 6(4), 779–783.
47. Kalaitzidou, K.; Crosby, A.J. "Adaptive polymer particles," *Appl. Phys. Lett.* **2008**, 93(4), 041910
48. Simpson, B.; Nunnery, G.; Tannenbaum, R.; Kalaitzidou, K. "Capture/release ability of thermo-responsive polymer particles," *J. Mater. Chem.* **2010**, 20(17), 3496–3501.
49. He, H.Y.; Guan, J.J.; Lee, J.L. "An oral delivery device based on self-folding hydrogels," *J. Control. Release* **2006**, 110(2), 339–346.
50. Guan, J.J.; He, H.Y.; Lee, L.J.; Hansford, D.J. "Fabrication of particulate reservoir-containing, capsulelike, and self-folding polymer microstructures for drug delivery," *Small* **2007**, 3(3), 412–418.
51. Guan, J.J.; He, H.Y.; Hansford, D.J.; Lee, L.J. "Self-folding of three-dimensional hydrogel microstructures," *J. Phys. Chem. B* **2005**, 109(49), 23134–23137.
52. Stoychev, G.; Pureskiy, N.; Ionov, L. "Self-folding all-polymer thermoresponsive microcapsules," *Soft. Matter* **2011**, 7, 3277–3279
53. Jeong, K.-U.; Jang, J.-H.; Kim, D.-Y.; Nah, C.; Lee, J.H.; Lee, M.-H.; Sun, H.-J.; Wang, C.-L.; Cheng, S.Z.D.; Thomas, E.L. "Three-dimensional actuators transformed from the programmed two-dimensional structures via bending, twisting and folding mechanisms," *J. Mater. Chem.* **2011**, 21, 6824–6830.
54. Azam, A.; Laffin, K.E.; Jamal, M.; Fernandes, R.; Gracias, D.H. "Self-folding micropatterned polymeric containers," *Biomed. Microdevices* **2011**, 13(1), 51–58.
55. Bassik, N.; Abebe, B.T.; Laffin, K.E.; Gracias, D.H. "Photolithographically patterned smart hydrogel based bilayer actuators," *Polymer* **2010**, 51(26), 6093–6098.
56. Kelby, T.S.; Wang, M.; Huck, W.T.S. "Controlled Folding of 2D Au–Polymer Brush Composites into 3D Microstructures," *Adv. Funct. Mater.* **2011**, 21(4), 652–657.
57. Laffin, K.E.; Morris, C.J.; Muqem, T.; Gracias, D.H. "Laser triggered sequential folding of microstructures," *Appl. Phys. Lett.* **2012**, 101(13), 131901
58. Bassik, N.; Brafman, A.; Zarafshar, A.M.; Jamal, M.; Luvsanjav, D.; Selaru, F.M.; Gracias, D.H. "Enzymatically Triggered Actuation of Miniaturized Tools," *J. Am. Chem. Soc.* **2010**, 132(46), 16314–16317.
59. Liang, H.Y.; Mahadevan, L. "Growth, geometry, and mechanics of a blooming lily," *Proc. Natl. Acad. Sci. U. S. A.* **2011**, 108(14), 5516–5521.
60. Liang, H.; Mahadevan, L. "The shape of a long leaf," *Proc. Natl. Acad. Sci. U. S. A.* **2009**, 106(52), 22049–22054.
61. Luchnikov, V.A.; Saito, Y.; Tzanis, L. "A Novel Fibrous Material Created by Self-Rolling of a Patterned Polymer Thin Film," *Macromol. Rapid. Comm.* **2012**, 33(16), 1404–1408.
62. Kumar, K.; Nandan, B.; Luchnikov, V.; Simon, F.; Vyalikh, A.; Scheler, U.; Stamm, M. "A Novel Approach for the Fabrication of Silica and Silica/Metal Hybrid Microtubes," *Chem. Mat.* **2009**, 21(18), 4282–4287.
63. Kumar, K.; Luchnikov, V.; Nandan, B.; Senkovskyy, V.; Stamm, M. "Formation of self-rolled polymer microtubes studied by combinatorial approach," *Eur. Polym. J.* **2008**, 44(12), 4115–4121.
64. Singamaneni, S.; McConney, M.E.; Tsukruk, V.V. "Swelling-Induced Folding in Confined Nanoscale Responsive Polymer Gels," *ACS. Nano* **2010**, 4(4), 2327–2337.
65. Shim, T.S.; Kim, S.-H.; Heo, C.-J.; Jeon, H.C.; Yang, S.-M. "Controlled Origami Folding of Hydrogel Bilayers with Sustained Reversibility for Robust Microcarriers," *Angew. Chem. Int. Edit.* **2012**, 51(6), 1420–1423.
66. Tanaka, T.; Okayama, M.; Kitayama, Y.; Kagawa, Y.; Okubo, M. "Preparation of "Mushroom-like" Janus Particles by Site-Selective Surface-Initiated Atom Transfer Radical Polymerization in Aqueous Dispersed Systems," *Langmuir* **2010**, 26(11), 7843–7847.

67. Leong, T.G.; Benson, B.R.; Call, E.K.; Gracias, D.H. "Thin Film Stress Driven Self-Folding of Microstructured Containers," *Small* **2008**, 4(10), 1605–1609.
68. Leong, T.G.; Randall, C.L.; Benson, B.R.; Zarafshar, A.M.; Gracias, D.H. "Self-loading lithographically structured microcontainers: 3D patterned, mobile microwells," *Lab. Chip.* **2008**, 8(10), 1621–1624.
69. Leong, T.G.; Randall, C.L.; Benson, B.R.; Bassik, N.; Stern, G.M.; Gracias, D.H. "Tetherless thermobiochemically actuated microgrippers," *Proc. Natl. Acad. Sci. U. S. A.* **2009**, 106(3), 703–708.
70. Behl, M.; Razzaq, M.Y.; Lendlein, A. "Multifunctional Shape-Memory Polymers," *Adv. Mater.* **2010**, 22(31), 3388–3410.
71. Zhang, X.; Pint, C.L.; Lee, M.H.; Schubert, B.E.; Jamshidi, A.; Takei, K.; Ko, H.; Gillies, A.; Bardhan, R.; Urban, J.J.; Wu, M.; Fearing, R.; Javey, A. "Optically- and Thermally-Responsive Programmable Materials Based on Carbon Nanotube-Hydrogel Polymer Composites," *Nano. Lett.* **2011**, 11(8), 3239–3244.
72. Liu, Y.; Boyles, J.K.; Genzer, J.; Dickey, M.D. "Self-folding of polymer sheets using local light absorption," *Soft. Matter.* **2012**, 8, 1764–1769.
73. Jager, E.W.H.; Inghanas, O.; Lundstrom, I. "Microrobots for micrometer-size objects in aqueous media: Potential tools for single-cell manipulation," *Science* **2000**, 288(5475), 2335–2338.
74. Feinberg, A.W.; Feigel, A.; Shevkoplyas, S.S.; Sheehy, S.; Whitesides, G.M.; Parker, K.K. "Muscular thin films for building actuators and powering devices," *Science* **2007**, 317(5843), 1366–1370.
75. Zakharchenko, S.; Sperling, E.; Ionov, L. "Fully biodegradable self-rolled polymer tubes: a candidate for tissue engineering scaffolds," *Biomacromolecules* **2011**, 12(6), 2211–2215.
76. Randall, C.L.; Kalinin, Y.V.; Jamal, M.; Shah, A.; Gracias, D.H. "Self-folding immunoprotective cell encapsulation devices," *Nanomed.-Nanotechnol.* **2011**, 7(6), 686–689.
77. Randall, C.L.; Kalinin, Y.V.; Jamal, M.; Manohar, T.; Gracias, D.H. "Three-dimensional microwell arrays for cell culture," *Lab. Chip.* **2011**, 11(1), 127–131.
78. Jamal, M.; Bassik, N.; Cho, J.H.; Randall, C.L.; Gracias, D.H. "Directed growth of fibroblasts into three dimensional micropatterned geometries via self-assembling scaffolds," *Biomaterials* **2010**, 31(7), 1683–1690.
79. Kalinin, Y.V.; Randhawa, J.S.; Gracias, D.H. "Three-Dimensional Chemical Patterns for Cellular Self-Organization," *Angew. Chem. Int. Edit.* **2011**, 50(11), 2549–2553.
80. Pedron, S.; van Lierop, S.; Horstman, P.; Penterman, R.; Broer, D.J.; Peeters, E. "Stimuli Responsive Delivery Vehicles for Cardiac Microtissue Transplantation," *Adv. Funct. Mater.* **2011**, 21(9), 1624–1630.
81. Yuan, B.; Jin, Y.; Sun, Y.; Wang, D.; Sun, J.; Wang, Z.; Zhang, W.; Jiang, X. "A Strategy for Depositing Different Types of Cells in Three Dimensions to Mimic Tubular Structures in Tissues," *Adv. Mater.* **2012**, 24(7), 890–896.
82. Kumar, K.; Nandan, B.; Formanek, P.; Stamm, M. "Fabrication of carbon microtubes from thin films of supramolecular assemblies via self-rolling approach," *J. Mater. Chem.* **2011**, 21(29), 10813–10817.
83. Jamal, M.; Zarafshar, A.M.; Gracias, D.H. "Differentially photo-crosslinked polymers enable self-assembling microfluidics," *Nat. Commun.* **2011**, 2, 527.

Ionov, L.

Biomimetic 3D self-assembling biomicroconstructs by spontaneous deformation of thin polymer films

***Journal of Materials Chemistry*** 2012, 22, 19366–19375

Cite this: *J. Mater. Chem.*, 2012, **22**, 19366

www.rsc.org/materials

## FEATURE ARTICLE

## Biomimetic 3D self-assembling biomicroconstructs by spontaneous deformation of thin polymer films

Leonid Ionov\*

Received 16th March 2012, Accepted 18th April 2012

DOI: 10.1039/c2jm31643a

Utilisation of spontaneous deformation of polymer films for fabrication of self-assembling constructs is a novel and very attractive research field. This manuscript overviews recent advance in the development and application of wrinkling, creasing and folding polymer films in biotechnology.

## Introduction: wrinkling, creasing, folding

Self-assembly and self-organization, being the driving principles of structure formation in nature, attract significant interest as promising concepts for the design of intelligent materials.<sup>1,2</sup> Thin polymer films with gradients of properties are the examples of self-assembling materials.<sup>3,4</sup> Due to inhomogeneous expansion/shrinking of different parts, such films are able to spontaneously form complex structures by wrinkling, creasing and folding and, thus, mimic mechanisms of development of animal organs, fruit growth and plant movement. Both creasing and wrinkling represent a bifurcation from a state of homogeneous deformation and typically occur when the substrate cannot be deformed (Fig. 1a and b). Wrinkles, wherein the surface of the material undulates sinusoidally but remains locally smooth, involve

a deviation from the homogeneous state by a field of strain that is infinitesimal in amplitude, but finite in space. By contrast, creases are localized folds that represent a deviation from the homogeneous state by a field of strain that is finite in amplitude, but infinitesimal in space.<sup>5</sup> Folding or bending is macroscopic deformation and occurs when the passive layer is soft and deformable (Fig. 1c). Utilization of these phenomena for the design of structured materials is highly attractive – they allow a very simple fabrication of very complex repetitive 2D and 3D patterns.<sup>6–12</sup> The focus of this review is to summarize the biotechnological applications of such polymer films.

## Wrinkling, creasing and folding in nature

Wrinkling and folding are extremely ubiquitous in nature. Wrinkles, for example, are generated during the growth of fruits. For instance, the Korean melon, which has just started to grow, is almost ideally spherical. Ridges appear during its growth and a small pumpkin has 10 equidistant longitudinal ridges. Further growth leads to an increase of the number of the ridges and a large pumpkin has about 20 ridges (Fig. 2a).<sup>13</sup> The ridges are generated by the inhomogeneous growth of different kinds of

Leibniz Institute of Polymer Research Dresden, Hohe Str. 6, 01069 Dresden, Germany. E-mail: ionov@ipfdd.de



Leonid Ionov

Leonid Ionov is a group leader at the Leibniz Institute of Polymer Research Dresden, Germany. He graduated from Lomonosov Moscow State University (Russia) and received a PhD in Polymer Chemistry in 2005 from Dresden University of Technology (Germany). He was working as a guest and post-doctoral researcher at the Eindhoven University of Technology (the Netherlands), Max Planck Institute of Molecular Cell Biology and Genetics (Germany) and at the Clarkson

University (USA). He is the author of more than 40 publications, several patent applications and book chapters. His research interests lie in the fields of stimuli-responsive and self-assembling materials.

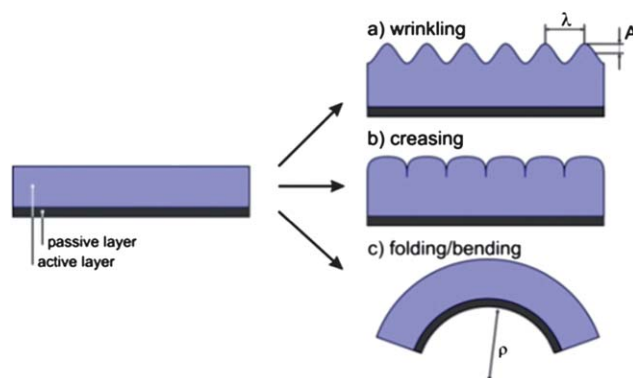
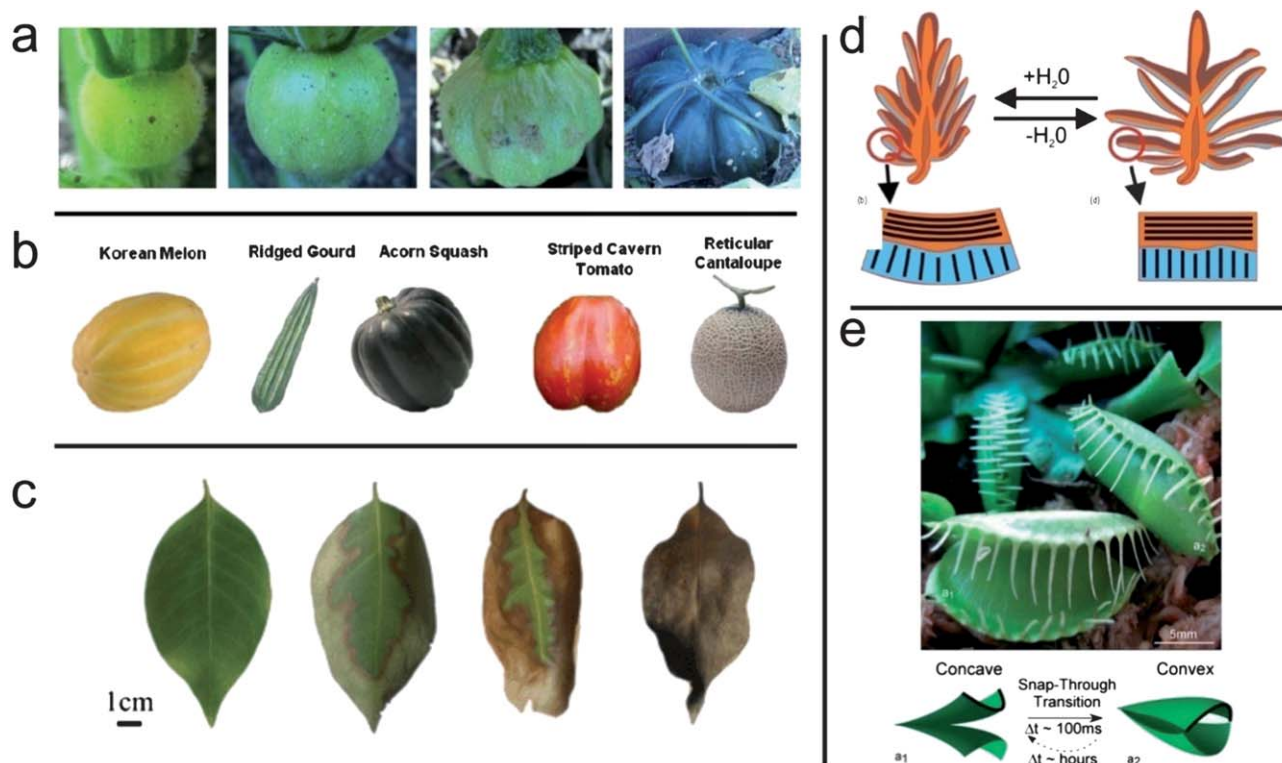


Fig. 1 Different scenario of deformation of thin films: wrinkling, creasing and folding.





**Fig. 2** Examples of wrinkling, creasing and folding systems in nature. (a) Morphology transition during the growth of a typical pumpkin (reprinted with permission of ref. 13, Copyright (2009) by Elsevier). (b) The morphologies of several fruits and vegetables<sup>13</sup> (reprinted with permission of ref. 13, Copyright (2009) by Elsevier). (c) Example of 4 different stages of dehydration of leaves from *Ligustrum lucidum*, where the nonuniform dehydration process and differential contraction are obvious.<sup>14</sup> (d) A sketch of actuation of scales in a pine cone upon drying and wetting (reprinted with permission of ref. 15, Copyright (2011) by Elsevier). (e) Snap-through of the Venus flytrap leaves from concave (a1) to convex (a2) occurs through the onset of an elastic instability films (reprinted with permission of ref. 19, Copyright (2007) by Wiley-VCH Verlag GmbH & Co. KGaA).

tissues and a variety of different patterns can appear (Fig. 2b). Wrinkles are often generated during drying. For examples, leaves, which are smooth when they are alive and saturated with water, start to curl up when they dry; that, again, is related to different volume changes of different tissues.<sup>14</sup>

The pine cone is an example of the folding system (Fig. 2d).<sup>15</sup> The pine cone is a well-known natural actuator in which the dead tissue that makes up the scales moves upon changes in humidity and allows the seeds inside the pine cone to be released. Each scale consists of two types of tissues, one consisting of cells in which the cellulose microfibrils are aligned along the length of the scale and the other in which they are perpendicular. Upon drying the interfacial matrix between the fibers shrinks on the lower half of the scales. The presence of the fibers leads to anisotropic contraction which is hindered by the stiffer surrounding tissue, thus leading to a bending of the scales. A similar mechanism, which is based on a bilayer structure, is used by *Aizoaceae* to protect seeds against drought and to release them when it is wet.<sup>16</sup> The folding and unfolding in both cases is relatively slow and occurs typically on the scale from several minutes to hours. Folding in Venus Flytrap (Fig. 2e) is much quicker – it has one of the fastest movements in the plant kingdom and it is able to close its “jaws” in about 100 ms.<sup>17,18</sup> In the “open” state the leaves are doubly curved. Upon stimulation, the plant ‘actively’ changes one of its principal natural curvatures by hydration that results in snapping and closing of the “jaws”.

### Wrinkling and creasing of engineered materials

Although the driving force for wrinkling and creasing is the same, the two modes of instability occur at very different critical strains, and hence, different critical linear expansions. There has been a wide range of critical values reported experimentally, 2.0–3.7, in different material systems. It was experimentally reported that a small stress results in wrinkling, and creases are formed at larger stresses.<sup>20</sup>

For an incompressible network, such as elastomeric poly-(dimethylsiloxane) (PDMS) coated with a thin hard skin, the compressive stress generated under bending is typically small, and formation of wrinkles with smooth and shallow surface undulations is often observed.<sup>21,22</sup> When the network becomes highly swollen, such as polyacrylamide gels in water, the initially free surfaces begin to touch each other, forming cusps in the gel in the form of localized sharp folds, or the so-called creasing instability.

At low compressive stresses, the wavelength ( $\lambda$ , Fig. 1) of the sinusoidal pattern is dependent on the thickness ( $d$ ) and mechanical properties of the film which is described as follows:<sup>23,24</sup>

$$\lambda = 2\pi d \left( \frac{\bar{E}_f}{3\bar{E}_s} \right)^{1/3} \quad (1)$$

where  $\bar{E} = E/(1 - \nu^2)$  is the plain-strain modulus, the subscript f and s refer to the film and substrate respectively, and  $\nu$  is the

Poisson's ratio. The critical strain required to wrinkle the film is independent of the physical properties of the film and substrate as follows:<sup>24,25</sup>

$$\varepsilon_c = \frac{1}{4} \left( \frac{3\bar{E}_f}{\bar{E}_s} \right)^{2/3} \quad (2)$$

According to these equations the wrinkling occurs as a specific wavelength independent of the amount of compressive strain, as long as the strain is above the critical value. However the amplitude ( $A$ , Fig. 1) of the wrinkling will increase as follows as the applied strain ( $\varepsilon$ ) increases:<sup>25,26</sup>

$$A = d \left( \frac{\varepsilon}{\varepsilon_c} - 1 \right)^{1/2} \quad (3)$$

As follows for eqn (1) the periodicity is controlled by mechanical properties of materials.

### Fabrication of wrinkled surfaces

Wrinkling and creasing may occur in two general cases of inhomogeneous films: the topmost layer either remains unchanged and the active layer shrinks<sup>27,28</sup> or the topmost layer swells more than bottom one<sup>5,20,29</sup> (Fig. 3). The first scenario occurs when the film surface is treated by photocrosslinking,<sup>27,28</sup> oxidation<sup>30,31</sup> and chemical vapour deposition.<sup>32–34</sup> The second scenario is observed, for example, during the swelling of the hydrogel with a vertical gradient of crosslinking density.<sup>20,29</sup> Specifically, the second scenario is associated with a greater expansion of the top layer relative to the bottom layer. While the swelling mismatch is one route, another route is the difference in the coefficient of thermal expansion.<sup>35</sup> Wrinkles can also be produced by local deformation of free standing elastic membranes, which can be done either by a liquid drop<sup>36</sup> or a needle.

Wrinkles can be generated not only on the flat surface but also on the surface of fibers and colloidal particles. It was found that a small compression in the shell of the fiber may induce, first, buckling characterized by sinusoidal patterns. While further compression may give rise to wrinkle-to-fold transition, entailing pitchfork-like patterns doubling the period of the first buckling. Such pattern transition is attributed to the constraint effect of the hard shell and the stretching/shearing ability of the soft core. The topographies incurred by both the first and second bifurcations can be tailored by modulating the geometric and mechanical properties of the structure (Fig. 4 left).<sup>38</sup> For example, wrinkled fibers were fabricated by using shape-memory polymer fibers which are coated by a metal shell. The shape memory fibers are first switched in their temporary shape and coated by the metal. Applied stimuli switch the shape memory fibers in their permanent shrunk shape that results in wrinkling on the metal shell.<sup>32</sup>

In a similar way wrinkles can be generated on the surface of colloidal core-shell particles when the core volume is reduced (Fig. 4 right).<sup>39</sup> The wrinkle morphology on the particle surface depends strongly on the particle size and film stress. It was experimentally demonstrated that the triangularly distributed dent-like and labyrinth-like patterns dominate in the cases of smaller and larger particles, respectively. With increasing film stress and/or substrate radius, the labyrinth-like buckling pattern

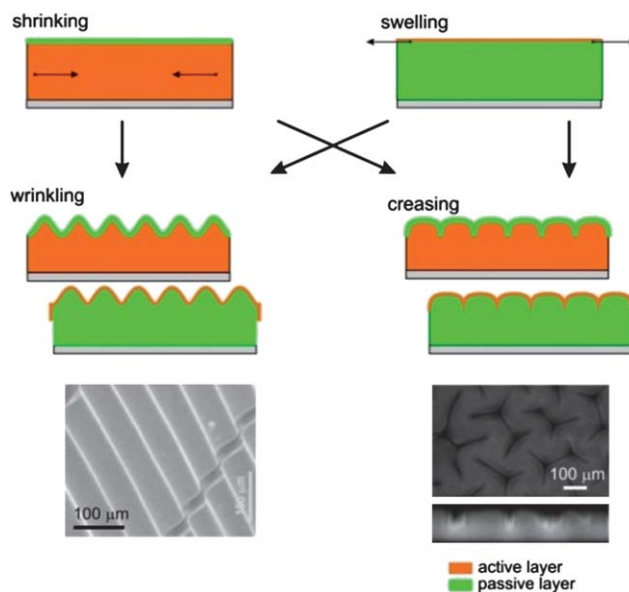


**Fig. 3** Two main approaches for generation of wrinkles and creases. Wrinkling and creasing occur when film is inhomogeneous and the topmost layer either remains unchanged and active layer shrinks or topmost layer swells more than bottom one. Examples of wrinkles (reprinted with permission of ref. 37, Copyright (2005) by The Nature Publishing Group) and creases (reprinted with permission of ref. 20, Copyright (2010) by Royal Society of Chemistry).

takes over. Both the buckling wavelength and the critical stress increase with the substrate radius.<sup>39,40</sup> In another experiment it was demonstrated that with increasing deformation, the sphere first exhibits a bucky ball-like wrinkling pattern and then undergoes a wrinkle-to-fold transition into labyrinth folded patterns. This transition involves dynamic movement, rotation, and coalescence of polygons formed during the initial buckling.<sup>41</sup> Janus particles with one side wrinkled can also be fabricated by non-equal shrinking of core-shell particles. For example, such particles were fabricated by UV light curing of one side of colloidal particles, which are swollen by a solvent. The cured hard skin on one side of the particles wrinkled after drying.<sup>42</sup>

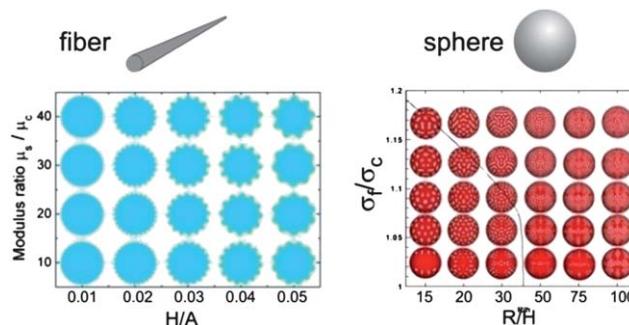


**Fig. 4** Diagrams of the critical buckling patterns of fibers (modulus ratio vs. ratio of shell thickness to core radius, reprinted with permission of ref. 38, Copyright (2010) by Royal Society of Chemistry) and sphere (normalized film nominal stress vs. the normalized substrate radius of curvature  $R/h$ , reprinted with permission of ref. 39, Copyright (2008) by The American Physical Society).

## Orientation of wrinkles/creases

Although wrinkling allows fabrication of highly periodic structures, the formed wrinkles are typically unordered (Fig. 5a and d). There are two main approaches to program wrinkling in a controlled way and designing of surfaces with well organized periodic wrinkle-like patterns. The first approach is based on the structuring of a polymer layer. Structuring can be performed either by site-selective crosslinking, decomposition or by applying topographically patterned surfaces. Whitesides was the first to use photopatterning to direct wrinkling. In particular, PDMS, which was soaked with benzophenone, was irradiated through the mask by UV light. As a result, mechanical properties of PDMS changed upon UV irradiation due to crosslinking. The patterned film was heated and irradiated and non-irradiated areas demonstrated different degrees of extension. The metal was deposited and the film was cooled down.<sup>22,33</sup> A similar approach was used by Crosby *et al.* In particular, they used site-selective oxidation of PDMS by ozone through the mask to generate pattern wrinkles.<sup>28,43</sup> Ohzono *et al.* used colloidal lithography as a mask to pattern the film in order to guide wrinkling.<sup>34</sup> Topographical patterning,<sup>44</sup> soft lithography and molding were used to fabricate complex wrinkles as well.<sup>45–48</sup> Writing with an ion beam was used to generate arbitrary patterns.<sup>49</sup> A very interesting approach was suggested by Crosby *et al.* They fabricated an ordered array of buckling membranes which were fixed on the wells.<sup>19,50</sup>

The second approach consists in controlled stretching of the film before surface treatment.<sup>51,52</sup> For example, uniaxially aligned wrinkles were produced by uniaxial stretching of the film. Simultaneous stretching in orthogonal directions allowed

fabrication of chevron patterns. Checkerboard patterns consisting of peaks and saddles were produced by two successive exposure–strain steps.<sup>53</sup>

## Properties and applications of wrinkling and creasing

Wrinkling is highly attractive for a number of applications due to the simplicity of fabrication of well ordered structures. For example, wrinkling was used for fabrication of super-hydrophobic rough surfaces with periodic two-level surface patterns. The first level of roughness is produced by the intrinsic nanoscale roughness of the film. The second level is produced by wrinkles.<sup>54</sup> Notably, the rough surfaces with uniaxially oriented wrinkles demonstrate anisotropic wetting properties which can be switched by stretching and compression.<sup>31</sup> Similar switching between wrinkled and smooth surfaces was used to design a surface with switchable adhesion.<sup>27,55</sup> In particular it was found that wrinkles generated after bringing two materials in contact enhance adhesion.<sup>56</sup> Friction properties can also be controlled by wrinkling. For example, the friction coefficient of a wrinkled surface is smaller than that of a flat one. Surfaces with uniaxially aligned wrinkles demonstrate anisotropy of friction as well. It was found that sliding perpendicular to the wrinkles is smaller than sliding parallel to the wrinkles.<sup>57</sup> Very importantly, wetting, adhesion and friction can be reversibly switched by “switching on” and “switching off” wrinkles, which can be achieved by treatment with a solvent.<sup>30</sup>

This transition between structured (wrinkled) and non-structured (smooth) states allows us to control optical properties. The smooth undeformed films are fully transparent whose wrinkling

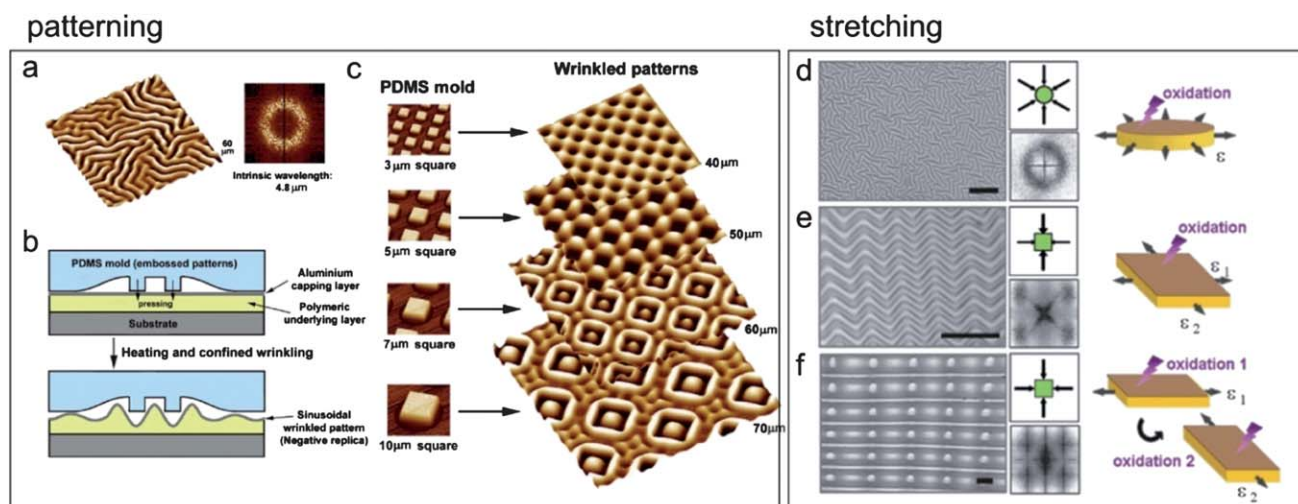


**Fig. 5** Two main approaches to program wrinkling: structuring (left) and controlled stretching (right). Left panel – (a) AFM micrograph of the isotropic wrinkles. (b) Schematic illustration of the roof collapse of the positive (protruding pattern) PDMS mold in bilayer wrinkling. The elastomeric mold is deformed to produce conformal wetting of the surface, which places pressure on the pattern. The wrinkles that are generated follow the contour of the PDMS mold pattern, resulting in a negatively replicated wrinkled structure. (c) AFM micrographs of self-organized wrinkle structures obtained through confinement-induced anisotropic wrinkling over the surface: (top to bottom) checkerboard pattern (3 μm period of the rectangular mold pattern), woven fabric array pattern (5 μm period), encircled dot array pattern (7 μm period), and encircled dot array separated by a tetrapod pattern (10 μm period). The *z* range of the AFM images is 800 nm (reprinted with permission of ref. 46, Copyright (2008) American Chemical Society). (Right panel, d–f) Optical micrographs and FFT of surface patterns generated by single and multi-axial strain fields (indicated by schematics) coupled with surface treatment. Patterns (d and e) are generated by a single exposure step and yield isotropic and chevron topologies. Pattern (f) yields a checkerboard pattern consisting of peaks and saddles, which has been produced by two successive exposure–strain steps. Scale bars are 20 μm (reprinted with permission of ref. 51, Copyright (2008) by Royal Society of Chemistry).



leads to switching of transmittance.<sup>30</sup> Crosby and Chan used buckling membranes, which are fixed on the wells, to generate an microlens arrays.<sup>58</sup> Due to their periodicity, wrinkled surfaces with periodicity in the visible range were used to obtain the structural colour.<sup>59</sup> The optical properties of such photonic structures can be tuned by stretching.<sup>60</sup>

Wrinkled surfaces were used as a stamp for printing<sup>61</sup> and a template for molding.<sup>62</sup> Wrinkles were also applied to arrange and separate<sup>37</sup> spherical<sup>63–65</sup> and anisotropic<sup>66</sup> colloidal particles as well as cells. For example, homogeneously wrinkled stamps can be used to produce linear arrays of gold nanoparticles and hydrogel microparticles over large areas by confined drying of nanoparticle solutions.<sup>63</sup> Depending on the dimensions of the grooves, the nanoparticles can be arranged into either single-line or double-line arrays, giving rise to marginally different optical responses through plasmon coupling. Anisotropic particles can be produced by crosslinking<sup>64,65</sup> of hydrogel particles which are aligned along the wrinkles and chemically linked to each other (Fig. 6a and b). Wrinkled surfaces can be applied to align mammalian cells as well.<sup>52,67</sup> Wrinkled surfaces with uniaxially aligned wrinkles allowed the uniaxial orientation of cells and reproducing the anisotropy seen in the heart.<sup>68</sup>

Programmed creasing was used to pattern proteins and cells. Hayward *et al.* developed biocompatible dynamic scaffolds

based on thin hydrogel coatings that reversibly hide and display surface chemical patterns in response to temperature changes. At room temperature, the gel absorbs water, triggering an elastic creasing instability that sequesters functionalized regions within tight folds on the surface (Fig. 7). Deswelling at 37 °C causes the gel surface to unfold, thereby regenerating the biomolecular patterns. Crease positions are directed by topographic features on the underlying substrate, and are translated into two-dimensional micrometre-scale surface chemical patterns through selective deposition of biochemically functionalized polyelectrolytes. These dynamic scaffolds are particularly promising for selective capture, sequestration and release of micrometre-sized beads, tunable activity of surface-immobilized enzymes and reversible encapsulation of adherent cells—which offer promise for incorporation within lab-on-a-chip devices or as dynamic substrates for cellular biology.<sup>48</sup>

Investigation of the formation of wrinkles is a quick and reliable method to probe mechanical, viscoelastic and fracture properties of polymer films<sup>25,69–75</sup> that is very important, for example, for organic electronics.<sup>76</sup> Using the spacing of these highly periodic wrinkles, the elastic modulus of the film was calculated by applying the well-established buckling mechanics. This new measurement platform was successfully applied to several systems displaying a wide range of thicknesses (nanometre to micrometre) and moduli (MPa to GPa).<sup>77</sup> It was also demonstrated that different kinds of wrinkles are formed depending on the viscoelastic properties of polymers.<sup>35</sup> In type I wrinkling, the elastic behaviour of high molecular weight polymers is still retained in the moderate temperature range so that the wrinkles are generated in such a way as to minimize the total free energy of the system. When the temperature is raised above the flow temperature of the polymer, however, the polymer changes into the viscous state and the wrinkling wavelength is determined by the stability equation of the dynamic approach, which leads to type II wrinkling. If the molecular weight of the polymer is low enough to lose its elastic characteristic, type III wrinkling governs the system and the wrinkles vanish after some period of fluctuation on the surface. In a similar way, wrinkling was used to probe mechanical properties of polymer brushes<sup>78</sup> or polymer multilayers.<sup>79</sup>

## Folding

Folding has the same origin as wrinkling and creasing – inhomogeneous change of volume. However, contrary to wrinkling and creasing, which are observed when the passive layer is rigid and undeformable, folding occurs when the passive layer is soft (Fig. 1). In fact all these phenomena are interconnected and the free-hanging film (part of it fixed on a rigid substrate) undergoes transition from wrinkling to folding. For small strain gradients, the film wrinkles, while for sufficiently large, a phase transition from wrinkling to bending occurs.<sup>80</sup>

Timoshenko<sup>81</sup> was the first to investigate bending of a bilayer which consisted of two materials with different expansion coefficients. He assumed that the bilayer can bend in only one direction and results in a bilayer with a uniform curvature

$$\frac{1}{\rho} = \frac{6(\varepsilon_2 - \varepsilon_1)(1 + m)^2}{h \left( 3(1 + m)^2 + (1 + mn) \left( m^2 + \frac{1}{mn} \right) \right)} \quad (4)$$

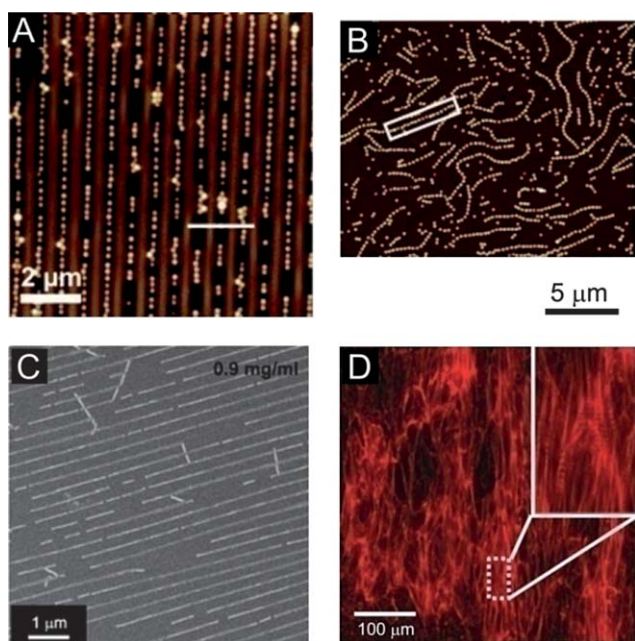


**Fig. 6** Alignment of particles and cells on wrinkled surfaces. (a) AFM images of microgel particles aligned in the wrinkles (reprinted with permission of ref. 65, Copyright (2011) by Royal Society of Chemistry). (b) Microgel particle chains generated by alignment in wrinkles followed by UV-crosslinking and subsequent release from the substrate (reprinted with permission of ref. 65, Copyright (2011) by Royal Society of Chemistry). (c) SEM phase images of aligned TMV on wrinkled PDMS substrate (reprinted with permission of ref. 66, Copyright (2009) by Royal Society of Chemistry). (d) Fluorescent microscopy images of hESC-CM cultured on wrinkled substrates for 2 days. Insets represent magnified regions where sarcomeric structures of hESC-CM are compared between conditions (reprinted with permission of ref. 68, Copyright (2011) by Wiley-VCH Verlag GmbH & Co. KGaA).

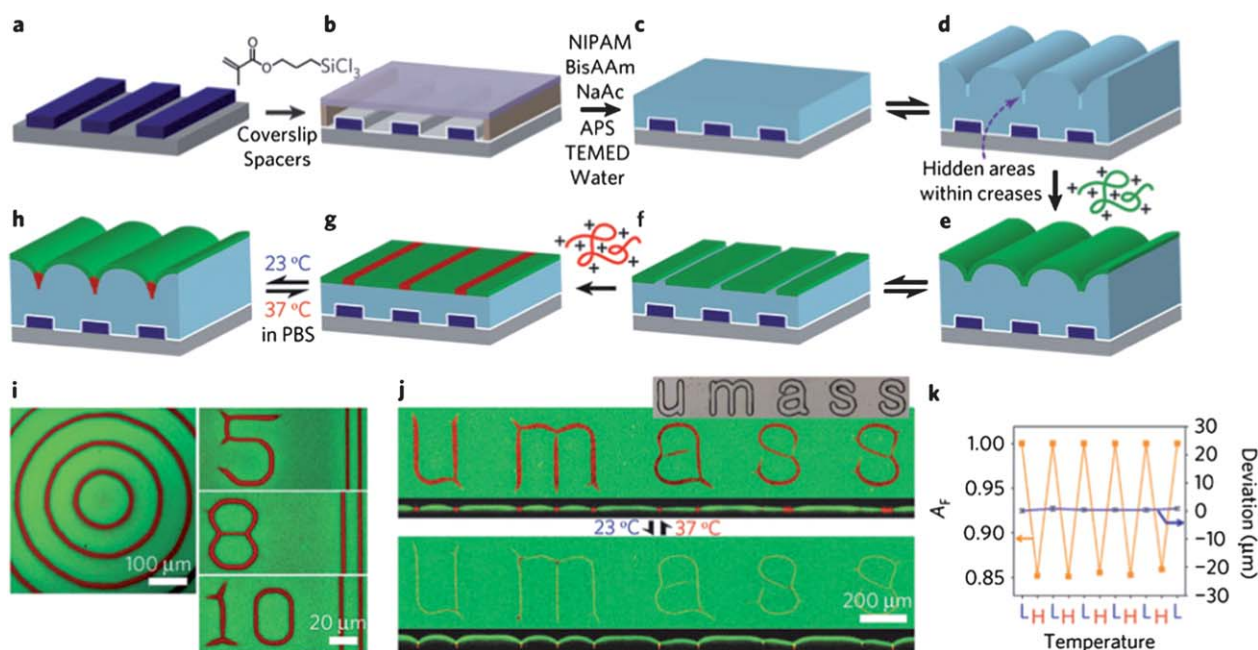


**Fig. 7** Patterning of proteins by controlled creasing. A topographically patterned substrate is lithographically fabricated. The substrate is modified with silane to promote covalent anchoring of the hydrogel layer, and assembled with a bare coverslip and spacers that define the hydrogel thickness into a channel into which an aqueous pre-gel solution is loaded by capillary action and polymerized. After detaching the coverslip, the surface-attached hydrogel is swelled, causing creases to form above the centres of elevated features on the substrate, thereby hiding certain areas of the surface. Areas that remain exposed are coated with PLL-g-PEG (green), then the hydrogel is deswelled to expose the previously hidden surface areas, into which a poly-electrolyte containing the desired biomolecular ligand (PLL-g-PEG-X, red) is selectively backfilled ligand-functionalized areas are then reversibly hidden and displayed through variations in temperature. In-plane projected images taken from LSCM at 37 °C for hydrogels bound to substrates patterned with concentric circles (left) and parallel lines with edge-to-edge separations corresponding to the displayed numbers of microns (right). The actuation of dynamic patterns is revealed by LSCM images (in-plane projections above and cross-sections below) of the hydrogel bound to the substrate lithographically patterned with the letters 'umass' (inset: optical micrograph of the substrate pattern) at 37 °C (top) and at 23 °C (bottom). *k*, Reproducibility of switching for 30 μm wide TRITC stripes templated by 60 μm wide raised parallel lines on the substrate is demonstrated by measuring the fraction of the exposed surface coated by FITC ( $A_F$ , yellow lines) and deviations in crease locations from the first to subsequent cycles (blue lines) and from the centres of elevated substrate features (error bars). 'L' and 'H' represent temperatures of 23 °C and 37 °C, respectively (reprinted with permission of ref. 48, Copyright (2010) by Nature Publishing Group).

$$\frac{E_1}{E_2} = n \quad (5)$$

$$\frac{a_1}{a_2} = m \quad (6)$$

where  $E$  is the elasticity modulus,  $a$  is the thickness of the layers,  $h$  is the total thickness ( $h = a_1 + a_2$ ),  $\epsilon$  is the stress of the films, and  $\rho$  is the radius of curvature. As seen from the eqn (4)–(6), the radius of curvature is inversely proportional to the film stress. Moreover, the radius of curvature first decreases and then increases with the increase of  $m$ . The resultant curvature is not very sensitive to the difference in stiffness between the two layers, and is mainly controlled by the actuation strain and the layer thickness. The Timoshenko equation applies to a beam bending in only one direction and does not predict the folding direction.

More recent models have considered complex bending of a bilayer in two dimensions. Mansfield found analytical solutions for large deflections of circular<sup>82</sup> and elliptical<sup>83</sup> plates having lenticular cross-sections with a temperature gradient through the thickness. For small gradients, the plates formed spherical caps, curved equally in all directions. At a critical gradient, a configuration with greater curvature in one direction became more

favorable. Because of the lens-shaped thickness profile, even though the elliptical plate had a major axis it showed no preferred direction for bending even for large deflections. Freund determined the strain at which the spherical cap, formed by the circular bilayer of uniform thickness, becomes unstable using low order polynomial solutions and finite element simulations.<sup>84</sup>

Later Smela *et al.* showed that short-side rolling was preferred in the case of free homogeneous actuation and that this preference increased with aspect ratio (ratio of length to width of the rectangular pattern).<sup>85</sup> Li *et al.*<sup>86</sup> and Schmidt<sup>87</sup> experimentally demonstrated the opposite scenario, namely a preference for long-side rolling, in the case where bilayers are progressively etched from a substrate. They observed that when the tube circumference was much larger than the width or the aspect ratio of the rectangle was high, rolling always occurred from the long side. When the tube circumference was much smaller than the width and the aspect ratio of the membrane pattern was not very high, the rolling resulted in a mixed yield of long- and short-side rolling, as well as a "dead-locked turnover" shape. Short-side rolling occurred at small aspect ratios when the deformed circumference is close to the width. In these self-rolling systems, the active component undergoes relatively small volume changes or actuation strains, which are nearly homogeneous over the

whole sample. Control of the rolling/folding direction is very important for programmed folding. For example, Schmidt demonstrated that introduction of wrinkles allows switching to short-side rolling.<sup>87</sup>

In inorganic self-rolling systems, the active component undergoes relatively small volume changes or actuation strains, which are nearly homogeneous over the whole sample. Hydrogels, however, demonstrate considerably different properties. First, hydrogels undergo large volume changes (up to 10 times) upon swelling and contraction. Second, the swelling of a hydrogel is often kinetically limited: due to slow diffusion of water through hydrogel, the parts which are closer to the edges swell first while the parts which are closer to the centre of the films swell later. Stoychev *et al.* investigated the folding of rectangular stimuli-responsive hydrogel-based polymer bilayers with different aspect ratios and relative thicknesses placed on a substrate.<sup>88</sup> It was found that long-side rolling dominates at high aspect ratios (ratio of length to width) when the width is comparable to the circumference of the formed tubes, which corresponds to a small actuation strain. Rolling from all sides occurs for a higher actuation strain, namely when the width and length considerably exceed the deformed circumference. In the case of moderate actuation, when the width and length are comparable to the deformed circumference, diagonal rolling is observed. Short-side rolling was observed very rarely and in combination with diagonal rolling. Based on experimental observations, finite-element modeling as well as energetic considerations, it was argued that bilayers placed on a substrate start to roll from corners due to quicker diffusion of water. Rolling from the long side starts later but dominates at high aspect ratios in agreement with energetic considerations. It was shown experimentally and by modeling that the main reasons for

a variety of rolling scenarios are (i) non-homogeneous swelling due to the presence of the substrate and (ii) adhesion of the polymer to the substrate.

### Complex folding

There are two general approaches for the design of self-folding films. The first approach is based on homogeneous bilayer films (Fig. 8, left). The approach is very simple and patterned bilayers are prepared by using one-step photolithography. The formed structures are, however, hinge-free and have rounded shapes such as tubes and capsules. Complexly patterned films where locally deposited active materials form hinges are used in the second approach (Fig. 8, right). An active material can undergo either reversible swelling/shrinking or an irreversible change of shape which is caused by melting. While the first method is experimentally complicated and is performed by using multi-step photolithography it allows fabrication of various figures with sharp and rounded edges such as cube, pyramids, capsules, *etc.*

There are many parameters which determine a folded shape. For example, the shape of a formed 3D object depends on the shape of the polymer films. The simplest case of a self-folding object is a tube which is formed by rectangular bilayers.<sup>89–95</sup> Helices of different kinds are formed by polymer bilayers with the gradually changing ratio between polymers.<sup>96</sup> Envelope-like capsules with rounded corners or nearly spherical ones are formed by the star-like polymer bilayers with four and six arms, respectively.<sup>94,95,97</sup> In these examples, simple rounded figures based on different combinations of fully or semi-folded tubes are formed. Moreover, because of the isotropy of mechanical properties of the bilayer, formation of hinges during folding of bilayers is considered to be impossible. Objects with sharp edges

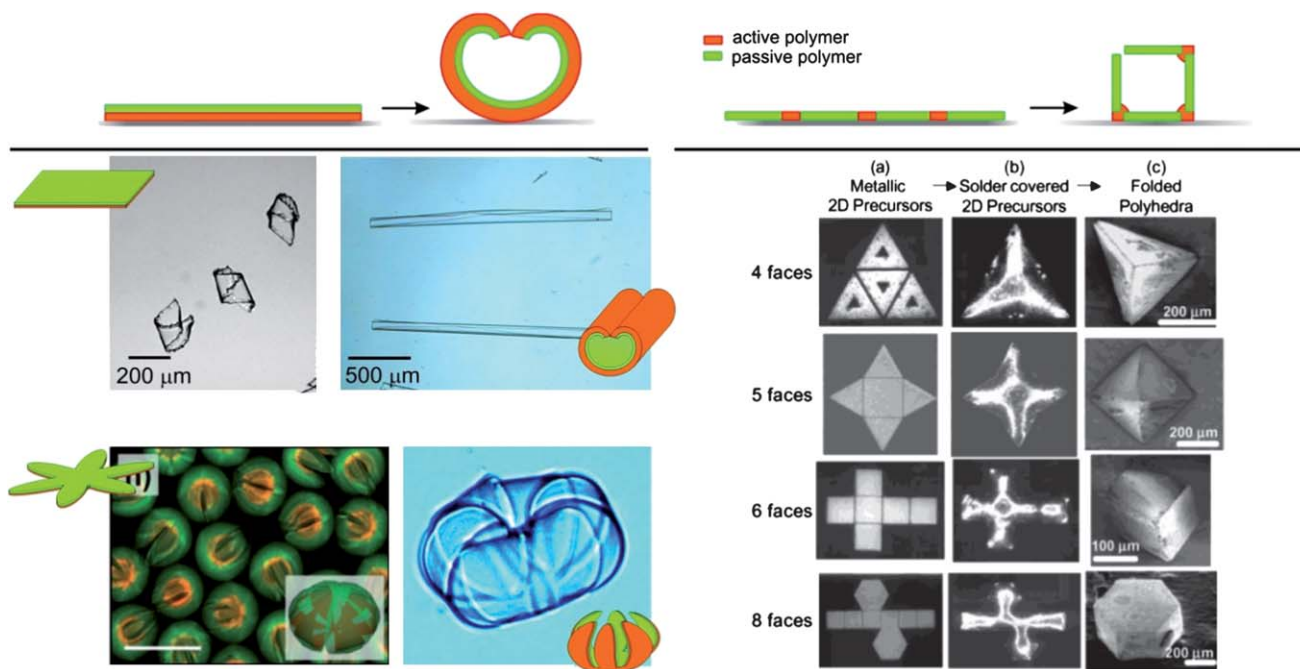


**Fig. 8** Two main approaches for fabrication of self-folding structures: (left) bilayers<sup>88,97</sup> (reprinted with permission of ref. 100, Copyright (2010) by Nature Publishing Group) and (right) patterned films (reprinted with permission of ref. 101, Copyright (2002) by Wiley-VCH Verlag GmbH & Co. KGaA).



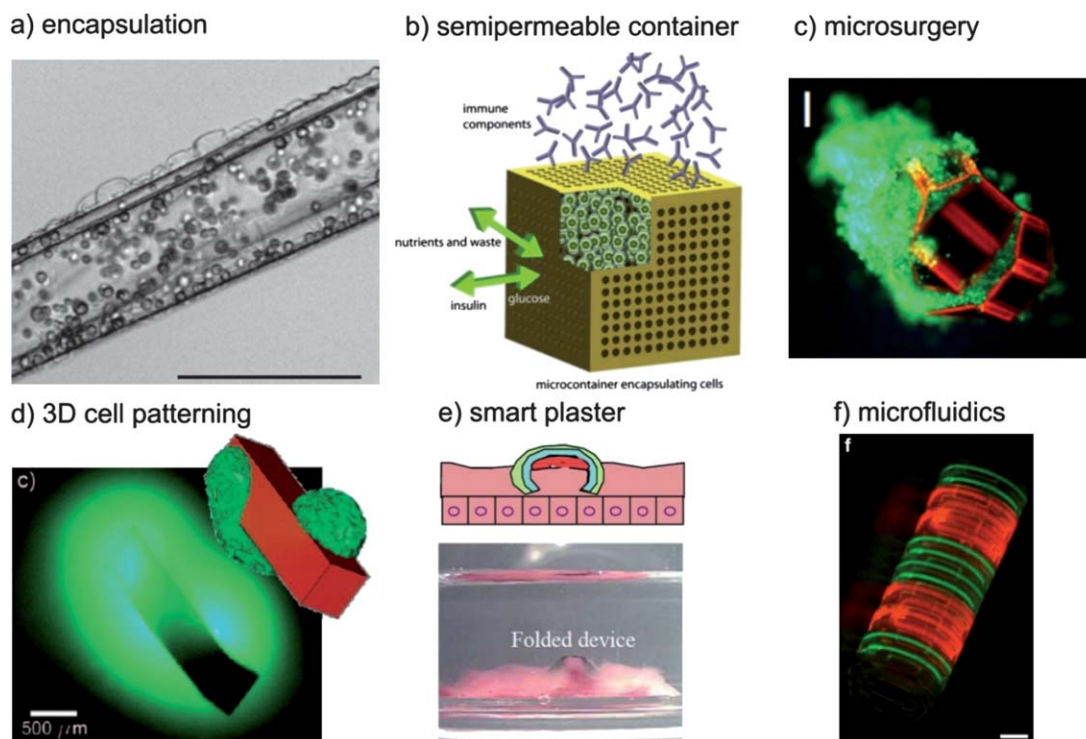


**Fig. 9** Examples of biomedical applications of self-folding films: (a) yeast cells encapsulation inside fully biodegradable self-rolled film (reprinted with permission of ref. 117, Copyright (2011) American Chemical Society), (b) scheme of artificial pancreas based on nanoporous self-folded devices: glucose and oxygen can penetrate through the pores of the folded device with encapsulated pancreas cell while immune components are unable to penetrate (reprinted with permission of ref. 118, Copyright (2011) by Elsevier), (c) self-folding microgripper with tissue (reprinted with permission of ref. 109, Copyright (2009) PNAS), (d) 3D cellular pattern produced by controlled diffusion of chemical through pores of self-folded object (reprinted with permission of ref. 121, Copyright (2002) by Wiley-VCH Verlag GmbH & Co. KGaA), (e) smart plasters which direct diffusion of drugs and prevent their leakage (reprinted with permission of ref. 93, Copyright (2006) by Elsevier), (f) 3D microfluidic device obtained by folding (reprinted with permission of ref. 122, Copyright (2011) by Nature Publishing Group).

are formed by the patterned bilayer where the active component is deposited locally. The active component can either swell/shrink or change its shape due to melting. In this way cubes and pyramids are formed by patterned bilayer with the active junction elements.<sup>96,98,99</sup> Importantly, in all reported cases folding runs in one step – active polymer changes its volume that results in simple bending.

Experimentally, the polymer films with different shapes can be obtained either by cutting,<sup>89–91</sup> using microwell-like substrates<sup>93–95</sup> or photolithography.<sup>92,97–99</sup> Cutting allows fabrication of millimetre large species with the rectangular shape, which form the tubes. The main advantage of this method is simplicity and applicability to almost all combinations of crosslinkable polymers. The use of microwell-like substrates is technically more complicated while it allows fabrication of polymer layers with different shapes such as rectangles or stars. Photolithography of bilayers allows large scale fabrication of self-folding objects of different shapes and sizes starting from several microns. The formed self-folding objects have rounded corners. The main disadvantage of this approach is the necessity to choose proper solvents for polymer deposition in a way that first polymer is not dissolved during deposition of the second polymer. Fabrication of patterned polymer films (Fig. 8, right) is technically the most complicated procedure and requires mask alignment during several steps of photolithography. On the other hand, it allows fabrication of the broadest range of shapes of self-folding objects.

### Properties and applications of folding

There are plenty of reports describing fabrication of self-folding films with different responsive properties. For example, there are pH-responsive systems based on polyelectrolytes,<sup>91,93,95,98,100,102–106</sup> thermoresponsive based on the gradient of thermal expansion,<sup>89,90</sup> melting of the polymer,<sup>99,107–109</sup> thermoresponsive polymers,<sup>92,97</sup> solvent,<sup>95,96,104,110</sup> electric signal,<sup>111,112,113</sup> and enzymes,<sup>114</sup> and light based on light-to-heat conversion.<sup>115,116</sup>

The one field of application of self-folding polymer thin films is the controlled encapsulation and release of drugs, particles and cells. Kalaitzidou demonstrated reversible adsorption–desorption of fluorescently labelled polyethyleneglycol, which is considered as a model drug, inside PDMS-gold tubes at 60–70 °C.<sup>89</sup> Gracias *et al.* demonstrated irreversible encapsulation of yeast cells inside self-folding SU8-PCL films upon heating above 60 °C.<sup>99</sup> Poly(*N*-isopropylacrylamide)-based self-folding films were also demonstrated to be suitable for reversible encapsulation of particles and yeast cells.<sup>92,97</sup> Cells were encapsulated upon cooling below 30 °C and could be released from the film, which is unfolded above 30 °C. This encapsulation and release is completely reversible and could be repeated many times. Very recently, fully biodegradable self-folding films, which consist of commercially available biodegradable polymers, were also used to encapsulate cells (Fig. 9a).<sup>117</sup> In fact there are many approaches which can be used for encapsulation of cells including LbL, microfluidic technique, and controlled

precipitation. The advantage of the self-folding approach is the possibility of reversible encapsulation and release. Self-folded objects with nanoporous walls and encapsulated cells were suggested as a prototype of artificial pancreas. The small molecules such as glucose and dissolved oxygen are able to pass through the pores while larger ones such as antibody are not. This size-selective permeability of self-folded capsules allows avoiding immune response that is highly demanded during transplantation of pancreas cells (Fig. 9b).<sup>118</sup> Gracias *et al.* used rigid metal-made self-folding microgrippers for capturing pieces of tissues for their controlled transport (Fig. 9c). Such systems are particularly attractive for non-invasive biopsy.<sup>109</sup> Self-folded objects were used as scaffolds for fabrication of 3D cellular constructs (Fig. 9d).<sup>119,120</sup> The controlled release of small molecules through the pores of self-folded microconstructs was used to spontaneously organize cells in a 3D environment.<sup>121</sup>

Self-folding films can also be used as smart plasters (Fig. 9e). Lee demonstrated this concept on the example of a millimetre sized poly(methyl methacrylate)–poly(2-hydroxyethyl methacrylate) bilayer with an attached mucoadhesive drug layer. The non-swelling PHEMA layer serves as a diffusion barrier, minimizing any drug leakage in the intestine. The resulting unidirectional release provides improved drug transport through the mucosal epithelium. The functionality of this device is successfully demonstrated *in vitro* using a porcine small intestine.<sup>93</sup>

There are several non-biorelated examples of applications of self-folding polymer films. Deposition of patterned metal on the polymer bilayer allowed fabrication of self-rolled tubes with a patterned conductive inner wall.<sup>91</sup> In another example, pyrolysis of polystyrene–poly(4-vinyl pyridine)–polydimethylsiloxane trilayer<sup>102</sup> was used for fabrication of silica tubes. Gracias used self-folding polymer films to fabricate self-assembled curved microfluidic networks (Fig. 9f).<sup>122</sup>

## Conclusions

Nature offers myriads of ideas for the design of novel materials with advanced properties. Wrinkling, creasing and folding often occur during development of organs or whole organisms and allow development of very complex shapes, which are required for efficient adaptation of living organisms to an ever changing environment. Very recently this concept was successfully transferred for the design of synthetic 2D and 3D structured polymer materials. Such biomimetic structured polymer systems were demonstrated to be highly promising for surface patterning, alignment, encapsulation and release of proteins, particles and cells. In spite of the fact that folding of films is promising for a variety of different applications, the main factor limiting its broad applications is fabrication using photolithography, which requires the use of expensive photomasks. Therefore, next efforts must be focused on solving this problem. Moreover, future efforts shall also be focused on the development of biomimetic polymer materials, which can be completely integrated into living organisms and be controlled by them.

## Acknowledgements

The author is grateful to DFG (grant IO 68/1-1) for financial support.

## Notes and references

- 1 A. Terfort, N. Bowden and G. M. Whitesides, *Nature*, 1997, **386**, 162–164.
- 2 G. M. Whitesides and B. Grzybowski, *Science*, 2002, **295**, 2418–2421.
- 3 T. G. Leong, A. M. Zafarshar and D. H. Gracias, *Small*, 2010, **6**, 792–806.
- 4 L. Ionov, *Soft Matter*, 2011, **7**, 6786–6791.
- 5 S. Cai, D. Chen, Z. Suo and R. C. Hayward, *Soft Matter*, 2012, **8**, 1301–1304.
- 6 S. Singamaneni and V. V. Tsukruk, *Soft Matter*, 2010, **6**, 5681–5692.
- 7 S. Yang, K. Khare and P. C. Lin, *Adv. Funct. Mater.*, 2010, **20**, 2550–2564.
- 8 T. R. Hendricks, W. Wang and I. Lee, *Soft Matter*, 2010, **6**, 3701–3706.
- 9 X. Chen and J. Yin, *Soft Matter*, 2010, **6**, 5667–5680.
- 10 A. Schweikart, N. Pazos-Perez, R. A. Alvarez-Puebla and A. Fery, *Soft Matter*, 2011, **7**, 4093–4100.
- 11 A. Schweikart and A. Fery, *Microchim. Acta*, 2009, **165**, 249–263.
- 12 J. Genzer and J. Groenewold, *Soft Matter*, 2006, **2**, 310–323.
- 13 J. Yin, X. Chen and I. Sheinman, *J. Mech. Phys. Solids*, 2009, **57**, 1470–1484.
- 14 H. Xiao and X. Chen, *Soft Matter*, 2011, **7**, 10794–10802.
- 15 J. W. C. Dunlop, R. Weinkamer and P. Fratzl, *Mater. Today*, 2011, **14**, 70–78.
- 16 M. J. Harrington, K. Razghandi, F. Ditsch, L. Guiducci, M. Rueggeberg, J. W. C. Dunlop, P. Fratzl, C. Neinhuis and I. Burgert, *Nat. Commun.*, 2011, **2**, 337.
- 17 J. M. Skotheim and L. Mahadevan, *Science*, 2005, **308**, 1308–1310.
- 18 Y. Forterre, J. M. Skotheim, J. Dumais and L. Mahadevan, *Nature*, 2005, **433**, 421–425.
- 19 D. P. Holmes and A. J. Crosby, *Adv. Mater.*, 2007, **19**, 3589–3593.
- 20 M. Guvendiren, J. A. Burdick and S. Yang, *Soft Matter*, 2010, **6**, 5795–5801.
- 21 E. Cerda and L. Mahadevan, *Phys. Rev. Lett.*, 2003, **90**, 074302.
- 22 W. T. S. Huck, N. Bowden, P. Onck, T. Pardo, J. W. Hutchinson and G. M. Whitesides, *Langmuir*, 2000, **16**, 3497–3501.
- 23 H. G. Allen, *Analysis and Design of Structural Sandwich Panels*, Pergamon Press, New York, 1969.
- 24 A. L. Volynskii, S. Bazhenov, O. V. Lebedeva and N. F. Bakeev, *J. Mater. Sci.*, 2000, **35**, 547–554.
- 25 J. Y. Chung, T. Q. Chastek, M. J. Fasolka, H. W. Ro and C. M. Stafford, *ACS Nano*, 2009, **3**, 844–852.
- 26 H. Q. Jiang, D. Y. Khang, J. Z. Song, Y. G. Sun, Y. G. Huang and J. A. Rogers, *Proc. Natl. Acad. Sci. U. S. A.*, 2007, **104**, 15607–15612.
- 27 E. P. Chan, E. J. Smith, R. C. Hayward and A. J. Crosby, *Adv. Mater.*, 2008, **20**, 711–716.
- 28 E. P. Chan and A. J. Crosby, *Soft Matter*, 2006, **2**, 324–328.
- 29 M. Guvendiren, S. Yang and J. A. Burdick, *Adv. Funct. Mater.*, 2009, **19**, 3038–3045.
- 30 H. S. Kim and A. J. Crosby, *Adv. Mater.*, 2011, **23**, 4188–4192.
- 31 J. Y. Chung, J. P. Youngblood and C. M. Stafford, *Soft Matter*, 2007, **3**, 1163–1169.
- 32 Y. Zhao, W. M. Huang and Y. Q. Fu, *J. Micromech. Microeng.*, 2011, **21**, 067007.
- 33 N. Bowden, S. Brittain, A. G. Evans, J. W. Hutchinson and G. M. Whitesides, *Nature*, 1998, **393**, 146–149.
- 34 T. Ohzono, S. I. Matsushita and M. Shimomura, *Soft Matter*, 2005, **1**, 227–230.
- 35 P. J. Yoo and H. H. Lee, *Macromolecules*, 2005, **38**, 2820–2831.
- 36 D. Vella, M. Adda-Bedia and E. Cerda, *Soft Matter*, 2010, **6**, 5778–5782.
- 37 K. Efimenko, M. Rackaitis, E. Manias, A. Vaziri, L. Mahadevan and J. Genzer, *Nat. Mater.*, 2005, **4**, 293–297.
- 38 Y.-P. Cao, B. Li and X.-Q. Feng, *Soft Matter*, 2012, **8**, 556–562.
- 39 G. X. Cao, X. Chen, C. R. Li, A. Ji and Z. X. Cao, *Phys. Rev. Lett.*, 2008, **100**, 036102.
- 40 J. Yin, Z. X. Cao, C. R. Li, I. Sheinman and X. Chen, *Proc. Natl. Acad. Sci. U. S. A.*, 2008, **105**, 19132–19135.
- 41 B. Li, F. Jia, Y. P. Cao, X. Q. Feng and H. J. Gao, *Phys. Rev. Lett.*, 2011, **106**, 234301.
- 42 A. C. Trindade, J. P. Canejo, L. F. V. Pinto, P. Patricio, P. Brogueira, P. I. C. Teixeira and M. H. Godinho, *Macromolecules*, 2011, **44**, 2220–2228.
- 43 M. Takahashi, T. Maeda, K. Uemura, J. X. Yao, Y. M. Tokuda, T. Yoko, H. Kaji, A. Marcelli and P. Innocenzi, *Adv. Mater.*, 2007, **19**, 4343–4346.

- 44 T. R. Hendricks and I. Lee, *Nano Lett.*, 2007, **7**, 372–379.
- 45 C. H. Lu, H. Mohwald and A. Fery, *Chem. Mater.*, 2008, **20**, 7052–7059.
- 46 P. J. Yoo and H. H. Lee, *Langmuir*, 2008, **24**, 6897–6902.
- 47 P. J. Yoo, K. Y. Suh, S. Y. Park and H. H. Lee, *Adv. Mater.*, 2002, **14**, 1383–1387.
- 48 J. Kim, J. Yoon and R. C. Hayward, *Nat. Mater.*, 2010, **9**, 159–164.
- 49 M. W. Moon, S. H. Lee, J. Y. Sun, K. H. Oh, A. Vaziri and J. W. Hutchinson, *Proc. Natl. Acad. Sci. U. S. A.*, 2007, **104**, 1130–1133.
- 50 D. P. Holmes, M. Ursiny and A. J. Crosby, *Soft Matter*, 2008, **4**, 82–85.
- 51 A. Chiche, C. M. Stafford and J. T. Cabral, *Soft Matter*, 2008, **4**, 2360–2364.
- 52 H. Vandeparre, S. Gabriele, F. Brau, C. Gay, K. K. Parker and P. Damman, *Soft Matter*, 2010, **6**, 5751–5756.
- 53 C. J. Rand, R. Sweeney, M. Morrissey, L. Hazel and A. J. Crosby, *Soft Matter*, 2008, **4**, 1805–1807.
- 54 P. C. Lin and S. Yang, *Soft Matter*, 2009, **5**, 1011–1018.
- 55 P. C. Lin, S. Vajpayee, A. Jagota, C. Y. Hui and S. Yang, *Soft Matter*, 2008, **4**, 1830–1835.
- 56 E. P. Chan, J. M. Karp and R. S. Langer, *J. Polym. Sci., Part B: Polym. Phys.*, 2011, **49**, 40–44.
- 57 C. J. Rand and A. J. Crosby, *J. Appl. Phys.*, 2009, **106**, 064913.
- 58 E. P. Chan and A. J. Crosby, *Adv. Mater.*, 2006, **18**, 3238–3242.
- 59 T. Xie, X. C. Xiao, J. J. Li and R. M. Wang, *Adv. Mater.*, 2010, **22**, 4390–4394.
- 60 C. J. Yu, K. O'Brien, Y. H. Zhang, H. B. Yu and H. Q. Jiang, *Appl. Phys. Lett.*, 2010, **96**, 041111.
- 61 M. Pretzl, A. Schweikart, C. Hanske, A. Chiche, U. Zettl, A. Horn, A. Boker and A. Fery, *Langmuir*, 2008, **24**, 12748–12753.
- 62 A. Schweikart, D. Zimin, U. A. Handge, M. Bennemann, V. Altstadt, A. Fery and K. Koch, *Macromol. Chem. Phys.*, 2010, **211**, 259–264.
- 63 N. Pazos-Perez, W. H. Ni, A. Schweikart, R. A. Alvarez-Puebla, A. Fery and L. M. Liz-Marzan, *Chem. Sci.*, 2010, **1**, 174–178.
- 64 C. H. Lu, H. Mohwald and A. Fery, *Soft Matter*, 2007, **3**, 1530–1536.
- 65 S. Hiltl, M. P. Schurings, A. Balaceanu, V. Mayorga, C. Liedel, A. Pich and A. Boker, *Soft Matter*, 2011, **7**, 8231–8238.
- 66 A. Horn, H. G. Schoberth, S. Hiltl, A. Chiche, Q. Wang, A. Schweikart, A. Fery and A. Boker, *Faraday Discuss.*, 2009, **143**, 143–150.
- 67 S. K. Smoukov, A. Bitner, C. J. Campbell, K. Kandere-Grzybowska and B. A. Grzybowski, *J. Am. Chem. Soc.*, 2005, **127**, 17803–17807.
- 68 A. Chen, D. K. Lieu, L. Freschauf, V. Lew, H. Sharma, J. X. Wang, D. Nguyen, I. Karakikes, R. J. Hajjar, A. Gopinathan, E. Botvinick, C. C. Fowlkes, R. A. Li and M. Khine, *Adv. Mater.*, 2011, **23**, 5785.
- 69 J. Y. Chung, J.-H. Lee, K. L. Beers and C. M. Stafford, *Nano Lett.*, 2011, **11**, 3361–3365.
- 70 J. Y. Chung, A. J. Nolte and C. M. Stafford, *Adv. Mater.*, 2011, **23**, 349–368.
- 71 E. A. Wilder, S. Guo, S. Lin-Gibson, M. J. Fasolka and C. M. Stafford, *Macromolecules*, 2006, **39**, 4138–4143.
- 72 J. Huang, M. Juskiewicz, W. H. de Jeu, E. Cerda, T. Emrick, N. Menon and T. P. Russell, *Science*, 2007, **317**, 650–653.
- 73 J.-H. Lee, J. Y. Chung and C. M. Stafford, *ACS Macro Lett.*, 2011, **1**, 122–126.
- 74 E. P. Chan, K. A. Page, S. H. Im, D. L. Patton, R. Huang and C. M. Stafford, *Soft Matter*, 2009, **5**, 4638–4641.
- 75 E. P. Chan, S. Kundu, Q. Lin and C. M. Stafford, *ACS Appl. Mater. Interfaces*, 2010, **3**, 331–338.
- 76 B. O'Connor, E. P. Chan, C. Chan, B. R. Conrad, L. J. Richter, R. J. Kline, M. Heeney, I. McCulloch, C. L. Soles and D. M. DeLongchamp, *ACS Nano*, 2010, **4**, 7538–7544.
- 77 C. M. Stafford, C. Harrison, K. L. Beers, A. Karim, E. J. Amis, M. R. Vanlandingham, H. C. Kim, W. Volksen, R. D. Miller and E. E. Simonyi, *Nat. Mater.*, 2004, **3**, 545–550.
- 78 H. Huang, J. Y. Chung, A. J. Nolte and C. M. Stafford, *Chem. Mater.*, 2007, **19**, 6555–6560.
- 79 A. J. Nolte, M. F. Rubner and R. E. Cohen, *Macromolecules*, 2005, **38**, 5367–5370.
- 80 P. Cendula, S. Kiravittaya, Y. F. Mei, C. Deneke and O. G. Schmidt, *Phys. Rev. B: Condens. Matter Mater. Phys.*, 2009, **79**, 085429.
- 81 S. Timoshenko, *J. Opt. Soc. Am.*, 1925, **11**, 233–255.
- 82 E. H. Mansfield, *Proc. R. Soc. London, Ser. A*, 1962, **268**, 316–327.
- 83 E. H. Mansfield, *Proc. R. Soc. London, Ser. A*, 1965, **288**, 396–417.
- 84 L. B. Freund, *J. Mech. Phys. Solids*, 2000, **48**, 1159–1174.
- 85 S. Alben, B. Balakrishnan and E. Smela, *Nano Lett.*, 2011, **11**, 2280–2285.
- 86 I. S. Chun, A. Challa, B. Derickson, K. J. Hsia and X. Li, *Nano Lett.*, 2010, **10**, 3927–3932.
- 87 P. Cendula, S. Kiravittaya, I. Monch, J. Schumann and O. G. Schmidt, *Nano Lett.*, 2011, **11**, 236–240.
- 88 G. Stoychev, S. Zakharchenko, S. Turcaud, J. W. C. Dunlop and L. Ionov, *ACS Nano*, 2012, DOI: 10.1021/nn300079f.
- 89 K. Kalaitzidou and A. J. Crosby, *Appl. Phys. Lett.*, 2008, **93**, 041910.
- 90 B. Simpson, G. Nunnery, R. Tannenbaum and K. Kalaitzidou, *J. Mater. Chem.*, 2010, **20**, 3496–3501.
- 91 V. Luchnikov, O. Sydorenko and M. Stamm, *Adv. Mater.*, 2005, **17**, 1177–1182.
- 92 S. Zakharchenko, N. Pureskiy, G. Stoychev, M. Stamm and L. Ionov, *Soft Matter*, 2010, **6**, 2633–2636.
- 93 H. Y. He, J. J. Guan and J. L. Lee, *J. Controlled Release*, 2006, **110**, 339–346.
- 94 J. J. Guan, H. Y. He, L. J. Lee and D. J. Hansford, *Small*, 2007, **3**, 412–418.
- 95 J. J. Guan, H. Y. He, D. J. Hansford and L. J. Lee, *J. Phys. Chem. B*, 2005, **109**, 23134–23137.
- 96 K.-U. Jeong, J.-H. Jang, D.-Y. Kim, C. Nah, J. H. Lee, M.-H. Lee, H.-J. Sun, C.-L. Wang, S. Z. D. Cheng and E. L. Thomas, *J. Mater. Chem.*, 2011, **21**, 6824–6830.
- 97 G. Stoychev, N. Pureskiy and L. Ionov, *Soft Matter*, 2011, **7**, 3277–3279.
- 98 N. Bassik, B. T. Abebe, K. E. Laflin and D. H. Gracias, *Polymer*, 2010, **51**, 6093–6098.
- 99 A. Azam, K. Laflin, M. Jamal, R. Fernandes and D. Gracias, *Biomed. Microdevices*, 2010, 1–8.
- 100 T. S. Shim, S.-H. Kim, C.-J. Heo, H. C. Jeon and S.-M. Yang, *Angew. Chem., Int. Ed.*, 2011, **51**, 1420–1423.
- 101 D. H. Gracias, V. Kavthekar, J. C. Love, K. E. Paul and G. M. Whitesides, *Adv. Mater.*, 2002, **14**, 235–238.
- 102 K. Kumar, B. Nandan, V. Luchnikov, F. Simon, A. Vyalikh, U. Scheler and M. Stamm, *Chem. Mater.*, 2009, **21**, 4282–4287.
- 103 K. Kumar, V. Luchnikov, B. Nandan, V. Senkovskyy and M. Stamm, *Eur. Polym. J.*, 2008, **44**, 4115–4121.
- 104 T. S. Kelby, M. Wang and W. T. S. Huck, *Adv. Funct. Mater.*, 2011, **21**, 652–657.
- 105 S. Singamaneni, M. E. McConney and V. V. Tsukruk, *Adv. Mater.*, 2010, **22**, 1263–1268.
- 106 S. Singamaneni, M. E. McConney and V. V. Tsukruk, *ACS Nano*, 2010, **4**, 2327–2337.
- 107 T. G. Leong, B. R. Benson, E. K. Call and D. H. Gracias, *Small*, 2008, **4**, 1605–1609.
- 108 T. G. Leong, C. L. Randall, B. R. Benson, A. M. Zarafshar and D. H. Gracias, *Lab Chip*, 2008, **8**, 1621–1624.
- 109 T. G. Leong, C. L. Randall, B. R. Benson, N. Bassik, G. M. Stern and D. H. Gracias, *Proc. Natl. Acad. Sci. U. S. A.*, 2009, **106**, 703–708.
- 110 D. P. Holmes, M. Roche, T. Sinha and H. A. Stone, *Soft Matter*, 2011, **7**, 5188–5193.
- 111 E. Smela, O. Inganas and I. Lundstrom, *Science*, 1995, **268**, 1735–1738.
- 112 E. W. H. Jager, O. Inganas and I. Lundstrom, *Science*, 2000, **288**, 2335–2338.
- 113 A. W. Feinberg, A. Feigel, S. S. Shevkoplyas, S. Sheehy, G. M. Whitesides and K. K. Parker, *Science*, 2007, **317**, 1366–1370.
- 114 N. Bassik, A. Brafman, A. M. Zarafshar, M. Jamal, D. Luvsanjav, F. M. Selaru and D. H. Gracias, *J. Am. Chem. Soc.*, 2010, **132**, 16314–16317.
- 115 X. Zhang, C. L. Pint, M. H. Lee, B. E. Schubert, A. Jamshidi, K. Takei, H. Ko, A. Gillies, R. Bardhan, J. J. Urban, M. Wu, R. Fearing and A. Javey, *Nano Lett.*, 2011, **11**, 3239–3244.
- 116 Y. Liu, J. K. Boyles, J. Genzer and M. D. Dickey, *Soft Matter*, 2012, **8**, 1764–1769.
- 117 S. Zakharchenko, E. Sperling and L. Ionov, *Biomacromolecules*, 2011, **12**, 2211–2215.
- 118 C. L. Randall, Y. V. Kalinin, M. Jamal, A. Shah and D. H. Gracias, *Nanomed.: Nanotechnol., Biol. Med.*, 2011, **7**, 686–689.
- 119 C. L. Randall, Y. V. Kalinin, M. Jamal, T. Manohar and D. H. Gracias, *Lab Chip*, 2011, **11**, 127–131.
- 120 M. Jamal, N. Bassik, J. H. Cho, C. L. Randall and D. H. Gracias, *Biomaterials*, 2010, **31**, 1683–1690.
- 121 Y. V. Kalinin, J. S. Randhawa and D. H. Gracias, *Angew. Chem., Int. Ed.*, 2011, **50**, 2549–2553.
- 122 M. Jamal, A. M. Zarafshar and D. H. Gracias, *Nat. Commun.*, 2011, **2**, 527.

Luchnikov, V.; Ionov, L. ; Stamm, M.

Self-rolled polymer tubes: novel tools for microfluidics, microbiology and drug-delivery systems

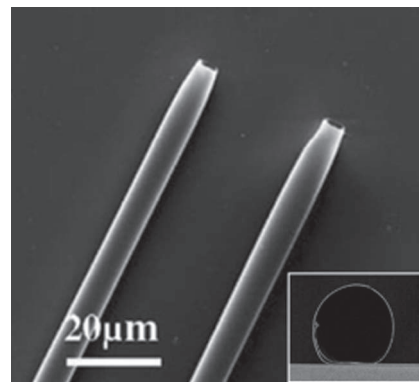
***Macromolecular Rapid Communications*** 2011, 32(24), 1943–1952



# Self-Rolled Polymer Tubes: Novel Tools for Microfluidics, Microbiology, and Drug-Delivery Systems

Valeriy Luchnikov,\* Leonid Ionov, Manfred Stamm

Recent work on the fabrication of tubular microstructures via self-rolling of thin, bilayer polymer films is reviewed. A bending moment in the films arises due to the swelling of one component of the bilayer in a selective solvent. The inner diameters of the tubes vary from hundreds of nanometers to dozens of micrometers. The position of the tubes on the substrate and their length can be preset by photolithographic patterning of the bilayer. Prior to rolling, the bilayers can be exposed to different methods of surface functionalization, providing opportunities for engineering the microtube inner surfaces for use in microfluidic circuits and "microbiological" applications. The self-rolling approach is promising for the development of novel drug- and cell-delivery systems, as well as for tissue engineering.



## 1. Introduction

Polymers can respond to external factors such as solvents, moisture, heat and light via a change in their specific volume in a much-more-pronounced manner than other materials can. In polymer films constrained by solid substrates, this leads to large internal stresses. When the films are not homogeneous in terms of their chemical content or mechanical characteristics, for instance when they consist of layers of different types of polymers or when the polymers are combined with coatings from inorganic materials (e.g., metals), internal stress relaxation can lead to quite spectacular effects. The most

well-known effect concerns the formation of patterns of wrinkles, which arises in systems consisting of a relatively hard outer layer on top of a softer elastic or viscoelastic substrate.<sup>[1]</sup> The wrinkles appear as a result of bending instabilities when the rigid skin layer is compressed due to the swelling or contraction of the substrate layer. Buckling and delamination are the internal relaxation modes (usually unwanted) that occur when the polymer film detaches from the substrate.

Another common mode of internal stress relaxation involves curling and rolling. This phenomenon is common for films that detach from a substrate and that are characterized by structural heterogeneity in the direction that is normal to the film surface. This heterogeneity can correspond to the different chemical compositions of the upper and outer layers of the films or to the gradient of the crosslinking density of the polymers, or it can be due to other reasons. A clear example of a nanoscale scrolled structure can be found in the fibres of the natural mineral asbestos chrysotile, which consists of nanosheets of magnesium, oxygen and silicon. The factor that causes rolling in this system is the difference in the lattice constants of

Dr. V. Luchnikov

Institut de Science des Matériaux de Mulhouse et Université  
Haute Alsace, 15 Rue Jean Starcky, Mulhouse 68057, France  
E-mail: valeriy.luchnikov@uha.fr

Dr. L. Ionov, Prof. M. Stamm

Leibniz Institute of Polymer Research Dresden, Hohe Str. 6,  
01069 Dresden, Germany



the layers. On the macroscale, self-rolling is commonly observed in drying plant leaves, clays, delaminated paintings etc. The self-rolling of thin solid films has been used for nearly 20 years as a powerful approach for the fabrication of micro- and nanoscale 3D objects, starting with structured quasi-2D films. Smela et al. were the first to report on the fabrication of polypyrrole-gold patterned films, which are able to form tubes and cubes in response to the application of an electric potential and to fold into different 3D structures.<sup>[2]</sup> Prinz et al. found that epitaxially grown semiconductor bilayers released from the substrate by selective etching of a sacrificial layer can curl into atomically smooth tubes that are only a few nanometers in width.<sup>[3,4]</sup> These tubes have since been reproduced by a number of research groups and have been examined in a number of applications. Prinz et al. fabricated microsyndes on the basis of free-standing self-rolled tubes and demonstrated the injection of DNA molecules into single cells via these syndes.<sup>[5]</sup> Schmidt et al. explored semiconductor tubes as nanoreactors,<sup>[6]</sup> waveguides for X-ray radiation,<sup>[7]</sup> microcompartments for living cells<sup>[8]</sup> and as self-propelling moving objects.<sup>[9]</sup> Liu et al. theoretically explored the formation of tubes as a result of an atomic-scale surface–stress imbalance.<sup>[10]</sup>

In 2005, we suggested an approach to fabricate microtubular cavities via the self-rolling of polymer bilayers.<sup>[11]</sup> The bending moment in our experiments originated from the unequal swelling of the polymers in selective solvents. The use of polymers as the tube-forming materials is advantageous for several reasons. Firstly, making very-thin polymer layers is a simple procedure that does not require the use of vacuum technologies (as in the case of metals and semiconductor films) and can be performed via spin or dip-coating from polymer solutions. Following this procedure, the polymers have a very broad range of physicochemical properties, which enables tuning of the mechanical, optical and chemical characteristics of the tubes to take place. Polymers are generally more biocompatible than metals and semiconductors, and this is very important in view of the potential biomedical applications of the tubes. Polymers are capable of a considerable change in volume and this makes them highly attractive for the design of actively moving materials<sup>[12]</sup> and for various microscale, 3D shapes via the "micro-origami" technique.<sup>[13]</sup> Finally, polymer surfaces can be easily patterned and functionalized with a number of surface-treatment methods such as plasma activation, photolithography, microcontact printing and many others. This last point is very important for the complex engineering of the inner walls of the tubes, which we consider as one of the most attractive possibilities provided by the self-rolling approach.

In the following sections, we review the main results in the field of polymer-based self-rolled tubes.



**Valeriy Luchnikov** has been a researcher at the French National Center of Scientific Research at the Institute of Material Science of Mulhouse since 2007. He graduated from the Novosibirsk State University in 1992, received a Ph.D. in chemical physics in 1996. His research interests include theoretical and experimental studies of micromechanics phenomena in thin polymer films, crystallization of polymers and the fabrication of novel carbon materials via ion-beam treatment of block-copolymer films. He is the author and coauthor of more than 40 publications, two book chapters and the holder of a patent.



**Leonid Ionov** is a group leader at the Leibniz Institute of Polymer Research, Dresden, Germany. He graduated from Lomonosov Moscow State University (Russia) and received a Ph.D. in polymer chemistry in 2005 from Dresden University of Technology (Germany). He is the author of more than 40 publications, several patent applications and book chapters. His research interests lie in the fields of stimuli-responsive and self-assembling materials. His current activities are focused on the application of stimuli-responsive self-folding films and self-rolling tubes for controlled encapsulation/release and for the design of novel biomaterials.



**Manfred Stamm** is professor of physical chemistry at Dresden University of Technology and head of the Institute of Physical Chemistry and Physics of Polymers at the Leibniz Institute of Polymer Research, Dresden. He obtained his diploma in solid-state physics at Frankfurt University in 1974, and received a Ph.D. at the Institute of Physical Chemistry of the University of Mainz. His interests include nanostructured materials, polymer (bio)interfaces and structure-property relationships of polymers. He is the author of more than 300 publications, the holder of 6 patents and the organizer of several international conferences.

## 2. Typical Fabrication Schemes and the Self-Rolling Mechanism of Polymer Bilayers

**Figure 1** illustrates a typical fabrication scheme that leads to the formation of polymer microtubes. A polymer bilayer, consisting of a polystyrene (PS) layer on top of a poly(4-vinyl pyridine) (P4VP) layer, is formed on the polished surface of a silicon wafer or other substrate (e.g., a glass slide) by means of dip- or spin-coating. Rolling, in this system,

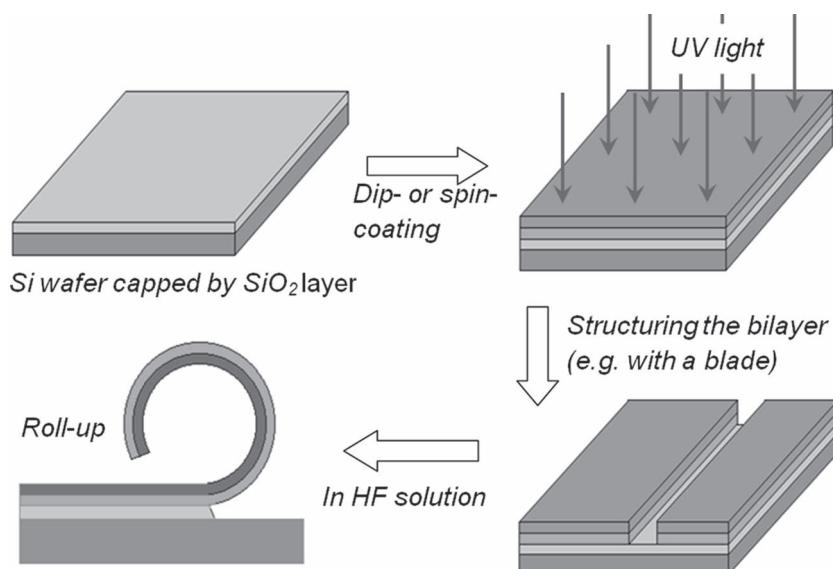


**Figure 1.** Typical fabrication scheme for self-rolled polymer tubes. Firstly, a polished silicon wafer with a surface  $\text{SiO}_2$  layer is cleaned in a piranha bath. A polymer bilayer is then formed on the wafer by dip- (or spin-) coating. As an example, a P4VP layer is formed from solution in chloroform, then a PS layer is deposited from solution in toluene. The polymers are crosslinked by UV radiation ( $\lambda = 254 \text{ nm}$ ). The openings are made by a sharp object such as a blade or a needle. The structured bilayer is put in diluted HF solution in water. The sacrificial  $\text{SiO}_2$  layer is dissolved. Swelling of the P4VP layer generates the bending moment in the bilayer and the rolling of the film.

the wafer in solutions of P4VP and PS in chloroform and toluene, respectively, so that the PS layer forms the outer part of the film. The bilayer is then crosslinked by exposure to short-wavelength ( $\lambda < 280 \text{ nm}$ ) UV light, which is known to lead to the generation of free radicals, chain scission and crosslinking of the PS<sup>[14]</sup> and P4VP.<sup>[15]</sup> The bilayer is structured through the formation of openings in the film via the use of a sharp object; for example, a needle or a blade. The wafer is finally put in a water solution of hydrofluoric acid, which removes the sacrificial  $\text{SiO}_2$  layer and liberates the film, which then rolls up due to swelling of the P4VP layer. The PS layer plays a double role: it protects the P4VP layer from contact with the acid media everywhere apart from at the rolling front, and it opposes the swelling of the P4VP layer, thus participating in the creation of the bending moment. Structuring of the film can also be performed by irradiation of the bilayer through a photomask (**Figure 2**). The patterned bilayer can be developed, prior to rolling, by washing

is achieved due to the selective swelling of the P4VP in a water solution of an acid, due to protonation of the pyridine rings. The bilayer is formed by dip- or spin-coating of

out the uncrosslinked polymer with organic solvents (e.g., chloroform or dichloromethane in the case of the PS–P4VP bilayer). Photopatterning allows for the creation of large

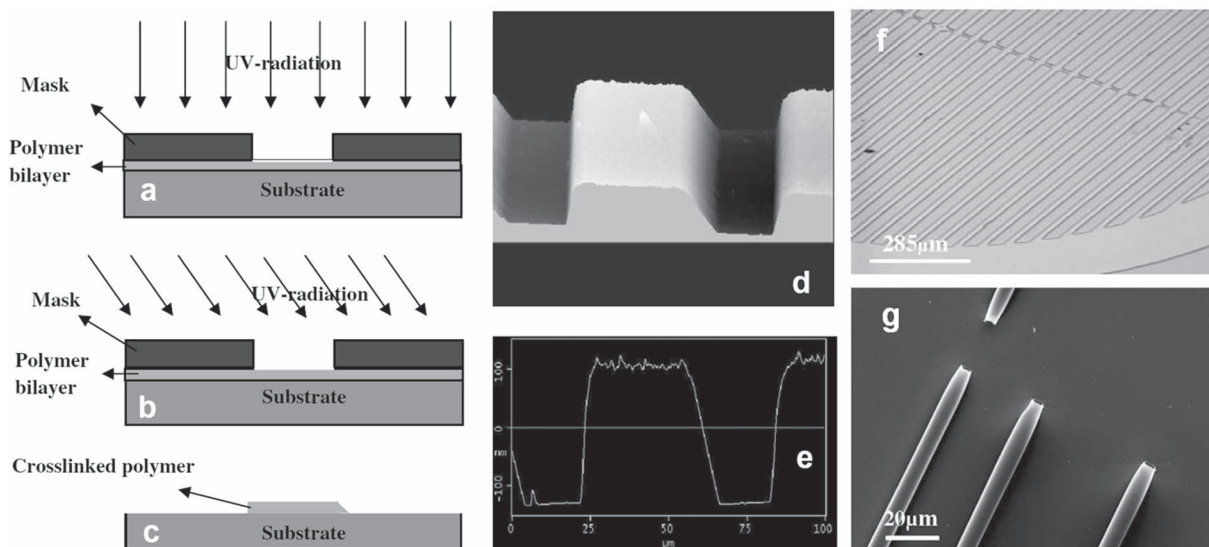


**Figure 2.** Photolithography route to fabrication of arrays of self-rolled tubes. (a) The sample is exposed to UV light at normal incidence. (b) The sample is exposed to UV light at a sharp incident angle. (c) A pattern develops after washing away the uncrosslinked polymer: the second exposure at an angle to the surface of the sample creates an asymmetric profile in the crosslinking density, which results in unidirectional rolling of the layers. (d) 3D AFM image of asymmetric polymer stripes. (e) Section profile of the AFM image. (f) The pattern is developed by washing away the uncrosslinked polymer with chloroform. (g) SEM micrograph of arrays of tubes. Reproduced with permission.<sup>[18]</sup> Copyright 2008, Elsevier.

■ Table 1. Typical conditions for the fabrication of self-rolled tubes.

P4VP layer thickness [nm]	PS layer thickness [nm]	UV dose [J·cm <sup>-2</sup> ]	1,4-Di-iodobutane crosslinking time and temperature [h, °C]	HCl or HF in water [wt%]	Radius of the tubes [μm]
90	50	1	-	0.1	30
90	50	12	-	0.1	7
57	45	8.2	-	0.1	5
25	25	0	2 h, 80 °C	0.01	1.5–2

arrays of tubes of standard dimensions.<sup>[16–18]</sup> The diameter of the formed tubes has been found to depend on both the ratio between the thicknesses of the polymer layers, as well as on the dose or irradiation level<sup>[18]</sup> (Table 1). Single tubes with exactly defined lengths can also be formed by focused ion-beam patterning of the bilayer films.<sup>[19]</sup>

The P4VP layer can also be crosslinked via the quaternization reaction in saturated 1,4-di-iodobutane vapour. Since the PS layer is in the glassy state at the temperatures at which the tubes are formed and exploited, its crosslinking via UV light is not necessary. The advantage of this approach is that extremely hazardous hydrofluoric acid can be excluded from the fabrication scheme, since the polymers are not covalently bound to the substrate (as may be the case with films that are irradiated with high doses of short-wavelength UV), and the dissolution of the sacrificial layer is not necessary. The films can then be rolled, for instance in hydrochloric acid or in alcohol solutions in water. Rolling the films in water solutions of dodecylbenzene sulfonic acid (DBSA) is extremely practical, as this leads to the formation of supramolecular complexes with pyridine rings, and also increases the effective volume of P4VP in the bottom film of the bilayer. After removal from the solution and the drying of the films, DBSA remains in the structure of P4VP, preventing the unrolling of the films or the collapse of the tubes, which sometimes occurs when the tube formation is performed in HF, HCl or alcohol solutions in water.

### 3. Composite Polymer-Metal and Ceramic Microtubes Produced via the Self-Rolling Approach

The self-rolling of polymer films can be exploited, not only in the formation of polymer tubes, but also in the design of tubes consisting of inorganic materials such as metals or ceramics. In this case, the rolling polymer bilayer can have the auxiliary function of a template, which may be removed, if necessary, from the final product via pyrolysis

or plasma treatment. This opens the way for the fabrication of 3D micro-objects that otherwise cannot be realized. In this section, we describe experiments regarding the fabrication of inorganic microtubes and composite organic–inorganic microtubes.<sup>[11,20–21]</sup>

Composite polymer–metal tubes can be prepared via vacuum sputtering of a thin metal layer on top of the polymer bilayer film or directly onto a single polymer layer (e.g., P4VP) that swells in a selective solvent (in the latter case, the

metallic film plays the role of the capping protective layer in the polymer bilayer).

When necessary, the organic component of a self-rolled tube can be removed by pyrolytic decomposition of the polymers. Gold constitutes a good choice of a material for the fabrication of composite tubes, since it is chemically inert (hence, thin Au films can withstand the action of acids used for rolling). Figure 3a–b shows a P4VP–PS–Au tube and the pure gold tube after the removal of the polymers via pyrolysis at 500 °C for 3 h in an oven. The complete removal of the organic component is verified by Fourier transform IR (FTIR) spectroscopy (Figure 3d). After pyrolysis, as expected, the organic moiety is removed, and only a silica fingerprint region at 1100 cm<sup>-1</sup> is observed, which comes from the silicon wafer. One of the potential applications of metallic microtubes is their use as IR-radiation waveguides. The electrical conductivity of the tubes provided by metallization of the rolling layers can also be exploited for heating the tubes and their interior, or for the generation of magnetic (Figure 4) and electrical fields inside the tubes. A current,  $I = 0.1$  A, generates a magnetic field inside the 200 mm-wide coil, as shown in Figure 4, which is estimated to be  $6 \times 10^{-4}$  T. Utilizing electrodes inside the tubes provides an excellent opportunity to integrate electrical and microfluidic circuits.

The self-rolling phenomenon can also be used to produce ceramic tubes when a ceramic precursor is introduced in the composition of the rolling layer. For instance, a thin film of polydimethylsiloxane (PDMS) can be rolled with the P4VP/PS bilayer, resulting in the formation of a PDMS–P4VP–PS trilayer polymer tube. Pyrolysis of these tubes at 700 °C for 4 h in an oxygen atmosphere converts the PDMS into silica and simultaneously removes the organic part of the tube (Figure 5).<sup>[21]</sup> Moreover, silica–metal tubes can be obtained when a metallic layer is introduced into the multilayer by vacuum sputtering prior to rolling.<sup>[21]</sup> Hybrid silica–metal microtubes are promising as a new type of hollow-core IR-radiation waveguide, to be used for high-power laser-radiation delivery in medical and industrial applications.<sup>[22]</sup> These tubes are also being



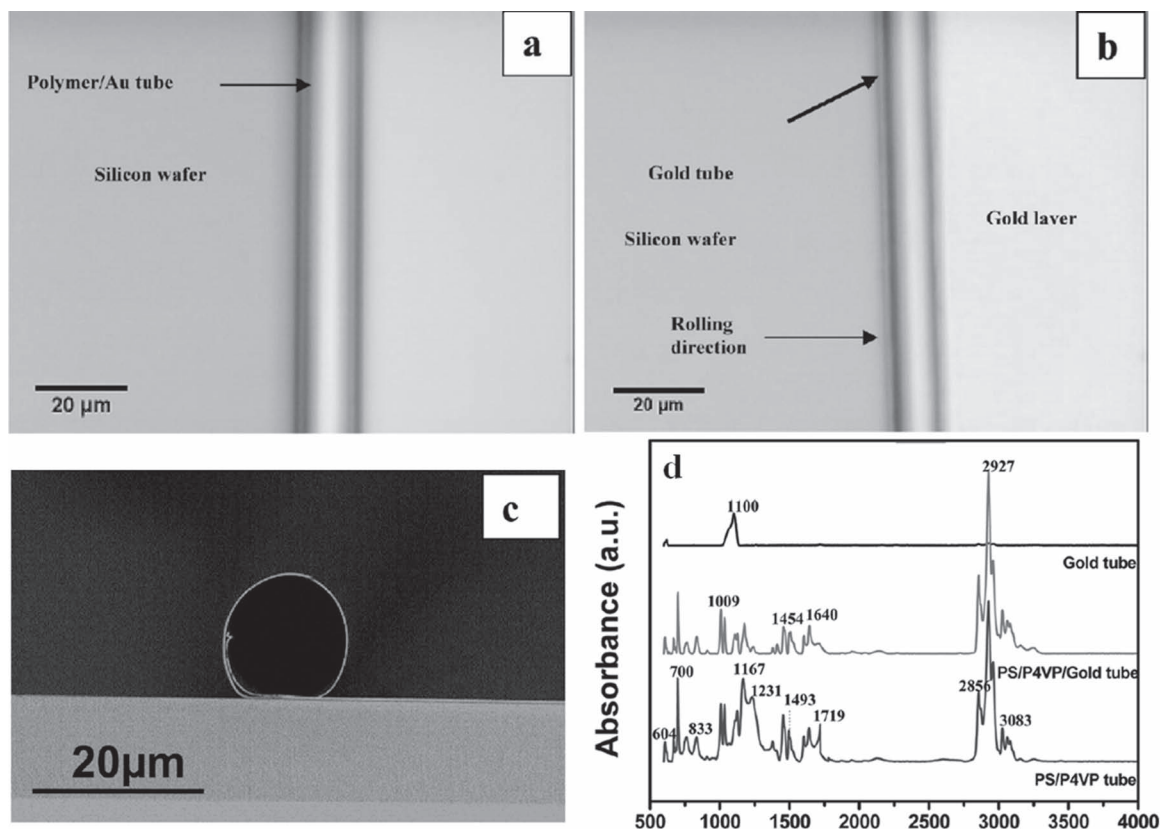


**Figure 3.** a–b) Optical micrographs of a gold tube before (a) and after (b) pyrolysis. c) Optical side-view of a gold tube after pyrolysis. (d) FTIR spectra of a PS–P4VP tube, the polymer with an inner gold layer and the tube after pyrolysis (only the gold remains). Reproduced with permission.<sup>[20]</sup> Copyright 2009, ACS Publications.

investigated as waveguides in soft X-ray diapason<sup>[23]</sup> that can be used as the building blocks for X-ray capillary optics.<sup>[24]</sup> Silica tubes with a metal coating of their inner walls, obtained by self-rolling and consecutive ceramization via pyrolysis, may also be good candidates for micro-capillary reactors in which the inner-metal coating plays the role of a metal catalyst.<sup>[25]</sup>

#### 4. Toroidal Microtubes

The self-rolling effect enables a new approach to the fabrication of micro- and nanocavities, which has attracted much attention as a means by which to trap light and matter in mesoscale volumes for the study of confinement effects, such as the inhibition or enhancement of the

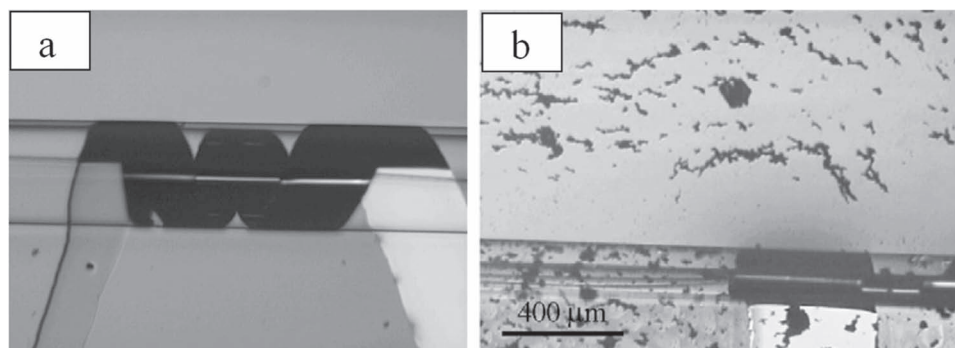


**Figure 4.** (a) A microsolonoid formed by rolling-up a gold, V-shaped stripe made on the surface of a P4VP–PS bilayer. The diameter of the tube is approximately 200  $\mu\text{m}$ . b) The action of an electrical current (0.1 A) passing through the rolled-up microsolonoid, with superparamagnetic particles (magnetite  $\text{Fe}_3\text{O}_4$ ) dispersed in water around the tube. The particles aggregate into bow-like features following the magnetic-field lines. Reproduced with permission.<sup>[16]</sup> Copyright 2007, Elsevier.

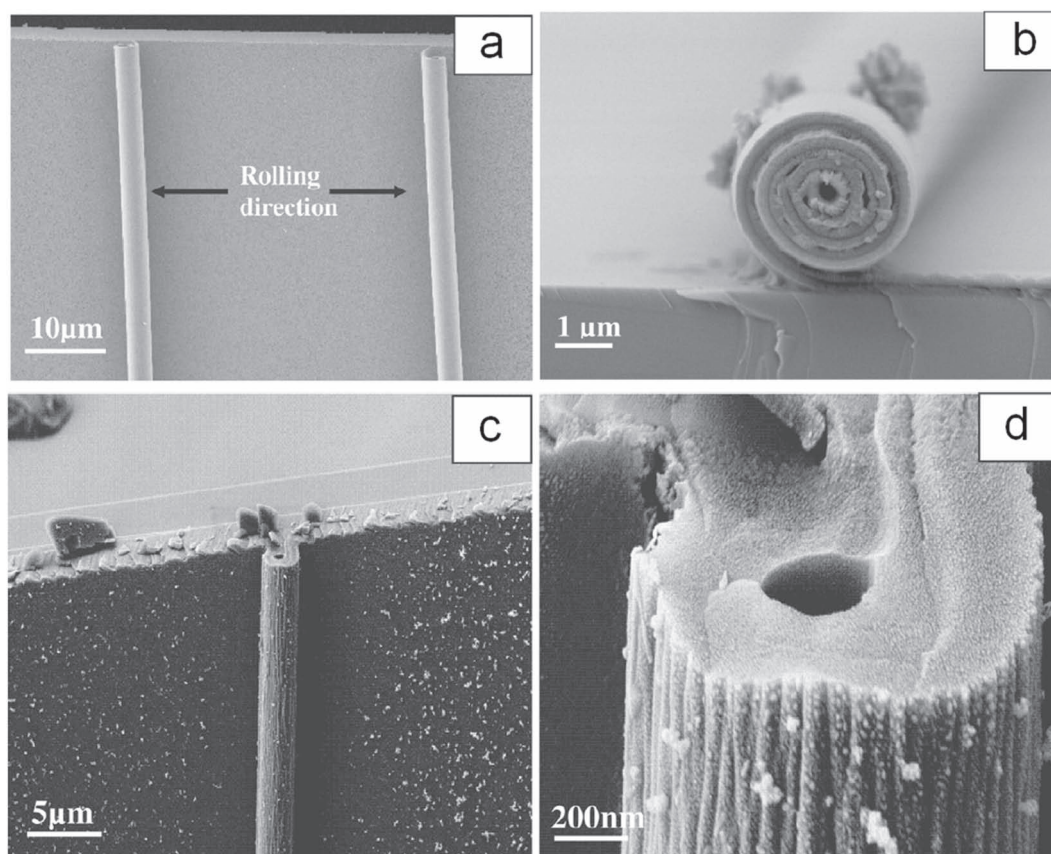


**Figure 5.** (a–d) SEM micrographs of a PDMS–PS–P4VP polymer tube before pyrolysis (a–b), and a silica tube after pyrolysis (c–d). (a) Tubes rolled in the opposite direction from the scratch. (b) Clearly visible rolled polymer layers at the open end of the tube. (c–d) SEM micrographs of a silica tube with an open end at lower (c) and higher (d) magnifications. Reproduced with permission.<sup>[21]</sup> Copyright 2009, ACS Publications.

spontaneous-radiation rate.<sup>[26]</sup> The toroidally shaped cavities are particularly interesting as quasi-1D compartments with periodic boundary conditions. We have shown<sup>[17]</sup> that such tubes can be realized by the self-rolling of bilayers from circular openings produced by photolithography

(**Figure 6**). In contrast to the case of the formation of straight tubes that can roll until the film is fully stable, self-rolling of toroidal tubes is self-constraining: it stops when the energy gain due to relaxation of the bending moment is compensated for by work on the in-plane

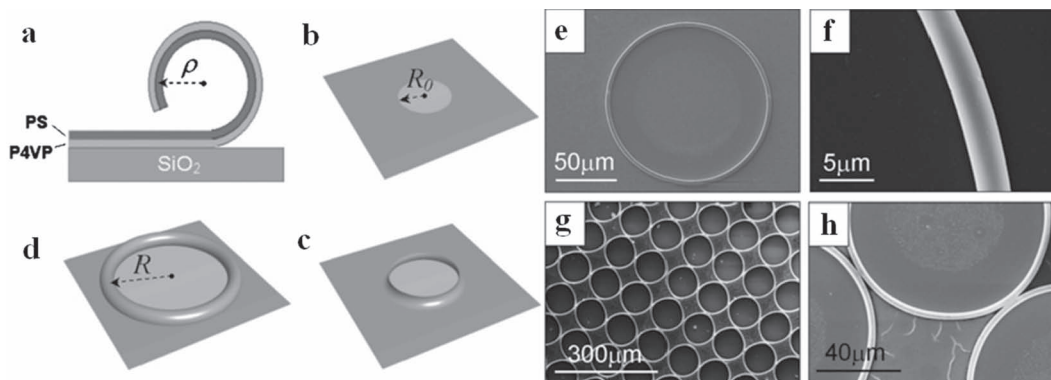


**Figure 6.** (a–d) The scheme of formation of the rolled-up toroidal microtubes: the structure of the polymer bilayer (a); a circular lithographic window in the film produced by the photolithography approach (b); the initial and the final stages of the toroid formation (c–d). (e–h) SEM micrographs of toroidal tubes: a single microtoroid (e–f); an array of microtoroids (g–h). Reproduced with permission.<sup>[17]</sup> Copyright 2008, Institute of Physics.



stretching of the film caused by the increasing radius of the torus. Toroidal tube formation can be described within the framework of a simple theory based on the minimization of the free-energy functional, which combines the contributions of the bending elastic energy and the in-plane-stretching elastic energy.<sup>[17]</sup> In particular, the theory relates the length of the rolled-up part of the bilayer to the effective Young's modulus of the film and its bending stiffness. This means that the formation of toroidal tubes may, in principle, be used for studies on the mechanical properties of thin polymer films.

## 5. Tubes with an Engineered Inner Surface

Probably the most interesting peculiarity of the self-rolling approach is the unprecedented freedom that it provides for engineering the inner surface of the tubes. Indeed, prior to enrolling, the bilayers can be exposed to a variety of surface-treatment techniques such as the aforementioned metallization, but also plasma chemical activation and the creation of nontrivial topological and chemical patterns on the inner walls of the microtubes by means of microcontact printing (**Figure 7**) or photolithography.

Tubes with patterned inner walls may be appropriate for numerous advanced applications in microfluidics, chromatography, catalysis and other fields. It is envisaged, for instance, that specific patterns may influence the growth and motility of living cells in the confined space of the tubes. Biomolecules anchored at specific positions inside the tubes may be explored for the design of biosensors, protein chromatography columns etc.

## 6. Self-Rolling Films for Biological Applications, Controlled Encapsulation and Release

Self-rolling films provide unique opportunities for the encapsulation of small objects such as molecules, or of larger ones such as particles and cells. This property is highly attractive for cell-delivery technology, the food industry and tissue engineering. The main limitations, however, come from the non-biodegradability and non-biocompatibility of self-folding films and the irreversibility of the folding, as well as from their sensitivity to stimuli in non-physiological ranges. In fact, the number of stimuli that can be used to trigger the folding of films is very limited. Cells are, for example, highly sensitive to even small changes of pH. Temperature appears to be the most suitable stimulus because cells readily withstand considerable changes of temperature.

Therefore, we have developed the first self-rolling films that are able to reversibly roll and unroll in response to a change of temperature in the physiological range of 30–37 °C. For the demonstration of the principle involved, bilayers of biodegradable and biocompatible polycaprolactone (PCL) and thermoresponsive poly(*N*-isopropylacrylamide) (PNIPAM) were fabricated and investigated.<sup>[27]</sup> Crosslinked PNIPAM hydrogels demonstrate temperature-switchable swelling. In particular, a PNIPAM hydrogel is highly swollen below 33 °C and its volume is approximately 10 times larger than that of its dry state. On the other hand, PNIPAM hydrogels shrink above 33 °C. It was observed that the PNIPAM–PCL layer is not deformed at a high temperature when the PNIPAM hydrogel is deswollen. Conversely, as soon as the temperature is reduced below the transition point, the PNIPAM hydrogel swells

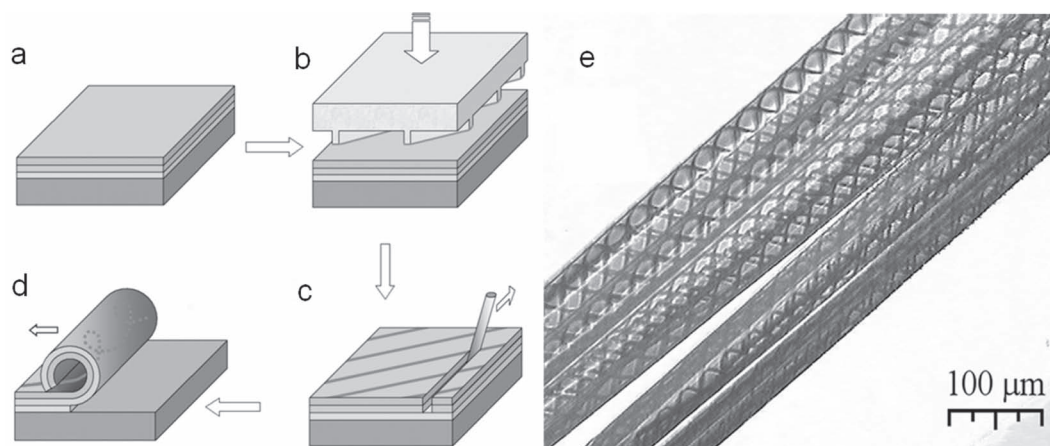


**Figure 7.** Fabrication of tubes with patterned inner surface. (a) Formation of the multilayer on a substrate (e.g., silicon wafer). (b) Patterning of the top layer (here by the use of microcontact printing). (c) Making lithographic openings (e.g., with the use of a sharp blade or needle). (d) Rolling-up the tube in a specific solvent. (e) A bunch of rolled-up tubes with helical patterns on the inner walls. Reproduced with permission.<sup>[11]</sup>

and the bilayer starts to deform (**Figure 8**). As result, tubes with different diameters are formed. It was found that the reversibility of folding depends on the topology of the formed tube. For example, tubes formed by a single revolution could completely unroll. On the other hand, tubes formed by multiple revolutions could not unroll, most probably due to steric hindrance. The most important finding is, however, that, independently from the character of the behaviour of tubes, both the unrolling and shrinking are completely reversible and can be repeated many times.

Tubes are the most primitive shape of folded polymer bilayers. More complicated shapes can be obtained using polymer bilayers with shapes different from the rectangular one. For example, star-like polymer bilayers are able to form envelope-like 3D capsules (**Figure 9**).<sup>[28]</sup> In both cases, when either tubes or capsules are formed, they can be readily used for the encapsulation of adsorbed microparticles and cells. The release of the encapsulated objects

depends on the reversibility of folding and is observed when one revolution is formed. The incorporation of magnetic nanoparticles in polymer bilayers allows for the fabrication of particles or cell-loaded folded objects that can be manipulated using a magnetic field, and this aspect is very important for targeted delivery.<sup>[27]</sup>

While PNIPAM–PCL bilayers are capable of both reversible and irreversible encapsulation of cells and particles, they are not very useful for in vivo applications. The main limitations come from the non-biodegradability and poor biocompatibility of PNIPAM. In order to address this issue, we designed fully biodegradable self-folding films. For this, polysuccinimide (PSI)–PCL bilayers were investigated.<sup>[29]</sup> Both PCL and PSI are hydrophobic and intrinsically water insoluble. PSI, however, is able to hydrolyze in a physiological-buffer environment, yielding water-swellable biodegradable poly(aspartic acid), which leads to the rolling of tubes and the encapsulation of cells. The main advantage of PSI is its relatively slow hydrolysis rate in a physiological

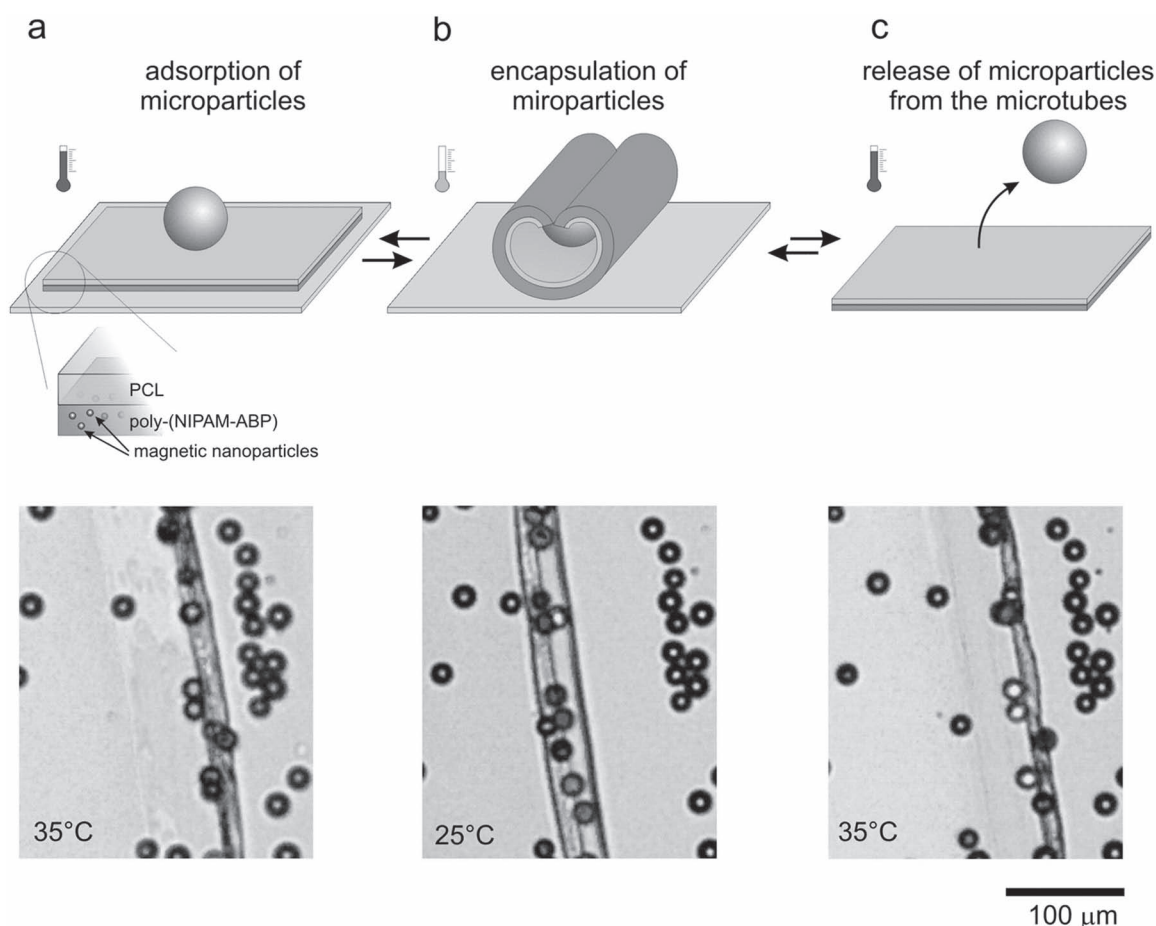


**Figure 8.** (a–c) Scheme of capture and release of microparticles by self-rolling microtubes. A thin film of a PNIPAM and PCL bilayer with admixed magnetic nanoparticles (a) is able to form a self-rolling tube and to encapsulate microparticles at reduced temperature (b); the particles can be released at an elevated temperature when the microtube is unrolled (c); optical-microscopy images of a PNIPAM–PCL bilayer with adsorbed microparticles at different temperatures are also shown. Reproduced with permission.<sup>[27]</sup> Copyright 2010, Royal Society of Chemistry.

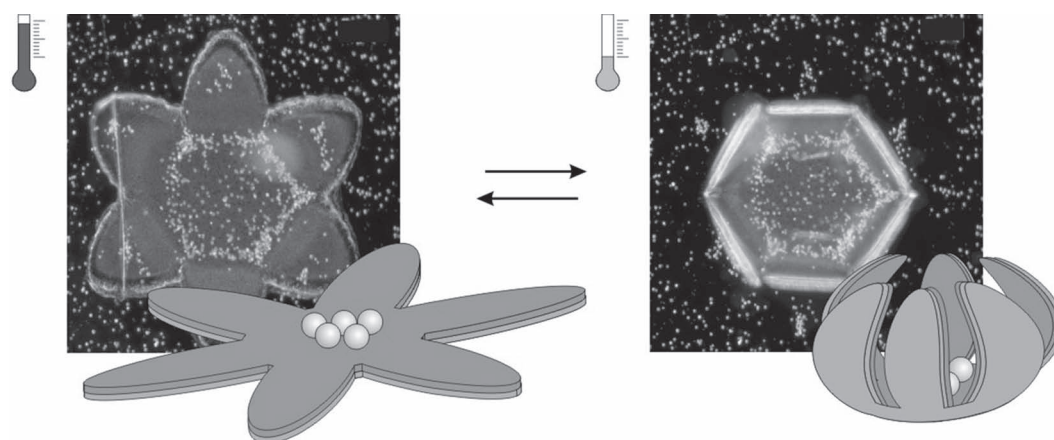


**Figure 9.** Encapsulation of yeast cells inside thermoresponsive self-folding capsules (dark-field optical microscopy). Yeast cells are adsorbed on the polymer bilayer at an elevated temperature. Cooling leads to the swelling of the thermoresponsive polymer and folding of the capsules. A second heating results in unfolding of the capsules and release of the cells. Reproduced with permission.<sup>[28]</sup> Copyright 2011, Royal Society of Chemistry.

buffer. It was found that PSI films start to swell only after 9 h of incubation. Self-rolling films demonstrate a similar behaviour and start to fold after 9 h. This delayed swelling and rolling could be very important for the efficient encapsulation of cells: they might have more time to adhere to the polymer film before irreversible rolling occurs.

## 7. Conclusion and Outlook

Spontaneous self-rolling of bilayer polymer films is a fascinating phenomenon with rich underlying physics. The curvature of the rolls and tubes depends on many factors, including the thickness of the individual layers, their Young's moduli and bending stiffness, the quality of the solvent with respect to each of the polymers and the degree of crosslinking. The dependencies of the tube diameters on these factors can be used for studies on the micromechanical properties of thin polymer films in reactive media. The analysis of the tube formation is relatively simple when it is done within the framework of linear elasticity theory.<sup>[17]</sup> However, a realistic theoretical description of the process should take into account finite plastic deformation of the polymers in the course of rolling. We plan to address this problem in future studies.

Apart from being interesting from the point of view of fundamental studies of the properties of thin films, the self-rolling of bilayers also turns out to be very promising for a number of applications. Bilayer self-rolling can be exploited for the encapsulation and controlled release of microparticles and living cells, which opens up new routes for the development of drug- and cell-delivery therapies. The release of cells and particles can be triggered remotely when a thermoresponsive polymer, such as PNIPAM, is used as one of the components of the bilayer film.

One of the most-attractive advantages of the self-rolling approach is in the complex engineering of the inner walls of the microtubes via modification of the bilayer films, prior to rolling, by a number of surface-treatment methods, such as metallization, plasma activation, and microcontact printing. Protein chromatography is one of the fields where such engineered tubes may find advanced applications. Enrolling of electrodes can provide an easy interface for electrical and microfluidic circuits.

The development of polymer self-rolled tubes has proceeded parallel to investigations of semiconductor and metallic rolled-up structures. Both fields have their advantages and realms of applications. The use of epitaxially grown films produces tubes whose diameters can be as small as a few nanometers. Semiconductor tubes are also interesting from the point of view of their electronic properties. Metallic Ti–Fe–Pt tubes were recently explored as microbots able to transport microparticles in microfluidic circuits. On the other hand, polymer tubes can be biocompatible and are therefore promising for biological and medical applications. A big advantage of polymers as materials for self-rolling bilayers is their easy processability. Indeed, thin polymer films can be produced by dip- or spin-coating from solutions in practically any chemical laboratory, without the need for expensive and rarely accessible equipment for molecular-beam epitaxy that is used for the fabrication of semiconductor bilayers. Polymers can have a large volumetric response to external environmental factors, such as moisture, pH, heat and electromagnetic radiation. This allows for easy control of the internal stress in the bilayer films and, consequently, of the diameters of the tubes. Moreover, it provides reversibility of the rolling, on which the design of our drug- and cell-delivery devices is based. Finally, polymers are very compatible with inorganic materials, such as metals, or

they can serve as the precursors for inorganic materials such as ceramics.

In conclusion, the design of microscale 3D objects via the self-rolling of polymer bilayer and multilayer films is an emerging field of research that has begun to find advanced applications in the soft-matter field.

**Acknowledgements:** We thank the Deutsche Forschungsgemeinschaft (SPP Priority Program 1165) and the Nanofun-Poly Network of Excellence for financial support.

Received: July 22, 2011; Revised: September 14, 2011; Published online: October 18, 2011; DOI: 10.1002/marc.201100482

**Keywords:** drug-delivery systems; functionalization of polymers; microencapsulation; microtubes; thin films

- [1] J. Genzer, J. Groenewold, *Soft Matter* **2006**, 2, 310.
- [2] E. Smela, O. Inganas, I. Lundstrom, *Science* **1995**, 268, 1735.
- [3] V. Ya. Prinz, V. A. Seleznev, V. A. Samoylov, A. K. Gutakovsky, *Microelectron. Eng.* **1996**, 30, 439.
- [4] V. Ya. Prinz, V. A. Seleznev, A. K. Gutakovsky, V. Preobrazhenski, A. V. Chehovsky, M. A. Putyato, M. A. Gavrilova, *Physica E* **2000**, 6, 828.
- [5] V. A. Seleznev, A. V. Prinz, V. Ya. Prinz, *Microelectron. Eng.* **2002**, 67–68, 782.
- [6] C. Deneke, N.-Y. Jin-Phillipp, I. Loa, O. G. Schmidt, *Appl. Phys. Lett.* **2004**, 84, 4475.
- [7] C. Deneke, O. G. Schmidt, *Appl. Phys. Lett.* **2006**, 89, 123121.
- [8] G. S. Huang, Y. F. Mei, D. J. Thurmer, E. Coric, O. G. Schmidt, *Lab Chip* **2009**, 9, 263.
- [9] S. Sanchez, A. A. Solovev, S. M. Harazim, O. G. Schmidt, *J. Am. Chem. Soc.* **2011**, 133, 701.
- [10] J. Zang, M. Huang, F. Liu, *Phys. Rev. Lett.* **2007**, 98, 146102.
- [11] V. Luchnikov, O. Sydorenko, M. Stamm, *Adv. Mater.* **2005**, 17, 1177.
- [12] L. Ionov, *J. Mater. Chem.* **2010**, 20, 3382.
- [13] L. Ionov, *Soft Matter* **2011**, 7, 6786.
- [14] B. G. Ranby, J. F. Rabek, *Photodegradation, Photo-oxidation and Photostabilization of Polymers*, Wiley, New York, USA **1975**, p. 167–172.
- [15] B. Harnish, J. T. Robinson, Z. Pei, O. Ramström, M. Yan, *Chem. Mater.* **2005**, 17, 4092.
- [16] V. Luchnikov, M. Stamm, *Physica E* **2007**, 37, 236.
- [17] V. Luchnikov, K. Kumar, M. Stamm, *J. Micromech. Microeng.* **2008**, 18, 035041.
- [18] K. Kumar, V. Luchnikov, B. Nandan, V. Senkovskyy, M. Stamm, *Eur. Polym. J.* **2008**, 44, 4115.
- [19] V. Luchnikov, M. Stamm, Ch. Akhmadaliev, L. Bischoff, B. Schmidt, *J. Micromech. Microeng.* **2006**, 16, 1602.
- [20] K. Kumar, B. Nandan, V. Luchnikov, E. B. Gowd, M. Stamm, *Langmuir* **2009**, 25, 7667.
- [21] K. Kumar, B. Nandan, V. Luchnikov, F. Simon, A. Vyalikh, U. Scheler, M. Stamm, *Chem. Mater.* **2009**, 21, 4282.
- [22] J. Harrington, *Fiber Integrated Optics* **2000**, 19, 211.
- [23] Y. Matsuura, T. Oyama, M. Miyagi, *Applied Optics* **2005**, 44, 6193.
- [24] M. A. Kumakhov, *Proc. SPIE* **1995**, 2515, 86.
- [25] C. H. Hornung, B. Hallmark, M. R. Mackley, I. R. Baxendale, S. V. Ley, *Adv. Synthesis Catal.* **2010**, 352, 1736.
- [26] E. M. Purcell, *Phys Rev* **1946**, 69, 681.
- [27] S. Zakharchenko, N. Pureskiy, G. Stoychev, M. Stamm, L. Ionov, *Soft Matter* **2010**, 6, 2633.
- [28] G. Stoychev, N. Pureskiy, L. Ionov, *Soft Matter* **2011**, 7, 3277.
- [29] S. Zakharchenko, E. Sperling, L. Ionov, *Biomacromolecules* **2011**, 12, 2211.

Ionov, L.

Soft microorigami: self-folding polymer films

***Soft Matter*** 2011, 7, 6786–6791.



Cite this: *Soft Matter*, 2011, **7**, 6786[www.rsc.org/softmatter](http://www.rsc.org/softmatter)

## TUTORIAL REVIEW

## Soft microorigami: self-folding polymer films

Leonid Ionov\*

Received 18th March 2011, Accepted 18th April 2011

DOI: 10.1039/c1sm05476g

Fabrication of 3D objects using folding of thin films is a novel and very attractive research field. The manuscript overviews recent advances in development and application of polymer films, which are able to fold and form 3D structures.

## Introduction

Engineering of complex 3D constructs is a highly challenging task for development of materials with novel optical properties, tissue engineering scaffolds, elements of micro- and nano-electronic devices. Three-dimensional materials can be fabricated using a variety of methods including two-photon photolithography, interference lithography, and molding (see the recent review of D. H. Gracias *et al.*<sup>1</sup>). Fabrication of 3D microobjects using controlled folding/bending of thin films—microorigami—is a novel and very attractive research field.<sup>1,2</sup> One of the advantages of this approach is the possibility of quick, reversible and reproducible fabrication of 3D hollow objects with controlled chemical properties and morphology of both the exterior and interior. The pioneering works in this field belong to Smela *et al.*<sup>3</sup> and Jager *et al.*<sup>4</sup> They were the first who started to work with self-folding films and demonstrated folding and unfolding of patterned gold films with polypyrrole hinges in response to an electric signal. Groups of O. G. Schmidt focused on the design of semiconductor and metal oxide self-rolled tubes and applied them for transport,<sup>5</sup> investigating behaviour of cells in confinement,<sup>6</sup> nanooptics<sup>7</sup> and energy storage elements.<sup>8</sup>

Gracias *et al.* developed approaches for design of metallic self-folding particles and demonstrated their applicability for design of self-assembling microelectronic devices, controlled encapsulation of cells, drugs and design of tissue engineering scaffolds.<sup>9–12</sup> Metallic self-folding thin films are also highly promising for optics<sup>13</sup> and photovoltaic power applications.<sup>14</sup>

On the other hand, due to their rigidity, limited biocompatibility and non-biodegradability, application of inorganic self-folding materials for biomedical purposes is limited. Polymers are more suitable for these purposes. First, there are many polymers changing their properties in physiological ranges of pH and temperature as well as polymers sensitive to biochemical processes.<sup>15</sup> Second, polymers undergo considerable and reversible changes in volume that allow design of a variety of actively moving microconstructs.<sup>16,17</sup> Third, there are a variety of biocompatible and biodegradable polymers.<sup>18</sup> This paper overviews the recent progress in development of polymer films, which are able to fold and form 3D microstructures. The main focus is to summarize polymer-based systems and to classify them with respect to way of fabrication, suitability for design of different 3D objects and applicability for biotechnology.

## Bending vs. expansion

Bending is essentially required for design of self-folding materials and allows conversion of semi-one-dimensional and two-dimensional objects into 2D and 3D ones, respectively. Typically bending is the result of either expansion or contraction of a material caused by changes in environmental conditions. In most cases the change in conditions, however, results in homogeneous expansion or contraction in all directions and does not lead to increase in dimensionality. Bending is produced as a result of inhomogeneous expansion/shrinking, which occurs with different magnitudes in different directions. Bending could be achieved either (i) by applying gradients of field to homogeneous materials or (ii) by applying non-gradient stimuli to inhomogeneous materials. The example of the first case is the bending of polyelectrolyte hydrogel during electrolysis.<sup>19</sup> The examples of the second group are the bending of liquid crystalline films,<sup>20</sup> hydrogels with the lateral gradient monomer concentration,<sup>21</sup> cantilever sensors<sup>22</sup> and shape-memory polymers.<sup>23</sup>

Leibniz Institute of Polymer Research Dresden, Hohe Str. 6, 01069 Dresden, Germany. E-mail: [ionov@ipfdd.de](mailto:ionov@ipfdd.de)



Leonid Ionov

Leonid Ionov is a group leader at the Leibniz Institute of Polymer Research Dresden (Germany). He received his PhD in Polymer Chemistry in 2005 from Dresden University of Technology (Germany) and made his postdoc at the Max Planck Institute of Molecular Cell Biology and Genetics (Germany) and Clarkson University (USA). His research is focused on stimuli-responsive and self-assembling materials.

## Design of self-folding films

In fact, design of self-folding objects using homogeneous materials is technically very complicated because a very complex spatial force gradient must be formed and kept for a considerable period of time. This, for example, can be achieved using surface tension by depositing a water droplet on a thin film.<sup>24</sup> The film folds immediately after the droplet is deposited. The formed 3D object changes its shape during drying of the droplet and unfolds when water is completely evaporated. In physiological buffer environment surface tension effects are, however, weak. Fabrication of self-folding objects using inhomogeneous films is more straightforward. The inhomogeneous films fold due to the difference in the properties of constituting materials in a pre-programmed manner, which is defined by the film structure/pattern.

To date, three general approaches for design of self-folding polymer films are reported (Fig. 1). The first approach is based on shape-memory polymers, which are partially liquid crystalline with directional anisotropy of properties (Fig. 1a). At low temperature the shape-memory materials are in their temporary shape. The films recover their permanent shape by heating. In second and third approaches two polymers are used. One of the polymers is passive and its properties remain unchanged. Another polymer is active and its volume or shape is changed when stimulus is applied. The second approach is based on the use of polymer bilayers (Fig. 1b). The active polymer swells or shrinks in response to the signal. The swelling in one direction is restricted by the passive polymer. As a result, the bilayer does not uniformly expand/shrink but folds and unfolds. The third approach is based on the use of patterned films of the passive polymer with insertion of an active one (Fig. 1c). The active polymer undergoes shape transition, which might be caused by surface forces, that results in folding of the film.

The shape of the formed 3D object depends on the shape of the polymer films (Fig. 2 and Table 1). The simplest case of a self-folding object is a tube.<sup>25–27,32–35</sup> Helixes of different kinds are formed by polymer bilayers with the gradually changing ratio

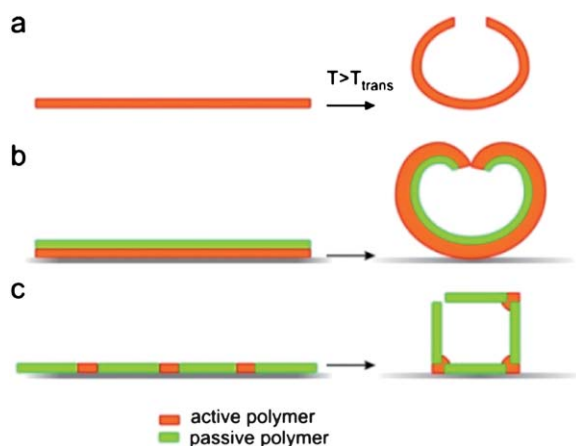


**Fig. 1** Approaches for design of self-folding polymer objects: (a) relaxation of shape-memory polymers, (b) folding of polymer bilayer due to expansion of one of the polymers and (c) folding of patterned polymer film caused by the shape change in one of the polymers.

between polymers.<sup>29</sup> Envelop-like capsules with rounded corners or nearly spherical ones are formed from the star-like polymer bilayers with four and six arms, respectively.<sup>27,28,35</sup> Cubes and pyramids are formed by patterned bilayers with the active junction elements.<sup>29,31,36</sup>

The polymer films with different shapes can be obtained either by cutting,<sup>25,26,32</sup> using microwell-like substrates<sup>27,34,35</sup> or photolithography<sup>28,31,33,36</sup> (Table 1). Cutting allows fabrication of millimetre size species with the rectangular shape, which form the tubes. The main advantage of this method is simplicity and applicability to almost all combinations of crosslinkable polymers. The use of microwell-like substrates is technically more complicated but allows fabrication of polymer layers with different shapes such as rectangles or stars. Photolithography of bilayers allows large-scale fabrication of self-folding objects of different shapes and sizes starting from several microns. The formed self-folding objects have rounded corners. The main disadvantage of this approach is the necessity to choose proper solvents for polymer deposition in the way that the first polymer is not dissolved during deposition of the second polymer. Fabrication of patterned polymer films (Fig. 1c) is the technically most complicated procedure and requires mask alignment during several steps of photolithography. On the other hand, it allows fabrication of the broadest range of shapes of self-folding objects.

## Stimuli

The use of polymers sensitive to different signals allows design of self-folding films folding upon immersion in solvent, change in pH, temperature, electric or biochemical signals (Table 2).

### pH-responsive

Self-folding films sensitive to pH are commonly designed using weak polyelectrolytes as active polymers. Luchnikov *et al.* demonstrated that polystyrene–poly(4-vinyl pyridine) bilayer<sup>26</sup> as well as polystyrene–poly(4-vinyl pyridine)–polydimethylsiloxane trilayer<sup>37</sup> are able to roll at low pH when poly(4-vinyl pyridine) is protonated and swells in water. The use of layers with two-dimensional gradient of thickness allowed thorough investigation of the folding.<sup>38</sup> It was found that the rate of rolling increased with the acidity of the solution. The tube diameter and the rate of rolling decreased with the increase in the UV exposure time. Moreover, the increase in thickness of PS results in increase in the diameter of tube.

Lee *et al.* used pH sensitive poly(methacrylic acid)–poly(2-hydroxyethyl methacrylate)<sup>34</sup> and poly(methacrylic acid) (PMAA)/polyEGDMA<sup>35</sup> patterned bilayer which folds in contact with biological fluids. It was not shown that the folding depends on pH. However, since weak polyelectrolyte poly(methacrylic acid) was used, the system is expected to respond to the pH signal. Gracias *et al.* fabricated millimetre size polyethylene glycol/poly(*N*-isopropylacrylamide-acrylic acid) bilayers which are able to snap in response to the pH signal.<sup>36</sup> One can also expect that this system is thermoresponsive. Huck *et al.* reported pH responsive gold–poly(methacryloxyethyl trimethylammonium chloride) brush patterned films which fold in response to the change in pH and salt concentration.<sup>30</sup>

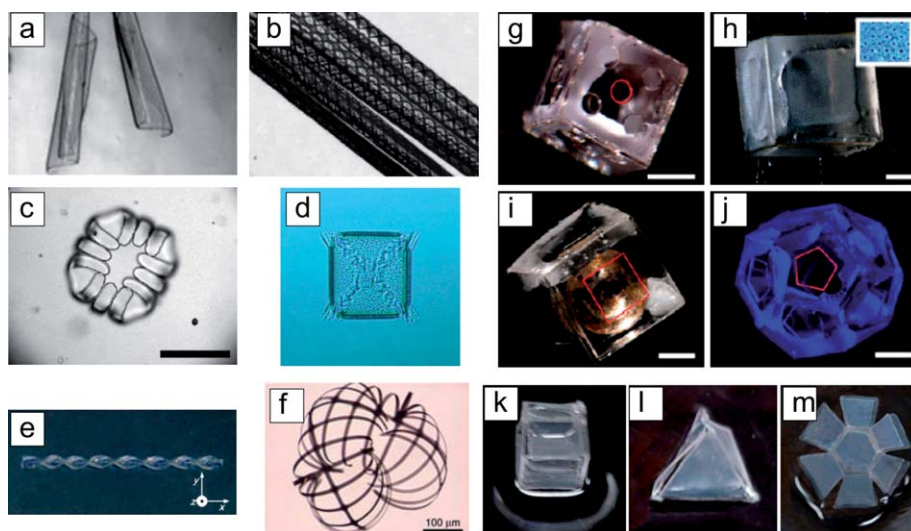


**Fig. 2** Examples of self-folding polymer films: tubes<sup>25,26</sup> (a and b: reproduced with permission, Copyright Wiley-VCH Verlag GmbH & Co. KGaA<sup>26</sup>), capsules<sup>27,28</sup> (c: reproduced with permission, Copyright Wiley-VCH Verlag GmbH & Co. KGaA<sup>27</sup>; d: Royal Society of Chemistry, Copyright<sup>28</sup>), helix<sup>29</sup> (e), hierarchically shaped tube<sup>30</sup> (f: reproduced with permission, Copyright Wiley-VCH Verlag GmbH & Co. KGaA<sup>30</sup>), cubes with porous walls<sup>29,31</sup> (g, h, and i: with kind permission from Springer Science + Business Media permission, Copyright<sup>31</sup>; k: Royal Society of Chemistry, Copyright<sup>29</sup>), dodecahedron<sup>31</sup> (j: with kind permission from Springer Science + Business Media permission, Copyright<sup>31</sup>), pyramid<sup>29</sup> (l: Royal Society of Chemistry, Copyright), and phlat ball<sup>29</sup> (m: Royal Society of Chemistry, Copyright).

## Thermoresponsive

Thermoresponsive self-folding films can be designed using continuous thermal expansion, melting, shape-memory transition or polymers which demonstrate the LCST (Low Critical Solution Temperature) behaviour in solutions. Kalaitzidou *et al.* used continuous volume expansion with temperature and demonstrated thermoresponsive rolling–unrolling of polydimethylsiloxane–gold bilayer tubes at 60–70 °C<sup>25,32</sup> which is due to different temperature expansion coefficients.

Gracias *et al.* used melting of polymers, which forms a droplet and forces patterned polymer films to fold. This was demonstrated on the example of patterned SU-8 photoresist–polycaprolactone film, which irreversibly folds at 60 °C (ref. 31) due to melting of polycaprolactone (Fig. 3). In order to reduce the transition temperature and make films more suitable for bio-related applications, Gracais *et al.* used photoresist hinges which are sensitive to temperatures around 40 °C.<sup>39–41</sup> The metal–polymer grippers irreversibly fold in response to temperature as well.

Lendlein *et al.* demonstrated the possibilities to design thermoresponsive macroscopic self-folding objects using shape-memory

polymers based on different poly( $\epsilon$ -caprolactone)s.<sup>23</sup> At low temperature the materials are in their temporary shape. The films recover their permanent shape and irreversibly fold by heating, which could be accompanied by a change in transparency. The exact size of the self-folding film as well as the temperature of transition was not given.

Polymer bilayers, where the active component is thermoresponsive poly(*N*-isopropylacrylamide)-based copolymer, are more suitable for encapsulation of cells. In aqueous media, poly(*N*-isopropylacrylamide)-based hydrogels reversibly swell and shrink below and above 33 °C. Moreover, the temperature of transition between swollen and shrunk states can be tuned by proper selection of the composition of copolymer. As a result, poly(*N*-isopropylacrylamide)–polycaprolactone patterned bilayers fold and unfold forming tubes of capsules below and above this temperature, respectively (Fig. 4).<sup>28,33</sup>

## Solvent responsive

Most examples of solvent-responsive self-folding films are the films, which fold upon immersion in aqueous media. Such films

**Table 1** Methods for fabrication of self-folding polymer films

Preparation method	Advantage	Disadvantage	Shapes of folded object	Ref.
Cutting	Simple, all crosslinkable polymers can be used	Limited shapes—mostly rectangular, large objects	Tubes	25,26,32
Microwells	All crosslinkable polymers can be used, variety of shapes	Requires fabrication of microwells	Tubes, capsules, and helices	27,34,35
Photolithography of bilayers	Simple, large scale fabrication, different sizes and shapes	Polymers must be deposited from selective solvents	Tubes and capsules	17,18
Photolithography of patterned layers	Large scale fabrication, different sizes and shapes	Complicated, requires special equipment	Tubes, capsules, cubes, and pyramids	23–25



**Table 2** Reported examples of self-folding polymer films

System	Stimuli	Folding range	Biodegradation	Reversibility	Ref.
<i>pH-responsive</i>					
Poly(4-vinyl pyridine)–polystyrene	PH	pH = 2	No	+	26
Poly(2-hydroxyethyl methacrylate)–poly(methacrylic acid)	PH	pH = 3–7.3	No	+	34
Poly(methacrylic acid)–polyethylene glycol	PH	No information	No	+	35
Poly( <i>N</i> -isopropylacrylamide- <i>co</i> -acrylic acid)–polyethylene glycol	PH	pH = 2.5–7.5	No	+	36
<b>Poly(methacryloxyethyl trimethylammonium chloride)–gold<sup>a</sup></b>	<b>PH, salt</b>	<b>Not given</b>	<b>No</b>	–	<b>30</b>
<b>Metals–photoresist<sup>a</sup></b>	<b>Acetic acid</b>	<b>&gt;60%</b>	<b>No</b>	–	<b>44</b>
<i>Solvent-responsive</i>					
Polyvinyl alcohol–chitosan	Water	Immediate folding	Partial	–	27
Chitosan–polyethylene glycol	Water	Immediate folding	Partial	–	35
Polydimethylsiloxane–polyurethane/2-hydroxyethyl methacrylate	Water	Immediate folding	No	–	29
<b>Poly(glycidyl methacrylate)–gold<sup>a</sup></b>	<b>Methanol</b>	<b>Immediate folding</b>	<b>No</b>	–	<b>30</b>
<i>Thermoresponsive</i>					
<b>Polydimethylsiloxane–gold<sup>a</sup></b>	<i>T</i>	<b>60–70 °C</b>	<b>No</b>	<b>+</b>	<b>25,32</b>
SU-8 photoresist–polycaprolactone	<i>T</i>	60 °C	Partial	–	31
Poly( <i>N</i> -isopropylacrylamide)–polycaprolactone	<i>T</i>	28–30 °C	Partial	+	28,33
Polycaprolactone	<i>T</i>	Unknown	Full	–	23
Poly(caprolactone- <i>co</i> -pentadecadolactone)	<i>T</i>	Unknown	Full	–	23
<b>Metals–photoresist<sup>a</sup></b>	<i>T</i>	<b>40–60 °C</b>	<b>No</b>	–	<b>39–41</b>
<i>Other</i>					
Polydimethylsiloxane–cardiomyocytes	Electric	10 V	Partial	+	42
<b>Metals–gelatine–carboxymethylcellulose<sup>a</sup></b>	<b>Enzyme</b>		<b>Partial</b>	<b>One circle</b>	<b>43</b>
<b>Polypyrrole–gold</b>	<b>Electric</b>	<b>1 V</b>	<b>No</b>	<b>+</b>	<b>3,4</b>

<sup>a</sup> Systems with inorganic components are in bold.

contain water-swallowable uncharged polymers. Lee *et al.* fabricated partially biodegradable polyvinyl alcohol–chitosan<sup>27</sup> and chitosan–poly(PEGMA-*co*-PEGDMA) bilayers<sup>35</sup> which fold in water due to swelling of polyvinyl alcohol and polyethylene glycol, respectively. Jeong and Jang *et al.* developed the approach for fabrication of millimetre size self-folding objects which are able to fold and form different 3D objects such as tubes, cubes, pyramids and helices.<sup>29</sup> Water-swallowable polydimethylsiloxane–polyurethane/2-hydroxyethyl methacrylate complex bilayers and patterned films were used. Since poly(vinyl alcohol), polyethylene

glycol and poly(2-hydroxyethyl methacrylate) are not polyelectrolytes, the swelling is expected to be independent of pH of aqueous media. These systems immediately fold upon immersion in aqueous media that hampers loading of cells.

Huck reported the example of the system which folds in methanol. This system is based on poly(glycidyl methacrylate) brush layers grafted to gold patterned films.<sup>30</sup>

### Other systems

Except for pH-, thermo- and solvent-responsive systems, there are also several examples of systems, which fold in response to

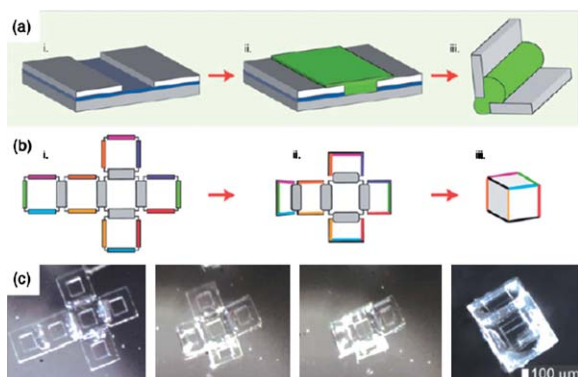


**Fig. 3** Thermoresponsive self-folding SU-8 photoresist–polycaprolactone thin films. (a) Fabrication: (i) a sacrificial layer was spin coated on a clean Si wafer. SU-8 panels were patterned using conventional photolithography. (ii) PCL was deposited in hinge gaps. (iii) 2D templates were lifted off via dissolution of the PVA layer in water and self-assembly occurred on heating above 58 °C. (b, i–iii) Schematic demonstrating self-folding of a cubic container. External “locking” hinges are colored in pairs to denote corresponding meeting edges. (c) Video capture sequence (over 15 s) showing a 1 mm sized, six-windowed polymeric container self-folding at 60 °C. With kind permission from Springer Science + Business Media permission, Copyright.<sup>31</sup>

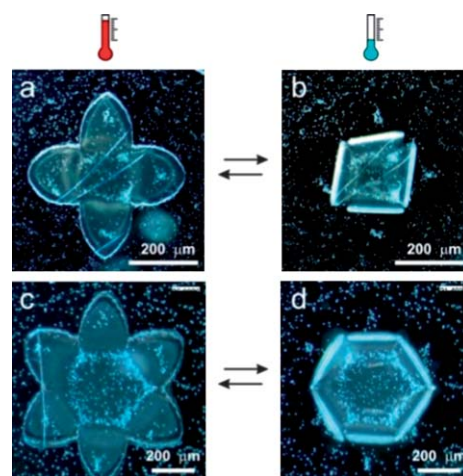


**Fig. 4** Encapsulation of yeast cells inside thermoresponsive poly(*N*-isopropylacrylamide)–polycaprolactone self-folding capsules. Yeast cells are adsorbed on the polymer bilayer at elevated temperatures (a and c). Cooling leads to swelling of the thermoresponsive polymer and folding of the capsules (b and d). Secondary heating results in unfolding of the capsules and release of the cells. Royal Society of Chemistry, Copyright.<sup>28</sup>

other stimuli such as the presence of enzymes or applied electric field. Smella<sup>3</sup> and Jager<sup>4</sup> *et al.*, who introduced the self-folding films, demonstrated folding and unfolding of patterned gold films with polypyrrole hinges in response to the electric signal. Whitesides *et al.* fabricated an electro-responsive self-folding bilayer, which consists of polydimethylsiloxane with the aligned cardiomyocytes.<sup>42</sup> The polymer–cell film adopted functional three-dimensional conformations when an electric signal is applied. These centimetre-scale constructs perform functions as diverse as gripping, pumping, walking, and swimming with fine spatial and temporal control.

Enzyme-sensitive self-folding films were developed for the first time by Gracias *et al.* The approach is based on the use of self-folding metallic grippers with active polymer hinges, which are sensitive to the presence of enzymes.<sup>43</sup> Two kinds of biodegradable polymers were used. The gripper, which is unfolded in the initial state, folds when the first polymer is degraded after addition of the first enzyme. The gripper unfolds when the second enzyme is added and the second polymer is degraded. As a result one circle of folding and unfolding is achieved.

## Applications

The main field of application of self-folding polymer thin films is the controlled encapsulation and release of drugs, particles and cells (Fig. 5). Kalaitzidou *et al.* demonstrated reversible adsorption–desorption of fluorescently labelled polyethylene glycol, which is considered as a model drug, inside PDMS–gold tubes at 60–70 °C.<sup>32</sup> Gracias *et al.* demonstrated irreversible encapsulation of yeast cells inside self-folding SU8–PCL films upon heating at above 60 °C.<sup>31</sup> Poly(*N*-isopropylacrylamide)-based self-folding films were also demonstrated to be suitable for reversible encapsulation of particles and yeast cells.<sup>28,33</sup> Cells were encapsulated upon cooling below 30 °C and could be released from the film, which is unfolded above 30 °C. This

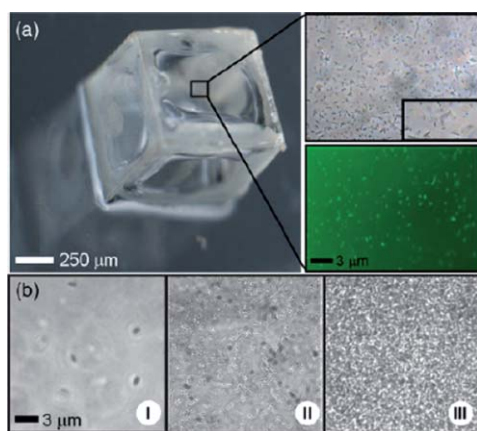


**Fig. 5** Bacterial encapsulation using self-folding SU-8 photoresist–polycaprolactone films. (a) Bright-field and fluorescence images of Syto 9 stained *E. coli* encapsulated within a polymer container, 24 h after encapsulation. (b) Bright-field time lapse images of bacteria within a polymeric container, taken at intervals of zero, 4 and 15 h following encapsulation by tumbling. With kind permission from Springer Science + Business Media permission, Copyright.<sup>31</sup>

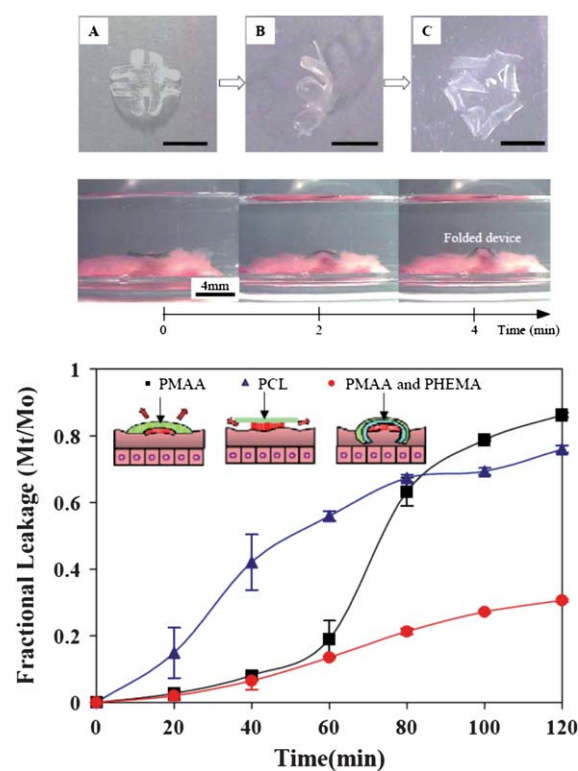


**Fig. 6** Self-folding polymer bilayer films as smart plaster. (Upper panel) Polymer bilayer is undeformed in dry states and folded in aqueous environment. (Middle panel) Folding of polymer bilayer on the mucus surface. (Lower panel) The fractional leakage of drug from the self-folded reservoir with different protection layers is the smallest (reproduced with permission, Copyright Elsevier<sup>34</sup>).

encapsulation and release is completely reversible and could be repeated many times (Fig. 4).

Self-folding films can also be used as smart plasters. Lee demonstrated this concept on the example of millimetre size poly(methyl methacrylate)–poly(2-hydroxyethyl methacrylate) bilayer with the attached mucoadhesive drug layer. The non-swelling PHEMA layer serves as a diffusion barrier, minimizing any drug leakage in the intestine. The resulting unidirectional release provides improved drug transport through the mucosal epithelium (Fig. 6). The functionality of this device is successfully demonstrated *in vitro* using a porcine small intestine.<sup>34</sup>

There are several non-biorelated examples of application of self-folding polymer films. Deposition of patterned metal on the polymer bilayer allowed fabrication of self-rolled tubes with patterned conductive inner wall.<sup>26</sup> In another example, pyrolysis of polystyrene–poly(4-vinyl pyridine)–polydimethylsiloxane tri-layer<sup>37</sup> was used for fabrication of silica tubes.

## Conclusions and outlook

The self-folding polymeric thin films are an emerging field, which only starts to develop. Till now, several examples of the polymer thin films folding due to immersion in aqueous environment, change in pH, temperature, electric signal or the presence of enzymes were demonstrated. The self-folding films are potentially very promising for controlled encapsulation and release of drugs



and cells. Here, cells are not locked inside an amorphous and densely crosslinked matrix, as it happens in the case of hydrogels, but are free to move. This is particularly important for design of tissue engineering scaffolds. The limited applicability of self-folding tubes for design of scaffolds is, on the one hand, due to their folding at non-physiological conditions. First, pH is not a favourable signal to trigger folding for encapsulation of cells. The use of temperature as stimulus is more suitable, since cells readily withstand temperature variation. On the other hand, most of the reported systems are non-biodegradable. There is only one report about the fully biodegradable self-folding polymer film. In future, these two problems must become the main focus of research in this field.

## Notes and references

- 1 T. G. Leong, A. M. Zarafshar and D. H. Gracias, *Small*, 2010, **6**, 792–806.
- 2 E. Hawkes, B. An, N. M. Benbernou, H. Tanaka, S. Kim, E. D. Demaine, D. Rus and R. J. Wood, *Proc. Natl. Acad. Sci. U. S. A.*, 2010, **107**, 12441–12445.
- 3 E. Smela, O. Inganäs and I. Lundström, *Science*, 1995, **268**, 1735–1738.
- 4 E. W. H. Jager, O. Inganäs and I. Lundström, *Science*, 2000, **288**, 2335–2338.
- 5 A. A. Solovev, S. Sanchez, M. Pumera, Y. F. Mei and O. G. Schmidt, *Adv. Funct. Mater.*, 2010, **20**, 2430–2435.
- 6 G. S. Huang, Y. F. Mei, D. J. Thurmer, E. Coric and O. G. Schmidt, *Lab Chip*, 2009, **9**, 263–268.
- 7 E. J. Smith, Z. Liu, Y. F. Mei and O. G. Schmidt, *Appl. Phys. Lett.*, 2009, **95**, 083104.
- 8 C. C. s. Bof Bufon, J. D. Cojal González, D. J. Thurmer, D. Grimm, M. Bauer and O. G. Schmidt, *Nano Lett.*, 2010, **10**, 2506–2510.
- 9 D. H. Gracias, J. Tien, T. L. Breen, C. Hsu and G. M. Whitesides, *Science*, 2000, **289**, 1170–1172.
- 10 T. Leong, Z. Y. Gu, T. Koh and D. H. Gracias, *J. Am. Chem. Soc.*, 2006, **128**, 11336–11337.
- 11 C. L. Randall, Y. V. Kalinin, M. Jamal, T. Manohar and D. H. Gracias, *Lab Chip*, 2011, **11**, 127–131.
- 12 M. Jamal, N. Bassik, J. H. Cho, C. L. Randall and D. H. Gracias, *Biomaterials*, 2010, **31**, 1683–1690.
- 13 S. Schwaiger, M. Broll, A. Krohn, A. Stemmann, C. Heyn, Y. Stark, D. Stickler, D. Heitmann and S. Mendach, *Phys. Rev. Lett.*, 2009, **102**, 163903.
- 14 X. Y. Guo, H. Li, B. Y. Ahn, E. B. Duoss, K. J. Hsia, J. A. Lewis and R. G. Nuzzo, *Proc. Natl. Acad. Sci. U. S. A.*, 2009, **106**, 20149–20154.
- 15 M. A. C. Stuart, W. T. S. Huck, J. Genzer, M. Müller, C. Ober, M. Stamm, G. B. Sukhorukov, I. Szleifer, V. V. Tsukruk, M. Urban, F. Winnik, S. Zauscher, I. Luzinov and S. Minko, *Nat. Mater.*, 2010, **9**, 101–113.
- 16 L. Ionov, *J. Mater. Chem.*, 2010, **20**, 3382–3390.
- 17 J. E. Comrie and W. T. S. Huck, *Macromol. Rapid Commun.*, 2008, **29**, 539–546.
- 18 P. X. Ma, *Adv. Drug Delivery Rev.*, 2008, **60**, 184–198.
- 19 G. H. Kwon, Y. Y. Choi, J. Y. Park, D. H. Woo, K. B. Lee, J. H. Kim and S.-H. Lee, *Lab Chip*, 2010, **10**, 1604–1610.
- 20 C. Ohm, M. Brehmer and R. Zentel, *Adv. Mater.*, 2010, **22**, 3366–3387.
- 21 Y. Klein, E. Efrati and E. Sharon, *Science*, 2007, **315**, 1116–1120.
- 22 F. Zhou, P. M. Biesheuvel, E. Y. Chou, W. Shu, R. Poetes, U. Steiner and W. T. S. Huck, *Nano Lett.*, 2008, **8**, 725–730.
- 23 M. Behl, M. Y. Razzaq and A. Lendlein, *Adv. Mater.*, 2010, **22**, 3388–3410.
- 24 C. Py, P. Reverdy, L. Doppler, J. Bico, B. Roman and C. N. Baroud, *Phys. Rev. Lett.*, 2007, **98**, 156103.
- 25 B. Simpson, G. Nunnery, R. Tannenbaum and K. Kalaitzidou, *J. Mater. Chem.*, 2010, **20**, 3496–3501.
- 26 V. Luchnikov, O. Sydorenko and M. Stamm, *Adv. Mater.*, 2005, **17**, 1177–1182.
- 27 J. J. Guan, H. Y. He, L. J. Lee and D. J. Hansford, *Small*, 2007, **3**, 412–418.
- 28 G. Stoychev, N. Pureskiy and L. Ionov, *Soft Matter*, 2011, **7**, 3277–3279.
- 29 K.-U. Jeong, J.-H. Jang, D.-Y. Kim, C. Nah, J. H. Lee, M.-H. Lee, H.-J. Sun, C.-L. Wang, S. Z. D. Cheng and E. L. Thomas, *J. Mater. Chem.*, 2011, **21**, 6824–6830.
- 30 T. S. Kelby, M. Wang and W. T. S. Huck, *Adv. Funct. Mater.*, 2011, **21**, 652–657.
- 31 A. Azam, K. Laflin, M. Jamal, R. Fernandes and D. Gracias, *Biomed. Microdevices*, 2010, 1–8.
- 32 K. Kalaitzidou and A. J. Crosby, *Appl. Phys. Lett.*, 2008, **93**, 041910.
- 33 S. Zakharchenko, N. Pureskiy, G. Stoychev, M. Stamm and L. Ionov, *Soft Matter*, 2010, **6**, 2633–2636.
- 34 H. Y. He, J. J. Guan and J. L. Lee, *J. Controlled Release*, 2006, **110**, 339–346.
- 35 J. J. Guan, H. Y. He, D. J. Hansford and L. J. Lee, *J. Phys. Chem. B*, 2005, **109**, 23134–23137.
- 36 N. Bassik, B. T. Abebe, K. E. Laflin and D. H. Gracias, *Polymer*, 2010, **51**, 6093–6098.
- 37 K. Kumar, B. Nandan, V. Luchnikov, F. Simon, A. Vyalikh, U. Scheler and M. Stamm, *Chem. Mater.*, 2009, **21**, 4282–4287.
- 38 K. Kumar, V. Luchnikov, B. Nandan, V. Senkovskyy and M. Stamm, *Eur. Polym. J.*, 2008, **44**, 4115–4121.
- 39 T. G. Leong, B. R. Benson, E. K. Call and D. H. Gracias, *Small*, 2008, **4**, 1605–1609.
- 40 T. G. Leong, C. L. Randall, B. R. Benson, A. M. Zarafshar and D. H. Gracias, *Lab Chip*, 2008, **8**, 1621–1624.
- 41 T. G. Leong, C. L. Randall, B. R. Benson, N. Bassik, G. M. Stern and D. H. Gracias, *Proc. Natl. Acad. Sci. U. S. A.*, 2009, **106**, 703–708.
- 42 A. W. Feinberg, A. Feigel, S. S. Shevkoplyas, S. Sheehy, G. M. Whitesides and K. K. Parker, *Science*, 2007, **317**, 1366–1370.
- 43 N. Bassik, A. Brafman, A. M. Zarafshar, M. Jamal, D. Luvsanjav, F. M. Selaru and D. H. Gracias, *J. Am. Chem. Soc.*, 2010, **132**, 16314–16317.
- 44 J. S. Randhawa, T. G. Leong, N. Bassik, B. R. Benson, M. T. Jochmans and D. H. Gracias, *J. Am. Chem. Soc.*, 2008, **130**, 17238–17239.

Ionov, L.

Actively-moving materials based on stimuli-responsive polymers

***Journal of Materials Chemistry*** 2010, 20, 3382.

# Actively-moving materials based on stimuli-responsive polymers†

Leonid Ionov\*

Received 2nd November 2009, Accepted 4th January 2010

First published as an Advance Article on the web 11th February 2010

DOI: 10.1039/b922718k

This review addresses recent developments in actively moving materials based on stimuli-responsive polymers on the scale from single molecules to polymer networks. The examples of application of stimuli-responsive polymers for design of actuators, sensors, active elements in microfluidic devices, materials with switchable optical properties as well as biomaterials are discussed. Emphasis is given to biohybrid materials consisting of synthetic and living components as well as stimuli-responsive materials inspired by nature.

## 1. Introduction

Active motion is intrinsic to living organisms on different levels of organization from individual animals or their groups down to a single molecule. Indeed, cells are equipped with various molecular machines, which allow their migration, division, sensing and adaptation.<sup>1</sup> For example, kinesin and dynein motor proteins transport vesicles inside cells and play important role in cell division, in intracellular transport of organelles as well as in cellular motility.<sup>2</sup> DNA and RNA motors replicate polynucleotides and repair them with high degree of reliability.<sup>3</sup> Myosin motor proteins perform steps along actin filaments causing muscular contraction and, thus, provide motion on the macroscopic scale.<sup>4</sup> Receptor protein molecules change their conformation (and chemical properties) in response to binding of molecules or ions and thereby provide cells mechanisms of sensing.<sup>5</sup> Animals use active motion on the microscale for defensive purposes as well. For example, movement of pigments and high-refractive index protein assemblies in cells is used by animals to adapt their coloration.<sup>6,7</sup> In fact, millions of years of evolution have forced animals to optimise these and other approaches for active-motion with respect to efficiency,

specificity and robustness. Therefore, learning lessons from nature and mimicking the behaviour of natural actively moving systems on different levels of sophistication is a challenging task for development of new generations of materials for biomedical applications, design of micromechanical systems, sensing *etc.*

Only recently, synthetic and natural stimuli-responsive polymers were introduced to address these challenging tasks. Stimuli-responsive polymers are polymers demonstrating considerable changes in properties in response to small variations of environmental conditions (see recent reviews<sup>8–12</sup>). To date a variety of polymers sensitive to environmental as well as to biochemical stimuli (light, pH, temperature, electric and magnetic field, chemicals)<sup>13</sup> have been developed, investigated and tested.<sup>14–21</sup> In many cases, stimuli induce formation of new covalent and non-covalent bonds often accompanied by changes in conformation of the polymer chains. These switching properties of the stimuli-responsive polymer chains allows one to consider them as elementary machines (actuators), that convert environmental signals into a mechanical response. The idea of this review is to present and discuss recent trends in the development of stimuli-responsive polymers for the design of actively moving materials on a scale from single polymer chains up to three-dimensional polymer networks. Emphasis is given to biohybrid materials consisting of synthetic and living components as well as materials inspired by nature.

Leibniz Institute of Polymer Research Dresden, Germany. E-mail: ionov@ipfdd.de; Fax: +493514658281; Tel: +493514658272

† This paper is part of a *Journal of Materials Chemistry* themed issue on Actively Moving Polymers. Guest editor: Andreas Lendlein.



Leonid Ionov

Leonid Ionov is a group leader at the Leibniz Institute of Polymer Research Dresden (Germany). He received his PhD in Polymer Chemistry in 2005 from Dresden University of Technology (Germany) and performed his Postdoc in the group of Stefan Diez (Max Planck Institute of Molecular Cell Biology and Genetics). His research is focused on stimuli-responsive and self-assembling materials.

## 2. Single polymer chains

Elementary polymer-based actively moving elements can consist of a singular polymer chain. In fact, a single polymer chain can reversibly switch its conformation upon change of environmental conditions and can, therefore, work as the simplest actuator. This principle was, for example, explored by Welch *et al.* He designed an electroresponsive molecular actuator based on a diblock-copolymer of a positively charged dendrimer and a negatively charged linear chain. Brownian dynamics simulations demonstrated the hybrid polyampholyte's ability to generate a force when an electric field is applied.<sup>22</sup>

A prototype molecular motor that has a "simple" internal structure was recently proposed by Potemkin *et al.*<sup>23</sup> Here, a single diblock-copolymer chain comprising "simple" monomer units is able to perform directed reptational motion being

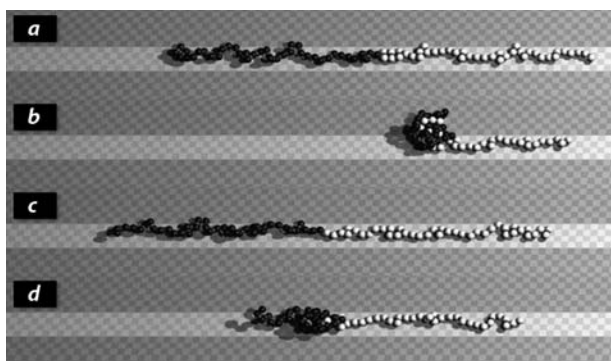


**Fig. 1** Schematic of reptation of block-copolymer chain on a striped surface upon cyclical change of conformation. Dark grey areas of the surface are “forbidden” for adsorption of the monomer units so the reptation can occur only along the bright grey stripe. Block A (black) is subjected to the periodical action of the external field that results in periodical collapse–readorption cycles. The block B (white) is always adsorbed. The location of the chain is shown at various moments of time:  $t_a < t_b < t_c < t_d$ . Reprinted with permission from ref. 23, Copyright Wiley-VCH Verlag GmbH & Co. KGaA.

adsorbed on a structured solid surface. One of the blocks of the copolymer is expected to be field responsive. Interactions between units of the block changed from repulsion to strong attraction, while between units of another block, only repulsion forces acted. The authors predict that the time-periodic collapse–readorption of the responsive block leads to the directed motion (reptation) of the chain along the “track” provided by the surface pattern. The rate and direction of this movement are controlled by energy parameters (the energy of adsorption as well as the attraction and repulsion of units), frequency of collapse–readorption effects, and composition of copolymer. From the physical viewpoint, such directional motion is possible if the following three conditions are satisfied: (i) the system receives external stimulus and energy that can be dissipated, (ii) the adsorbed molecule has anisotropic properties *e.g.* an anisotropic molecular friction, and (iii) the surface provides adhesion and direction of the motion (“track”). The authors analysed the case when external forces act only on one of the blocks leading to its periodical collapse readorption (Fig. 1). This situation can physically be realized if, for example, one of the blocks contains photosensitive groups whose interactions can be controlled by light. Another possibility to induce collapse and readorption comprises an exposure of the molecule to different vapours.

### 3. Surface-grafted polymer films (brushes)

Surface-immobilized stimuli-responsive polymer layers are another kind of actively-moving materials.<sup>24,25</sup> Fixation of a polymer chain by one end allows design of stimuli-responsive surfaces that can be used as sensors, nanotransport tools as well as systems with switchable catalytic and enzymatic activity.

#### 3.1 Surfaces with switchable topographies

Switching of the conformation of surface-grafted polymer chains often results in change of height (thickness) and/or topography of a polymer layer. The height changes of polyelectrolytes brushes in response to the presence of ions of different size and

valence were recently actively explored by Huck and colleagues.<sup>26</sup> Binding of counter ions to polymer chains changes the swelling and the hydrophilic/hydrophobic properties of the polymer layer. The reversible changes in height of synthetic<sup>27,28</sup> and natural<sup>29</sup> polymer layers grafted inside narrow pores were also used for the design of microfluidic systems with environmentally controllable fluid flow.<sup>30–32</sup> Moreover, reversible changes of the height of a polymer layer can be used for design of environmental sensors.<sup>33–35</sup>

Micro- and nanopatterned as well as gradient grafted polymer layers demonstrate both switching of the thickness and topography. Nano- and micropatterned one-component polymer brushes can be prepared by photolithography,<sup>36,37</sup> scanning probe lithography,<sup>32,38</sup> electron beam lithography,<sup>39–41</sup> micro-contact printing.<sup>42</sup> Alternatively, nanopatterned stimuli-responsive brushes can be prepared on biological objects as templates.<sup>43,44</sup> Nanoconfinement can strongly influence the properties of grafted polymer layers. First, nanopatterned polymer brushes undergo reversible swelling in both lateral and vertical directions.<sup>45</sup> Moreover, Huck *et al.* have demonstrated that nanopatterned thermoresponsive poly(2-(2-methoxyethoxy)-ethyl methacrylate) brushes reveal a considerable broadening of the collapse transition and an increase of the degree of vertical swelling.<sup>46</sup> Grafting of two<sup>47–49</sup> or more<sup>50</sup> types of polymer chains in a laterally-resolved manner allows more complicated response. For example, patterned brushes of two oppositely charged polyelectrolytes provide reversible switching of wettability, charge and topography in an inverse manner.<sup>51</sup>

Recently, surface-structured stimuli-responsive polymer brushes have been used for design of patterned surfaces with the patterns whose size can be changed in response to a variation of the environmental conditions, rather than local treatment.<sup>52</sup> The approach is based on structured surface-immobilization of thermoresponsive poly(*N*-isopropylacrylamide) (PNIPAM) copolymers with different transition temperatures. In aqueous environment, PNIPAM (homopolymer) reversibly changes its solubility at the low critical solution temperature (LCST = 33 °C). However, the LCST can be gradually increased or decreased by incorporation of additional hydrophobic or hydrophilic comonomers, respectively. Likewise, the LCST can be tuned by varying the ratio of both added comonomer types. Using this principle, a surface containing lateral LCST gradients was fabricated by laying down opposing gradients of hydrophilic and hydrophobic poly(*N*-isopropylacrylamide) copolymers. Across this surface, polymers with LCST above or below the actual temperature of the surrounding solvent were collapsed or swollen, respectively.

#### 3.2 Control of nanoparticles motion by topography switching

Several research groups explored reversible swelling of surface-grafted polymer chains in response to change of environmental conditions as a means to control vertical and lateral motion of micro- and nanoparticles. For example, homopolymer<sup>33–35,53</sup> and diblock-copolymer<sup>54</sup> brushes were used to move adsorbed metal or semiconductor nanoparticles in the vertical direction by switching the conformation of polymer chains. Here, the advantage of diblock-copolymer brushes is the possibility to freeze the vertical position of nanoparticles by drying.

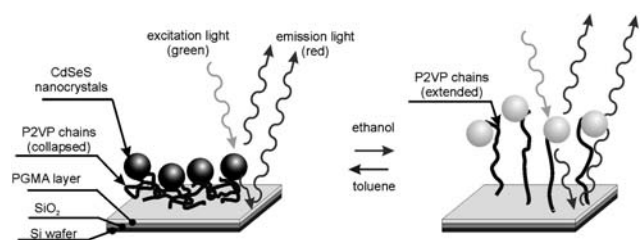


**Fig. 2** Schematic of a polymeric sensor based on a surface-grafted polymer layer with fluorescent nanocrystals. Hydrophobic nanocrystals are adsorbed on a stimuli-responsive polymer layer grafted onto a reflecting substrate. The light emitted by nanocrystals can undergo either constructive or destructive interference depending on their distance to the substrate. The nanocrystal–surface distance depends on the conformation of the polymer chains and changes in different solvents. The change in height is therefore reported by a variation in the detected fluorescence intensity. Reprinted with permission of ref. 35, Copyright Wiley-VCH Verlag GmbH & Co. KGaA.

Depending on the interactions of the solvent with the polymer block where nanoparticles are linked to, the nanoparticles can be either positioned on the surface or can be hidden in the vicinity of a substrate. In many cases, the change of conformation of polymer chains causes changes of the interactions between the attached particles including plasmonic effect, fluorescence quenching or light interference, that can be used for design of environmental<sup>33–35,53,55,56</sup> and biochemical<sup>57</sup> sensors. One possibility consists in incorporation of fluorescent nanocrystals into polymer layers grafted onto reflecting surfaces (Fig. 2). Switching of the conformation of polymer chains results in change of the distance between the nanocrystals and the substrates. As a result, the character of interference between the light that is directly emitted by a nanoparticle and the light that is reflected by the mirror surface changes. Consequently, the intensity of the detected fluorescence light depends on the conformation of grafted polymer chains. The main advantages of this approach are extreme instrumental simplicity, high spatial precision of the measurements, and fast signal response.

Santer *et al.* extended the concept of particle movement by polymer brushes and used them for lateral movement of

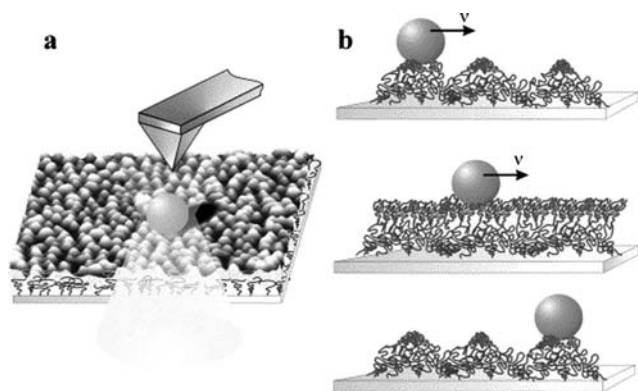


**Fig. 3** (a) Scheme of a transport of colloidal particles by block-copolymer brush. (b) During topography switching accompanied by changes in the interfacial energy, the ‘arms’ of the brush grasp the nano cargo and move it along a surface. Reprinted with permission of ref. 58, copyright 2004 Elsevier.

adsorbed nanoobjects (Fig. 3).<sup>58,59</sup> The essential idea is that different topographical and chemical configurations of the polymer brushes together with drastic changes in surface energy and potential landscape during a phase transition can cause the polymer chains to grasp or release a nano-object successively, moving it across a surface (Fig. 3). In the absence of a directional driving force the movement of particles is random and non-directional. To direct the motion, R  he recently developed an approach based on nanoscale gradient brushes.<sup>60</sup>

### 3.3 Switchable surfaces from one-component grafted polymer layers

Switching of the conformation of surface grafted polymer chains is one approach for design of surfaces with switchable properties. Along this line, Zhulina *et al.* explored the phase diagram of a single-component surface-grafted polymer layer at different grafting densities and interactions with solvent.<sup>61</sup> They predicted switching between morphologies of pinned micelles and a swollen brush layer by varying the solvent quality. In good solvent conditions polymer chains are swollen and completely screen the substrate. On the other hand, in poor solvent conditions polymer chains try to avoid unfavourable contacts with solvent and form compact micelles leaving the substrate partially accessible to the environment. Thereby, the grafted polymer chains can either completely or partially cover the substrate that can be used for design of switchable surfaces.<sup>62</sup>

### 3.4 Switchable surfaces from multicomponent polymer layers

Another possibility for design of switchable surfaces based on reversible motion of surface grafted polymer chains consists in incorporation of active elements (nanoparticles or proteins) in the polymer layer. Switching of the conformation of polymer chains results in switching of the accessibility of these active elements. Thereby, active elements are accessible or inaccessible when polymer chains are collapsed or swollen, respectively. Minko *et al.* have used this principle for design of composite surfaces with adaptive adhesion prepared by grafting of poly-(ethylene glycol) (PEG) chains between fluorinated particles;<sup>63,64</sup> PEG and fluorinated particles are non-sticky in aqueous and dry environments, respectively. It was shown experimentally that PEG chains are collapsed on air and are hidden under fluorinated particles which results in non-adhesive properties of the composite surface in the dry state. On the other hand, in an aqueous environment non-sticky PEG chains swell and screen sticky particles, which also results in non-adhesive properties in an aqueous environment.

Another possibility to use the conformational changes of polymer chains is to design systems with switchable catalytic and enzymatic activity. Typically, active species (enzymes or catalysts) are incorporated in the polymer layer. Switching of the conformation of polymer chains results in switching of the accessibility of these active species and, as a result, leads to a change of their apparent activity. Following this concept, Ballauff *et al.* incorporated silver nanoparticles in to a thermoresponsive polymer brush grafted onto spherical microparticles.<sup>65</sup> By changing the conformation of the polymer chains, they



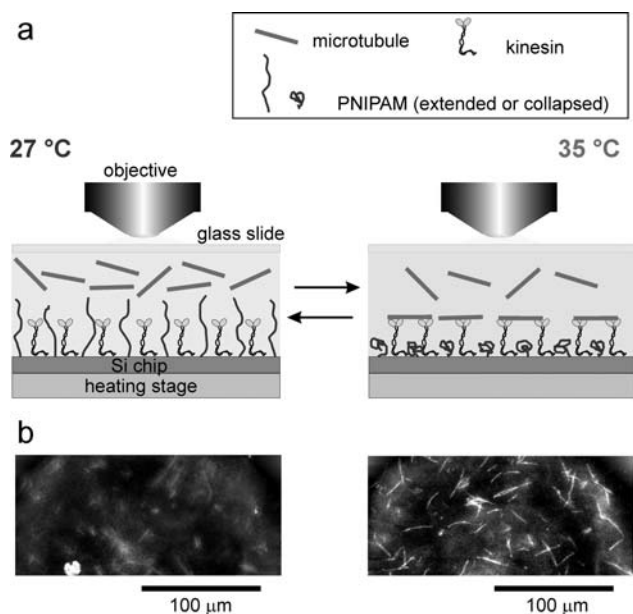


**Fig. 4** Switching of gliding motility of microtubules on a thermoresponsive poly(*N*-isopropylacrylamide) (PNIPAM) surface with adsorbed kinesin motor protein. (a) Schematics of the experimental setup. Repeated changes in temperature resulted in the reversible switching of PNIPAM chains between the extended conformation (where microtubules are repelled from the surface and cannot bind to the kinesin heads) and the collapsed conformation (where microtubules can glide unhindered on the kinesin molecules). (b) Fluorescence micrographs of rhodamine-labeled microtubules on a substrate surface with grafted PNIPAM chains and adsorbed kinesin. No gliding of microtubules is observed at 27 °C (left image) while the microtubules glide at 35 °C (right image). Reprinted with permission of ref. 66, copyright 2006 American Chemical Society.

controlled the accessibility of the nanoparticles and in this way were able to reversibly switch their catalytic activity.

Ionov<sup>66</sup> *et al.* have used similar approach to control biomolecular transport by temperature. The approach is based on the fabrication of a composite surface where functional kinesin motor-molecules are adsorbed onto a substrate between surface-grafted polymer chains of thermoresponsive poly(*N*-isopropylacrylamide). It was demonstrated that motor-driven microtubules undergo reversible landing, gliding and release in response to conformational changes of the polymer chains (Fig. 4). Moreover, it was demonstrated that such systems can be used for dynamic sorting of protein assemblies *in vitro*.<sup>66,67</sup>

### 3.5 Switchable surfaces from mixed homopolymer and block-copolymer brushes

Grafting of two or more types of polymer chains allows design of an interesting class of responsive materials—mixed homopolymer or block-copolymer brushes.<sup>68</sup> Mixed polymer brushes consist of two or more sorts of polymers randomly grafted to a substrate. The mechanism of responsiveness of the mixed brushes is different from homopolymer brushes. Polymer chains of different sorts try to avoid unfavourable contacts and undergo lateral vs. vertical nanoscale separation, the character of which depends on the incompatibility of the polymers and the

interaction with surrounding media (solvent). Depending on interaction of polymer chains with the surrounding solvent, these brushes can be switched between the states when polymer chains of one or the other kind are swollen and dominate at the topmost polymer layer.<sup>69</sup> By selection of appropriate solvent one can achieve a whole spectrum of intermediate states. Mixed and block copolymer brushes have been recently used for design of surfaces with switchable wettability,<sup>70–72</sup> adhesion,<sup>73</sup> control of protein adsorption,<sup>74</sup> and were applied for design of active elements in microfluidic devices.<sup>37,75</sup>

Mixed polyelectrolyte (PEL) brushes represent a particularly interesting case of mixed polymer brushes. Mixed PEL brushes consist of two oppositely charged polyelectrolytes.<sup>76–79</sup> Being responsive to pH and salt concentration, thin polymer films from mixed PEL brushes are of high interest for the regulation of protein adsorption,<sup>74</sup> surface wetting,<sup>71,75,76</sup> stability of pH-responsive colloids,<sup>80,81</sup> for the development of “smart” coatings,<sup>51</sup> microfluidic devices,<sup>75</sup> enzyme-controlled Pickering emulsions,<sup>82</sup> *etc.* Block-copolymer<sup>83,84</sup> or random copolymer polyampholyte brushes<sup>85,86</sup> where electrostatic interactions play an important role in the phase behaviour of the tethered polyampholyte chains, behave similarly to mixed PEL brushes.

Recently, Minko’s group introduced a novel approach to create an electrochemical gating system of mixed PEL brushes grafted to an electrode surface and explored the switchable properties of these mixed polymer brushes by change of pH. The morphological transitions in mixed polymer brushes associated with the electrode surface resulted in the opening, closing, or precise tuning of their permeability for ion transport through the channels formed in the nanostructured thin film in response to an external stimulus (pH change). In comparison to a homopolymer brush system, the mixed brush demonstrates much broader variation of ion transport through the thin film.<sup>27</sup>

### 3.6 Actuator based on cantilevers with grafted polymer layers

Design of sensors based on the responsive properties of surface-grafted polymer chains is a very important and promising research direction. Typically, the swelling or collapse of polymer layers is detected by measuring the thickness or the optical properties of incorporated nanoparticles.

Another very promising approach for design of actuators and sensors relies on one-side modification of AFM cantilevers with stimuli-responsive polymer brushes.<sup>87</sup> Swelling of polymer chains and steric repulsion between them causes cantilever bending, which is detected by deflection of a laser beam. In fact, the use of cantilevers allows amplification of the small signal produced by swelling of polymer chains, which means that the cantilever-brush-based actuators can act as highly sensitive probes. Using this approach, cantilevers modified with polymer brushes are used for design of pH,<sup>88,89</sup> solvent,<sup>90</sup> or salt<sup>91</sup> sensors.

## 4. Polymer networks, hydrogels and films

Hydrogels refer to the three-dimensional polymer networks imbibed with aqueous solutions. There are many reports describing design of hydrogels sensitive to light, pH, temperature, biochemical processes, electric and magnetic fields.<sup>92–94</sup> Exposure to one or multiple stimuli causes reversible

contraction/swelling of hydrogels. The reversible changes in size and shape of hydrogels have found broad applications for design of micromechanical and drug delivery systems, as well as for microfluidic devices and sensors (see recent reviews<sup>95,96</sup>).

#### 4.1 Actuators

Applying external signal changes the properties of stimuli-responsive hydrogels while removal of stimuli returns hydrogels to the initial state. The repeated changes of stimuli are therefore needed to achieve cyclical changes in hydrogel size. To achieve this goal, one has to apply the stimuli in a cyclical manner. Alternatively, a very intriguing approach based on use of Belousov–Zhabotinsky (BZ) reaction<sup>97</sup> has been suggested to control swelling and collapse of hydrogels in a spatio-temporal manner. The BZ reaction is well known as a non-equilibrium dissipative reaction and generates autonomous oscillations in the redox potential. For example, Yoshida fabricated gels exhibiting autonomous peristaltic motion without external stimuli, which were prepared by copolymerizing temperature-responsive *N*-isopropylacrylamide, with ruthenium tris(2,2′-bipyridine) ( $\text{Ru}(\text{bpy})_3$ ) as the catalyst for the Belousov–Zhabotinsky (BZ) reaction, and used it for directed particle transport (Fig. 5).<sup>98</sup> BZ reaction results in local swelling of the hydrogel that changes over time. As result, a moving wave of swollen hydrogel is formed. The wave provides peristaltic motion of the adsorbed microparticles. In another approach, Maeda fabricated a self-oscillating gel actuator without external stimuli by producing a gradient structure, which generates a pendulum motion by fixing one edge of the gel.<sup>99</sup>

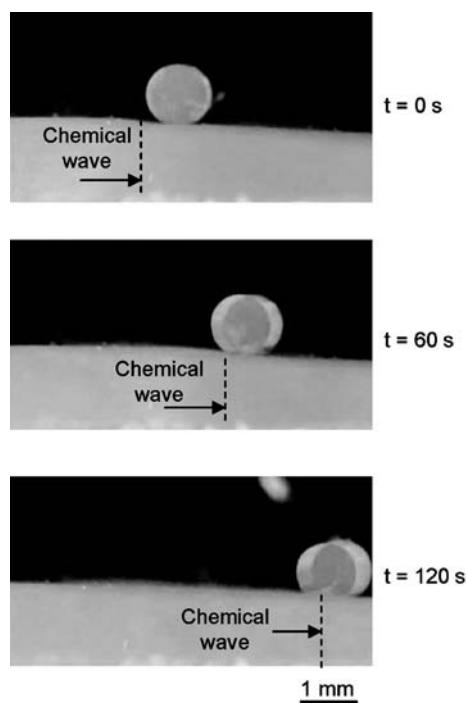


**Fig. 5** Use of Belousov–Zhabotinsky reaction in a redox-sensitive gel for transportation of particles. The particle is transported along the chemical wave due to spatially resolved swelling and collapse of hydrogel. Reprinted with permission of ref. 98, copyright 2009 American Chemical Society.

Similarly to surface-grafted polymer layers, the reversible swelling/deswelling of hydrogels can be used for design of sensors and active elements in microfluidic devices. For example, smart polymer-based micromechanical devices can be designed with reversible swelling/deswelling stimuli-responsive polyelectrolyte membranes.<sup>100,101</sup> More complex systems consist of thermoresponsive hydrogel films with a gradient of composition<sup>102</sup> or two-layered structures.<sup>103</sup> These composite films possess an inherent bending character for which the bending direction and curvature do not depend on the direction of an external stimulus, *e.g.*, an electric field, but on the nanostructure and design of the gels. Similarly, stimuli-induced deformation of crosslinked two-layered polymer networks was used by Luchnikov *et al.* for fabrication of self rolling polymeric microtubes with a patterned inner surface.<sup>104</sup> He fabricated patterned polystyrene–poly(2-vinylpyridine) bilayers. These bilayers rolled and formed a tube in acidic environment because of the selective swelling of poly(2-vinyl pyridine).

Aizenber and Sidorenko recently described a very fascinating approach for design of hydrogel-based actuators. They fabricated a thin hydrogel films with incorporated high-aspect ratio rods. Collapse or swelling of the thin hydrogel layer caused change of orientation of the rods<sup>105,106</sup> These hydrogel films were, in particular, used for design of surfaces with “conventional” and “reverse” switching behaviour. These surfaces revealed conventional switching—hydrophilic after exposure to water and hydrophobic after drying if the rods are fixed on the surfaces. They could achieve reverse switching—hydrophobic after exposure to water and hydrophilic after drying—by using hydrogel films with non-fixed rods. Swelling or collapse of the polymer layer changed orientation of the nanorods and thus changed the wetting behaviour. Due to the contraction of the polymer film upon drying, nanocolumns redirect the tensile forces from the gel into a lateral actuation that results in a tilt of the partially exposed nanostructures. The tilt angle is controlled by the volume change of the gel and can be therefore regulated by the appropriate choice of the polymer. Re-hydration of the sample leads to swelling and relaxation of the hydrogel. This results in normal orientation of the bristles (Fig. 6).<sup>107</sup>

In fact, reversible swelling/deswelling of hydrogels is reminiscent to contraction/relaxation of muscles. Lee *et al.* have used this property of hydrogels and fabricated pH-sensitive hydrogel actuators mimicking the shape and motion of octopus and sperm.<sup>108</sup> Such aquabots are able to produce directional motion in response to change of electrochemical potential and can be potentially used for biomedical applications to sense and destroy certain microorganisms.

#### 4.2 Sensors

There are several approaches to design sensors based on hydrogels. One approach is based on direct detection of the changes of hydrogel volume or mass. This, for example, can be done by ellipsometry, quartz microbalance (for hydrogel thin films) or scattering techniques (for hydrogel particles).<sup>109</sup> A second approach consists in immobilization of a hydrogel to a AFM cantilever.<sup>110</sup> Swelling of hydrogel deforms the cantilever similarly to polymer brushes (see above). Another approach for design of hydrogel-based sensors is incorporation of

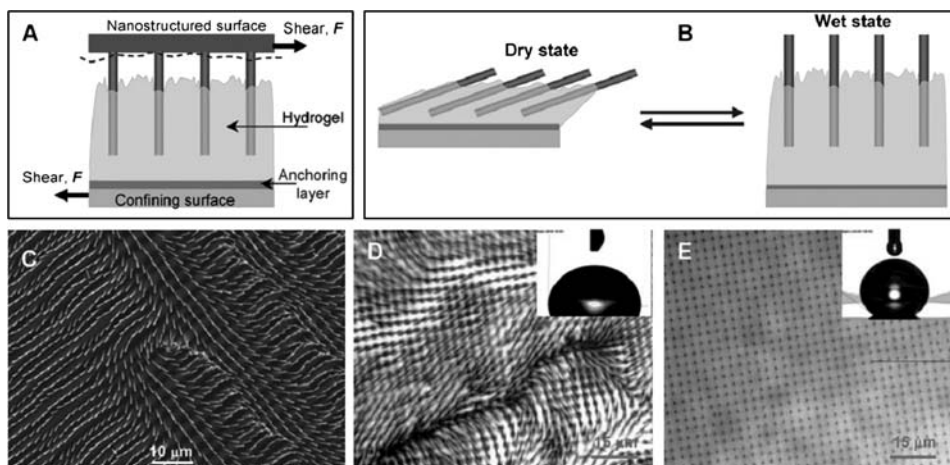


**Fig. 6** Gel-embedded array of rigid setae (GEARS) designed to provide a reverse response to exposure to water. (A) Schematic of the setae transfer into the hydrogel layer attached to the confining solid surface modified with the PGMA anchoring layer upon *in situ* synthesis. (B) Schematic illustration of the dynamic rearrangement of the GEARS in the dry and wet states. (C) Representative SEM image of the GEARS bristle in the dry state. (D) Optical microscopy analysis of the dry GEARS surface reveals highly tilted setae. The surface is relatively hydrophilic (D, inset). (E) Optical microscopy analysis of the same region as in (D) in a humid atmosphere reveals setae standing perpendicular to the surface and its hydrophobic character (E, inset). Reprinted with permission of ref. 107, copyright 2008 Royal Society of Chemistry.

semiconductor or metal nanoparticles into the hydrogel matrix. In this case, particles serve as optically active probes. Contraction/swelling of hydrogels switches interactions between nanoparticles that results in change of optical properties.<sup>111–115</sup>

#### 4.3 Microfluidic devices

One of the first reports describing the use of stimuli-responsive hydrogels as active elements in microfluidic devices was reported by Beebe *et al.*<sup>116</sup> They used pH sensitive hydrogels. Later on, the approach was extended to temperature-, enzyme-, light- and electric field-responsive polymers.<sup>117,118</sup> For lab-on-a-chip applications, the use of light and electric field as stimuli hold promise since they allow switching with both high spatial and temporal resolution. For example, Richter and co-workers explored possibilities to control liquid flow by stimuli-responsive hydrogels. In particular, they used hydrogels as pumps and gates which control liquid flow in microfluidic devices.<sup>119,120</sup> They fabricated electrically controlled arrays of heating elements to locally heat thermoresponsive hydrogels and in this way designed a display, which can be used for blind reading. Recently, Minko *et al.* have developed an approach for fabrication of porous hydrogel membranes and used them for biochemically controlled gating of liquid flow.<sup>121–123</sup>

#### 4.4 Switchable optical devices

Switching of macroscopic geometrical parameters of hydrogels was recently explored for design of materials with switchable optical properties. Lyon *et al.* suggested to use switchable hydrogel particles as lenses with tunable focal length.<sup>124</sup> Potentially, the hydrogel particles can be assembled in hexagonally packed arrays and are used for fabrication of miniaturized elements of different size.<sup>125</sup> Jiang *et al.* have used hydrogel actuators integrated into a microfluidic system serving as a container for a liquid droplet. The hydrogel reacts to stimuli by adjustment of the shape—and hence focal length—of the

droplet.<sup>126</sup> Another approach for design of switchable lenses was explored by Crosby *et al.* This work presented a simple, robust, biomimetic responsive surface based on an array of microlens shells that snap from one curvature (*e.g.*, concave) to another curvature (*e.g.*, convex) when a critical stress develops in the shell structure.<sup>127</sup>

Photonic crystals with switchable optical properties are another type of smart optical devices, which can be designed using stimuli-responsive polymers. An assembly of switchable hydrogel particles with incorporated high-refractive index particles in opal-like periodic structures or a hydrogel matrix filled with close-packed high refractive index particles are two possible ways for designing devices with switchable optical properties.<sup>128–131</sup> In both approaches, reversible swelling/deswelling of polymer results in changes of periodicity of lattice that causes switching of optical properties. Here mechanical treatment,<sup>132</sup> temperature,<sup>129</sup> light, magnetic<sup>133</sup> and electric<sup>134</sup> fields are stimuli to switching optical properties. Similar to hydrogel-particle composites, stimuli-induced swelling of block copolymers was used for design of opal-like photonic crystals with switchable optical properties.<sup>135</sup> Notably, this mechanism of switching of periodicity of high-refractive index protein assemblies is used by squids to tune their coloration.<sup>6</sup>

Recently, Akashi *et al.* have explored another bioinspired approach for design of materials with tunable coloration. The authors designed bioinspired light-modulation material that imitates the behaviour of pigment cells of squids and octopuses based on hydrogels with included pigments.<sup>136</sup> The mechanism of light modulation is due to reversible volume change of dense coloured gel particles, *i.e.* light modulation is caused by a synergistic effect between the change of the area of light absorption and the absorption of colorant in gels.

#### 4.5 Biomaterials

Stimuli-responsive hydrogels are a topic of intensive investigation directed towards design of novel biomedical materials.

A very broadly investigated approach for design of drug delivery systems is based on controlled release of drugs from temperature and light responsive hydrogels. Being initially saturated with a drug, hydrogel particles are injected in a living organism. The elevated temperature in the inflamed tissue or localized illumination with light causes contraction of hydrogel particles and release of drug molecules. On the other hand, it is known that behaviour of cells (differentiation, growth, apoptosis) depends on geometrical constraints. To address this problem, Pelah has developed an approach to reversibly deform cell shape using a thermoresponsive polymeric actuator.<sup>137</sup>

Whitesides designed biohybrid materials from engineered tissue and synthetic polymer thin film. The construct was built by culturing neonatal rat ventricular cardiomyocytes on PDMS film micropatterned with ECM to promote spatially ordered, two-dimensional myogenesis. The centimetre-scale constructs performed diverse gripping, pumping, walking and swimming with good spatial and temporal control and were able to generate forces as high as 4 mN mm<sup>-2</sup>.<sup>138</sup>

## 5. Other actively moving materials

Besides single-molecule actuators, grafted polymer layers and hydrogels, which are used for design of actively moving materials, liquid crystals and shape-memory polymers deserve particular interest. For example, a very promising approach for controlled bending of polymer free-standing films was introduced by Ikeda *et al.* They showed that a single film of a liquid-crystal network containing an azobenzene chromophore can be repeatedly and precisely bent along any chosen direction by using linearly polarized light.<sup>139</sup> This striking photomechanical effect results from a photoselective volume contraction and may be useful in the development of high-speed actuators for microscale or nanoscale applications, for example in microrobots in medicine or optical microw tweezers.

Shape-memory polymers are another example of actively moving polymer-based materials. Shape memory results from a combination of polymer morphology and specific processing conditions and can be understood in terms of polymer functionalization rather than as an intrinsic property of the polymer chains. By conventional processing the polymer is formed into its initial, permanent shape. Afterwards, in a process called programming, a polymer sample is deformed and fixed in the temporary shape. Upon application of an external stimulus (light<sup>140–142</sup> or temperature<sup>143–145</sup>), the polymer recovers its initial permanent shape. Thus, conventional shape-memory polymers have a dual-shape capability and consist of at least one phase which can form physical crosslinks. Recently, Lendlein and co-workers introduced triple-shape memory polymers.<sup>146</sup> Triple-shape memory polymers can move from a first shape to a second shape and from there to a third shape, where both shape changes are induced by temperature increases. This triple-shape capability is obtained for multiphase polymer networks after application of a complex stepwise thermomechanical programming process. Shape memory polymers have been successfully used for design of switchable photonic structures,<sup>147</sup> self-healing materials,<sup>148</sup> fibers<sup>149</sup> and bioinspired switchable adhesives.<sup>150</sup>

## 6. Summary and outlook

This review presents recent trends in the development of stimuli-responsive polymers for design of actively moving materials. In most approaches polymers sensitive to environmental signal (pH, temperature, light) influenced were used. On the other hand, there are a growing number of publications reporting design of systems sensitive to biochemical stimuli (mostly enzymes). Both environmentally and biochemically sensitive systems have been developed for design of actuators, sensors, active elements in microfluidic devices, as smart optical elements, as well as biomaterials.

Recently a new class of responsive materials based on surface structured (Janus) colloidal particles has been reported.<sup>12,80,151</sup> Janus particles were already introduced to be highly efficient as catalytic systems, as drug-carriers, as building blocks of self-assembling materials, as optical and rheological probes, as well as functional elements for design of electronic paper devices. Furthermore, one expects that the controlled rotational movement of Janus particles can be, for example, used for electronic paper devices, smart surfaces with switchable wettability and adhesion.

In fact, recent trends in the development of polymers sensitive to biochemical and biophysical process in cells can lead to the appearance of a next generation of smart actively moving materials. Along this line, Whitesides, for example, designed biohybrid materials from an engineered tissue and a synthetic polymer thin film.<sup>138</sup> Such materials can be considered as first steps towards the design of synthetic biomaterials, which are programmed directly for specific processes in a human body. In future one can think about a thin film of synthetic materials, which are deposited on skin and change its adhesion or friction by signals from the human body.

## Acknowledgements

The author is grateful to VW Foundation (Grant 03N8712) and DFG (Grant IO 68/1-1) for financial support. Manfred Stamm, Alla Synytska, Georgi Stoychev, Nikolay Puretskiy and Svetlana Zakharchenko are acknowledged for fruitful comments on manuscript.

## References

- 1 A. L. Barabási and Z. N. Oltvai, *Nat. Rev. Genet.*, 2004, **5**, 101–115.
- 2 P. Schwillle and S. Diez, *Crit. Rev. Biochem. Mol. Biol.*, 2009, **44**, 223–242.
- 3 J. Bath and A. J. Turberfield, *Nat. Nanotechnol.*, 2007, **2**, 275–284.
- 4 F. Tama and C. L. Brooks, *Annu. Rev. Biophys. Biomol. Struct.*, 2006, **35**, 115–133.
- 5 A. N. Lin and Z. G. Liu, *Cell Res.*, 2008, **18**, 327–327.
- 6 W. J. Crookes, L. L. Ding, Q. L. Huang, J. R. Kimbell, J. Horwitz and M. J. McFall-Ngai, *Science*, 2004, **303**, 235–238.
- 7 R. Vaia and J. Baur, *Science*, 2008, **319**, 420–421.
- 8 C. D. H. Alarcón, S. Pennadam and C. Alexander, *Chem. Soc. Rev.*, 2005, **34**, 276–285.
- 9 A. Kumar, A. Srivastava, I. Y. Galaev and B. Mattiasson, *Prog. Polym. Sci.*, 2007, **32**, 1205–1237.
- 10 S. Dai, P. Ravi and K. C. Tam, *Soft Matter*, 2009, **5**, 2513–2533.
- 11 J. F. Mano, *Adv. Eng. Mater.*, 2008, **10**, 515–527.
- 12 A. Sun and J. Lahann, *Soft Matter*, 2009, **5**, 1555–1561.
- 13 R. J. Mart, R. D. Osborne, M. M. Stevens and R. V. Ulijn, *Soft Matter*, 2006, **2**, 822–835.

- 14 M. A. Cole, N. H. Voelcker, H. Thissen and H. J. Griesser, *Biomaterials*, 2009, **30**, 1827–1850.
- 15 A. L. Hook, N. H. Voelcker and H. Thissen, *Acta Biomater.*, 2009, **5**, 2350–2370.
- 16 J. Zhou, T. K. Tam, M. Pita, M. Ornatska, S. Minko and E. Katz, *ACS Appl. Mater. Interfaces*, 2009, **1**, 144–149.
- 17 I. Tokarev, V. Gopishetty, J. Zhou, M. Pita, M. Motornov, E. Katz and S. Minko, *ACS Appl. Mater. Interfaces*, 2009, **1**, 532–536.
- 18 P. D. Thornton, R. J. Mart, S. J. Webb and R. V. Ulijn, *Soft Matter*, 2008, **4**, 821–827.
- 19 T. O. McDonald, H. L. Qu, B. R. Saunders and R. V. Ulijn, *Soft Matter*, 2009, **5**, 1728–1734.
- 20 T. K. Tam, J. Zhou, M. Pita, M. Ornatska, S. Minko and E. Katz, *J. Am. Chem. Soc.*, 2008, **130**, 10888.
- 21 L. Ionov and S. Diez, *J. Am. Chem. Soc.*, 2009, **131**, 13315–13319.
- 22 P. M. Welch, *Nano Lett.*, 2005, **5**, 1279–1283.
- 23 O. E. Perelstein, V. A. Ivanov, Y. S. Velichko, P. G. Khalatur, A. R. Khokhlov and I. I. Potemkin, *Macromol. Rapid Commun.*, 2007, **28**, 977–980.
- 24 I. Luzinov, S. Minko and V. V. Tsukruk, *Soft Matter*, 2008, **4**, 714–725.
- 25 I. Luzinov, S. Minko and V. V. Tsukruk, *Prog. Polym. Sci.*, 2004, **29**, 635–698.
- 26 O. Azzaroni, A. A. Brown and W. T. S. Huck, *Adv. Mater.*, 2007, **19**, 151–154.
- 27 M. Motornov, R. Sheparovych, E. Katz and S. Minko, *ACS Nano*, 2008, **2**, 41–52.
- 28 B. Yameen, M. Ali, R. Neumann, W. Ensinger, W. Knoll and O. Azzaroni, *Nano Lett.*, 2009, **9**, 2788–2793.
- 29 F. Xia, W. Guo, Y. D. Mao, X. Hou, J. M. Xue, H. W. Xia, L. Wang, Y. L. Song, H. Ji, O. Y. Qi, Y. G. Wang and L. Jiang, *J. Am. Chem. Soc.*, 2008, **130**, 8345–8350.
- 30 H. J. Zhang and Y. Ito, *Langmuir*, 2001, **17**, 8336–8340.
- 31 Y. Ito, Y. S. Park and Y. Imanishi, *Langmuir*, 2000, **16**, 5376–5381.
- 32 M. Kaholek, W. K. Lee, B. LaMattina, K. C. Caster and S. Zauscher, *Nano Lett.*, 2004, **4**, 373–376.
- 33 I. Tokareva, S. Minko, J. H. Fendler and E. Hutter, *J. Am. Chem. Soc.*, 2004, **126**, 15950–15951.
- 34 S. Westenhoff and N. A. Kotov, *J. Am. Chem. Soc.*, 2002, **124**, 2448–2449.
- 35 L. Ionov, S. Sapra, A. Synytska, A. L. Rogach, M. Stamm and S. Diez, *Adv. Mater.*, 2006, **18**, 1453.
- 36 R. Dong, S. Krishnan, B. A. Baird, M. Lindau and C. K. Ober, *Biomacromolecules*, 2007, **8**, 3082–3092.
- 37 L. Ionov, S. Minko, M. Stamm, J. F. Gohy, R. Jerome and A. Scholl, *J. Am. Chem. Soc.*, 2003, **125**, 8302–8306.
- 38 Q. He, A. Kuller, M. Grunze and J. B. Li, *Langmuir*, 2007, **23**, 3981–3987.
- 39 M. Steenackers, A. Kueller, N. Ballav, M. Zharnikov, M. Grunze and R. Jordan, *Small*, 2007, **3**, 1764–1773.
- 40 U. Schmelter, A. Paul, A. Kuller, M. Steenackers, A. Ulman, M. Grunze, A. Golzhauser and R. Jordan, *Small*, 2007, **3**, 459–465.
- 41 M. Kaholek, W.-K. Lee, J. Feng, B. LaMattina, D. J. Dyer and S. Zauscher, *Chem. Mater.*, 2006, **18**, 3660–3664.
- 42 R. R. Shah, D. Merceyes, M. Husemann, I. Rees, N. L. Abbott, C. J. Hawker and J. L. Hedrick, *Macromolecules*, 2000, **33**, 597–605.
- 43 L. Ionov, V. Bocharova and S. Diez, *Soft Matter*, 2009, **5**, 67–71.
- 44 J. Couet and M. Biesalski, *Macromolecules*, 2006, **39**, 7258–7268.
- 45 M. Patra and P. Linse, *Nano Lett.*, 2006, **6**, 133–137.
- 46 A. M. Jonas, Z. J. Hu, K. Glinel and W. T. S. Huck, *Nano Lett.*, 2008, **8**, 3819–3824.
- 47 Y. Liu, V. Klep and I. Luzinov, *J. Am. Chem. Soc.*, 2006, **128**, 8106–8107.
- 48 M. Husemann, M. Morrison, D. Benoit, J. Frommer, C. M. Mate, W. D. Hinsberg, J. L. Hedrick and C. J. Hawker, *J. Am. Chem. Soc.*, 2000, **122**, 1844.
- 49 R. Konradi and J. Ruhe, *Langmuir*, 2006, **22**, 8571–8575.
- 50 F. Zhou, Z. J. Zheng, B. Yu, W. M. Liu and W. T. S. Huck, *J. Am. Chem. Soc.*, 2006, **128**, 16253–16258.
- 51 A. Synytska, M. Stamm, S. Diez and L. Ionov, *Langmuir*, 2007, **23**, 5205–5209.
- 52 L. Ionov, A. Synytska and S. Diez, *Adv. Funct. Mater.*, 2008, **18**, 1501–1508.
- 53 O. Tagit, N. Tomczak, E. M. Benetti, Y. Cesa, C. Blum, V. Subramaniam, J. L. Herek and G. J. Vancso, *Nanotechnology*, 2009, **20**, 185501.
- 54 K. Yu, H. F. Wang and Y. C. Han, *Langmuir*, 2007, **23**, 8957–8964.
- 55 T. Kang, S. Hong, I. Choi, J. J. Sung, Y. Kim, J. S. Hahn and J. Yi, *J. Am. Chem. Soc.*, 2006, **128**, 12870–12878.
- 56 M. Mitsuishi, Y. Koishikawa, H. Tanaka, E. Sato, T. Mikayama, J. Matsui and T. Miyashita, *Langmuir*, 2007, **23**, 7472–7474.
- 57 I. Tokareva, I. Tokarev, S. Minko, E. Hutter and J. H. Fendler, *Chem. Commun.*, 2006, 3343–3345.
- 58 S. Santer and J. Ruhe, *Polymer*, 2004, **45**, 8279–8297.
- 59 S. Santer, A. Kopyshv, J. Donges, H. K. Yang and J. Ruhe, *Adv. Mater.*, 2006, **18**, 2359.
- 60 C. Schuh, S. Santer, O. Prucker and J. Ruhe, *Adv. Mater.*, 2009, **21**, 4706–4710.
- 61 E. B. Zhulina, T. M. Birshtein, V. A. Priamitsyn and L. I. Klushin, *Macromolecules*, 1995, **28**, 8612.
- 62 L. Ionov, B. Zdyrko, A. Sidorenko, S. Minko, V. Klep, I. Luzinov and M. Stamm, *Macromol. Rapid Commun.*, 2004, **25**, 360–365.
- 63 R. Sheparovych, M. Motornov and S. Minko, *Adv. Mater.*, 2009, **21**, 1840.
- 64 R. Sheparovych, M. Motornov and S. Minko, *Langmuir*, 2008, **24**, 13828–13832.
- 65 Y. Lu, Y. Mei, M. Drechsler and M. Ballauff, *Angew. Chem., Int. Ed.*, 2006, **45**, 813–816.
- 66 L. Ionov, M. Stamm and S. Diez, *Nano Lett.*, 2006, **6**, 1982–1987.
- 67 L. Ionov, M. Stamm and S. Diez, *Nano Lett.*, 2005, **5**, 1910–1914.
- 68 S. Minko, *Polym. Rev.*, 2006, **46**, 397–420.
- 69 A. Sidorenko, S. Minko, K. Schenk-Meuser, H. Duschner and M. Stamm, *Langmuir*, 1999, **15**, 8349–8355.
- 70 S. Minko, M. Muller, M. Motornov, M. Nitschke, K. Grundke and M. Stamm, *J. Am. Chem. Soc.*, 2003, **125**, 3896–3900.
- 71 L. Ionov, N. Houbenov, A. Sidorenko, M. Stamm, I. Luzinov and S. Minko, *Langmuir*, 2004, **20**, 9916–9919.
- 72 L. Ionov, A. Sidorenko, M. Stamm, S. Minko, B. Zdyrko, V. Klep and I. Luzinov, *Macromolecules*, 2004, **37**, 7421–7423.
- 73 H. Retsos, G. Gorodyska, A. Kiriy, M. Stamm and C. Creton, *Langmuir*, 2005, **21**, 7722–7725.
- 74 L. Ionov, N. Houbenov, A. Sidorenko, M. Stamm and S. Minko, *Biointerphases*, 2009, **4**, FA45–FA49.
- 75 L. Ionov, N. Houbenov, A. Sidorenko, M. Stamm and S. Minko, *Adv. Funct. Mater.*, 2006, **16**, 1153–1160.
- 76 N. Houbenov, S. Minko and M. Stamm, *Macromolecules*, 2003, **36**, 5897–5901.
- 77 K. Roodenko, Y. Mikhaylova, L. Ionov, M. Gensch, M. Stamm, S. Minko, U. Schade, K. J. Eichhorn, N. Esser and K. Hinrichs, *Appl. Phys. Lett.*, 2008, **92**, 103102.
- 78 Y. Mikhaylova, L. Ionov, J. Rappich, M. Gensch, N. Esser, S. Minko, K. J. Eichhorn, M. Stamm and K. Hinrichs, *Anal. Chem.*, 2007, **79**, 7676–7682.
- 79 K. Hinrichs, D. Aulich, L. Ionov, N. Esser, K. J. Eichhorn, M. Motornov, M. Stamm and S. Minko, *Langmuir*, 2009, **25**, 10987–10991.
- 80 S. Berger, A. Synytska, L. Ionov, K. J. Eichhorn and M. Stamm, *Macromolecules*, 2008, **41**, 9669–9676.
- 81 M. Motornov, R. Sheparovych, R. Lupitsky, E. MacWilliams, O. Hoy, I. Luzinov and S. Minko, *Adv. Funct. Mater.*, 2007, **17**, 2307–2314.
- 82 M. Motornov, J. Zhou, M. Pita, I. Tokarev, V. Gopishetty, E. Katz and S. Minko, *Small*, 2009, **5**, 817–820.
- 83 N. Ayres, C. D. Cyrus and W. J. Brittain, *Langmuir*, 2007, **23**, 3744–3749.
- 84 A. Akinchina and P. Linse, *Langmuir*, 2007, **23**, 1465–1472.
- 85 S. Sanjuan and Y. Tran, *Macromolecules*, 2008, **41**, 8721–8728.
- 86 N. Cheng, A. A. Brown, O. Azzaroni and W. T. S. Huck, *Macromolecules*, 2008, **41**, 6317–6321.
- 87 S. Singamaneni, M. C. LeMieux, H. P. Lang, C. Gerber, Y. Lam, S. Zauscher, P. G. Datskos, N. V. Lavrik, H. Jiang, R. R. Naik, T. J. Bunning and V. V. Tsukruk, *Adv. Mater.*, 2008, **20**, 653–680.
- 88 F. Zhou, P. M. Biesheuvel, E. Y. Chol, W. Shu, R. Poetes, U. Steiner and W. T. S. Huck, *Nano Lett.*, 2008, **8**, 725–730.
- 89 F. Zhou, W. M. Shu, M. E. Welland and W. T. S. Huck, *J. Am. Chem. Soc.*, 2006, **128**, 5326–5327.
- 90 G. G. Bumbu, M. Wolkenhauer, G. Kircher, J. S. Gutmann and R. Berger, *Langmuir*, 2007, **23**, 2203–2207.



- 91 A. Valiaev, N. I. Abu-Lail, D. W. Lim, A. Chilkoti and S. Zauscher, *Langmuir*, 2007, **23**, 339–344.
- 92 S. Bhattacharya, F. Eckert, V. Boyko and A. Pich, *Small*, 2007, **3**, 650–657.
- 93 Z. Y. Meng, M. H. Smith and L. A. Lyon, *Colloid Polym. Sci.*, 2009, **287**, 277–285.
- 94 C. D. Jones and L. A. Lyon, *J. Am. Chem. Soc.*, 2003, **125**, 460–465.
- 95 S. K. Ahn, R. M. Kasi, S. C. Kim, N. Sharma and Y. X. Zhou, *Soft Matter*, 2008, **4**, 1151–1157.
- 96 I. Tokarev and S. Minko, *Soft Matter*, 2009, **5**, 511–524.
- 97 A. N. Zaikin and A. M. Zhabotinsky, *Nature*, 1970, **225**, 535.
- 98 Y. Murase, S. Maeda, S. Hashimoto and R. Yoshida, *Langmuir*, 2009, **25**, 483–489.
- 99 S. Maeda, Y. Hara, R. Yoshida and S. Hashimoto, *Macromol. Rapid Commun.*, 2008, **29**, 401–405.
- 100 S. Haider, S. Y. Park and S. H. Lee, *Soft Matter*, 2008, **4**, 485–492.
- 101 T. F. Otero, *J. Mater. Chem.*, 2009, **19**, 681–689.
- 102 T. A. Asoh, M. Matsusaki, T. Kaneko and M. Akashi, *Adv. Mater.*, 2008, **20**, 2080.
- 103 P. D. Topham, J. R. Howse, C. J. Crook, S. P. Armes, R. A. L. Jones and A. J. Ryan, *Macromolecules*, 2007, **40**, 4393.
- 104 V. Luchnikov, O. Sydorenko and M. Stamm, *Adv. Mater.*, 2005, **17**, 1177.
- 105 B. Pokroy, A. K. Epstein, M. C. M. Persson-Gulda and J. Aizenberg, *Adv. Mater.*, 2009, **21**, 463.
- 106 A. Sidorenko, T. Krupenkin, A. Taylor, P. Fratzl and J. Aizenberg, *Science*, 2007, **315**, 487–490.
- 107 A. Sidorenko, T. Krupenkin and J. Aizenberg, *J. Mater. Chem.*, 2008, **18**, 3841–3846.
- 108 G. H. Kwon, J. Y. Park, J. Y. Kim, M. L. Frisk, D. J. Beebe and S. H. Lee, *Small*, 2008, **4**, 2148–2153.
- 109 A. Richter, G. Paschew, S. Klatt, J. Lienig, K. F. Arndt and H. J. P. Adler, *Sensors*, 2008, **8**, 561–581.
- 110 J. Z. Hilt, A. K. Gupta, R. Bashir and N. A. Peppas, *Biomed. Microdevices*, 2003, **5**, 177–184.
- 111 V. Kozlovskaya, E. Kharlampieva, B. P. Khanal, P. Manna, E. R. Zubarev and V. V. Tsukruk, *Chem. Mater.*, 2008, **20**, 7474–7485.
- 112 I. Tokarev, I. Tokareva and S. Minko, *Adv. Mater.*, 2008, **20**, 2730.
- 113 Y. J. Gong, M. Y. Gao, D. Y. Wang and H. Mohwald, *Chem. Mater.*, 2005, **17**, 2648–2653.
- 114 M. Kuang, D. Y. Wang and H. Mohwald, *Adv. Funct. Mater.*, 2005, **15**, 1611–1616.
- 115 J. Li, X. Hong, Y. Liu, D. Li, Y. W. Wang, J. H. Li, Y. B. Bai and T. J. Li, *Adv. Mater.*, 2005, **17**, 163.
- 116 D. J. Beebe, J. S. Moore, J. M. Bauer, Q. Yu, R. H. Liu, C. Devadoss and B. H. Jo, *Nature*, 2000, **404**, 588.
- 117 X. F. Zeng and H. R. Jiang, *Appl. Phys. Lett.*, 2008, **93**, 151101.
- 118 D. T. Eddington, R. H. Liu, J. S. Moore and D. J. Beebe, *Lab Chip*, 2001, **1**, 96–99.
- 119 A. Richter, D. Kuckling, S. Howitz, T. Gehring and K. F. Arndt, *J. Microelectromech. Syst.*, 2003, **12**, 748–753.
- 120 A. Richter, S. Klatt, G. Paschew and C. Klenke, *Lab Chip*, 2009, **9**, 613–618.
- 121 V. Gopishetty, Y. Roiter, I. Tokarev and S. Minko, *Adv. Mater.*, 2008, **20**, 4588–4593.
- 122 M. Pita, T. K. Tam, S. Minko and E. Katz, *ACS Appl. Mater. Interfaces*, 2009, **1**, 1166.
- 123 I. Tokarev, M. Orlov, E. Katz and S. Minko, *J. Phys. Chem. B*, 2007, **111**, 12141–12145.
- 124 J. Kim, M. J. Serpe and L. A. Lyon, *J. Am. Chem. Soc.*, 2004, **126**, 9512–9513.
- 125 H. Wu, T. W. Odom and G. M. Whitesides, *J. Am. Chem. Soc.*, 2002, **124**, 7288.
- 126 L. Dong, A. K. Agarwal, D. J. Beebe and H. Jiang, *Nature*, 2006, **442**, 551.
- 127 D. P. Holmes and A. J. Crosby, *Adv. Mater.*, 2007, **19**, 3589.
- 128 H. Fudouzi and Y. N. Xia, *Adv. Mater.*, 2003, **15**, 892.
- 129 K. Matsubara, M. Watanabe and Y. Takeoka, *Angew. Chem., Int. Ed.*, 2007, **46**, 1688–1692.
- 130 K. Ueno, K. Matsubara, M. Watanabe and Y. Takeoka, *Adv. Mater.*, 2007, **19**, 2807.
- 131 K. U. Jeong, J. H. Jang, C. Y. Koh, M. J. Graham, K. Y. Jin, S. J. Park, C. Nah, M. H. Lee, S. Z. D. Cheng and E. L. Thomas, *J. Mater. Chem.*, 2009, **19**, 1956–1959.
- 132 J. R. Lawrence, G. H. Shim, P. Jiang, M. G. Han, Y. R. Ying and S. H. Foulger, *Adv. Mater.*, 2005, **17**, 2344.
- 133 J. P. Ge, Y. X. Hu and Y. D. Yin, *Angew. Chem., Int. Ed.*, 2007, **46**, 7428–7431.
- 134 K. Ueno, J. Sakamoto, Y. Takeoka and M. Watanabe, *J. Mater. Chem.*, 2009, **19**, 4778–4783.
- 135 J. J. Walsh, Y. Kang, M. R. A. and T. E. L., *Adv. Mater.*, 2009, **21**, 3078–3081.
- 136 R. Akashi, H. Tsutsui and A. Komura, *Adv. Mater.*, 2002, **14**, 1808–1811.
- 137 A. Pelah, R. Seemann and T. M. Jovin, *J. Am. Chem. Soc.*, 2007, **129**, 468–469.
- 138 A. W. Feinberg, A. Feigel, S. S. Shevkoplyas, S. Sheehy, G. M. Whitesides and K. K. Parker, *Science*, 2007, **317**, 1366–1370.
- 139 Y. L. Yu, M. Nakano and T. Ikeda, *Nature*, 2003, **425**, 145–145.
- 140 K. C. Hribar, R. B. Metter, J. L. Ifkovits, T. Troxler and J. A. Burdick, *Small*, 2009, **5**, 1830–1834.
- 141 A. Lendlein, H. Y. Jiang, O. Junger and R. Langer, *Nature*, 2005, **434**, 879–882.
- 142 H. Y. Jiang, S. Kelch and A. Lendlein, *Adv. Mater.*, 2006, **18**, 1471–1475.
- 143 A. Lendlein and S. Kelch, *Angew. Chem., Int. Ed.*, 2002, **41**, 2034–2057.
- 144 A. Lendlein, J. r. Zotzmann, Y. Feng, A. Alteheld and S. Kelch, *Biomacromolecules*, 2009, **10**, 975–982.
- 145 P. Miaudet, A. Derre, M. Maugey, C. Zakri, P. M. Piccione, R. Inoubli and P. Poulin, *Science*, 2007, **318**, 1294–1296.
- 146 M. Behl, I. Bellin, S. Kelch, W. Wagermaier and A. Lendlein, *Adv. Funct. Mater.*, 2009, **19**, 102–108.
- 147 J.-H. Jang, C. Y. Koh, K. Bertoldi, M. C. Boyce and E. L. Thomas, *Nano Lett.*, 2009, **9**, 2113–2119.
- 148 E. L. Kirkby, J. D. Rule, V. L. Michaud, N. R. Sottos, S. R. White and J. A. E. Manson, *Adv. Funct. Mater.*, 2008, **18**, 2253–2260.
- 149 F. L. Ji, Y. Zhu, J. L. Hu, Y. Liu, L. Y. Yeung and G. D. Ye, *Smart Mater. Struct.*, 2006, **15**, 1547–1554.
- 150 S. Reddy, E. Arzt and A. del Campo, *Adv. Mater.*, 2007, **19**, 3833.
- 151 T. Isojima, M. Lattuada, J. B. Vander Sande and T. A. Hatton, *ACS Nano*, 2008, **2**, 1799.

Leonid Ionov, Cordula Reuther, Robert Tucker, Stefan Diez

Freely programmable patterning of protein bioactivity on surfaces using visible light –  
“green” photopatterning

*Submitted*

# **Programmable patterning of protein bioactivity on surfaces using visible light**

Cordula Reuther<sup>\*,+</sup>, Leonid Ionov<sup>\*,a</sup>, Stefan Diez<sup>\*,+</sup>

<sup>\*</sup> Max Planck Institute of Molecular Cell Biology and Genetics, Dresden, Germany

<sup>+</sup> B CUBE - Center for Molecular Bioengineering, Technische Universität Dresden, Dresden, Germany

<sup>a</sup> Current address: <sup>1</sup>Leibniz Institute of Polymer Research Dresden e.V., Dresden, Germany

EMAIL ADDRESS OF CORRESPONDING AUTHOR: [diez@bcube-dresden.de](mailto:diez@bcube-dresden.de)

## **Abstract**

We report on the spatially controlled patterning of multiple proteins with micro-scale precision using visible light. Based on localized light-to-heat conversion combined with a thermo-responsive polymer layer we demonstrate specific patterning of different proteins side by side without the need for specific linker molecules. Additionally, due to the temperature-dependent conformation of the polymer layer, protein accessibility could be switched dynamically in a global as well as local manner.

## Text body

Patterning functional proteins onto artificial substrates is of interest for the development of nanotechnology, tissue engineering, biosensors, and cell biology [1-13]. Towards this end, a number of chemical patterning methods based on optical lithography [14, 15], atomic force microscopy (AFM) [16, 17], printing techniques [18], chemical vapor deposition (CVD) [19, 20] have been applied recently. While each of these methods provides particular advantages, a general trade-off between spatial resolution, throughput and maximum pattern size exists. For example, AFM-based techniques can be used to place small numbers of functional proteins with nanometer lateral resolution, but are limited to low writing speeds and small pattern sizes. Optical methods, such as light-based activation of functional groups or ligands on surfaces [21], overcome these limitations as they often offer sufficient resolution combined with the potential for high through-put production. However, when based on conventional lithography, expensive metal masks are needed and only predefined patterns can be created. Moreover, the high-energy of the ultraviolet radiation ( $\lambda \sim 350$  nm) often needed to trigger the photoactivation of proteins or protein-binding molecules can be harmful for biological material [22]. Continuous illumination with light can also lead to the photogeneration of highly reactive radicals - causing undesirable effects including protein conformational changes and loss of biological function.

Here, we present an approach that allows the programmable patterning of proteins in-situ as well as the local activation of enzymes. Our method is based on using homogeneous wide-field illumination by visible light to locally heat the surface and switch the conformation of a thermo-responsive polymer coating. Specifically, layers of thermo-responsive poly(N-isopropylacrylamide) (PNIPAM) are applied to control the binding of functional proteins onto surfaces as well as their accessibility from solution [23-25]. We demonstrate that the specific patterning of multiple kinds of proteins side by side by sequential processing without the need for specific linker molecules or elaborate surface preparation. The advantage of this photothermal patterning approach is that, due to the use of visible light, it is inoffensive for proteins as well as versatile regarding the wavelength range. It thus simultaneously enables global and local switching of protein bioactivity.



A schematic of our experimental set-up is shown in Figure 1A. The sample consisted of a glass substrate coated with a ‘light-to-heat’ converting (LHC) layer. In order to enable efficient conversion of light into heat we decided on employing carbon. Carbon, in contrast to other light absorbing materials like silicon and gold, possesses low reflectance and high absorption values over the whole visible wavelength range. Carbon was therefore the most flexible coating material with respect to the wavelength used for the LHC process. For the patterning experiments, PNIPAM chains were grafted onto the carbon surface. In aqueous solution these polymer chains are dehydrated above the lower critical solution temperature (LCST; 32 °C) and assume a collapsed conformation. In this configuration proteins can be adsorbed in-between the polymer chains onto the surface. In contrast, below the LCST, the polymer chains are hydrated and assume an extended conformation. They then repel proteins from the surface and screen surface-bound proteins from solution. The coated sample was assembled into a flow-cell and mounted to a peltier element that enabled global temperature regulation. For local heating, the geometrical shapes of various diaphragms with different sizes were imaged onto the coated samples.

To successfully pattern or activate functional molecules on the sample surface it was important that the temperature in the illuminated area was higher than the LCST of PNIPAM but lower than the thermal denaturation temperature of the proteins. Therefore, we characterized the light-induced heating on the carbon layers experimentally. We employed a biomolecular transport system to measure the local temperature distribution on the surface *in-situ*. In particular, we performed *in vitro* gliding motility assays, in which microtubules were propelled over a surface covered with ATP-hydrolyzing kinesin-1 motor proteins, on a carbon-coated glass sample without PNIPAM. Because the enzymatic activity of kinesin-1 and thus the microtubule gliding velocity is temperature-dependent, the local temperature values could be determined using a velocity-temperature calibration curve [26]. The temperature of the peltier element was kept constant at 23.5 °C. In a cyclic order the surface was then locally illuminated by a 20 µm wide circular pattern for 2 s alternating with taking an fluorescence image of the microtubules within 100 ms exposure time. As the microtubules were labeled by Alexa 488 we applied a wavelength of 561 nm for local illumination to avoid photo-bleaching. The point-to-point velocities as well as the position of the microtubules gliding across the locally illuminated surface were obtained by microtubule tracking based on the open-source software FIESTA [27]. The local temperature values were determined according to the

velocity-temperature calibration curve from [26] and are plotted in Figure 1B as function of the distance between the microtubule center and the center of the illuminated circle. We found that the temperature rose in the illuminated area above 32 °C and reached values of up to 40 °C. The temperature dropped sharply to an average temperature of about 27 °C in the immediate vicinity, which was, though slightly higher than the peltier temperature, still well below the LCST of PNIPAM. Without illumination, the surface temperature set by the peltier element was verified by average microtubule speeds which corresponded to 23 °C. When increasing the laser intensity, microtubules moving into the illuminated areas detached from the surface. This effect was presumably caused by irreversible denaturation of the kinesin-1 motor proteins evidenced also the fact that no microtubule gliding was observed on these areas when the temperature was lowered later on. This implies that the generated temperatures were well above 40 °C. In contrast, control experiments on surfaces without carbon layers did not show any velocity increase (data not shown).

To further investigate the potential of the photothermal patterning technique with respect to resolution and scalability the temperature distribution was modeled using the Comsol™ software. Our simulations predict that the size of the “programmed” area, i.e. the area where the local temperature was above the LCST of PNIPAM, increases with the volumetric heat release (Fig. 1C), the width of the diaphragm opening (Fig. 1D), and the peltier temperature. The experimentally determined temperature distribution (Fig. 1B) was in good agreement with the simulated distribution for a 20 µm wide circular diaphragm and a volumetric heat release of  $3 \cdot 10^{13} \text{ W/m}^3$ . Interestingly, the experimental temperature drop in the immediate vicinity was even steeper than the simulated one. The observed impact of the width of the illuminated pattern on the induced heating (Fig. 1D) presumably results from an increased relative heat-dissipation at the rims of the smaller patterns and implies that the laser power needs to be adjusted for different pattern sizes. The dependence on the peltier temperature can be instrumental in generating steeper temperature profiles by applying a lower peltier temperature in conjunction with higher laser power. Moreover, our modeling showed that steady-state conditions of local heating and heat dissipations are reached within about 100 ms. As the conformational change of PNIPAM is fast [28], the illumination duration necessary for successful protein patterning can thus be determined by the time necessary for sufficient protein adsorption on the surface.

Figure 1

On the example of streptavidin molecules labeled with Alexa Fluor 488 we tested the ability of our experimental set-up to photothermally pattern proteins (Fig. 2). Specifically, patterning experiments were performed by incubating streptavidin solutions onto PNIPAM-layers grafted to carbon-glass samples. The samples were kept at low temperature, e.g. 21°C, so that the PNIPAM was swollen and therefore protein-repelling. For illuminating the surface a laser beam with  $\lambda = 561$  nm was applied to avoid bleaching of the fluorescently labeled molecules during patterning. For each pattern the surface was illuminated for 1 min in order to allow the streptavidin molecules to bind out of solution. Before imaging the resulting protein patterns, unbound protein was washed out. First, a sample was illuminated several times through a circular diaphragm (diameter = 12.8  $\mu\text{m}$ ) with varying laser power. Between each illumination step the stage was shifted. The fluorescence images in Fig. 2B show that the pattern size increased with increasing laser power. At a laser duty cycle below 30% the induced heating was not sufficient to switch the conformation of the PNIPAM chains, and thus no streptavidin molecules bound to the surface. For a laser duty cycle of about 40% the patterned circle had a diameter of about 12  $\mu\text{m}$ , corresponding to the projected size of the diaphragm opening. Moreover, the whole area of the circle showed relatively uniform fluorescence intensity. At higher laser duty cycles the pattern size increased but also showed decreasing fluorescence intensity in the center. The increasing temperature, especially in the center of the pattern, probably caused this intensity decrease due to damage of the proteins or the fluorescent dye. In a second experiment, circular streptavidin patterns were created using different sizes of the diaphragm opening (Fig. 2C). The laser duty cycle in each illumination step was adjusted so that the resulting patterns had about the size of the diaphragm opening. The smallest circles that we achieved in our configuration and applying a laser duty cycle of 100% had a diameter of about 5  $\mu\text{m}$ . Both experiments proved that proteins can be patterned reproducibly onto PNIPAM-coated carbon-glass samples via photothermal patterning. Moreover, the results comply qualitatively very well with the theoretical predictions.

Figure 2

The possibility of sequential patterning is important for specifically adsorbing different kinds of proteins side by side. In one experiment (Fig. 3A) we tested whether streptavidin molecules labeled with three different dyes (Alexa 405, 430 and 488) can be patterned consecutively next to each other. These dyes were chosen such that each of it was distinguishable using a distinct excitation wavelength / emission filter combination. For patterning the proteins the substrate surface was illuminated by laser light with  $\lambda = 561$  nm through a circular diaphragm ( $d = 12,8$   $\mu\text{m}$ ). In-between three sequential illumination steps the different protein solutions were exchanged and the microscope stage was shifted 20  $\mu\text{m}$  in y-direction. Afterwards images were taken using following excitation wavelengths and emission filters:  $\lambda_{\text{ex}} = 405$  nm and BP 450/50 for Alexa Fluor 405;  $\lambda_{\text{ex}} = 488$  nm and BP 535/30 for Alexa Fluor 488;  $\lambda_{\text{ex}} = 405$  nm and BP 535/30 for Alexa Fluor 430. The images as well as the color overlay of the three imaging configurations clearly show that each of the differently labeled protein molecules was patterned very specifically just in one of the formerly illuminated areas. Thus, the patterned proteins must have been protected against further protein binding by the swollen chains of the thermoresponsive polymer.

In another experiment two different kinds of proteins, namely fluorescent streptavidin and unlabeled kinesin-1 molecules, were patterned. Alexa Fluor 488 streptavidin was patterned by locally illuminating the sample twice through a rectangular diaphragm ( $a = 3.2$   $\mu\text{m}$  and  $b = 12.8$   $\mu\text{m}$ ). The stage was shifted by 10  $\mu\text{m}$  in Y-direction in-between the illumination steps. Afterwards unlabeled kinesin-1 molecules were patterned similarly with three illumination steps. For visualizing the successful patterning of kinesin-1 as well as the functionality of the molecules microtubules were allowed to interact with the pattern. For this, microtubule solution containing adenylyl-imidodiphosphate (AMPPNP), a non-hydrolysable analogue of ATP, was added to the flow-cell. The temperature of the sample was then raised to 35°C to globally collapse the PNIPAM chains on the entire surface and allow microtubules to bind to the patterned kinesin-1 molecules. The immobilized microtubules (red) (Fig. 3B) visualize the position of the kinesin-1 pattern in the formerly illuminated area and next to the streptavidin pattern (green). Upon adding ATP containing motility solution to the system bound microtubules were released from the pattern and new microtubules started to bind to as well as to glide across the patterned kinesin-1 molecules (Fig. 3C). These gliding microtubules demonstrated that photothermally adsorbed proteins kept their biological function and were not denatured.

### Figure 3

Besides globally activating kinesin-1 patterns we also tested to locally activate biomolecular transport on surfaces homogeneously covered with kinesin-1 molecules. Thus, a regular kinesin-1 gliding motility assay was performed at 35°C. After adjusting the temperature to 20°C microtubules were released from the surface, demonstrating the functionality of the PNIPAM. The surface was then illuminated continuously through a circular diaphragm ( $d = 20\text{ }\mu\text{m}$ ) with laser light ( $\lambda = 561\text{ nm}$ ; laser duty cycle: 30%) while keeping the backside of the substrate surface at 24°C by the means of a peltier element. Microtubules started to land and glide exclusively in the photo-thermally heated area within less than one minute of illumination (Fig. 4). The microtubules were gliding with an average speed of  $0.96\text{ }\mu\text{m/s}$ , but also showed point-to-point velocities of up to  $1.5\text{ }\mu\text{m/s}$ . These values correspond to temperatures of  $T = 32\text{ }^{\circ}\text{C}$  and  $T = 40.5\text{ }^{\circ}\text{C}$ , respectively. The activation was reversible and could be repeated. This experiment provided reasonable evidence that enzymes like kinesin-1 can be locally activated by light quite easily on homogeneously covered surfaces.

### Figure 4

In summary, we used visible light to locally collapse a thermo-responsive polymer on carbon-coated glass substrates by light to heat conversion. Thereby, patterns of functional proteins were formed in-situ. Importantly, in addition to uniform patterns with different geometries and sizes we were able to demonstrate specific patterning of multiple kinds of proteins on the same surface without the need for specific linker molecules or elaborate surface preparation by sequential illumination steps. Moreover, in our system patterns can be reversibly activated and deactivated in a local and global manner, respectively. We are convinced that applying higher laser powers can further reduce the minimal pattern size. We expect that this technique can find wide application as a method of simple and quick fabrication of programmable protein microarrays for bio- and nanotechnological applications in lab-on-chip systems.

Local motility activation also possible in channel structures? for specific binding, transport and release of microtubules, in combination with electrical heating



## Materials and Methods

The experiments were performed in 2-mm-wide flow cells self-built from a sample, a PEGylated coverslip [29] and two pieces of parafilm. The back of the sample was colored with black permanent marker to block the autofluorescence of the thermal contact. The sample was then mounted on a peltier element [30] with heat transfer compound for keeping it at defined temperature. The peltier was coupled to a power supply and a thermometer (Physitemp BAT-10).

**Motors and Microtubules.** Wild type kinesin-1 (full length *Drosophila melanogaster*) was expressed in *Escherichia coli* and purified applying a published protocol [31]. Microtubules were polymerized from 5  $\mu$ L of porcine brain tubulin [32] (4 mg/mL; labeled with different fluorophores as stated elsewhere) in BRB80 buffer (80 mM potassium PIPES, pH 6.9, 1 mM EGTA, 1 mM  $MgCl_2$ ) with 4 mM  $MgCl_2$ , 1 mM Mg-GTP and 5% DMSO at 37 °C. After 30 min, the microtubule polymers were stabilized and diluted 100-fold in room-temperature BRB80 containing 10  $\mu$ M taxol.

**Kinesin-1 gliding motility assay.** A casein-containing solution (0.5 mg/ml in BRB80) was perfused into the flow-cell and allowed to adsorb to the surface for 5 min. Then a 10  $\mu$ g/ml kinesin-1 solution in BRB80 buffer containing 1mM Mg-ATP and 0.2 mg/ml casein (BRB80CA) was perfused. After 5 – 10 min a microtubule containing solution (Motility solution: BRB80 with 10 mM taxol, microtubules (equivalent of 32 nM tubulin) 1 mM ATP, 40 mM D-glucose, 55  $\mu$ g/ml glucose oxidase, 11mg/ml catalase, 10 mM dithiothreitol (DTT)) was added to the cell and imaging was started.

**PNIPAM samples.** The method for grafting PNIPAM onto the carbon-coated glass surface (carbon-coating was performed by the Fraunhofer IWS (Dresden, Germany)) was adapted from Ionov et al. [33]. Briefly, carbon-coated substrates were spin-coated (2000rpm, 500rpm/s, 30 s) with a 0.01% polyglycidyl methacrylate (PGMA,  $M_n$  = 65000 g/mol) solution in chloroform. The PGMA was annealed at 130 °C for 20 min in a vacuum oven. After annealing the substrates were placed in hot chloroform (70 °C) in order to remove unbound PGMA. Poly(N-isopropylacrylamide) (PNIPAM,  $M_n$  = 45000 g/mol) was dissolved in

chloroform (1% solution). The surface of the substrates was then completely covered with a droplet of the PNIPAM solution. After the chloroform evaporated, the substrates were placed in the vacuum oven at 160 °C for 60 min to anneal the PNIPAM. Unbound PNIPAM was removed by washing the substrates in hot chloroform (70 °C).

**Patterning of proteins.** The PNIPAM sample was kept at low temperature (15-25°C) when the patterning solution (Streptavidin solution (0.125 mg/ml) containing a fluorescently labeled streptavidin conjugates (Alexa Fluor 405 or 430 or 488; Invitrogen) in BRB80 or Kinesin-1 solution (20 µg/ml) containing 0.5 mg/ml casein, 1mM Mg-ATP and 10 mM dithiothreitol (DTT) in BRB80) was perfused into the flow-cell. The sample was then locally illuminated with laser light ( $\lambda = 561$  nm;  $\lambda = 488$  nm for kinesin-1 patterning) through a 63x water immersion objective (Zeiss, numerical aperture NA=1.2) for 1 min using a DirectFRAP unit (Zeiss) with a diaphragm wheel. After patterning non-adsorbed protein was removed by multiple perfusions with BRB80CA. For sequential patterning of different proteins these steps were repeated. In the last step either antifade solution (BRB80 with 40 mM D-glucose, 55 µg/ml glucose oxidase, 11mg/ml catalase and 10 mM dithiothreitol (DTT)) or microtubule containing solution was added to the cell.

Thereby the diaphragm, located within the optical path of the used microscope, was illuminated by the visible light of an expanded laser beam. As a result, the desired pattern was illuminated with homogeneous intensity.

**Imaging.** Fluorescence images were obtained using a Zeiss Axio Observer inverted optical microscope with a 63x water immersion objective (NA = 1.2). For data acquisition, a spinning disc scan head (Yokogawa CSU-X1) with two cameras (Zeiss AxiCam MRm and Roper evolve 515 EMCCD) was used in conjunction with AxioVision software (Zeiss). Images were acquired with an exposure time of 100 ms.

**Acknowledgements:** The authors like to thank C. Bräuer for laboratory assistance / expression of kinesin-1. The work was financially supported by the Max-Planck-Society,

BMBF (grant ), VW (grant ), the European Research Council (NanoTrans, ERC starting grant 242933).

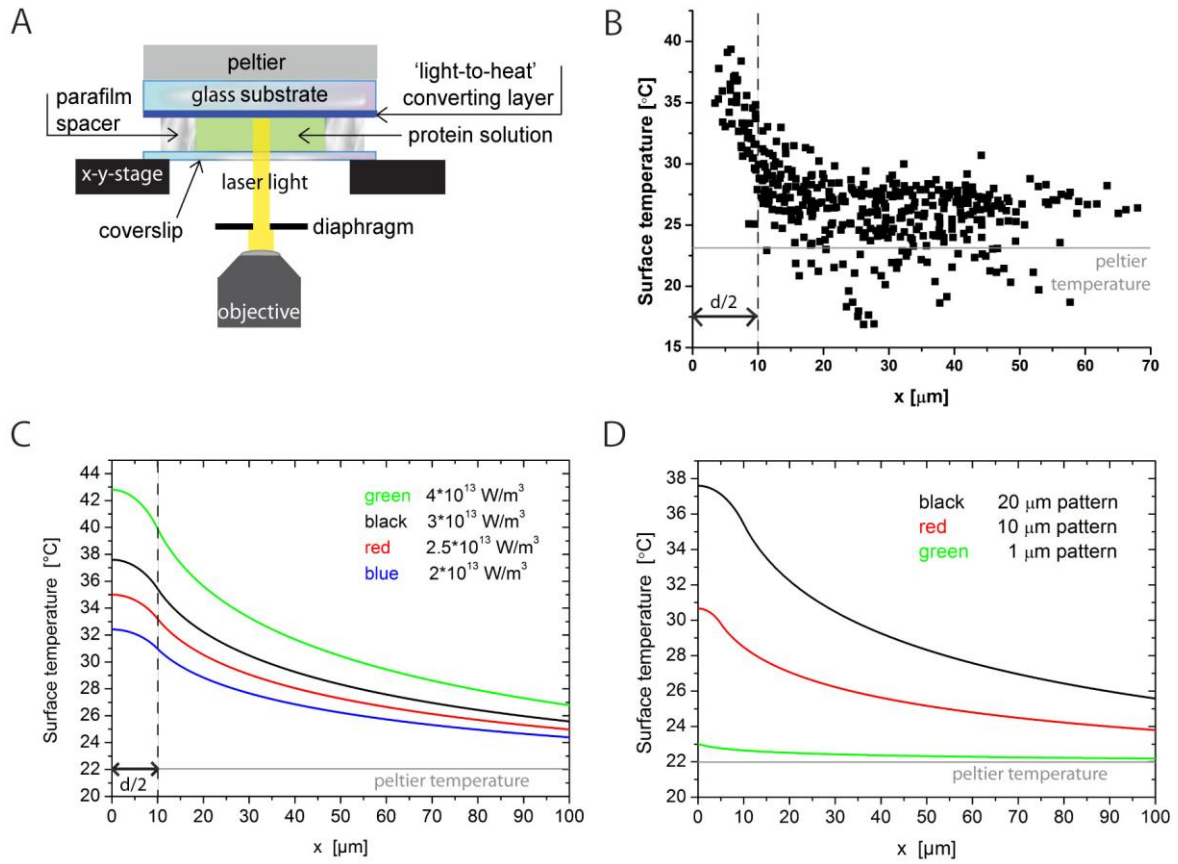


**Figure 1. Light-induced heating on carbon-coated glass surfaces.** (A) Experimental set-up for local heating with visible laser light. The glass substrate to be optically patterned is coated with a 'light-to-heat' converting carbon layer and is mounted to a peltier element for temperature regulation on the upper side of the flow-cell. (B) Experimentally determined temperature distribution on a surface heated through a circular pattern (diameter  $d = 20 \mu\text{m}$ ). The point-to-point velocities of microtubules gliding across the locally illuminated area were obtained by FIESTA [27]. Applying a temperature-velocity-calibration curve the corresponding temperature values were determined and plotted as function of the distance between the microtubule center and the center of the illuminated area (center of the illuminated area at  $x = 0$ ). (C) Simulated temperature profiles in dependence of the volumetric heat release rate of a 45 nm thick carbon layer upon absorption of light. The width of the simulated illumination pattern was  $20 \mu\text{m}$ . (D) Simulated temperature profiles in dependence of the width of the illuminated patterns. The volumetric heat release rate was kept constant at  $3 \times 10^{13} \text{ W/m}^3$ .

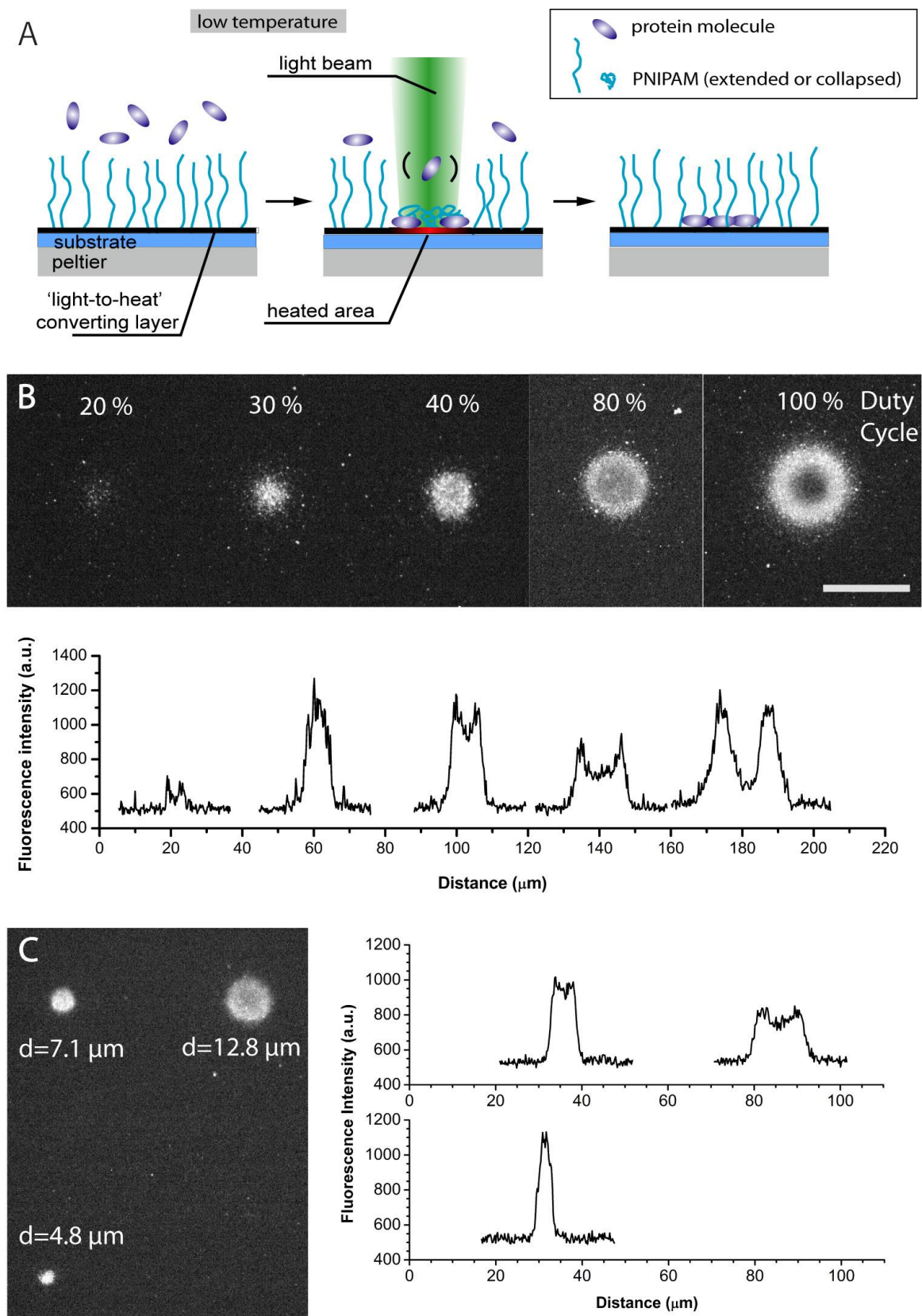


**Figure 2. Photothermal patterning of protein molecules.** (A) Schematic illustration of photothermal protein patterning. Localized heating upon illumination causes the collapse of



*the thermoresponsive polymer, resulting in adsorption of proteins in the illuminated areas. When the illumination is removed, the photopatterned proteins remain entrapped in the polymer layer, and the swollen polymer chains prevent further protein binding. (B) Fluorescence images of Alexa Fluor 488 streptavidin patterned sequentially with increasing laser duty cycle ( $\lambda = 561$  nm; maximal power output 3.6 mW) and a circular diaphragm ( $d = 12.8$   $\mu\text{m}$ ). The corresponding fluorescence intensity across the center of each circle is depicted below. (C) Fluorescence images (left) and fluorescence intensity (right) of Alexa Fluor 488 streptavidin patterned sequentially with different diaphragm sizes and size-adapted laser power ( $\lambda = 561$  nm). (Scale bar represents 20  $\mu\text{m}$ .)*

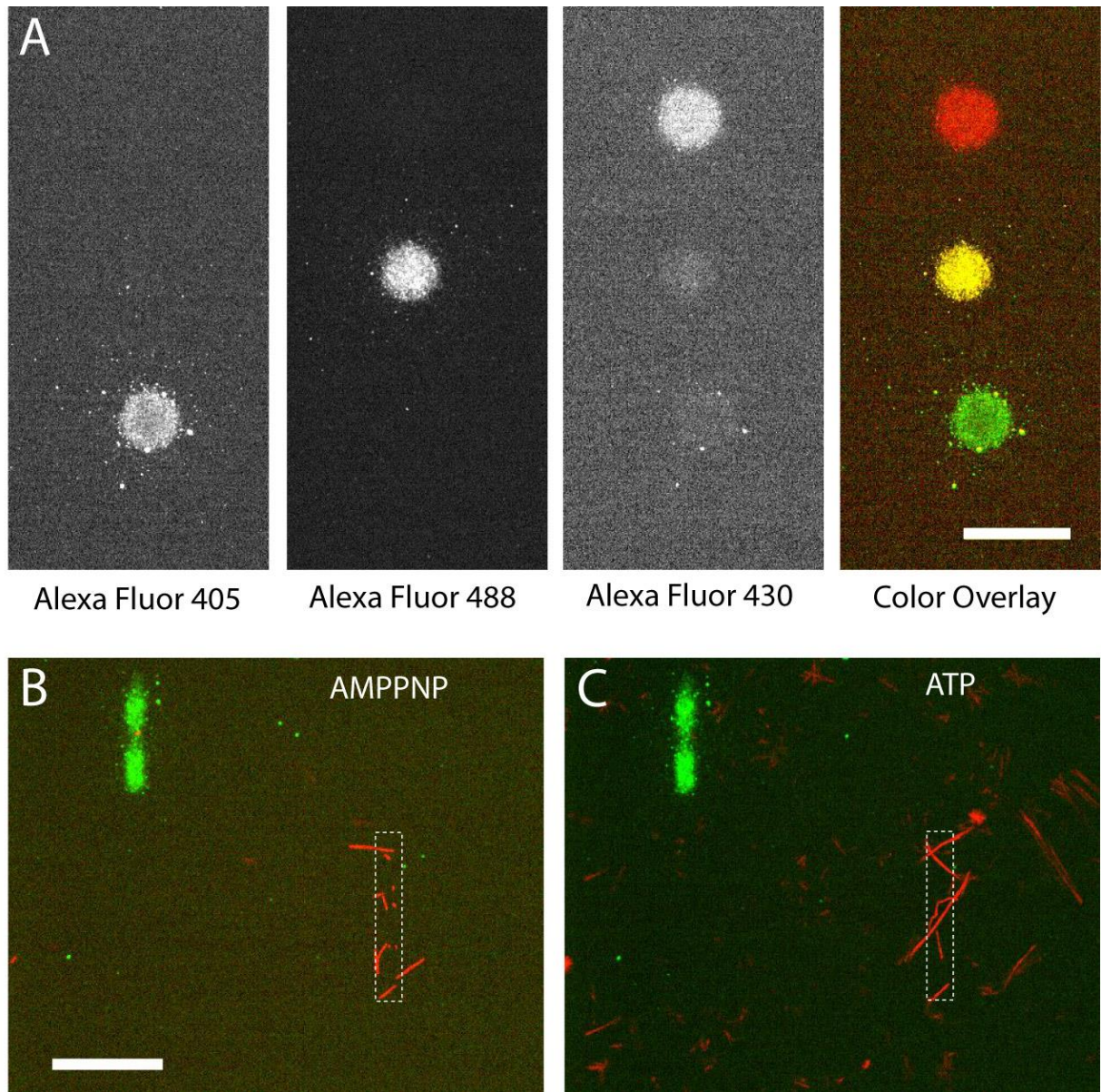


**Figure 3. Sequential patterning of different proteins.** (A) Streptavidin molecules labeled with three different dyes were consecutively patterned next to each other using laser light with  $\lambda = 561$  nm (circular diaphragm,  $d = 12.8$   $\mu\text{m}$ ). Fluorescence images were taken using following excitation wavelengths and emission filters:  $\lambda_{\text{ex}} = 405$  nm and BP 450/50 for Alexa Fluor 405;  $\lambda_{\text{ex}} = 488$  nm and BP 535/30 for Alexa Fluor 488;  $\lambda_{\text{ex}} = 405$  nm and BP 535/30 for Alexa Fluor 430. The right image is a color overlay of the three imaging configurations. (B) Color overlay of the fluorescence images of the patterned Alexa Fluor 488 streptavidin (green) and microtubules (red) immobilized on the kinesin-1 pattern via the non-hydrolysable ATP-analogue AMPPNP. Alexa Fluor 488 streptavidin was patterned by locally illuminating the sample twice through a rectangular diaphragm ( $a = 3.2$   $\mu\text{m}$  and  $b = 12.8$   $\mu\text{m}$ ). The stage was shifted by 10  $\mu\text{m}$  in Y-direction in-between the illumination steps. Afterwards unlabeled

*kinesin-1* molecules were patterned similarly with three illumination steps. To activate the resulting *kinesin-1* pattern the surface was globally heated to 35 °C. (C) Color overlay of the fluorescence image of patterned Alexa Fluor 488 streptavidin (green) and the maximum projection of moving microtubules (red) on the *kinesin-1* pattern. Gliding microtubules demonstrated the functionality of the molecules. (Scale bars represent 20  $\mu\text{m}$ .)

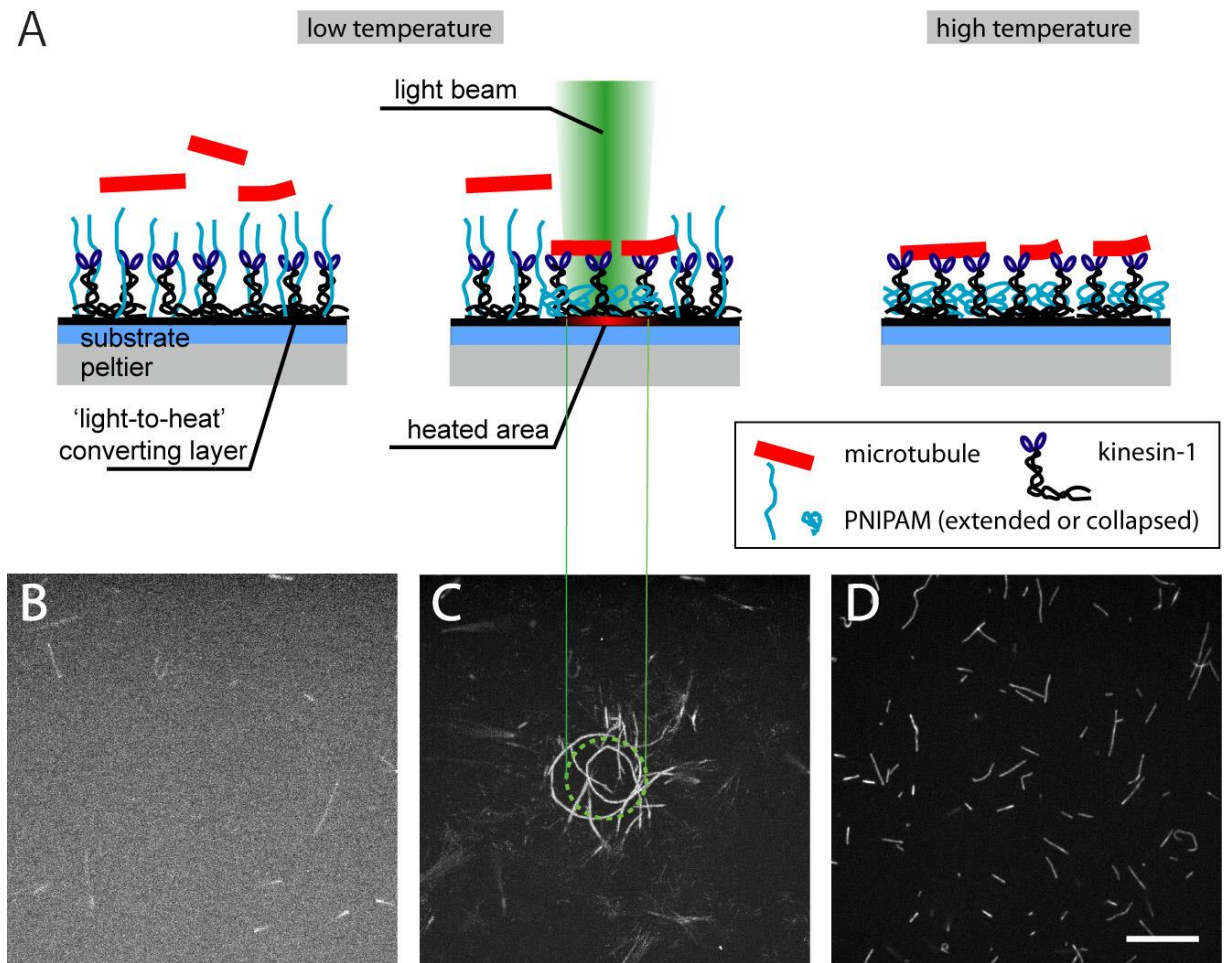


**Figure 4. Local activation of kinesin-1 by light-induced heating of a PNIPAM coated surface.** (A) Schematic illustrations of the surface configuration during the experiment in one field of view. The corresponding fluorescence images are shown in B to D. (B) Keeping the sample at 20 °C swollen PNIPAM chains prevented microtubules in solution from binding to the surface-bound kinesin-1 molecules. (C) Localized illumination with laser light ( $\lambda = 561$  nm) and subsequent conversion of light into heat caused the collapse of the thermoresponsive polymer chains. The surface-bound kinesin-1 molecules were locally activated and became accessible for microtubule binding. The maximum projection of moving microtubules revealed that kinesin-1 molecules were only activated in the illuminated and heated area and not in the surface parts around. (D) Globally heating the sample to 35 °C activated all surface-bound kinesin-1 molecules and allowed microtubules to bind and move. (Scale bar represents 20  $\mu\text{m}$ .)



## References

1. Khademhosseini, A., et al., *Microscale technologies for tissue engineering and biology*. Proceedings of the National Academy of Sciences of the United States of America, 2006. **103**(8): p. 2480-2487.
2. Folch, A. and M. Toner, *Microengineering of cellular interactions*. Annual Review of Biomedical Engineering, 2000. **2**: p. 227-+.
3. Li, N., A. Tourovskaia, and A. Folch, *Biology on a Chip: Microfabrication for Studying the Behavior of Cultured Cells*. Critical Reviews™ in Biomedical Engineering, 2003. **31**((5&6)): p. 423–488.
4. Raghavan, S. and C.S. Chen, *Micropatterned environments in cell biology*. Advanced Materials, 2004. **16**(15): p. 1303-1313.
5. Sniadecki, N., et al., *Nanotechnology for cell-substrate interactions*. Annals of Biomedical Engineering, 2006. **34**(1): p. 59-74.
6. Falconnet, D., et al., *Surface engineering approaches to micropattern surfaces for cell-based assays*. Biomaterials, 2006. **27**(16): p. 3044-3063.
7. Chen, C.S., et al., *Geometric control of cell life and death*. Science, 1997. **276**(5317): p. 1425-1428.
8. McBeath, R., et al., *Cell shape, cytoskeletal tension, and RhoA regulate stem cell lineage commitment*. Developmental Cell, 2004. **6**(4): p. 483-495.
9. Senaratne, W., L. Andruzzi, and C.K. Ober, *Self-Assembled Monolayers and Polymer Brushes in Biotechnology: Current Applications and Future Perspectives*. Biomacromolecules, 2005. **6**(5): p. 2427-2448.
10. Besson, E., et al., *A novel and simplified procedure for patterning hydrophobic and hydrophilic SAMs for microfluidic devices by using UV photolithography*. Langmuir, 2006. **22**(20): p. 8346-8352.
11. Babacan, S., et al., *Evaluation of antibody immobilization methods for piezoelectric biosensor application*. Biosensors & Bioelectronics, 2000. **15**(11-12): p. 615-621.
12. Feng, C.L., et al., *Reactive microcontact printing on block copolymer films: Exploiting chemistry in microcontacts for sub-micrometer patterning of biomolecules*. Advanced Materials, 2007. **19**(2): p. 286-+.
13. Reuther, C., et al., *Biotemplated nanopatterning of planar surfaces with molecular motors*. Nano Letters, 2006. **6**(10): p. 2177-2183.
14. Allen, R.D., *Trends in patterning materials for advanced lithography*. Journal of Photopolymer Science and Technology, 2007. **20**(3): p. 453-455.
15. Yamaguchi, M., et al., *Protein patterning using a microstructured organosilane layer fabricated by VUV light lithography as a template*. Colloids and Surfaces a-Physicochemical and Engineering Aspects, 2006. **284**: p. 532-534.
16. Tinazli, A., et al., *Native protein nanolithography that can write, read and erase*. Nat Nano, 2007. **2**(4): p. 220-225.
17. David S. Ginger, H.Z.C.A.M., *The Evolution of Dip-Pen Nanolithography*. Angewandte Chemie International Edition, 2004. **43**(1): p. 30-45.
18. Xia, Y.N. and G.M. Whitesides, *Soft lithography*. Angewandte Chemie-International Edition, 1998. **37**(5): p. 551-575.



19. Slocik, J.M., et al., *Site-specific patterning of biomolecules and quantum dots on functionalized surfaces generated by plasma-enhanced chemical vapor deposition*. Advanced Materials, 2006. **18**(16): p. 2095-+.
20. Jung, J.M., et al., *Gold-conjugated protein nanoarrays through block-copolymer lithography: From fabrication to biosensor design*. Small, 2006. **2**(8-9): p. 1010-1015.
21. Holden, M.A. and P.S. Cremer, *Light Activated Patterning of Dye-Labeled Molecules on Surfaces*. J. Am. Chem. Soc., 2003. **2003**(125): p. 8074-8075.
22. Gerhardt, K.E., M.I. Wilson, and B.M. Greenberg, *Ultraviolet wavelength dependence of photomorphological and photosynthetic responses in Brassica napus and Arabidopsis thaliana*. Photochem Photobiol, 2005. **81**(5): p. 1061-8.
23. Ionov, L., M. Stamm, and S. Diez, *Reversible switching of microtubule motility using thermoresponsive polymer surfaces*. Nano Lett, 2006. **6**(9): p. 1982-7.
24. Huber, D.L., et al., *Programmed Adsorption and Release of Proteins in a Microfluidic Device*. Science, 2003. **301**: p. 352-354.
25. Ionov, L. and S. Diez, *Environment-friendly photolithography using poly(N-isopropylacrylamide)-based thermoresponsive photoresists*. Journal of the American Chemical Society, 2009. **131**(37): p. 13315-9.
26. Schroeder, V., et al., *Dynamic Guiding of Motor-Driven Microtubules on Electrically Heated, Smart Polymer Tracks*. Nano Letters, 2013. **13**(7): p. 3434-3438.
27. Ruhnow, F., D. Zwicker, and S. Diez, *Tracking single particles and elongated filaments with nanometer precision*. Biophysical Journal. **100**(11): p. 2820-8.
28. Ye, X.D., et al., *How many stages in the coil-to-globule transition of linear homopolymer chains in a dilute solution?* Macromolecules, 2007. **40**(14): p. 4750-4752.
29. Papra, A., N. Gadegaard, and N.B. Larsen, *Characterization of ultrathin poly(ethylene glycol) monolayers on silicon substrates*. Langmuir, 2001. **17**(5): p. 1457-1460.
30. Korten, T. and S. Diez, *Setting up roadblocks for kinesin-1: mechanism for the selective speed control of cargo carrying microtubules*. Lab Chip, 2008. **8**(9): p. 1441-7.
31. Coy, D.L., M. Wagenbach, and J. Howard, *Kinesin takes one 8-nm step for each ATP that it hydrolyzes*. J Biol Chem, 1999. **274**(6): p. 3667-71.
32. Castoldi, M. and A.V. Popov, *Purification of brain tubulin through two cycles of polymerization-depolymerization in a high-molarity buffer*. Protein Expr Purif, 2003. **32**(1): p. 83-8.
33. Ionov, L., A. Synytska, and S. Diez, *Temperature-induced size-control of bioactive surface patterns*. Advanced Functional Materials, 2008. **18**(10): p. 1501-1508.

Stoychev, G.; Turcaud, S.; Dunlop, J.; Ionov, L.

Hierarchical multi-step folding of polymer bilayers

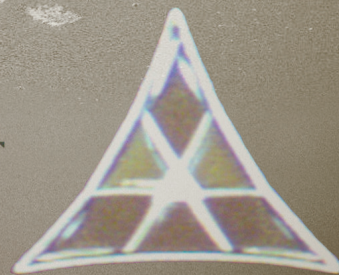
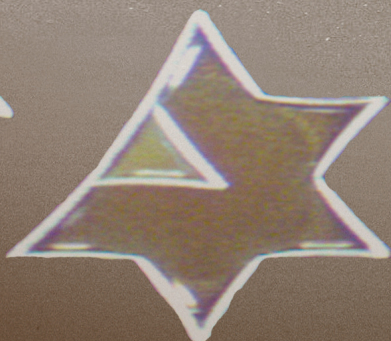
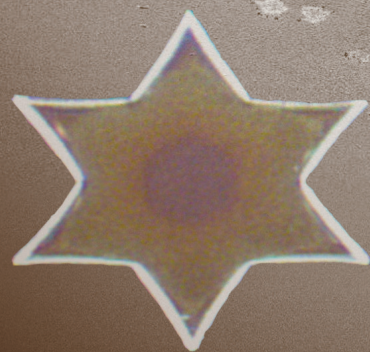
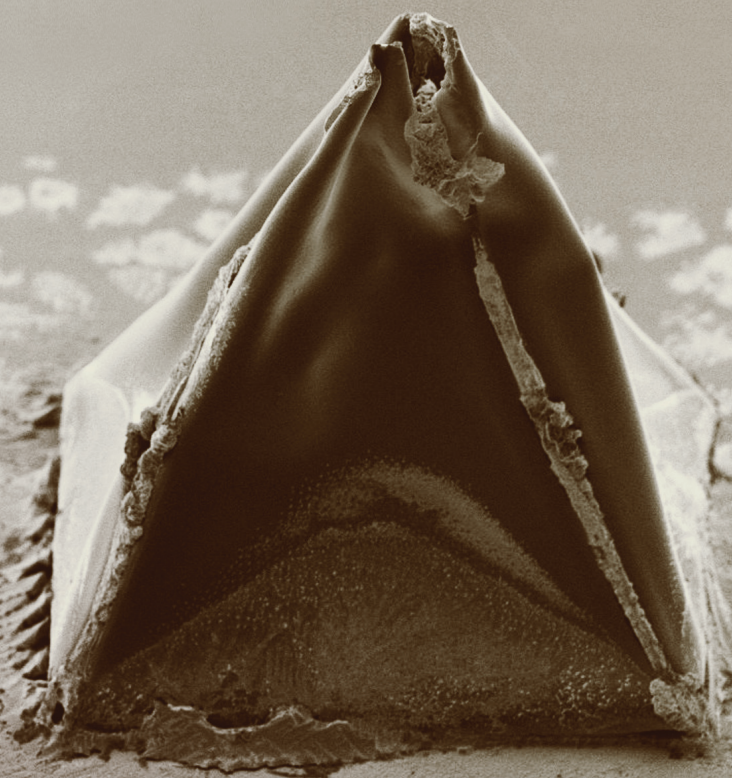
***Advanced Functional Materials*** 2013, 23, 2295–2300.



Vol. 23 • No. 18 • May 13 • 2013

[www.afm-journal.de](http://www.afm-journal.de)

# ADVANCED FUNCTIONAL MATERIALS



WILEY-VCH



# Hierarchical Multi-Step Folding of Polymer Bilayers

Georgi Stoychev, Sébastien Turcaud, John W. C. Dunlop, and Leonid Ionov\*

**A highly complex multi-step folding of isotropic stimuli-responsive polymer bilayers resulting in a variety of 2D and 3D structures is reported. Experimental observations allow determination of empirical rules, which can be used to direct the folding of polymer films in a predictable manner. In particular, it is demonstrated that these rules can be used for the design of a 3D pyramid. The understanding and know-how attained in this study allow the very simple design of highly complex, self-folding 3D objects and open new horizons for 3D patterning, important for the design of microfluidic devices, biomaterials, and soft electronics.**

## 1. Introduction

Nature offers an enormous arsenal of ideas for the design of novel materials with superior properties and interesting behavior. In particular, self-assembly and self-organization, which are fundamental to structure formation in nature, attract significant interest as promising concepts for the design of intelligent materials.<sup>[1]</sup> Self-folding stimuli-responsive polymer films are exemplary biomimetic materials<sup>[2]</sup> and can be viewed as model systems for bioinspired actuation. Such films, on one hand, mimic movement mechanisms in certain plant organs<sup>[3,4]</sup> and, on the other hand, are able to self-organize and form complex 3D structures.<sup>[5]</sup> These self-folding films consist of two polymers with different properties. Because of the nonequal expansion of the two polymers, these films are able to form tubes,<sup>[6,7]</sup> capsules<sup>[8]</sup> or more complex structures.<sup>[9]</sup> Similar to origami, the self-folding polymeric films provide unique possibilities for the straightforward fabrication of highly complex 3D microstructures with patterned inner and outer walls that cannot be achieved using other technologies.

There are two general approaches for the design of self-folding films. The first approach is based on the use of complexly patterned films, where locally deposited active materials form hinges.<sup>[10]</sup> Homogenous bilayer films are used in the

second approach.<sup>[11]</sup> Because of the isotropy of the mechanical properties of the bilayer, the formed structures are hinge-free and have rounded shapes. Importantly, in all reported cases, folding runs in one step. On the other hand there are reports that folding in nature can have a very complex character, which strongly depends on the geometry and swelling path<sup>[12]</sup> that may result in multistep folding (development of curvature in different directions).<sup>[3]</sup> In this contribution, we demonstrate that the shape of isotropic polymer bilayers is able to direct folding

in a sophisticated manner leading to even more complex hierarchical folding than in nature. In particular, films can undergo sequential folding steps by forming various 3D shapes with sharp hinges. By analyzing the folding patterns we elucidated empirical rules, cross-checked by analytical considerations and backed up with finite-element simulations, which allow the folding to be directed, leading to the design of specific 3D shapes. We also highlight the importance of path-dependency in the activation of the actuator, which enables to lock it in a local energy minimum, which can differ from the global one.

## 2. Results and Discussions

For the experiments we used polymer films consisting of two layers of photo-crosslinked polymers: the active layer being a random thermoresponsive copolymer poly(N-isopropylacrylamide-co-acrylic acid) (P(NIPAM-AA)) and the passive layer being poly(methylmethacrylate) (PMMA) (Figure 1). The bilayer, prepared as described elsewhere,<sup>[7]</sup> is located on a silica wafer in such a way that the active and passive polymers are the bottom and top layers, respectively. The bilayer is undeformed in PBS 0.1 M pH = 7.4 environment at  $T > 70^\circ\text{C}$  and folding occurs after cooling below  $70^\circ\text{C}$  (Figure 1).

Due to the relatively slow diffusion rate of water inside the P(NIPAM-AA) layer, actuation is driven by the progression of the diffusion front, along which the hydrogel starts to swell. This induces a path-dependency in the folding pattern as the bilayer is not homogeneously activated, but progressively swells as water diffuses from the lateral sides. The investigation of swelling was performed in a qualitative manner by observing the color change of the films which, due to light interference, reflects the change in optical path length (OPL) (Figure 2). The OPL varies as a function of the film thickness and refractive index, which in turn depends on the swelling degree.<sup>[13]</sup> The nonswollen elliptical and star-like films have a homogenous blue (Figure 2a) and reddish (Figure 2d) color, respectively. The difference in the color of both films is caused by their different

G. Stoychev, Dr. L. Ionov  
Leibniz Institute of Polymer Research Dresden  
Hohe Str. 6, D-01069 Dresden, Germany  
E-mail: ionov@ipfdd.de

G. Stoychev  
Technische Universität Dresden  
Physical Chemistry of Polymer Materials  
01062 Dresden, Germany  
S. Turcaud, Dr. J. W. C. Dunlop  
Department of Biomaterials  
Max Planck Institute of Colloids and Interfaces  
Am Mühlenberg 1, D-14424, Potsdam, Germany



DOI: 10.1002/adfm.201203245

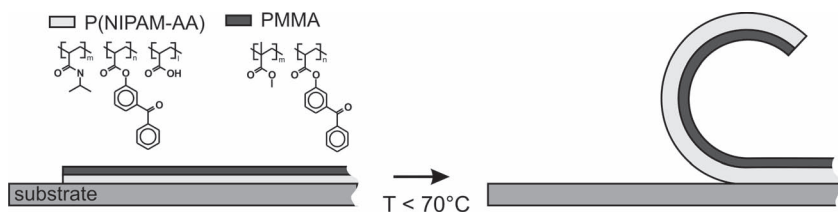


**Figure 1.** Scheme of folding of a bilayer polymer film consisting of two polymers: hydrophobic PMMA and thermoresponsive hydrogel P(NIPAM-AA).

starting thicknesses (Figure 2). The color of the films starts to change immediately after immersion in water at 25 °C, with the elliptical film becoming redder while the star-like film becomes green (Figure 2b,e). The changes of color in both cases start from the outer periphery of the bilayer film. As the active layer is confined between a water-impermeable silicon wafer and hydrophobic PMMA, this suggests that water can only penetrate inside the layer from the lateral sides.<sup>[14]</sup> The depth of water penetration along the perimeter of the film (activation depth) is uniform in both cases in the first moments of swelling. The differences in the swelling behavior between the two shapes appear after several seconds of incubation in water. The activation pattern depends on the external shape of the bilayers, with the position of the diffusion front (the activation depth) depending on the distance to the tissue border. This can be seen clearly in the differences of the activation patterns in the convex shapes like ellipse (Figure 2b), and concave ones like star (Figure 2d). For the star-like bilayers, the tips

of the triangular-like arms swell faster than their base and their polygonal central part. This can be explained by the fact that after a certain time the diffusion fronts on either side of the arms intersect resulting in faster swelling. The experimental results show that the swelling starts from the periphery of the films and that the activation profile strongly depends on the shape of the film as confirmed by simple finite element simulations (see Figure 2c,f).

We next modeled and experimentally investigated the folding of circular/elliptical and star-like films. Modeling predicts that multiple wrinkles are formed along the perimeter of folding bilayer when it is edge-activated (Figure 2g). The spatial wavelength of the wrinkles is proportional to the activation depth ( $d$ ) as observed in the wrinkles of leaves due to excessive radial edge-growth<sup>[15]</sup> and solved analytically in the context of geometrically nonlinear elasticity.<sup>[16]</sup> As the activation depth increases, the number of wrinkles decreases as  $P/d$ , where  $P$  is the perimeter of the shape (Figure 2h). The fact that there is both a gradient in radial- (edge-activation) and transversal direction (bilayer), results in a combination of wrinkling and bending, respectively (Figure 2g,h). In full agreement with the modeling predictions, experimental results show that the number of wrinkles decreases during folding (Figure 2i-l). Due to the transversal bending effect, the wrinkles actually evolve into local partial tubes as the activation depth increases. We observed that, at some point, the wrinkles stop to merge and their number remains constant. The probability of merging of two tubes depends on the angle ( $\beta$ , Figure 2h) between them. Experimentally, we found that the critical value of  $\beta$  below which merging of folded tubes was not observed is ca. 120–150°, which corresponds to 6–8 wrinkles when starting with a circular shape (inset in Figure 2h and Figure S3 in the Supporting Information). Based on these experimental observations we derived the first folding rule: “Bilayer polymer films placed on a substrate start to fold from their periphery and the number of formed wrinkles/tubes decreases until the angle between adjacent wrinkles/tubes approaches 130°”.

After the number of wrinkles/tubes along the perimeter of the bilayer film stopped to change the bilayers are locked for some time until the subsequent folding step occurs. For example, the wrinkled semi-ellipse bends towards its base (Figure 3a). To explain the origin of the second step of folding we considered the geometry of the film after the first folding step. As mentioned, wrinkling of a bilayer leads to the formation of tubes along the perimeter of the film. Considering the fact that the rigidity of the tubes is higher than that of the undeformed films, the polygonal shapes are stiffened by this tube formation, and therefore possess a

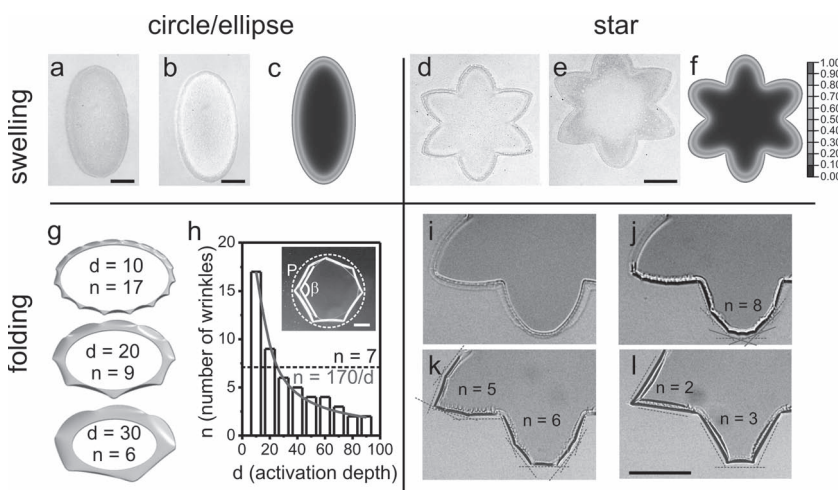


**Figure 2.** Swelling (upper panels) and first step of folding (lower panels) of circular/elliptical (left panels) and star-like (right panels) bilayer polymer films. a,b,d,e) Microscopy snapshots of swelling elliptical and star-like P(NIPAM-AA)/PMMA bilayers immediately after immersion in water (a,d) and after ca. 60 s incubation (b,e); c,f) Color map of the calculated swelling (from 0 to 1) controlled by water diffusion in the active monolayer with a lateral constant boundary condition (blue is non swollen) dependent on shape obtained by finite element simulations; g) Finite element simulations of wrinkling of a bilayer crown representing the activated edge in case of a circular shape; h) The number of wrinkles is inversely proportional to the activation depth. Dashed line corresponds to the experimental observation of heptahedrons (inset) when folding is typically stopped in the case of circular shapes. The red line corresponds to  $n = 170/d$ . i–l) Two rays of six-ray star during wrinkling, decrease of number of wrinkles is observed. a, b)  $H_{\text{PNIPAM}} = 35$  nm,  $H_{\text{PMMA}} = 400$  nm; d,e)  $H_{\text{PNIPAM}} = 35$  nm,  $H_{\text{PMMA}} = 500$  nm; i–l)  $H_{\text{PNIPAM-AA}} = 1200$  nm,  $H_{\text{PMMA}} = 400$  nm, scale bar is 200  $\mu\text{m}$ .



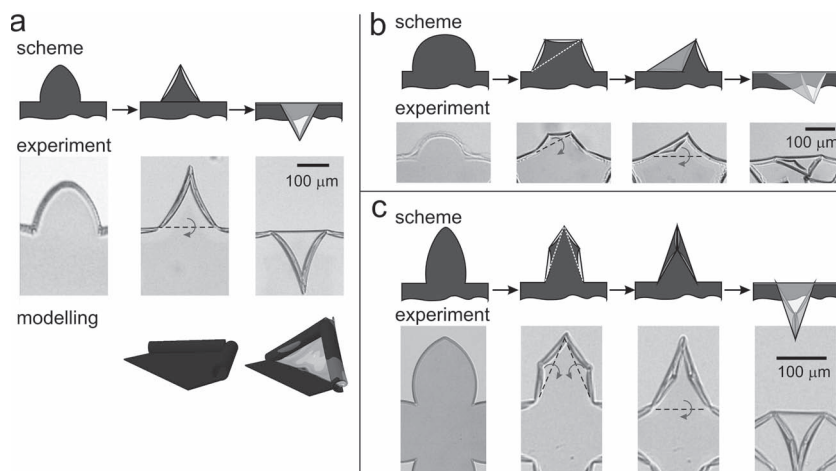


**Figure 3.** Schematic illustration, experimental observation, and modeling of the second step of folding of the elliptical arms depending on their shape. a)  $H_{(\text{PNIPAM-AA})} = 1200 \text{ nm}$ ,  $H_{\text{PMMA}} = 170 \text{ nm}$ ; b)  $H_{(\text{PNIPAM-AA})} = 1200 \text{ nm}$ ,  $H_{\text{PMMA}} = 400 \text{ nm}$ ; c)  $H_{(\text{PNIPAM-AA})} = 900 \text{ nm}$ ,  $H_{\text{PMMA}} = 170 \text{ nm}$ .

number of weak points located at the intersection of the tubes, i.e., at the vertices. These points act like hinges and folding is only observed along the lines connecting them (dashed line in Figure 3a). The formation of hinges during folding of isotropic bilayers, which to our knowledge has not been reported in the literature, is induced by the progressive activation from the lateral sides and the folded shapes are controlled by the initial shapes of the bilayers. This leads to the second rule of the folding: *“After the wrinkles along the perimeter of the film form tubes, further folding proceeds along the lines connecting the vertexes of the folded film”*.

In case there are more than two hinges in the film, a question arises: upon which connecting line will the folding occur? The number of hinges is largely determined by the shape of the semi-ellipses. The regular semi-ellipse, which has a triangular shape after the first step of folding, simply bends toward the base along the line connecting the two bottom vertexes (dashed line in Figure 3a). If the semi-ellipse is more rounded, it forms a trapezoid after the first-step of folding (Figure 3b). In the second step of folding, the trapezoid bends along one of the lines connecting the opposite top and bottom vertexes (dashed line in the second image from the left in Figure 3b). Next, the formed triangle bends towards its base along the line connecting the two bottom vertexes. The elongated semi-ellipse forms four folds after the first step of folding (Figure 3c). Interestingly, the semi-ellipse folds further along the lines connecting the vertexes at the base and the top vertex and no folding along the lines connecting neither the vertexes of the middle nor the ones at the base is observed. Looking at the evolution of the activation pattern through time (diffusion profile see Figure 2), we observe that the lines connecting the hinges can only be used if they are within the activated pattern (red). Thus, the third rule of the folding states: *“the folding goes along the lines which are closer to the periphery of the films”*.

Six-ray stars demonstrate the formation of very complex structures (Figure 4). Notably simultaneous folding of all rays

is observed very rarely and in most cases triangles (Figure 4g) were formed. We investigated the folding in a time-resolved manner in order to explain the formation of the triangles (Figure 5). Similar to the experiment demonstrated in Figure 2, wrinkles get longer and bend transversally into tubes (Figure 5b) thus increasing the rigidity of the ray. Next, one of the rays folds towards the center of the star (II in Figure 5c). Folding of this ray leads to the formation of a rigid semi-rolled tube, which is formed by the folded ray and the tubular shoulders of the adjacent rays (Figure 5c). The angle between the base of the folded ray and the shoulders of the neighboring arms is close to  $180^\circ$  (Figure 5c). In this configuration, the weak points located at the intersection between I–II and II–III has disappeared and rays I and III (Figure 5c) cannot bend anymore. As a result, only three remaining rays (IV, V, VI) can bend. If ray V folds, no additional rays can bend (Figure 4l).

If ray IV folds (Figure 5d) ray V is blocked. Finally, ray VI can fold leading to the formation of a triangle (Figure 5e). The discussed principle can be easily applied to understand the formation of the other observed figures (Figure 4c–l, Supporting Information Figure S2 and Figure S3). In fact, several factors can be held responsible for the observed symmetry breaking (rays do not fold at the same time) such as inhomogeneities in the films and shape imperfections resulting in small deviations from the symmetric diffusion profile. Based on these experimental observations, one can derive the fourth folding rule: *“Folding of the rays may result in blocking of the neighboring rays if the angle between the base of the folded ray and the shoulders of the neighboring rays is close to  $180^\circ$ ”*.

Finally, we applied the derived rules for the design of truly 3D structures—pyramids. In fact, the reason why six-ray star formed flattened folded structures is their short arms and the hindering of folding of rays. Therefore, in order to fabricate pyramids we increased the relative length of the rays and changed the angle between them by decreasing their number (Figure 6a,b). The rays of the fabricated four-ray stars first wrinkle along their perimeter (Figure 6c, d). Four tubes are formed along the perimeter of each ray (first rule, Figure 6c), which then collapse two by two and form triangles (second rule, Figure 6d). Since the angle between the folds located on the shoulders of each ray is considerably smaller than  $180^\circ$ , the folding of rays is not self-interfering (forth rule) and all rays fold in the direction of the center of the star (third rule) thus forming a hollow pyramid (Figure 6e–g) that is supported by simulations (Figure 6h). In fact these rules are also applicable to other shapes such as rectangles. As an example we included two-step folding of rectangles (Supporting Information Figure S4).

We observed that, in general, folding rules are applicable to all thickness (we performed many experiments with different thicknesses). The difference between the thin and thick films are in minor. For example, we observe that when star-like thin fold than all six arms (Figure 4d,k) can fold inside because rigidity of the film is not that high. In the

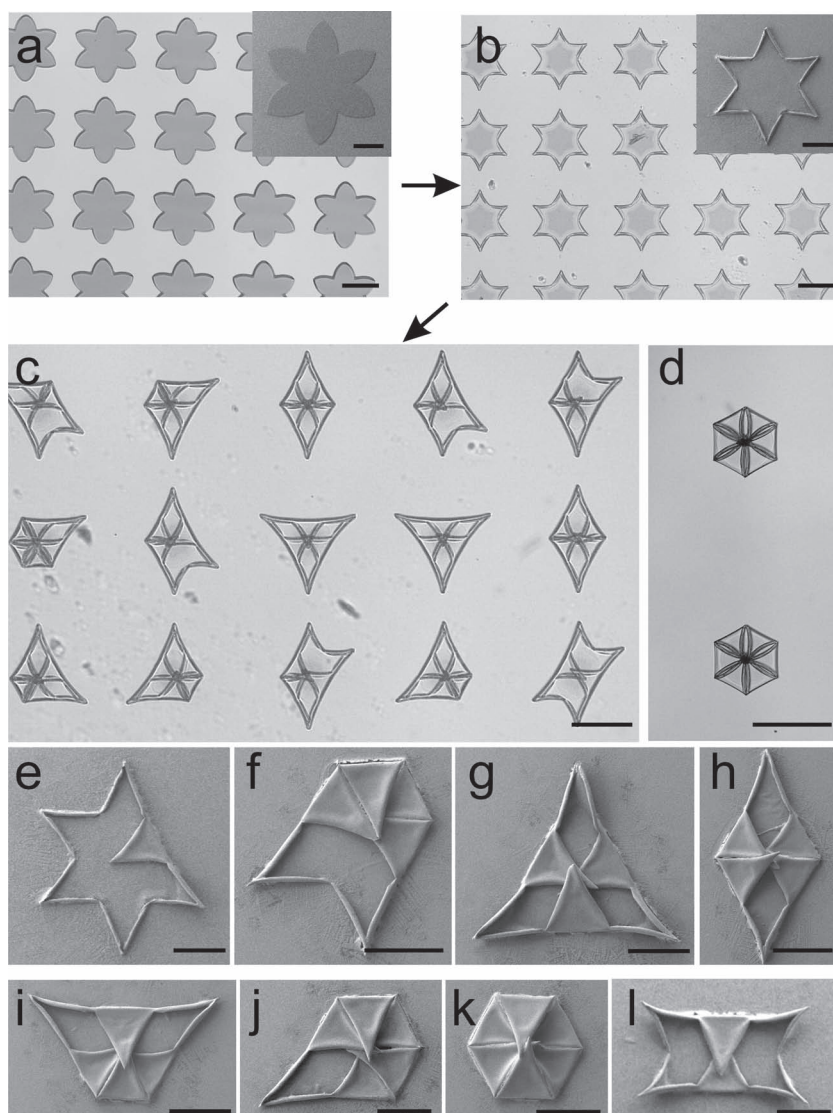


**Figure 4.** Examples of structures obtained by progressive edge-activation of six-ray star-like bilayers. a) Patterned bilayers; b) First step of actuation: wrinkles collapse into tubes; c–l) Second step of actuation: rays fold leading to several configurations depending on the order of folding. Scale bars are 200  $\mu\text{m}$ ,  $H_{(\text{NIPAM-AA})} = 1200 \text{ nm}$ ,  $H_{\text{PMMA}} = 260 \text{ nm}$ .

case of thick films, we typically observed folding of 3–4 arms (Figure 4g,l).

### 3. Conclusions

In conclusion, we investigated the actuation of patterned bilayers placed on a substrate. Due to the edge-activation of the bilayers, the observed deformed shapes differ from the classical ones obtained by homogeneous activation. We found that films can demonstrate several kinds of actuation behavior such as wrinkling, bending and folding that result in a variety of shapes. It was demonstrated that one can introduce hinges into the folded structure by proper design of the bilayer's external shape through diffusion without having to use site selective

deposition of active polymers. Experimental observations lead us to derive four empirical rules backed up by theoretical understanding as well as simulations. We then demonstrated how those rules can be used to direct the folding of edge-activated polymer bilayers through a concrete example—the design of a 3D pyramid. We believe that the derived understanding and know-how will allow very simple design of highly complex, self-folding 3D objects and will open new horizons for 3D patterning which is highly important for the design of microfluidic devices, biomaterials, soft electronics, etc.

### 4. Experimental Section

**Materials:** N-isopropylacrylamide (NIPAM, Aldrich), 4-hydroxybenzophenone (Fluka), polycaprolactone ( $M_n = 70\,000$ – $90\,000$  Da, Aldrich), benzophenone (Aldrich) and acryloyl chloride (Fluka) were used as received. Methyl methacrylate (MMA, Aldrich) and acrylic acid were purified by filtration through  $\text{Al}_2\text{O}_3$  column before polymerization.

**Synthesis of 4-Acryloylbenzophenone (BA):** 4-Hydroxybenzophenone (20 g, 0.1009 mol), diisopropylethylamine (19.3 mL, 0.1110 mol) and 80 mL of methylene chloride were added into 200 mL three-necked round-bottom flask fitted with an overhead stirrer, a thermometer, and an addition funnel with acryloyl chloride (9.02 mL, 0.1110 mol) solution in 20 mL of methylene chloride. The acryloyl chloride solution was added dropwise into the flask under cooling ( $0$ – $5^\circ\text{C}$ ) for ca 3 h. The methylene chloride was removed by rotary evaporation. The residue was washed with 80 mL of 20% HCl, 80 mL of saturated solution of sodium hydrocarbonate and dried over sodium sulphate. The solution was passed through a silica gel column with chloroform as the eluent. Chloroform was removed by rotary evaporator. Finally, 24.44 g (95%) of ABP was obtained.  $^1\text{H}$  NMR ( $\text{CDCl}_3$ , 500 MHz): 6.05 (dd,  $J_1 = 10.40$ ,  $J_2 = 1.26$ , 1H), 6.34 (dd,  $J_1 = 10.40$ ,  $J_3 = 17.34$ , 1H), 6.64 (dd,  $J_3 = 17.34$ ,  $J_2 = 1.26$ , 1H), 7.27 (m, 2H), 7.49 (m, 2H), 7.59 (m, 1H), 7.80 (m, 2H), 7.86 (m, 2H).

**Synthesis of P(NIPAM-AA-BA):** BA (0.28 g, 1.12 mmol); NIPAM (6 g, 51.57 mmol), AA (0.2556 g, 3.36 mmol), AIBN (0.01632 g, 0.38 mmol) were added in 50 mL flask. Components were dissolved in 30 mL ethanol and degassed with nitrogen for 30 min. The mixture was purged with nitrogen for 30 min. The polymerization was carried at  $70^\circ\text{C}$  under nitrogen atmosphere with mechanical stirring overnight. After cooling, the mixture was poured in 750 mL diethyl ether, the precipitate was filtered and dried in vacuum at  $40^\circ\text{C}$ .

**Synthesis of P(MMA-BA):** 6.3 g MMA (62.7 mmol), 0.24 g BA (0.96 mmol) and 0.05 g AIBN (0.31 mmol) were dissolved in 30 mL of toluene. The mixture was purged with nitrogen for 30 min. The polymerization was carried at  $70^\circ\text{C}$  under nitrogen atmosphere with mechanical stirring overnight. After cooling, the mixture was poured in 750 mL diethyl ether, the precipitate was filtered and dried in vacuum at  $40^\circ\text{C}$ .

**Preparation of Polymer Bilayers:** In a typical experiment, poly-(NIPAM-BA) was dip-coated from its ethanol solution on silica wafer substrate. P(MMA-BA) was dip-coated from toluene solution on the

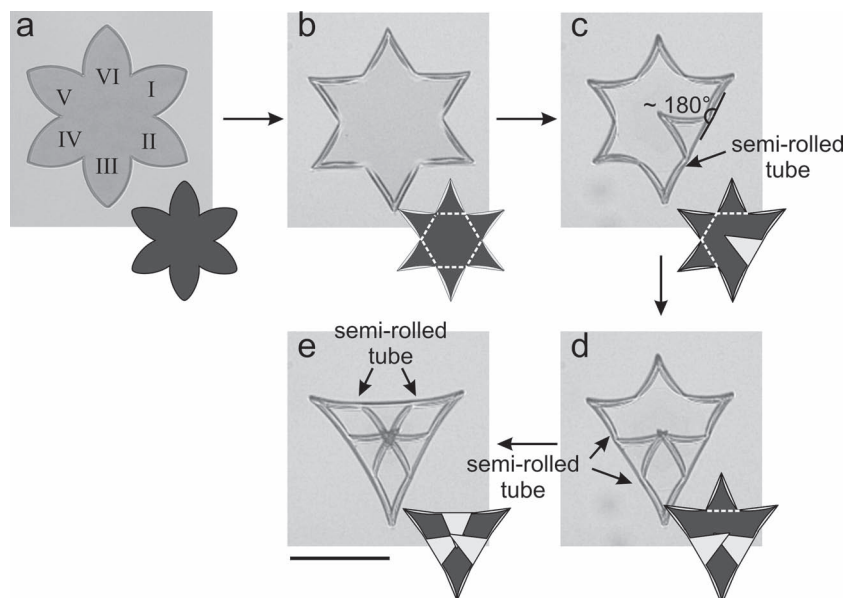


**Figure 5.** Microscopy snap-shots illustrating the mechanism of formation of triangles during actuation of a six-ray stars. Scale bar is 200  $\mu\text{m}$ ,  $H_{(\text{PNIPAM-AA})} = 1200 \text{ nm}$ ,  $H_{\text{PMMA}} = 170 \text{ nm}$ .

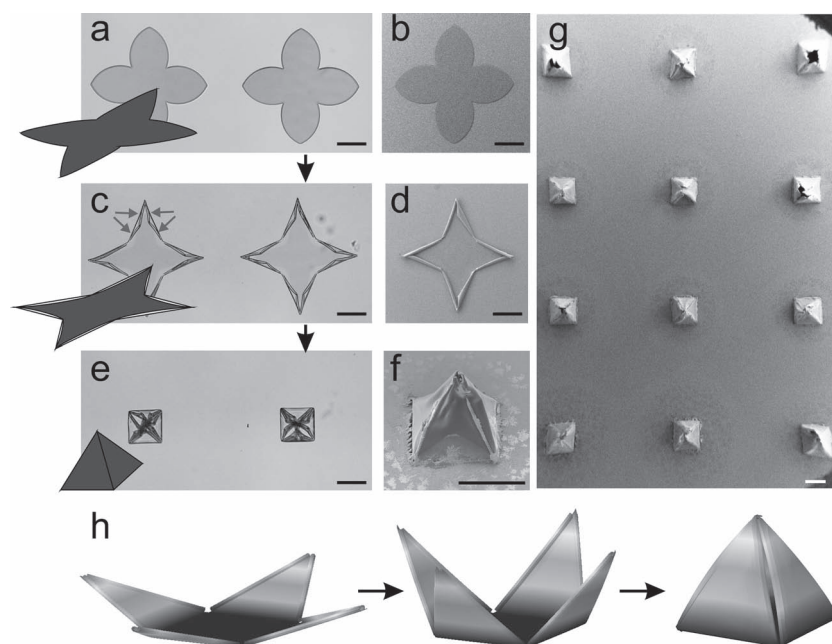


**Figure 6.** Sequential actuation of four-ray stars leads to the formation of pyramids. a,b) unactivated film; c,d) after wrinkling of the ray periphery into tubes, arrows indicate four wrinkles formed on each arm during first step of folding; e–g) after folding of rays leading to the formation of pyramids. Scale bar is 200  $\mu\text{m}$ ,  $H_{(\text{PNIPAM-AA})} = 1200 \text{ nm}$ ;  $H_{\text{PMMA}} = 260 \text{ nm}$ . h) Simulated folding of four-arm star.

poly-(NIPAM-BA) film. The bilayer film was illuminated through a photomask (Toppan Photomasks inc.) by halogen lamp for 40 min to crosslink the polymers. The illuminated film was rinsed in chloroform in order to remove the polymers from non-irradiated areas. The prepared bilayers were then dried again in air before experiment and contained

no water. The observation of bilayer was performed by Axiovert Zeiss Microscope using 5 $\times$  and 10 $\times$  air objectives.

**Numerical Simulations:** Simulations were performed in Abaqus v6.11 using the standard finite-element method. In order to simulate the diffusion process in the active layer we performed a 2D heat transfer analysis with imposed temperature on the free perimeter of the shapes (circle, semi-ellipsoid) and constant diffusive properties. This resulted in a time-dependent temperature distribution that mimics the swelling process. The resulting nodal temperatures at an early point in time were then applied to the corresponding 3D bilayer shapes having a mismatch in expansion properties (passive layer has 0 thermal expansion, while the active layer has in-plane expansion coefficients of 1). Due to symmetries only the relevant part of the bilayers were simulated in order to reduce computational costs. The resultant actuated shape was obtained through a geometrically nonlinear static step. For more detailed information see ref. [14]. Doing this, we assumed that diffusion-driven actuation follows a quasistatic process in which the timescales of diffusion and actuation are clearly separated. The progression of the diffusion front is slow (s) while the resultant mechanical actuation is fast (ms). This enabled us to consider the two phenomena separately thereby neglecting potential couplings between swelling and mechanical properties. Results are only qualitative, as the actual material characteristics of the hydrogels were not measured. However, the actuation pattern, and thus the number of wrinkles, only depends on the depth of the differential edge-activation named “activation depth” in this paper. This enabled us to predict and confirm the experimental actuation patterns with simple normalized properties.

## Supporting Information

Supporting Information is available from the Wiley Online Library or from the author.

## Acknowledgements

The authors are grateful to DFG (Grant IO 68/1-1) and IPF for financial support. The authors are grateful to K.-J. Eichhorn and R. Schulze (IPF) for assistance with ellipsometry.

Received: November 5, 2012  
Published online: November 26, 2012

- [1] a) A. Terfort, N. Bowden, G. M. Whitesides, *Nature* **1997**, *386*, 162;  
b) G. M. Whitesides, B. Grzybowski, *Science* **2002**, *295*, 2418.
- [2] a) T. G. Leong, A. M. Zarafshar, D. H. Gracias, *Small* **2010**, *6*, 792;  
b) L. Ionov, *Soft Matter* **2011**, *7*, 6786.



- [3] M. J. Harrington, K. Razghandi, F. Ditsch, L. Guiducci, M. Rueggeberg, J. W. C. Dunlop, P. Fratzl, C. Neinhuis, I. Burgert, *Nat. Commun.* **2011**, 2, 337.
- [4] a) J. W. C. Dunlop, R. Weinkamer, P. Fratzl, *Mater. Today* **2011**, 14, 70; b) J. M. Skotheim, L. Mahadevan, *Science* **2005**, 308, 1308; c) L. Mahadevan, S. Rica, *Science* **2005**, 307, 1740.
- [5] M. Jamal, A. M. Zarafshar, D. H. Gracias, *Nat. Commun.* **2011**, 2, 527.
- [6] S. Zakharchenko, E. Sperling, L. Ionov, *Biomacromolecules* **2011**, 12, 2211.
- [7] S. Zakharchenko, N. Pureskiy, G. Stoychev, M. Stamm, L. Ionov, *Soft Matter* **2010**, 6, 2633.
- [8] G. Stoychev, N. Pureskiy, L. Ionov, *Soft Matter* **2011**, 7, 3277.
- [9] A. Azam, K. Laflin, M. Jamal, R. Fernandes, D. Gracias, *Biomed. Microdevices* **2011**, 1, 51.
- [10] D. H. Gracias, V. Kavthekar, J. C. Love, K. E. Paul, G. M. Whitesides, *Adv. Mater.* **2002**, 14, 235.
- [11] G. S. Huang, Y. F. Mei, D. J. Thurmer, E. Coric, O. G. Schmidt, *Lab Chip* **2009**, 9, 263.
- [12] a) H. Y. Liang, L. Mahadevan, *Proc. Natl. Acad. Sci. USA* **2011**, 108, 5516; b) H. Liang, L. Mahadevan, *Proc. Natl. Acad. Sci. USA* **2009**, 106, 22049.
- [13] a) I. Jung, J. S. Rhyee, J. Y. Son, R. S. Ruoff, K. Y. Rhee, *Nanotechnology* **2012**, 23, 025708; b) J. Henrie, S. Kellis, S. M. Schultz, A. Hawkins, *Opt. Express* **2004**, 12, 1464.
- [14] G. Stoychev, S. Zakharchenko, S. Turcaud, J. W. C. Dunlop, L. Ionov, *ACS Nano* **2012**, 6, 3925.
- [15] M. Marder, E. Sharon, S. Smith, B. Roman, *Europhys. Lett.* **2003**, 62, 498.
- [16] B. Audoly, A. Boudaoud, *C. R. Acad. Sci., Ser. IIb: Mec.* **2002**, 330, 831.

Zakharchenko, S.; Puretskiy, N.; Stoychev, G.; Waurisch, C.; Hickey, S.G.;  
Eychmüller, A.; Sommer, J.U.; Ionov, L.

Stimuli-responsive hierarchically self-assembled 3D porous polymer-based structures  
with aligned pores

***Journal of Materials Chemistry B*** 2013, 1, 1786-1793.

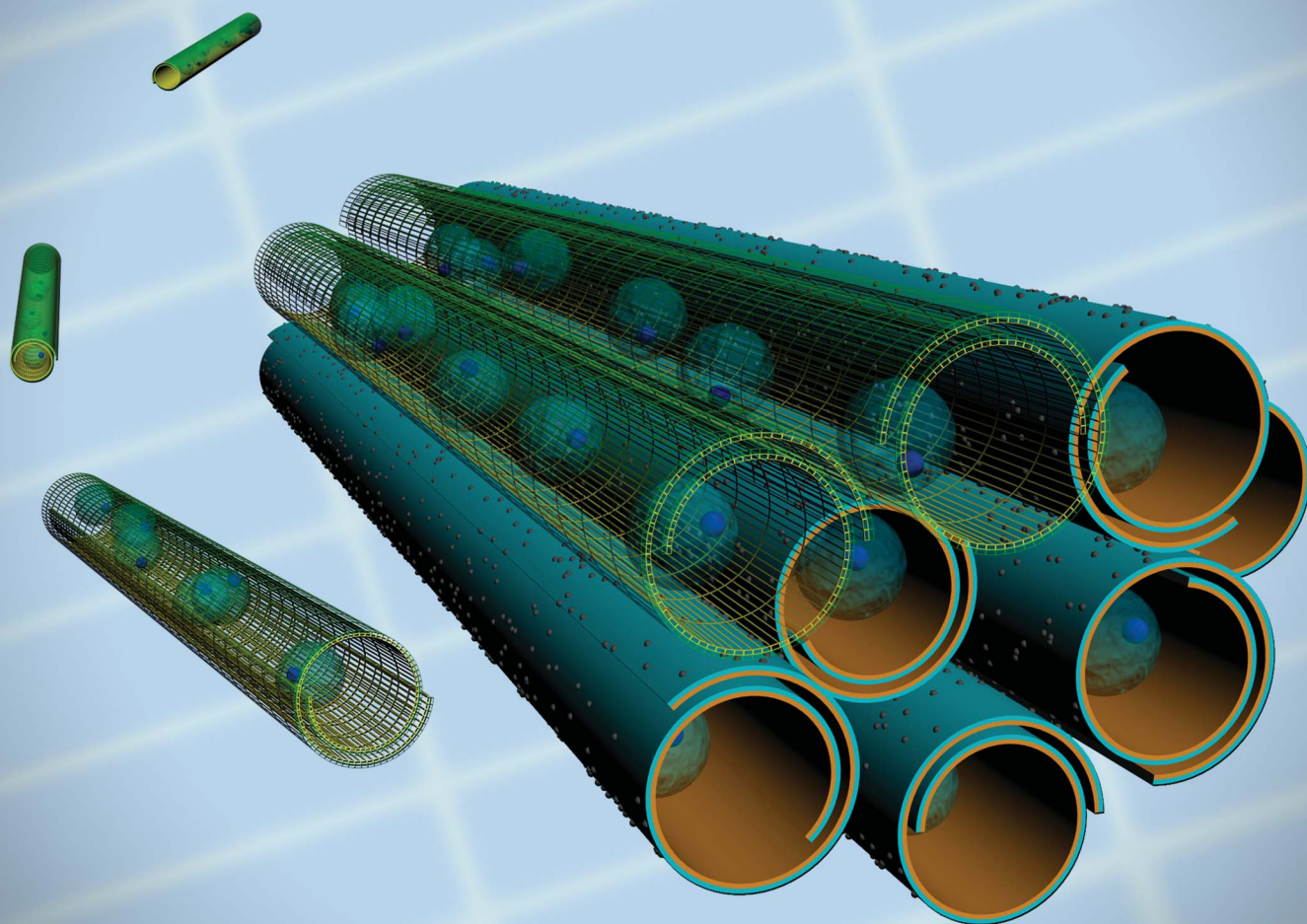


# Journal of Materials Chemistry B

Materials for biology and medicine

[www.rsc.org/MaterialsB](http://www.rsc.org/MaterialsB)

Volume 1 | Number 13 | 7 April 2013 | Pages 1767–1870



ISSN 2050-750X

RSC Publishing

**PAPER**

Leonid Ionov *et al.*  
Stimuli-responsive hierarchically self-assembled 3D porous polymer-based structures with aligned pores

## PAPER

## Stimuli-responsive hierarchically self-assembled 3D porous polymer-based structures with aligned pores†

Cite this: *J. Mater. Chem. B*, 2013, **1**, 1786

Svetlana Zakharchenko,<sup>ab</sup> Nikolay Puretskiy,<sup>ab</sup> Georgi Stoychev,<sup>ab</sup> Christian Waurisch,<sup>c</sup> Stephen G. Hickey,<sup>c</sup> Alexander Eychemüller,<sup>c</sup> Jens-Uwe Sommer<sup>ad</sup> and Leonid Ionov<sup>\*a</sup>

We have developed a novel approach for the fabrication of self-assembled porous materials with uniaxial tubular pores. The approach is based on the use of microtubes formed by stimuli-induced rolling of polymer bilayers consisting of hydrophobic and stimuli-responsive hydrophilic polymers. Different objects, for example yeast cells, can be encapsulated inside the tubes during their rolling. The self-rolled tubes filled with the yeast cells are capable of controlled self-assembly and form a uniaxial tubular homogeneously filled scaffold. Moreover, our approach allows design of porous materials with the pores having different properties.

Received 10th October 2012  
Accepted 12th December 2012

DOI: 10.1039/c2tb00231k

[www.rsc.org/MaterialsB](http://www.rsc.org/MaterialsB)

## Introduction

Materials with uniaxially aligned/oriented pores have huge potential for a number of applications including design of self-healing materials,<sup>1,2</sup> functional ceramics,<sup>3</sup> membranes for separation and sensing,<sup>4</sup> photonic crystals,<sup>5–7</sup> catalyst support,<sup>8</sup> light-weight materials,<sup>9</sup> vibration-damping materials,<sup>9</sup> heat insulating materials,<sup>10</sup> photovoltaic applications,<sup>11</sup> microanalytics,<sup>12</sup> and tissue engineering.<sup>13–21</sup> Moreover, many kinds of tissues such as bones,<sup>13</sup> vascular tissue,<sup>14,15</sup> cardiac tissue,<sup>16–18</sup> and nerves<sup>19,20</sup> have either tubular or uniaxially aligned porous structures. In order to mimic the tubular structural environment, phase separation techniques,<sup>14,15,22</sup> polymer fiber templating,<sup>16,19,20</sup> directed foaming,<sup>23</sup> directional freezing,<sup>14,24–27</sup> prototyping,<sup>17</sup> uniaxial stretching of porous materials,<sup>28</sup> or natural porous materials such as wood<sup>3</sup> were used. In these approaches the separate tubes or scaffold with tubular structure are first fabricated and then filled with a material. This “post-filling” strategy suffers, however, often from non-homogenous filling of the porous scaffold.

Self-folding films offer a very elegant solution to the problem of non-homogenous distribution inside the pores.<sup>29–31</sup> The self-

folding films consist of two kinds of materials, which can be either inorganic<sup>32</sup> or organic.<sup>33–37</sup> Internal stress is produced due to different volume changes of these materials upon application of appropriate stimuli that result in the deformation of the bilayer film and formation of 3D objects with various shapes such as tubes, cubes or capsules.<sup>29,30,38</sup> Self-folding films based on polymers are particularly attractive for biotechnological and lab-on-chip applications due to their sensitivity to stimuli in the physiological range, biocompatibility and biodegradability.<sup>37,39–41</sup> The main advantage of self-folding films is that they can be filled before self-assembly and formation of tubes (folding) that provides the desired homogeneity of filling.<sup>29,37,40</sup> Moreover self-rolled tubes are able to provide structural anisotropy. Our approach consists of the fabrication of homogeneously filled self-rolled tubes and their self-assembly into complex 3D constructs with uniaxially aligned pores (Fig. 1). The approach was demonstrated for the example of encapsulation of yeast cells.

## Experimental part

## Materials

Acrylic acid (AA, Aldrich), methyl methacrylate (MMA, Aldrich), and 2-(dimethylamino)ethyl methacrylate (DMAEMA, Aldrich) were purified by filtration through an Al<sub>2</sub>O<sub>3</sub> column before polymerisation. *N*-Isopropylacrylamide (NIPAM, Aldrich) was recrystallized from hexane. 4-Hydroxybenzophenone (Fluka), acryloyl chloride (Fluka), *N,N*-diisopropylethylamine (Aldrich), 2,2'-azobis(2-methylpropionitrile) (AIBN, Fluka), *N,N,N',N',N''*-pentamethyldiethylenetriamine (PMDTA, Aldrich), 2-bromoisobutyrate (EBiB, Aldrich), and copper(II) bromide (CuBr<sub>2</sub>, Aldrich) were used as received. Cadmium oxide (CdO, 99.5%), 1-octadecene (ODE, 90%), oleic acid (OlAc, 90%), *n*-tri-octylphosphine oxide (TOPO, 99%), sulfur powder (99.98%) and

<sup>a</sup>Leibniz Institute of Polymer Research Dresden, Hohe Str. 6, D-01069 Dresden, Germany. E-mail: [ionov@ipfdd.de](mailto:ionov@ipfdd.de)

<sup>b</sup>Technische Universität Dresden, Physical Chemistry of Polymer Materials, 01062 Dresden, Germany

<sup>c</sup>Technische Universität Dresden, Physical Chemistry/Electrochemistry, Bergstrasse 66b, 01062 Dresden, Germany

<sup>d</sup>Technische Universität Dresden, Institute for Theoretical Physics, Zellescher Weg 17, 01069 Dresden, Germany

† Electronic supplementary information (ESI) available: Movies of assembly and disassembly of self-rolled tubes can be found in the ESI. See DOI: 10.1039/c2tb00231k

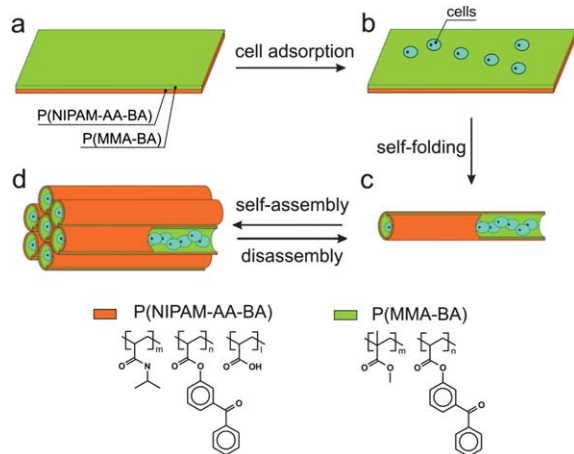


**Fig. 1** Fabrication of tubular self-assembling structures filled with cells using self-rolled tubes. (a) Unfolded patterned bilayer consisting of two polymers: red represents hydrophilic p(NIPAM-AA-BA) and green represents hydrophobic p(MMA-BA); (b) cells are adsorbed on the top of an unfolded bilayer; (c) cells are encapsulated inside the rolled film; and (d) self-rolled tubes are assembled together forming a porous construct homogeneously filled with cells.

zinc acetate ( $\text{Zn}(\text{Ac})_2$ , 99.99%) were purchased from Aldrich. Hexadecylamine (HDA, >99%) and *n*-trioctylphosphine (TOP) were obtained from Fluka and selenium powder (99.99%) was purchased from ChemPur. All chemicals were used without further treatment, except TOP, which was purified by distillation. All solvents were used as received.

### Synthesis of 4-acryloylbenzophenone (BA)

4-Hydroxybenzophenone (20 g, 0.1009 mol), *N,N*-diisopropylethylamine (19.3 ml, 0.1110 mol) and 80 ml of methylene chloride were added into a 200 ml three-necked round-bottom flask fitted with an overhead stirrer, a thermometer and an addition funnel with acryloyl chloride (9.02 ml, 0.1110 mol) solution in 20 ml of methylene chloride. The acryloyl chloride solution was added drop-wise into the flask under cooling (0–5 °C) for *ca.* 3 hours. The methylene chloride was removed by rotary evaporation. The residue was washed with 80 ml of 20% HCl, 80 ml of a saturated solution of sodium hydrocarbonate and dried over sodium sulfate. The solution was passed through a silica gel column with chloroform as the eluent. Chloroform was removed using a rotary evaporator. Finally, 24.44 g (95%) of ABP was obtained.  $^1\text{H}$  NMR ( $\text{CDCl}_3$ , 500 MHz): 6.05 (dd,  $J_1 = 10.40$ ,  $J_2 = 1.26$ , 1H), 6.34 (dd,  $J_1 = 10.40$ ,  $J_3 = 17.34$ , 1H), 6.64 (dd,  $J_3 = 17.34$ ,  $J_2 = 1.26$ , 1H), 7.27 (m, 2H), 7.49 (m, 2H), 7.59 (m, 1H), 7.80 (m, 2H), 7.86 (m, 2H).

### Synthesis of p(NIPAM-AA-BA)

NIPAM (6.4798 g, 55.62 mmol), BA (0.224 g, 0.89 mmol); AA (0.1912 g, 2.66 mmol), and AIBN (0.0507 g, 0.31 mmol) were dissolved in 30 ml of ethanol and the mixture was degassed with nitrogen for 30 minutes. The polymerization was carried out at 70 °C with mechanical stirring for 24 hours. Then the p(NIPAM-AA-BA) polymerization mixture was cooled to room temperature and poured slowly into 750 ml of diethyl ether. The precipitated

polymer was filtered and dried under vacuum. Molecular weight of the obtained polymer is  $M_n = 24 \text{ kg mol}^{-1}$ ,  $M_w = 80 \text{ kg mol}^{-1}$ . LCST (water)  $\approx 30^\circ\text{C}$ , LCST (PBS buffer 0.15 M, pH 7.4)  $\approx 40^\circ\text{C}$ .

### Synthesis of p(MMA-ABP)

MMA (4.5 g, 44.95 mmol), BA (0.182 g, 0.73 mmol) and AIBN (0.075 g, 0.46 mmol) were dissolved in 25 ml of *N,N*-dimethylformamide (DMF). The mixture was purged with nitrogen for 30 min. The polymerization was carried out at 70 °C under nitrogen atmosphere with mechanical stirring overnight. After cooling down to room temperature, the mixture was poured into 800 ml diethyl ether, and the precipitate was filtered and dried under vacuum at 40 °C. Molecular weight of the obtained polymer is  $M_n = 13 \text{ kg mol}^{-1}$ ,  $M_w = 37 \text{ kg mol}^{-1}$ .

### Preparation and modification of silica particles

Silica particles (SP-1000) were prepared by the Stöber synthesis with further modification with (3-aminopropyl)triethoxysilane (SP-NH<sub>2</sub>) and 2-bromo-2-methylpropionyl bromide (SP-Br) as described earlier.<sup>42</sup>

### Polymerisation of 2-(dimethylamino)ethyl methacrylate (DMAEMA)

1 g of SP-Br particles was placed in a 50 ml round-bottom flask and 15 ml DMF were added. The mixture was sonicated for 10 min. Further 15 ml of DMAEMA, 190  $\mu\text{l}$  of 0.5 M solution *N,N,N',N',N'',N'''*-pentamethyldiethylenetriamine (PMDTA) in DMF, 190  $\mu\text{l}$  of 0.1 M solution copper(II) bromide ( $\text{CuBr}_2$ ) in DMF, and 0.75  $\mu\text{l}$  of ethyl 2-bromoisobutyrate (EBiB) were added. To remove the excess of oxygen from the reaction mixture, nitrogen was bubbled through the reaction mixture for 10 min. Then, 400  $\mu\text{l}$  tin(II) 2-ethylhexanoate were added to the reaction mixture and the flask was placed on an oil bath at 101 °C and stirred at 700 rpm. After 1 hour the flask was removed from the oil bath and the particles were centrifuged and washed several times with DMF and ethanol and dried in a vacuum oven at 50 °C overnight. Approximately 1 g of SP-PDMAEMA particles was obtained. The thickness of the polymer brushes, grafted from the particles, was estimated by the parallel reaction on a modified silica wafer and the value of *ca.* 60 nm determined. Molecular weight of PDMAEMA obtained as a side product is  $M_w = 21 \text{ kg mol}^{-1}$ .

### Synthesis of quantum dots

CdSe QDs with a maximum in the fluorescence at 605 nm were synthesized following a modified procedure of Qu and Peng.<sup>43</sup> In detail, a 25 ml flask was loaded with 8 ml ODE, 2 g TOPO, 2 g HDA and 4 ml  $\text{Cd}(\text{oleate})_2$  (0.1 M in ODE). This mixture was degassed under reduced pressure at 100 °C for 60 minutes. Subsequently, the mixture was heated under inert atmosphere to the desired injection temperature of 270 °C. Into this hot solution 0.4 mmol selenium dissolved in 2 ml ODE and 2 ml TOP was quickly injected. The nanoparticles were allowed to grow for 20 minutes at 245 °C. Particle growth was stopped by cooling the reaction flask with cold water and simultaneous



injection of 6 ml of toluene. The resulting particles were then purified by repeated precipitation with an iso-propanol-methanol mixture and redissolved in toluene.

Green emitting CdSe/Cd<sub>1-x</sub>Zn<sub>x</sub>Se<sub>1-y</sub>S<sub>y</sub>/ZnS QDs with a maximum in the fluorescence at 540 nm were synthesized following a procedure of Bae *et al.*<sup>44</sup> Therefore, in a 100 ml flask 51.4 mg CdO, 733.6 mg Zn(Ac)<sub>2</sub>, 5.5 ml OAc and 20 ml ODE were degassed under reduced pressure at 120 °C until Zn(oleate)<sub>2</sub> formation was completed. Subsequently, the mixture was heated to 310 °C. After the solution turned colorless, indicating a complete Cd(oleate)<sub>2</sub> formation, 0.4 mmol selenium and 4 mmol sulfur in 3 ml TOP were quickly injected. After 10 minutes growth time at 300 °C the reaction was stopped by cooling the reaction flask with cold water. The crude solution was diluted with chloroform and then purified by repeated precipitation with acetone and redissolved in chloroform.

### Fabrication of polymer bilayers and self-rolled tubes

The bilayer films were produced using dip-coating. First p(NIPAM-AA-BA) containing an additional 10 wt% of 4-hydroxybenzophenone was deposited on a silica wafer substrate from ethanol solutions. Next, p(MMA-BA) was dip-coated from toluene, which is a selective solvent, on the top of p(NIPAM-AA-BA) films. The polymer bilayers were irradiated with UV light (254 nm) through a mask with a typical pattern size of 200 µm to 1600 µm. UV irradiation activates benzophenone fragments and leads to the cross-linking of the irradiated areas. By rinsing in chloroform, non-crosslinked polymers were removed and patterned bilayer films were formed on the substrate. The tubes were fabricated by exposure of patterned bilayers to PBS (0.15 M, pH 7.4) at room temperature followed by fast rolling within 5–10 minutes.

### Preparation of fluorescent tubes

To prepare fluorescent tubes for confocal microscopy, the same procedure as described above was used. To achieve fluorescence, small amounts of either red emitting (CdSe) or green emitting (CdSe/Cd<sub>1-x</sub>Zn<sub>x</sub>Se<sub>1-y</sub>S<sub>y</sub>/ZnS) quantum dots were admixed into the p(MMA-BA) toluene solution used for dip-coating.

### Tube aggregates preparation and alignment

Tube dispersion was prepared by washing the rolled tubes from the substrate with a small amount (2–3 ml) of water into a glass vial. To assemble the tubes, a water dispersion of PDMAEMA-covered SiO<sub>2</sub> particles (85 mg l<sup>-1</sup>) was added to the tube dispersion. The amount of added particles was calculated with respect to 25–30% saturation of the tube surface with particles and under the assumption of hexagonal close packing and complete adsorption of all particles onto the tube surface. A water dispersion of tubes and oppositely charged particles was carefully shaken for 10–15 min, which resulted in tube agglomerate formation. Tubes in aggregates were aligned by pulling out from water with a needle.

### Experiments with yeast cells

To adsorb yeast cells, patterned polymer bilayers were exposed to a water dispersion of the cells for 20 min at room temperature. Next, the excess water was removed and replaced with PBS buffer (0.15 M, pH 7.4) that resulted in the rolling of the tubes and encapsulation of the cells within 30 min to 1 hour. Agglomerates with encapsulated yeast cells were incubated in Alpha medium w/o nucleosides (Biochrom AG) at 25 °C for 24 hours.

### Microscopy

For confocal imaging, a Zeiss LSM 780 NLO microscope equipped with a Zeiss Plane-Apochromat 20×/0.8 air objective was used. Samples were excited at 405 nm and imaged using a GaAsP spectral detector with 32 channels (detector range was set to 400–700 nm) in Lambda-mode. Spectral unmixing has been achieved using Zen 2010 B Software. The obtained image stacks were processed and analyzed using ImageJ. For light microscopy imaging, a Zeiss Axio microscope equipped with Zeiss 5×, 10×, 20× and 50× air objectives was used.

### SEM

Scanning electron microscopy was performed using a Zeiss NEON 40 microscope with an acceleration voltage of 3 kV using secondary electron detection on samples sputtered with platinum (3 nm).

## Results and discussions

In order to demonstrate the proof of principle, we used pH-responsive self-rolling polymer bilayer films. The bilayer consists of a hydrophilic stimuli-responsive poly(*N*-isopropylacrylamide-*co*-acrylic acid-*co*-benzophenoneacrylate) (p(NIPAM-AA-BA)) bottom layer and hydrophobic poly(methylmethacrylate-*co*-benzophenoneacrylate) (p(MMA-BA)) top layer (Fig. 1a). The polymers were synthesized using free radical polymerization as described earlier.<sup>37,38</sup> These polymers are expected to be biocompatible.<sup>45,46</sup> The bilayer films were fabricated by sequential deposition of p(NIPAM-AA-BA) and p(MMA-BA) layers on a silicon substrate using dipcoating. The formed bilayer was patterned by irradiation with UV light through a photomask that causes photoactivation of the benzophenone fragments and crosslinking of the polymers. The irradiated film was rinsed with chloroform or acetone in order to remove non-crosslinked polymers leaving rectangular bilayers (Fig. 2a). Afterwards the films were dried at 80 °C in a vacuum oven for 24 h to remove traces of solvents.

The random copolymer of *N*-isopropylacrylamide, acrylic acid and benzophenone acrylate p(NIPAM-AA-BPA) demonstrates pH-dependent swelling in an aqueous environment. Swelling in distilled water (pH = 5.5) at room temperature is, however, very slow and the bilayer remains undeformed for a considerable time – approximately 1 h. The transition temperature and the swelling/rolling rate increase with the increase of ionic strength and pH of the aqueous solution that is due to boosted dissociation of acrylic acid (pK<sub>a</sub> = 5.5). For example, transfer of the bilayer into a PBS 0.15 M, pH = 7.4, buffer leads

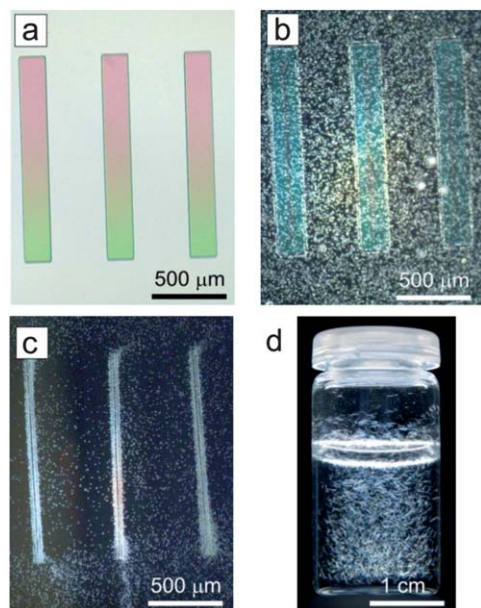


**Fig. 2** Polymer bilayers at different stages of processing. (a) Bright field microscopy image of the patterned bilayer after photolithography and development; (b) dark field microscopy image after adsorption of yeast cells (in water, at room temperature); (c) dark field microscopy image after tube rolling and encapsulation of the cells (in PBS pH 7.4 buffer, at RT); and (d) photograph of aqueous dispersion of self-rolled tubes.

to very quick rolling, and the formation of tubes occurs in 5–10 minutes (Fig. 2b and c). The average diameter of the tubes is *ca.* 20  $\mu\text{m}$  and the length is 1.5 mm, which is defined by the size of the pattern. After rolling, the tubes can be released from the substrate and washed with water into a glass vial, where they chaotically flow without forming aggregates (Fig. 2d). The tubes can be unrolled and encapsulated materials can be released depending on the number of rolls.<sup>37</sup>

In order to assemble the tubes, they were transferred into millipore water and a small amount<sup>47</sup> of water dispersion of 1  $\mu\text{m}$  large  $\text{SiO}_2$  particles with a grafted positively charged 60 nm thick polyelectrolyte poly((2-dimethylamino)ethyl methacrylate) (PDMAEMA) brush layer was added (Fig. 3a). The particle-tube dispersion was carefully shaken, which led to fast (10–20 min) aggregation of the tubes due to the formation of a polyelectrolyte complex between the charged groups on the particle (amino, PDMAEMA) and the tube (carboxylic, PAA) surfaces (Fig. 3b–e). On the other hand, injection of an excess of particles<sup>48</sup> did not lead to aggregation of the tubes. The tubes are also unable to aggregate without the addition of the particles. In the first case, the surface of the tubes is not saturated with the particles, and tubes have a “patchy” surface consisting of areas with negative charge (polymer surface) and areas with positive charge (particles). As a result of the interactions between positive and negative patches, the tubes are able to adhere to each other. In the second case, the tube surface is quickly saturated with positively charged particles, leading to charge inversion of the tube surface. These positively charged tubes covered with the particles repel each other due to electrostatic interaction and are unable to assemble.

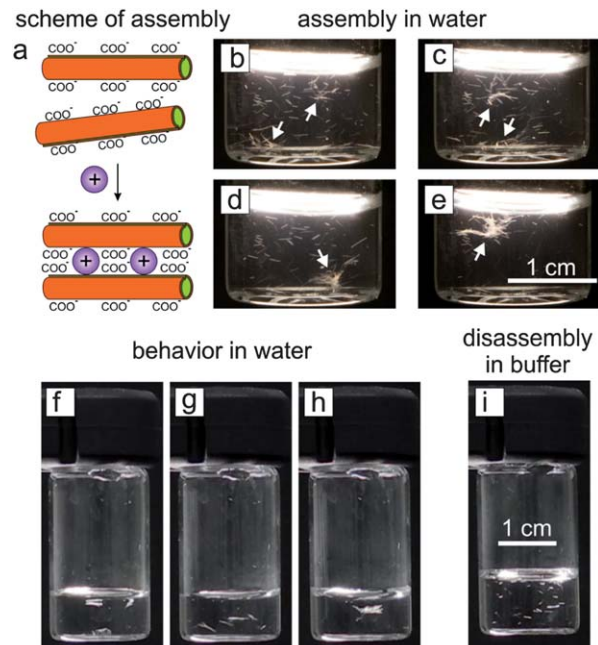


**Fig. 3** Self-assembly of self-rolled tubes: (a) scheme of physical crosslinking of tubes by oppositely charged particles; (b–e) optical photographs of microtubes during self-assembly ( $c = 180$  tubes per ml); (f and g) optical photographs of microtube aggregates in water after shaking ( $c = 90$  tubes per ml); and (i) optical photographs of the disassembly of microtube aggregates in PBS buffer.

The formed aggregates are mechanically stable in Millipore water. Upon intensive shaking, they can break apart into smaller aggregates, which however, re-assemble again (Fig. 3f–h). The aggregates are less stable in a saline buffer environment. For example, fresh aggregates easily break apart into smaller ones or separate tubes after transfer to PBS 0.15 M, pH = 7.4 buffer (Fig. 3i). In fact, an increase of ionic strength leads to screening of the charges of the carboxylic and amino groups that results in weakening of the bonds between the tubes and disassembly. Transfer of the tubes obtained by disassembly of aggregates back into pure water leads to restoration of the electrostatic interactions and re-agglomeration of the tubes (not shown). The self-rolled tubes, thus, demonstrate the ability to undergo reversible stimuli-controlled assembly–disassembly.

Next, we modelled the self-assembly of the tubes. The tubes are linked by multiple non-covalent bonds formed between the tube surface and brush layer on the particles. While a small number of non-covalent bonds is relatively weak and can be easily broken, the probability to break many non-covalent bonds is small. We followed different scenarios of aggregation by considering the assembly of 3 tubes (Fig. 4). All three tubes are separate at the beginning (Fig. 4a). Let us consider that the green tube sticks to the blue one (Fig. 4b), and finally the red tube sticks to the aggregate of blue and green (Fig. 4c). Since the contact area between the green and the blue tubes is not large, they can rotate with a characteristic rotational time  $-t_1$ . As soon as both tubes align with each other, the contact area between them will increase and further rotation will be suppressed. On the other hand, the time that is needed for the red tube to reach



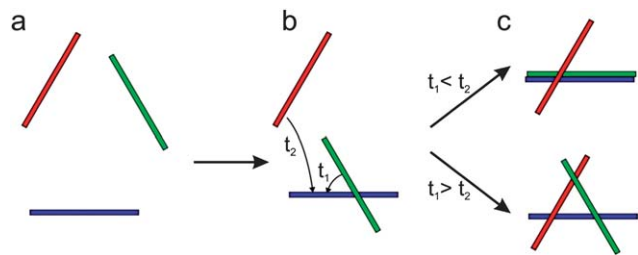


**Fig. 4** Scheme of the agglomeration of 3 tubes in dispersion. All three tubes are separate in the first moment. The green tube sticks to the blue one and, finally, the red tube sticks to the aggregate of blue and green ones.  $t_1$  and  $t_2$  are the times needed for rotation of the green tube and diffusion of the red tube, respectively.

the aggregate shall be denoted by  $t_2$ . If  $t_1 \gg t_2$  the green and blue tubes will not have enough time to align. In this case, the red tube will stick to both tubes and stabilize the disordered structure by forming additional bonds. In the opposite case for  $t_1 \ll t_2$  the green and the blue tubes will be able to orient parallel to each other before the red tubes stick to them. This scenario can easily be extended to a larger number of tubes. The rotational time ( $t_1$ ) for a thin rigid rod scales with the third power of the length of the rod, i.e.  $t_1 \sim l^3$ .<sup>49</sup> The translational time ( $t_2$ ) is given by the diffusion of the rod over the average distance between two rods,  $\xi \sim c^{-1/3}$ , where  $c$  denotes the concentration of tubes/rods. The diffusion coefficient for the translational diffusion of the rod can be assumed to scale as  $D \sim 1/l$ .<sup>49</sup> The typical distance over which the tubes can diffuse during time  $t_1$  is thus given by  $\xi \sim l$ . Therefore, one can expect that if the distance between the tubes is much larger than their own length, the formation of more ordered agglomerates is expected. The characteristic concentration scales accordingly as  $c^* \sim 1/l^3$ . The distance between the tubes illustrated in Fig. 3b–e, as calculated from their concentration, is ca.  $d = 1.8$  mm, which is comparable to their length  $l = 1.6$  mm. Therefore, one can expect the formation of both ordered and unordered agglomerates in this case. Moreover, the tubes in the aggregates, which were obtained from more ( $c = 250$  tubes per ml, Fig. 5c–e) and less ( $c = 90$  tubes per ml, Fig. 3f–h) concentrated dispersions, are less and more ordered, respectively. Apparently, self-assembly of self-rolled tubes is close to self-assembly of lyotropic liquid crystals and is expected to depend on the aspect ratio (ratio of length to diameter). The detailed investigation of the effects of aspect ratio and size of the tubes on their self-assembly is, however, beyond the scope of this manuscript.

The tubes strongly align in one direction when a force is applied. This, for example, occurs when the aggregates are pulled out from the water with a needle (Fig. 5). Moreover, aggregates where tubes are aligned are more stable compared to ones where the tubes are disordered – the aligned aggregates do not break apart in the PBS buffer. The character of tube orientation corresponds to orientation in nematic liquid crystals – tubes are oriented in one direction while their centers of mass are unordered. We estimated a two-dimensional degree of tube orientation ( $S$ ) using eqn (1).<sup>50</sup> It was found that the orientation

degree in the sample illustrated in Fig. 5f–h ( $c = 50$  tubes per ml) is extremely high,  $S = 0.98$ . Tubes in the sample illustrated in Fig. 5c–e, which was obtained by assembly at higher concentration of microtubes ( $c = 250$  tubes per ml), have an apparently lower orientation degree.

$$S = \frac{\langle 3(\cos \theta)^2 - 1 \rangle}{2} \quad (1)$$

We estimated the porosity of the formed agglomerates by considering the inner diameter of the tubes, wall thickness as well as packing density of the tubes. The inner diameter ( $d_{\text{inn}}$ ) varies in the range of 10–100  $\mu\text{m}$ , the thickness ( $d_{\text{wall}}$ ) of the swollen wall is ca. 1–5  $\mu\text{m}$  depending on the thickness of polymer layers. The maximal packing density of cylinders is ca. 0.91. The porosity ( $P$ , ratio of pore volume to total volume), which was estimated using eqn (2), varies in the range  $P = 76$ –90%.

$$S = \frac{(0.5d_{\text{inn}})^2}{0.91(0.5d_{\text{inn}} + d_{\text{wall}})^2} \quad (2)$$

Next, we demonstrated the possibilities for fabrication of complex porous architectures consisting of microtubes with different properties. In particular, we fabricated two types of porous structures formed by tubes of two sorts which are labelled with green and red fluorescent quantum dots admixed to a PMMA layer. In one experiment, tubes of one sort (red ones) were assembled by crosslinking with colloidal particles and stretched by pulling with a needle. The formed aggregate of uniaxially aligned tubes was immersed in dispersions of tubes of the second sort (green ones). The negatively charged green tubes stuck to the positively charged particle patches presented on the aggregate of red tubes (Fig. 6a and b), starting to form a “core-shell” structure. In the second experiment, green tubes were mixed with an excess of PDMAEMA-coated particles in PBS buffer that terminates aggregation, and incubated together for 30 min. The particle-coated but not agglomerated green tubes were added to a dispersion of red ones in water, and as a result an agglomerate (Fig. 6c and d) consisting of randomly distributed red and green tubes was formed (cross-sections in Fig. 6e and f).

Finally, we explored the possibility of fabricating a porous self-assembled construct where tubular pores are filled with cells (Fig. 7). For this, we adsorbed yeast cells from a water dispersion on the top of a patterned unfolded p(NIPAM-AA-BA)/p(MMA-BA) bilayer. After the yeast cells had settled down from their aqueous dispersion, the water was replaced with PBS (pH 7.4) buffer to stimulate rolling of the tubes and encapsulation of the yeast cells. The tubes filled with cells were washed from the substrate with several milliliters of water into a glass vial. Afterwards, the tubes were assembled into agglomerates by shaking together with a small amount of oppositely charged particles. The assembled tubes were aligned by pulling them out from the water with a needle (similar to the previous experiments, Fig. 7a), transferring them into the culture medium and incubating them for 24 h at room temperature. The number of cells in the tubes increased significantly, which indicates the viability of yeast cells as well as free diffusion of

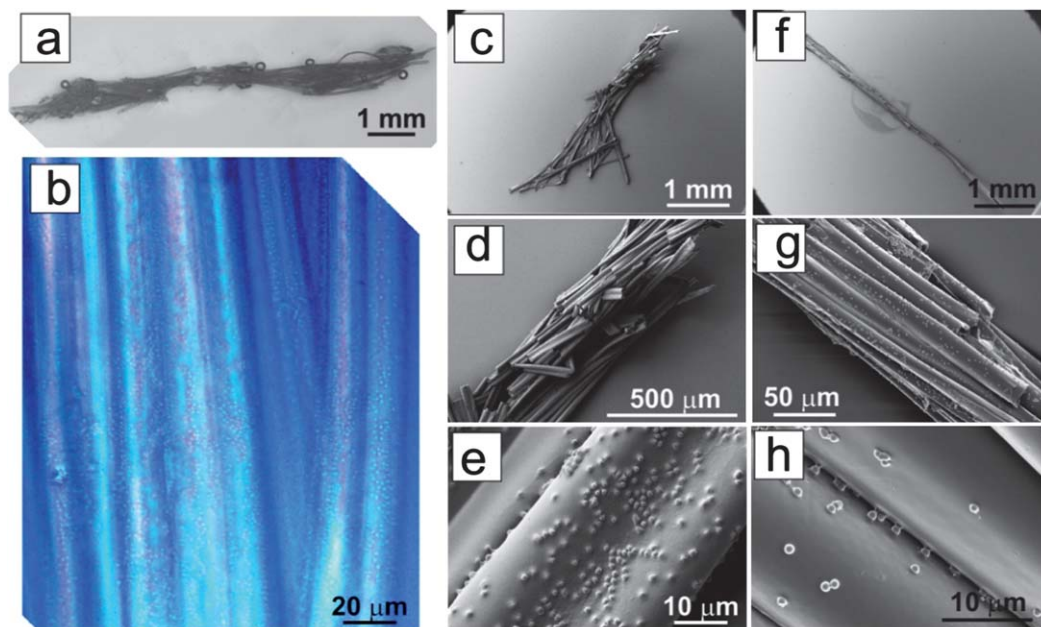


**Fig. 5** Aligned self-assembled self-rolled tubes. (a and b) Optical microscopy, (c–h) scanning electron microscopy images of two aggregates (c–e and f–h) formed by self-rolled tubes crosslinked by positively charged particles and aligned by pulling out from the water with a needle.

nutrition molecules into the tubes (Fig. 7b). In this experiment we fabricated tubes with a small diameter ( $d = 20 \mu\text{m}$ ), which is very close to the size of the yeast cells ( $d = 5 \mu\text{m}$ ), in order to demonstrate the advantage of our method. Obviously, post-filling of narrow tubes, which are disconnected from the tubular network, with cells is almost impossible due to the slow migration of cells into the narrow tubes. Indeed, some tubes,

which were occasionally not filled with cells during tube formation, remaining empty after incubation in the cell culture medium. For example, tube 1 (Fig. 7a) was empty after cell encapsulation and it remained empty after 24 h of incubation in the cell culture medium. In contrast, tube 2, which was initially partly filled with yeast cells, is completely filled with yeast cells after incubation. In this experiment yeast cells were used for

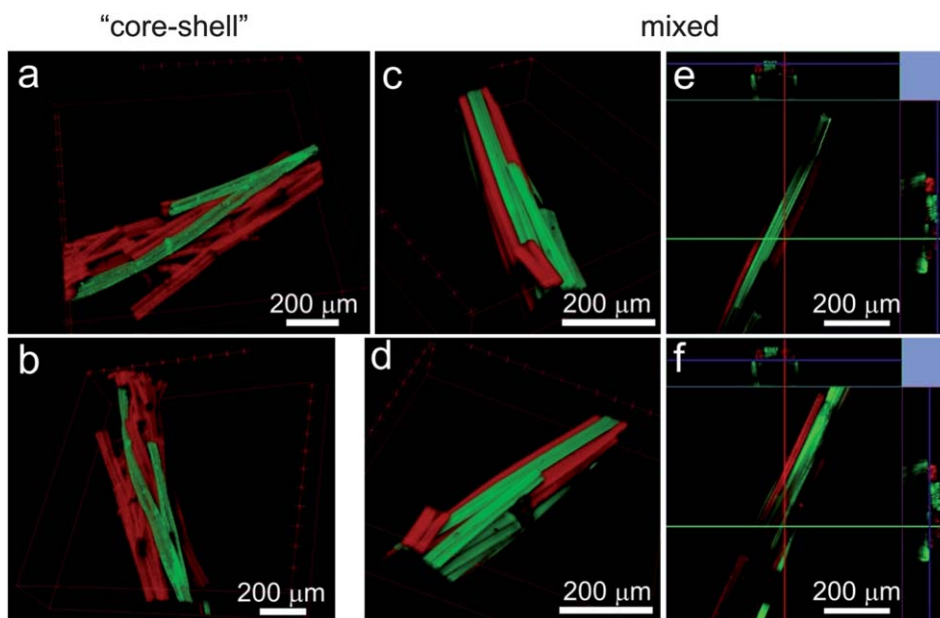


**Fig. 6** Confocal microscopy images of assemblies of microtubes with different colors. (a and b) 3D reconstruction of a “core-shell” porous scaffold, where green tubes are immobilized on an assembly of red ones. (c and d) 3D reconstruction of a “mixed” porous scaffold, where green tubes are first coated by PDMAEMA particles and then assembled together with red ones. (e and f) cross-section of a mixed scaffold (c and d) in different planes. Due to low penetration depth of light beam, imaging of the whole aggregate was not possible.

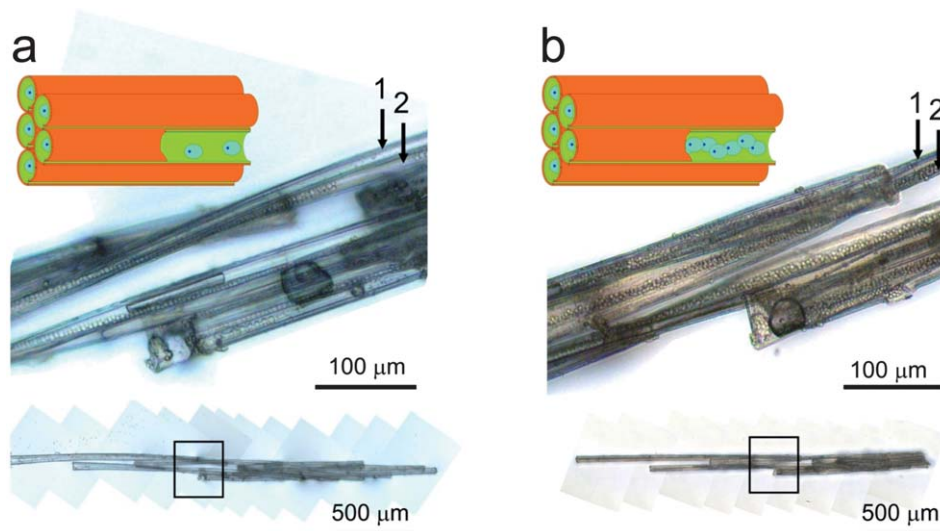


**Fig. 7** Porous 3D construct obtained by self-assembly of self-rolled tubes filled with yeast cells: (a) directly after self-assembly; (b) after 1 day of incubation in the cell culture medium. The images in the lower panel are the microscopy snapshots of the whole cell-filled agglomerate. The images in the middle panel are the magnifications of the areas restricted by rectangles. Tubes 1 and 2 are empty and partially filled with yeast cells, respectively right after assembly. Tube 1 remains empty after incubation in the cell culture medium. Tube 2 is completely filled with cells after incubation in the cell culture medium.

demonstration of the proof of the concept. In fact it was demonstrated that the number of yeast cells increases with time and cells receive enough nutrition, which might be the issue in the narrow tubes. Previous research demonstrated that mammalian cells can also be encapsulated inside tubes,<sup>51</sup> which potentially allows fabrication of 3D scaffolds for tissue engineering.

## Conclusion

We have developed a novel approach for the fabrication of self-assembled porous scaffolds with uniaxial tubular pores. The approach is based on the use of microtubes formed by the stimuli-induced rolling of rectangular bilayers consisting of hydrophobic and stimuli-responsive hydrophilic polymers. Any micrometer-sized objects, for example yeast cells, can be encapsulated inside the tubes during their rolling. The self-rolled tubes filled with yeast cells can be easily assembled into a uniaxial tubular scaffold homogeneously filled with the cells. The main advantage of this approach is the possibility to homogeneously fill the pores with any kind of matter – inorganic, organic or living. Moreover, the approach allows design of porous materials with complex architectures formed by tubes of different sorts.

The developed approach is versatile and very simple. Indeed, the preparation of polymer films does not require expensive equipment and is easy to perform. The polymers, which were used in this paper, are however not biodegradable. On the other hand since the approach is generic, a variety of polymers with different properties such as biodegradability and electric conductivity can be used, which allows design of novel materials with advanced properties for biomedical purposes, microelectronic, 3D light-emitting devices, catalysis and energy storage.

## Acknowledgements

The authors are grateful to DFG (Grant IO 68/1-1) and IPF for financial support. The authors are grateful to Stefan Diez (B CUBE, Dresden and MPI-CBG) and Jan Peychl (Light Microscopy Facility, MPI-CBG) for assistance with confocal microscopy experiments.

## Notes and references

- 1 K. S. Toohey, N. R. Sottos, J. A. Lewis, J. S. Moore and S. R. White, *Nat. Mater.*, 2007, **6**, 581–585.
- 2 A. P. Esser-Kahn, P. R. Thakre, H. F. Dong, J. F. Patrick, V. K. Vlasko-Vlasov, N. R. Sottos, J. S. Moore and S. R. White, *Adv. Mater.*, 2011, **23**, 3654–3658.
- 3 P. Greil, T. Lifka and A. Kaindl, *J. Eur. Ceram. Soc.*, 1998, **18**, 1961–1973.
- 4 B. J. Hinds, N. Chopra, T. Rantell, R. Andrews, V. Gavalas and L. G. Bachas, *Science*, 2004, **303**, 62–65.
- 5 K. A. Kilian, L. M. H. Lai, A. Magenau, S. Cartland, T. Bocking, N. Di Girolamo, M. Gal, K. Gaus and J. J. Gooding, *Nano Lett.*, 2009, **9**, 2021–2025.
- 6 B. H. King, A. Gramada, J. R. Link and M. J. Sailor, *Adv. Mater.*, 2007, **19**, 4044–4048.
- 7 D. Hermann, M. Diem, S. F. Mingaleev, A. Garcia-Martin, P. Wolffe and K. Busch, *Phys. Rev. B: Condens. Matter Mater. Phys.*, 2008, 77.
- 8 M. F. L. Johnson and W. E. Stewart, *J. Catal.*, 1965, **4**, 248–252.
- 9 H. Nakajima, *Prog. Mater. Sci.*, 2007, **52**, 1091–1173.
- 10 R. Prasher, *J. Appl. Phys.*, 2006, **100**, 064302.
- 11 E. Khaleghi, E. Olevsky and M. Meyers, *J. Am. Ceram. Soc.*, 2009, **92**, 1487–1491.
- 12 F. Feil, V. Cauda, T. Bein and C. Bräuchle, *Nano Lett.*, 2012, **12**(3), 1354–1361.

- 13 M. J. Yaszemski, R. G. Payne, W. C. Hayes, R. Langer and A. G. Mikos, *Biomaterials*, 1996, **17**, 175–185.
- 14 H. Ma, J. Hu and P. X. Ma, *Adv. Funct. Mater.*, 2010, **20**, 2833–2841.
- 15 X. Hu, H. Shen, F. Yang, J. Bei and S. Wang, *Biomaterials*, 2008, **29**, 3128–3136.
- 16 L. R. Madden, D. J. Mortisen, E. M. Sussman, S. K. Dupras, J. A. Fugate, J. L. Cuy, K. D. Hauch, M. A. Laflamme, C. E. Murry and B. D. Ratner, *Proc. Natl. Acad. Sci. U. S. A.*, 2010, **107**, 15211–15216.
- 17 G. C. Engelmayr, M. Y. Cheng, C. J. Bettinger, J. T. Borenstein, R. Langer and L. E. Freed, *Nat. Mater.*, 2008, **7**, 1003–1010.
- 18 H. Kenar, G. T. Kose, M. Toner, D. L. Kaplan and V. Hasirci, *Biomaterials*, 2011, **32**, 5320–5329.
- 19 D. Yucel, G. T. Kose and V. Hasirci, *Biomacromolecules*, 2010, **11**, 3584–3591.
- 20 J. Li, T. A. Rickett and R. Shi, *Langmuir*, 2008, **25**, 1813–1817.
- 21 W. N. Bian and N. Bursac, *Biomaterials*, 2009, **30**, 1401–1412.
- 22 P. X. Ma and R. Zhang, *J. Biomed. Mater. Res.*, 2001, **56**, 469–477.
- 23 L. M. Mathieu, T. L. Mueller, P. E. Bourban, D. P. Pioletti, R. Muller and J. A. E. Manson, *Biomaterials*, 2006, **27**, 905–916.
- 24 H. F. Zhang, I. Hussain, M. Brust, M. F. Butler, S. P. Rannard and A. I. Cooper, *Nat. Mater.*, 2005, **4**, 787–793.
- 25 H. Zhang and A. I. Cooper, *Adv. Mater.*, 2007, **19**, 1529–1533.
- 26 H. F. Zhang, J. Long and A. I. Cooper, *J. Am. Chem. Soc.*, 2005, **127**, 13482–13483.
- 27 S. Stokols and M. H. Tuszynski, *Biomaterials*, 2004, **25**, 5839–5846.
- 28 Y. Nakamichi, Y. Hirai, H. Yabu and M. Shimomura, *J. Mater. Chem.*, 2011, **21**, 3884–3889.
- 29 L. Ionov, *Soft Matter*, 2011, **7**, 6786–6791.
- 30 T. G. Leong, A. M. Zarafshar and D. H. Gracias, *Small*, 2010, **6**, 792–806.
- 31 B. Yuan, Y. Jin, Y. Sun, D. Wang, J. Sun, Z. Wang, W. Zhang and X. Jiang, *Adv. Mater.*, 2012, **24**, 890–896.
- 32 G. Huang and Y. Mei, *Adv. Mater.*, 2012, **24**, 2517–2546.
- 33 T. G. Leong, C. L. Randall, B. R. Benson, N. Bassik, G. M. Stern and D. H. Gracias, *Proc. Natl. Acad. Sci. U. S. A.*, 2009, **106**, 703–708.
- 34 J. S. Randhawa, T. G. Leong, N. Bassik, B. R. Benson, M. T. Jochmans and D. H. Gracias, *J. Am. Chem. Soc.*, 2008, **130**, 17238–17239.
- 35 P. Cendula, S. Kiravittaya, I. Monch, J. Schumann and O. G. Schmidt, *Nano Lett.*, 2011, **11**, 236–240.
- 36 G. S. Huang, Y. F. Mei, D. J. Thurmer, E. Coric and O. G. Schmidt, *Lab Chip*, 2009, **9**, 263–268.
- 37 S. Zakharchenko, N. Pureskiy, G. Stoychev, M. Stamm and L. Ionov, *Soft Matter*, 2010, **6**, 2633–2636.
- 38 G. Stoychev, S. Zakharchenko, S. Turcaud, J. W. C. Dunlop and L. Ionov, *ACS Nano*, 2012, **6**, 3925–3934.
- 39 S. Zakharchenko, E. Sperling and L. Ionov, *Biomacromolecules*, 2011, **12**, 2211–2215.
- 40 G. Stoychev, N. Pureskiy and L. Ionov, *Soft Matter*, 2011, **7**, 3277–3279.
- 41 M. Jamal, A. M. Zarafshar and D. H. Gracias, *Nat. Commun.*, 2011, **2**, 527.
- 42 N. Pureskiy and L. Ionov, *Langmuir*, 2011, **27**, 3006–3011.
- 43 L. Qu and X. Peng, *J. Am. Chem. Soc.*, 2002, **124**, 2049–2055.
- 44 W. K. Bae, K. Char, H. Hur and S. Lee, *Chem. Mater.*, 2008, **20**, 531–539.
- 45 J.-H. Kim and T. R. Lee, *Chem. Mater.*, 2004, **16**, 3647–3651.
- 46 K. W. Lye, H. Tideman, J. C. G. Wolke, M. A. W. Merckx, F. K. C. Chin and J. A. Jansen, *Clin. Oral Implan. Res.*, 2011, DOI: 10.1111/j.1600-0501.2011.02388.x.
- 47 The amount of particles was taken with respect to cover 25–30% of outer surface of tubes.
- 48 Amount of particles is more than required to cover all tubes.
- 49 M. Doi and S. F. Edwards, *The Theory of Polymer Dynamics*, Clarendon Press, 1988.
- 50 L. Onsager, *Ann. N. Y. Acad. Sci.*, 1949, **51**, 627–659.
- 51 S. Pedron, S. van Lierop, P. Horstman, R. Penterman, D. J. Broer and E. Peeters, *Adv. Funct. Mater.*, 2011, **21**, 1624–1630.

Stoychev, G.; Zakharchenko, S.; Turcaud, S.; Dunlop, J.; Ionov, L.

Shape programmed folding of stimuli-responsive polymer bilayers

***ACS Nano*** 2012, 6 (5), 3925–3934



# Shape-Programmed Folding of Stimuli-Responsive Polymer Bilayers

Georgi Stoychev,<sup>†,\*</sup> Svetlana Zakharchenko,<sup>†,\*</sup> Sébastien Turcaud,<sup>§</sup> John W. C. Dunlop,<sup>§</sup> and Leonid Ionov<sup>†,\*</sup>

<sup>†</sup>Leibniz Institute of Polymer Research Dresden, Hohe Straße 6, D-01069 Dresden, Germany and Department of Biomaterials, <sup>‡</sup>Technische Universität Dresden, Physical Chemistry of Polymer Materials, 01062 Dresden, Germany, and <sup>§</sup>Max Planck Institute of Colloids and Interfaces, Am Mühlenberg 1, D-14424, Potsdam, Germany

**D**esign of hollow 3D objects such as capsules and tubes is highly demanded for cell encapsulation, drug delivery and design of self-healing materials.<sup>1</sup> Most approaches for fabrication of capsules are based on the use of particles or fibers as templates, which are covered by functional materials. Hollow functional structures are, thus, formed after the removal of the core. Recently, the use of self-folding films that are able to form different 3D structures was suggested as a template-free alternative to the traditional template-based approaches.<sup>2,3</sup> The main advantage of self-folding films is the possibility to transfer a pattern, created on the surface of the unfolded film, into the inner and outer walls of the folded 3D structure.<sup>4–6</sup>

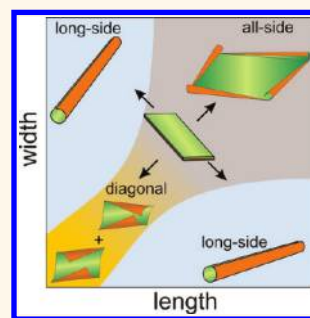
Inorganic and polymer-based bilayers are examples of self-folding films, which fold due to relaxation of internal stresses originated from dissimilar properties of the two layers, such as lattice mismatch, thermal expansion, or swellability. Inorganic-based self-folding films are promising for a variety of fields including transport,<sup>7</sup> nanooptics,<sup>8</sup> energy storage elements,<sup>9</sup> photovoltaic power applications,<sup>10</sup> optics,<sup>11</sup> and engineering of scaffolds,<sup>12–15</sup> as well as being suitable to investigate the role of confinement on cell behavior.<sup>16</sup> Polymer-based self-folding films, on the other hand, are particularly promising for biotechnological applications such as encapsulation of cells<sup>17,18</sup> and design of biomaterials.<sup>19</sup> These and other applications require precise control of the folding for fabrication of 3D objects with a defined shape. In particular, it was demonstrated that the resulting shape of the folded 3D object can be controlled by the shape of the original bilayer. For example, rectangular bilayers form tubes,<sup>17</sup> while star-like bilayers are able to form envelope-like capsules.<sup>18</sup>

Generally, the rolling of a rectangular bilayer may occur according to three different

**ABSTRACT** We investigated the folding of rectangular stimuli-responsive hydrogel-based polymer bilayers with different aspect ratios and relative thicknesses placed on a substrate. It was found that long-side rolling dominates at high aspect ratios (ratio of length to width) when the width is comparable to the circumference of the formed tubes, which corresponds to a small actuation strain.

Rolling from all sides occurs for higher actuation,

namely when the width and length considerably exceed the deformed circumference. In the case of moderate actuation, when both the width and length are comparable to the deformed circumference, diagonal rolling is observed. Short-side rolling was observed very rarely and in combination with diagonal rolling. On the basis of experimental observations, finite-element modeling and energetic considerations, we argued that bilayers placed on a substrate start to roll from corners due to quicker diffusion of water. Rolling from the long-side starts later but dominates at high aspect ratios, in agreement with energetic considerations. We have shown experimentally and by modeling that the main reasons causing a variety of rolling scenarios are (i) non-homogenous swelling due to the presence of the substrate and (ii) adhesion of the polymer to the substrate.



**KEYWORDS:** thermoresponsive · polymer · bilayer · tube · folding

scenarios: long-side, short-side, and diagonal rolling (see Figure 1). The effects of film shape on the character of folding were experimentally investigated on examples of purely inorganic and composite polyaniline–inorganic bilayers. Smela *et al.* showed that short-side rolling was preferred in the case of free homogeneous actuation and that this preference increased with aspect ratio (ratio of length to width of rectangular pattern).<sup>20</sup> Li *et al.* experimentally demonstrated the opposite scenario<sup>21</sup> in the case where bilayers are progressively etched from a substrate, namely a preference for long-side rolling. They observed that when the tube circumference was much larger than the width, or the aspect ratio of the rectangle was high, rolling always occurred from the long side. When the tube circumference was much smaller than the width

\* Address correspondence to ionov@ipfdd.de.

Received for review January 7, 2012 and accepted April 24, 2012.

Published online April 24, 2012  
10.1021/nn300079f

© 2012 American Chemical Society

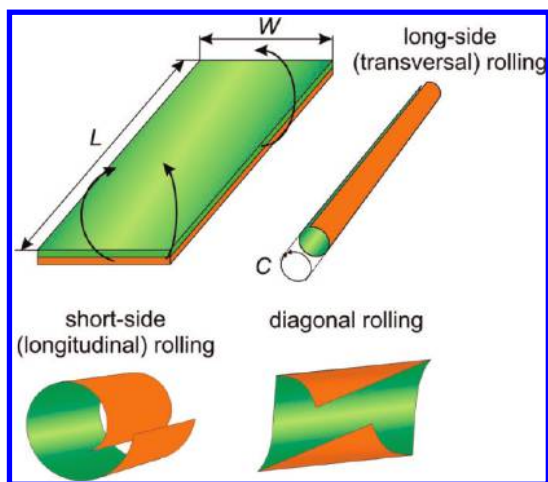


**Figure 1.** Scheme of rolling of a polymer bilayer according to different scenarios: short-side, long-side, and diagonal rolling.

and the aspect ratio of the rectangular bilayer was not very high, the rolling resulted in a mixed yield of long- and short-side rolling, as well as a “dead-locked turnover” shape. Short-side rolling occurred at small aspect ratios when the deformed circumference is close to the width. In these self-rolling systems, the active component undergoes relatively small volume changes or actuation strains, which are nearly homogeneous over the whole sample. Hydrogel films, which are also able to fold, demonstrate considerably different properties.<sup>22–24</sup> First, hydrogels undergo large volume changes (up to 10 times) upon swelling and contraction. Second, the swelling of a hydrogel is often kinetically limited: due to slow diffusion of water through a hydrogel, the parts that are closer to the edges swell first, while the parts that are closer to the center of the films swell later. Thus, the actuation profile inside the active layer is heterogeneous. In this paper we investigate the effects of shape, size, and rolling curvature on the direction of folding of rectangular polymer bilayers placed on a substrate, where the bottom component is a stimuli-responsive hydrogel.

## EXPERIMENTAL OBSERVATIONS

**Experimental Preparation.** Two families of polymeric bilayers, made of an active and a passive layer, are studied. The passive component is either hydrophobic polycaprolactone (PCL) or random copolymer poly(methylmethacrylate-co-benzophenone acrylate) (P(MMA-BA)). The active component is a thermoresponsive hydrogel formed either by photo-cross-linked poly(*N*-isopropylacrylamide-co-acrylic acid-co-benzophenone acrylate) (P(NIPAM-AA-BA)) or by poly(*N*-isopropylacrylamide-co-benzophenone acrylate) (P(NIPAM-BA)). Thermoresponsive hydrogels swell and shrink at reduced and elevated temperature, respectively. The passive hydrophobic P(MMA-BA) and PCL layers restrict swelling of the active hydrogel. As a result, the

bilayer made of these polymers does not uniformly expand/shrink but folds and unfolds due to swelling and collapse of the hydrogel layer.

P(NIPAM-AA-BA)/P(MMA-BA) and P(NIPAM-BA)/PCL bilayers were prepared using photolithography, as described earlier.<sup>17</sup> First, we prepared two sets of patterned bilayers of P(NIPAM-AA-BA)/P(MMA-BA), which differ in thickness ( $H$ ) of the P(MMA-BA) layer, which results in different rolling curvature. One set formed narrow tubes with a diameter  $d = 20 \mu\text{m}$  ( $H_{\text{P(MMA-BA)}} = 500 \text{ nm}$ ;  $H_{\text{P(NIPAM-AA-BA)}} = 1200 \text{ nm}$ ), while the second set forms wider tubes with diameters in the range  $d = 70\text{--}90 \mu\text{m}$  ( $H_{\text{P(MMA-BA)}} = 1200 \text{ nm}$ ;  $H_{\text{P(NIPAM-AA-BA)}} = 1200 \text{ nm}$ ). Rectangular bilayers of different lengths ( $L = 100\text{--}1000 \mu\text{m}$ ) and aspect ratios (ratio of length ( $L$ ) to width ( $W$ ),  $A = L/W = 1\text{--}8$ ) were fabricated using specially designed photomasks. After removal of the non-cross-linked polymer, the patterned bilayers were exposed to PBS solution (pH = 7.4) at room temperature. As a result, photo-cross-linked P(NIPAM-AA-BA) swelled, leading to rolling of the bilayer and formation of tubes. The folded films formed by each set of bilayers were then mapped by optical microscopy in order to assess the rolling radius as well as the deformation pattern (see Figures 2 and 3).

**Experimental Results.** It was found that the final diameter of the tube is independent of the size of the bilayer ( $L$ ,  $W$ ), but everything else being equal (Young modulus of active and passive layer as well as activation strain), it is solely controlled by the relative thickness of the active and passive layers<sup>25</sup> and, thus, is (almost) constant for each set of experiments. The direction of rolling strongly depends on the size and shape of the films as well as on the thickness of the active and passive layer (see Figure 4). We distinguished four general types of rolling: long-side rolling, diagonal rolling, short-side rolling, and mixed all-side rolling, which is a combination of the first three types. The character of preferential rolling is plotted as a function of the absolute values of width, length, and aspect ratio, as well as normalized values, which are obtained by dividing the length or width by the typical circumference of the rolled tube ( $C = \pi d$ , Figure 1).

Three types of rolling were observed when narrow tubes ( $d = 20 \mu\text{m}$ ) are formed: long-side, diagonal, and all-side rolling (see Figure 4a). It must be noted that no short-side rolling was observed. The all-side rolling (see Figure 2, a1–3, b1–2) occurs when the width of the films considerably exceeds the circumference of rolling for aspect ratios of 1 or 2. A decrease of the width for an aspect ratio of 2 or more results in preferential long-side rolling (see Figure 2, b3, c1–3, d1–3), when the normalized length is more than 2. Depending on the ratio of width ( $W$ ) to circumference ( $C$ ), incompletely rolled tubes ( $W/C < 1$ ), completely rolled tubes ( $W/C \approx 1$ ), or doubled tubes ( $W/C \geq 2$ ) are formed. A further decrease of the length leads to a mixture between

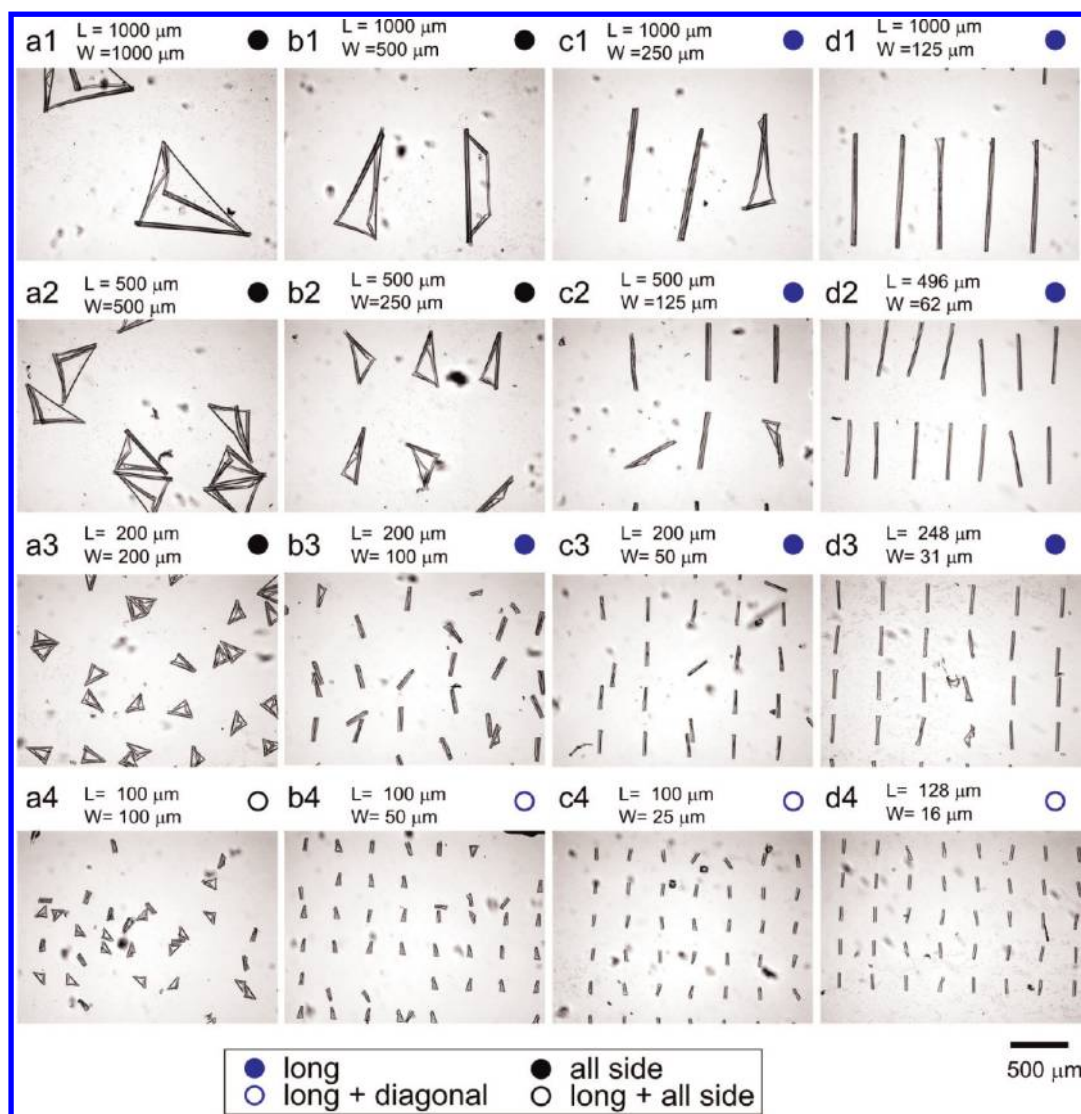


Figure 2. Microscopy snapshots of folded P(NIPAM-AA-BA)-P(MMA-BA) bilayers of different length ( $L$ ) and width ( $W$ ) that form narrow tubes of diameter  $d = 20 \mu\text{m}$ ;  $H_{\text{P(MMA-BA)}} = 500 \text{ nm}$ ;  $H_{\text{P(NIPAM-AA-BA)}} = 1200 \text{ nm}$ .

long-side and diagonal or all-side rolling (see Figure 2, a4, b4, c4, and d4). The most promising parametric window for potential applications, such as microfluidics<sup>24</sup> and cell encapsulation,<sup>17</sup> is thus bilayers with an aspect ratio of 4 or more.

Different rolling behavior is observed when wide tubes ( $d = 70\text{--}90 \mu\text{m}$ ) are formed (see Figure 4b). First, the films with the highest aspect ratio slightly bend and almost do not roll because of the large circumference (see Figure 3, d1–4). Second, other bilayers roll either according to diagonal or all-side rolling scenarios. Diagonal rolling is observed in the cases of square films ( $L/W = 1$ ) when two opposite corners bend toward each other (see Figure 3, a1–4). “Tick or check mark-like” structures (see for example Figure 3, c1, the film in the middle) in combination with diagonal rolling are observed in almost all cases at  $L/W > 1$  when either adjacent or opposite corners bend toward each other. Bending from short sides was observed

in combination with diagonal rolling only in one case (see Figure 3, b4).

The results obtained for narrow (Figure 2 and 4a) and wide (Figure 3 and 4b) tubes plotted as a function of normalized length and width are not fully identical. Figure 4b is shifted to larger values of  $L/C$ . The reason for this effect is not completely clear and could be due to effects related to heterogeneities in the swelling behavior, which are hard to fully consider. On the other hand, there is a clear correlation between the results given in Figure 4a and b, which is qualitatively summed up in Figure 4c. For example, all-side rolling is observed when both length and width considerably exceed the deformed circumference. Diagonal rolling is observed when  $L = W$ , and both are comparable to the circumference. Mixtures of diagonal rolling and the formation of “tick or check mark-like” structures (tube in the middle of Figure 3, c1) are observed when  $L > W$  and both  $L$  and  $W$  are comparable to the circumference.



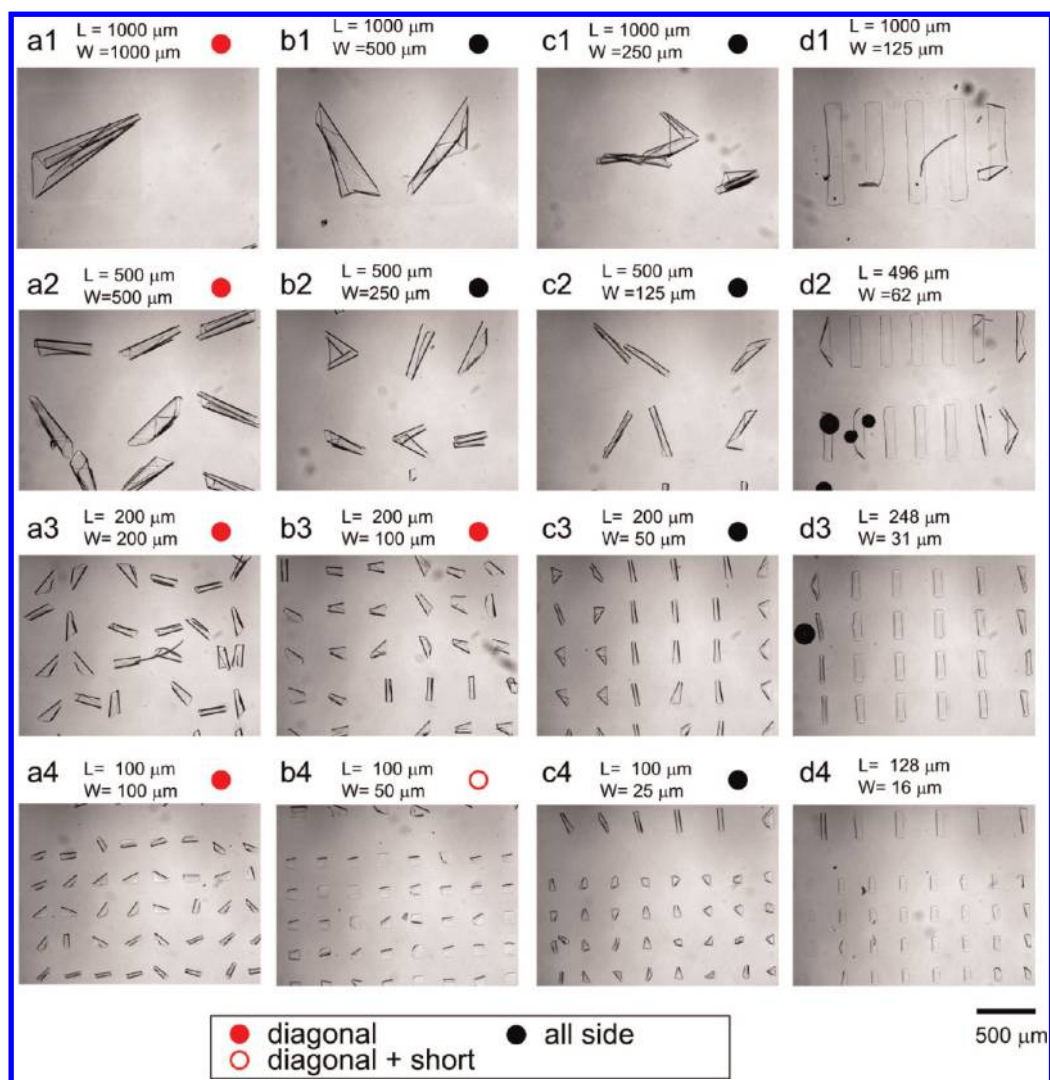
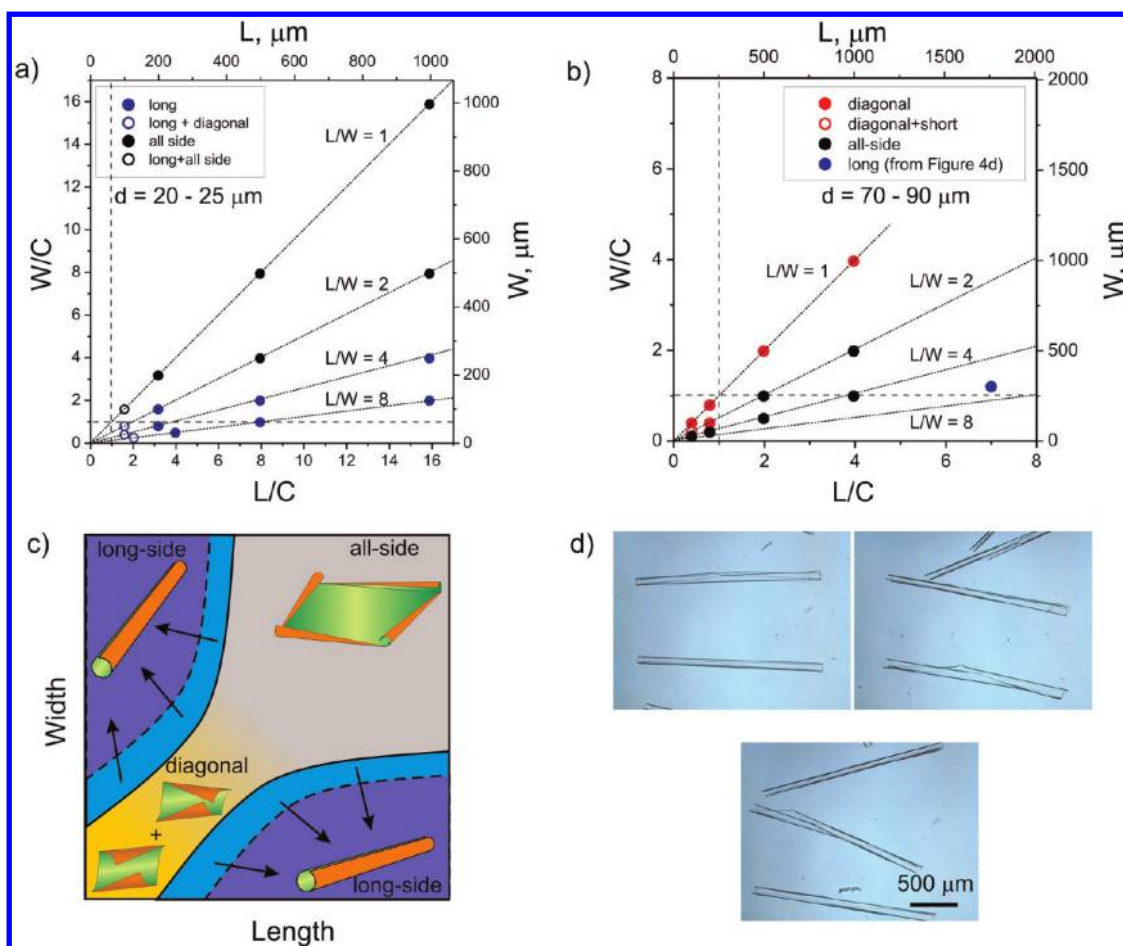


Figure 3. Microscopy snapshots of folded P(NIPAM-AA-BA)-P(MMA-BA) bilayers with different length ( $L$ ) and width ( $W$ ) that form wide tubes of diameter  $d = 70\text{--}90\text{ }\mu\text{m}$ ;  $H_{\text{P(MMA-BA)}} = 1200\text{ nm}$ ;  $H_{\text{P(NIPAM-AA-BA)}} = 1200\text{ nm}$ .

The long-side rolling takes place when the length considerably exceeds the deformed circumference ( $L/C > 4$ ) and the aspect ratio is larger than 4. As a result, long tubes are formed, at least in the case of narrow tubes ( $d = 20\text{ }\mu\text{m}$ ). In order to test the hypothesis that long tubes are formed when  $L/C > 4$  and  $W \approx C$  also in the case of wide tubes ( $d = 70\text{--}90\text{ }\mu\text{m}$ ), we investigated rolling of  $1800\text{ }\mu\text{m} \times 300\text{ }\mu\text{m}$  large bilayer tubes ( $H_{\text{P(MMA-BA)}} = 1200\text{ nm}$ ,  $H_{\text{P(NIPAM-AA-BA)}} = 1200\text{ nm}$ ,  $W/C = 1.2$ ;  $L/C = 7.5$ ). Indeed, rolling resulted in preferential formation of long tubes (see Figure 4d), in agreement with our predictions.

**Mechanism of Rolling.** In order to clarify the variety of observed rolling scenarios, we experimentally investigated swelling and rolling of the bilayers. Rolling was investigated first using members of the second family of patterned bilayers formed by poly(*N*-isopropylacrylamide-co-benzophenone acrylate) and polycaprolactone with high aspect ratio ( $L/W = 6$ ,  $H_{\text{PCL}} = 300\text{ nm}$ ,

$H_{\text{P(NIPAM-BA)}} = 750\text{ nm}$ ).<sup>17</sup> Initially, the polymer films were immersed in warm water, where the active P(NIPAM-BA) hydrogel monolayer is shrunk. The temperature was gradually decreased, and rolling was observed. Diagonal rolling started from corners and stopped when two rolling fronts met each other (Figure 5a). Long-side rolling started later (Figure 5b) but eventually dominated, leading to a switching of the diagonally rolled corners to long-side rolled (Figure 5c,d). The formed double tubes were unrolled at elevated temperature (Supporting Information, Movie S1). The central part of the rolled bilayer, which has a shape of a line (Figure 5e), is still adhered to the substrate after rolling because the bilayer remains almost undeformed there. This adhesion area directs long-side rolling during the second cycle of temperature decrease and prevents short-side rolling. The second rolling, thus, proceeded similar to the first one: rolling starts from the corners and then switches to long-side rolling.



**Figure 4.** Dependence of preferential rolling direction of P(NIPAM-AA-BA)–P(MMA-BA) bilayers on the size and shape of the films when (a) narrow ( $d = 20\text{--}25\text{ }\mu\text{m}$ ,  $H_{\text{P(MMA-BA)}} = 500\text{ nm}$ ;  $H_{\text{P(NIPAM-AA-BA)}} = 1200\text{ nm}$ ) and (b) wide ( $d = 70\text{--}90\text{ }\mu\text{m}$ ,  $H_{\text{P(MMA-BA)}} = 1200\text{ nm}$ ;  $H_{\text{P(NIPAM-AA-BA)}} = 1200\text{ nm}$ ) tubes are formed. Dashed lines correspond to  $L/C = 1$  and  $W/C = 1$  ( $L$  and  $W$  are length and width of the film, respectively;  $C$  is the circumference of the rolled tube). (c) Schematic diagram of rolling scenario as a function of length and width. Arrows indicate how the diagram changes when circumference ( $C$ ) increases. (d) Examples of wide tubes ( $d = 80\text{ }\mu\text{m}$ ,  $H_{\text{P(MMA-BA)}} = 1200\text{ nm}$ ;  $H_{\text{P(NIPAM-AA-BA)}} = 1200\text{ nm}$ ) formed by rolling of  $1800\text{ }\mu\text{m} \times 300\text{ }\mu\text{m}$  large bilayers (corresponds to the blue point in part b).

In order to explain the fact that rolling starts from the corners, we experimentally investigated the swelling process. This was performed in a qualitative manner by observing changes in the interference pattern of white light with the bilayer during swelling. In order to avoid bending and folding of the bilayer during swelling, a very thin P(NIPAM-AA-BA) layer ( $H = 35\text{ nm}$ ) under a thick P(MMA-BA) layer ( $H = 400\text{ nm}$ ) was used. Due to the effect of interference of light, which is mirrored from the top and bottom surfaces of the bilayer, the changes of colors (see Figure 6) reflect changes in the film thickness. It is observed that the color of the films starts to change at the corners first, which confirms the assumption that edge-activation of the active layer due to slow water diffusion into the hydrogels is at the origin of the experimentally observed fact that rolling starts at corners. Thus, on the basis of the observations of rolling and swelling mechanisms, we can argue that diffusion determines folding in the first moments of folding, while

adhesion seems to play a decisive role at later stages of folding.

## THEORETICAL CONSIDERATIONS

**Diffusion-Driven Actuation.** The observed long-side folding of rectangular bilayers for some specific shape parameters contradicts the bending of bilayer actuators, which occurs along the short side.<sup>20,25</sup> However, this holds under the assumption that the active layer is homogeneously activated and that there is no interaction with a substrate. This is the case of a freely floating bilayer, where diffusion of water inside the hydrogel layer is not restricted by any substrate. It was confirmed that such freely floating bilayers undergo short-side rolling that is similar to the behavior of standard actuators (Figure 7a). As the studied bilayers are placed on a substrate, it is reasonable to assume that diffusion of water inside the active monolayer upon activation ( $T < T_{\text{critic}}$ ) occurs primarily through its lateral sides. Additionally, not only does the substrate



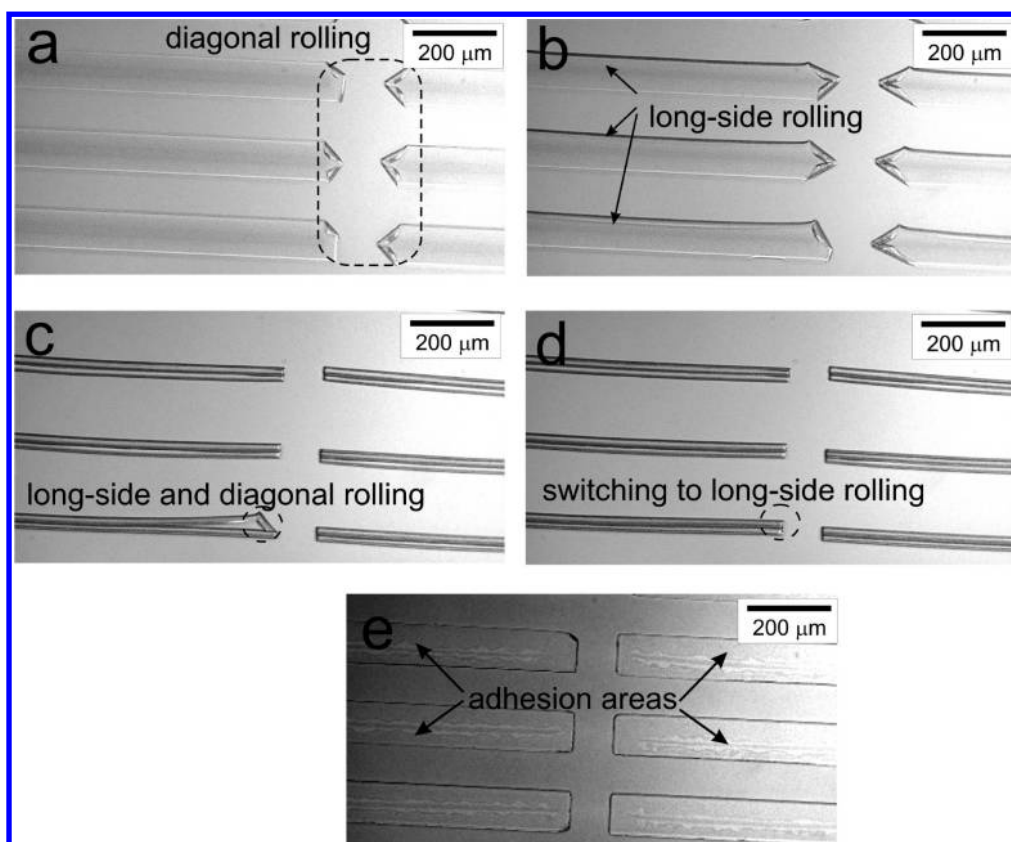


Figure 5. Time-resolved rolling of the P(NIPAM-BA)–PCL bilayer ( $H_{\text{PCL}} = 300 \text{ nm}$ ,  $H_{\text{P(NIPAM-BA)}} = 750 \text{ nm}$ ,  $930 \mu\text{m} \times 90 \mu\text{m}$ ); diameter of the tube  $d = 41 \mu\text{m}$  (a–e, supplementary Movie S1).

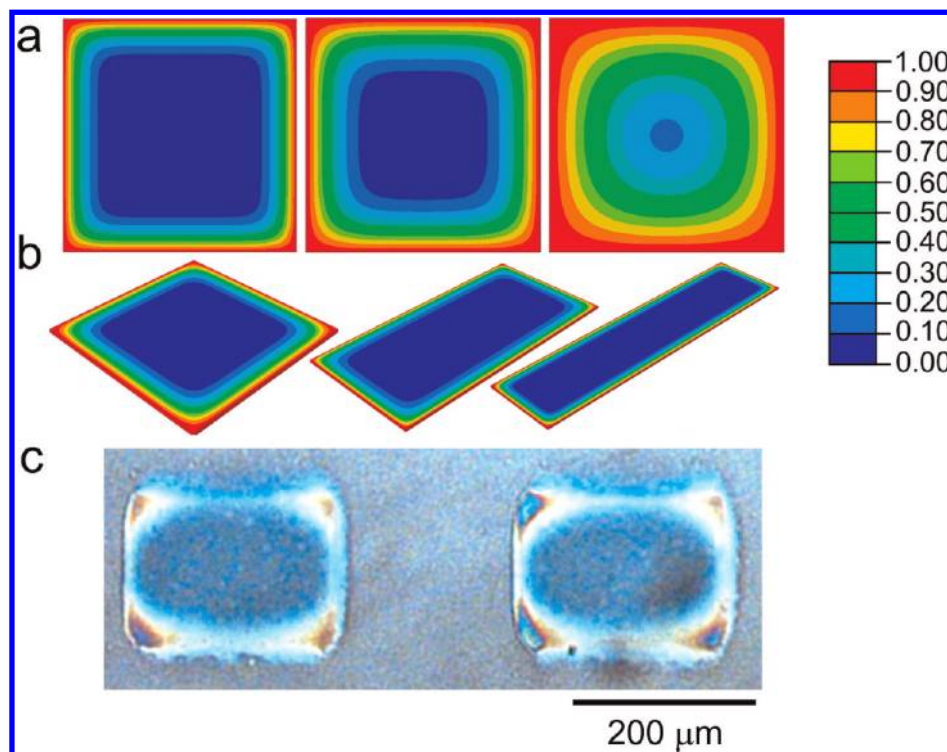
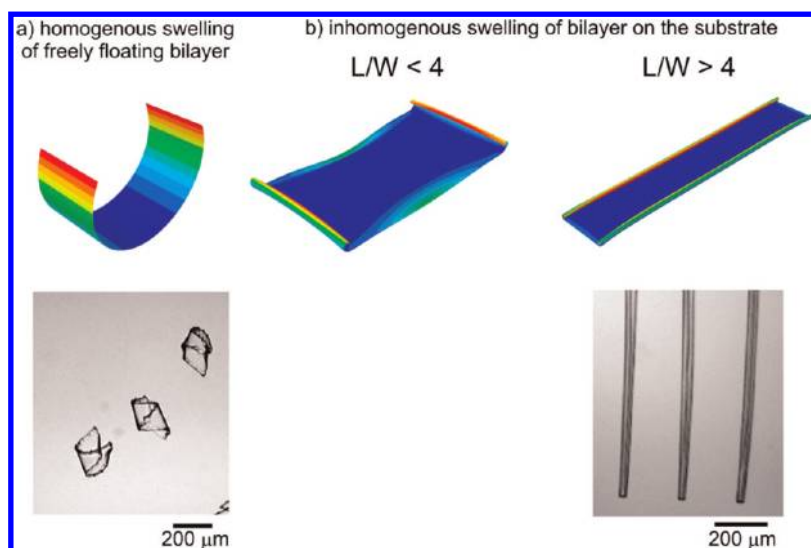


Figure 6. Color map of the calculated swelling (from 0 to 1) controlled by water diffusion in the active monolayer with a lateral constant boundary condition (blue is nonswollen) dependent on time (a) and shape (b) obtained by finite-element simulations as well as experimentally obtained microscopy snapshot of swollen P(NIPAM-BA)–PMMA bilayer ( $H_{\text{P(MMA-BA)}} = 400 \text{ nm}$ ;  $H_{\text{P(NIPAM-AA-BA)}} = 35 \text{ nm}$ ) after few seconds of swelling (c).



**Figure 7.** Simulation and experimentally observed folding of rectangular bilayers at different conditions: (a) freely floating rectangular bilayer (homogeneous swelling, supplementary Movie S2); (b) rectangular bilayer on substrate (inhomogeneous swelling, supplementary Movie S1).

confine diffusion, it also exerts adhesion forces to the bottom surface of the bilayer that impede actuation until a certain threshold of detachment forces is reached. This means that bending, which requires detachment of the substrate, occurs only for a sufficient activation strain. In particular, nonswollen areas do not bend.

**Finite-Element Simulations.** The diffusion pattern is assumed to obey a classical diffusion law (Fick's law) with a constant imposed boundary condition on the lateral sides of the active monolayer. Well known in one dimension, the two-dimensional diffusion pattern was obtained through a finite-element simulation using ABAQUS at different time points for different monolayer shapes (aspect ratio). Diffusion of water inside a hydrogel can be described as a first approximation by steady-state heat diffusion inside a medium with constant diffusivity. We used linear three-dimensional diffusion elements (DC3D8), in order to be able to apply the resulting activation field to actuate bilayers subsequently, and applied a constant boundary condition on the lateral surfaces. The solvent diffusion, however, is a very complex process that is quite difficult to fully describe because the boundary conditions of diffusion change as the film deforms and detaches from the substrate. We aimed to discuss diffusion in the very first moments of swelling, when the film starts to deform, as we believe that subsequent deformation of the film is largely determined by its starting deformation. The simulation allowed us to predict an inhomogeneous two-dimensional diffusion pattern that eventually becomes homogeneous after a sufficient time (see Figure 6a,b).

Subsequently, we applied the obtained thermal field at different time points to a bilayer of the same aspect ratio. Both layers of the bilayer are made of a

linear elastic material with a normalized Young modulus of 1 and a Poisson ratio of 0.3. This crude simplification relies on the fact that the stiffness contrast between the active and the passive layer does not significantly affect the rolling radius of a bilayer.<sup>25</sup> The bottom layer possesses in-plane thermal expansion coefficients equal to 1, whereas the top layer is thermally inactive. In order to understand the influence of substrate adhesion, we imposed a fixed kinematical boundary condition at an internal rectangular bottom surface, scaled from the external shape. We used a fine mesh of first-order eight-node elements with reduced integration (C3D8R), which are able to follow the large displacements at reasonable cost. The deformed shape corresponding to an edge activation of the bilayer at a given time point in the diffusion process was calculated in a static step taking nonlinear geometric effects into account. Adaptive meshing techniques were used to avoid large distortions in mesh elements upon actuation. We compared the obtained results with the one obtained using the Riks method and found no discrepancy between the predicted deformed shapes. Surprisingly, convergence using a combination of adaptive meshing techniques on a fine mesh with a static nonlinear geometric step proved to be better than using the Riks method. This simple uncoupled model already shows that sharp activation strains near the edges combined with an internal constraint of the bottom layer produces interesting deformation patterns for different aspect ratios. In particular, the model predicts that short- and long-side rolling is more favorable at  $L/W < 4$  and  $L/W > 4$ , respectively (see Figure 7b).

The appearance of all-side and diagonal rolling in experiments at smaller aspect ratios accounts for the fact that no preferential direction appears for bending

deformations. Also, imperfections of the material properties of the polymer film and substrate can be responsible for the observed symmetry-breaking.

**Energetic Considerations.** The fact that edge activation of a constrained bilayer leads to long-side rolling is also suggested by plate theory. The elastic energy of plate-like objects can be decomposed into a stretching and a bending term according to Föppl von Kármán plate theory,<sup>26</sup> in which the in-plane strains are integrated over the thickness taking into account the edge activation. This formulation describes accurately the elastic energy of a bilayer plate upon edge activation and can be solved numerically (this will be done in a subsequent paper). Another approach, which is less subtle, but that also leads to accurate results, is solving the 3D mechanical problem by a finite-element method. Essentially the problem can be described in the following way: we make an additive decomposition of the total strain in the active layer into an eigenstrain (or swelling strain) and an elastic strain  $\varepsilon_{kl}^T = \varepsilon_{kl}^{eg} + \varepsilon_{kl}^e$ . The eigenstrain is given as  $\varepsilon_{ij}^{eg} = \alpha \delta_{ij}$ , where  $\delta_{ij}$  is the Kronecker delta tensor, and isotropic swelling is assumed in the current model. The amount of swelling depends on the swelling coefficient  $\alpha$ , which in turn can vary spatially according to the solution of the diffusion equation. As the active layer is constrained by the passive layer, geometric incompatibilities result in elastic strains and thus stresses through Hooke's law,  $\sigma_{ij} = E_{ijkl} \varepsilon_{kl}^e$ . The final shape of the structure upon changes in the spatial distribution and magnitude of  $\alpha$  is calculated by minimizing the elastic energy of the system. For further details of the finite-element method see, for example, ref 27. With the stretching term being linear in thickness, while the bending term is cubic, bending deformations are favored when the plate is sufficiently thin. Unlike in a beam-like bilayer, actuation triggers a biaxial expansion field inside the plate, which creates internal stresses in the long and in the short direction of the plate. Relaxation of internal stresses perpendicular to the edge of the bilayer will lead to bending, whereas relaxation of internal stresses parallel to the edge of the bilayer will produce stretching that will eventually lead to wrinkling, as in the edge of long leaves.<sup>28</sup> Because of the presence of the substrate, internal stresses perpendicular to the edge of the bilayer are more easily relaxed, leading to simple bending, while internal stresses parallel to the edge of the bilayer produce simple stretching. As the aspect ratio increases, it is thus less costly to relax stresses into bending on the long side than on the short side. This explains qualitatively why long-side rolling is observed as the aspect ratio increases.

Finite-element modeling and energetic considerations show that the experimentally observed appearance of long tubes for large aspect ratios and high activation strains are due to (i) non-homogenous swelling due to slow lateral diffusion, as well as (ii) adhesion of the bilayer to the substrate, constraining

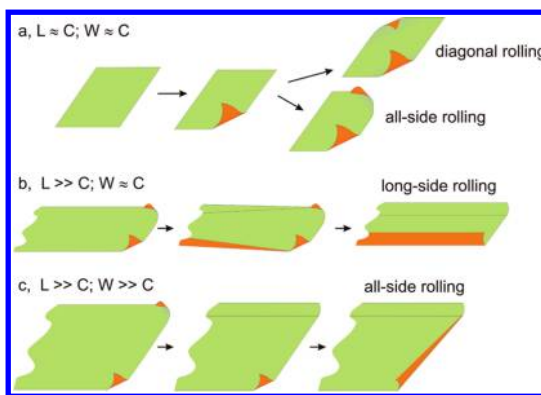


**Figure 8.** Schematic of rolling leading to diagonal rolling, long-side rolling, and all-side rolling.

the deformations. Both these factors are caused by the specific arrangement of the experiment: (i) polymer bilayer is deposited on the substrate and (ii) active polymer is the bottom layer.

**Rolling Scenario.** Finally, by considering modeling and experimental results, the following scenario of rolling of hydrogel-based polymer bilayer lying on a substrate is assigned. The rolling starts from the edges due to faster diffusion of water from the lateral surfaces, which then are able to detach from the substrate and to bend. Rolling can start either from two adjacent (for example Figure 3, d2, right lower polymer film, or Figure 3, b2, left upper film) or opposite edges (almost all polymer films in Figure 2, a2) or from all corners simultaneously, which is less probable if the bilayer is small due to the presence of imperfections and becomes energetically unfavorable once a sufficient actuation strain is reached. Rolling is almost immediately finished if the deformed circumference is comparable to the size of the bilayer. As a result, diagonally rolled tubes are formed if rolling starts from two opposite corners (Figure 8a), and “tick or check mark-like” structures (for example Figure 3, c1, the film in the middle) are formed if rolling starts from two adjacent corners.

A more complicated scenario is observed when the width of the films is smaller and the length is considerably larger than the deformed circumference. Rolling starts at the corners first, like before, but long-side rolling starts later (Figure 8b and Figure 5) and is energetically favored. Rolling along the short side is unfavorable because it implies more stored stretching energy along the long side. Further long-side rolling makes diagonally rolled corners unfavorable and leads to the switching of bent corners to a “long-side rolling” scenario. Depending on the width of the film compared to the deformed circumference, either an incompletely rolled tube is formed or the two long-side rolling fronts collide into a completely rolled or doubled tube.

If the deformed circumference is considerably smaller than the width and length of the films

(which implies a high activation strain), then rolling starts first from corners and then continues along all sides (Figure 8c). The rolling fronts do not collide until several revolutions are made, which were shown to be almost irreversible.<sup>17</sup> As a result, already rolled fronts are unable to unroll and irreversible all-side rolling is observed.

## CONCLUSIONS

We investigated in detail folding of rectangular stimuli-responsive hydrogel-based polymer bilayers located on a substrate with different lengths, widths, and thicknesses. It was found that long-side rolling dominates at high aspect ratios (ratio of length to width) when the width is comparable to the circumference of the formed tubes. Rolling from all sides occurs when the width and length considerably exceed this circumference. Diagonal or all-side rolling is observed when the width and length are comparable to the circumference. Short-side rolling was observed very rarely and in combination with diagonal rolling. On the basis of both experimental observations and

theoretical assumptions, we argued that bilayers placed on a substrate start to roll from corners due to quicker diffusion of water. Rolling from long-side starts later but dominates at high aspect ratio due to energetic considerations. We have shown experimentally and by finite-element modeling confirmed by theoretical considerations that the main reasons causing a variety of rolling scenarios are (i) non-homogenous swelling due to slow diffusion of water in hydrogels and (ii) adhesion of polymer to a substrate until a certain threshold. Moreover, non-homogenous swelling determines folding in the first moments, while adhesion plays a decisive role at later stages of folding.

The films that we investigated are fabricated on the microscale. On the other hand, the knowledge obtained in this work is applicable to thinner films to direct their folding in order to form tubes with diameter in the nano range. We believe that the obtained knowledge can be particularly helpful for the design of self-folding objects with highly complex shapes and provides an interesting model system for path-dependent actuation.

## EXPERIMENTAL PART

**Materials.** *N*-Isopropylacrylamide (NIPAM, Aldrich), 4-hydroxybenzophenone (Fluka), polycaprolactone ( $M_n = 70\,000$ – $90\,000$ , Aldrich), benzophenone (Aldrich), and acryloyl chloride (Fluka) were used as received. Methyl methacrylate (MMA, Aldrich) was purified by filtration through an  $Al_2O_3$  column before polymerization.

**Synthesis of 4-Acryloylbenzophenone (BA).** 4-Hydroxybenzophenone (20 g, 0.1009 mol), diisopropylethylamine (19.3 mL, 0.1110 mol), and 80 mL of methylene chloride were added into a 200 mL three-necked round-bottom flask fitted with an overhead stirrer, a thermometer, and an addition funnel with acryloyl chloride (9.02 mL, 0.1110 mol) solution in 20 mL of methylene chloride. The acryloyl chloride solution was added dropwise into the flask under cooling (0–5 °C) for ca. 3 h. The methylene chloride was removed by rotary evaporation. The residue was washed with 80 mL of 20% HCl and 80 mL of a saturated solution of sodium hydrocarbonate and dried over sodium sulfate. The solution was passed through a silica gel column with chloroform as the eluent. Chloroform was removed by rotary evaporator. Finally, 24.44 g (95%) of BA was obtained.  $^1H$  NMR ( $CDCl_3$ , 500 MHz): 6.05 (dd,  $J_1 = 10.40$ ,  $J_2 = 1.26$ , 1H), 6.34 (dd,  $J_1 = 10.40$ ,  $J_3 = 17.34$ , 1H), 6.64 (dd,  $J_3 = 17.34$ ,  $J_2 = 1.26$ , 1H), 7.27 (m, 2H), 7.49 (m, 2H), 7.59 (m, 1H), 7.80 (m, 2H), 7.86 (m, 2H).

**Synthesis of P(NIPAM-BA).** BA (0.02253 g, 0.089 mmol; 0.04551 g, 0.18 mmol; 0.11737 g, 0.47 mmol), NIPAM (1 g, 0.0885 mol), and azobisisobutyronitrile (AIBN) (0.01453 g, 0.089 mmol) were added in 10 mL test tubes. Components were dissolved in 6 mL of 1,4-dioxane and degassed with nitrogen for 30 min. Test tubes were tightly sealed and placed into a shaker (70 °C, 90 rpm) for 24 h. Then the P(NIPAM-BA) polymerization mixtures were cooled to room temperature and poured slowly into diethyl ether. Products were filtered and dried under vacuum.

**Synthesis of P(MMA-BA).** A 6.2803 g amount of MMA (62.72 mmol), 0.2405 g of BA (0.96 mmol), and 0.052 g of AIBN (0.31 mmol) were dissolved in 30 mL of toluene. The mixture was purged with nitrogen for 30 min. The polymerization was carried at 70 °C under a nitrogen atmosphere with mechanical stirring overnight. After cooling, the mixture was poured in

750 mL of diethyl ether, and the precipitate was filtered and dried under vacuum at 40 °C.

**Preparation of Polymer Bilayers.** In a typical experiment, poly(NIPAM-BA) was dip-coated from its ethanol solution on a silica wafer substrate. Polycaprolactone with 2–5 mass % of benzophenone or P(MMA-BA) was spin-coated from a toluene solution on poly(NIPAM-BA) film. The bilayer film was illuminated through a specially designed photomasks by a halogen lamp for 40 min to cross-link polymers. The illuminated film was rinsed in chloroform in order to remove polymers in nonirradiated areas.

**Conflict of Interest:** The authors declare no competing financial interest.

**Acknowledgment.** The authors are grateful to DFG (Grant IO 68/1-1) and IPF for financial support. We also thank Yves Bréchet for discussions about the FE simulations.

**Supporting Information Available:** Movies of long-side (Figure S, S1) and short-side (Figure 7a, S2) rolling. This material is available free of charge via the Internet at <http://pubs.acs.org>.

## REFERENCES AND NOTES

- Esser-Kahn, A. P.; Odom, S. A.; Sottos, N. R.; White, S. R.; Moore, J. S. Triggered Release from Polymer Capsules. *Macromolecules* **2011**, *44*, 5539–5553.
- Ionov, L. Soft Microorigami: Self-Folding Polymer Films. *Soft Matter* **2011**, *7*, 6786–6791.
- Leong, T. G.; Zarafshar, A. M.; Gracias, D. H. Three-Dimensional Fabrication at Small Size Scales. *Small* **2010**, *6*, 792–806.
- Randhawa, J. S.; Kanu, L. N.; Singh, G.; Gracias, D. H. Importance of Surface Patterns for Defect Mitigation in Three-Dimensional Self-Assembly. *Langmuir* **2010**, *26*, 12534–12539.
- Luchnikov, V.; Sydorenko, O.; Stamm, M. Self-Rolled Polymer and Composite Polymer/Metal Micro- and Nanotubes with Patterned Inner Walls. *Adv. Mater.* **2005**, *17*, 1177–1182.
- Cho, J. H.; Gracias, D. H. Self-Assembly of Lithographically Patterned Nanoparticles. *Nano Lett.* **2009**, *9*, 4049–4052.



7. Solovev, A. A.; Sanchez, S.; Pumera, M.; Mei, Y. F.; Schmidt, O. G. Magnetic Control of Tubular Catalytic Microbots for the Transport, Assembly, and Delivery of Micro-objects. *Adv. Funct. Mater.* **2010**, *20*, 2430–2435.
8. Smith, E. J.; Liu, Z.; Mei, Y. F.; Schmidt, O. G. System Investigation of a Rolled-Up Metamaterial Optical Hyperlens Structure. *Appl. Phys. Lett.* **2009**, *95*, 083104.
9. Bof Bufon, C. C. s.; Cojal González, J. D.; Thurmer, D. J.; Grimm, D.; Bauer, M.; Schmidt, O. G. Self-Assembled Ultra-Compact Energy Storage Elements Based on Hybrid Nanomembranes. *Nano Lett.* **2010**, *10*, 2506–2510.
10. Guo, X. Y.; Li, H.; Ahn, B. Y.; Duoss, E. B.; Hsia, K. J.; Lewis, J. A.; Nuzzo, R. G. Two- and Three-Dimensional Folding of Thin Film Single-Crystalline Silicon for Photovoltaic Power Applications. *Proc. Natl. Acad. Sci. U. S. A.* **2009**, *106*, 20149–20154.
11. Schwaiger, S.; Broll, M.; Krohn, A.; Stemmann, A.; Heyn, C.; Stark, Y.; Sticklerbhas, D.; Heitmann, D.; Mendach, S. Rolled-Up Three-Dimensional Metamaterials with a Tunable Plasma Frequency in the Visible Regime. *Phys. Rev. Lett.* **2009**, *102*, 163903.
12. Gracias, D. H.; Tien, J.; Breen, T. L.; Hsu, C.; Whitesides, G. M. Forming Electrical Networks in Three Dimensions by Self-Assembly. *Science* **2000**, *289*, 1170–1172.
13. Leong, T.; Gu, Z. Y.; Koh, T.; Gracias, D. H. Spatially Controlled Chemistry Using Remotely Guided Nanoliter Scale Containers. *J. Am. Chem. Soc.* **2006**, *128*, 11336–11337.
14. Randall, C. L.; Kalinin, Y. V.; Jamal, M.; Manohar, T.; Gracias, D. H. Three-Dimensional Microwell Arrays for Cell Culture. *Lab Chip* **2011**, *11*, 127–131.
15. Jamal, M.; Bassik, N.; Cho, J. H.; Randall, C. L.; Gracias, D. H. Directed Growth of Fibroblasts into Three Dimensional Micropatterned Geometries via Self-Assembling Scaffolds. *Biomaterials* **2010**, *31*, 1683–1690.
16. Huang, G. S.; Mei, Y. F.; Thurmer, D. J.; Coric, E.; Schmidt, O. G. Rolled-Up Transparent Microtubes as Two-Dimensionally Confined Culture Scaffolds of Individual Yeast Cells. *Lab Chip* **2009**, *9*, 263–268.
17. Zakharchenko, S.; Pureskiy, N.; Stoychev, G.; Stamm, M.; Ionov, L. Temperature Controlled Encapsulation and Release Using Partially Biodegradable Thermo-Magneto-Sensitive Self-Rolling Tubes. *Soft Matter* **2010**, *6*, 2633–2636.
18. Stoychev, G.; Pureskiy, N.; Ionov, L. Self-Folding All-Polymer Thermoresponsive Microcapsules. *Soft Matter* **2011**, *7*, 3277–3279.
19. Zakharchenko, S.; Sperling, E.; Ionov, L. Fully Biodegradable Self-Rolled Polymer Tubes: a Candidate For Tissue Engineering Scaffolds. *Biomacromolecules* **2011**, *12*, 2211–2215.
20. Alben, S.; Balakrishnan, B.; Smela, E. Edge Effects Determine the Direction of Bilayer Bending. *Nano Lett.* **2011**, *11*, 2280–2285.
21. Chun, I. S.; Challa, A.; Derickson, B.; Hsia, K. J.; Li, X. Geometry Effect on the Strain-Induced Self-Rolling of Semiconductor Membranes. *Nano Lett.* **2010**, *10*, 3927–3932.
22. Stuart, M. A. C.; Huck, W. T. S.; Genzer, J.; Muller, M.; Ober, C.; Stamm, M.; Sukhorukov, G. B.; Szleifer, I.; Tsukruk, V. V.; Urban, M.; *et al.* Emerging Applications of Stimuli-Responsive Polymer Materials. *Nat. Mater.* **2010**, *9*, 101–113.
23. Singamaneni, S.; McConney, M. E.; Tsukruk, V. V. Swelling-Induced Folding in Confined Nanoscale Responsive Polymer Gels. *ACS Nano* **2010**, *4*, 2327–2337.
24. Jamal, M.; Zarafshar, A. M.; Gracias, D. H. Differentially Photo-Crosslinked Polymers Enable Self-Assembling Microfluidics. *Nat. Commun.* **2011**, *2*, 527.
25. Timoshenko, S. Analysis of Bi-Metal Thermostats. *J. Opt. Soc. Am. Rev. Sci. Instrum.* **1925**, *11*, 233–255.
26. Audoly, B.; Pomeau, Y. *Elasticity and Geometry: from Hair Curls to The Non-Linear Response of Shells*; Oxford University Press: Oxford, 2010.
27. Zienkiewicz, O. C.; Taylor, R. L. *Finite Element Method for Solid and Structural Mechanics*, 6th ed.; Elsevier: New York, 2005.
28. Liang, H. Y.; Mahadevan, L. Growth, Geometry, and Mechanics of a Blooming Lily. *Proc. Natl. Acad. Sci. U. S. A.* **2011**, *108*, 5516–5521.



Zakharchenko, S.; Sperling, E.; Ionov, L.

Fully biodegradable self-rolled polymer tubes: a candidate for tissue engineering scaffolds

***Biomacromolecules*** 2011, 12 (6), 2211–2215

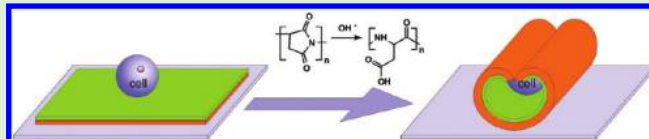
# Fully Biodegradable Self-Rolled Polymer Tubes: A Candidate for Tissue Engineering Scaffolds

Svetlana Zakharchenko, Evgeni Sperling, and Leonid Ionov\*

Leibniz Institute of Polymer Research Dresden, Hohe Str. 6, D-01069 Dresden, Germany

**S** Supporting Information

**ABSTRACT:** We report an approach for the fabrication of fully biodegradable self-rolled tubes based on patterned polysuccinimide/polycaprolactone bilayers. These polymers are biocompatible, biodegradable, produced industrially, and are already approved for biomedical purposes. Both polycaprolactone and polysuccinimide are hydrophobic and intrinsically water-insoluble. Polysuccinimide, however, hydrolyzes in physiological buffer environment yielding water-swelling polyaspartic acid that causes the rolling of the polymer bilayer and formation of tubes. We demonstrate the possibility to encapsulate yeast cells using self-rolled tubes.



## INTRODUCTION

The design of three-dimensional (3D) scaffolds that provide a suitable environment for the growth and division of cells is a keynote procedure for development of efficient approaches for regeneration of tissues and organs. To be suitable for tissue engineering, the scaffolds must fulfill many requirements such as biocompatibility, biodegradability, and porosity as well as proper chemical and mechanical environment mimicking properties of the extracellular matrix. Most of the developed approaches for fabrication of scaffolds can be classified either as “bottom-up” or “top-down” ones. “Bottom-up” ones include phase separation techniques and self-assembling materials.<sup>1–3</sup> Examples of “top-down” ones are electrospinning<sup>4</sup> and microfabrication.<sup>5–9</sup> Many “top-down” approaches suffer from inhomogeneous cells seeding caused by slow migration of cells inside the scaffold. As an alternative, cells might be seeded in situ during the formation of the scaffold. This, for example, can be done using self-assembling peptide hydrogels (molecular “bottom-up”). After self-assembly of the peptides, cells remain entrapped in the polymer network with the size of the mesh smaller than the cell size. The migration of cells inside such scaffolds is restricted.

Recently, a combination of “top-down” and “bottom-up” approaches was introduced for the design of scaffolds. Cells were encapsulated inside relatively large poly(ethylene glycol) (PEG) hydrogel microbricks which were allowed to self-assemble in 3D superstructures of defined shape.<sup>10,11</sup> The advantages of such mesoscale self-assembling systems are: (i) homogeneous seeding of the cells and (ii) simplicity to form large superstructures with different shapes. On the other hand, the applicability of the developed approach is limited due to the nonbiodegradability of the cross-linked PEG hydrogel and the small size of the pores, which is intrinsic to many hydrogel-based scaffolds.

Wrapping by thin films, which form self-rolled tubes<sup>12</sup> or self-folding particles,<sup>13</sup> is an alternative approach for the encapsulation of cells. Self-rolled tubes are thin bilayers which are able to roll due to internal stress produced as a result of thermal

expansion, lattice mismatch, or swelling. The self-rolled tubes, being intrinsically anisotropic, are structurally close to muscle, nerve, and bone tissues. Moreover, microtubes form pores with sizes up to hundreds of micrometers, which is more suitable for the design of scaffolds due to free migration of cells. Encapsulation of cells using wrapping was recently realized on the example of self-rolling tubes made of inorganic materials.<sup>14</sup> Cell-seeded rolled tubes can be potentially assembled into complex submillimeter- and microporous 3D structures<sup>15</sup> with homogeneously distributed cells. It was demonstrated that cells can be encapsulated inside the tubes with diameter in the range of tens of micrometers without the use of harmful UV light. The use of inorganic materials for the fabrication of self-rolling tubes, however, does not allow their application for medical purposes. Recently, Luchnikov et al. demonstrated that self-rolling tubes could be designed using polymers.<sup>16</sup> They showed self-rolling of poly(4-vinylpyridine)/polystyrene bilayer film in acidic environment (pH = 2). On the other hand, Kalaitzidou et al. demonstrated thermoresponsive rolling-unrolling of PDMS/gold tubes at 60–70 °C.<sup>17,18</sup> Gracias et al. developed an approach for the design of self-folding particles made of patterned SU-8 photoresist-polycaprolactone films, which irreversibly fold at 60 °C.<sup>19</sup> The nonbiodegradability and non-biocompatibility of these polymers as well as the difficulty to locally control such low pH values and the high temperature hamper the application of these systems in medicine as well.<sup>20</sup> More recently, we reported fabrication of partially biodegradable magneto-temperature sensitive microtubes and capsules able to capture and release cells in a response to change of temperature in the physiological range between 25 and 33 °C.<sup>21,22</sup> These tubes, based on the use of two polymers—one thermoresponsive poly(*N*-isopropylacrylamide)-based copolymer and hydrophobic

**Received:** March 3, 2011

**Revised:** April 26, 2011

**Published:** April 27, 2011

polycaprolactone (PCL)—can also hardly be used for the fabrication of tissue engineering scaffolds due to the nonbiodegradability and the poor biocompatibility of poly(*N*-isopropylacrylamide).

In this manuscript we report, for the first time, the fabrication of fully biodegradable self-rolled tubes. The tubes are based on cross-linked polysuccinimide/polycaprolactone bilayer. These polymers are biocompatible, biodegradable,<sup>23,24</sup> produced industrially, and were already approved for biomedical purposes. Both polycaprolactone and polysuccinimide are hydrophobic and intrinsically water-insoluble. Polysuccinimide, however, is able to hydrolyze in physiological buffer environment, yielding water-swelling biodegradable polyaspartic acid,<sup>25</sup> which leads to rolling of the tubes and encapsulation of cells (Figure 1).

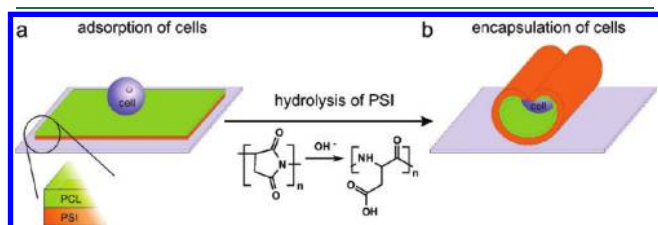


**Figure 1.** Scheme of the formation of self-rolled tubes. Polysuccinimide (PSI)/polycaprolactone (PCL) bilayer is deposited on a substrate. Slow hydrolysis of polysuccinimide in physiological buffer (pH = 7.4) yields polyaspartic acid, which leads to the rolling of the tubes and encapsulation of cells.

## EXPERIMENTAL SECTION

**Materials.** L-Aspartic acid (Aldrich), 85% phosphoric acid (Aldrich), polycaprolactone ( $M_n = 70000\text{--}90000$  g/mol, Aldrich), and 4-hydroxybenzophenone (Aldrich) were used as received.

**Synthesis of Polysuccinimide (PSI).** PSI was synthesized by acid-catalyzed thermal polycondensation of L-aspartic acid. A typical synthesis procedure was as follows. Powdery L-aspartic acid (20 g, 150 mmol) and 85% *o*-phosphoric acid (10 g, 87 mmol) were kept at 200 °C for 6.5 h under nitrogen flow. The mixture was cooled to room temperature and dissolved in *N,N*-dimethylformamide (DMF). The solution was poured into a large amount of deionized water, and the precipitate was washed several times with water until the filtered water became neutral. The obtained PSI was characterized by GPC:  $M_n = 15700$  g/mol,  $M_w = 44900$  g/mol,  $M_w/M_n = 2.86$ .

### Fabrication of the Polymer Bilayers and Self-Rolled Tubes.

The bilayers were produced by photolithography. For this, thin films (70–400 nm) of PSI containing 1 wt % of 4-hydroxybenzophenone with respect to the amount of the polymer were deposited on silicon wafer by spincoating from DMF solution. Next, thin films (70–500 nm) of PCL containing 4 wt % of 4-hydroxybenzophenone were deposited from toluene solution, which is a selective solvent, on top of the PSI film. The polymer bilayers were patterned by irradiation with UV light through a mask. UV irradiation activates benzophenone fragments, which produces free radicals and led to cross-linking in the irradiated areas. As a result, patterned bilayer films were formed on the substrate. The self-rolling tubes were fabricated by long-time exposure of the bilayer in PBS (0.15 M, pH = 7.4).

**Experiments with Yeast Cells.** Yeast cells encapsulated inside the tube were incubated in Dulbecco's modified Eagle's medium: Nutrient Mixture F-12. All experiments with yeast cells were carried out at 25 °C.

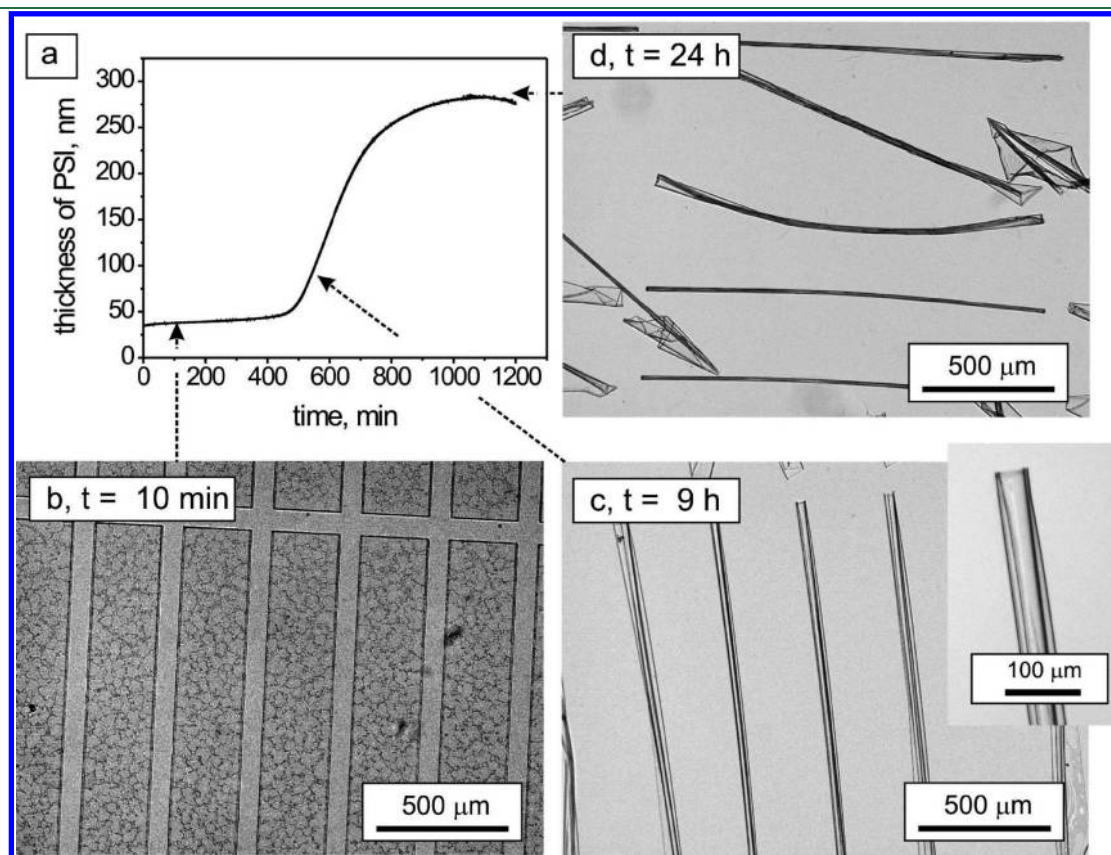


**Figure 2.** Swelling of photocross-linked polysuccinimide films (a) and morphologies of self-rolling tubes ( $th(\text{PSI}) = 200$  nm;  $th(\text{PCL}) = 86$  nm, pattern  $1800\ \mu\text{m} \times 300\ \mu\text{m}$ ) on different stages of rolling; (b) after 10 min of incubation; (c) after 9 h of incubation,  $d = 55\ \mu\text{m}$ ; (d) after 24 h of incubation,  $d = 25\ \mu\text{m}$ .

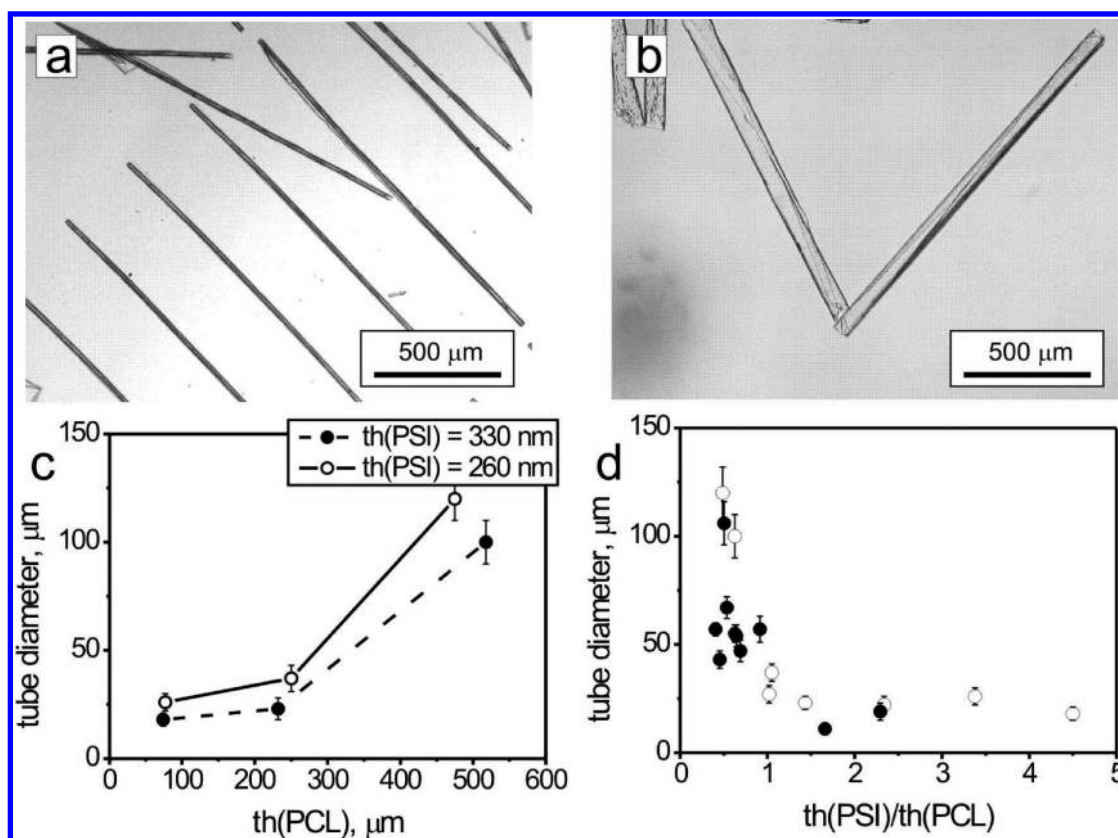


**Figure 3.** Examples of microtubes with different diameters of (a) 22  $\mu\text{m}$  or (b) 100  $\mu\text{m}$  as well as the dependence of the tube diameter on the thickness of PCL (c) and the th(PSI)/th(PCL) ratio (d). The empty circles in (d) correspond to samples prepared by dipcoating without further treatment, solid circles correspond to PSI/PCL films annealed at 60  $^{\circ}\text{C}$  and cooled down to -196  $^{\circ}\text{C}$ .

## RESULTS AND DISCUSSION

First the swelling of photo-cross-linked PSI thin film in physiological buffer (PBS 0.15 M, pH = 7.4) at  $T = 25^{\circ}\text{C}$  was investigated. Considering the fact that pH of culture media is often very close to pH of PBS, the swelling behavior of PSI is expected to be similar in both cases. The PSI film was deposited on silica wafer from DMF solution by spin-coating. To avoid dewetting of the polymer film caused by slow evaporation of the solvent, the samples were quickly heated up to 170  $^{\circ}\text{C}$  on a heating plate. The obtained PSI films were very smooth, and the rms roughness was below 1 nm. In PBS buffer at 25  $^{\circ}\text{C}$  PSI film swelled that resulted in increase of its thickness by ca. 8–10 times: from 35 to 283 nm after 24 h of hydrolysis. Considering the fact that the PSI layer is homogeneously cross-linked, the final degree of swelling of the thicker layers is expected to be similar: 8–10 times.

The swelling of the PSI film had a step-like character (Figure 2a). The thickness of PSI increased slightly during the first period (0–9 h), and strong swelling started after 8–9 h of incubation in buffer. The swelling was nearly completed after 24 h. The observed step-like characters of the swelling are most probably due to diffusion-limited penetration of water in the hydrophobic PSI layer. In the beginning, water starts to diffuse slowly in the hydrophobic PSI layer hydrolyzing it. As soon as a threshold amount of succinimide groups is hydrolyzed, the PSI layer starts to swell to a higher degree due to repulsion between the formed negatively charged carboxylic groups. As a result, the diffusion of water in the polymer layer increases that leads to a faster hydrolysis of the remaining succinimide groups. In fact, the

delayed hydrolysis of PSI films can be considered as an advantage because cells might have enough time to bind to the surface of the polymer bilayer and spread before the tube is formed.

The PSI/PCL bilayers were produced using photolithography. First, the PSI was deposited from its DMF solution using spincoating. PCL was deposited in the same manner from toluene solution. A small amount of 4-hydroxybenzophenone was added to both polymers to provide possibility to cross-link them using UV light. The benzophenone derivatives, which generates free radicals upon irradiation with UV light,<sup>26</sup> have already been applied for photo-cross-linking of biodegradable biomaterials.<sup>27</sup> Notably, other similar compounds including benzophenone, 4-carboxybenzophenone, and 2,4-dihydroxybenzophenone were found to be almost inefficient for the cross-linking of the polymers. This may be related to a difference in the adsorption spectra or the quantum yield. After illumination with UV light, the noncross-linked polymer was removed by sequential rinsing in chloroform and DMF where PCL and PSI are respectively soluble. To avoid cytotoxicity, the rest of the DMF were removed by rinsing in large amount of ethanol. The cross-linked polymers are expected to be biodegradable as well since they still contain the carbon–oxygen and carbon–nitrogen bonds of the original polymers. The obtained patterned bilayers were used for rolling experiments.

The obtained PSI/PCL bilayers were incubated in PBS. The bilayers, which appeared patchy due to the crystalline PCL, remain unchanged during the first 9 h at  $T = 25^{\circ}\text{C}$  (Figure 2b). The rolling started after 9 h of incubation and incompletely rolled tubes ( $d = 55 \mu\text{m}$ , Figure 2c) were formed. Further incubation led to a shrinkage of the tubes and a decrease of their diameter



( $d = 25 \mu\text{m}$ , Figure 2d). The formed tubes could be easily detached from the silicon substrate due to the swelling of the polyaspartic acid (hydrolyzed PSI). The decrease of the tube diameter with time is in qualitative agreement with the Timoshenko equation.<sup>28</sup> According to the Timoshenko equation, higher stress in the film, which is proportional to the swelling degree, leads to a smaller diameter of the tubes. The step-like rolling behavior of PSI/PCL bilayer correlates very well with the step-like character of swelling of the PSI layer.

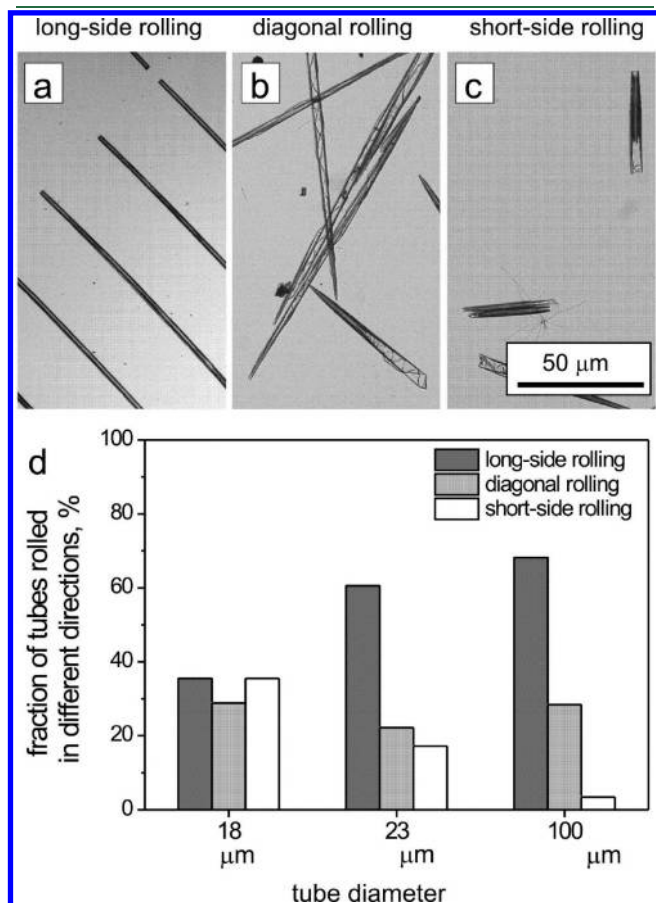


**Figure 4.** Different morphologies of tubes formed by a rolling PSI/PCL bilayer: (a) long-side rolling; (b) diagonal rolling; (c) short side rolling. Fraction of the microtubes rolled in different directions depending on the tube diameter (d, pattern  $1800 \mu\text{m} \times 300 \mu\text{m}$ ). Approximately 50 microtubes were analyzed in each case.

It was found that the rolling of thick bilayers often results in peeling of the polymer films, which might be caused by the rigidity of the microcrystalline PCL layer. The microcrystalline structure of PCL was also most probably the origin of the defects of rolling (Figure 2d). To prevent the formation of large PCL crystallites, polymer bilayers were heated up to  $60^\circ\text{C}$  to melt the PCL and then quickly cooled down by liquid nitrogen  $T = -196^\circ\text{C}$ . This thermal treatment resulted in a decrease of the size of the crystallites from tens of micrometers to less than a micrometer (images not shown) and improved the rolling in many cases.

Next, the effect of the thickness of the polymer layers on the diameter of the formed tubes was investigated. It was found that tubes diameter increased with the increase of thickness of the PCL layer as well as with the decrease of the thickness of the PSI layer (Figure 3a–c). These results were obtained for tubes after 24 h of rolling when no further change of the tube diameter with time was observed. Moreover, PSI/PCL bilayers prepared with and without thermal treatment demonstrated similar dependence of the tube diameter on the ratio between thicknesses of the polymers layers (Figure 3d). In general, the smaller was the ratio of the thickness of the PSI layer to the thickness of PCL layer ( $r = \text{th(PSI)}/\text{th(PCL)}$ ) the larger the diameter of the formed tubes (Figure 3d). Since strain in the film is related to the difference between the thickness of the PSI in swollen and dry states, these findings are in a qualitative agreement with the Timoshenko equation as well.<sup>28</sup> Using this principle, we explored the possibilities to fabricate tubes with a diameter more than  $50 \mu\text{m}$  using both the decrease of the thickness of the PSI ( $\text{th(PSI)} = 67 \text{ nm}$ ;  $\text{th(PCL)} = 132 \text{ nm}$ ;  $r = 0.5$ ) and the increase of thickness of the PCL layer ( $\text{th(PSI)} = 260 \text{ nm}$ ;  $\text{th(PCL)} = 473 \text{ nm}$ ;  $r = 0.54$ ). Notably, tubes were formed only in the second case because very thin PSI layer made the tubes too soft and the tubes were easily deformed and smashed by the liquid stream. In fact, tubes of a diameter ranging from  $10 \mu\text{m}$  up to more than  $100 \mu\text{m}$  can be fabricated. Tubes with the size  $100 \mu\text{m}$  or more are particularly promising for the design of porous scaffolds.<sup>29</sup>

Contrary to previously investigated PNIPAM/PCL system,<sup>21</sup> which rolled predominately in one direction, PSI/PCL bilayers were able to roll in different directions. We distinguished three cases: long-side rolling, diagonal rolling, and short-side rolling (Figure 4). The probability to roll in each of these directions depended on the ratio of the final diameter of the tubes to the size of the pattern and the number of the possible revolutions. The bilayer rolled in all directions equally if tubes with the smallest diameter were formed. The increase of the diameter led to the formation of tubes with predominately long-side rolling. To

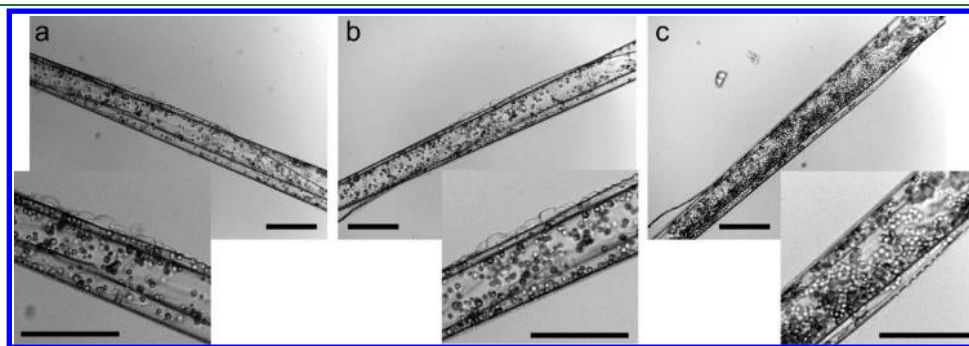


**Figure 5.** PSI/PCL self-rolled tube (a) after encapsulation of yeast cells in PBS buffer, (b) directly after the transfer to the nutrition media, and (c) after 14 h of incubation in the nutrition media. Scale bar is  $100 \mu\text{m}$ .



explain the obtained results we assign the following scenario of rolling. Water starts to diffuse and hydrolyzes PSI along the perimeter of the patterned polymer bilayer. The bilayer loses its contact with the substrate at the point where adhesion to the substrate is the smallest, starts to roll, and makes several revolutions. Considering the fact that the tubes are unable to unroll or change their morphology if they are produced by multiple revolutions,<sup>21</sup> the direction of rolling of the whole thin tube is determined by the direction of rolling in the initial period of time. As a result, tubes with a small diameter roll in all directions with similar probability. On the other hand, tubes with larger diameter are formed by single revolution. These tubes have more possibilities to change their morphology and to find energetically more favorable state during the rolling.<sup>30</sup>

Finally, we tested the possibility to encapsulate yeast cells using biodegradable self-rolled tubes. The bakery yeast cells were adsorbed on patterned PSI/PCL bilayer from PBS pH = 7.4 buffer. After 27 h of incubation, the PSI/PCL bilayer formed tubes with diameter 80–100  $\mu\text{m}$  with encapsulated yeast cells (Figure 5a). The number of cells remained approximately constant in PBS. One microtube with encapsulated yeast cells was transferred into the nutrition media (Figure 5b) and further incubated for 14 h. Incubation in nutrition media led to proliferation and division of the yeast cells that increased their number. This was an indication of nontoxicity and availability of free space for new cells as well as on the permeability of the tubes for nutrition.

## CONCLUSIONS AND OUTLOOK

We reported an approach for fabrication the fully biodegradable self-rolled tubes, which are suitable for the encapsulation of cells. Our approach is based on the fabrication of polymer bilayers where both components are water-insoluble polymers: polycaprolactone and polysuccinimide. Polysuccinimide is able to slowly hydrolyze and swell in a physiological buffer environment leading to self-rolling of the polymer bilayer and the formation of microtubes. We also demonstrated that the self-rolled tubes can be used for encapsulation of cells, which proliferate and divide inside the tube. Since the used polymers are biocompatible, biodegradable, and produced industrially and are approved for biomedical purposes, the proposed approach is of practical interest for controlled cell delivery and the design of scaffolds for tissue engineering.

## ASSOCIATED CONTENT

**S Supporting Information.** Movie of self-rolled tube with encapsulated yeast cells (avi format). This material is available free of charge via the Internet at <http://pubs.acs.org>.

## AUTHOR INFORMATION

### Corresponding Author

\*E-mail: [ionov@ipfdd.de](mailto:ionov@ipfdd.de) (L.I.).

## ACKNOWLEDGMENT

The authors are grateful to Manfred Stamm and Georgi Stoychev for fruitful discussions. This work was supported by the Leibniz Institute of Polymer Research Dresden.

## REFERENCES

- (1) Whitesides, G. M.; Grzybowski, B. *Science* **2002**, 295 (5564), 2418–2421.
- (2) Zhang, S. G. *Biotechnol. Adv.* **2002**, 20 (5–6), 321–339.
- (3) Ball, P. *Nature* **1994**, 367 (6461), 323–324.
- (4) Reneker, D. H.; Chun, I. *Nanotechnology* **1996**, 7 (3), 216–223.
- (5) Liu, V. A.; Bhatia, S. N. *Biomed. Microdevices* **2002**, 4 (4), 257–266.
- (6) Yu, T. Y.; Ober, C. K. *Biomacromolecules* **2003**, 4 (5), 1126–1131.
- (7) Ward, J. H.; Bashir, R.; Peppas, N. A. *J. Biomed. Mater. Res.* **2001**, 56 (3), 351–360.
- (8) Luo, Y.; Shoichet, M. S. *Nat. Mater.* **2004**, 3 (4), 249–253.
- (9) Gillette, B. M.; Jensen, J. A.; Tang, B. X.; Yang, G. J.; Bazargan-Lari, A.; Zhong, M.; Sia, S. K. *Nat. Mater.* **2008**, 7 (8), 636–640.
- (10) Zamanian, B.; Masaeli, M.; Nichol, J. W.; Khabiry, M.; Hancock, M. J.; Bae, H.; Khademhosseini, A. *Small* **2010**, 6 (8), 937–944.
- (11) Du, Y. A.; Lo, E.; Ali, S.; Khademhosseini, A. *Proc. Natl. Acad. Sci. U.S.A.* **2008**, 105 (28), 9522–9527.
- (12) Solovev, A. A.; Sanchez, S.; Pumera, M.; Mei, Y. F.; Schmidt, O. G. *Adv. Funct. Mater.* **2010**, 20 (15), 2430–2435.
- (13) Randall, C. L.; Kalinin, Y. V.; Jamal, M.; Manohar, T.; Gracias, D. H. *Lab Chip* **2011**, 11 (1), 127–131.
- (14) Huang, G. S.; Mei, Y. F.; Thurmer, D. J.; Coric, E.; Schmidt, O. G. *Lab Chip* **2009**, 9 (2), 263–268.
- (15) Randhawa, J. S.; Kanu, L. N.; Singh, G.; Gracias, D. H. *Langmuir* **2010**, 26 (15), 12534–12539.
- (16) Luchnikov, V.; Sydorenko, O.; Stamm, M. *Adv. Mater.* **2005**, 17 (9), 1177.
- (17) Kalaitzidou, K.; Crosby, A. J. *Appl. Phys. Lett.* **2008**, 93 (4), 041910.
- (18) Simpson, B.; Nunnery, G.; Tannenbaum, R.; Kalaitzidou, K. *J. Mater. Chem.* **2010**, 20 (17), 3496–3501.
- (19) Azam, A.; Laffin, K.; Jamal, M.; Fernandes, R.; Gracias, D. *Biomed. Microdevices* **2010**, 1–8.
- (20) Zakharchenko, S.; Pureskiy, N.; Stoychev, G.; Stamm, M.; Ionov, L. *Soft Matter* **2010**, 6 (12), 2633–2636.
- (21) Ionov, L. *Soft Matter* **2011** No. DOI: 10.1039/C1SM05476G.
- (22) Stoychev, G.; Pureskiy, N.; Ionov, L. *Soft Matter* **2011**, 7, 3277–3279.
- (23) Low Kim, C.; Wheeler, A. P.; Koskan Larry, P. Commercial Poly(aspartic acid) and Its Uses. In *Hydrophilic Polymers*; American Chemical Society: Washington, DC, 1996; Vol. 248, pp 99–111.
- (24) Klein, T.; Moritz, R.-J.; Graupner, R. *Polyaspartates and Polysuccinimide*; Wiley-VCH Verlag GmbH & Co. KGaA: New York, 2000.
- (25) Thombre, S. M.; Sarwade, B. D. *J. Macromol. Sci., Part A: Pure Appl. Chem.* **2005**, 42 (9), 1299–1315.
- (26) Prucker, O.; Naumann, C. A.; Ruhe, J.; Knoll, W.; Frank, C. W. *J. Am. Chem. Soc.* **1999**, 121 (38), 8766–8770.
- (27) Claeysens, F.; Hasan, E. A.; Gaidukeviciute, A.; Achilleos, D. S.; Ranella, A.; Reinhardt, C.; Ovsianikov, A.; Shizhou, X.; Fotakis, C.; Vamvakaki, M.; Chichkov, B. N.; Farsari, M. *Langmuir* **2009**, 25 (5), 3219–3223.
- (28) Timoshenko, S. J. *Opt. Soc. Am.* **1925**, 11 (3), 233–255.
- (29) Karageorgiou, V.; Kaplan, D. *Biomaterials* **2005**, 26 (27), 5474–5491.
- (30) Chun, I. S.; Challa, A.; Derickson, B.; Hsia, K. J.; Li, X. *Nano Lett.* **2010**, 10 (10), 3927–3932.

Stoychev, G.; Puretskiy, N.; Ionov, L.

Self-folding all-polymer thermoresponsive microcapsules

***Soft Matter*** 2011, 7, 3277-3279.

Cite this: *Soft Matter*, 2011, **7**, 3277

www.rsc.org/softmatter

## COMMUNICATION

## Self-folding all-polymer thermoresponsive microcapsules†

Georgi Stoychev, Nikolay Puretskiy and Leonid Ionov\*

Received 21st January 2011, Accepted 22nd February 2011

DOI: 10.1039/c1sm05109a

**We design partially biodegradable thermoresponsive self-folding capsules capable of controlled capture and release of cells. The proof of principle is demonstrated on the example of star-like patterned polycaprolactone-poly(*N*-isopropylacrylamide) bilayers, which reversibly encapsulate/release yeast cells in response to a temperature signal.**

Encapsulation of cells is a very important task for the design of scaffolds for tissue engineering.<sup>1–5</sup> To date, cells were encapsulated predominately using physically or chemically crosslinked hydrogels.<sup>6,7</sup> In one general approach, cells are dispersed in a solution of monomers or polymer precursors, which are crosslinked and form a matrix with included cells. Hydrogels, therefore, provide both mechanical resistivity as well as suitable aqueous environment for the cell.

Recently self-rolling tubes and self-folding microcapsules were successfully introduced for encapsulation of cell as well.<sup>8,9</sup> Self-rolling tubes are a thin bilayer, which is able to roll due to internal stress produced as result of thermal expansion or lattice mismatch.<sup>10,11</sup> Self-folding capsules are based on the similar principle and were designed as patterned metallic layer with active metallic or polymeric junction elements.<sup>12</sup> Contraction and expansion of the junctions result in folding and unfolding of the metallic film, respectively. To date, self-rolling tubes and self-folding capsules were designed predominantly using inorganic materials that restrict their medical applications. There are several examples of polymer based self-rolling tubes and self-folding capsules. Luchnikov *et al.*, for example, showed the self-rolling of polystyrene-poly(2-vinylpyridine) bilayer film in an acidic environment (pH = 2).<sup>13</sup> Kalaitzidou *et al.* demonstrated thermoresponsive rolling-unrolling of PDMS-gold-made tubes at 60–70 °C.<sup>14,15</sup> Gracias and co-workers developed an approach for the design of self-folding capsules made of patterned SU-8 photoresist - polycaprolactone film, which irreversibly fold at 60 °C.<sup>12</sup> The difficulty to locally control such low pH values and the high temperature hampers the application of these systems in medicine.

Recently, we reported the fabrication of partially biodegradable magneto-temperature sensitive microtubes, which are able to capture and release objects up to 10 µm in size in response to varying the

temperature in the range of 25–33 °C.<sup>16</sup> In our approach, two polymers were used. First one is thermoresponsive poly(*N*-isopropylacrylamide). In aqueous media, poly(*N*-isopropylacrylamide) (PNIPAM) reversibly changes its solubility at 33 °C. Due to its thermoresponsive properties, PNIPAM has already been applied for cell culturing,<sup>17</sup> directed protein adsorption,<sup>18</sup> control of biomolecular motors,<sup>19,20</sup> protein purification,<sup>21</sup> photolithography<sup>22</sup> and drug delivery.<sup>23</sup> The second polymer is hydrophobic and water-insoluble polycaprolactone (PCL). Both polymers were deposited on a substrate in the form of crosslinked bilayer. Swelling and shrinking of PNIPAM resulted in reversible rolling of the bilayer and the formation of tubes.

Here we report the fabrication of partially biodegradable thermoresponsive star-shaped self-folding capsules. The general idea is to use a polymer bilayer, where one component is biodegradable hydrophobic polycaprolactone (PCL) and another is thermoresponsive hydrogel (PNIPAM). This bilayer has the shape of a star with several arms (Fig. 1). The crosslinked PNIPAM layer swells and shrinks in response to temperature. The PCL layer restricts swelling of the PNIPAM in one direction. As a result, the star-like bilayer made of these polymers does not uniformly expand/shrink but folds and unfolds due to swelling and collapse of PNIPAM, respectively. In order to demonstrate the approach, four- and six-arm self-folding capsules were fabricated and applied for reversible encapsulation of yeast cells.

The patterned star-like bilayers were first produced using photolithography. A small amount of photocrosslinker, benzophenone derivatives, was introduced to both polymers in order to provide sensitivity to UV light. For this, poly(*N*-isopropylacrylamide) copolymer containing 1 mol% of 4-acryloylbenzophenone comonomer (poly(NIPAM-ABP)) was prepared. The poly(NIPAM-ABP) had a slightly lower cloud point ( $T = 28$  °C) than the PNIPAM homopolymer did ( $T = 33$  °C). A thick film ( $h = 4$  µm) of

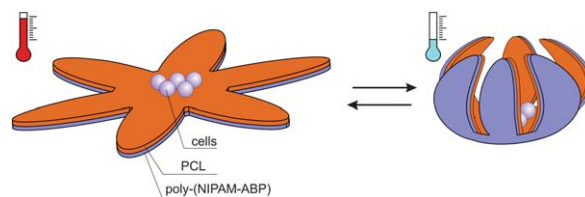


**Fig. 1** A scheme of the folding star-shaped polymer bilayer. Swelling of the thermoresponsive hydrogel layer at lower temperature increases stress in the film that results in bending of the star arms and folding.

Leibniz Institute of Polymer Research Dresden, Hohe Str. 6, 01069 Dresden, Germany. E-mail: ionov@ipfdd.de

† Electronic Supplementary Information (ESI) available: Movies of reversible folding-unfolding as well as encapsulation and release of yeast cells. See DOI: 10.1039/c1sm05109a/

poly(NIPAM-ABP) was deposited on a silicon wafer substrate from 8% ethanol solution by dipcoating. Next, the thick PCL film ( $h = 4 \mu\text{m}$ ) containing 6 mol% of 4-hydroxybenzophenone was deposited from 5% toluene solution on the top of the poly(NIPAM-ABP) film. The polymer bilayer was patterned by irradiation using deep UV (254 nm) light through a mask. UV irradiation activated the benzophenone fragments, which produced free radicals and led to cross-linking in the irradiated areas. As a result, patterned bilayer films were formed on the substrate. The films were not soluble in organic solvents as well as in water, indicating the formation of a network.

Next, folding of the patterned bilayers in aqueous environment was investigated. It was found that star-like bilayer films remain undeformed at  $T > 28^\circ\text{C}$  (Fig. 2 a,e). The arms of the bilayer started to bend when the temperature decreased below the cloud point of poly-(NIPAM-ABP) (Fig. 2 b,f). The bending was typically completed after 5–10 s. The thickness of the polymer layers was adjusted in such a way that the arms make a half-turn. Experimentally it was found that  $4 \mu\text{m}$  thick poly-(NIPAM-ABP) and PCL layers allowed complete and partial folding of the four-arm and six-arm stars, respectively. (Fig. 2 c,g). The use of thicker PCL and thinner poly-(NIPAM-ABP) layer led to a larger curvature radius and incomplete folding of the capsules. On the other hand, thinner PCL and thicker poly-(NIPAM-ABP) resulted in a smaller curvature radius and multiple rolling of the arms to form tubes. The folded polymer layer stayed bound to the substrate because the centers of both the four- and six-arm stars remained almost undeformed at moderately low temperature ( $T = 20^\circ\text{C}$ ) for a long time. The capsules were released from the substrate after further cooling ( $T < 10^\circ\text{C}$ ) due to strong swelling of the poly-(NIPAM-ABP) layer that resulted in considerable deformation of the central part. Increasing the temperature led to a shrinking of poly-(NIPAM-ABP) layer and unfolding of the capsules. The unfolding was completely reversible and no residual deformation of the polymer bilayer was observed, even after several folding-unfolding cycles.

Finally, the possibility to encapsulate and release yeast cells using self-folding star-like polymer bilayers was demonstrated. For this,

backing yeast cells were deposited on the patterned polymer bilayer from buffer dispersion at elevated temperature when poly-(NIPAM-ABP) is shrunk (Fig. 3 a,c). The surface density of the cells was in the range  $2000\text{--}10000 \text{ cells mm}^{-2}$  depending on the sample. A decrease in the temperature resulted in swelling of the poly-(NIPAM-ABP) and led to folding of the polymer capsules and encapsulation of the cells (Fig. 3 b,d). The yeast cells became accessible to the environment and could be removed from the polymer surface by liquid stream upon unfolding at elevated temperature when the poly-(NIPAM-ABP)

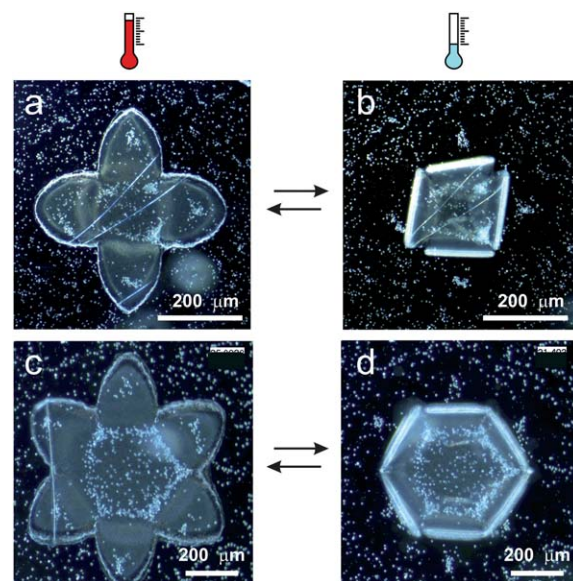


**Fig. 3** Encapsulation of yeast cells inside the thermoresponsive self-folding capsules (dark field optical microscopy). Yeast cells are adsorbed on the polymer bilayer at elevated temperature. Cooling leads to swelling of the thermoresponsive polymer and folding of the capsules. Further heating results in unfolding of the capsules and release of the cells. See supplementary movies S3 and S4.

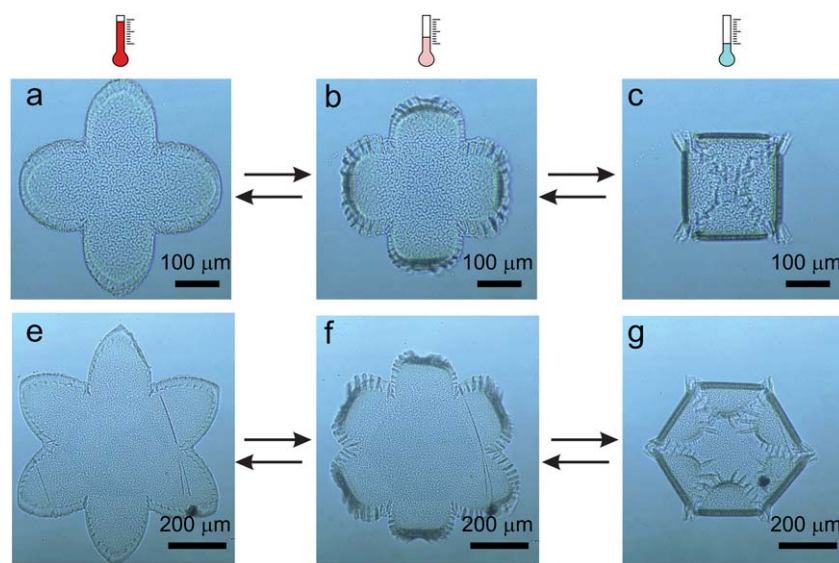


**Fig. 2** Bright field optical microscopy images of self-folding of the star-like patterned polymer bilayer. The polymer bilayer is undeformed at elevated temperatures when the poly-(NIPAM-ABP) layer is shrunk. Cooling results in swelling of poly-(NIPAM-ABP) layer and folding of the bilayer. See supplementary movies S1 and S2.



layer is shrunk. It was also observed that cells were concentrated in the center of the capsules after several folding cycles, which was caused by their sliding from the arms during folding. These experiments demonstrated the possibility for encapsulation and release of cells using self-folding capsules.

## Conclusions

In conclusion, we demonstrated the design of partially biodegradable thermoresponsive self-folding capsules capable of controlled capture and release of cells. The proof of the principle was demonstrated on the example of star-like patterned polycaprolactone-poly(*N*-isopropylacrylamide) bilayer, which reversibly encapsulates/releases yeast cells in response to a temperature signal. The developed approach can potentially be used to control the activity of bacteria and fungi by switching their accessibility to the environment. Moreover, the cell-loaded capsules can be assembled into 3D scaffolds which are highly promising for tissue engineering.

## Experimental part

### Materials

*N*-isopropylacrylamide (NIPAM, Aldrich), 4-hydroxybenzophenone (Fluka), polycaprolactone ( $M_n = 70000$ – $90000$ , Aldrich), benzophenone (Aldrich), 2,2'-Azobis(2-methylpropionitrile) (AIBN, Fluka), *N,N*-diisopropylethylamine (Aldrich) and acryloyl chloride (Fluka) were used as received. Solvents were also used as received.

### Synthesis of 4-acryloylbenzophenone (ABP)

4-Hydroxybenzophenone (20 g, 0.1009 mol), *N,N*-diisopropylethylamine (19.3 ml, 0.1110 mol) and 80 ml of methylene chloride were added to 200 ml three-necked round-bottom flask fitted with an overhead stirrer, a thermometer, and an addition funnel with acryloyl chloride (9.02 ml, 0.1110 mol) solution in 20 ml of methylene chloride. The acryloyl chloride solution was added dropwise into the flask under cooling (0–5 °C) for ca 3 h. The methylene chloride was removed by rotary evaporation. The residue was washed with 80 ml of 20% HCl, 80 ml of saturated solution of sodium hydrocarbonate and dried over sodium sulfate. The solution was passed through a silica gel column with chloroform as the eluent. Chloroform was removed by rotary evaporator. Finally, 24.44 g (95%) of ABP was obtained.  $^1\text{H}$  NMR ( $\text{CDCl}_3$ , 500 MHz): 6.05 (dd,  $J_1 = 10.40$ ,  $J_2 = 1.26$ , 1H), 6.34 (dd,  $J_1 = 10.40$ ,  $J_3 = 17.34$ , 1H), 6.64 (dd,  $J_3 = 17.34$ ,  $J_2 = 1.26$ , 1H), 7.27 (m, 2H), 7.49 (m, 2H), 7.59 (m, 1H), 7.80 (m, 2H), 7.86 (m, 2H).

### Synthesis of poly-(NIPAM-ABP)

ABP (0.02253 g, 0.089 mmol), NIPAM (1 g, 8.85 mmol), AIBN (0.01453 g, 0.089 mmol) were added in 10 ml test tubes. Components

were dissolved in 6 ml 1,4-dioxane and degassed with nitrogen for 30 min. Test tubes were tightly sealed and placed into a shaker (70 °C, 90 rpm) for 24 h. Then the mixtures were cooled to room temperature and poured slowly into diethyl ether. Products were filtered and dried under vacuum.

## Acknowledgements

The authors are grateful to Manfred Stamm for fruitful discussions. DFG (Grant IO 68/1-1) and Volkswagen Foundation are acknowledged for financial support.

## References

- 1 S. Levenberg and R. Langer, in *Current Topics in Developmental Biology*, Vol. 61, Elsevier Academic Press Inc, San Diego, 2004, vol. 61, p. 113.
- 2 F. Couet, N. Rajan and D. Mantovani, *Macromol. Biosci.*, 2007, **7**, 701–718.
- 3 G. C. Gurtner, M. J. Callaghan and M. T. Longaker, *Annu. Rev. Med.*, 2007, **58**, 299–312.
- 4 B. V. Slaughter, S. S. Khurshid, O. Z. Fisher, A. Khademhosseini and N. A. Peppas, *Adv. Mater.*, 2009, **21**, 3307–3329.
- 5 N. A. Peppas, J. Z. Hilt, A. Khademhosseini and R. Langer, *Adv. Mater.*, 2006, **18**, 1345–1360.
- 6 K. M. Park, S. Y. Lee, Y. K. Joung, J. S. Na, M. C. Lee and K. D. Park, *Acta Biomater.*, 2009, **5**, 1956–1965.
- 7 W. X. Wang, H. Liang, R. C. Al Ghanami, L. Hamilton, M. Fraylich, K. M. Shakesheff, B. Saunders and C. Alexander, *Adv. Mater.*, 2009, **21**, 1809.
- 8 G. S. Huang, Y. F. Mei, D. J. Thurmer, E. Coric and O. G. Schmidt, *Lab Chip*, 2009, **9**, 263–268.
- 9 M. Jamal, N. Bassik, J. H. Cho, C. L. Randall and D. H. Gracias, *Biomaterials*, 2010, **31**, 1683–1690.
- 10 A. B. Vorob'ev and V. Y. Prinz, *Semicond. Sci. Technol.*, 2002, **17**, 614–616.
- 11 S. V. Golod, V. Y. Prinz, V. I. Mashanov and A. K. Gutakovskiy, *Semicond. Sci. Technol.*, 2001, **16**, 181–185.
- 12 A. Azam, K. Laflin, M. Jamal, R. Fernandes and D. Gracias, *Biomed. Microdevices*, 2010, 1–8.
- 13 V. Luchnikov, O. Sydorenko and M. Stamm, *Adv. Mater.*, 2005, **17**, 1177.
- 14 K. Kalaitzidou and A. J. Crosby, *Appl. Phys. Lett.*, 2008, **93**.
- 15 B. Simpson, G. Nunnery, R. Tannenbaum and K. Kalaitzidou, *J. Mater. Chem.*, 2010, **20**, 3496–3501.
- 16 S. Zakharchenko, N. Pureskiy, G. Stoychev, M. Stamm and L. Ionov, *Soft Matter*, 2010, **6**, 2633–2636.
- 17 N. Yamada, T. Okano, H. Sakai, F. Karikusa, Y. Sawasaki and Y. Sakurai, *Makromol. Chem. Rapid Commun.*, 1990, **11**, 571–576.
- 18 D. L. Huber, R. P. Manginell, M. A. Samara, B. I. Kim and B. C. Bunker, *Science*, 2003, **301**, 352–354.
- 19 L. Ionov, M. Stamm and S. Diez, *Nano Lett.*, 2006, **6**, 1982–1987.
- 20 L. Ionov, A. Synytska and S. Diez, *Adv. Funct. Mater.*, 2008, **18**, 1501–1508.
- 21 I. Y. Galaev and B. Mattiasson, *Trends Biotechnol.*, 1999, **17**, 335–340.
- 22 L. Ionov and S. Diez, *J. Am. Chem. Soc.*, 2009, **131**, 13315–13319.
- 23 C. D. H. Alarcon, S. Pennadam and C. Alexander, *Chem. Soc. Rev.*, 2005, **34**, 276–285.



Zakharchenko, S.; Puretskiy, S.; Stoychev, G.; Stamm, M.; Ionov, L.  
Temperature controlled encapsulation and release using partially biodegradable  
thermo-magneto-sensitive self-rolling tubes  
***Soft Matter*** 2010, 12, 2633-2636.

# Temperature controlled encapsulation and release using partially biodegradable thermo-magneto-sensitive self-rolling tubes†

Svetlana Zakharchenko, Nikolay Puretskiy, Georgi Stoychev, Manfred Stamm and Leonid Ionov\*

Received 10th March 2010, Accepted 26th April 2010

First published as an Advance Article on the web 21st May 2010

DOI: 10.1039/c0sm00088d

**We suggest a new approach for controlled encapsulation and release of microparticles, cells and drugs using thin bilayer films of thermoresponsive and biodegradable polymers, which are able to form self-rolling tubes. The magnetic nanoparticles are incorporated in the thermoresponsive layer in order to provide the microtubes sensitivity to magnetic field. We demonstrate reversible rolling and unrolling of the polymer films, reversible capture and release of microparticles in response to change of temperature as well as manipulation of particle-loaded microtubes using external magnetic field. The suggested approach can be successfully implemented for controlled delivery of drugs and cells in living organisms as well as to design scaffolds for tissue engineering.**

Development of approaches for controlled delivery of drugs and cells in living organisms is very important for medicine and regenerative therapy.<sup>1–5</sup> Stimuli-responsive polymers were demonstrated to be particularly promising for these applications due to their ability to reversibly change physical and chemical properties in response to environmental signal.<sup>6,7</sup> To date, several approaches based on polymers sensitive either to pH or to temperature signals have been developed and tested. For example, small drug molecules can be delivered using stimuli-responsive hydrogel particles and released from them due to stimuli-induced contraction.<sup>8–10</sup> On the other hand, cells can be delivered and released in a controlled manner using polymer systems able to undergo sol–gel transition.<sup>11,12</sup>

In this manuscript, we suggest a new approach for controlled encapsulation and release of cells and drugs using stimuli-responsive polymers. This approach is based on the use of self-rolling tubes. The tubes can be formed by thin films, which spontaneously roll due to internal stress. Recently, self-rolling tubes made of inorganic materials<sup>13,14</sup> were demonstrated to be suitable for encapsulation of yeast cells.<sup>15</sup> Inorganic materials, however, do not allow direct use of these tubes for cell delivery inside living organisms. More recently, Luchnikov *et al.* demonstrated that self-rolling tubes could be designed using polymers.<sup>16</sup> They showed self-rolling of polystyrene–poly-(2-vinylpyridine) bilayer film in acidic environment (pH = 2). On the other hand, Kalaitzidou and Crosby demonstrated thermoresponsive rolling–unrolling of PDMS–gold made tubes at 60–70 °C.<sup>17</sup> The non-biodegradability and non-biocompatibility of these polymers as well as the difficulty to locally control such low pH values and the high

temperature hamper the use of these systems for biotechnological applications. Here we report the design of partially biodegradable magneto-temperature sensitive microtubes able to capture and release objects with size up to 10 µm in response to change of temperature in the range of 25–33 °C. In our approach, two polymers—one thermoresponsive poly(*N*-isopropylacrylamide)-based copolymer and hydrophobic polycaprolactone (PCL)—are used. In aqueous media, poly(*N*-isopropylacrylamide) (PNIPAM) homopolymer reversibly changes its solubility at the Low Critical Solution Temperature (LCST = 33 °C). Due to its thermoresponsive properties, PNIPAM has been already applied for cell culturing,<sup>18</sup> directed protein adsorption,<sup>19</sup> control of biomolecular motors,<sup>20,21</sup> protein purification,<sup>22</sup> photolithography<sup>23</sup> and drug delivery.<sup>6</sup> The second polymer—hydrophobic and water-insoluble polycaprolactone (PCL)—is deposited on top of the PNIPAM layer. The two-layer film made of these polymers is able to self-roll and unroll due to swelling and collapse of PNIPAM at low and elevated temperatures, respectively (Fig. 1). We demonstrate that this rolling and unrolling can be used for encapsulation and release of microparticles. Moreover, magnetic nanoparticles were incorporated in the thermoresponsive layer in order to provide microtubes sensitivity to magnetic field.

The microtubes were first produced using photolithography. Small amount of photocrosslinker—benzophenone derivatives—was added to both polymers in order to provide sensitivity to UV light. For this, we prepared poly(*N*-isopropylacrylamide) copolymer containing 1 mol% of 4-acryloylbenzophenone comonomer (poly(NIPAM-ABP)). The poly(NIPAM-ABP) had slightly lower LCST (LCST = 28 °C) than the PNIPAM homopolymer (LCST = 33 °C). Thin films (200–500 nm) of poly(NIPAM-ABP) were deposited on silicon wafer substrate by spin-coating. Next, thin film (40–300 nm) of PCL containing 1–3 mol% of pure benzophenone was deposited from toluene solution, which is selective solvent, on the top of poly(NIPAM-ABP) film. The polymer bilayer was patterned by irradiation with UV light through a mask. UV irradiation activated benzophenone fragments, which produced free radicals and led to crosslinking in the irradiated areas. As a result, patterned bilayer films were formed on the substrate. The films were not soluble in organic solvents as well as in water and do not split into films of individual polymers that indicated the formation of a network.

Next, we investigated the formation of self-rolling polymer tubes in aqueous environment as well as the capture of microparticles. We found that bilayer films remain undeformed at  $T > 28$  °C and start to roll and form tubes when the temperature decreases below the LCST of poly(NIPAM-ABP). The rolling of the tubes is very fast and is completed after 1–3 s when 1–3 revolutions are made. The following heating affects the morphology of the formed microtube. In particular, the microtubes produced by single revolution are able to unroll almost

Leibniz Institute of Polymer Research Dresden, Hohe Str. 6, 01069 Dresden, Germany. E-mail: ionov@ipfdd.de

† Electronic supplementary information (ESI) available: Movies of tube formation, particle capture by rolling tubes, reversible encapsulation and release of particles and flow of particle-loaded tubes in a magnetic field. See DOI: 10.1039/c0sm00088d

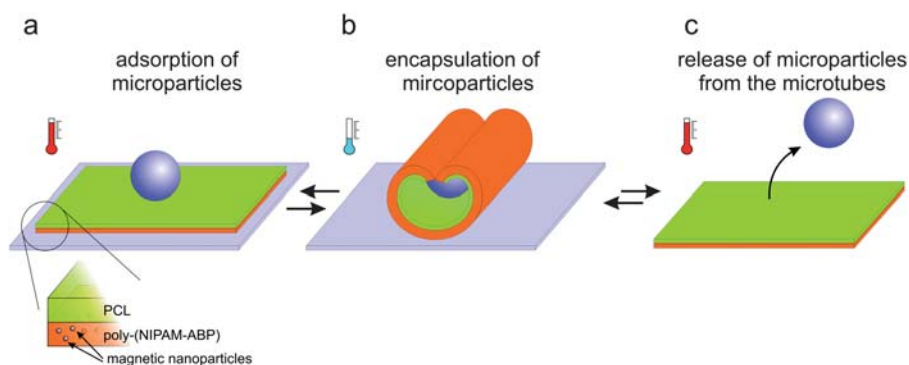


**Fig. 1** Scheme of capture and release of microparticles by self-rolling microtubes. Thin film of poly(*N*-isopropylacrylamide-*co*-4-acryloylbenzophenone) (poly(NIPAM-ABP) and polycaprolactone (PCL)) with admixed magnetic nanoparticles (a) is able to form self-rolling tube and to encapsulate microparticles at reduced temperature (b). The particle can be released at elevated temperature when the microtube is unrolled (c).

completely at elevated temperatures when the poly(NIPAM-ABP) is collapsed. Meanwhile tubes formed by multiple revolutions shrink at elevated temperature and are unable to unroll. Both shrinking and unrolling are very rapid (1–5 seconds), completely reversible and can be repeated many times.

Second, we tested the possibility to load microtubes with 10  $\mu\text{m}$   $\text{SiO}_2$  particles as well as to release them. For this, microparticles were adsorbed from their aqueous dispersion on patterned polymer two-layer film at elevated temperature when poly(NIPAM-ABP) is collapsed and microtubes are not formed. Decrease of the temperature resulted in swelling of the poly(NIPAM-ABP) and led to the formation of microtubes with encapsulated microparticles (Fig. 2). We observed two mechanisms of particle encapsulation—microparticles were either encapsulated inside rolls or entrapped between the rolls. The microparticles encapsulated inside rolls produced by multiple rolling cannot be released at elevated temperature due to inability of microtubes to unroll and remain entrapped inside the microtubes. On the other hand, microparticles encapsulated inside one-revolution rolls (Fig. 3, ESI† Movie S3) and between the rolls are able to leave the microtubes at elevated temperatures when thermoresponsive polymer is collapsed. These experiments demonstrated the possibilities to encapsulate, trap and release particles using self-rolling tubes.

Finally, we tested the possibility to manipulate particle-loaded microtubes using magnetic field. For this, we prepared microtubes containing 0.7 mass% of oleic acid-coated  $\text{Fe}_3\text{O}_4$  nanoparticles<sup>24</sup> in the thermoresponsive layer and loaded them with microparticles. We found that the freely flowing particle-loaded microtubes start to move in the direction of the magnet when it is applied (Fig. 4, ESI† Movie S4). The direction of the microtubes flow can be immediately

switched by changing the position of the magnet, thus demonstrating the possibility to manipulate the microtubes using magnetic field.

In conclusion, we demonstrated the design of partially biodegradable thermo- and magneto-sensitive self-rolling tubes capable of controlled capture and release of objects with size up to 10  $\mu\text{m}$ , which is the size of living cells. The main advantages of these tubes are (1) improved biocompatibility and biodegradability, (2) possibility to release encapsulated objects as well as (3) ability to manipulate them using magnetic field. Since simple methods such as dipcoating and photolithography were used, the reported method can be easily scaled up for production of large quantities of microtubes. Comparing to the other methods for drug and cell delivery such as hollow capsules, gel particles and vesicles, the presented approach gives opportunity of controlled release of large objects such as cells by stimuli-induced unrolling of tubes. Potentially, the cell-loaded tubes can be also assembled into 3D scaffolds. In this case, the advantage of microtubes comparing to cell-loaded hydrogel particles is a structural and mechanical anisotropy, which is intrinsic to many kinds of tissues including bones, muscles, *etc.* We foresee that the demonstrated approach can be successfully implemented for controlled delivery of drugs and cells in living organisms as well as for the design scaffolds for tissue engineering.

## Experimental part

### Materials

*N*-Isopropylacrylamide (NIPAM, Aldrich), 4-hydroxybenzophenone (Fluka), polycaprolactone ( $M_n = 70\,000\text{--}90\,000$ , Aldrich),

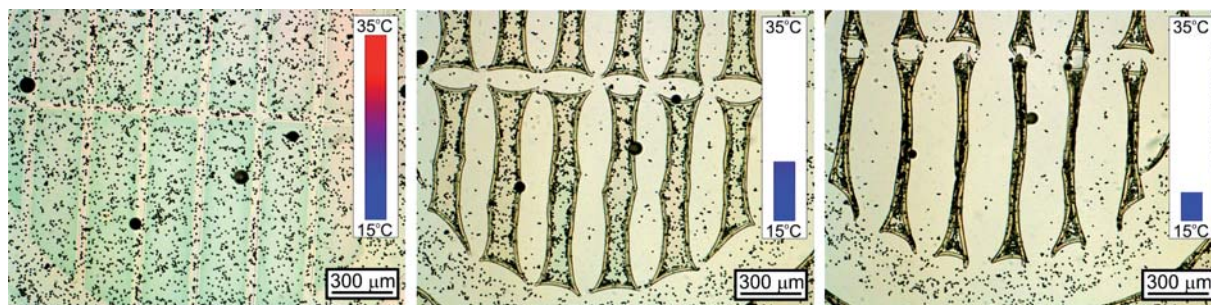


**Fig. 2** Microscopy snapshots of encapsulation of microparticles by self-rolling tubes upon cooling. (See ESI†, Movies S1 and S2.)

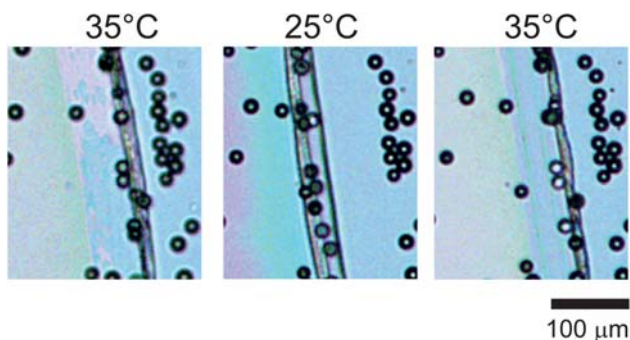


**Fig. 3** Encapsulation and release of microparticles from microtube at different temperatures. (See ESI†, Movie S3.) The one-revolution microtubes unroll at elevated temperature thus releasing the particles.



**Fig. 4** Magneto-sensitive properties of microtubes. Microscopy snapshots of microparticle-loaded microtubes containing magnetic nanoparticles flowing in the applied magnetic field. (See ESI†, Movie S4.) Arrows show the direction of flow.

benzophenone (Aldrich) and acryloyl chloride (Fluka) were used as received.

#### Synthesis of 4-acryloylbenzophenone (ABP)

4-Hydroxybenzophenone (20 g, 0.1009 mol), diisopropylethylamine (19.3 ml, 0.1110 mol) and 80 ml of methylene chloride were added into 200 ml three-necked round-bottom flask fitted with an overhead stirrer, a thermometer, and an addition funnel with acryloyl chloride (9.02 ml, 0.1110 mol) solution in 20 ml of methylene chloride. The acryloyl chloride solution was added dropwise into the flask under cooling (0–5 °C) for *ca.* 3 hours. The methylene chloride was removed by rotary evaporation. The residue was washed with 80 ml of 20% HCl, 80 ml of saturated solution of sodium hydrocarbonate and dried over sodium sulfate. The solution was passed through a silica gel column with chloroform as the eluent. Chloroform was removed by a rotary evaporator. Finally, 24.44 g (95%) of ABP was obtained. <sup>1</sup>H NMR (CDCl<sub>3</sub>, 500 MHz): 6.05 (dd, *J*<sub>1</sub> = 10.40, *J*<sub>2</sub> = 1.26, 1H), 6.34 (dd, *J*<sub>1</sub> = 10.40, *J*<sub>3</sub> = 17.34, 1H), 6.64 (dd, *J*<sub>3</sub> = 17.34, *J*<sub>2</sub> = 1.26, 1H), 7.27 (m, 2H), 7.49 (m, 2H), 7.59 (m, 1H), 7.80 (m, 2H), 7.86 (m, 2H).

#### Synthesis of poly-(NIPAM-ABP)

ABP (0.02253 g, 0.089 mmol; 0.04551 g, 0.18 mmol; 0.11737 g, 0.47 mmol), NIPAM (1 g, 0.0885 mol), AIBN (0.01453 g, 0.089 mmol) were added in 10 ml test tubes. Components were dissolved in 6 ml 1,4-dioxane and degassed with nitrogen for 30 minutes. Test tubes were tightly sealed and placed into a shaker (70 °C, 90 rpm) for 24 hours. Then the mixtures were cooled to room temperature and

poured slowly into diethyl ether. Products were filtered and dried under vacuum.

#### Synthesis of magnetic particles

The oleic acid stabilized iron oxide nanoparticles were prepared as described in ref. 24. Briefly, FeCl<sub>3</sub> and FeCl<sub>2</sub> were dissolved in 40 ml of deionized water. The solution was heated at 80 °C for 1 h while being stirred. A solution of 0.1 ml oleic acid in 5 ml acetone was added to the heated salt solution. Then 5 ml of NH<sub>4</sub>OH (30% w/w) were added rapidly to it. Further additions of oleic acid were made in five 0.2 ml (undiluted) volumes over 5 min intervals. The crystal growth was allowed to proceed for 30 min at 80 °C with constant stirring. The suspension was then cooled to room temperature. The suspended particles were flocculated by acetone and were washed five times with acetone and methanol mixture (equal volumes) to remove the excess oleic acid and were recovered by magnetic decantation.

#### Preparation of self-rolling tubes

In a typical experiment, poly(NIPAM-ABP) was spin-coated from its chloroform solution on silica wafer substrate. Polycaprolactone with 2–5 mass% of benzophenone was spin-coated from toluene solution on poly(NIPAM-ABP) film. The bilayer film was illuminated through TEM grid by halogen lamp for 15 min to crosslink polymers. The illuminated film was rinsed in chloroform in order to remove polymers in non-irradiated areas.

#### Acknowledgements

The authors are grateful to Alexander Sidorenko (USP) for fruitful discussions. DFG (Grant IO 68/1-1) and Volkswagen Foundation are acknowledged for financial support.

#### Notes and references

- 1 S. Levenberg and R. Langer, in *Current Topics in Developmental Biology*, ed. Gerald P. Schatten, Elsevier Academic Press Inc, San Diego, 2004, vol. 61, p. 113–134.
- 2 F. Couet, N. Rajan and D. Mantovani, *Macromol. Biosci.*, 2007, **7**, 701–718.
- 3 G. C. Gurtner, M. J. Callaghan and M. T. Longaker, *Annu. Rev. Med.*, 2007, **58**, 299–312.
- 4 B. V. Slaughter, S. S. Khurshid, O. Z. Fisher, A. Khademhosseini and N. A. Peppas, *Adv. Mater.*, 2009, **21**, 3307–3329.
- 5 N. A. Peppas, J. Z. Hilt, A. Khademhosseini and R. Langer, *Adv. Mater.*, 2006, **18**, 1345–1360.
- 6 C. D. H. Alarcon, S. Pennadam and C. Alexander, *Chem. Soc. Rev.*, 2005, **34**, 276–285.
- 7 P. M. Mendes, *Chem. Soc. Rev.*, 2008, **37**, 2512–2529.
- 8 Y. Qiu and K. Park, *Adv. Drug Delivery Rev.*, 2001, **53**, 321–339.
- 9 J. Jagur-Grodzinski, *Polym. Adv. Technol.*, 2010, **21**, 27–47.
- 10 T. R. Hoare and D. S. Kohane, *Polymer*, 2008, **49**, 1993–2007.
- 11 K. M. Park, S. Y. Lee, Y. K. Joong, J. S. Na, M. C. Lee and K. D. Park, *Acta Biomater.*, 2009, **5**, 1956–1965.
- 12 W. X. Wang, H. Liang, R. C. Al Ghanami, L. Hamilton, M. Fraylich, K. M. Shakesheff, B. Saunders and C. Alexander, *Adv. Mater.*, 2009, **21**, 1809–1813.
- 13 A. B. Vorob'ev and V. Y. Prinz, *Semicond. Sci. Technol.*, 2002, **17**, 614–616.
- 14 S. V. Golod, V. Y. Prinz, V. I. Mashanov and A. K. Gutakovskiy, *Semicond. Sci. Technol.*, 2001, **16**, 181–185.
- 15 G. S. Huang, Y. F. Mei, D. J. Thurmer, E. Coric and O. G. Schmidt, *Lab Chip*, 2009, **9**, 263–268.

- 
- 16 V. Luchnikov, O. Sydorenko and M. Stamm, *Adv. Mater.*, 2005, **17**, 1177–1182.
- 17 K. Kalaitzidou and A. J. Crosby, *Appl. Phys. Lett.*, 2008, **93**, 041910.
- 18 N. Yamada, T. Okano, H. Sakai, F. Karikusa, Y. Sawasaki and Y. Sakurai, *Makromol. Chem. Rapid Commun.*, 1990, **11**, 571–576.
- 19 D. L. Huber, R. P. Manginell, M. A. Samara, B. I. Kim and B. C. Bunker, *Science*, 2003, **301**, 352–354.
- 20 L. Ionov, M. Stamm and S. Diez, *Nano Lett.*, 2006, **6**, 1982–1987.
- 21 L. Ionov, A. Synytska and S. Diez, *Adv. Funct. Mater.*, 2008, **18**, 1501–1508.
- 22 I. Y. Galaev and B. Mattiasson, *Trends Biotechnol.*, 1999, **17**, 335–340.
- 23 L. Ionov and S. Diez, *J. Am. Chem. Soc.*, 2009, **131**, 13315–13319.
- 24 D. Maity and D. C. Agrawal, *J. Magn. Magn. Mater.*, 2007, **308**, 46–55.



**Ionov, L.;** Synytska, A.; Kaul, E.; Diez S.

Protein-resistant polymer coatings based on surface-adsorbed poly(aminoethyl methacrylate)/poly(ethylene glycol) copolymers

***Biomacromolecules*** 2010, *11* (1), 233–237.

# Protein-Resistant Polymer Coatings Based on Surface-Adsorbed Poly(aminoethyl methacrylate)/Poly(ethylene glycol) Copolymers

Leonid Ionov,<sup>\*,†,‡</sup> Alla Synytska,<sup>‡</sup> Elisabeth Kaul,<sup>‡</sup> and Stefan Diez<sup>†</sup>

Max-Planck-Institute of Molecular Cell Biology and Genetics, Pfotenhauer Str. 108, 01307 Dresden, Germany, and Leibniz Institute of Polymer Research Dresden e.V., Hohe Str. 6, D-01069 Dresden, Germany

Received September 22, 2009; Revised Manuscript Received November 25, 2009

We report on the protein-resistant properties of glass substrates coated with novel copolymers of 2-aminoethyl methacrylate hydrochloride and poly(ethylene glycol) methyl ether methacrylate (AEM-PEG). In comparison to currently available protein-blocking polymer systems, such as poly-L-lysine-poly(ethylene glycol), silane-based poly(ethylene glycol), and poly(ethylene glycol) brushes prepared by surface-initiated polymerization, the proposed AEM-PEG offers the combined advantages of low cost, simplicity of use, and applicability in aqueous solutions. We demonstrate the capability of AEM-PEG to block the surface binding of globular proteins (tubulin), their assemblies (microtubules), and functional motor proteins (kinesin-1). Moreover, we demonstrate the applicability of AEM-PEG for surface patterning of proteins in microfluidic devices.

## Introduction

Reducing the nonspecific adsorption of proteins on surfaces is important for biomedical, bioanalytical, and bionanotechnology applications.<sup>1–6</sup> Currently, poly(ethylene glycol) (PEG) based polymers with different architectures are widely used for this purpose. The methods to immobilize PEG on different substrates include the grafting or adsorption of functionalized PEGulating agents and surface-initiated polymerization.<sup>7–12</sup> Among these methods, the ones that can be easily utilized in an aqueous environment for lab-on-chip systems deserve particular interest. For example, graft copolymers of poly-L-lysine (PLL) with PEG side chains (PLL-PEG) were shown to adsorb from biological buffer solutions onto a variety of substrate materials including glass and metal oxides.<sup>13,14</sup> Thereby, the positively charged PLL backbone sticks to the negatively charged substrates (providing stability for the adsorbed layer) and the PEG side chains stretch away from the surface (forming the protein-resistant layer). However, despite the widely demonstrated applicability of PLL-PEG for surface blocking, for generating of protein patterns and gradients, as well as for cell adhesion studies,<sup>15,16</sup> PLL-PEG is rather expensive.

Here we report on the synthesis and the investigation of the protein-repellent properties of a low-cost PLL-PEG analog. In particular, we prepared random copolymers of 2-aminoethyl methacrylate and poly(ethylene glycol) methyl ether methacrylate (AEM-PEG, Figure 1). AEM-PEG comprises a positively charged backbone and PEG side chains, thus, mimicking the structure of PLL-PEG. We tested the protein-resistant properties of glass substrates modified by AEM-PEG and compared our results to surface blockings based on PLL-PEG as well as silane-based poly(ethylene glycol) (silane-PEG).<sup>17</sup>

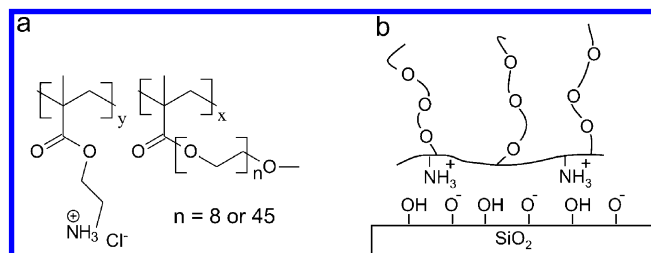


**Figure 1.** Characteristics of poly(ethylene glycol) methyl ether methacrylate and 2-aminoethyl methacrylate hydrochloride (AEM-PEG). (a) Chemical structure of AEM-PEG. The number of monomer units are denoted by  $x$  and  $y$  and the length of the PEG side chains is given by  $n$ . (b) Schematic representation of AEM-PEG adsorption onto negatively charged surfaces.

## Experimental Section

**Chemicals.** 2-Aminoethyl methacrylate hydrochloride (AEM, Aldrich), 2,2'-azobis(2-methylpropionitrile) (AIBN, Fluka), *N,N*-dimethylformamide (DMF, Fluka), PLL(20)-g(3.2)-PEG(5) (Surface Solutions, batch SZ24-3, 20.6.2005), and 2-[methoxy(polyethyleneoxy)propyl]trimethoxysilane (ABCR) were used as received. The poly(ethylene glycol) methyl ether methacrylate,  $M_n = 475$  (PEG475, Aldrich), and poly(ethylene glycol) methyl ether methacrylate 50% water solution,  $M_n = 2080$  (PEG2K, Aldrich), were purified by passing through an  $Al_2O_3$  column.

**Fabrication of Silane-PEG Substrates.** Piranha-cleaned glass substrates were incubated in 2.3 mg/mL toluene solution of 2-[methoxy(polyethyleneoxy)propyl]trimethoxysilane for 18 h. The substrates were rinsed several times in toluene, ethanol, and pure water.

**Synthesis of AEM-PEG Copolymers.** Poly(ethylene glycol) methyl ether methacrylate (1 g) with different molecular weights, a variable amount of 2-aminoethyl methacrylate hydrochloride, and 2 mg of AIBN were dissolved in 5 mL of water/DMF 1:1 mixture. Polymerization was performed under a nitrogen atmosphere for 24 h. The resulting polymer solution was diluted to a concentration of 1 mg/mL and used for further experiments. Obtained polymers were defined as AEM $\alpha$ -PEG $\beta$ , where  $\alpha$  is the molecular weight of PEG side chains (475 stands for 475 g/mol, 2080 stands for 2080 g/mol), and  $\beta$  is the mass of AEM in milligrams used for the synthesis of polymers. For example, sample

\* To whom correspondence should be addressed. Current address: Leibniz Institute of Polymer Research Dresden e.V., Hohe Str. 6, D-01069 Dresden, Germany. E-mail: ionov@ipfdd.de; ionov@mpi-cbg.de.

<sup>†</sup> Max-Planck-Institute of Molecular Cell Biology and Genetics.

<sup>‡</sup> Leibniz Institute of Polymer Research Dresden e.V.

PEG2K-AEM6.5 was prepared using 1 g of poly(ethylene glycol) methyl ether methacrylate ( $M_n = 2080$  g/mol) and 6.5 mg of 2-aminoethyl methacrylate hydrochloride. Degree of polymerization was estimated by SEC using dimethylacetamide as eluting solvent. For determination of composition we applied NMR ( $\text{CDCl}_3$ ). We found that NMR spectra of copolymers as prepared (no purification after the synthesis) and after dialysis against water for 7 days are quantitatively similar. In fact, the ratio between peaks corresponding the PEG side chains ( $\delta \approx 3.65$ ) and AEM groups ( $\delta \approx 3.65$  and  $\delta \approx 3.4$ ) did not change after dialysis.

**Polymer Adsorption Experiments.** Glass coverslips or silica wafers cleaned in piranha solution ( $\text{H}_2\text{SO}_4$  and  $\text{H}_2\text{O}_2$  2:1) at 70 °C for 40 min and were used as substrates. Narrow channels ( $3 \times 18 \times 0.1$  mm) were fabricated between the cleaned glass coverslips and formed the flow cells for further experiments. The channel was filled with PEG-AEM copolymers solution (1 mg/mL in pure water). After about 10 min the channel was rinsed with BRB80 (80 mM PIPES/KOH pH = 6.9, 1 mM EGTA, 1 mM  $\text{MgCl}_2$ ) buffer.

**Adsorption of Microtubules and Tubulin.** Taxol-stabilized, rhodamine-labeled microtubules ( $\sim 30$  nM tubulin, 1 mM ATP, 1 mM  $\text{MgCl}_2$ , 10  $\mu\text{M}$  Taxol, and oxygen scavenger mix; all in BRB80 buffer) were prepared as described elsewhere.<sup>2</sup> Unpolymerized tubulin was not removed. The substrates were exposed to the microtubule/tubulin solutions for 5 min. Afterward, not-adsorbed microtubules and tubulin were removed by rinsing with BRB80 (containing 10  $\mu\text{M}$  Taxol).

**Microtubule Motility Experiments.** Motility experiments were performed in flow channels with adsorbed polymers. A casein-containing solution (0.5 mg/mL in BRB80) was perfused into the flow cell and allowed to adsorb to the surfaces for 5 min. Next, 50  $\mu\text{L}$  of a motor solution containing 2  $\mu\text{g/mL}$  wild-type kinesin-1 in BRB80 (full length drosophila conventional kinesin expressed in bacteria and purified as described in ref 18) was perfused into the flow cell and allowed to adsorb for 5 min. Thereafter, a motility solution containing rhodamine-labeled taxol-stabilized microtubules<sup>2,19</sup> was applied.

**Ellipsometry.** The thickness of the polymer layers was measured at  $\lambda = 633$  nm and an angle of incidence of 70° (in dry state) and of 68° (in specially designed cell for in situ measurements) with a null-ellipsometer (Multiscope, Optrel Berlin) as described elsewhere.<sup>20,21</sup> The density of PEG-side chains in the polymer layer adsorbed on the glass ( $\Gamma_{\text{PEG}}$ ) and the distance between individual PEG chains on the surface ( $D$ ) were calculated using eqs 1 and 2, respectively:

$$\Gamma_{\text{PEG}}(\text{mg/m}^2) = H \cdot \rho \cdot (1 - \varphi_{\text{AEM}}^{\text{mass}}) \quad (1)$$

$$D(\text{nm}^{-1}) = \sqrt{\frac{M_{\text{PEG}}}{\Gamma_{\text{PEG}} \cdot N_A}} \quad (2)$$

where  $H$  is the dry thickness of the adsorbed polymer layer,  $\rho$  is the bulk mass density of polymer,  $\varphi_{\text{AEM}}^{\text{mass}}$  is the mass fraction of AEM,  $M_{\text{PEG}}$  is the molecular weight of PEG,  $N_A$  is Avogadro's number.

**Fluorescence Microscopy.** Fluorescence images were obtained using an Axiovert 200 M inverted microscope with a 20 $\times$  objective (Zeiss, Oberkochen, Germany) equipped with a FluoArc lamp. For data acquisition a standard TRITC filterset (excitation: HQ 535/50; dichroic: Q 565 LP; emission: HQ 610/75, Chroma Technology) in conjunction with a Micromax 512 BFT camera (Photometrics, Tucson, AZ) and a MetaMorph imaging system (Universal Imaging, Downingtown, PA) were used.

**Electrokinetic Measurements.** The streaming potential measurements were carried out with the Electrokinetic Analyzer (EKA) by Anton Paar GmbH, Graz, Austria, using a special rectangular cell (developed and constructed at the Leibniz Institute of Polymer Research, Dresden, Germany) for small flat pieces. Details of the measuring technique and the used device are reported elsewhere.<sup>22,23</sup> The zeta potential was calculated according to Smoluchowski.<sup>24</sup>

## Results and Discussions

**Adsorption of Polymers.** Two series of AEM-PEG copolymers with different lengths of the PEG side chains (Figure 1) were synthesized using free radical polymerization. The obtained copolymers were denominated as AEM $\alpha$ -PEG $\beta$ , where  $\alpha$  is the mass of AEM in milligrams per gram of PEG monomer used for synthesis and  $\beta$  is the molecular weight of the PEG (in g/mol). The degree of polymerization varied between 600–1000 monomer units. While the obtained polymers were all water soluble, increasing the fraction of AEM resulted in gelation of the polymer water solutions.

We studied the adsorption of AEM-PEG copolymers on negatively charged glass surfaces ( $\text{IEP}_{\text{GLASS}} = 2$ ; Figure 2). It was found that the thickness of the adsorbed polymer layers as function of the composition exhibited a peak-like character (Figure 2a and b).<sup>25,26</sup> The incorporation of small amounts of positively charged AEM groups in the polymer chains first resulted in a sharp increase of the polymer adsorption. This behavior indicates that a minimum number of positively charged groups per chain are required for sustained polymer adsorption to the surface. On the other hand, at larger AEM amounts the layer thickness decreased due to the lower number of PEG side chains per polymer molecule. Importantly, this decrease was not linear. We believe that this nonlinearity results from internal electrostatic repulsions of AEM groups (leading to an increased footprint of the polymer coils on the surface) and from repulsions between the charged polymer coils themselves.

We calculated the distances between individual (AEM-bound) PEG chains on surface and compared these values to the gyration radii of PEG chains of similar molecular weight (Figure 2d). The distance was found to be minimal for the polymers AEM3.2-PEG475 and AEM3.2-PEG2080. It is important to note that these minimal distances were almost equal to the gyration radii of free PEG chains with similar molecular weight<sup>27</sup> in aqueous environment. This indicates that, although the (AEM-bound) PEG chains are not in the brush regime, they completely shield the glass substrate.

Zeta potential measurements proved the substrate shielding by the adsorbed polymers. While the glass substrate was strongly negatively charged ( $\zeta = -60$  mV at pH = 5), the adsorbed AEM-PEG polymers reduced the negative charge. The most pronounced reduction in surface charge was observed for AEM3.2-PEG2080 and AEM230-PEG475 (Figure 3). In these cases, the glass substrates were almost uncharged. Considering the low thickness of the adsorbed AEM230-PEG475 layer (see Figure 2b), we can assume that the main reason for the charge reduction is the large amount of AEM in the polymer chains. On the other hand, the adsorbed AEM3.2-PEG2080 layer was significantly thicker and the reduction in surface charge was most likely caused by the formation of a relatively dense PEG layer (see Figure 2b and d).

Combining the results on polymer adsorption, we predict that AEM $\alpha$ -PEG2080 copolymers with  $\alpha$  in the range from 1.6 to 6.5 will most efficiently prevent the surface adsorption of proteins. These polymers form the thickest and the densest PEG layers, while at the same time, they completely reduce the negative surface charge.

**Protein Adsorption.** We tested the adsorption of fluorescently labeled proteins to AEM-PEG coated surfaces on the examples of tubulin (globular protein with a size of about 5 nm) and in vitro reconstructed microtubules (protein assemblies with a diameter of about 25 nm and lengths of several tens of  $\mu\text{m}$ ; Figures 4 and 5). In addition, we investigated the binding

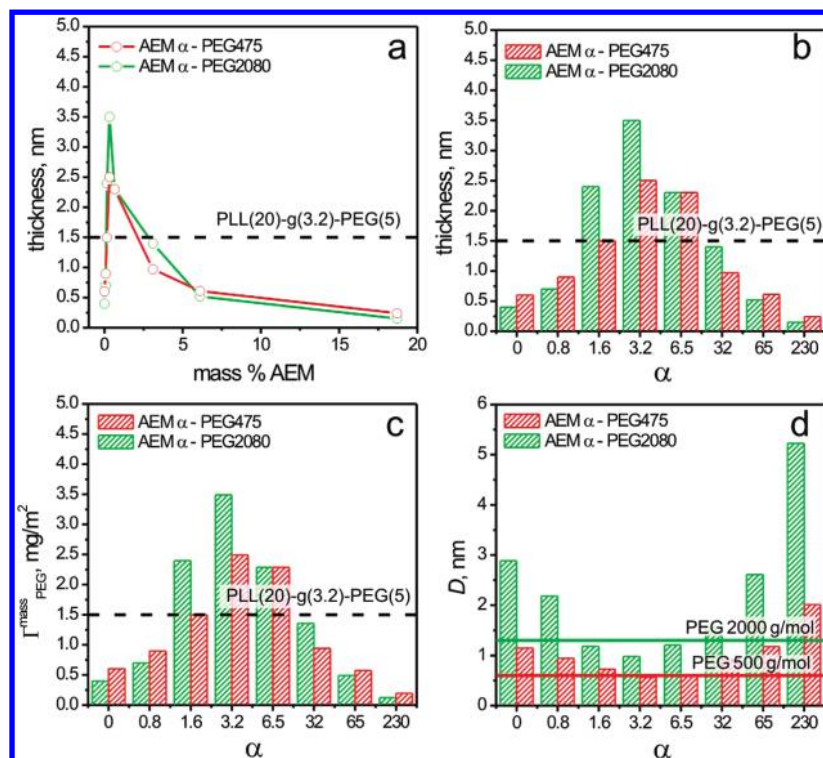


**Figure 2.** Surface adsorption of AEM-PEG to glass. (a and b) Two different representations of the thickness of adsorbed AEM $\alpha$ -PEG2080 (green) and AEM $\alpha$ -PEG475 (red) copolymers as function of their composition. (c) Calculated grafting density and (d) distance between individual (AEM-bound) PEG chains vs AEM-PEG composition. For comparison, the thickness (dashed lines in a and b) and the grafting density (dashed line in c) of adsorbed PLL(20)-g(3.2)-PEG(5) layers are plotted. Moreover, the gyration radii of PEG with molecular weights of 500 g/mol and 2000 g/mol in water (red and green lines in d) are given for reference.

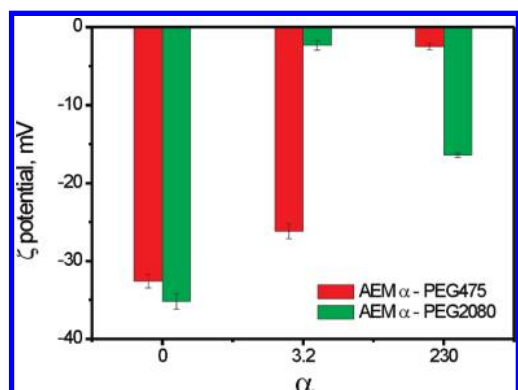


**Figure 3.** Zeta potential of glass surfaces with adsorbed PEG-AEM copolymers at pH = 5 and 1 mM KCl.

of unlabeled kinesin-1 motor proteins, which the presence on the surface was probed in microtubule gliding assays (Figure 6).

When applying a solution containing rhodamine-labeled microtubules and unpolymerized rhodamine-labeled tubulin to glass surfaces treated with AEM6.5-PEG2080 (Figure 4a) and AEM3.2-PEG2080 (Figure 4b), we observed very low protein binding comparable to a glass surface treated with silane-PEG (Figure 4c). Surprisingly, we found PLL(20)-g(3.2)-PEG(5) to be rather inefficient in surface blocking (Figure 4d), comparable to untreated (piranha-cleaned) surfaces without polymers (Figure 4e) and surfaces treated with AEM-PEG copolymers with high amounts of AEM (images not shown). On those samples, microtubules were not prevented from binding to the surface and a significantly increased fluorescent background signal originating from unpolymerized tubulin was observed. We believe that the sticking of microtubules on the PLL-PEG coated

glass substrate is due to the high density of accessible positively charged lysine groups. On the other hand, as it was reported by Textor et al.<sup>14</sup> and by Vogel et al. in<sup>16</sup> the optimization of the length of PEG side chains and the composition of PLL-PEG allows for very efficient blocking of adsorption of model proteins and kinesin motor proteins.

Varying the polymer composition, we found that, for all AEM amounts, copolymers with longer PEG chains ( $\beta = 2080$ ) more efficiently suppressed protein adsorption than shorter PEG chains ( $\beta = 475$ ; Figure 5). For compositions with  $\alpha < 32$ , independent of the actual AEM amount, no binding of microtubules was observed and the amount of bound tubulin was low.

To further demonstrate the efficiency of surface blocking, we adsorbed kinesin-1 motor proteins<sup>28</sup> on different PEG-modified surfaces and assayed the gliding motility of microtubules.<sup>29</sup> We found that microtubules (i) were gliding (with normal speed of 800 nm/s) on untreated glass surfaces without polymers, (ii) got stuck immotile on PLL-PEG-coated glass surfaces, and (iii) did not bind at all to glass surfaces coated with AEM6.5-PEG2080, AEM3.2-PEG2080, and silane-PEG coated glasses.

We also tested the protein-repellent properties of the polymer layer after treatment in different environment. For this we applied PBS, pH = 7.4, 100  $\mu$ M, BRB 80, pH = 6.9, buffers as well as organic solvents (ethanol and acetone). We found the protein-repellent properties of the polymer layer are kept after exposure to these media.

**Surface Patterning.** Finally, we tested the applicability AEM-PEG copolymers for surface structuring in microfluidic devices. In a flow cell formed between two glass coverslips, we filled half of the channel with a AEM6.5-PEG2080 solution. After incubation for 10 min, the solution was removed and replaced by a motility solution containing kinesin-1 motor



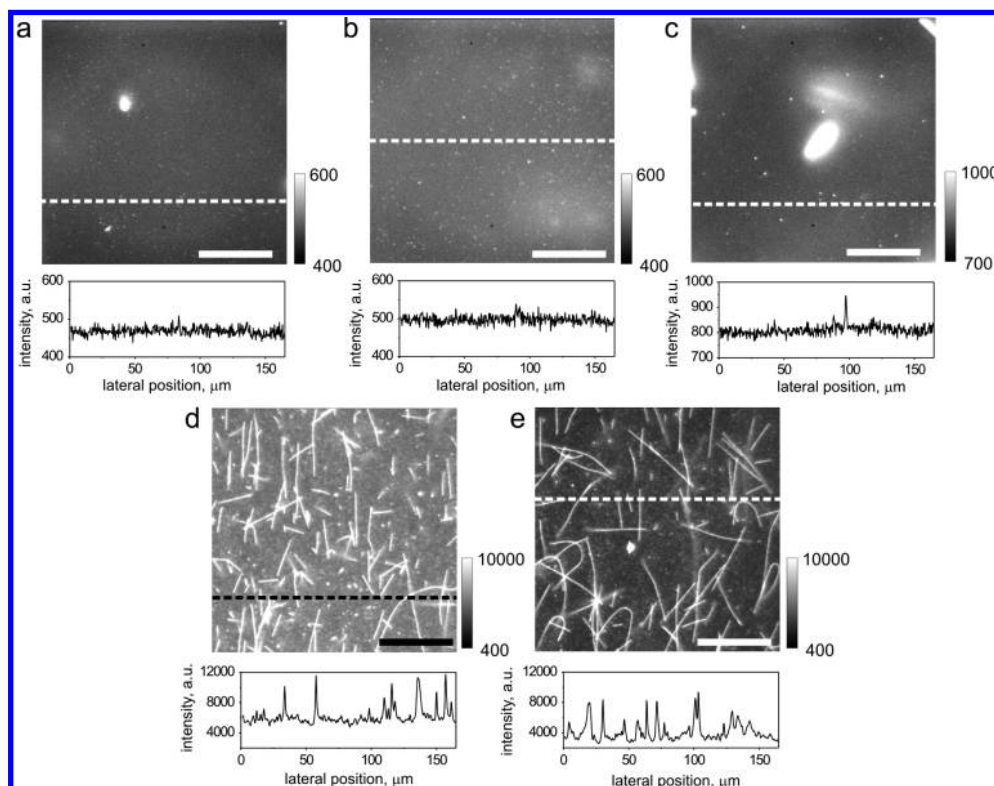


**Figure 4.** Adsorption of fluorescent tubulin and microtubules on differently treated glass surfaces: (a) AEM6.5-PEG2080, (b) AEM3.2-PEG2080, (c) silane-PEG, (d) PLL(20)-g(3.2)-PEG(5), and (e) piranha-cleaned glass without polymers. The surfaces were incubated with the protein solutions for 5 min and carefully rinsed with unfluorescent buffer solution before imaging. Intensity profiles along the dashed lines in the fluorescence micrographs (scale bar 50  $\mu\text{m}$ ) are given below the images. The bright spots in the images a, b, and c are microtubules floating freely in solution.

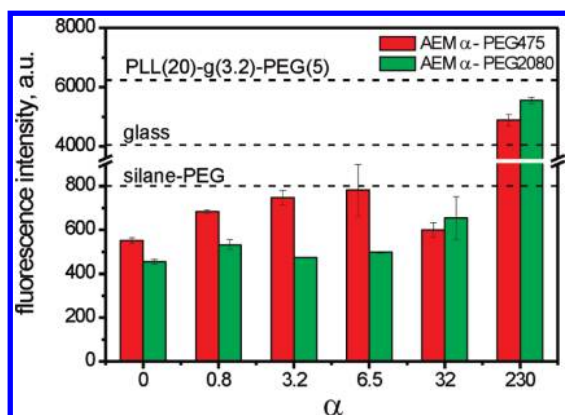


**Figure 5.** Background fluorescence intensities of rhodamine-labeled tubulin adsorbed on glass substrates treated with different AEM-PEG copolymers (evaluated from images as exemplarily shown in Figure 4). Intensity values on piranha-cleaned as well as silane-PEG and PLL(20)-g(3.2)-PEG(5)-coated glass surfaces are given for reference.

protein. In microtubule motility assays we then observed a well-defined border between the untreated and the formerly polymer-covered areas.

In conclusion, we designed novel polymers, which are highly suitable to prevent the adsorption of proteins on glass surfaces. The proposed polymers show unique combination of advantages (such as low price, simplicity of use, applicability in water solutions) over widely used PLL-PEG, silane-PEG, and PEG brushes prepared by surface-initiated polymerization. We believe that these advantages will make the developed polymers

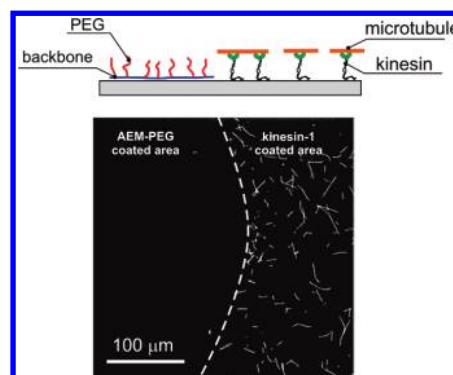


**Figure 6.** Surface patterning of kinesin-1 using AEM-PEG. Before the whole flow cell was incubated with kinesin-1 motors, half of the glass surfaces were treated with AEM6.5-PEG2080. Rhodamine-labeled microtubules were then gliding on the areas formerly not-covered by AEM-PEG, while no motility was observed on the areas with adsorbed polymer.

attractive for many future applications including the chemical structuring of surfaces in microfluidic devices and the design of bioanalytical chips in general.

**Acknowledgment.** The authors are thankful to Ms. Franziska Jäkel and Dr. Cornelia Bellman for zeta potential measurements. This work was supported by the BMBF (Grant 03N8712), the Volkswagen Foundation, the DFG (Grants SY125/1-1 and IO 68/1-1), and the Max-Planck-Society.

## References and Notes

- (1) Harris, J. M.; Chess, R. B. *Nat. Rev. Drug Discovery* **2003**, 2, 214–221.



- (2) Ionov, L.; Stamm, M.; Diez, S. *Nano Lett.* **2005**, *5*, 1910–1914.
- (3) Desai, T. A. *Med. Eng. Phys.* **2000**, *22*, 595–606.
- (4) Suh, K. Y.; Seong, J.; Khademhosseini, A.; Laibinis, P. E.; Langer, R. *Biomaterials* **2004**, *25*, 557–563.
- (5) Sofia, S. J.; Premnath, V.; Merrill, E. W. *Macromolecules* **1998**, *31*, 5059–5070.
- (6) Langer, R.; Peppas, N. A. *AIChE J.* **2003**, *49*, 2990–3006.
- (7) Otsuka, H.; Nagasaki, Y.; Kataoka, K. *Curr. Opin. Colloid Interface Sci.* **2001**, *6*, 3–10.
- (8) Harder, P.; Grunze, M.; Dahint, R.; Whitesides, G. M.; Laibinis, P. E. *J. Phys. Chem. B* **1998**, *102*, 426–436.
- (9) Du, H.; Chandaroy, P.; Hui, S. W. *Biochim. Biophys. Acta* **1997**, *1326*, 236–248.
- (10) Lee, S. W.; Laibinis, P. E. *Biomaterials* **1998**, *19*, 1669–1675.
- (11) Zhang, F.; Kang, E. T.; Neoh, K. G.; Wang, P.; Tan, K. L. *Biomaterials* **2001**, *22*, 1541–1548.
- (12) Unsworth, L. D.; Sheardown, H.; Brash, J. L. *Langmuir* **2005**, *21*, 1036–1041.
- (13) Huang, N. P.; Michel, R.; Voros, J.; Textor, M.; Hofer, R.; Rossi, A.; Elbert, D. L.; Hubbell, J. A.; Spencer, N. D. *Langmuir* **2001**, *17*, 489–498.
- (14) Kenausis, G. L.; Voros, J.; Elbert, D. L.; Huang, N. P.; Hofer, R.; Ruiz-Taylor, L.; Textor, M.; Hubbell, J. A.; Spencer, N. D. *J. Phys. Chem. B* **2000**, *104*, 3298–3309.
- (15) Falconnet, D.; Csucs, G.; Grandin, H. M.; Textor, M. *Biomaterials* **2006**, *27*, 3044–3063.
- (16) Brunner, C.; Wahnes, C.; Vogel, V. *Lab Chip* **2007**, *7*, 1263–1271.
- (17) Hubbell, J. A.; Elbert, D.; Hill-west, J. L.; Drumheller, P. D.; Chowdhury, S.; Sawhney, A. S. Multifunctional organic polymers. U.S. Patent 5,462,990, 1995.
- (18) Coy, D. L.; Wagenbach, M.; Howard, J. J. *Biol. Chem.* **1999**, *274*, 3667–3671.
- (19) Ionov, L.; Stamm, M.; Diez, S. *Nano Lett.* **2006**, *6*, 1982–1987.
- (20) Ionov, L.; Zdyrko, B.; Sidorenko, A.; Minko, S.; Klep, V.; Luzinov, I.; Stamm, M. *Macromol. Rapid Commun.* **2004**, *25*, 360–365.
- (21) Ionov, L.; Sidorenko, A.; Eichhorn, K. J.; Stamm, M.; Minko, S.; Hinrichs, K. *Langmuir* **2005**, *21*, 8711–8716.
- (22) Simon, F.; Werner, C.; Bellmann, C. *Tech. Mess.* **1996**, *63*, 447.
- (23) Bellmann, C.; Synytska, A.; Caspari, A.; Drechsler, A.; Grundke, K. *J. Colloid Interface Sci.* **2007**, *309*, 225–230.
- (24) Smoluchowski, M. In *Handbuch der Elektrizität und des Magnetismus*; Graetz, L., Ed.; Barth Verlag: Leipzig, 1921; Vol. II, p 366.
- (25) Elbert, D. L.; Hubbell, J. A. *Chem. Biol.* **1998**, *5*, 177–183.
- (26) Konradi, R.; Pidhatika, B.; Muhlebach, A.; Textor, M. *Langmuir* **2008**, *24*, 613–616.
- (27) Tanaka, S.; Ataka, M.; Onuma, K.; Kubota, T. *Biophys. J.* **2003**, *84*, 3299–3306.
- (28) Howard, J. *Nature* **1997**, *389*, 561–567.
- (29) Katira, P.; Agarwal, A.; Fischer, T.; Chen, H. Y.; Jiang, X.; Lahann, J.; Hess, H. *Adv. Mater.* **2007**, *19*, 3171–3176.

BM901082Y

Ionov, L.; Diez S.

Environment-friendly photolithography using poly-(N-isopropylacrylamide)-based  
thermoreponsive photoresist

***Journal of American Chemical Society*** 2009, 131(37), 13315-13319.

## Environment-Friendly Photolithography Using Poly(*N*-isopropylacrylamide)-Based Thermoresponsive Photoresists

Leonid Ionov<sup>\*,†,‡</sup> and Stefan Diez<sup>†</sup>

Max-Planck-Institute of Molecular Cell Biology and Genetics, Pfotenhauer Str. 108,  
01307 Dresden, Germany, and Leibniz Institute of Polymer Research Dresden, Hohe Str. 6,  
01069 Dresden, Germany

Received April 3, 2009; E-mail: ionov@ipfdd.de; ionov@mpi-cbg.de

**Abstract:** We report a novel approach for the temperature-triggered development of water-soluble photoresists based on photocleavable poly(*N*-isopropylacrylamide) copolymers. These copolymers are soluble in an aqueous environment below their Lower Critical Solution Temperature (LCST). Upon UV irradiation, the photocleavable groups are deprotected resulting in an increased LCST. Thus, the illuminated parts of spin-coated copolymer layers dissolve at higher temperatures than the surrounding areas, leading to pattern development. The photoresist can finally be completely removed at low temperature. We demonstrate the applicability of this novel photolithographic approach by the patterning of fluorescent proteins.

Development of photopatterning technology is of importance for microelectronics,<sup>1</sup> sensor design,<sup>2,3</sup> microfluidics,<sup>4,5</sup> biotechnology,<sup>6–8</sup> bioanalytics,<sup>9,10</sup> and tissue engineering.<sup>11</sup> Thereby, different compounds undergoing photoinduced degradation<sup>12</sup> or cross-linking<sup>13</sup> are implemented as photoresists for fabrication of structured surfaces. In fact, the design of photosensitive compounds determines the applicability of any particular sort of photolithography. For example, water-soluble photoresists<sup>12,14</sup> are of particular interest for the *in situ* patterning of proteins and cells<sup>15–17</sup> under biologically relevant conditions. Recently, various photoresists that are water-soluble and can be developed in

an aqueous environment have been designed. However, most of them undergo immediate development upon illumination. This causes an undesired contamination of the surrounding due to the uncontrolled release of dissolved photoresists.

Here, we demonstrate a novel approach for the design of photoresists which can be fully processed in aqueous environment but which development is triggered by temperature. Our design is based on random copolymers of poly(*N*-isopropylacrylamide) (PNIPAM) with photocleavable groups. In an aqueous environment, PNIPAM (homopolymer) reversibly changes its solubility at the Low Critical Solution Temperature (LCST = 33 °C). Due to its thermoresponsive properties, PNIPAM has been already applied for cell culturing,<sup>18</sup> directed protein adsorption,<sup>19</sup> control of biomolecular motors,<sup>20</sup> protein purification,<sup>21</sup> and drug delivery.<sup>22</sup> In our approach, we incorporated hydrophobic 2-nitrobenzyl photocleavable groups into the PNIPAM chains and prepared random poly(2-nitrobenzyl acrylate-co-*N*-isopropylacrylamide) copolymers (poly(NIPAM-NBA)) resulting in a lowered LCST. Upon UV irradiation, the LCST of the copolymers increases due to the formation of poly(acrylic acid-co-*N*-isopropylacrylamide) (poly(NIPAM-AA)). Consequently, when photostructured copolymer layers

<sup>†</sup> Max-Planck-Institute of Molecular Cell Biology and Genetics.

<sup>‡</sup> Leibniz Institute of Polymer Research Dresden.

- (1) Beh, W. S.; Kim, I. T.; Qin, D.; Xia, Y. N.; Whitesides, G. M. *Adv. Mater.* **1999**, *11* (12), 1038–1041.
- (2) Ionov, L.; Minko, S.; Stamm, M.; Gohy, J. F.; Jerome, R.; Scholl, A. *J. Am. Chem. Soc.* **2003**, *125* (27), 8302–8306.
- (3) Synytska, A.; Stamm, M.; Diez, S.; Ionov, L. *Langmuir* **2007**, *23* (9), 5205–5209.
- (4) Zhao, B.; Moore, J. S.; Beebe, D. J. *Science* **2001**, *291* (5506), 1023–1026.
- (5) Ionov, L.; Houbenov, N.; Sidorenko, A.; Stamm, M.; Minko, S. *Adv. Funct. Mater.* **2006**, *16* (9), 1153–1160.
- (6) Revzin, A.; Russell, R. J.; Yadavalli, V. K.; Koh, W. G.; Deister, C.; Hile, D. D.; Mellott, M. B.; Pishko, M. V. *Langmuir* **2001**, *17* (18), 5440–5447.
- (7) Ionov, L.; Synytska, A.; Diez, S. *Adv. Funct. Mater.* **2008**, *18* (10), 1501–1508.
- (8) Falconnet, D.; Csucs, G.; Grandin, H. M.; Textor, M. *Biomaterials* **2006**, *27* (16), 3044–3063.
- (9) Duffy, D. C.; McDonald, J. C.; Schueller, O. J. A.; Whitesides, G. M. *Anal. Chem.* **1998**, *70* (23), 4974–4984.
- (10) Blawas, A. S.; Reichert, W. M. *Biomaterials* **1998**, *19* (7–9), 595–609.
- (11) Kaihara, S.; Borenstein, J.; Koka, R.; Lalan, S.; Ochoa, E. R.; Ravens, M.; Pien, H.; Cunningham, B.; Vacanti, J. P. *Tissue Engineering* **2000**, *6* (2), 105–117.
- (12) Yamada, S.; Mrozek, T.; Rager, T.; Owens, J.; Rangel, J.; Willson, C. G.; Byers, J. *Macromolecules* **2004**, *37* (2), 377–384.
- (13) Trakhtenberg, S.; Warner, J. C.; Nagarajan, R.; Bruno, F. F.; Samuelson, L. A.; Kumar, J. *Chem. Mater.* **2006**, *18* (12), 2873–2878.

- (14) Lin, Q. H.; Steinhäusler, T.; Simpson, L.; Wilder, M.; Medeiros, D. R.; Willson, C. G.; Havard, J.; Frechet, J. M. J. *Chem. Mater.* **1997**, *9* (8), 1725–1730.
- (15) Doh, J.; Irvine, D. J. *J. Am. Chem. Soc.* **2004**, *126* (30), 9170–9171.
- (16) Doh, J.; Irvine, D. J. *Proc. Natl. Acad. Sci. U.S.A.* **2006**, *103* (15), 5700–5705.
- (17) Katz, J. S.; Doh, J.; Irvine, D. J. *Langmuir* **2006**, *22* (1), 353–359.
- (18) Yamada, N.; Okano, T.; Sakai, H.; Karikusa, F.; Sawasaki, Y.; Sakurai, Y. *Makromol. Chem., Rapid Commun.* **1990**, *11* (11), 571–576.
- (19) Huber, D. L.; Manginell, R. P.; Samara, M. A.; Kim, B. I.; Bunker, B. C. *Science* **2003**, *301* (5631), 352–354.
- (20) Ionov, L.; Stamm, M.; Diez, S. *Nano Lett.* **2006**, *6* (9), 1982–1987.
- (21) Galaev, I. Y.; Mattiasson, B. *Trends Biotechnol.* **1999**, *17* (8), 335–340.
- (22) Alarcon, C. D. H.; Pennadam, S.; Alexander, C. *Chem. Soc. Rev.* **2005**, *34* (3), 276–285.

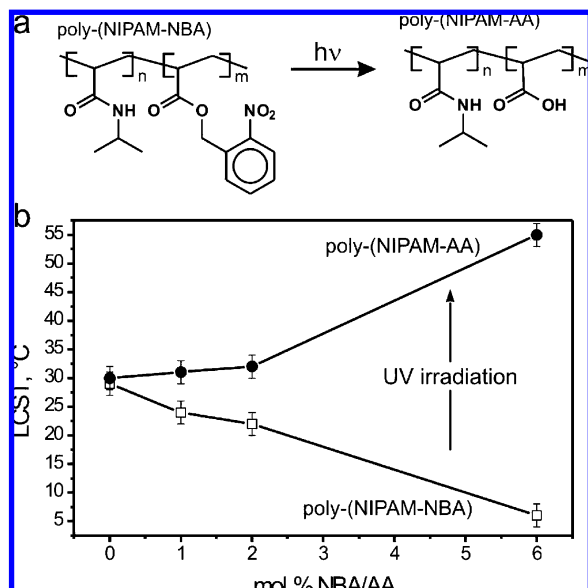


**Figure 1.** Properties of photocleavable PNIPAM copolymers. (a) Schematic conversion of poly(NIPAM-NBA) into poly(NIPAM-AA) upon UV irradiation. (b) Thermoresponsive behavior (Low Critical Solution Temperature, LCST) of poly(NIPAM-NBA) (□) and poly(NIPAM-AA) (●) in PBS 100 mM buffer (pH = 7) as a function of copolymer composition.

are cooled down from a high temperature (where they are insoluble), poly(NIPAM-AA) and poly(NIPAM-NBA) dissolve in a sequential manner.

We have synthesized poly(NIPAM-NBA) with different fractions of photocleavable comonomer as described elsewhere<sup>7</sup> and investigated its thermoresponsive behavior in an aqueous environment (Figure 1). We found that the incorporation of nitrobenzyl acrylate reduced the LCST<sup>23</sup> by more than 20 °C. The conversion of hydrophobic nitrobenzyl acrylate groups into carboxylic acid occurred upon irradiation with UV light (Figure 1a). The LCST of the polymer thereby significantly increased due to the formation of hydrophilic groups. This remarkable change in the thermoresponsive behavior of PNIPAM-based copolymers after UV irradiation, in combination with the possibility to deposit it onto substrates from aqueous solutions, allows their use as photoresists with thermotrigged development.

The general concept of this novel type of photolithography using PNIPAM-based photoresists is illustrated in Figure 2. A thin film of poly(NIPAM-NBA) (Figure 2a) is deposited on a substrate and irradiated with UV light through a mask at elevated temperature (Figure 2b). Reducing the temperature slightly below the LCST of the poly(NIPAM-AA) leads to pattern development in the biological buffer (Figure 2c). While proteins can bind to the patterned surface everywhere (Figure 2d), proteins adsorbed to the top of the photoresist are removed by lowering the temperature below the LCST of the poly(NIPAM-NBA) (Figure 2e).

To experimentally demonstrate the thermotrigged development of the PNIPAM-based photoresist, we spin-coated 100–150 nm thick films of poly(NIPAM-NBA) (6 mol % of NBA,  $M_w$  = 114 000; PDI = 1.7, LCST = 6 °C) with an admixed small amount of fluorescent nanoparticles<sup>24</sup> on a glass substrate.

Illumination with the UV light through a mask caused the photocleavage of nitrobenzyl groups and changed the optical properties of the photoresist. As a result, the contrast between illuminated and nonilluminated areas could be detected using epi-fluorescence microscopy (Figure 3a). The illuminated polymer was removed by rinsing in PBS buffer at 25 °C (below LCST of poly(NIPAM-AA) which is  $T$  = 55 °C) leading to pattern development (Figure 3b). The photoresist pattern was completely removed by rinsing in cold PBS buffer at 4 °C (below LCST of poly(NIPAM-NBA) which is 6 °C) (Figure 3c).

We quantified the thickness of the photoresist layer on each step of processing using null-ellipsometry. For this, we spin-coated a thin layer of the photoresist (87 nm) onto a silicon wafer and illuminated half of the film with UV light for 10 min. After 20 min of development in PBS buffer at room temperature (corresponds to Figure 2c and 3b), we found that the thickness of the photoresist in illuminated areas was reduced down to 0.1 nm, while the thickness in nonilluminated areas was reduced only slightly (down to 72 nm). After additional rinsing in PBS buffer at  $T$  = 4 °C for 20 min, the thickness of the photoresist in nonilluminated areas was completely removed; the thickness was reduced down to 0.1 nm. In agreement with the results of null-ellipsometry, fluorescence microscopy shows that the amount of photoresist in nonilluminated areas is slightly reduced after development at room temperature (reduce of fluorescence after development, Figure 3a and b). Moreover, fluorescence intensity in developed areas is almost equal to that after complete removal of the photoresist (Figure 3b and c). Thus, we can argue that the photoresist film can be completely removed both in the illuminated areas after development at room temperature and in the nonilluminated areas at reduced temperature.

We tested the potential of our method for the *in situ* photoresist development in microfluidic devices. For this, fluorescent neutravidin-coated 200 nm large beads were adsorbed on poly(NIPAM-NBA) (with 1 mol % of NBA) from an aqueous environment at temperature  $T$  = 35 °C (above the LCST of the deprotected poly(NIPAM-AA), see Figure 1b). The polymer layer was then illuminated through a 100× oil objective (1.4 numerical aperture) by UV light. We observed that the particles stayed attached to the illuminated polymer if the surrounding temperature was higher than the LCST of poly(NIPAM-AA) (Figure 4a; note that due to photobleaching the fluorescent beads in the illuminated area appear slightly dimmer than those in the surrounding area.). The illuminated polymer dissolved, and the fluorescent beads were released after the temperature was reduced below the LCST of the photo-deprotected polymer (Figure 4b). Further cooling down to  $T$  = 8 °C removed the photoresist completely (Figure 4c).<sup>25</sup> This experiment demonstrated the possibility for *in situ* patterning using poly(NIPAM-NBA) photoresists.

Finally, we demonstrated the applicability of the developed method for protein patterning. Poly(NIPAM-NBA) (with 6 mol % of NBA and admixed red-fluorescent CdSeS quantum dots, as tested in the experiment illustrated in Figure 3) was used as a photoresist. After illumination through a mask and development at moderate temperature ( $T$  = 30 °C), fluorescent casein

(23) The LCST of all polymers were measured in PBS 100 mM buffer, pH = 7.

(24) Nanoparticles were used to make the polymer fluorescent and detectable using fluorescence microscopy. The CdSeS nanocrystals were kindly provided by Dr. A. Rogach (LMU).

(25) We note that the efficient development of photoresist inside a narrow channel occurred at lower temperatures than the LCST of poly(NIPAM-AA). This finding can be attributed to slow polymer dissolution because no stirring was applied and the process was limited by diffusion.

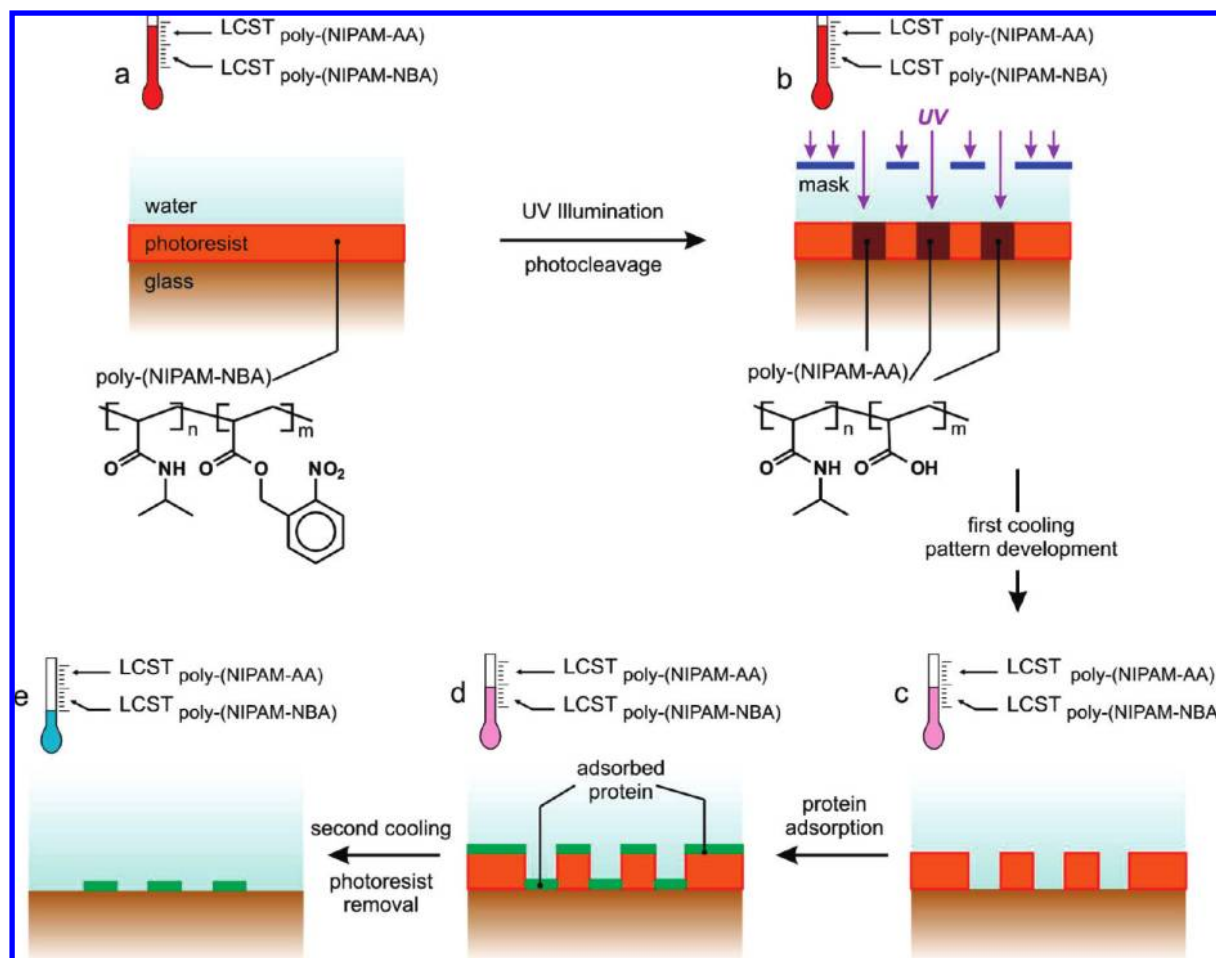


**Figure 2.** Scheme of photopatterning using PNIPAM-based photoresists with temperature-triggered development. Thermoresponsive poly(2-nitrobenzyl acrylate-co-*N*-isopropylacrylamide) is deposited as photoresist onto a substrate (a). Illumination of the photoresist (b) results in photocleavage of nitrobenzyl acrylate groups, increasing the LCST. After the photoresist pattern is developed at slightly lower temperature (c), proteins are adsorbed (d). The photoresist (together with the proteins on top) can be completely removed in aqueous environment at low temperatures (e).

(10 mg/mL) was adsorbed to the patterned surface. The unbound casein was then washed out by rinsing in warm PBS buffer ( $T = 30\text{ }^{\circ}\text{C}$ ),<sup>26</sup> and the residual photoresist was removed by rinsing in cold PBS buffer ( $T = 4\text{ }^{\circ}\text{C}$ ). The thickness of the casein layer as measured by null-ellipsometry is 2.4 nm. We observed a clear pattern of fluorescent casein (green) on the surface (Figure 5a) and a minor residual red signal in the areas which were covered by the photoresist (Figure 5b). On the other hand, we did not observe the red signal if the experiment was performed using the polymer without added fluorescent nanocrystals (images are not shown). Therefore, we attribute the red signal in the areas previously occupied by the nonilluminated photoresist to precipitation of water-insoluble fluorescent nanoparticles, which were added to photoresist.<sup>24</sup>

Because carboxylic groups are formed upon illumination of poly(NIPAM-NBA), we expect that our thermoresponsive photoresist can demonstrate pH-dependent development similarly to the pH-sensitive photoresist developed by Irvine.<sup>15</sup> Therefore, our photoresist can be used in the same way as it was suggested by Irvine: it can be deposited onto a positively charged substrate and form a bilayer after patterning.<sup>15</sup> On the other hand, since negatively charged glass was used as the substrate, the photoresist could be completely removed in illuminated areas after pattern development

at moderate temperature and in nonilluminated areas after additional rinsing at low temperature. In contrast to the photoresist developed by Irvine, our photoresist can be developed by applying different temperatures.

In conclusion, we developed a novel approach for the design of environment-friendly (water-soluble/water-developing) photoresists with stimuli-triggered development based on photocleavable copolymers of poly(*N*-isopropylacrylamide). The proposed photoresists possess a unique combination of advantages: (i) they are soluble in biological buffers, (ii) their photocleaved products are soluble in an aqueous environment as well, and (iii) their development is triggered by temperature in physiological buffer in a controllable way and no change of pH is required. We demonstrated the applicability of the presented method for *in situ* patterning inside microfluidic channels and for protein patterning on surfaces. We foresee a strong potential of our method for patterning and harvesting proteins, particles, and cells in microfluidic devices, where all procedures have to be performed in biological buffers.

## Experimental Section

**Materials.** *N*-Isopropylacrylamide (NIPAM, Aldrich), acetone (Aldrich), anhydrous dichloromethane (Aldrich), triethylamine (Fluka), 2-nitrobenzyl alcohol (Fluka), acryloyl chloride (Fluka), *N,N,N',N'',N'''*-pentamethyldiethylenetriamine (PMDTA, Aldrich),

(26) Warm buffer was used to prevent further pattern development.



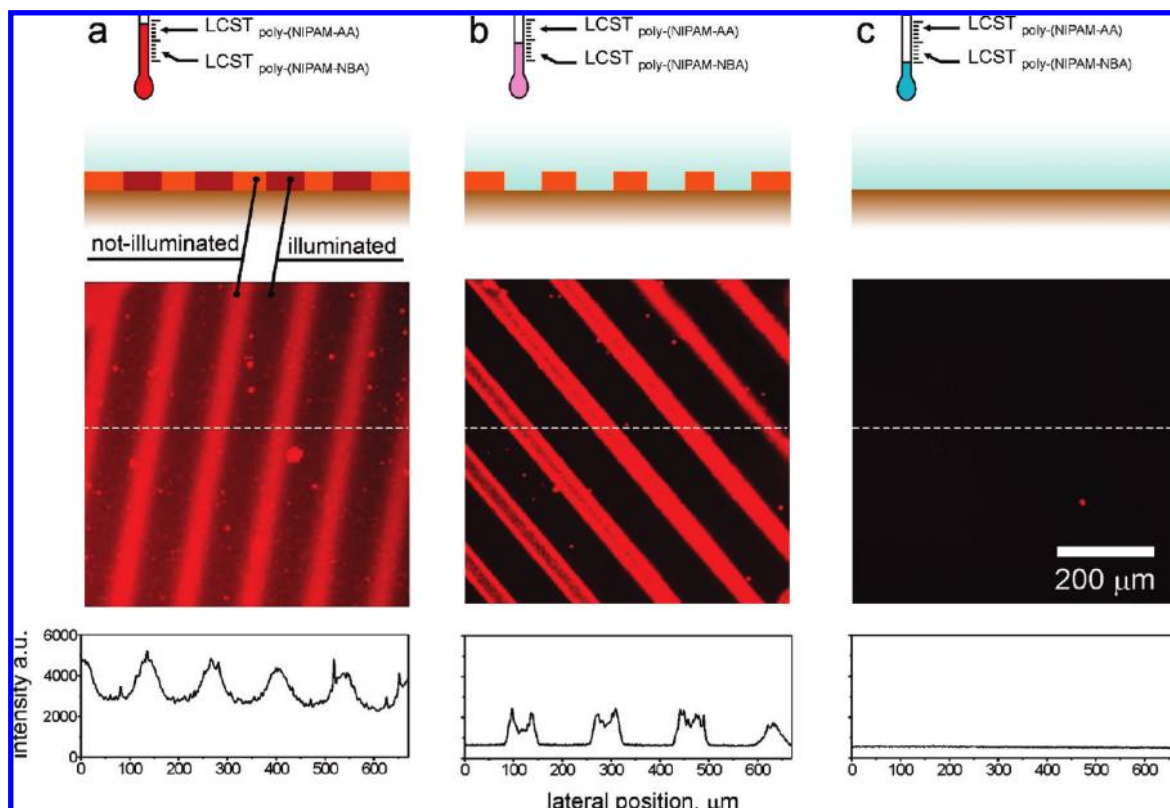


**Figure 3.** Fluorescence micrographs of poly(NIPAM-NBA) photoresist (% NBA = 6 mol %;  $M_w = 114\,000$ ; PDI = 1.7;  $\text{LCST}_{\text{poly(NIPAM-NBA)}} = 6\text{ }^\circ\text{C}$ ;  $\text{LCST}_{\text{poly(NIPAM-AA)}} = 55\text{ }^\circ\text{C}$ ) with admixed fluorescent CdSeS nanocrystals<sup>16</sup> at different stages of processing: (a) after illumination; (b) after development at 25 °C; and (c) after cooling to 4 °C.

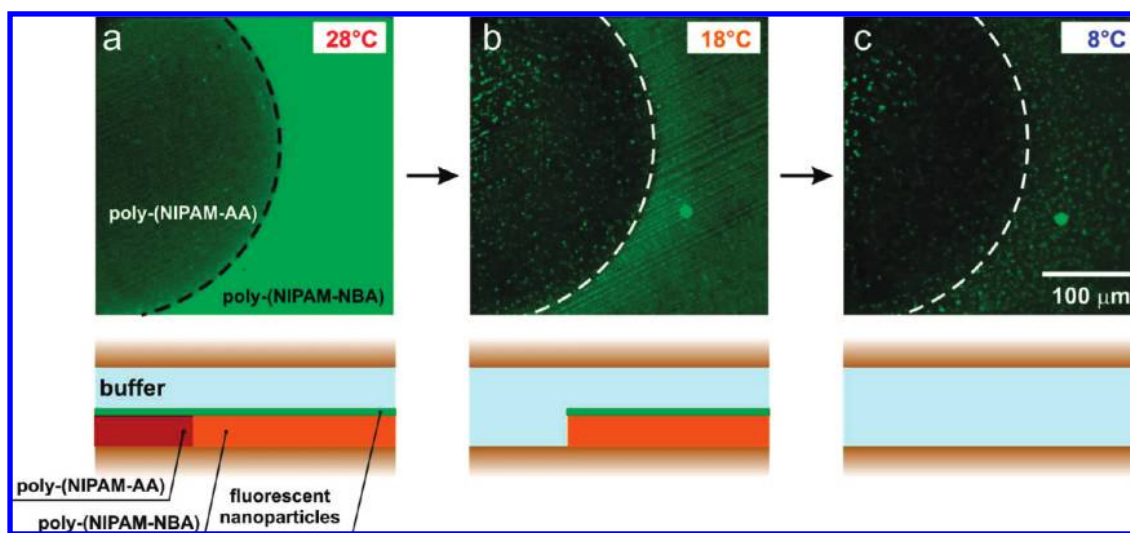


**Figure 4.** Fluorescence micrographs of in situ temperature-triggered development of poly(NIPAM-NBA) photoresist (% NBA = 1 mol %;  $\text{LCST}_{\text{poly(NIPAM-NBA)}} = 25\text{ }^\circ\text{C}$ ;  $\text{LCST}_{\text{poly(NIPAM-AA)}} = 29\text{ }^\circ\text{C}$ ;  $M_w = 25\,000$ ; PDI = 1.5) at different temperatures.

ethyl-2-bromoisobutyrate (EBiB), ethylenediamine (ED, Fluka), anhydrous dichloromethane (Aldrich), 2-bromo-2-methylpropanoyl bromide (BMPB, Aldrich), triethylamine (Fluka), L-ascorbic acid (Sigma), and copper bromide (Aldrich) were used as received.

**Synthesis of 2-Nitrobenzyl Acrylate (NBA).** 3 g ( $1.9 \times 10^{-2}$  mol) of 2-nitrobenzyl alcohol and 2.1 g ( $2 \times 10^{-2}$  mol) of triethylamine were dissolved in 20 mL of anhydrous dichloromethane, and 1.7 mL ( $2 \times 10^{-2}$  mol) of acryloyl chloride were added dropwise to the resulting solution. Stirring continued for 1 h. After filtering out the resulting salt, the filtrate was concentrated and purified by column chromatography (packed material: silica

gel; eluent: hexane/ethyl acetate = 10/1). Thus, 2.7 g of an oily liquid were recovered and confirmed to be 2-nitrobenzyl acrylate by NMR spectroscopy.  $\delta = 5.6$  (s, 2H),  $\delta = 5.8\text{--}6.5$  (m, 3H),  $\delta = 7.1\text{--}8.1$  (m, 4H).

**Synthesis of Poly(NIPAM-NBA) Copolymers.** The poly(NIPAM-NBA) copolymer with 6 mol % of NBA was prepared according to the following procedure. *N*-Isopropylacrylamide (4 g,  $3.5 \times 10^{-2}$  mol), 2-nitrobenzyl acrylate (465 mg,  $2.25 \times 10^{-3}$  mol), and EBiB (8 mg,  $4.1 \times 10^{-5}$  mol) were dissolved in 6 mL of acetone solution of  $\text{CuBr}_2$  (0.4 mg,  $1.8 \times 10^{-6}$  mol) and PMDTA (0.31 mg,  $1.8 \times 10^{-6}$  mol). The reaction solution was added to the

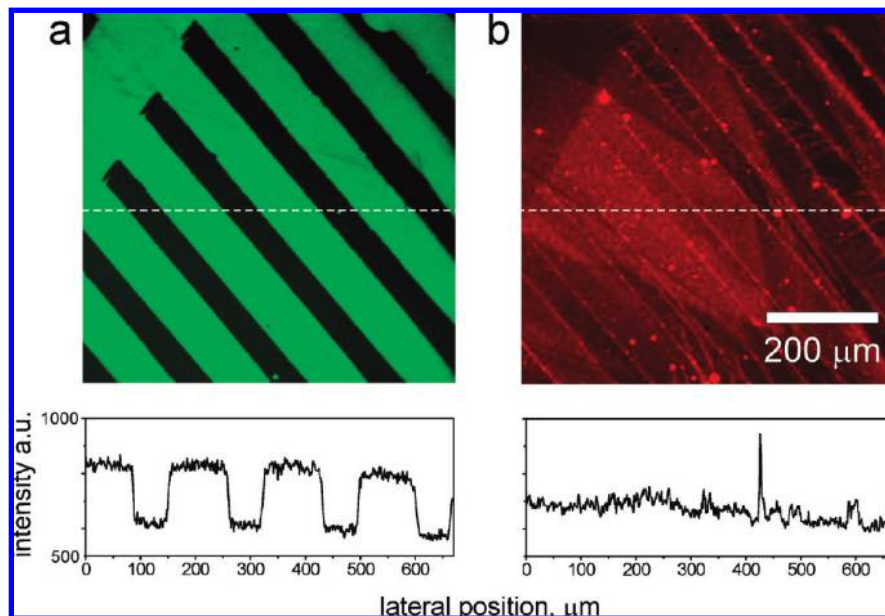


**Figure 5.** Fluorescence micrographs of a FITC-casein pattern obtained by photolithography using poly(NIPAM-NBA) (% NBA = 6 mol %;  $M_w$  = 114 000; PDI = 1.7;  $LCST_{poly(NIPAM-NBA)} = 6\text{ }^{\circ}\text{C}$ ;  $LCST_{poly(NIPAM-AA)} = 55\text{ }^{\circ}\text{C}$ ) photoresist with added CdSeS fluorescent nanocrystals. (a) Signal of FITC-casein (green) and (b) signal of poly(NIPAM-NBA) with admixed CdSeS quantum dots with partial cross-talk from the FITC-casein and from precipitated fluorescent nanocrystals (red).

tube and sealed with a rubber septum; a solution of L-ascorbic acid (18 mg,  $1 \times 10^{-4}$  mol) in water (0.5 mL) was injected. The vial was placed in a  $70\text{ }^{\circ}\text{C}$  oil bath. The polymerization was carried out under stirring and was stopped after 4 h. The polymer was precipitated in diethylether. The copolymers with different composition were prepared using a similar route. The LCST of polymers was measured in PBS 100 mM buffer, pH = 7.

**Fluorescent Microscopy.** Fluorescence images were obtained using an Axiovert 200 M inverted microscope with a  $10\times$  objective (Zeiss, Oberkochen, Germany) equipped with a FluoArc lamp. For data acquisition a standard TRITC filterset (excitation: HQ 535/50; dichroic: Q 565 LP; emission: HQ 610/75, Chroma Technology)

and FITC filterset (excitation: HQ 480/40, dichroic: Q 505 LP, emission: HQ 535/75, Chroma Technology, Rockingham, VT) in conjunction with a Micromax 512 BFT camera (Photometrics, Tucson, AZ) and a MetaMorph imaging system (Universal Imaging, Downingtown, PA) were used.

**Acknowledgment.** Petra Treppe (IPF Dresden) is acknowledged for technical support. This work was supported by the BMBF (Grant 03N8712), the Volkswagen Foundation, and the Max-Planck-Society.

JA902660S

Ionov, L.; Bocharova, V.; Diez, S.

Biotemplated synthesis of stimuli-responsive nanopatterned polymer brushes on  
microtubules

***Soft Matter*** 2009, 5, 67–71.

# Biotemplated synthesis of stimuli-responsive nanopatterned polymer brushes on microtubules

Leonid Ionov,<sup>\*a</sup> Vera Bocharova<sup>b</sup> and Stefan Diez<sup>a</sup>

Received 31st July 2008, Accepted 8th September 2008

First published as an Advance Article on the web 23rd September 2008

DOI: 10.1039/b813295j

We report the synthesis of nanostructured stimuli-responsive polymer brushes using atom transfer radical polymerisation initiated on protein filaments of the cytoskeleton. In particular, we used microtubules and prepared thermoresponsive poly-(*N*-isopropylacrylamide) brushes with incorporated fluorescent groups. The use of microtubules as templates for fabrication of “soft” polymeric nanostructures on surfaces opens new possibilities for the design of functional materials.

Nanostructured surfaces are of growing interest for information storage,<sup>1</sup> microfluidics,<sup>2</sup> design of smart materials,<sup>3</sup> biotechnology,<sup>4</sup> microelectronics,<sup>5</sup> photonic applications<sup>6</sup> *etc.* Thereby, the use of biological objects as templates for the design of the nanostructures offers a range of advantages.<sup>7</sup> In particular, selective molecular recognition and proof-reading during the build-up of biomolecules can provide a high degree of uniformity in the possible structures. Different biomacromolecules and their assemblies including DNA, viral capsids, cytoskeleton filaments and protein crystals were successfully applied as templates for the fabrication of inorganic nanostructured materials (see recent review<sup>7</sup>). On the other hand, design of functional organic nanostructures<sup>8–10</sup> using biotemplating is still an almost unexplored field.

Microtubules, which are cylindrical protein filaments with outer diameters of about 24 nm and lengths up to tens of micrometres, deserve a particular interests as templates.<sup>11–14</sup> First, microtubules can be easily formed by self-assembly of tubulin dimers. Second, microtubules are able to form segmented structures with different functionality in a controlled manner.<sup>15</sup> Third, a number of approaches to control position as well as orientation of microtubules on artificial substrates are available.<sup>16–20</sup> This makes microtubules highly promising for templated synthesis of complex materials.

Here, we demonstrate the fabrication of stimuli-responsive nanopatterned polymer brushes using microtubules as templates. In particular, we report on the “grafting from” synthesis of thermoresponsive poly-(*N*-isopropylacrylamide)—PNIPAM—brushes by atom transfer radical polymerisation (ATRP) initiated on microtubules. The outer surfaces of microtubules contain reactive amino groups providing the possibility for chemical modification with fluorescent and other functional groups. In our approach, we substituted the amino groups with reactive groups capable of

initiating ATRP and grew polymer chains from surface-adsorbed microtubules (Fig. 1).

Rhodamine-labelled microtubules (fluorescent emission in the red wavelength range) were prepared by self-assembly of  $\alpha,\beta$ -tubulin dimers (see Experimental part). The microtubules were then adsorbed on DDS-coated glass surfaces by perfusing them in buffer solution through a narrow channel between two glass cover slips. The adsorbed microtubules were crosslinked by glutaraldehyde, which reacted with lysine residues and formed chemical links between neighbouring amino groups (Fig. 2a). Because part of the glutaraldehyde molecules did not react bifunctionally with the lysine residues, the outer surface of the crosslinked microtubules then contained aldehyde groups. Initiator groups were then immobilized onto the crosslinked microtubules by sequentially treating them with 2,2'-(ethylenedioxy)bis(ethylamine) and bromo-2-methylpropanoyl bromide (see Experimental part for details). The initiator-modified microtubules possessed a rod-like shape, which remained undeformed after multiple rinsings in different organic solvents (Fig. 2b). Using the simplified ATRP developed by Matyjaszewski *et al.*,<sup>21</sup> we demonstrated the polymerisation of *N*-isopropylacrylamide with small addition (2 wt%) of fluorescein *o*-acrylate (Fig. 2c). Most strikingly, the diameters of the polymer-modified microtubules were substantially increased and their shape was often deformed.

The role of fluorescein *o*-acrylate (fluorescent emission in the green wavelength range) was to make the synthesized polymer brushes

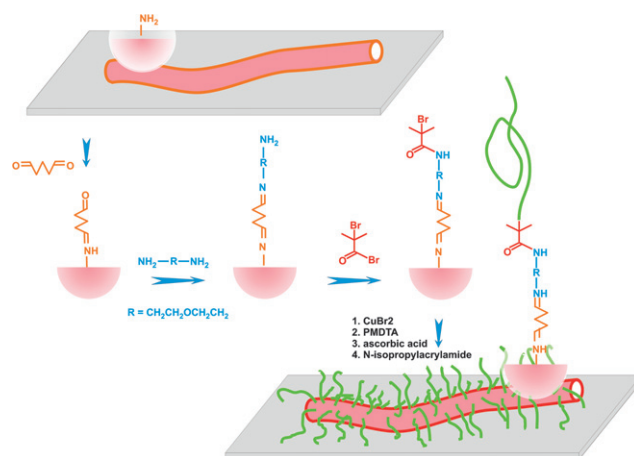


**Fig. 1** Schematic diagram of microtubule modification and polymer grafting. The polymer chains were grown from microtubules that were adsorbed on a hydrophobic glass substrate and sequentially crosslinked with glutaraldehyde, amino-functionalised using 2,2'-(ethylenedioxy)-bis(ethylamine) and modified by 2-bromo-2-methylpropanoyl bromide.

<sup>a</sup>Max-Planck-Institute of Molecular Cell Biology and Genetics, Pfotenhauerstrasse 108, 01307 Dresden, Germany. E-mail: ionov@mpi-cbg.de

<sup>b</sup>Leibniz Institute of Polymer Research Dresden e.V., Hohe Str. 6, 01069 Dresden, Germany

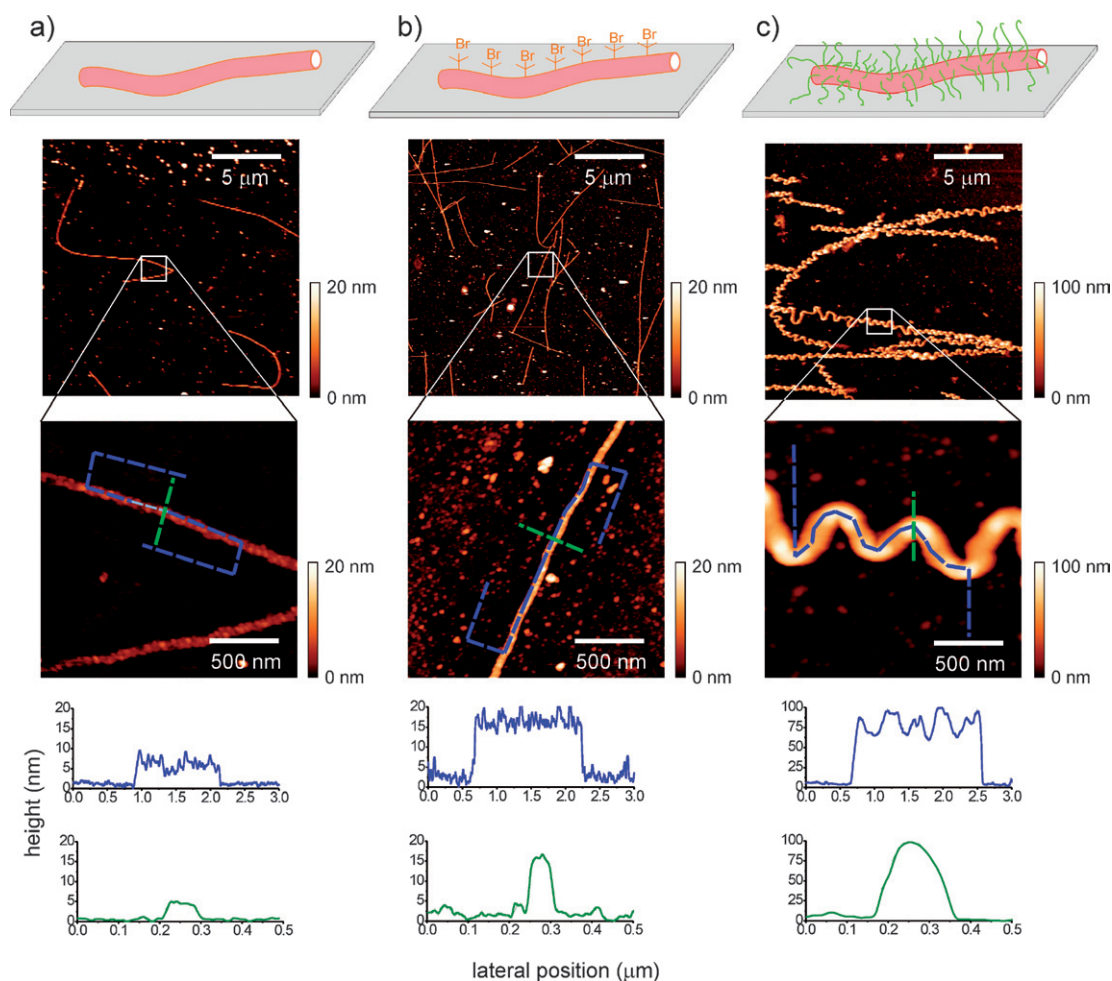


**Fig. 2** Morphology of microtubules at different stages of the modification procedure. AFM images (middle panel) of microtubules (a) after crosslinking with glutaraldehyde, (b) after immobilization of initiator, and (c) after grafting of poly-(*N*-isopropylacrylamide–fluorescein *o*-acrylate) ( $M_n = 69\,000\text{ g mol}^{-1}$ ,  $M_w = 152\,000\text{ g mol}^{-1}$ ). Cross-sections (bottom panel) are given along the paths indicated with the corresponding colour on the AFM images. No tip-deconvolution was performed.

detectable by fluorescence microscopy. Verifying the successful synthesis of the polymer chains on the microtubule we found that the originally “red-fluorescent” microtubules became additionally “green-fluorescent” after polymerisation (Fig. 3).

In order to investigate the structural changes of the microtubule in detail, we imaged the same area of interest by AFM before and after the polymerisation (Fig. 4). These measurements revealed that the contour length of the microtubules increased by up to 100%. On the other hand, the end-to-end distance of the surface-attached microtubules remained almost unchanged. We attribute the increase of the contour length to stretching within and between the tubulin dimers caused by steric repulsions between the grafted polymer chains rather than to high temperature and interactions with solvents.<sup>22</sup>

We estimated the grafting densities of the polymer chains per microtubule length ( $\Gamma_{\text{length}}$ ) and area ( $\Gamma_{\text{area}}$ ) using the following equations:<sup>23</sup>

$$\Gamma_{\text{length}} = \frac{S_{\text{SEC}} \rho_{\text{PNIPAM}} N_A}{M_w} \quad (1)$$

$$\Gamma_{\text{area}} = \Gamma_{\text{length}} / C_{\text{SEC}} \quad (2)$$

where  $S_{\text{SEC}}$  is the cross-sectional area of the polymer-modified microtubule,  $\rho_{\text{PNIPAM}}$  is the polymer mass density,  $M_w$  is the weight averaged molecular weight,  $N_A$  is the Avogadro constant, and  $C_{\text{SEC}}$  is the arc-length over the surface of a given section cut perpendicularly to the microtubule. Thereby  $S_{\text{SEC}}$  is derived experimentally as the integrated area of the cross-section of a polymer-modified microtubule as shown in Fig. 2c (lowest panel). Here, the contribution from the microtubule before the polymerisation is neglected.  $C_{\text{SEC}}$  is determined as the circumference of the initiator-modified microtubule as shown in Fig. 2b (lowest panel). For the estimation of  $S_{\text{SEC}}$  and  $C_{\text{SEC}}$  the AFM curves have been corrected for the tip radius. We derived grafting densities of  $\Gamma_{\text{length}} \approx 40\text{ chains nm}^{-1}$  ( $\Gamma_{\text{area}} \approx 0.3\text{ chains nm}^{-2}$ ) and  $\Gamma_{\text{length}} \approx 42\text{ chains nm}^{-1}$  ( $\Gamma_{\text{area}} \approx 0.32\text{ chains nm}^{-2}$ ) for the data presented in Fig. 2 and 4, respectively. The average distance  $D$  between grafting sites could then be calculated by  $D = \Gamma_{\text{area}}^{-1/2} \approx 1.8\text{ nm}$ . This value is substantially smaller than the gyration radius of PNIPAM chains with similar molecular weights in the collapsed state ( $R_g \approx 20\text{ nm}$ ).<sup>29</sup> Consequently, the polymer-grafted shell can be considered as a brush-like one.



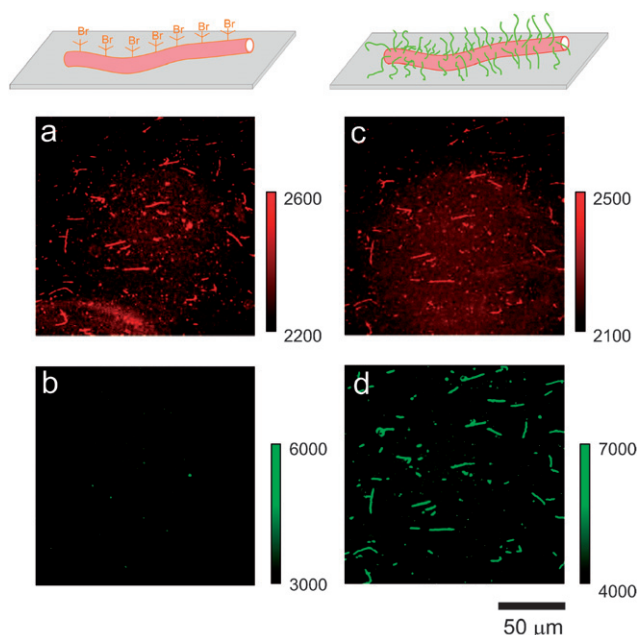


**Fig. 3** Epi-fluorescent images of surface-adsorbed microtubules after immobilization of initiator (a: microtubule signal, b: polymer signal) and after grafting of poly-(*N*-isopropylacrylamide–fluorescein *o*-acrylate) ( $M_n = 59\,000\text{ g mol}^{-1}$ ,  $M_w = 136\,000\text{ g mol}^{-1}$ ) (c: microtubule signal, d: polymer signal).

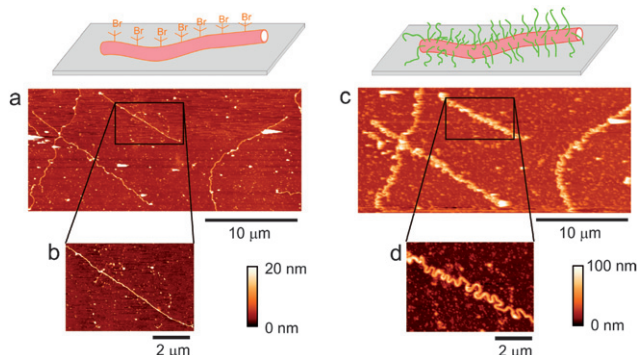


**Fig. 4** AFM images of microtubules in the same area of interest before (a, b) and after (c, d) grafting of poly-(*N*-isopropylacrylamide–fluorescein *o*-acrylate) ( $M_n = 47\,000\text{ g mol}^{-1}$ ,  $M_w = 122\,000\text{ g mol}^{-1}$ ). No tip-deconvolution of AFM images was performed.

We explored the correlation between the grafted amount of polymer chains and the number of amino acid residues, which were able to react with  $\alpha$ -bromoisobutyryl bromide initiator for the polymerisation. Microtubules are composed of about 13 protofilaments made up of  $\alpha$ , $\beta$ -tubulin dimers (repeat length 8 nm). Each  $\alpha$ , $\beta$ -tubulin dimer contains 34 lysine, 42 arginine and 50 serine amino acid residues, corresponding to  $N \approx 200$  of potential grafting sites per nanometre of microtubule length. On the other hand, since the contour length of microtubules increased after polymerisation, the apparent density of potential grafting sites decreased by a factor of  $L_{C-POL}/L_C$ , where  $L_{C-POL}$  and  $L_C$  are the contour lengths of the microtubules after and before polymerisation. The apparent density of potential grafting sites  $N_{POL}$  was found to be  $N_{POL} = 130\text{ nm}^{-1}$

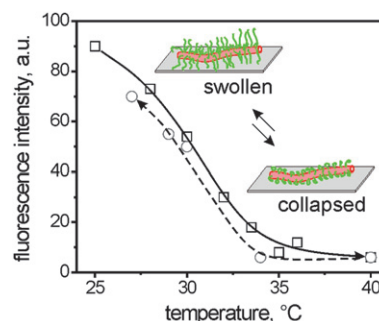


**Fig. 5** Switching of PNIPAM grafted on microtubules. Dependence of fluorescence intensity of poly-(*N*-isopropylacrylamide–fluorescein *o*-acrylate) brushes on temperature upon heating (open squares, solid line) and cooling (open circles, dashed line).

(data from Fig. 2) and  $N_{POL} = 100\text{ nm}^{-1}$  (data from Fig. 4) meaning that about  $\Gamma_{\text{length}}/N_{POL} = 30\%–40\%$  reactive amino acid residues initiated growth of polymer chains<sup>23</sup>

Finally, we investigated the switching behaviour of the grafted poly-(*N*-isopropylacrylamide) brushes in an aqueous environment. We found that the fluorescence intensity of the polymer chains (obtained from images as in Fig 3d) gradually decreased with increasing temperature (Fig. 5), reaching almost zero at the low critical solution temperature of PNIPAM ( $T = 33\text{ °C}$ ). The reason for this effect was, most probably, fluorophore quenching by the collapsed polymer chains<sup>24–26</sup> indicating that the polymer chains were capable of switching. Given the optical resolution of our imaging system, we did, on the other hand, not detect any morphological changes of the PNIPAM-decorated microtubules as a result of the polymer swelling and collapse.

In conclusion, we presented a novel approach for the design of nanopatterned polymer brushes based on the use of biological templates. Using microtubules as templates, we fabricated thermoresponsive nanopatterned poly-(*N*-isopropylacrylamide) brushes which can be further used for design of responsive material systems<sup>27</sup> and biomolecular switches.<sup>28</sup> We believe that microtubule-based polymeric materials will be of interest for a variety of nanotechnological and microelectronic applications.

## Experimental part

### Materials

2,2'-(Ethylenedioxy)bis(ethylamine) (Aldrich), glutaraldehyde (Sigma-Aldrich), *N*-isopropylacrylamide (NIPAM, Aldrich), acetone (Aldrich), *N,N,N',N''*-pentamethyldiethylenetriamine (PMDTA, Aldrich), ethyl-2-bromoisobutyrate (EbiB, Aldrich), ethylenediamine (ED, Fluka), dimethyldichlorosilane (DDS, Fluka), anhydrous dichloromethane (Aldrich), 2-bromo-2-methylpropanoyl bromide (BMPB, Aldrich), triethylamine (Fluka), L-ascorbic acid (Sigma), fluorescein *o*-acrylate (FA, Aldrich), copper (ii) bromide (Aldrich) were used as received.

### Preparation of DDS-coated glasses

Piranha-cleaned glass substrates were treated by DDS (125  $\mu\text{L}$ ) solution in 250 mL of trichloroethylene over a period of 60 min. The DDS-coated glasses were rinsed several times in methanol and water.

DDS was used to prevent the adsorption of ethylenediamine and immobilization of initiator on the glass substrate.

### Preparation of microtubules

Rhodamine-labelled microtubules were grown from 10  $\mu\text{L}$  of bovine brain tubulin (4 mg  $\text{mL}^{-1}$ , mixture of 1 rhodamine-labelled/3 unlabelled tubulin units) in BRB80 buffer (80 mM potassium PIPES, pH 6.9, 1 mM EGTA, 1 mM  $\text{MgCl}_2$ ) with 4 mM  $\text{MgCl}_2$ , 1 mM Mg-guanosine 5'-triphosphate sodium salt, and 5% DMSO at 37 °C. After 30 min, the microtubules were stabilized and 100-fold diluted in room-temperature BRB80 containing 10  $\mu\text{M}$  taxol.

### Modification of microtubules

Grown microtubules were purified from free tubulin by centrifuging at 40 000 rpm for 10 min. The supernatant was substituted with 10  $\mu\text{M}$  taxol solution in BRB80 buffer. The microtubules were perfused and adsorbed in 2 mm wide flow cells self-built from two DDS-coated coverslips (Corning, 22  $\times$  22  $\mu\text{m}^2$  and 18  $\times$  18  $\text{mm}^2$ ) and two pieces of double-sided sticky tape (Scotch 3M, thickness 0.1 mm). The non-adsorbed microtubules were washed out by perfusing 10  $\mu\text{M}$  taxol in BRB80. The 1% and 3% solution of glutaraldehyde in 10  $\mu\text{M}$  taxol in BRB80 were subsequently perfused for 5 min in the flow cell to crosslink the microtubules. Final crosslinking was performed by 25% water solution of glutaraldehyde over a period of 20 min. The crosslinked microtubules were subsequently treated with 100% 2,2'-(ethylenedioxy)bis(ethylamine) for 20 min. The initiator was immobilized on microtubules from a solution of BMPB (0.96 g, 4.2  $\times 10^{-3}$  mol) and triethylamine (0.72 g, 7  $\times 10^{-3}$  mol) in anhydrous dichloromethane (100 mL) over a period of 2 h. The modified microtubules were rinsed in dichloromethane 2 $\times$ , ethanol 2 $\times$  and dried with nitrogen flux.

### Grafting of polymer on microtubules

Polymer was grafted on initiator-modified microtubules as follows: NIPAM (2 g, 1.75  $\times 10^{-2}$  mol), FA (40 mg, 1  $\times 10^{-4}$  mol), EBIB (0.65 mg, 3.3  $\times 10^{-6}$  mol),  $\text{CuBr}_2$  (0.35 mg, 1.6  $\times 10^{-6}$  mol), PMDTA (1.3 mg, 8  $\times 10^{-6}$  mol) were dissolved in 2 mL of acetone. The reaction solution was added to the tube containing the DDS-glass substrate with adsorbed initiator-modified microtubules. After the tube was sealed with a rubber septum, a solution of L-ascorbic acid (18 mg, 1  $\times 10^{-4}$  mol) in water (0.06 mL) was injected. The vial was placed in a 70 °C oil bath. The polymerisation was stopped after 1 h. The polymer obtained in solution was collected by precipitation in diethyl ether and used for determination of molecular weight. It is believed that these values should be close to those of the grafted polymer brushes. The substrates with polymer-modified microtubules were rinsed several times in hot chloroform and acetone. DMAC–2%  $\text{H}_2\text{O}$ –LiCl (3 g  $\text{L}^{-1}$ ) was used as eluent for GPC.

### Epi-fluorescent microscopy

Fluorescence images were obtained using an Axiovert 200M inverted microscope with a 40 $\times$  objective (Zeiss, Oberkochen, Germany) equipped with FluoArc lamp. For data acquisition standard TRITC (excitation: HQ 535/50; dichroic: Q 565 LP; emission: HQ 610/75, Chroma Technology) and FITC (excitation: HQ 480/40; dichroic: Q 505 LP; emission: HQ 535/50, Chroma Technology) filter sets in

conjunction with a Micromax 512 BFT camera (Photometrics, Tucson, AZ) and a MetaMorph imaging system (Universal Imaging, Downingtown, PA) were used.

### Atomic force microscopy

AFM studies were performed with a Dimension 3100 (Digital Instruments, Inc., Santa Barbara, CA) microscope. Tapping mode was used to map the film morphology at ambient conditions.

### Acknowledgements

M. Stamm, A. Synytska (IPF Dresden) and T. Korten are acknowledged for fruitful discussions and careful reading of the manuscript. Petra Treppe (IPF Dresden) is acknowledged for technical support. This work was supported by the BMBF (Grant 03N8712), the Volkswagen Foundation and the Max-Planck-Society.

### Notes and references

- 1 H. Sato and T. Homma, *J. Nanosci. Nanotechnol.*, 2007, **7**, 225–231.
- 2 L. Ionov, N. Houbenov, A. Sidorenko, M. Stamm and S. Minko, *Adv. Funct. Mater.*, 2006, **16**, 1153–1160.
- 3 A. Sidorenko, T. Krupenkin, A. Taylor, P. Fratzl and J. Aizenberg, *Science*, 2007, **315**, 487–490.
- 4 M. J. Dalby, N. Gadegaard, R. Tare, A. Andar, M. O. Riehle, P. Herzyk, C. D. W. Wilkinson and R. O. C. Oreffo, *Nat. Mater.*, 2007, **6**, 997–1003.
- 5 E. Menard, M. A. Meitl, Y. Sun, J. U. Park, D. J. L. Shir, Y. S. Nam, S. Jeon and J. A. Rogers, *Chem. Rev.*, 2007, **107**, 1117–1160.
- 6 A. Boker, J. He, T. Emrick and T. P. Russell, *Soft Matter*, 2007, **3**, 1231–1248.
- 7 S. Sotiropoulou, Y. Sierra-Sastre, S. S. Mark and C. A. Batt, *Chem. Mater.*, 2008, **20**, 821–834.
- 8 C. Reuther, L. Hajdo, R. Tucker, A. A. Kasprzak and S. Diez, *Nano Lett.*, 2006, **6**, 2177–2183.
- 9 Z. Niu, J. Liu, L. A. Lee, M. A. Bruckman, D. Zhao, G. Koley and Q. Wang, *Nano Lett.*, 2007, **7**, 3729–3733.
- 10 M. Young, D. Willits, M. Uchida and T. Douglas, *Annual Review of Phytopathology*, 2008, **46**, 361–384.
- 11 C. Brunner, C. Wahnes and V. Vogel, *Lab Chip*, 2007, **7**, 1263–1271.
- 12 S. Behrens, K. Rahn, W. Habicht, K. J. Bohm, H. Rosner, E. Dinjus and E. Unger, *Adv. Mater.*, 2002, **14**, 1621–1625.
- 13 S. Hiayama, T. Inoue, T. Shima, Y. Moritani, T. Suda and K. Sutoh, *Small*, 2008, **4**, 410–415.
- 14 M. Platt, G. Muthukrishnan, W. O. Hancock and M. E. Williams, *J. Am. Chem. Soc.*, 2005, **127**, 15686–15687.
- 15 G. D. Bachand, S. B. Rivera, A. K. Boal, J. Gaudioso, J. Liu and B. C. Bunker, *Nano Lett.*, 2004, **4**, 817–821.
- 16 L. Ionov, M. Stamm and S. Diez, *Nano Lett.*, 2006, **6**, 1982–1987.
- 17 F.-U. Gast, P. S. Dittrich, P. Schwill, M. Weigel, M. Mertig, J. Opitz, U. Queitsch, S. Diez, B. Lincoln, F. Wottawah, S. Schinkinger, J. Guck, J. Käs, J. Smolinski, K. Salchert, C. Werner, C. Duschl, M. S. Jäger, K. Uhlig, P. Geggier and S. Howitz, *Microfluid. Nanofluid.*, 2006, **2**, 21–36.
- 18 M. G. L. van den Heuvel, M. P. De Graaff and C. Dekker, *Science*, 2006, **312**, 910–914.
- 19 B. M. Hutchins, M. Platt, W. O. Hancock and M. E. Williams, *Small*, 2007, **3**, 126–131.
- 20 R. Tucker, P. Katira and H. Hess, *Nano Lett.*, 2008, **8**, 221–226.
- 21 K. Matyjaszewski, H. C. Dong, W. Jakubowski, J. Pietrasik and A. Kusumo, *Langmuir*, 2007, **23**, 4528–4531.
- 22 We found that the morphology of the glutamate-crosslinked microtubules with immobilized initiator did not change after boiling in acetone.
- 23 The estimation is based on the assumption that the mass density of grafted polymer is identical to that of the bulk polymer. Moreover, precise evaluation of the grafting density is hampered by the polydispersity of the polymer chains. Use of  $M_n$  instead of  $M_w$  reduces the calculated grafting density by factor of  $M_w/M_n \approx 2.2$ .

- 
- 24 S. Morita, F. Tsunomori and H. Ushiki, *Eur. Polym. J.*, 2002, **38**, 1863.
- 25 Intensity of fluorescein acrylate slightly increases with temperature.
- 26 The measured decrease in fluorescence intensity was not related to a direct temperature dependence of the fluorescence as we did not find such dependence in control experiments (data not shown).
- 27 M. Kaholek, W. K. Lee, S. J. Ahn, H. W. Ma, K. C. Caster, B. LaMattina and S. Zauscher, *Chem. Mater.*, 2004, **16**, 3688–3696.
- 28 J. Hyun, W. K. Lee, N. Nath, A. Chilkoti and S. Zauscher, *J. Am. Chem. Soc.*, 2004, **126**, 7330–7335.
- 29 X. H. Wang and C. Wu, *Macromolecules*, 1999, **32**, 4299.

Ionov, L.; Synytska A.; Diez S.

Temperature-induced size-control of bioactive surface patterns

***Advanced Functional Materials*** 2008, 18, 1501-1507.

DOI: 10.1002/adfm.200800017

# Temperature-Induced Size-Control of Bioactive Surface Patterns\*\*

By Leonid Ionov,\* Alla Synytska, and Stefan Diez

We present a novel method to produce bioactive surface patterns whose size can be changed in response to a variation of the environmental conditions, rather than local treatment. Our approach is based on the structured surface-immobilization of thermoresponsive poly(*N*-isopropylacrylamide) (PNIPAM) polymer chains with different transition temperatures. We experimentally demonstrate how the size of an area in which a particular polymer is collapsed or swollen can be controlled by ambient temperature. We show the temperature-induced size-control of a bioactive surface pattern by embedding functional motor proteins into the switchable polymer layers.

## 1. Introduction

Micropatterned surfaces are widely used for biotechnological applications such as cell culture, bioanalytics, and tissue engineering.<sup>[1–8]</sup> Although many approaches exist to fabricate sophisticated surface patterns, for example based on micro-contact printing, electron beam lithography, or dip-pen lithography<sup>[1–5,9–11]</sup>, they are almost entirely limited to producing fixed patterns that can not be intentionally modified under physiological conditions. However, patterns that could be generated or modified on demand in aqueous environment would tremendously extend the applicability of structured surfaces. In order to achieve such *in-situ* treatment in a localized manner a number of optical<sup>[12–15]</sup> and electrochemical techniques have been proposed.<sup>[16–19]</sup> For example, structured illumination of a surface containing light-sensitive groups was used to irreversibly add and remove pattern elements.<sup>[14,20]</sup> Reconfigurable optical patterning was shown based on reversibly-isomerizable chemical groups<sup>[13,15]</sup> and application of such surfaces was demonstrated for light-programmed cell adsorption.<sup>[12,13]</sup> However, most of the optical strategies use UV illumination, which is often harmful to biological species.

Here we demonstrate a new method to produce bioactive surfaces with patterns whose size can be changed in response to variation of the environmental conditions, rather than local treatment. Our design is based on the patterned surface-immobilization of thermoresponsive poly(*N*-isopropylacrylamide) (PNIPAM) polymer chains. In aqueous environments, PNIPAM (homopolymer) chains undergo reversible collapse or swelling above or below the Low Critical Solution Temperature (LCST = 33 °C), respectively. However, the LCST can be gradually increased or decreased by incorporation of additional hydrophobic or hydrophilic comonomers, respectively. Likewise, the LCST can be tuned by varying the ratio of both added comonomer types. Using this principle, we fabricated a surface containing lateral LCST gradients by laying down opposing gradients of hydrophilic and hydrophobic PNIPAM-copolymers (Fig. 1a–c). Across this surface, polymers whose LCST is above or below the actual temperature of the surrounding were collapsed or swollen, respectively. We further showed that changes in ambient temperature could alter the size of the area in which a particular polymer was collapsed or swollen (Fig. 1d). By embedding functional proteins into the switchable polymer layers we demonstrated the temperature-induced size-control of bioactive surface patterns.

[\*] Dr. L. Ionov, Dr. S. Diez  
Max-Planck-Institute of Molecular Cell Biology and Genetics  
Pfotenhauerstrasse 108, 01307 Dresden (Germany)  
E-mail: ionov@mpi-cbg.de

Dr. A. Synytska  
Leibniz Institute of Polymer Research Dresden e.V.  
Hohe Strasse 6, 01069 Dresden (Germany)

[\*\*] The authors are grateful to Prof. Manfred Stamm and the Leibniz Institute of Polymer Research Dresden for the opportunity to perform polymer synthetic experiments. Hartmut Komber (Leibniz Institute of Polymer Research Dresden) is acknowledged for NMR investigations. Wolfgang Birnbaum and Dirk Kuckling (TU Dresden) are acknowledged for the determination of the polymer molecular masses. The kind help of Chris Gell (MPI-CBG) and Laurel Rohde (CRTD Dresden) on the manuscript was highly appreciated. This work was supported by the BMBF (Grant 03N8712), the Volkswagen Foundation and the Max-Planck-Society.

## 2. Results and Discussion

First, we prepared and characterized the thermal behavior of the different thermoresponsive PNIPAM copolymers. Random copolymers with hydrophobic *tert*-butyl acrylate (tBA) and hydrophilic acrylic acid (AA) comonomers were synthesized. The hydrophobic tBA monomer units included in the PNIPAM chains (% tBA = 6 mol % in monomer mixture) reduced the LCST to about 25 °C as measured in a pure aqueous environment. The tBA was hydrolyzed into hydrophilic acrylic acid (AA) in an acidic environment (Fig. 2). The LCST of poly(NIPAM-AA) was found to be 33 °C in a pure



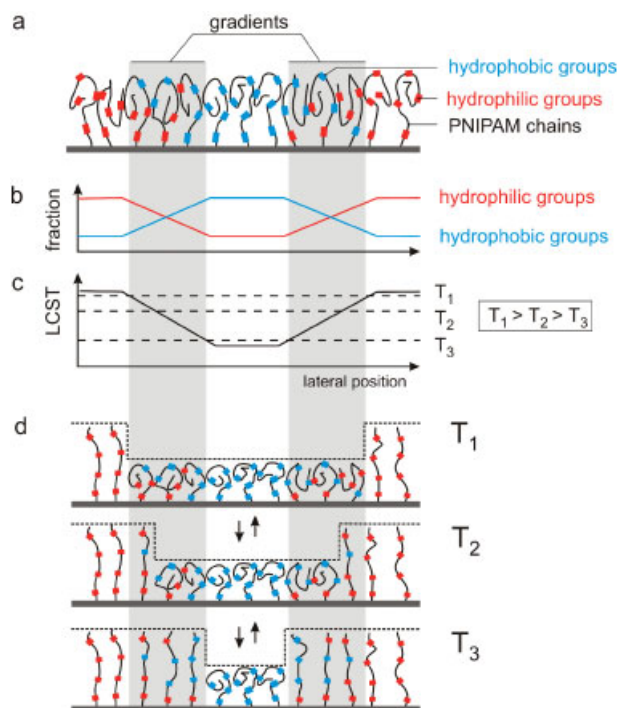


**Figure 1.** Concept of surfaces with size-controlled patterns. a) and b) Lateral gradients of thermoresponsive PNIPAM copolymers with hydrophobic or hydrophilic groups are formed on the surface. c) The Low Critical Solution Temperature (LCST) of PNIPAM copolymers changes gradually with the ratio of hydrophobic to hydrophilic groups. The dashed lines indicate three examples of ambient temperatures  $T_1$ ,  $T_2$ , and  $T_3$ . d) Polymer chains with an LCST below and above ambient temperatures  $T_1$ ,  $T_2$ , and  $T_3$  are collapsed and swollen, respectively. As a result, the size of the area containing the collapsed polymer depends on the ambient temperature and can be reversibly tuned.

aqueous environment and 50–65 °C in salty buffer solutions (points at tBA:AA = 0:4 ratio in Fig. 3).

To demonstrate that the LCST of poly(NIPAM-tBA-AA) copolymers gradually changes with the ratio of hydrophilic to hydrophobic components, we prepared a series of poly(NIPAM-tBA-AA) copolymers containing different tBA to AA ratios. As expected, the LCST decreased gradually as the tBA to AA ratio increased (Fig. 3). Moreover, the LCST depended on the ionic strength of the aqueous solution. Attributable to changing the balance between intramolecular hydrogen bonds and hydrogen bonds with water<sup>[21]</sup> an increase in ionic strength lead to (i) a pronounced increase in the LCST of PNIPAM copolymers that have AA as the predominant

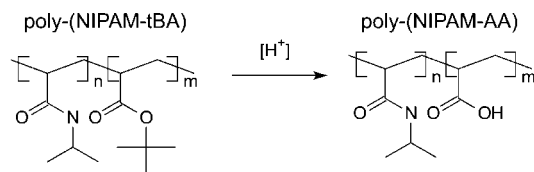


**Figure 2.** Hydrolysis of poly(NIPAM-tBA) copolymer to poly(NIPAM-AA) in an acidic environment.

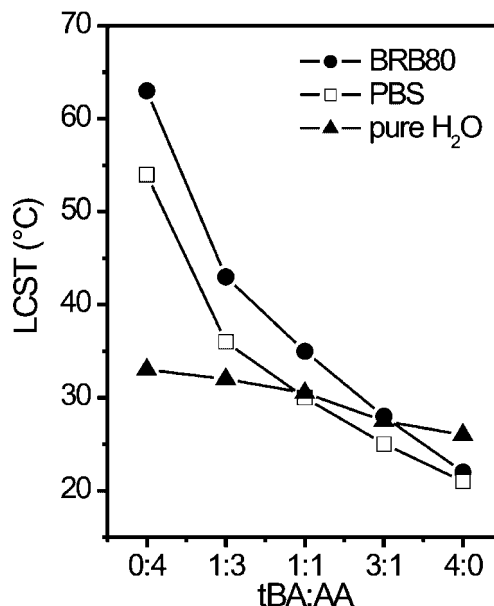


**Figure 3.** The LCST of poly(NIPAM-tBA-AA) copolymers (% tBA + % AA in monomer mixture is 6 mol %) in different aqueous environments: 80 mM Brinkley Reassembly Buffer (BRB80, pH = 6.9), 100 mM Phosphate Buffered Saline (PBS, pH = 7.5) and pure water.

co-monomer and (ii) a decrease in the LCST for PNIPAM copolymers that have tBA as the predominant co-monomer.

Next, we fabricated surface-immobilized PNIPAM copolymer layers and investigated their swelling behavior. A poly(NIPAM-tBA) layer grafted to the surface of the silicon wafer was prepared using surface-initiated atom-transfer radical polymerization (see Experimental).<sup>[22]</sup> The thickness of the polymer layer in the dry state was  $h_{\text{DRY}} = 33$  nm, and the polymer molecular weight was  $M_w = 253000$ , polymer dispersity index  $\text{PDI} = 1.8$ . A poly(NIPAM-AA) layer was obtained by hydrolysis of the poly(NIPAM-tBA) layer in methanesulfonic acid.<sup>[23]</sup> Ellipsometric investigations revealed that the poly(NIPAM-AA) layer was thicker than the poly(NIPAM-tBA) layer at both high and low temperatures as the result of electrostatic repulsions between negatively charged carboxylic groups (Table 1).

To visually inspect the swelling of both poly(NIPAM-tBA) and poly(NIPAM-AA) layers in a spatially resolved manner, we adsorbed fluorescent protein onto the polymer layers and employed fluorescence interference contrast (FLIC) microscopy.<sup>[24]</sup> FLIC microscopy is based on interference effects between the direct excitation and emission light with reflected light from the surface leading to a periodic modulation of the detected emission intensity as function of height above the surface (Fig. 4a). Due to a half wavelength phase shift upon reflection on the mirror (silica-silicon interface), fluorescent molecules are almost invisible if located directly on the mirror. The intensity increases as the distance between the fluorescent molecules and the mirror grows, and it passes through the maximum at a distance of about a quarter of a wavelength.

**Table 1.** Height  $h$  and refractive index  $n$  of poly(NIPAM-tBA) and poly(NIPAM-AA) grafted layers obtained by ellipsometry in BRB80 at different temperatures. The initial thickness of the poly(NIPAM-tBA) layer in dry state was  $h_{\text{DRY}} = 33$  nm.

Polymer	$T$ [°C]	$h$ [nm]	$n$	$h \times n$ [nm]
poly(NIPAM-tBA)	16	86.2	1.39	120
	55	27.2	1.52	42
poly(NIPAM-AA)	16	118.7	1.37	163
	55	46.9	1.44	67

FLIC microscopy thus allows obtaining information about the vertical position of fluorescent objects in the vicinity to a reflecting surface with high spatial accuracy.<sup>[25,26]</sup> The intensity can be expressed by the following equation:<sup>[27]</sup>

$$I(h) = I_0 \left( 2 \cdot (1 - r_f)^2 + 8r_f \sin^2 \left( \frac{2\pi}{\lambda_{\text{EX}}} (n_{\text{SiO}_2} \cdot h_{\text{SiO}_2} + n_{\text{PGMA}} \cdot h_{\text{PGMA}} + n_{\text{PNIPAM}} \cdot h) \right) \right) \times \left( 2 \cdot (1 - r_f)^2 + 8r_f \sin^2 \left( \frac{2\pi}{\lambda_{\text{EM}}} (n_{\text{SiO}_2} \cdot h_{\text{SiO}_2} + n_{\text{PGMA}} \cdot h_{\text{PGMA}} + n_{\text{PNIPAM}} \cdot h) \right) \right) \quad (1)$$

where,  $I_0$  serves as a proportionality factor. Refractive indices for the PNIPAM layer, PGMA with initiator and  $\text{SiO}_2$  are represented by  $n_{\text{PNIPAM}}$ ,  $n_{\text{PGMA}} = 1.5$  and  $n_{\text{SiO}_2} = 1.46$ .  $h_{\text{SiO}_2} = 1.4$  nm is the oxide thickness,  $h_{\text{PGMA}} = 2.2$  nm is the height of PGMA layer, and  $h$  is the height of the fluorophores above the oxide surface. The reflection coefficient is represented by  $r_f$ . A set of optical filters defining the excitation and emission wavelengths,  $\lambda_{\text{EX}} = 565$  nm and  $\lambda_{\text{EM}} = 610$  nm, has been used.

Experimentally, we incubated the polymer layers with rhodamine-labelled tubulin ( $1 \text{ mg ml}^{-1}$  in BRB80 buffer) at  $T = 65^\circ\text{C}$ . Because, both the poly(NIPAM-tBA) and poly(NIPAM-AA) layers were collapsed at this temperature, the tubulin molecules readily adsorbed onto the polymer surface.<sup>[28]</sup> Unadsorbed protein was removed by multiple rinsing in BRB80 buffer at  $18^\circ\text{C}$  where the polymer chains were

swollen. When imaging the surfaces by FLIC microscopy at low temperature ( $T < 20^\circ\text{C}$ , when both polymers were swollen) we found that the poly(NIPAM-tBA) area was brighter than the poly(NIPAM-AA) area (Fig. 4b). The opposite behavior was observed when the polymers were collapsed high temperature ( $T = 55^\circ\text{C}$ ). We note that this change in fluorescence intensity mainly originated from the changed distance of the fluorescent proteins from the surface rather than from desorption or temperature induced changes in the quantum yield of the fluorophores.<sup>[29]</sup> To clarify the differences in the fluorescence intensities of poly(NIPAM-tBA) and poly(NIPAM-AA) areas we refer to the polymer layer thicknesses and refractive index values as measured by ellipsometry (Table 1). Considering the ellipsometric results, we expected that the intensity of the collapsed poly(NIPAM-AA) and collapsed poly(NIPAM-

tBA) areas must be relatively low because the  $h \times n$  values correspond to a position close to the first minimum on the FLIC curve (Table 1, Fig. 4c). The  $h \times n$  values of the swollen poly(NIPAM-tBA) and swollen poly(NIPAM-AA) areas correspond to the positions right before and after the first maximum, respectively, and the apparent fluorescence is predicted to be strong. Thus the observed degree of fluorescence in poly(NIPAM-tBA) area is consistent with our expectation (Fig. 4c and d). The difference between the expected and observed behavior in the collapsed and swollen states of the poly(NIPAM-AA) area was likely caused by a larger thickness of the poly(NIPAM-AA) layer than detected by ellipsometry.

To directly investigate the switching of the polymer layers by FLIC microscopy we prepared a flow channel ( $3 \text{ mm} \times 18 \text{ mm} \times 0.1 \text{ mm}$ ) between a glass coverslip and the silicon

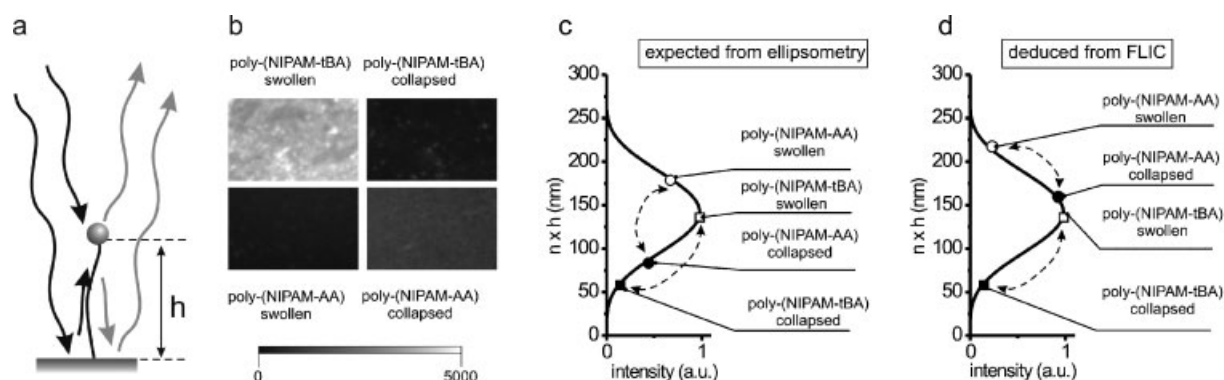


**Figure 4.** Fluorescent Interference Contrast (FLIC) microscopy of poly(NIPAM-tBA) and poly(NIPAM-AA) surfaces. a) Interference of exciting (black line) and emitted (gray line) light near a reflecting surface. b) Observed fluorescence of rhodamine-labelled tubulin adsorbed onto poly(NIPAM-tBA) and poly(NIPAM-AA) layers in swollen ( $T < 20^\circ\text{C}$ ) and collapsed ( $T = 55^\circ\text{C}$ ) states. c) and d)  $h \times n$  values for poly(NIPAM-tBA) (squares) and poly(NIPAM-AA) (circles) layers in swollen (open symbols) and collapsed (solid symbols) states as measured by ellipsometry (measured height values are projected onto the theoretical FLIC curve (c) and deduced from FLIC (measured intensity values are projected onto the theoretical FLIC curve (d)).

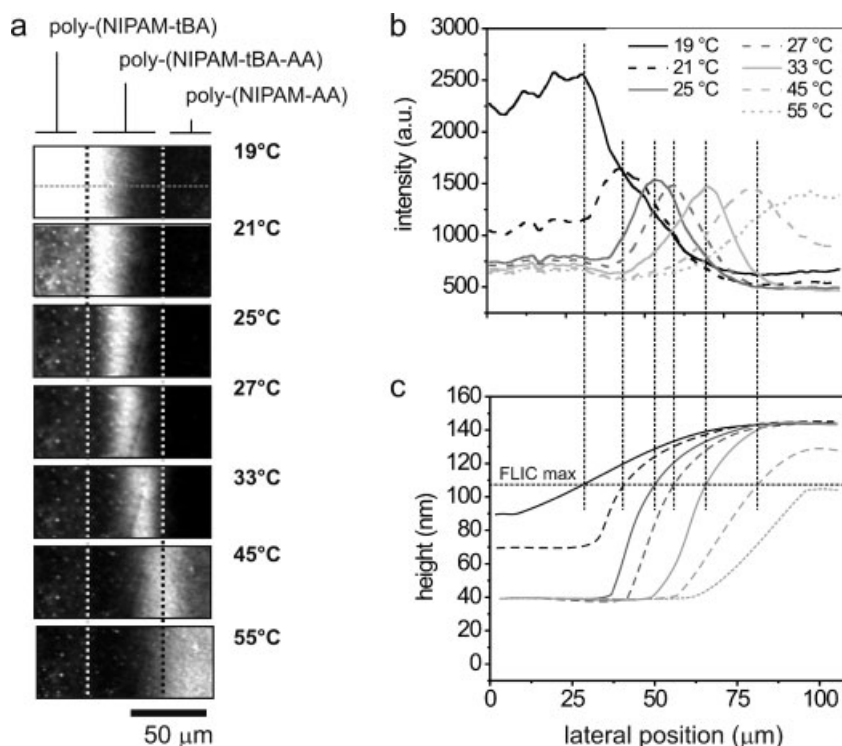


**Figure 5.** Switching of the height profile of the poly(NIPAM-tBA-AA) gradient layer. a) FLIC images of the poly(NIPAM-tBA-AA) layer with adsorbed rhodamine-labeled tubulin at different temperatures. Intensity profile (b) and qualitatively reconstructed height profile (c) along gray dotted line in (a) of the polymer layer at different temperatures. The initial thickness of the poly(NIPAM-tBA) layer in the dry state was  $h_{\text{DRY}} = 33$  nm.

chip with the polymer layer using double-stick tape. The channel was filled half with water and half with methanesulfonic acid. Due to diffusion at the boundary between water and methanesulfonic acid a gradient of poly(NIPAM-tBA-AA) was formed amidst the fully hydrolyzed poly(NIPAM-AA) and the unhydrolyzed poly(NIPAM-tBA) areas. After about 20 s the channel was rinsed with water from the opposite side. FLIC images of adsorbed fluorescent tubulin (same preparation as described above) revealed a strong fluorescent signal on the poly(NIPAM-tBA) area and a weak signal at the poly(NIPAM-AA) area at low temperature ( $T < 20^\circ\text{C}$ ) (Fig. 5a). At high temperature ( $T > 50^\circ\text{C}$ ) the poly(NIPAM-AA) appeared brighter than the poly(NIPAM-tBA) area. This behavior was expected from the results shown in Figure 4. However, most interestingly, a bright, spatially confined band in the poly(NIPAM-tBA-AA) gradient area was detected at temperatures between  $21^\circ\text{C}$  and  $50^\circ\text{C}$ .

Considering equation 1, this bright band represents the maximum of the FLIC curve at  $n \times h \approx 140$  nm (see also Fig. 4c and d). The lateral coordinate of this band shifted towards the poly(NIPAM-AA) areas when the temperature increased (Fig. 5b). This directly indicates that the height and/or refractive index profile of the polymer layer changes with temperature. Since the difference in the refractive indices in the swollen versus the collapsed polymers is rather small – namely  $100\% \times \frac{n_{\text{collapsed}} - n_{\text{swollen}}}{n_{\text{collapsed}}} = 100\% \times \frac{1.52 - 1.37}{1.52} \approx 10\%$  (Table 1) – the change in the intensity profile along the sample was mainly caused by changes in the height of the polymer

layer. A qualitative reconstruction of the height profile of the polymer layer at different temperatures is shown in Figure 5c.<sup>[30]</sup> Here, one can see an obvious gradual shift of the border between the swollen and the collapsed areas. This border was not completely step-like due to the unsharp transition between the collapsed and the swollen polymer chain conformations. In this particular experiment, the border between the collapsed and the swollen areas was reversibly shifted by about  $50\ \mu\text{m}$ , but shifts up to  $120\ \mu\text{m}$  were obtained in additional experiments. Importantly, the changes in the size of the collapsed and the swollen areas were fully reversible (data not shown).

In order to fabricate circular patterns whose diameter can be controlled by temperature, we synthesized a thermoresponsive polymer layer based on random copolymerization of NIPAM with hydrophobic photolabile 2-nitrobenzyl acrylate (NBA). The LCST of the poly(NIPAM-NBA) copolymer ( $M_w = 114000$ ,  $\text{PDI} = 1.7$ , obtained by polymerization of a mixture of

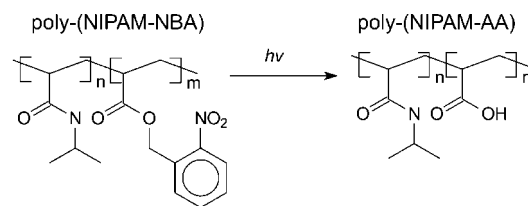


**Figure 6.** Conversion of poly(NIPAM-NBA) copolymer into poly(NIPAM-AA) upon UV illumination.

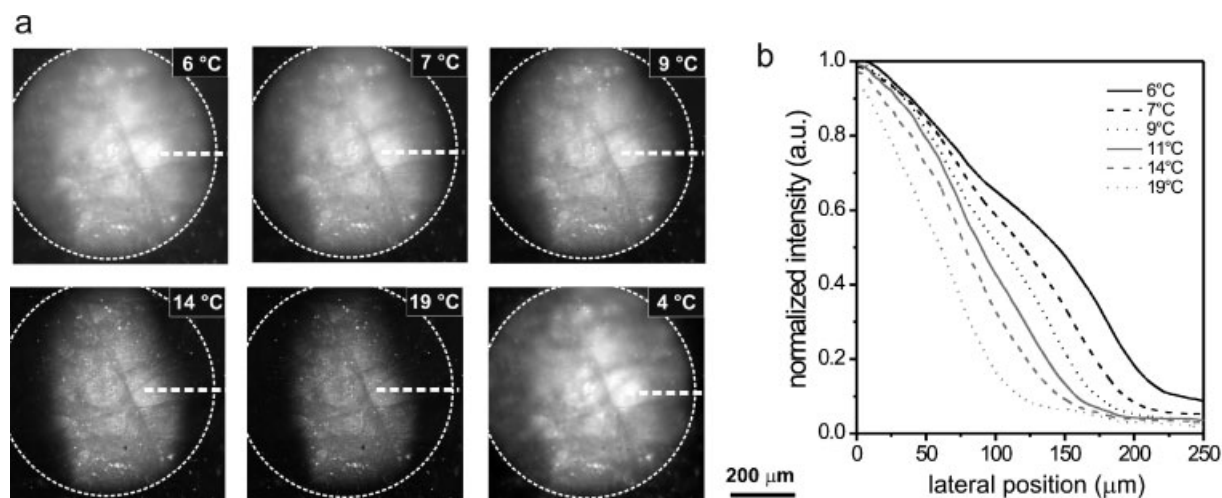


**Figure 7.** Switching the size of a circular poly(NIPAM-NBA-AA) pattern. a) FLIC images of rhodamine-labelled tubulin on poly(NIPAM-NBA-AA) pattern at different temperatures. The size of the swollen (bright) area changes with temperature. b) Normalized fluorescence intensity profiles of the polymer layer at different temperatures along the white dashed line in (a). The initial thickness of the poly(NIPAM-NBA) layer in the dry state was  $h_{\text{DRY}} = 15.7$  nm

94 mol % NIPAM and 6 mol % NBA) was about 7 °C in BRB80 buffer. We then illuminated a part of the poly(NIPAM-NBA) layer with UV light ( $\lambda = 360$  nm) using a 100 $\times$  microscope objective. This resulted in the localized cleavage (deprotection) of the hydrophobic 2-nitrobenzyl groups and the formation of hydrophilic carboxylic groups (Fig. 6) in a circular area with diameter of about 0.5 mm. The LCST of the fully deprotected polymer was more than 90 °C. Because, in our case, the degree of deprotection gradually decreased from the center of the illuminated area towards the edges we obtained a two-dimensional poly(NIPAM-NBA-AA) gradient.

Using FLIC microscopy (with fluorescent tubulin, as described above) we observed a decrease in the fluorescence intensity in the center of the deprotected area as well as a decrease in the size of the bright area upon raising the temperature (Fig. 7a and b). This behavior is attributed to the collapse of the polymer chains and thus a decrease in the detected fluorescence intensity in a spatially varying manner. Remarkably, when the temperature was lowered back to the initial value the size of the swollen area was fully recovered (Fig. 7a, lower right image). This observation indicates the reversibility of the switching process. We note, that smaller patterns can be fabricated on demand by UV-illumination through a mask.<sup>[31]</sup>

To demonstrate the temperature-induced size-control of bioactive surface patterns, we assayed the gliding motility of microtubules on kinesin-coated poly(NIPAM-tBA-AA) gradient surfaces. Microtubules are hollow, cylindrical, protein filaments with an outer diameter of 24 nm. They can be formed *in vitro* by self-assembly of tubulin-heterodimers reaching lengths of up to several tens of micrometers. Kinesin<sup>[32,33]</sup> is an ATP-hydrolysing enzyme that moves vesicles and organelles along microtubules in a cellular environment.<sup>[34]</sup> Recently, it

was shown that microtubules can reversibly land and release (in response to collapsing and swelling of the polymer chains) on composite surfaces where kinesin molecules were embedded in a homopolymer PNIPAM layer.<sup>[35]</sup> Here, we adsorbed kinesin on poly(NIPAM-tBA-AA) gradient surfaces (similar to those presented in Fig. 5a) at  $T = 37$  °C. We then lowered the temperature to 17 °C which caused swelling of both poly(NIPAM-tBA) and poly(NIPAM-AA) and led to the release of weakly adsorbed kinesin. We then imaged the gliding motility of rhodamine-labelled microtubules on the kinesin molecules that were entrapped in the thin polymer layer by timelapse fluorescence microscopy. At a temperature of  $T = 21$  °C, which is slightly above the LCST of poly(NIPAM-tBA), we found that microtubules were gliding only on the poly(NIPAM-tBA) surface area where the polymer chains were collapsed and did not repel the microtubules (Fig. 8). Increasing the temperature up to  $T = 41$  °C led to a laterally progressing collapse of the poly(NIPAM-tBA-AA) and allowed the microtubules to land on the exposed kinesin molecules in the gradient area. Cooling back down to  $T = 21$  °C deactivated the poly(NIPAM-tBA-AA) gradient area again. The associated swelling of the polymer chains repelled the gliding microtubules and prevented the landing of microtubules on the kinesin molecules in this area. This reversible size control of the active kinesin pattern could be repeated multiple times.

### 3. Conclusions

In summary, we presented a new concept to design bioactive patterned surfaces whose size can be controlled by altering the ambient conditions. In one set of experiment, we generated



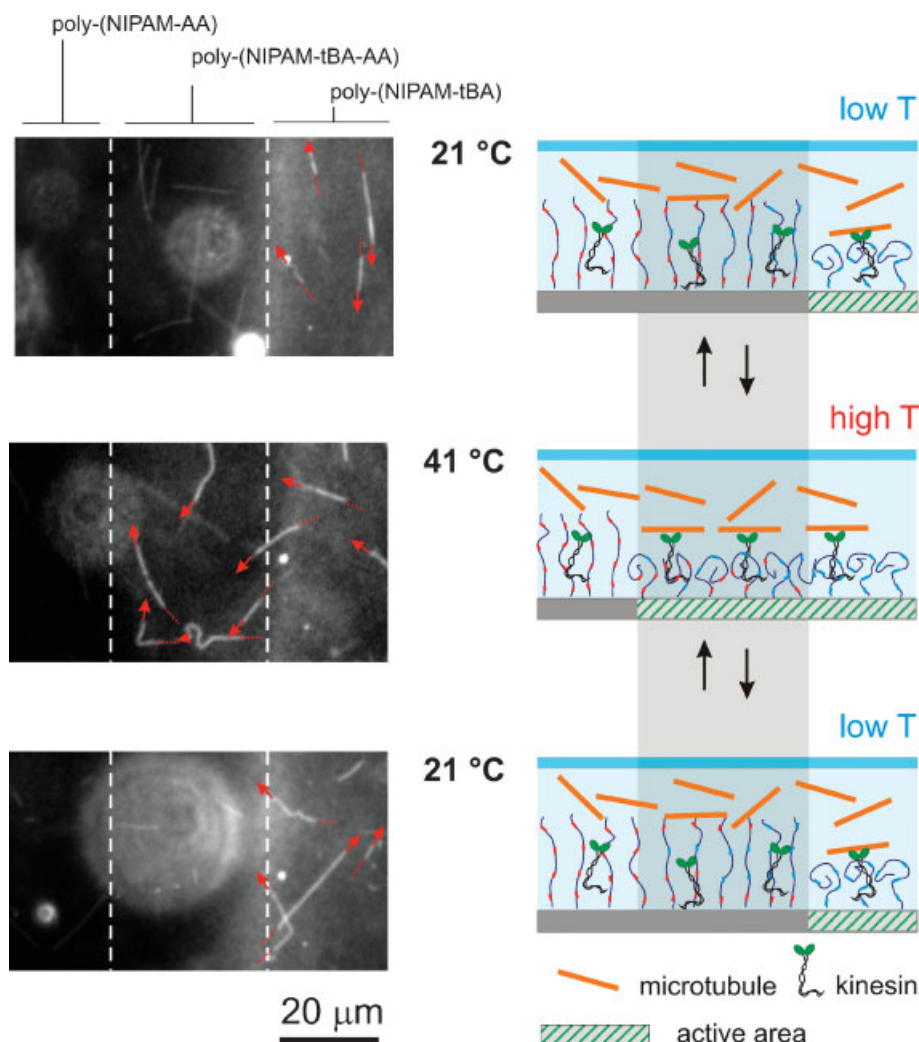


**Figure 8.** Temperature-induced size-control of bioactive surface patterns. Left panel: Fluorescence images of rhodamine-labeled microtubules driven by kinesin motors on a substrate surface with grafted poly(NIPAM-tBA-AA) gradient. Actively gliding microtubules were determined by timelapse microscopy and are indicated by the red arrowheads (direction of movement) and the dotted lines (traveled path during the preceding frames). White circular patterns in the fluorescent images arise from microtubules, which are diffusing in solution out of focus. Right panel: Schematic diagram of polymer conformation and gliding motility. Repeated changes in temperature resulted in the reversible switching of the polymer chains between the extended conformation (repelling microtubules from the surface) and the collapsed conformation (enabling gliding motility of microtubules).

lateral gradients composed of thermoresponsive poly(*N*-isopropylacryl amide – *tert*-butyl acrylate – acrylic acid) copolymers by local hydrolysis using methanesulfonic acid. On these gradients we showed that the border between the collapsed and the swollen polymer areas could be reversibly shifted by up to 120 μm when raising or lowering the temperature between 21 °C and 50 °C. Utilizing kinesin-driven motility of microtubules, we demonstrated the applicability of these gradients for the temperature-induced size-control of bioactive surface patterns. In a second set of experiments we generated circular gradients of poly(*N*-isopropylacryl amide – 2-nitrobenzyl acrylate – acrylic acid) by UV irradiation. It is thus possible to use photolithography to produce switchable polymer gradients with customized layouts. We note, that

the temperature range over which switching occurs can be precisely tuned by selecting the appropriate copolymer composition. We believe that this novel strategy to produce surface patterns whose size and shape can be reversibly switched *in-situ* will be of interest for a variety of biotechnological applications, such as programmed cell adhesion, viability and differentiation.

#### 4. Experimental

**Materials:** Highly polished single-crystal silicon wafers of {100} orientation (Semiconductor Processing Co.) were used as a substrate. *N*-isopropylacrylamide (NIPAM, Aldrich), acetone (Aldrich), *N,N,N'*,



*N,N'*-pentamethyldiethylenetriamine (PMDTA, Aldrich), ethyl-2-bromoisobutyrate (EBiB), ethylenediamine (ED, Fluka), anhydrous dichloromethane (Aldrich), 2-bromo-2-methylpropanoyl bromide (BMPB, Aldrich), triethylamine (Fluka), L-ascorbic acid (Sigma), copper bromide (Aldrich), 2,2'-azobis(2-methylpropionitrile) (AIBN), methane sulfonic acid (Merck) were used as received. *tert*-butyl acrylate (tBA, Fluka) was distilled under nitrogen steam prior to polymerization. Polyglycidyl methacrylate (PGMA) ( $M_n = 84\,000\text{ g mol}^{-1}$ ) was synthesized by free radical polymerization of glycidyl methacrylate (Aldrich).

**Synthesis of 2-Nitrobenzyl Acrylate (NBA):**  $3\text{ g}$  ( $1.9 \times 10^{-2}\text{ mol}$ ) of 2-nitrobenzyl alcohol,  $2.1\text{ g}$  ( $2 \times 10^{-2}\text{ mol}$ ) of triethylamine were dissolved in  $20\text{ ml}$  of anhydrous dichloromethane, and  $1.7\text{ ml}$  ( $2 \times 10^{-2}\text{ mole}$ ) of acryloyl chloride was added drop-wise to the resulting solution. Stirring continued for one hour. After filtering out the resulting salt, the filtrate was concentrated and purified by column chromatography (packed material: silica gel; eluent: hexane/ethyl acetate = 10/1). Thus,  $2.7\text{ g}$  of an oily liquid was recovered and confirmed to be 2-nitrobenzyl acrylate by NMR spectroscopy.  $^1\text{H-NMR}$  ( $500.13\text{ MHz}$ ,  $\text{CDCl}_3$   $\delta$ ):  $5.6$  (s, 2H),  $5.8\text{--}6.5$  (m, 3H),  $7.1\text{--}8.1$  (m, 4H).

**Synthesis of Poly(NIPAM-tBA-AA) Random Copolymers:** Poly(NIPAM-tBA-AA) random copolymers were synthesized by free radical polymerization. For this,  $2\text{ g}$  ( $0.0177\text{ mol}$ ) of NIPAM, *tert*-butyl acrylate and acrylic acid (total  $1.12 \times 10^{-3}\text{ mol}$ ) and  $8\text{ mg}$  of AIBN ( $4.9 \times 10^{-5}\text{ mol}$ ) were dissolved in  $4\text{ ml}$  acetone. Polymerization was carried out in an argon atmosphere for  $1.5\text{ h}$ .

**Surface-Initiated Polymerization:** The silicon wafers were first cleaned in an ultrasonic bath for  $30\text{ min}$ , placed in a hot piranha solution (3:1 concentrated sulphuric acid and 30% hydrogen peroxide; the mixture reacts violently with organic solvents and should be handled with care) for  $1\text{ h}$ , and then rinsed several times with MilliQ water. The thickness of silicon oxide was measured to be  $1.3\text{ nm}$  after the cleaning procedure. A thin layer of PGMA ( $1.75\text{ nm}$ ) was deposited on top of the chips by spincoating  $0.02\%$  PGMA solution in chloroform at  $2000\text{ rpm}$  and annealing at  $110^\circ\text{C}$  for  $10\text{ min}$ . Afterwards, the wafers were rinsed in a  $1.5\%$  ethanol solution of ethylenediamine (ED) for  $2\text{ h}$ . The wafers were carefully rinsed in  $2 \times$  in ethanol,  $2 \times$  in ethanol/water mixture in ultrasonic bath and dried with nitrogen flux. The thickness of the PGMA + ED layer was  $1.65\text{ nm}$ . The wafers were rinsed in a solution of BMPB ( $0.96\text{ g}$ ,  $4.2 \times 10^{-3}\text{ mol}$ ) and triethylamine ( $0.72\text{ g}$ ,  $7 \times 10^{-3}\text{ mol}$ ) in anhydrous dichloromethane ( $100\text{ ml}$ ). The wafer were rinsed in dichloromethane  $2 \times$  and dried with nitrogen flux. The thickness of the PGMA + ED + BMPB layer was  $1.85\text{ nm}$ .

Poly(NIPAM-tBA) and poly(NIPAM-NBA) random copolymer brushes were prepared as follows: NIPAM ( $4\text{ g}$ ,  $3.5 \times 10^{-2}\text{ mol}$ ), tBA ( $288\text{ mg}$ ,  $2.25 \times 10^{-3}\text{ mol}$ ) or NBA ( $465\text{ mg}$ ,  $2.25 \times 10^{-3}\text{ mol}$ ) EBiB ( $8\text{ mg}$ ,  $4.1 \times 10^{-5}\text{ mol}$ ) were dissolved in  $6\text{ ml}$  of acetone solution of  $\text{CuBr}_2$  ( $0.4\text{ mg}$ ,  $1.8 \times 10^{-6}\text{ mol}$ ) and PMDTA ( $0.31\text{ mg}$ ,  $1.8 \times 10^{-6}\text{ mol}$ ). The reaction solution was added to the tube containing the wafer with immobilized initiator. After the tube was sealed with a rubber septum, a solution of L-ascorbic acid ( $18\text{ mg}$ ,  $1 \times 10^{-4}\text{ mol}$ ) in water ( $0.5\text{ ml}$ ) was injected. The vial was placed in a  $70^\circ\text{C}$  oil bath. The polymerization was carried out under stirring and was stopped after  $4\text{ h}$ .

**Ellipsometry:** The thickness of the polymer layers was measured at  $\lambda = 633\text{ nm}$  and an angle of incidence of  $70^\circ$  with a SENTECH SE-402 microfocus ellipsometer as described elsewhere [36,37].

**Fluorescent Microscopy:** Fluorescence images were obtained using an Axiovert 200M inverted microscope with a  $20 \times$  objective (Zeiss, Oberkochen, Germany) equipped with FluoArc lamp. For data acquisition a standard TRITC filterset (excitation: HQ 535/50; dichroic: Q 565 LP; emission: HQ 610/75, Chroma Technology) in conjunction with a Micromax 512 BFT camera (Photometrics, Tucson, AZ) and a MetaMorph imaging system (Universal Imaging, Downingtown, PA) were used.

Received: January 01, 2008

- [1] A. Khademhosseini, R. Langer, J. Borenstein, J. P. Vacanti, *Proc. Natl. Acad. Sci. USA* **2006**, *103*, 2480.
- [2] A. Folch, M. Toner, *Annu. Rev. Biomed. Eng.* **2000**, *2*, 227.
- [3] N. Li, A. Tourovskaia, A. Folch, *Crit. Rev. Biomed. Eng.* **2003**, *31*, 423.
- [4] S. Raghavan, C. S. Chen, *Adv. Mater.* **2004**, *16*, 1303.
- [5] N. Sniadecki, R. A. Desai, S. A. Ruiz, C. S. Chen, *Ann. Biomed. Eng.* **2006**, *34*, 59.
- [6] D. Falconnet, G. Csucs, H. M. Grandin, M. Textor, *Biomaterials* **2006**, *27*, 3044.
- [7] C. S. Chen, M. Mrksich, S. Huang, G. M. Whitesides, D. E. Ingber, *Science* **1997**, *276*, 1425.
- [8] R. McBeath, D. M. Pirone, C. M. Nelson, K. Bhadriraju, C. S. Chen, *Develop. Cell* **2004**, *6*, 483.
- [9] Y. N. Xia, G. M. Whitesides, *Angew. Chem. Int. Ed.* **1998**, *37*, 551.
- [10] R. D. Piner, J. Zhu, F. Xu, S. H. Hong, C. A. Mirkin, *Science* **1999**, *283*, 661.
- [11] Y. N. Xia, J. A. Rogers, K. E. Paul, G. M. Whitesides, *Chem. Rev.* **1999**, *99*, 1823.
- [12] J. Edahiro, K. Sumaru, Y. Tada, K. Ohi, T. Takagi, M. Kameda, T. Shinbo, T. Kanamori, Y. Yoshimi, *Biomacromolecules* **2005**, *6*, 970.
- [13] A. Higuchi, A. Hamamura, Y. Shindo, H. Kitamura, B. O. Yoon, T. Mori, T. Uyama, A. Umezawa, *Biomacromolecules* **2004**, *5*, 1770.
- [14] J. Nakanishi, Y. Kikuchi, T. Takarada, H. Nakayama, K. Yamaguchi, M. Maeda, *J. Am. Chem. Soc.* **2004**, *126*, 16314.
- [15] H. S. Lim, J. T. Han, D. Kwak, M. H. Jin, K. Cho, *J. Am. Chem. Soc.* **2006**, *128*, 14458.
- [16] C. Zhao, I. Witte, G. Wittstock, *Angew. Chem. Int. Ed.* **2006**, *45*, 5469.
- [17] H. Kaji, M. Kanada, D. Oyamatsu, T. Matsue, M. Nishizawa, *Langmuir* **2004**, *20*, 16.
- [18] H. Kaji, K. Tsukidate, T. Matsue, M. Nishizawa, *J. Am. Chem. Soc.* **2004**, *126*, 15026.
- [19] X. Y. Jiang, R. Ferrigno, M. Mrksich, G. M. Whitesides, *J. Am. Chem. Soc.* **2003**, *125*, 2366.
- [20] B. Zhao, J. S. Moore, D. J. Beebe, *Science* **2001**, *291*, 1023.
- [21] J. D. Debord, L. A. Lyon, *Langmuir* **2003**, *19*, 7662.
- [22] K. Matyjaszewski, H. C. Dong, W. Jakubowski, J. Pietrasik, A. Kusumo, *Langmuir* **2007**, *23*, 4528.
- [23] A. Synytska, M. Stamm, S. Diez, L. Ionov, *Langmuir* **2007**, *23*, 5205.
- [24] A. Lambacher, P. Fromherz, *Appl. Phys. A* **1996**, *63*, 207.
- [25] J. Kerssemakers, J. Howard, H. Hess, S. Diez, *Proc. Natl. Acad. Sci. USA* **2006**, *103*, 15812.
- [26] L. Ionov, S. Sapra, A. Synytska, A. L. Rogach, M. Stamm, S. Diez, *Adv. Mater.* **2006**, *18*, 1453.
- [27] Y. Kaizuka, J. T. Groves, *Biophys. J.* **2004**, *86*, 905.
- [28] D. L. Huber, R. P. Manginell, M. A. Samara, B.-I. Kim, B. C. Bunker, *Science* **2003**, *301*, 352.
- [29] To prove this, we observed the fluorescence of protein adsorbed onto PNIPAM layer grafted onto special silicon chip with set of four different thicknesses of silicon oxide. This experiment, which allows reconstruction of FLIC curve and obtaining the value of  $h \times n$  does show that the distance between fluorescent protein and surface change when polymer collapses or swells.
- [30] The height profile has been reconstructed taking into account the following consideration. For simplicity, we assumed that refractive index of polymer layer has an intermediate value between that of the polymer in the collapsed and the swollen states ( $n = 1.4$ ). The Maximum of the intensity corresponds to the condition of  $n \times h \approx 140\text{ nm}$  (Fig. 3). The height of the poly(NIPAM-tBA) area corresponds to the position before first maximum and is  $h \approx 110\text{ nm}$ . The intensity profiles have been corrected with respect to changes of intensity of the fluorescence with temperature.

- [31] J. Opitz, F. Braun, R. Seidel, W. Pompe, B. Voit, M. Mertig, *Nanotechnology* **2004**, *15*, 717.
- [32] J. Howard, *Nature* **1997**, *389*, 561.
- [33] J. Howard, *Mechanics of Motor Proteins and the Cytoskeleton*, Sinauer Press, Sunderland, MA **2001**.
- [34] R. D. Vale, *Cell* **2003**, *112*, 467.
- [35] L. Ionov, M. Stamm, S. Diez, *Nano Lett.* **2006**, *6*, **1982**.
- [36] S. Minko, S. Patil, V. Datsyuk, F. Simon, K. J. Eichhorn, M. Motornov, D. Usov, I. Tokarev, M. Stamm, *Langmuir* **2002**, *18*, 289.
- [37] L. Ionov, A. Sidorenko, K.-J. Eichhorn, M. Stamm, S. Minko, K. Hinrichs, *Langmuir* **2005**, *21*, 8711.
-

Synytska, A; Stamm, M.; Diez, S.; Ionov, L.

Simple and fast method for the fabrication of switchable bicomponent micro-patterned polymer surfaces

***Langmuir*** 2007, 23(9), 5205-5209.

# Simple and Fast Method for the Fabrication of Switchable Bicomponent Micropatterned Polymer Surfaces

Alla Synytska and Manfred Stamm

Leibniz-Institute of Polymer Research, 01069 Dresden, Germany

Stefan Diez and Leonid Ionov\*

Max-Planck-Institute of Molecular Cell Biology and Genetics, 01307 Dresden, Germany

Received December 13, 2006. In Final Form: February 8, 2007

We report on the fabrication of micropatterned polymer surfaces that allow the reversible inversion of surface topography, charge, and wettability. Micropatterned surfaces were prepared by grafting two oppositely charged polyelectrolytes (poly(acrylic acid) and poly(2-vinylpyridine)) using a combination of photolithography, “lift off”, and “grafting to” techniques. The switchable surfaces are of interest in microprinting and for the design of microfluidic devices and programmed protein adsorption.

## Introduction

Micropatterned surfaces are of considerable importance for microelectronics, printing technology, microfluidic and microanalytical devices, information storage, biosensors, etc.<sup>1–5</sup> Topographical relief and/or a contrast of physicochemical properties—such as wettability, charge, and fluorescence—are generated via a number of techniques including photolithography, microcontact printing, and dip-pen technology.<sup>1,4,6</sup> However, once a pattern is generated, it cannot be easily changed on the fly. This limits the usability of a patterned surface to a single specific application, and new microstructures have to be fabricated for new applications. Therefore, it is desirable to develop methods for the fabrication of structured surfaces with switchable and rewritable patterns.<sup>7–9</sup> One approach toward this goal is based on the site-selective deposition of stimuli-responsive materials forming self-assembled monolayers (SAM) or polymer brushes. On such surfaces, the topographical and physicochemical properties can be locally triggered by external control over the environmental conditions. For example, one-component structured layers of temperature sensitive polymers or weak polyelectrolytes have been used for site-selective swelling as a result of changing temperature or pH, respectively.<sup>10–13</sup> Novel surface properties are expected when two or more kinds of polymer

chains<sup>14–19</sup> are grafted onto the same substrate. Along these lines, we recently demonstrated the fabrication of bicomponent polymer surfaces where hydrophobic/hydrophilic patterns appeared or disappeared depending on the environmental conditions.<sup>17</sup> However, the fabrication of patterned two- and multi-component switchable surfaces is still not a trivial task.<sup>20</sup> Commonly, for the fabrication of patterned surfaces, researchers use surface initiated polymerization,<sup>14–20</sup> which requires high purification of the monomers and special conditions for polymerization procedures.

Here, we report on a simple and fast method for the fabrication of bicomponent micropatterned polymer surfaces with switchable properties using a combination of photolithography, “lift off”, and “grafting to” techniques. We demonstrate the unique behavior of bicomponent micropatterned surfaces that allow the switching of surface topography, wettability, and charge in an inverse manner. The basis of these stimuli-responsive surfaces is the site-selective grafting of two oppositely charged polyelectrolytes (Figure 1). Depending on the pH of the surroundings, one kind of the polymer chains is swollen (charged and hydrophilic), while the other is collapsed (uncharged and hydrophobic). The main advantage of such surfaces is their capability of inverse switching, for example, hydrophilic patterns can be reversibly converted into hydrophobic ones and vice versa, via external stimuli.

## Experimental Procedures

Carboxyl-terminated poly(*tert*-butyl acrylate) (PBA-COOH,  $M_n = 42\,000$  g/mol,  $M_w = 47\,000$  g/mol) and carboxyl-terminated poly(2-vinylpyridine) (P2VP-COOH,  $M_n = 39\,200$  g/mol,  $M_w = 41\,500$  g/mol), synthesized by anionic polymerization, were purchased from Polymer Source, Inc. Polyglycidyl methacrylate

\* Corresponding author. E-mail: ionov@mpi-cbg.de.

- (1) Geissler, M.; Xia, Y. N. *Adv. Mater.* **2004**, *16*, 1249–1269.
- (2) Smith, R. K.; Lewis, P. A.; Weiss, P. S. *Prog. Surf. Sci.* **2004**, *75*, 1–68.
- (3) Ulman, A. *Chem. Rev.* **1996**, *96*, 1533–1554.
- (4) Xia, Y. N.; Whitesides, G. M. *Angew. Chem., Int. Ed.* **1998**, *37*, 551–575.
- (5) Zhao, B.; Brittain, W. J. *Prog. Polym. Sci.* **2000**, *25*, 677–710.
- (6) Xia, Y. N.; Rogers, J. A.; Paul, K. E.; Whitesides, G. M. *Chem. Rev.* **1999**, *99*, 1823–1848.
- (7) Hu, Z. B.; Chen, Y. Y.; Wang, C. J.; Zheng, Y. D.; Li, Y. *Nature* **1998**, *393*, 149–152.
- (8) Luzinov, I.; Minko, S.; Tsukruk, V. V. *Prog. Polym. Sci.* **2004**, *29*, 635–698.
- (9) Senaratne, W.; Andruzzi, L.; Ober, C. K. *Biomacromolecules* **2005**, *6*, 2427–2448.
- (10) Ito, Y.; Chen, G. P.; Guan, Y. Q.; Imanishi, Y. *Langmuir* **1997**, *13*, 2756–2759.
- (11) Kaholek, M.; Lee, W. K.; LaMattina, B.; Caster, K. C.; Zauscher, S. *Nano Lett.* **2004**, *4*, 373–376.
- (12) Kaholek, M.; Lee, W. K.; Ahn, S. J.; Ma, H. W.; Caster, K. C.; LaMattina, B.; Zauscher, S. *Chem. Mater.* **2004**, *16*, 3688–3696.
- (13) Kaholek, M.; Lee, W. K.; Feng, J.; LaMattina, B.; Dyer, D. J.; Zauscher, S. *Chem. Mater.* **2006**, *18*, 3660–3664.

- (14) Xu, F. J.; Song, Y.; Cheng, Z. P.; Zhu, X. L.; Zhu, C. X.; Kang, E. T.; Neoh, K. G. *Macromolecules* **2005**, *38*, 6254–6258.
- (15) Liu, Y.; Klep, V.; Luzinov, I. *J. Am. Chem. Soc.* **2006**, *128*, 8106–8107.
- (16) Yu, K.; Cong, Y.; Fu, J.; Xing, R. B.; Zhao, N.; Han, Y. C. *Surf. Sci.* **2004**, *572*, 490–496.
- (17) Ionov, L.; Minko, S.; Stamm, M.; Gohy, J. F.; Jerome, R.; Scholl, A. *J. Am. Chem. Soc.* **2003**, *125*, 8302–8306.
- (18) Feng Zhou, L. J.; Weimin, L.; Qunji, X. *Macromol. Rapid Commun.* **2004**, *25*, 1979–1983.
- (19) Prucker, O.; Habicht, J.; Park, I. J.; Ruhe, J. *Mater. Sci. Eng., C* **1999**, *8–9*, 291–297.
- (20) Zhou, F.; Zheng, Z.; Yu, B.; Liu, W.; Huck, W. T. S. *J. Am. Chem. Soc.* **2006**, *128*, 16253–16258.

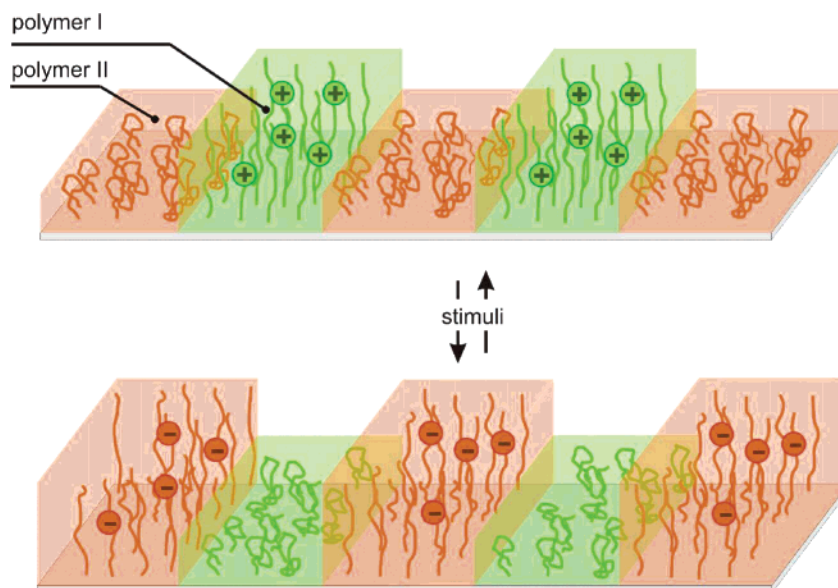


**Figure 1.** Concept of inversely and reversibly switchable micropatterned surfaces consisting of two oppositely charged polyelectrolytes. Depending on the surrounding conditions, one polymer is swollen (charged and hydrophilic), while the other is collapsed (uncharged and hydrophobic), thereby demonstrating the inverse switching of topography, wettability, and charge.

(PGMA) ( $M_n = 84\,000$  g/mol) was synthesized by free radical polymerization of glycidyl methacrylate (Aldrich). Methanesulfonic acid (Fluka) was used without additional purification. Casein fluorescein isothiocyanate (FITC-Casein) was purchased from Sigma. A photoresist (Clariant PL 177) and developer (AZ developer) were purchased from Microchemicals.

Highly polished single-crystal silicon wafers of {100} orientation (Semiconductor Processing Co.) were used as a substrate. The wafers were first cleaned in an ultrasonic bath for 30 min, placed in a hot piranha solution (3:1 concentrated sulfuric acid and 30% hydrogen peroxide; the mixture reacts violently with organic solvents and should be handled with care) for 1 h, and then rinsed several times with MilliQ water.

PBA/P2VP micropatterning was achieved using the following procedure: first, the surface of a Si wafer was coated with a thin film (1.5 nm) of PGMA from a 0.01% solution in chloroform. Next, a thick layer (several micrometers) of the photoresist was spin-coated onto the PGMA-coated wafer. UV illumination through a mask and development resulted in the formation of topographical patterns of photoresist on the PGMA surface. Afterward, a thin (25 nm) film of PBA-COOH was spin-coated from a 0.5% solution in toluene. The remaining photoresist was decomposed by a second UV illumination and removed together with the covering PBA film by rinsing in the developer ("lift off"). As a result, patches of the PBA-COOH film were left on top of the PGMA layer. Annealing at 150 °C for 2 h led to a chemical reaction between the terminal carboxylic groups of PBA-COOH and the epoxy groups of PGMA, resulting in the formation of a grafted PBA layer. Ungrafted polymer was washed out by multiple rinses in chloroform. Next, a thick film (200 nm) of P2VP-COOH was spin-coated from a 1% solution in chloroform on the top of the PBA patterned surface. Annealing at 150 °C led to grafting of P2VP-COOH to the areas unoccupied by grafted PBA. Finally, PBA was hydrolyzed with methanesulfonic acid for 5 min, yielding poly(acrylic acid) (PAA).<sup>21</sup> The typical thicknesses of the PBA and P2VP grafted layers were found to be 11 and 5 nm, respectively, as measured by ellipsometry. The thickness of the PBA layer was reduced after hydrolysis to PAA by about 40% to 7 nm.

The thickness of the polymer layers was measured at  $\lambda = 633$  nm and an angle of incidence of 70° with a SENTECH SE-402 microfocus ellipsometer as described elsewhere.<sup>22,23</sup> Advancing contact angles of water were measured using DSA-10 Krüss equipment. The mixed

**Table 1.** Dissociation Constants (pK),<sup>24–26</sup> IEP, and Advancing Water Contact Angles of P2VP and PAA<sup>a</sup>

polymer	pK	IEP	advancing water contact angle (deg)	
			pH = 2	pH = 10
PAA	5.5	3.2	70	20
P2VP	2.3	6.7	25	75

<sup>a</sup> Dissociation constants are given for polymer chains in solution. Values of the advanced water contact angles were determined on monocomponent polymer films (thickness 8–10 nm in the dry state) grafted onto silicon wafers coated with a PGMA anchoring layer (see Experimental Procedures).

brush was exposed to an aqueous solution (of specified pH) for 2 min, dried, and used for contact angle experiments. AFM studies were performed with a Dimension 3100 (Digital Instruments, Inc.) microscope. The tapping mode was used to map the film morphology at ambient conditions. Optical microscopy was performed using an Axiovert 200 M microscope (Zeiss). For fluorescence measurements, a standard FITC filter set (excitation: HQ 480/40; dichroic: Q 505 LP; emission: HQ 535/75, Chroma Technology) was used.

## Results and Discussion

To fabricate micropatterned polymer surfaces that are switchable in aqueous environments, we used poly-(2-vinylpyridine) (P2VP) and poly(acrylic acid) (PAA). These polymers reversibly change their conformation and charge depending on the pH. The PAA chains are negatively charged and extended at pH > 5.5, while the P2VP chains are positively charged and extended at pH < 2.3 (see pK and IEP values in Table 1). Both polymers are uncharged and collapsed for all other pH values. Surface grafted films of PAA and P2VP demonstrate reversible switching from moderately hydrophobic to hydrophilic behavior after treatment with alkali and acidic water, respectively (see values of advancing contact angle in Table 1).

Micropatterning was performed by a combination of photolithography, "lift off", and "grafting to" techniques (Figure 2 and Experimental Procedures). In brief, silicon wafers were coated

(21) Tao, G.; Gong, A.; Lu, J.; Sue, H.-J.; Bergbreiter, D. E. *Macromolecules* **2001**, *34*, 7672–7679.

(22) Minko, S.; Patil, S.; Datsyuk, V.; Simon, F.; Eichhorn, K. J.; Motornov, M.; Usov, D.; Tokarev, I.; Stamm, M. *Langmuir* **2002**, *18*, 289–296.

(23) Ionov, L.; Sidorenko, A.; Stamm, M.; Minko, S.; Zdyrko, B.; Klep, V.; Luzinov, I. *Macromolecules* **2004**, *37*, 7421–7423.



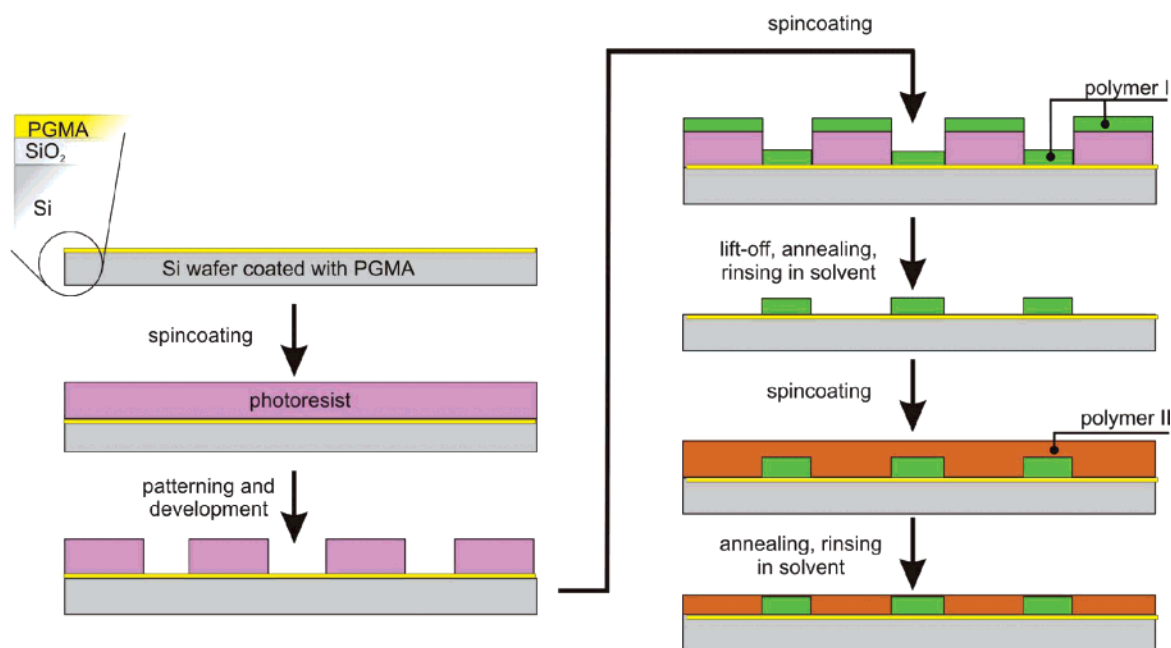


**Figure 2.** Preparation of micropatterned bicomponent polymer grafted layers using a combination of photolithography, “lift off”, and “grafting to” techniques. Polymer I: PBA and polymer II: P2VP. After the micropatterned PBA/P2VP surfaces had been fabricated, PBA was hydrolyzed yielding PAA (not shown in the scheme).

with a 1.5 nm thick film of PGMA, which served as a coupling agent for carboxyl-terminated polymers.<sup>27</sup> Next, the photoresist was spin-coated, illuminated through a mask, and developed. Afterward, a 25 nm thick film of PBA-COOH was spin-coated, and the left over photoresistor and covering PBA film were removed after additional UV exposure by rinsing in the developer. The resulting patches of the PBA-COOH film on the top of the PGMA layer were annealed at elevated temperatures. This leads to a chemical reaction between epoxy groups on the surface and carboxylic groups at the tail of the polymer chains, resulting in formation of the grafted PBA pattern. The thickness of the grafted polymer film was essentially determined by the diffusion of the polymer chains through the layer of already grafted polymer chains and can be controlled by the time and temperature of annealing.<sup>28</sup> Next, P2VP-COOH was spin-coated on the top of the PBA patterned surface and grafted at elevated temperature. Finally, PBA was hydrolyzed yielding PAA.<sup>21</sup> The typical thicknesses of the PAA and P2VP grafted layers were found to be about 7 and 5 nm, respectively. Generally, the advantage of our technique is the combination of (i) high chemical stability of the obtained polymer layer (polymer chains are chemically anchored to the substrate), (ii) easy control over the molecular weight as well as the grafting density of the polymer, and (iii) simplicity of the fabrication procedure.

We investigated the topography of the patterned surfaces using atomic force microscopy (AFM). After treating the surfaces with pure water (pH = 6.7) and drying with nitrogen (Figure 3a,b, cross-section 1), we found the PAA features to be elevated above the P2VP area. However, exposure of the surface to HCl vapor inverted the surface topography: the collapsed PAA features

were lower than the now elevated P2VP structures (Figure 3b–d, cross-section 3). This inverse switching resulted from electrostatic interactions within the polymer layer. Repulsion between the charged groups (carboxyl groups in alkalic medium and protonated pyridine rings in acidic medium) caused the swelling of the respective polymer, incorporating water molecules from the moderately humid air atmosphere (Figure 3d). Interestingly, the degree of switching could be controlled by the extent of exposure to the HCl vapor. The pattern was incompletely switched after a single 2–3 s exposure to HCl, when the heights of the PAA and P2VP features were approximately identical (cross-section 2). Full switching was achieved after a second exposure to HCl vapor (cross-section 3). We note that the patterned PAA/P2VP surface could be switched back to the initial state by rinsing in alkalic or pure water. We observed that such reversible switching between opposite states could be repeated more than 10 times (data not shown). Because the polymer layer was dried by nitrogen flux at room temperature, the polymers still contained water molecules. Therefore, we expect that the observed morphological behavior measured in air is qualitatively similar to one in solvent.<sup>29,30</sup>

Intriguingly, the switching of the surface topography was accompanied by the switching of the surface properties with regard to hydrophobicity. Local condensation of water droplets revealed a distinct contrast between P2VP and PAA areas (Figure 4a). After exposure to pure water (pH = 6.7), very small water droplets wetted the hydrophobic P2VP area, whereas larger drops occurred on the hydrophilic PAA area. The inverse scenario was observed after exposure of the patterned surface to acidic water (pH = 2). The observed switching between hydrophobic and hydrophilic surface properties was applied to the generation of various liquid patterns (Figure 4b). Using the PAA/P2VP pattern shown in Figure 3, where PAA formed nearly square-shaped

(24) Sidorenko, A.; Minko, S.; Schenk-Meuser, K.; Duschner, H.; Stamm, M. *Langmuir* **1999**, *15*, 8349–8355.

(25) Currie, E. P. K.; Sieval, A. B.; Fleer, G. J.; Stuart, M. A. C. *Langmuir* **2000**, *16*, 8324–8333.

(26) Houbenon, N.; Minko, S.; Stamm, M. *Macromolecules* **2003**, *36*, 5897–5901.

(27) Iyer, K. S.; Zdyrko, B.; Malz, H.; Pionteck, J.; Luzinov, I. *Macromolecules* **2003**, *36*, 6519–6526.

(28) Ionov, L.; Zdyrko, B.; Sidorenko, A.; Minko, S.; Klep, V.; Luzinov, I.; Stamm, M. *Macromol. Rapid Commun.* **2004**, *25*, 360–365.

(29) Lin, Y.-H.; Teng, J.; Zubarev, E. R.; Shulha, H.; Tsukruk, V. V. *Nano Lett.* **2005**, *5*, 491–495.

(30) Julthongpipit, D.; Lin, Y.-H.; Teng, J.; Zubarev, E. R.; Tsukruk, V. V. *J. Am. Chem. Soc.* **2003**, *125*, 15912–15921.

(31) Wu, X. Z.; Wu, J. Q.; Pawliszyn, J. *Electrophoresis* **1995**, *16*, 1474–1478.

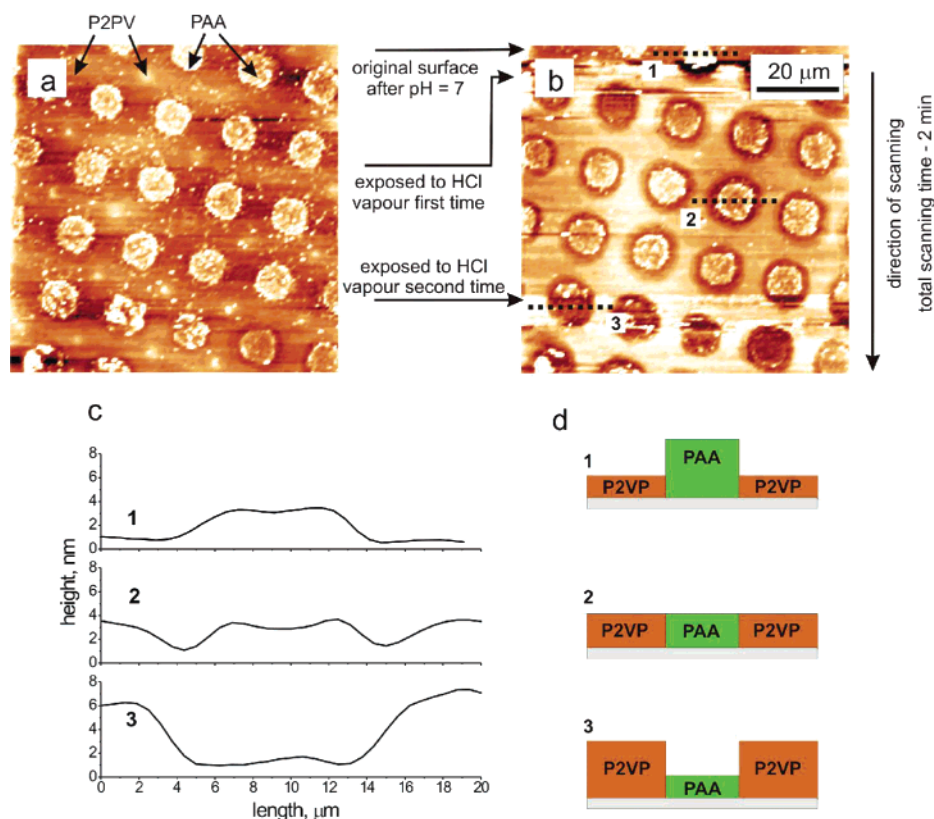


**Figure 3.** Surface topography of patterned PAA/P2VP under various conditions. (a) AFM image after exposure to pure water (pH = 6.7). (b) In situ observation of topography switching upon exposure to HCl vapor. First, the surface was treated with pure water (pH = 6.7, cross-section 1) and then exposed to HCl vapor twice (cross-sections 2 and 3). (c) Quantification of the topographical profiles from panel b. (d) Schematic diagram of the switching. The PAA features are swollen after exposure to pure water (cross-section 1). Exposure to HCl vapor leads to the depression of PAA, while P2VP becomes protonated and swollen (cross-sections 2 and 3). AFM scanning was performed in air at room temperature. The heights at the edges of the polymer pattern appear to be slightly elevated due to 1-D horizontal second-order flattening of the AFM image during scanning.

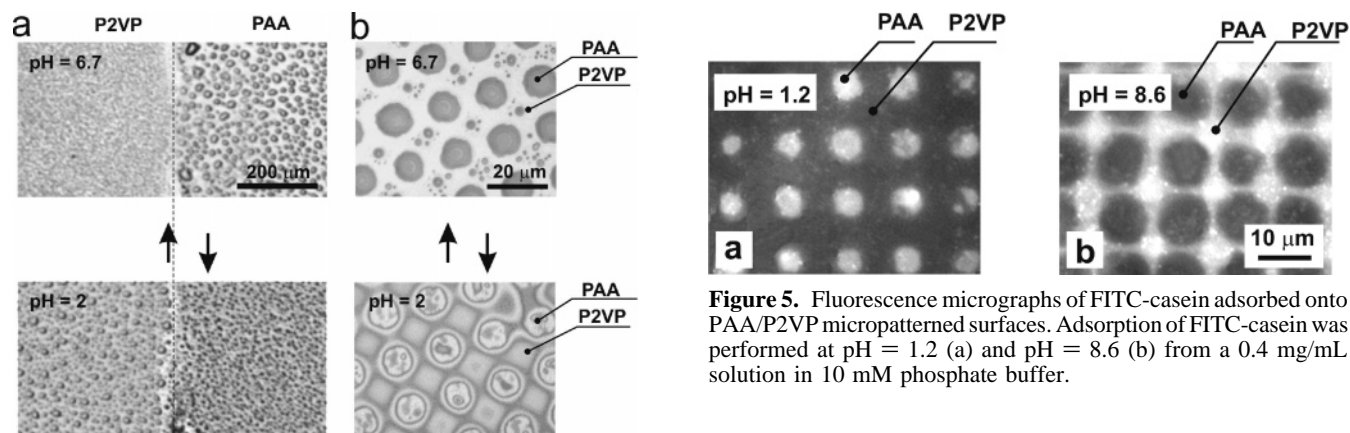


**Figure 4.** Adsorption of water droplets on structured PAA and P2VP surfaces. Optical bright-field microscopy of water droplets on a PAA/P2VP boundary (a) and microstructure (b) at different pH values. Water selectively wetted the P2VP or PAA areas at low or high pH, respectively.

patches between P2VP stripes, we generated either arrays of individual water droplets (Figure 4b, upper panel) or networks of checkered water channels (Figure 4b, lower panel) depending on the surrounding pH. Water selectively wetted the hydrophilic areas and did not spread over the hydrophobic ones. Notably, we observed the formation of smaller water droplets in the center of hydrophobic areas (PAA at pH = 2 and P2VP at pH = 6.7) probably caused by the dewetting of thin water films on the

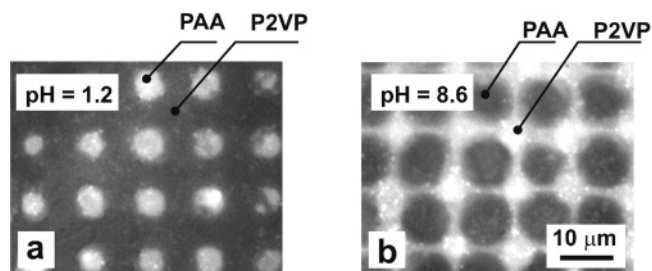


**Figure 5.** Fluorescence micrographs of FITC-casein adsorbed onto PAA/P2VP micropatterned surfaces. Adsorption of FITC-casein was performed at pH = 1.2 (a) and pH = 8.6 (b) from a 0.4 mg/mL solution in 10 mM phosphate buffer.

hydrophobic surface. Importantly, the shape of the liquid pattern was switched by merely changing the environmental conditions.

To test the usability of the inversely switchable surface for programmed protein adsorption, we applied fluorescently labeled proteins (FITC-casein) to the micropatterned PAA/P2VP surfaces. We observed that FITC-casein selectively adsorbed onto the PAA features at pH = 1.2 and to the P2VP features at pH = 8.6 (Figure 5). The selective adsorption of FITC-casein onto areas occupied by one of the polymers can be readily explained by considering electrostatic interactions. As stated earlier, P2VP is charged positively at pH < 2.3, and PAA is negatively charged at pH > 5.5 (Table 1). FITC-casein has an IEP of 7.63,<sup>31</sup> thus being charged negatively above this point and positively below. Therefore repelled from the P2VP features at low pH and from the PAA features at high pH can adsorb on polymer surfaces due

to hydrophobic interactions or hydrogen bonds in the absence of electrostatic repulsion.

In summary, we have developed a straightforward method for the preparation of switchable micropatterned polymer surfaces based on bicomponent polyelectrolyte layers. This method utilizes a “grafting to” approach instead of the widely used surface initiated polymerization. This makes the preparation of bicomponent patterned polymer grafted layers simple and quick. We demonstrated that our approach allows the inverse and reversible switching of surface topography, wettability, and charge. This approach can be easily extended for the fabrication of multi-component ( $n > 2$ ) micropatterned polymer surfaces by repeating the structuring cycle multiple times. We foresee a large potential of inversely switchable micropatterned surfaces for (i) micro-

printing where the topographical features of the polymer layer can be used as a master that is switchable via external stimuli, (ii) microfluidic devices where liquid movement (direction, speed, etc.) can be easily manipulated by pH, and (iii) microanalytical purposes where chemicals and proteins can be deposited in a switchable site-selective manner (programmed protein adsorption).

**Acknowledgment.** The authors are grateful to Robert Tucker for helpful comments on the manuscript. This work was supported by the DFG (Grant SPP 1164), the BMBF (Grant 03N8712), and the Volkswagen Foundation.

LA063601Y

Ionov, L.; Stamm, M.; Diez, S.

Reversible switching of microtubule motility using thermoresponsive polymer surfaces

***Nano Letters*** 2006, 6(9), 1982 – 1987.

# Reversible Switching of Microtubule Motility Using Thermoresponsive Polymer Surfaces

Leonid Ionov,<sup>†,‡</sup> Manfred Stamm,<sup>‡</sup> and Stefan Diez<sup>\*,†</sup>

Max-Planck-Institute of Molecular Cell Biology and Genetics, Pfotenhauerstrasse 108,  
01307 Dresden, Germany, and Leibniz Institute of Polymer Research Dresden,  
Hohe Strasse 6, 01069 Dresden, Germany

Received May 19, 2006; Revised Manuscript Received July 20, 2006

## ABSTRACT

We report a novel approach for the dynamic control of gliding microtubule motility by external stimuli. Our approach is based on the fabrication of a composite surface where functional kinesin motor-molecules are adsorbed onto a silicon substrate between surface-grafted polymer chains of thermoresponsive poly(*N*-isopropylacrylamide). By external temperature control between 27 and 35 °C, we demonstrate the reversible landing, gliding, and releasing of motor-driven microtubules in response to conformational changes of the polymer chains. Our method represents a versatile means to control the activity of biomolecular motors, and other surface-coupled enzyme systems, in bionanotechnological applications.

The development of methods to transport and manipulate nano-objects in engineered environments is a challenging task toward the design of miniaturized bionanodevices. While atomic force microscopy and optical tweezers have recently been applied for the positioning of nanoparticles, polymer molecules, and proteins<sup>1–5</sup> their applicability is limited to single molecules at a time. An alternative method of nanomanipulation, which holds the promise to be applicable in a highly parallel manner, is the *in vitro* use of biomolecular motors.

One well-studied motor protein is kinesin,<sup>6,7</sup> an ATP-hydrolyzing enzyme that moves in a cellular environment vesicles and organelles along microtubules.<sup>8</sup> Microtubules are hollow, cylindrical, protein filaments that can be formed *in vitro* by self-assembly of tubulin heterodimers. Microtubules have an outer diameter of 24 nm and can be as long as several micrometers. *In vitro* gliding motility assays, where microtubules are propelled over a substrate by surface-bound kinesin molecules in the presence of ATP, have been widely used to study the interaction between motor proteins and microtubules.<sup>7</sup>

Recently, the kinesin–microtubule system has been successfully implemented into synthetic environments in order to facilitate technological tasks such as nanotransport and nanostructuring.<sup>9–12</sup> In such applications, a highly specific, spatiotemporal control over the transport activity is desired. Static spatial control over the motility has been achieved by

topographical or/and chemical surface modifications of substrate.<sup>13–15</sup> Moreover, electrical fields<sup>16–18</sup> and hydrodynamic flow<sup>19,20</sup> have been used to dynamically influence the motion of gliding filaments. Temporal control has also been achieved by manipulating the ATP concentration either by buffer exchange<sup>20,21</sup> or by ATP uncaging.<sup>9</sup>

In this paper, we report an approach to control the motility of gliding microtubules using stimuli-responsive polymer surfaces. In particular, we fabricated composite surfaces where functional kinesin motor molecules were adsorbed onto a silicon substrate between surface-grafted polymer chains of thermoresponsive poly(*N*-isopropylacrylamide) (PNIPAM).<sup>22,23</sup> In aqueous solution the PNIPAM polymer chains hydrate to form extended structures when the temperature is below the lower critical solution temperature (LCST, 32–33 °C for PNIPAM<sup>24</sup>) but become compact structures by dehydration when heated above the LCST. We used this effect to repel gliding microtubules from the surface at 27 °C while they were able to land and glide at 35 °C (Figure 1).

**Fabrication of PNIPAM Gradient Surfaces.** To determine the optimal polymer surface density for the temperature-controlled switching of microtubule motility, we performed our experiments on a PNIPAM layer with a lateral gradient of the grafting density. Gradient PNIPAM layers were prepared via a two-step procedure similar to the methods described elsewhere.<sup>12,25</sup> In brief, highly polished single-crystal silicon wafers of {100} orientation with a native silicon oxide layer (1.6 nm) (Semiconductor Processing Co.) were used as substrates. Silicon chips, which were

\* Corresponding author. E-mail: diez@mpi-cbg.de.

<sup>†</sup> Max-Planck-Institute of Molecular Cell Biology and Genetics.

<sup>‡</sup> Leibniz Institute of Polymer Research Dresden.



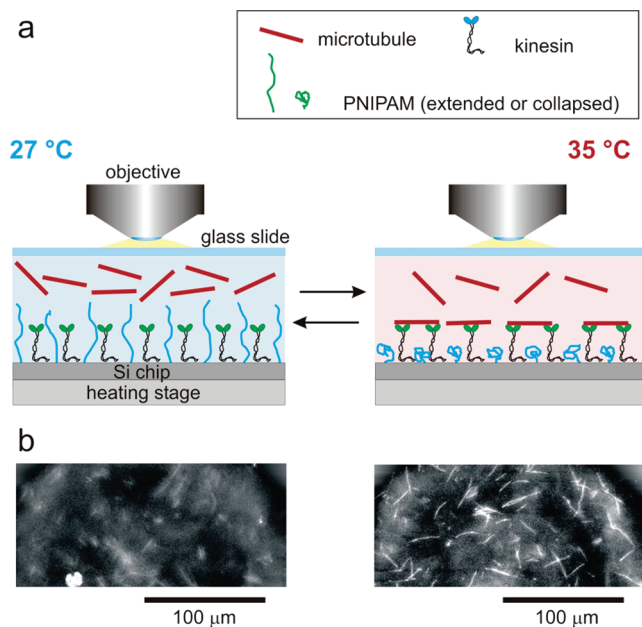


**Figure 1.** Gliding motility of microtubules on a thermoresponsive PNIPAM surface with adsorbed kinesin. (a) Schematics of the experimental setup. Repeated changes in temperature resulted in the reversible switching of PNIPAM chains between the extended conformation (where microtubules are repelled from the surface and cannot bind to the kinesin heads) and the collapsed conformation (where microtubules can glide unhindered on the kinesin molecules). (b) Fluorescence micrographs of rhodamine-labeled microtubules on a substrate surface with grafted PNIPAM chains ( $\Gamma_{\text{PNIPAM}} \approx 6 \text{ mg/m}^2$ ) and adsorbed kinesin. No gliding of microtubules is observed at 27 °C (left image) while the microtubules glide at 35 °C (right image).

cut from the wafers in different sizes, were first ultrasonically cleaned in chloroform for 30 min, placed in hot piranha solution (3:1 concentrated sulfuric acid and 30% hydrogen peroxide) for 1 h, and finally rinsed several times with high-purity water. A thin layer of polyglycidyl methacrylate (PGMA,  $M_n = 84\,000 \text{ g/mol}$ , synthesized by free radical polymerization) was deposited on top of the chips by spin-coating of a 0.01% PGMA solution in chloroform and annealed at 110 °C for 5 min. Afterward, a thick film (200 nm) of carboxy terminated poly(*N*-isopropylacrylamide) (PNIPAM-COOH,  $M_n = 49\,900 \text{ g/mol}$ , PDI = 1.46, synthesized by anionic polymerization, purchased from Polymer Source, Inc.) was spin-coated on top of the PGMA layer from a 2% solution in chloroform and annealed for 1 h on a stage exhibiting a temperature gradient. The temperature changed gradually from 130 to 180 °C along the 50-mm length of the sample. Upon heating, the chemical reaction between the terminating carboxyl groups of the PNIPAM and the epoxy groups of the PGMA resulted in the formation of the grafted PNIPAM layer with a gradient in the grafting density caused by the temperature dependence of the grafting kinetics. Nongrafted polymer was removed using Soxhlet extraction in chloroform for 3 h.

The thickness profile of the one-dimensional PNIPAM-gradient was determined by ellipsometric mapping using a SENTECH SE-402 scanning microfocus ellipsometer at  $\lambda = 633 \text{ nm}$  at an angle of incidence of 70°. The thicknesses

**Table 1.** Correlation of the Measured Thickness of the PNIPAM Layer in the Dry State with the Grafting Density, the Number of Individual Polymer Chains per Surface Area, the Average Distance between Individual Polymer Chains, and the Expected Thickness of the Polymer Layer in Water at 27 °C

$h_{\text{PNIPAM,dry}}$ (nm)	$\Gamma_{\text{PNIPAM}}$ (mg/m <sup>2</sup> )	$S_{\text{PNIPAM}}$ (μm <sup>-2</sup> )	$D_{\text{PNIPAM}}$ (nm)	$h_{\text{PNIPAM,water,27}^\circ\text{C}}$ (nm)
1.6	1.6	19500	7.1	13–16
5.1	5.1	62500	4.0	41–51
6.0	6.0	73500	3.7	48–60

of the polymer layers obtained from ellipsometry corresponded to a four-layer model Si/SiO<sub>2</sub>/PGMA/PNIPAM where it was assumed that the polymer films (PGMA and PNIPAM) have the same refractive index as the corresponding bulk polymers. Because the thickness of a PNIPAM layer strongly depends on the degree of swelling, we will further on use the grafting density  $\Gamma_{\text{PNIPAM}}$  rather than the thickness  $h_{\text{PNIPAM}}$  of the polymer layer. With a polymer mass density  $\rho$  of about 1000 kg/m<sup>3</sup>, the grafting density is given by  $\Gamma_{\text{PNIPAM}} = h_{\text{PNIPAM,dry}}\rho$ , where  $h_{\text{PNIPAM,dry}}$  is the measured ellipsometric thickness of the PNIPAM layer in the dry state. The number of individual polymer chains per surface area  $S_{\text{PNIPAM}}$  is related to the grafting density by  $S_{\text{PNIPAM}} = \Gamma_{\text{PNIPAM}}N_A/M_n$ , where  $N_A$  is the Avogadro number and  $M_n$  is the averaged molecular weight of PNIPAM. The averaged distance between individual polymer chains can be estimated by  $D_{\text{PNIPAM}} = S_{\text{PNIPAM}}^{1/2}$ . Concerning the behavior of a PNIPAM layer in water, it is known that the thickness at 35 °C is approximately the same as that in the dry state, whereas the thickness increases about 8–10 times upon swelling at 27 °C.<sup>26</sup> A summary of the PNIPAM characteristics for three different grafting densities is given in Table 1. Figure 2a shows that the PNIPAM grafting density gradually increased with lateral position  $x$  on our sample, where  $x = 0$  is assigned to the position with the lowest grafting density.

**Preparation of Microtubule Motility Assays.** Motility experiments were performed in a 5-mm-wide flow cell constructed from a silicon chip containing the PNIPAM gradient, a cover slip (Corning, 50 × 24 mm<sup>2</sup>), and two pieces of double-sided sticky tape (Scotch 3M, thickness 0.1 mm). A casein-containing solution (0.5 mg/mL in BRB8 (80 mM PIPES)/KOH pH 6.9, 1 mM EGTA, 1 mM MgCl<sub>2</sub>) was perfused into the flow cell and allowed to adsorb to the surfaces for 5 min. Next, 50 μL of a motor solution containing 2 μg/mL wild-type kinesin in BRB80 (full length drosophila conventional kinesin expressed in bacteria and purified as described in ref 27) was perfused into the flow cell and allowed to adsorb for 5 min. Depending on the conditions of the experiments, the casein and kinesin solutions were adsorbed at 27 or 35 °C. Thereafter, a motility solution containing rhodamine-labeled taxol-stabilized microtubules<sup>12</sup> was applied. To perform the motility experiments under conditions where the binding and unbinding of microtubules to/from the surface is in equilibrium, unbound microtubules were not washed out.

**Temperature Control and Optical Imaging.** For the data in Figures 2, 3, and 5, the temperature in the flow cell was

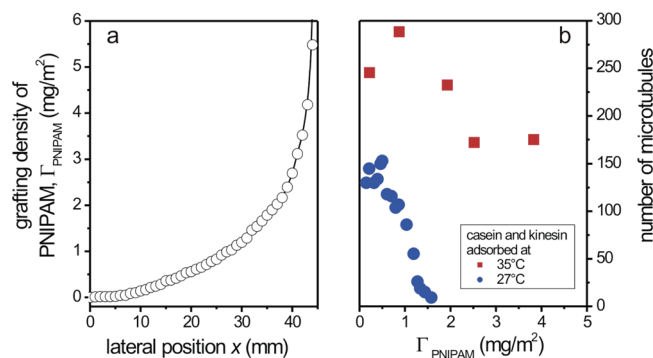


**Figure 2.** Characterization of the gradient PNIPAM layer. (a) Ellipsometric mapping of the gradient PNIPAM layer in the dry state. (b) Number of gliding microtubules per field of view vs PNIPAM grafting density. Casein and kinesin solutions were perfused at either 27 °C (blue circles) or 35 °C (red squares). Perfusion of motility solution and microscopic imaging were performed at 27 °C.

adjusted by using a Tempcontrol 37-2 digital unit (PeCon GmbH, Germany) which simultaneously controlled the temperature of the objective and the sample holder. Fluorescent images were obtained using an Axiovert 200M inverted microscope with a 40 $\times$  oil immersion objective (Zeiss, Oberkochen, Germany) in conjunction with a Cool-Snap HQ camera (Photometrics, Tucson, AZ) in 2  $\times$  2 binning mode yielding a field of view of 226  $\times$  169  $\mu\text{m}^2$ . Because the time scale in these experiments was slow and the flow cell was thermally well coupled to the objective by immersion oil as well as to the sample holder by heat conducting paste, the temperature values indicated by the Tempcontrol unit were used for data evaluation. To obtain the data in Figure 4 the silicon chip was directly attached to a Peltier element (50 mm  $\times$  50 mm, Conrad Electronic GmbH, Hirschau, Germany) by heat conducting paste. Heating and cooling were then performed by changing the electrical polarity on the Peltier element by a conventional power supply. In this experiment the temperature was recorded by a BAT-10 multipurpose thermometer (Physitemp Instruments, Clifton, NJ) and a 20 $\times$  air objective (Zeiss, Oberkochen, Germany) in conjunction with a MicroMax 512 BFT back-illuminated CCD camera (Photometrics, Tucson, AZ) was used for image acquisition. Image processing was performed using MetaMorph software (Universal Imaging, Downingtown, PA).

In the following, we report on the characterization of microtubule motility on the gradient PNIPAM surfaces at constant temperature (experiments 1 and 2) and the reversible switching of motility on selected locations along the gradient (experiments 3 and 4).

**Adsorption of Casein and Kinesin on Extended PNIPAM Chains (Experiment I).** We started with the investigation of microtubule motility after adsorbing casein and kinesin onto the PNIPAM gradient layer at 27 °C; i.e., when the PNIPAM chains were in the extended state. When investigating microtubule motility at 27 °C, we found that the number of gliding microtubules decreased strongly with increasing PNIPAM grafting density (Figure 2b, blue circles) and no microtubules were observed at  $\Gamma_{\text{PNIPAM}} > 1.6$  mg/

m<sup>2</sup>. This behavior is in accordance with earlier experiments<sup>12</sup> where casein and kinesin were adsorbed onto a gradient layer of poly(ethylene glycol), a polymer with similar protein repelling properties as PNIPAM at 27 °C. However, in the range where motility occurred, the gliding velocity of microtubules was independent of the amount of grafted PNIPAM,  $v = 0.84 \pm 0.08$   $\mu\text{m/s}$  (mean  $\pm$  standard deviation, averaged for all polymer densities, data obtained from at least 20 gliding microtubules per polymer density).

When the temperature of the flow cell was raised from 27 to 35 °C, the gliding velocity increased to  $v = 1.22 \pm 0.07$   $\mu\text{m/s}$ , as expected from the faster rate of ATP hydrolysis.<sup>21</sup> However, the number of gliding microtubules—observed at  $\Gamma_{\text{PNIPAM}} = 1.6$  mg/m<sup>2</sup>—increased only marginally and remained constant upon further cyclic changes of the temperature. We conclude that in the range of grafting densities where motility was observed the number of PNIPAM chains was too small to significantly influence the microtubule–kinesin interactions.

**Adsorption of Casein and Kinesin on Collapsed PNIPAM Chains (Experiment II).** In a second experiment, we incubated a PNIPAM gradient layer of the same kind as used in experiment I with casein and kinesin at 35 °C. At this temperature, the PNIPAM chains were collapsed and the perfused proteins were able to bind on all positions along the polymer gradient (information obtained from the perfusion of fluorescent casein, data not shown). The flow cell was then cooled to 27 °C. This particular cooling step was performed in order to release the kinesin molecules, which might have initially adsorbed onto the PNIPAM chains themselves at 35 °C.<sup>23</sup> The nonadsorbed kinesin was then removed from the flow cell by perfusion of the microtubule-containing motility solution at 27 °C. We assume that after this procedure, the majority of bound kinesin molecules are attached to the substrate between the PNIPAM chains and there is no kinesin in solution. Further switching of the PNIPAM layer between collapsed and extended states should not influence the total concentration of kinesin molecules on the surface. When investigating microtubule motility at 27 °C (similar as in experiment I), we observed that—at any given PNIPAM grafting density—the number of gliding microtubules was higher than that in experiment I and motility was observed up to grafting densities of 4 mg/m<sup>2</sup> and higher (Figure 2b, red squares). However, similar to experiment I, the number of gliding microtubules gradually decreased with increasing  $\Gamma_{\text{PNIPAM}}$ .

The results from experiments I and II show that the use of a PNIPAM gradient layer allows the fabrication of surface gradients of active kinesin. Our finding that the gliding velocity did not change along the gradient indicates that the bioactivity of individual kinesin molecules is independent of the PNIPAM grafting density. Moreover, we observed only very few stuck microtubules. This indicates a high percentage of active motor molecules on the polymer surface, since it is known that inactive motors tend to stick microtubules to the surface.

When casein and kinesin were adsorbed to the surface at 27 °C, we found that the grafting density of PNIPAM—at

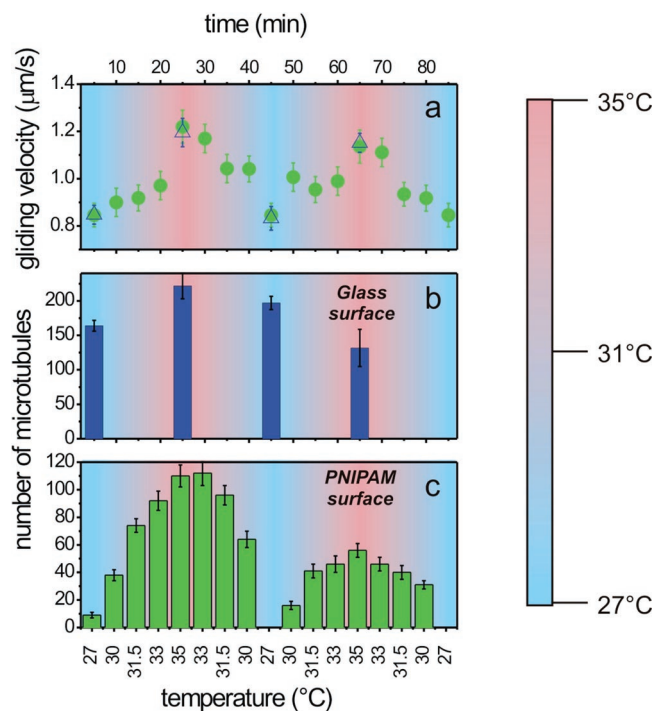


**Figure 3.** Temperature-induced changes of gliding microtubule motility. (a) Dependence of the averaged gliding velocity with the temperature on the PNIPAM surface (green circles) and glass (blue triangles). (b) Number of gliding microtubules on the glass surface. The measurements were performed at 27 and 35 °C only, but motility also occurred at intermediate temperatures. (c) Number of gliding microtubules during two sequential cycles of heating and cooling at  $\Gamma_{\text{PNIPAM}} \approx 6 \text{ mg/m}^2$  (see also Supporting Information). Casein and kinesin were adsorbed at 35 °C. The underlain color code is used for qualitative comparison.

which motility was observed—was insufficient to influence microtubule motility in a temperature-induced way. Therefore, we concluded that the adsorption of casein and kinesin at 35 °C (when the PNIPAM chains are in the collapsed state and higher kinesin densities can be bound to the surface) will be advantageous when aiming for the temperature-induced switching of motility.

**Reversible Switching of Microtubule Motility (Experiment III).** To demonstrate the temperature-induced switching of microtubule motility, we incubated a PNIPAM gradient surface with casein and kinesin at 35 °C. We then gradually raised and lowered the temperature between 27 and 35 °C and investigated the gliding motion of microtubules at  $\Gamma_{\text{PNIPAM}} \approx 6 \text{ mg/m}^2$ . Again, the gliding velocity was found to change in phase with the temperature both on the polymer and on the glass surface of the flow cell (Figure 3a). While the number of gliding microtubules did not change significantly on the glass side (Figure 3b), a pronounced temperature dependence became apparent on the polymer surface (Figure 3c and Supporting Information).<sup>28</sup> Upon the gradual increase of the temperature, the number of gliding microtubules significantly increased. Upon cooling, this number lowered until eventually no gliding microtubules were observed at 27 °C. The same behavior was observed during a second, consecutive cycle of heating and cooling. The slightly lower number of gliding microtubules during the

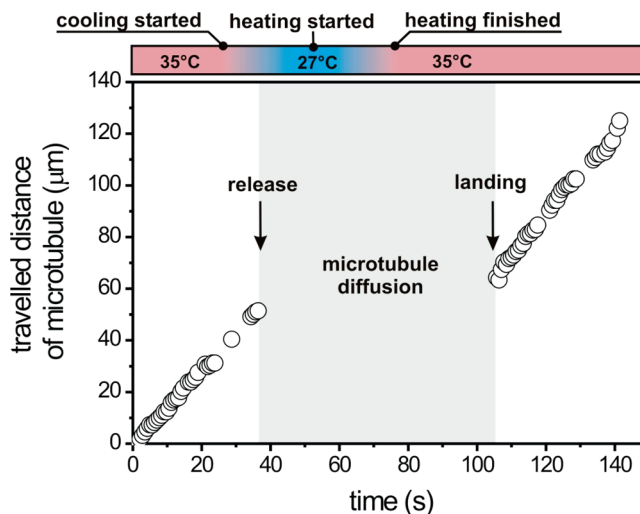


**Figure 4.** Behavior of a single microtubule during rapid cooling and heating of the PNIPAM–kinesin surface. Plotted is the traveled distance of one microtubule (as determined by manual tracking of the trailing end of the microtubule) as a function of time. The corresponding temperature conditions are indicated in the upper panel. The microtubule first glided at 35 °C with constant velocity, released when the temperature was lowered to 27 °C, and diffused in the solution close to the surface. During the diffusive period, tracking of the microtubule was not possible. After the surface was heated to 35 °C again the microtubule rebound after about 20 s and was gliding again at constant velocity.

second cycle was most likely due to partial denaturation of the adsorbed kinesin. Note, that a similar effect was observed on the glass surface, where the number of gliding microtubules decreased to about 60% of the initial value during the second temperature cycle.

To obtain the data in Figure 3, heating and cooling were performed slowly and emphasis was on performing the measurements under conditions where the gliding microtubules were in equilibrium with the ones in solution. To perform measurements on a faster time scale, we extended our experimental setup by a Peltier element. This way we were able to switch the temperature in the flow cell between 27 and 35 °C within about 25 s. We observed that the release of microtubules occurred almost concurrent with the temperature decrease from 35 to 27 °C. In contrast, landing started only about 20 s after the temperature had risen to 35 °C again. This time lag was presumably caused by the limited diffusion of the released microtubules back to the kinesins on the surface. Figure 4 shows a typical example of the behavior of a single microtubule during the rapid cooling and heating of the PNIPAM–kinesin surface ( $\Gamma_{\text{PNIPAM}} \approx 6 \text{ mg/m}^2$ ).

**Temperature-Controlled Sorting of Microtubules (Experiment IV).** Similar to experiment III, we incubated a PNIPAM gradient surface with casein and kinesin at 35 °C but investigated the gliding motility at a location with a less dense PNIPAM layer ( $\Gamma_{\text{PNIPAM}} \approx 5 \text{ mg/m}^2$ ). We again observed a periodic increase and decrease of the number of gliding microtubules upon heating and cooling (Figure 5a). However, cooling did not lead to a complete release of microtubules at 27 °C. We found that the cyclic change of the temperature was accompanied by a cyclic change of the



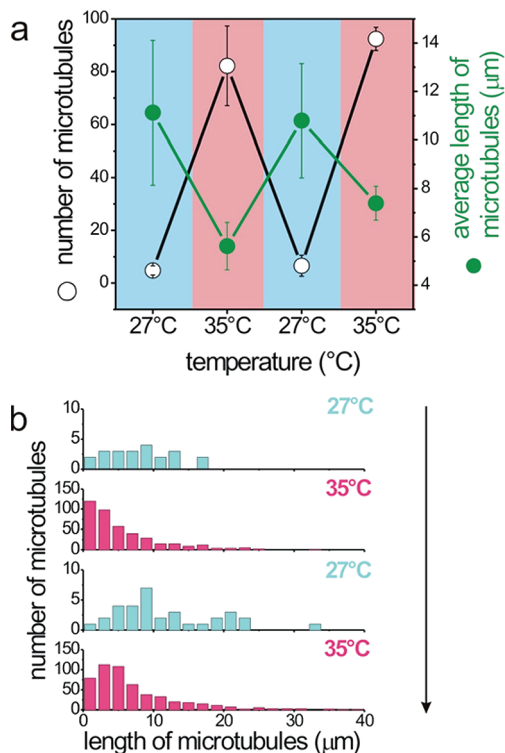


**Figure 5.** Dependence of the number and the length of motile microtubules on temperature at  $\Gamma_{\text{PNIPAM}} \approx 5 \text{ mg/m}^2$ . (a) Average microtubule length (green, filled circles) and number of microtubules (black, open circles) per field of view as function of temperature. (b) Histograms of microtubule lengths at different temperatures (data represent total length distributions of microtubules in four fields of view). The cyclic change of temperature was accompanied by a cyclic change of the average microtubule length. The arrow shows the temporal order of the experiments.

average microtubule length (Figure 5a). Analysis of the length distributions of gliding microtubules revealed that cooling predominantly caused the release of the shorter microtubules (Figure 5b). This finding can be explained as follows: Swelling of the PNIPAM chains leads to the screening of part of the kinesin motors. Consequently, the average distance between neighboring kinesin molecules that can be reached by the microtubules significantly increases. Because for continuous gliding, microtubules always need to be in contact with at least two kinesin motors at one time, the variable motor density leads to a sorting effect of the microtubules according to their length similar to the static phenomenon described in ref 12.

The release of the gliding microtubules in experiments III and IV can be understood by the dimension of the swollen PNIPAM layer at 27 °C (see Table 1). At high grafting densities the length of the extended PNIPAM chains exceeds the height of about 15–20 nm at which kinesin-driven microtubules are assumed to hover above the surface.<sup>29</sup> Thus, the kinesin heads are likely be hidden within the surrounding PNIPAM chains. Heating leads to a collapse of the PNIPAM chains and makes the kinesin molecules accessible for the microtubules.

In summary, we developed a novel approach for the in vitro control of microtubule motility on kinesin-coated substrates using stimuli-responsive polymers. Reversible

switching of motility was achieved by the covalent attachment of a thermoresponsive PNIPAM onto Si chips where kinesin motors were subsequently adsorbed. We observed that microtubules were able to land and glide on the composite PNIPAM–kinesin surface at 35 °C but were repelled from the surface at 27 °C. Moreover, we demonstrated the applicability of the composite PNIPAM–kinesin layer for the stimuli-controlled sorting of microtubules according to their length.

We believe that the reported method can be implemented for the control of microtubule guiding in various nanotechnological applications. For example, patches of PNIPAM polymer grafted onto the bottoms of narrow grooves could be used for the externally controlled gating of nanotransport: microtubules could pass the gate if the PNIPAM patch is locally heated but would be expelled at room temperature. Such a configuration could also be applied for the thermocontrolled sorting of microtubules according to their length when microtubules of length shorter than a threshold value cannot pass such a gate. Because the presented method operates in a temperature range that does not impact the functioning of most biological systems, we foresee a strong potential of the system for the external control over a wide range of surface-coupled enzyme systems.

**Acknowledgment.** We thank C. Bräuer for technical assistance, as well as C. Leduc, C. Reuther, B. Schroth-Diez, and A. Synytska for helpful comments on the manuscript. T. Pompe and the members of our group are kindly acknowledged for fruitful discussions. We are grateful to the DFG (Grant B10 within priority program Reactive Polymers SFB287) and the BMBF (Grant 03N8712) for financial support.

**Supporting Information Available:** A sequence of fluorescent images of microtubules gliding over a PNIPAM–kinesin surface (field of view  $226 \times 169 \mu\text{m}$ , PNIPAM grafting density of about  $6 \text{ mg/m}^2$ ) at different temperatures. This material is available free of charge via the Internet at <http://pubs.acs.org>.

## References

- (1) Postma, H. W. C.; Sellmeijer, A.; Dekker, C. *Adv. Mater.* **2000**, *12*, 1299.
- (2) Shu, L. J.; Schluter, A. D.; Ecker, C.; Severin, N.; Rabe, J. P. *Angew. Chem., Int. Ed.* **2001**, *40*, 4666.
- (3) MacDonald, M. P.; Paterson, L.; Volke-Sepulveda, K.; Arlt, J.; Sibbett, W.; Dholakia, K. *Science* **2002**, *296*, 1101–1103.
- (4) Schenning, A. P. H. J.; Jonkheijm, P.; Hofkens, J.; De Feyter, S.; Asavei, T.; Cotlet, M.; De Schryver, F. C.; Meijer, E. W. *Chem Commun* **2002**, 1264–1265.
- (5) Svoboda, K.; Schmidt, C. F.; Schnapp, B. J.; Block, S. M. *Nature* **1993**, *365*, 721–727.
- (6) Howard, J. *Nature* **1997**, *389*, 561–567.
- (7) Howard, J. *Mechanics of Motor Proteins and the Cytoskeleton*; Sinauer Press: Sunderland, MA, 2001.
- (8) Vale, R. D. *Cell* **2003**, *112*, 467–480.
- (9) Hess, H.; Clemmens, J.; Qin, D.; Howard, J.; Vogel, V. *Nano Lett.* **2001**, *1*, 235–239.
- (10) Hiratsuka, Y.; Tada, T.; Oiwa, K.; Kanayama, T.; Uyeda, T. Q. P. *Biophys. J.* **2001**, *81*, 1555–1561.
- (11) Hess, H.; Bachand, G. D.; Vogel, V. *Chem–Eur. J.* **2004**, *10*, 2110–2116.
- (12) Ionov, L.; Stamm, M.; Diez, S. *Nano Lett.* **2005**, *5*, 1910–1914.

- (13) Clemmens, J.; Hess, H.; Lipscomb, R.; Hanein, Y.; Bohringer, K. F.; Matzke, C. M.; Bachand, G. D.; Bunker, B. C.; Vogel, V. *Langmuir* **2003**, *19*, 10967–10974.
- (14) Hess, H.; Clemmens, J.; Matzke, C. M.; Bachand, G. D.; Bunker, B. C.; Vogel, V. *Appl. Phys. A: Mater. Sci. Process.* **2002**, *75*, 309–313.
- (15) vandenHeuvel, M. G. L.; Butcher, C. T.; Smeets, R. M. M.; Diez, S.; Dekker, C. *Nano Lett.* **2005**, *5*, 1117–1122.
- (16) Riveline, D.; Ott, A.; Julicher, F.; Winkelmann, D. A.; Cardoso, O.; Lacapere, J. J.; Magnusdottir, S.; Viovy, J. L.; Gorre-Talini, L.; Prost, J. *Eur. Biophys. J. Biophys. Lett.* **1998**, *27*, 403–408.
- (17) Asokan, S. B.; Jawerth, L.; Carroll, R. L.; Cheney, R. E.; Washburn, S.; R. Superfine, R. *Nano Lett.* **2003**, *3*, 431–437.
- (18) van den Heuvel, M. G. L.; De Graaff, M. P.; Dekker, C. *Science* **2006**, *312*, 910–914.
- (19) Prots, I.; Stracke, R.; Unger, E.; Bohm, K. J. *Cell Biol. Int.* **2003**, *27*, 251–253.
- (20) Gast, F.-U.; Dittrich, P. S.; Schwille, P.; Weigel, M.; Mertig, M.; Opitz, J.; Queitsch, U.; Diez, S.; Lincoln, B.; Wottawah, F.; Schinkinger, S.; Guck, J.; Käs, J.; Smolinski, J.; Salchert, K.; Werner, C.; Duschl, C.; Jäger, M. S.; Uhlig, K.; Geggier, P.; Howitz, S. *Microfluid. Nanofluid.* **2006**, *2*, 21–36.
- (21) Bohm, K. J.; Stracke, R.; Baum, M.; Zieren, M.; Unger, E. *FEBS Lett.* **2000**, *466*, 59–62.
- (22) Nath, N.; Chilkoti, A. *Adv. Mater.* **2002**, *14*, 1243–1246.
- (23) Huber, D. L.; Manginell, R. P.; Samara, M. A.; Kim, B.-I.; C. Bunker, B. *Science* **2003**, *301*, 352–354.
- (24) Sun, T. L.; Wang, G. J.; Lin, F.; Biqian, L.; Yongmei, M.; Lei, J.; Zhu, D.-B. *Angew. Chem.* **2004**, *116*, 361.
- (25) Ionov, L.; Zdyrko, B.; Sidorenko, A.; Minko, S.; Klep, V.; Luzinov, I.; Stamm, M. *Macromol. Rapid Commun.* **2004**, *25*, 360–365.
- (26) Schmaljohann, D.; Nitschke, M.; Schulze, R.; Eing, A.; Werner, C.; Eichhorn, Y. J. *Langmuir* **2005**, *21*, 2317–2322.
- (27) Coy, D. L.; Wagenbach, M.; Howard, J. *J. Biol. Chem.* **1999**, *274*, 3667–3671.
- (28) We note that the number of microtubules gliding on the glass surface is approximately two times higher than that on the polymer surface. This is most probably due to stronger affinity of kinesin to glass than to the polymer surface at the chosen grafting density.
- (29) Hunt, A.; Howard, J. *Biophys. J.* **1993**, *64*, A263–A263.

NL0611539



Ionov, L.; Sapra, S.; Synytska, A; Rogach, A. L.; Stamm, M.; Diez, S.

Fast and spatially resolved environmental sensing using grafted composite layers of stimuli-responsive polymers and semiconductor nanocrystals

***Advanced Materials*** 2006, 18(11), 1453-1457.

DOI: 10.1002/adma.200502686

## Fast and Spatially Resolved Environmental Probing Using Stimuli-Responsive Polymer Layers and Fluorescent Nanocrystals\*\*

By Leonid Ionov,\* Sameer Sapra, Alla Synytska, Andrey L. Rogach, Manfred Stamm, and Stefan Diez\*

The development of chemical and biological sensors is of growing interest for many analytical applications, including the monitoring of environmental and industrial processes and the quality control of nutrition and water, as well as for medical and security purposes. In recent sensor approaches, the change in fluorescence of organic dyes or inorganic nanoparticles in different environments has been widely used to detect various ions and chemical substances.<sup>[1–12]</sup> In most of the cases, the environmental changes lead to quenching of the fluorescence<sup>[8–10]</sup> or to a shift of the emission spectrum due to energy transfer.<sup>[5,11,12]</sup> In such applications, semiconductor nanocrystals have several advantages over organic fluorescent dyes. In particular, nanocrystals have a high photostability, broad absorption spectra in combination with a narrow and symmetric emission band, and high molar absorbance.<sup>[5]</sup>

Here, we report a novel approach for the design of environmental sensors based on fluorescence interference contrast (FLIC)<sup>[13]</sup> of semiconductor nanocrystals near a reflecting silicon surface (Fig. 1). FLIC arises from the interference between light that is directly emitted (or absorbed) by a nanoparticle and the light that is reflected by the mirror surface. Consequently, the intensity of the detected fluorescence light

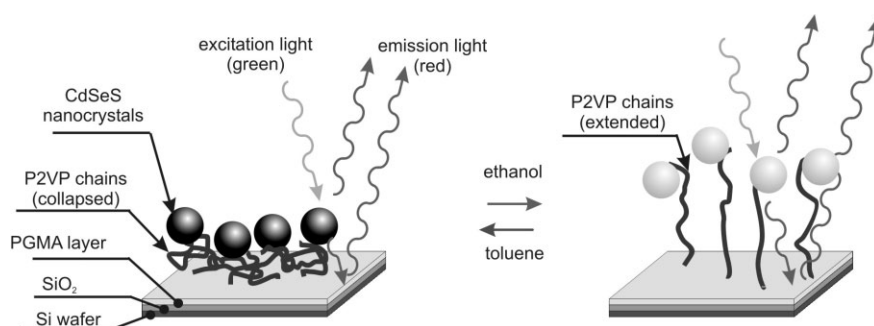


**Figure 1.** Schematic of the polymeric sensor. Hydrophobic nanocrystals are adsorbed on a stimuli-responsive polymer layer that was previously grafted onto a reflecting substrate. The nanocrystal-surface distance depends on the conformation of the polymer chains and changes in different solvents. The change in height is then reported by a variation in the detected fluorescence intensity.

becomes a periodic function of the nanoparticle distance from the surface. The period of this function is determined by the wavelength of the light and the refractive index of the surrounding medium. Fluorescent nanoparticles located in close proximity to the mirror surface will appear dark, while particles about a quarter-wavelength away will appear with maximum brightness. Inserting a polymer layer, whose thickness depends on the environmental conditions, provides a simple and cheap strategy for the design of a sensor. Using the swelling behavior of a poly(2-vinyl pyridine) (P2VP) polymer layer anchored to a silica wafer, we use the sensor for precise measurements of solvent composition with unprecedented spatial and temporal resolution.

The P2VP polymer layer was grafted onto chips from a Si wafer with a native  $\text{SiO}_2$  layer of thickness  $H_{\text{SiO}_2} = 1.6$  nm (precoated with PGMA,  $H_{\text{PGMA}} = 1.5$  nm, see Experimental). The thickness of the dry P2VP layer was measured by ellipsometry to be  $H^{\text{DRY}} = 7.6 \text{ nm} \pm 0.5 \text{ nm}$ , corresponding to a grafting density of about  $0.1 \text{ chains nm}^{-2}$ . Because the distance between the grafting points ( $d = 3.5$  nm) was smaller than the gyration radius of the P2VP polymer coils ( $R_g \approx 5$  nm), the polymer layer was considered brushlike. The surface of the P2VP layer was smooth with a root mean square roughness less than 0.3 nm, as measured by atomic force microscopy (AFM). We found that the P2VP brush undergoes a completely reversible change in thickness in different solvents. In toluene (a “poor” solvent), the polymer layer had a thickness of  $H^{\text{TOLUENE}} = 9 \text{ nm} \pm 1 \text{ nm}$  while in ethanol (a “good” solvent) the P2VP brush swelled by a factor of about 2.5 to a thickness of  $H^{\text{ETHANOL}} = 19.6 \text{ nm} \pm 1 \text{ nm}$  (values measured by ellipsometry without attached nanocrystals).

[\*] Dr. L. Ionov, Dr. S. Diez  
Max-Planck-Institute of Molecular Cell Biology and Genetics  
01307 Dresden (Germany)  
E-mail: ionov@mpi-cbg.de; diez@mpi-cbg.de  
Dr. L. Ionov, Dr. A. Synytska, Prof. M. Stamm  
Leibniz-Institute of Polymer Research  
01069 Dresden (Germany)  
Dr. S. Sapra, Dr. A. L. Rogach  
Photonics and Optoelectronics Group  
Physics Department and CeNS  
Ludwig-Maximilians-Universität München  
80799 München (Germany)

[\*\*] We thank J. Kerssemakers and J. Helenius for help with the experimental work and J. Feldmann for helpful discussions, as well as K.-J. Eichhorn and R. Schulz for support with the ellipsometry. Andor Technology (Belfast, Northern Ireland) is greatly acknowledged for the generous loan of the high-speed EMCCD camera. The authors are grateful to the DFG (grant SPP 1164) and the BMBF (grant 03N8712) for financial support. S. Sapra is thankful to the Humboldt-Foundation for funding his research stay in Germany.

Hydrophobic CdSeS nanocrystals (emitting at 570 nm, see Figs. 2a and b) were adsorbed from a 1 mM toluene solution onto the P2VP brush during 30 s. Non- or weakly adsorbed particles were removed by rinsing with toluene. Changes in the surface morphology (Fig. 2c) and the appearance of a fluorescence signal indicated the incorporation of nanocrystals into the polymer layer. While there was no chemical bonding between the nanocrystals and the polymer chains, the nanocrystals were held in the polymer matrix, most likely due to hydrophobic–hydrophobic interaction. Stability of this interaction was verified by an unchanged fluorescence intensity after rinsing the surface in various solvents and subsequent drying. Atomic force microscopy (AFM) images (Fig. 2c) showed that the nanocrystals covered approximately 5 % of the brush surface.

We found that the fluorescence intensity of the CdSeS nanocrystals adsorbed onto the P2VP brush strongly depended on the surrounding solvent (Fig. 3). To show that the observed fluorescence changes are a measure of the changes in the P2VP layer thickness, the polymer–nanocrystal layer was partly removed by scratches with a diamond knife in a cross-like pattern. While the fluorescence intensity was low in a dry environment (Fig. 3a, i), the intensity increased significantly when a toluene droplet was deposited on the brush surface (Fig. 3a, ii). The increase in fluorescence intensity became even more pronounced when toluene was replaced by ethanol (Fig. 3a, iii). Intensity profiles across one of the scratches are given in Figure 3b. The slight increase in the fluorescence intensity in the scratched areas after depositing of toluene and ethanol was attributed to reflections of the fluorescent light within the liquid droplets. Notably, the solvent-induced switching of the fluorescence intensity was found to be completely reversible and reproducible. Figure 3c shows averaged values of the

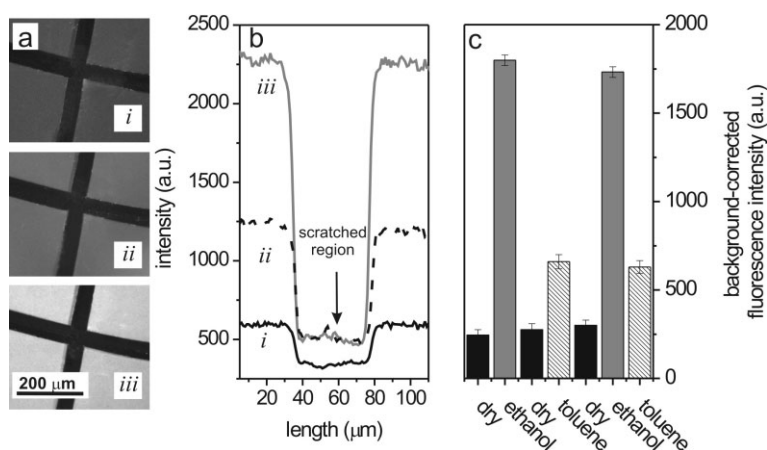


**Figure 3.** Fluorescence of the CdSeS–P2VP brush layer. a) Fluorescence microscopy images of the CdSeS–P2VP brush layer in the dry state (i), wetted with a droplet of toluene (ii), and wetted with a droplet of ethanol (iii). For contrast, thin stripes of the polymer–nanocrystal layer were removed using a diamond knife. b) Intensity profiles across one of the scratches in (a). c) Multiple cycles of solvent application and drying. Average intensity values are corrected for the background fluorescence measured in the scratched areas. Plotted are the average intensity values  $\pm$  the standard deviation for areas of 200  $\mu\text{m} \times 200 \mu\text{m}$ .

background-corrected fluorescence intensities for multiple cycles of solvent application and drying on the same chip. To rule out that the observed changes in fluorescence were the result of a chemical interaction of the solvent with the nanocrystals themselves we performed control experiments using the same layer system on glass. No dependence of the fluorescence intensity on the surrounding environment was found.

We investigated how well the intensity variations could be used to measure the thickness of polymer layers. For that, we performed measurements on a Si chip with four different thicknesses of SiO<sub>2</sub> (Fig. 4, method similar to one reported by Braun et al.).<sup>[14]</sup> The simultaneous recording of all four intensity signals allowed each individual environmental condition to be fit by the following equation:<sup>[15]</sup>

$$I(h) = I_0 \left( 2 \cdot (1 - r_f)^2 + 8r_f \sin^2 \left( \frac{2\pi}{\lambda_{EX}} (n_{\text{SiO}_2} \cdot h_{\text{SiO}_2} + n \cdot h) \right) \right) \times \left( 2 \cdot (1 - r_f)^2 + 8r_f \sin^2 \left( \frac{2\pi}{\lambda_{EM}} (n_{\text{SiO}_2} \cdot h_{\text{SiO}_2} + n \cdot h) \right) \right) \quad (1)$$

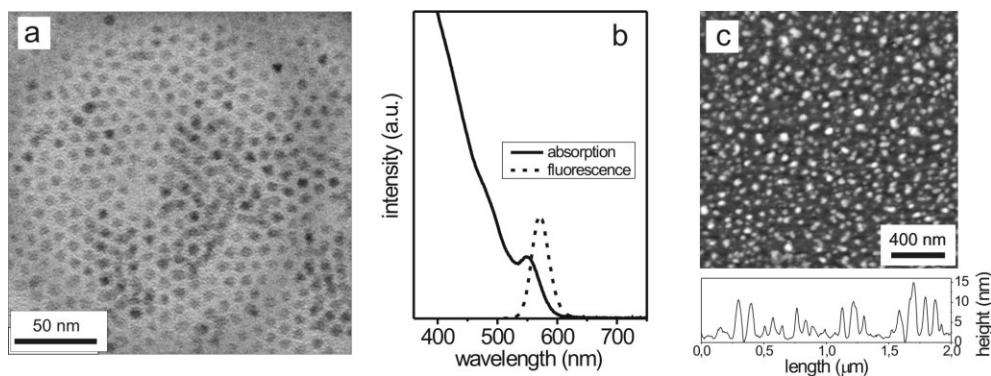


**Figure 2.** Characterization of the semiconductor nanocrystals. a) Transmission electron microscopy (TEM) image of the nanocrystals. b) Absorption and emission spectra of the nanocrystals. c) AFM image of the P2VP brush after adsorption of the nanocrystals.

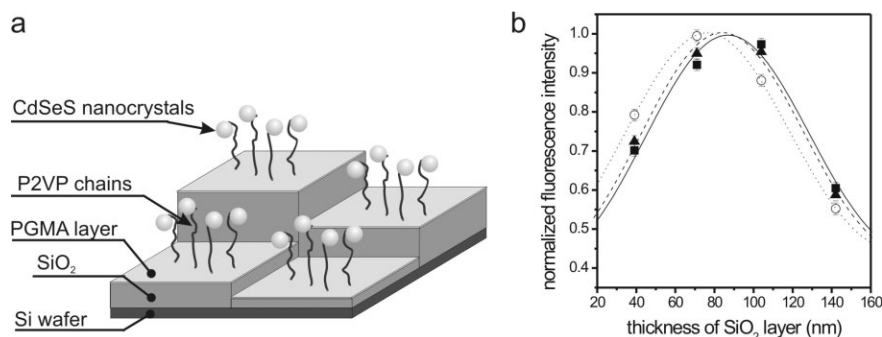


**Figure 4.** Quantification of the thickness of the polymer layer by FLIC. a) Schematic of the simultaneous intensity measurements at four different thicknesses of SiO<sub>2</sub>. b) Normalized fluorescence intensity values of the CdSeS–P2VP brush layer on the SiO<sub>2</sub> steps: ■: dry sample, ▲: after deposition of the toluene droplet, ○: after deposition of the ethanol droplet. FLIC curves are fitted using Equation 1 for the dry sample (solid line), the sample in toluene (dashed line), and in ethanol (dotted line).

where  $I_0$  serves as a proportionality factor. Refractive indices for the polymer layer and the SiO<sub>2</sub> layer are represented by  $n$  and  $n_{\text{SiO}_2} = 1.46$ , respectively.  $h_{\text{SiO}_2}$  is the oxide thickness and  $h$  is the height above the oxide surface. The excitation and emission wavelengths,  $\lambda_{\text{EX}}$  and  $\lambda_{\text{EM}}$ , are 565 nm and 610 nm, respectively. The reflection coefficient is represented by  $r_f$ .

In our fitting procedure using Equation 1 (Fig. 4b), we kept the refractive index of the polymer layer constant and equal to that obtained from the ellipsometric measurement (Table 1) while the other parameters ( $r_f$ ,  $I_0$ , and  $h$ ) were varied. For each environmental condition, we thus obtained a height value,  $h$ , which represents the distance between the

**Table 1.** Values of the parameters as obtained by fitting the experimental data of Figure 4 using Equation 1. Also included is the ellipsometry data as obtained for the polymer layers without nanocrystals. The thickness of the polymer layer represents the sum of the thickness of the anchoring PGMA layer and the thickness of the P2VP grafted layer. The typical error in the determination of the polymer layer using ellipsometry is  $\pm 1$  nm.

Conditions	FLIC				Ellipsometry $H_{\text{PGMA}} + H_{\text{P2VP}}$ [nm]
	$I_0$	$r_f$	$h$ [nm]	$n$	
Ethanol	39.8	0.11	20.9	1.46	21.1
Toluene	37.0	0.11	12.1	1.58	10.5
Dry	37.0	0.11	9.1	1.59	9.1

nanocrystals and the SiO<sub>2</sub> surface. Note that the height values derived from our FLIC approach are nearly identical to the ellipsometric data (Table 1). The shift in the curves in Figure 4b represents the different contributions of the polymer layers to the absolute height of the nanocrystals above the reflecting Si/SiO<sub>2</sub> interface.

We performed two specific experiments in order to demonstrate the applicability of the presented polymer–nanocrystal system for environmental sensing. In the first experiment we utilized the CdSeS–P2VP brush layer for sensing the composition of liquid mixtures. As the conformation of the individual

polymer chains will gradually depend on the mixing ratio between a “good” and a “poor” solvent, the thickness of the polymer layer should also vary between the extremes, as determined above for ethanol and toluene. In fact, we did find a strongly linear relationship between the observed fluorescence intensity of our sensor system and the ethanol–toluene mixing ratio (Fig. 5a). Using this plot as calibration, the composition of an unknown ethanol–toluene mixture can be determined easily. In the second experiment, we demonstrated the applicability of the polymer–nanocrystal system for the real-time monitoring of liquid flow. For that purpose we constructed a flow chamber

(width 2 mm, height 50  $\mu\text{m}$ ) consisting of a glass cover slip on one side and a Si chip with the polymer–nanocrystal system on the other. We then recorded on a charge-coupled device (CCD) camera (image acquisition with 100 frames per second) how the front of an ethanol droplet fills such a closed channel (Fig. 5b). While the dry area on the surface appears

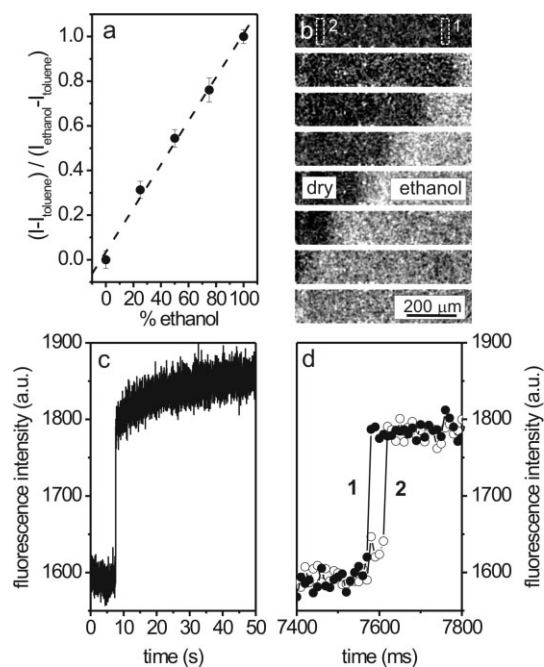


**Figure 5.** Sensory applications of P2VP–CdSeS layers. a) Dependence of the normalized fluorescence intensity  $(I - I_{\text{toluene}}) / (I_{\text{ethanol}} - I_{\text{toluene}})$  as a function of the ethanol content in the toluene–ethanol mixture.  $I_{\text{toluene}}$  and  $I_{\text{ethanol}}$  denote the measured intensities for 100% toluene or ethanol, respectively. b) Sequence of fluorescence microscopy images during ethanol perfusion (from the right) into a flow cell with a P2VP–CdSeS layer. The time interval between consecutive images is 10 ms. c,d) Time-dependence of the detected fluorescence intensity from (b) over 50 s at location 1 and over 400 ms at locations 1 and 2. It can be observed that the P2VP–CdSeS layer responds within less than 10 ms. The flow rate of the solvent inside the channel was 0.015  $\text{m s}^{-1}$ .

dark, the part of the surface that is wetted by ethanol shows an increased intensity due to the increased distance of the nanocrystals from the surface.

Although complete switching of the P2VP–CdSeS layer finishes after about 1–3 min of swelling, the first sharp response of the signal occurs in less than 10 ms (Figs. 5c and d). Thus, this very fast response of the polymer layers will allow the use of the polymer–nanocrystal layers for ultrafast sensing and for the dynamic investigation of the properties of polymer grafted layers in contact with liquids or other surfaces.

Although other methods, such as imaging ellipsometry, allow the precise mapping of the properties of thin films, the present method has distinct advantages. Using a high-speed camera, we demonstrated the possibility to acquire 100 spatially resolved images per second and even faster data acquisition is possible. On the contrary, the typical acquisition time associated with imaging ellipsometry is about 1 min. Moreover, if spatial information is not required, the detection system can be reduced to a light-emitting diode for fluorescence excitation and a photodiode for emission measurements. A simple and compact sensor should be realizable. The main factors that limit the applicability of our sensor are related to the chemical stability of the polymer layer and the nanocrystals. For example, we found that the CdSeS nanocrystals used in our experiments decomposed at < pH 3. Concerning the thickness of the used polymer layers we note that the difference between the compacted and swollen state is required to be less than 120 nm (half the period of the FLIC curve). However, the actual position on the periodic FLIC curve can be tuned by the thickness of the underlying SiO<sub>2</sub> layer.

To conclude, we have developed a novel strategy for the design of fluorescent environmental sensors. Our method is based on nanocrystals incorporated into polymer layers grafted onto reflecting surfaces. The main advantages of our approach are extreme instrumental simplicity, high spatial precision of the measurements and a fast signal response. We foresee a large potential of such sensors for the in situ monitoring of mixing and separation processes, as well as for the control of the composition of liquid mixtures in microfluidic devices. Our sensing strategy can be extended to aqueous environments when appropriate polymers are used. For example, polyelectrolyte layers are responsive to pH and ionic strength, while poly(*N*-isopropyl acrylamide) is sensitive to temperature. In addition, we believe that our method can contribute to a further understanding of the dynamic properties of ultrathin polymer films and their interaction with environmental components ranging from ions and inorganic nanoparticles to proteins and cells.

## Experimental

Highly polished single-crystal silicon wafers of {100} orientation with either 1.8 nm or 148 nm thick silicon oxide layers (Semiconductor Processing Co) were used as substrates. The wafers were cleaned with chloroform in an ultrasonic bath for 30 min, placed in piranha solution (3:1 concentrated sulfuric acid and 30 % hydrogen peroxide)

for 1 h, and rinsed several times with water. Polyglycidylmethacrylate (PGMA) (number-average molecular weight,  $M_n = 84\,000 \text{ g mol}^{-1}$ ) was synthesized by free radical polymerization of glycidyl methacrylate (Aldrich). Carboxyl-terminated poly(2-vinyl pyridine) (P2VP-COOH,  $M_n = 39\,200 \text{ g mol}^{-1}$ , weight-average molecular weight,  $M_w = 41\,500 \text{ g mol}^{-1}$ ) was purchased from Polymer Source, Inc. The silicon wafers with patches of silicon oxide of different thicknesses were prepared using step-by-step etching in 10 % HF [14].

P2VP brush layers were prepared via a two-step procedure [16]. In brief, a thin layer of PGMA (ca. 1.5 nm) was deposited by spin-coating from a 0.01 % solution in chloroform and annealed at 110 °C for 5 min. On top, a thin film of P2VP-COOH (2 % solution in chloroform) was spin-coated and annealed for 5 h at 150 °C. Ungrafted polymer was removed using Soxhlet extraction in chloroform for 3 h.

Hydrophobic CdSeS nanocrystals were prepared by the method described in the literature [17]. Typically, CdO (0.05 g), oleic acid (0.46 g), and 15 mL tri-*n*-octylamine were mixed in a three-necked flask and heated to 300 °C under inert atmosphere. A solution of Se (0.0021 g) and S (0.0124 g) in 1 mL tri-*n*-octylphosphine was swiftly injected into the hot solution and the reaction was allowed to proceed for 5 min. This leads to bright-orange emitting nanocrystals (quantum yield ca. 50 %) with a narrow size distribution as is seen in the TEM images in Figure 2a. The average particle size is 4.8 nm. By varying the Se/S ratio nanocrystals with emissions ranging between violet and red can be prepared.

The thickness of polymer layers in the dry state was measured at  $\lambda = 632.8 \text{ nm}$  and an angle of incidence of 70° with a null-ellipsometer in a polarizer compensator–sample analyzer (Multiscop, Optrel Berlin) as described elsewhere [18,19]. From the obtained values, we calculated the distance between grafting points by the following equation:

$$d = (H \rho N_A / M_w)^{-1/2} \quad (2)$$

where  $H$  is the ellipsometric thickness,  $\rho$  is the mass density (for simplicity we used  $\rho = 1 \text{ g cm}^{-3}$ ),  $N_A$  is Avogadro's number, and  $M_w$  is the molecular weight. "In situ" ellipsometric measurements were performed to examine the swelling behavior of the polymer brush in different media. An ellipsometric cell with thin glass walls fixed at a known angle (68°) from the sample plane was used [20].

AFM studies were performed with a Dimension 3100 (Digital Instruments, Inc., Santa Barbara, CA) microscope. Tapping mode was used to map the film morphology at ambient conditions. We estimated the surface coverage of adsorbed nanocrystals by the following equation:

$$\varphi = 100 \% N \pi d^2 / 4A \quad (3)$$

where  $d$  is the diameter of the nanocrystals and  $N$  is the number of nanocrystals detected per area  $A$ .

Fluorescence images were obtained using an Axiovert 200M inverted microscope with a 10× objective (Zeiss, Oberkochen, Germany). For data acquisition (Figs. 3 and 4) a CoolSnap HQ Camera (Photometrics, Tucson, AZ) was used in conjunction with a MetaMorph imaging system (Universal Imaging, Downingtown, PA). The data in Figure 5 were obtained using an iXon DV 887-BI electron-multiplied CCD camera (Andor Technology, Belfast, Northern Ireland). The following filter set was used for imaging: Excitation: HQ 535/50, Dichroic: Q 565 LP, Emission: HQ 610/75 (Chroma Technology, Rockingham, VT).

Received: December 15, 2005  
Final version: February 21, 2006  
Published online: April 26, 2006

- [1] H. A. Ho, M. Bera-Aberem, M. Leclerc, *Chem. Eur. J.* **2005**, *11*, 1718.
- [2] R. Nutiu, Y. Li, *Chem. Eur. J.* **2004**, *10*, 1868.



- [3] N. L. Rosi, C. A. Mirkin, *Chem. Rev.* **2005**, *105*, 1547.
- [4] A. P. de Silva, H. Q. Gunaratne, T. Gunnlaugsson, A. J. M. Huxley, C. P. McCoy, J. T. Rademacher, T. E. Rice, *Chem. Rev.* **1997**, *97*, 1515.
- [5] I. L. Medintz, H. T. Uyeda, E. R. Goldman, H. Mattoussi, *Nat. Mater.* **2005**, *4*, 435.
- [6] E. Pringsheim, D. Zimin, O. S. Wolfbeis, *Adv. Mater.* **2001**, *13*, 819.
- [7] A. Ueno, *Adv. Mater.* **1993**, *5*, 132.
- [8] C. Bo, Y. Ying, Z. Zhentao, Z. Ping, *Chem. Lett.* **2004**, *33*, 1608.
- [9] Y. F. Chen, Z. Rosenzweig, *Anal. Chem.* **2002**, *74*, 5132.
- [10] S. Westenhoff, N. A. Kotov, *J. Am. Chem. Soc.* **2002**, *124*, 2448.
- [11] E. R. Goldman, I. L. Medintz, J. L. Whitley, A. Hayhurst, A. R. Clapp, H. T. Uyeda, J. R. Deschamps, M. E. Lassman, H. Mattoussi, *J. Am. Chem. Soc.* **2005**, *127*, 6744.
- [12] I. L. Medintz, E. R. Goldman, M. E. Lassman, J. M. Mauro, *Bioconjugate Chem.* **2003**, *14*, 909.
- [13] A. Lambacher, P. Fromherz, *Appl. Phys. A* **1996**, *63*, 207.
- [14] D. Braun, P. Fromherz, *Appl. Phys. A* **1997**, *65*, 341.
- [15] Y. Kaizuka, J. T. Groves, *Biophys. J.* **2004**, *86*, 905.
- [16] I. Tokareva, S. Minko, J. H. Fendler, E. Hutter, *J. Am. Chem. Soc.* **2004**, *126*, 15 950.
- [17] E. Jang, S. Jun, L. Pu, *Chem. Commun.* **2003**, 2964.
- [18] S. Minko, S. Patil, V. Datsyuk, F. Simon, K. J. Eichhorn, M. Motorov, D. Usov, I. Tokarev, M. Stamm, *Langmuir* **2002**, *18*, 289.
- [19] L. Ionov, B. Zdyrko, A. Sidorenko, S. Minko, V. Klep, I. Luzinov, M. Stamm, *Macromol. Rapid Commun.* **2004**, *25*, 360.
- [20] N. Houbenov, S. Minko, M. Stamm, *Macromolecules* **2003**, *36*, 5897.

Ionov, L.; Stamm, M.; Diez, S.

Size sorting of protein assemblies using polymeric gradient surfaces

***Nano Letters*** 2005, 5(10), 1910-1914.

# Size Sorting of Protein Assemblies Using Polymeric Gradient Surfaces

Leonid Ionov,<sup>†,‡</sup> Manfred Stamm,<sup>‡</sup> and Stefan Diez<sup>\*,†</sup>

Max-Planck-Institute of Molecular Cell Biology and Genetics, Pfotenhauerstrasse 108,  
01307 Dresden, Germany, and Leibniz Institute of Polymer Research Dresden,  
Hohe Str. 6, 01069 Dresden, Germany

Received June 28, 2005; Revised Manuscript Received August 26, 2005

## ABSTRACT

We report on a novel approach for the size-dependent fractionation of protein assemblies on polymeric surfaces. Using a simple temperature gradient method to generate one-dimensional gradients of grafted poly(ethylene glycol), we fabricated silicon-oxide chips with a gradually changing surface density of kinesin motor molecules. We demonstrate that such a bioactive surface can be used to sort gliding microtubules according to their length. To our knowledge, this is the first example of the self-organized sorting of protein assemblies on surfaces.

**Introduction.** Surfaces that change their properties gradually in one or more directions are applied successfully for combinatorial and high-throughput investigations in numerous research areas. Detailed scanning of such gradient surfaces allowed, for example, the thorough investigation of dewetting processes,<sup>1</sup> the morphological and wetting phenomena of polymer thin films,<sup>2–7</sup> as well as the measurement of the cloud point.<sup>1</sup> Thereby, the gradient approach allows for a substantial acceleration of data collection in multiparameter spaces combined with a significant reduction in the variance of the results due to experimental conditions. Moreover, gradient surfaces have recently become increasingly attractive for the investigation of proteins and cells.<sup>8–15</sup> Simultaneous control over the position and density of proteins on a surface constitutes a powerful means to investigate their properties. Until now, gradients of proteins on the surface have been generated by varying the dose of light during protein photoimmobilization,<sup>13</sup> by the controlled adsorption of nanoparticles with immobilized proteins,<sup>12</sup> by adsorption on gradient self-assembled monolayers<sup>16</sup> and on gradient surface-immobilized polymer layers prepared using controlled corona discharge,<sup>17</sup> as well as by ink-jet methods.<sup>18</sup> Such gradient surfaces have, for example, been used to study the effects of ligand/receptor density on biological recognition<sup>9,19</sup> and polyvalency.<sup>20</sup>

In this work, we report on the use of gradient surfaces for the sorting of protein assemblies according to their size. In particular, we demonstrate the sorting of gliding microtubules on surfaces that are coated with a gradually changing density of kinesin motor proteins (Figure 1). Microtubules are

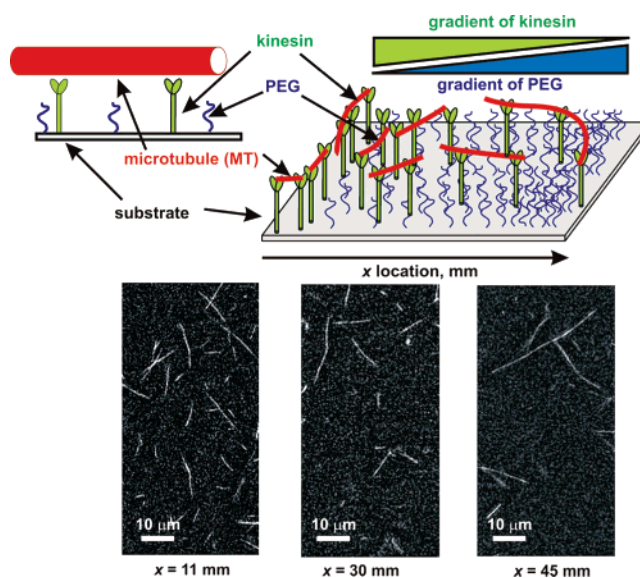


**Figure 1.** Gliding motility of microtubules on a poly(ethylene glycol) (PEG)-gradient surface with immobilized kinesin. Upper part: schematic diagram of the motility system. Although the grafting density of PEG increases from left to right, the kinesin gradient is formed in the opposite direction. Lower part: fluorescence micrographs of gliding microtubules taken at three different locations along the gradient surface. At lower kinesin density, the number of microtubules per field of view decreases, whereas the average length of the microtubules increases (see also supporting information).

hollow, cylindrical protein filaments that can be formed in vitro by self-assembly of tubulin-heterodimers. They have an outer diameter of 25 nm and can be as long as 10–50 μm. Kinesin is an ATP-hydrolyzing motor protein that moves vesicles and organelles along microtubules in the cellular environment.<sup>16,21–26</sup> In vitro gliding motility assays, where

\* Corresponding Author: E-mail: diez@mpi-cbg.de.

<sup>†</sup> Max-Planck-Institute of Molecular Cell Biology and Genetics.

<sup>‡</sup> Leibniz Institute of Polymer Research Dresden.

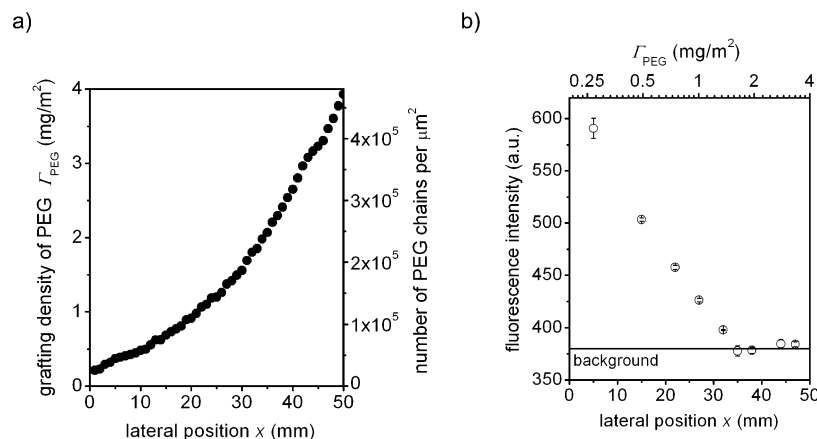


**Figure 2.** PEG density and GFP-kinesin binding. (a) Grafting density PEG and number of PEG chains per  $\mu\text{m}^2$  as a function of the lateral position on the substrate surface. (b) Fluorescence intensity of surface-bound GFP-kinesin vs lateral position and PEG grafting density. The solid line indicates the background fluorescence measured in the absence of GFP-kinesin.

microtubules are propelled over a glass coverslip by surface-bound kinesin molecules, have been used to study the interaction between motor proteins and microtubules.<sup>27–30</sup> Moreover, the kinesin-microtubule system has been implemented successfully into synthetic environments in order to facilitate tasks such as nanotransport and nanostructuring.<sup>30</sup> In such applications, control over the kinesin surface density and the microtubule length is crucial because the maximum force that can be generated depends strongly on these parameters. In particular, the length distribution of microtubules that are grown in vitro is very broad. Methods to separate microtubules according to their length, while keeping their fragile structure intact, are therefore highly desirable but have, to our knowledge, not been reported to date.

Being a processive motor, a single kinesin molecule can move a whole microtubule over the surface without letting go of it.<sup>25,31</sup> The kinesin surface density and the length of the microtubule then determine if the microtubule subsequently leaves the surface or is grabbed by one or more other motors. Thus, the use of surfaces with gradually increasing distances between kinesin molecules is suited to sort microtubules according to their length.

We prepared kinesin gradients by adsorption of kinesin molecules onto surfaces with previously formed gradients in the grafting density of poly(ethylene glycol) (PEG). Poly(ethylene glycol) prevents the binding of proteins to surfaces and is used widely for the design of protein-resistant coatings.<sup>32–35</sup> Recently, it was demonstrated that the adsorption of proteins on PEG-modified surfaces decreases with increasing PEG grafting density.<sup>36</sup> Therefore, the use of surfaces with a gradually changing density of PEG chains is an appropriate way to prepare surface concentration gradients of proteins. We show that the adsorbed kinesin retains its bioactivity and can be used for the sorting of microtubules. To our knowledge, this is the first report about the active sorting of objects on a surface according to their size.

**Fabrication of Gradient Surfaces.** Highly polished single-crystal silicon wafers (final chip size  $50 \times 10 \text{ mm}^2$ ,

{100} orientation, obtained from Semiconductor Processing Co.) with a native silicon oxide layer of 1.6 nm thickness were used as surface substrates. The wafers were cleaned in an ultrasonic bath with chloroform for 30 min, placed in hot piranha solution (3:1 concentrated sulfuric acid and 30% hydrogen peroxide) for 1 h, and rinsed several times with water. Subsequently, a thin layer of polyglycidyl methacrylate (PGMA) (thickness about 1.5 nm) was deposited by spin-coating a 0.01% PGMA solution in methylethyl ketone (MEK, VWR). PGMA ( $M_n = 84\,000 \text{ g/mol}$ ) was synthesized by free radical polymerization of glycidyl methacrylate (Aldrich) in MEK at  $60^\circ\text{C}$  using azobisisobutyronitrile (Aldrich) as the initiator. The obtained polymer was purified by multiple precipitations from MEK solution in diethyl ether. On top of the PGMA layer, a thin film (thickness about 200 nm) of PEG-NH<sub>2</sub> (2% solution in chloroform, PEG-NH<sub>2</sub>,  $M_n = 5\,000 \text{ g/mol}$ ,  $M_w = 5\,400 \text{ g/mol}$ , Polymer Source, Inc.) was spin-coated and annealed for 1 h on a stage with a 1D temperature gradient. The temperature changed gradually from  $40$  to  $90^\circ\text{C}$  along the 50-mm length of the sample. Upon heating, the chemical reaction between the terminating amino groups of the PEG and the epoxy groups of the PGMA results in the formation of the grafted PEG layer with a gradient in the grafting density caused by the temperature dependence of the grafting kinetics. The thin layer of PGMA thereby served as a macromolecular anchoring layer.<sup>37</sup> Ungrafted polymer was removed using Soxhlet extraction in chloroform for 3 h. The main advantages of our method to produce PEG-gradient surfaces are that it (i) allows for a precise control of the grafted amount of PEG and (ii) can be performed without any special equipment.

**Characterization of the Surface Gradients.** The grafting density,  $\Gamma_{\text{PEG}}$ , of the one-dimensional PEG-gradient was determined by ellipsometric mapping using a SENTECH SE-402 scanning microfocus ellipsometer at  $\lambda = 633 \text{ nm}$  at an angle of incidence of  $70^\circ$  with a lateral resolution defined by the beam spot of about  $20 \mu\text{m}$ . Figure 2a shows that the amount of surface-immobilized PEG chains increases gradually with lateral position  $x$  on the sample ( $x = 0$  at the edge with the lowest grafting density of the PEG layer).

Kinesin binding experiments were performed in a 5-mm-wide flow cell constructed from a silicon chip containing the PEG gradient,<sup>38</sup> a coverslip<sup>39</sup> (Corning, 50 × 24 mm<sup>2</sup>), and two pieces of double-sided sticky tape (Scotch 3M, thickness 0.1 mm). A casein-containing solution (0.5 mg/mL in BRB80) was perfused into the flow cell and allowed to adsorb to the surfaces for 5 min. This step originates from the commonly used protocol for gliding microtubule motility (as applied later on for the sorting application) and serves to reduce the denaturation of kinesin as well as prevent the sticking of microtubules to the surface. To quantify the binding of motor proteins, we perfused 50  $\mu$ L of motor solution (containing 27.4  $\mu$ g/mL kinesin labeled with the green-fluorescent protein (GFP) in BRB80) into the flow cell and allowed it to adsorb for 5 min. Afterward, an oxygen scavenger mix (20 mM D-Glucose, 0.020 mg/mL glucose oxidase, 0.008 mg/mL catalase, 1%  $\beta$ -mercaptoethanol) was perfused into the flow cell in order to reduce photobleaching and to remove unbound GFP-kinesin. Fluorescent images were obtained using an Axiovert 200M inverted microscope with a 40x oil immersion objective (Zeiss, Oberkochen, Germany). For data acquisition, a CoolSnap HQ Camera (Photometrics, Tucson, AZ) in 2 × 2 binning mode (yielding a field of view with an effective area of 226 × 169  $\mu$ m<sup>2</sup>) was used in conjunction with the MetaMorph imaging system (Universal Imaging, Downingtown, PA). Figure 2b shows data of the measured fluorescence (each value representing the averaged intensity over 7 fields of view) as function of the lateral position,  $x$ . The gradual decrease of fluorescence intensity with increasing grafting density of PEG indicates the formation of a 1D gradient of surface concentration of kinesin. No GFP-labeled kinesin molecules were detected to bind to the surface at PEG densities higher than 1.8 mg/m<sup>2</sup> where the measured fluorescence values corresponded to the background fluorescence measured in the absence of GFP-kinesin. This background is attributed mainly to auto fluorescence in our experimental setup and to residual back-reflected excitation light.

**Microtubule Motility on Gradient Surfaces.** Surfaces with a gradually changing density of kinesin were prepared as described above using a motor solution containing 2  $\mu$ g/mL wild-type kinesin (full length drosophila conventional kinesin expressed in bacteria and purified as described in ref 40). Thereafter, motility solution containing rhodamine-labeled taxol-stabilized microtubules<sup>41</sup> (~30 nM tubulin, 1 mM ATP, 1 mM MgCl<sub>2</sub>, 10  $\mu$ M taxol, and oxygen scavenger mix; all in BRB80 buffer) was perfused into the cell. To perform the motility experiments under conditions where the binding and unbinding of microtubules to/from the surface is in equilibrium, we did not wash out unbound microtubules. Imaging was started 10 min after perfusion of the microtubules into the flow chamber. It was found that the number of microtubules gliding over the PEG-kinesin gradient surface decreases linearly with the lateral position on the chip (Figure 3, green circles). However, the speed of the gliding microtubules was independent of the PEG grafting density and thus the kinesin surface density (Figure 3, red triangles). These observations demonstrate clearly, that (i)

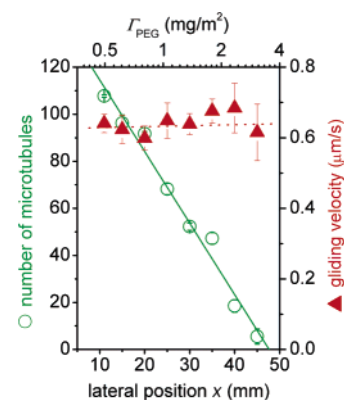


**Figure 3.** Characterization of gliding motility on PEG-kinesin gradient surfaces. Number of gliding microtubules per field of view (green circles) and gliding velocity (red triangles) vs lateral position and PEG grafting density. Plotted are average values  $\pm$  standard deviation derived from at least four time-lapse movies at each position.

the use of a PEG gradient layer allows the fabrication of surface density gradients of functional kinesin molecules and (ii) the activity of individual kinesin molecules is independent of the amount of grafted PEG underneath. In fact, we observed only very few immobile microtubules that were attached to the surface but did not move. This indicates a low amount of inactive motor molecules on the surface because it is known that inactive motors tend to inhibit MT gliding. Notably, we found gliding microtubules at grafting densities of PEG up to  $\Gamma = 3$  mg/m<sup>2</sup>. This finding is in contrast to the fluorescent measurements of GFP-kinesin (Figure 2b), where the surface seems to block protein absorption for PEG densities of  $\Gamma > 1.8$  mg/m<sup>2</sup>. This difference might be the result of the limited detection sensitivity in Figure 2b (see above). However, it could also be a sign of steric hindrance effects, that is, kinesin molecules that are labeled with a GFP molecule (diameter about 4 nm) at their tails might need more unblocked surface area to bind to than wild-type kinesin.

**Size Sorting of Gliding Microtubules.** Analysis of the length distribution of the gliding microtubules on the gradient surfaces showed that shorter microtubules disappeared gradually at positions with increased PEG-grafting density (Figure 4a). We found that the average length of microtubules increased from 6 to 13  $\mu$ m (Figure 4b) at increasing PEG grafting densities from 0.5 to 2.2 mg/m<sup>2</sup>. The length of the shortest motile microtubules, which provides an estimate of the distance between active kinesin molecules, was found to increase from less than 1  $\mu$ m to about 5  $\mu$ m over the evaluated range of PEG densities.

To explain the obtained results, we can make the following considerations: microtubules whose length,  $l$ , is larger than the average spacing,  $L_K$ , between neighboring kinesin molecules can continuously glide over the surface (i.e., they will very likely find a second kinesin to be propelled by before detaching from the first one). However, if  $l < L_K$ , then the probability to find a microtubule of length  $l$  on a surface with a kinesin density  $\rho_K = 1/L_K^2$  will be proportional to the microtubule landing rate  $\eta_{\text{landing}} = \alpha \cdot \rho_K \cdot l$  and the



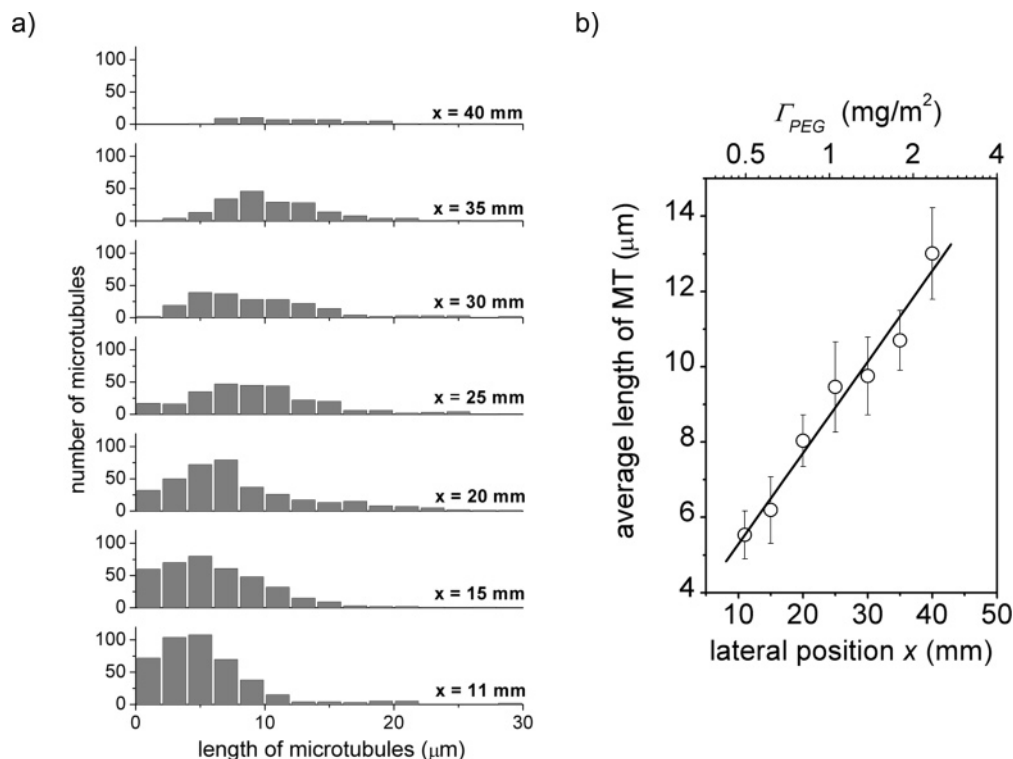


**Figure 4.** Dependence of the length of motile microtubules on the PEG-kinesin density. (a) Histograms of microtubule lengths at different lateral positions on the substrate (data represent typical length distributions of microtubules in four fields of view) (b) Average microtubule length as function of the lateral position and PEG grafting density. Error bars show the standard deviation for four fields of view at each lateral position.

gliding time on the surface  $t_{\text{gliding}} = l/u_{\text{gliding}}$  with  $u_{\text{gliding}}$  being the microtubule gliding velocity and  $\alpha$  being a constant. Thus, longer microtubules have a higher probability of landing on the surface and a lower probability of leaving it. Consequently, for a given microtubule length (or a range of lengths), the fraction of gliding microtubules will depend linearly on the kinesin surface density, which has been measured in Figure 2b via GFP-fluorescence to be a linear function of the lateral position on the gradient chip. In fact, such behavior can be demonstrated in Figure 5 where the data from Figure 4a (pooled for the 3–6  $\mu\text{m}$  and 6–9  $\mu\text{m}$  length ranges) has been plotted normalized to the number of microtubules present in the initial distribution (as inferred from the  $x = 11$  mm data). The number of short microtubules (length range between 3 and 6  $\mu\text{m}$ , open circles) monotonically decreases along the lateral position on the chip. Looking at longer microtubules (length range between 6 and 9  $\mu\text{m}$ , filled triangles), it becomes apparent that the fraction of gliding microtubules first stays constant and only decreases from a certain lateral position on the chip.

In summary, we have developed a novel method for the surface-based sorting of protein assemblies according to their size. As an example, we have demonstrated experimentally that surfaces with a gradually changing density of kinesin molecules can be used for the size fractionation of gliding microtubules. To our knowledge, this approach constitutes the first example of the self-organized sorting of protein assemblies on surfaces. We note that the sorting depended highly on the functionality of the surface-bound kinesin motors, which actively transported the microtubules to be

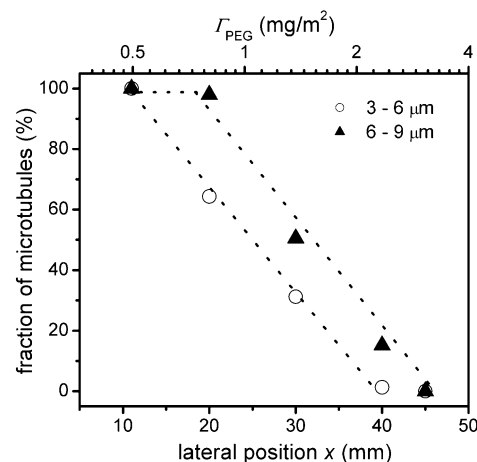


**Figure 5.** Fraction of gliding microtubules (normalized by the initial distribution) as a function of the lateral position on the gradient surface. Although a linear decrease is observed for 3–6  $\mu\text{m}$  long microtubules starting from  $x = 11$  mm, the fraction of microtubules with 6–9  $\mu\text{m}$  length decreases only after some initial plateau. The dotted lines in the figure serve only to guide the eye and shall illustrate the general behavior of the data.

sorted. In this way, motor proteins are very well suited to test the functional implementation of proteins into artificial environments because gliding filament motility can be used readily as read-out of retained protein activity. In regard to nanotechnological applications of the kinesin-microtubule transport system, our method might provide a means to obtain microtubules with narrow length distributions. The motile microtubules could be directed into collection reservoirs by

hydrodynamic flow perpendicular to the direction of the gradient in order to collect the different lengths after separation on the surface.<sup>42</sup> In general, we foresee a large potential of the reported method for further investigations of motor protein activity, as well as for high-throughput screening and combinatorial investigations of protein properties and interactions between proteins.

**Acknowledgment.** We thank C. Reuther, C. Bräuer, and J. Kerssemakers for assistance with the experiments, R. Clark and J. Howard for providing the GFP-labeled kinesin, and G. Brouhard, C. Dinu, J. Helenius, B. Nitzsche, E. Schäffer, and B. Schroth-Diez for helpful comments on the manuscript. We are also grateful to the DFG (grant SFB 287) and the BMBF (grant 03N8712) for financial support.

**Supporting Information Available:** Movie of gliding microtubule motility at three kinesin densities on the gradient surface. This material is available free of charge via the Internet at <http://pubs.acs.org>.

## References

- Meredith, J. C.; Smith, A. P.; Karim, A.; Amis, E. J. *Macromolecules* **2000**, *33*, 9747–9756.
- Ionov, L.; Zdyrko, B.; Sidorenko, A.; Minko, S.; Klep, V.; Luzinov, I. *Macromol. Rapid Commun.* **2004**, *25*, 360–365.
- Ionov, L.; Sidorenko, A.; Stamm, M.; Minko, S.; Zdyrko, B.; Klep, V.; Luzinov, I. *Macromolecules* **2004**, *37*, 7421–7423.
- Ionov, L.; Houbenov, N.; Sidorenko, A.; Luzinov, I.; Minko, S.; Stamm, M. *Langmuir* **2004**, *20*, 9916–9919.
- Smith, A. P.; Douglas, J. F.; Meredith, J. C.; Amis, E. J.; Karim, A. *J. Polym. Sci., Polym. Phys. Ed.* **2001**, *18*, 2141–2158.
- Smith, A. P.; Meredith, J. C.; Douglas, J. F.; Amis, E. J.; Karim, A. *Phys. Rev. Lett.* **2001**, *87*, 015503.
- Wu, T.; Efimenko, K.; Vlcek, P.; Subr, V.; Genzer, J. *Macromolecules* **2003**, *36*, 2448–2453.
- Halfter, W. *J. Neurosci.* **1996**, *16*, 4389–4401.
- Caelen, I.; Bernard, A.; Juncker, D.; Michel, B.; Heinzlmann, H.; Delamarche, E. *Langmuir* **2000**, *16*, 9125–9130.
- Mao, H.; Yang, T.; Cremer, P. S. *J. Am. Chem. Soc.* **2002**, *124*, 4432–4435.
- Fosser, K. A.; Nuzzo, R. G. *Anal. Chem.* **2003**, *75*, 5775–5782.
- Krämer, S.; Xie, H.; Gaff, J.; Williamson, J. R.; Tkachenko, A. G.; Nouri, N.; Feldheim, D. A.; Feldheim, D. L. *J. Am. Chem. Soc.* **2004**, *126*, 5388–5395.
- Caelen, I.; Gao, H.; Sigrist, H. *Langmuir* **2002**, *18*, 2463–2467.
- Smith, J. T.; Tomfohr, J. K.; Wells, M. C.; Beebe, T. P.; Kepler, T. B.; Reichert, W. M. *Langmuir* **2004**, *20*, 8279–8286.
- Baier, H.; Bonhoeffer, F. *Science* **1992**, *255*, 472–475.
- Riepl, M.; Ostblom, M.; Lundström, I.; Svensson, S. C. T.; Denier van der Gon, A. W.; Schäferling, M.; Liedberg, B. *Langmuir* **2005**, *21*, 1042–1050.
- Lee, J. H.; Jeong, B. J.; Lee, H. B. *J. Biomed. Mater. Res.* **1997**, *34*, 105–114.
- Pardo, L.; Wilson, W. C.; Boland, J.; Boland, T. *Langmuir* **2003**, *19*, 1462–1466.
- Butler, J. E.; Ni, L.; Nessler, R.; Joshi, K. S.; Suter, M.; Rosenberg, B.; Chang, J.; Brown, W. R.; Cantarero, L. A. *J. Immunol. Methods* **1992**, *150*, 77.
- Cairo, C. V.; Gestwicki, J. E.; Kanai, M.; Kiessling, L. L. *J. Am. Chem. Soc.* **2002**, *124*, 1615–1619.
- Howard, J. *Mechanics of Motor Proteins and the Cytoskeleton*; Sinauer Press: Sunderland, Massachusetts, 2001.
- Howard, J. *Nature* **1997**, *389*, 561–567.
- Coy, D. L.; Hancock, W. O.; Wagenbach, M.; Howard, J. *Nat. Cell Biol.* **1999**, *1*, 288–292.
- Howard, J.; Hyman, A. A. *Nature* **2003**, *422*, 753–758.
- Howard, J.; Hudspeth, A. J.; Vale, R. D. *Nature* **1989**, *342*, 154–158.
- Diez, S.; Reuther, C.; Dinu, C.; Seidel, R.; Mertig, M.; Pompe, W.; Howard, J. *Nano Lett.* **2003**, *3*, 1251–1254.
- Hess, H.; Clemmens, J.; Howard, J.; Vogel, V. *Nano Lett.* **2002**, *2*, 113–116.
- Clemmens, J.; Hess, H.; Lipscomb, R.; Hanein, Y.; Bohringer, K. F.; Matzke, C. M.; Bachand, G. D.; Bunker, B. C.; Vogel, V. *Langmuir* **2003**, *19*, 10967–10974.
- Hess, H.; Matzke, C. M.; Doot, R. K.; Clemmens, J.; Bachand, G. D.; Bunker, B. C.; Vogel, V. *Nano Lett.* **2003**, *3*, 1651–1655.
- Hess, H.; Bachand, G. D.; Vogel, V. *Chem.—Eur. J.* **2004**, *10*, 2110–2116.
- Hancock, W. O.; Howard, J. *J. Cell Biol.* **1998**, *140*, 1395–1405.
- Lee, J. H.; Lee, H. B.; Andrade, J. D. *Prog. Polym. Sci.* **1995**, *20*, 1043–1079.
- Elbert, D. L.; Hubbell, J. A. *Annu. Rev. Mater. Sci.* **1996**, *26*, 365–394.
- Harris, J. M. *Poly(ethylene glycol) Chemistry. Biotechnical and Biomedical Applications*; Plenum Press: New York, 1992.
- Recent Advances in Marine Biotechnology*; Fingerman, M., Nagabhushanam, R., Thompson, M. F., Eds.; Science Publishers: Enfield, NH, 1999; Vol. 3.
- Vanderah, D. J.; La, H.; Naff, J.; Silin, V.; Rubinson, K. A. *J. Am. Chem. Soc.* **2004**, *126*, 13639–13641.
- Zdyrko, B.; Klep, V.; Luzinov, I. *Langmuir* **2003**, *19*, 10179–10187.
- To quantify the amount of surface-bound GFP-kinesin via fluorescence measurements, we used silicon wafers with a 75-nm oxide layer (obtained from GeSiM mbH, Rossendorf) in order to avoid destructive interference effects present at low oxide thickness.
- Before usage, the coverslips were immersed in a PEG solution that consisted of 5 mM 2-[methoxypoly-(ethyleneoxy)propyl]-trimethoxysilane (90%, ABCR Karlsruhe) and 0.08% hydrochloric acid (36%) in toluene. After 12 h, the coverslips were rinsed and sonicated in toluene, ethanol, and water. The PEG layer on the glass coverslip prevented kinesin and microtubule binding to that side of the flow cell.
- Coy, D. L.; Wagenbach, M.; Howard, J. *J. Biol. Chem.* **1999**, *274*, 3667–3671.
- Rhodamine-labeled microtubules were polymerized from 10  $\mu$ L of bovine brain tubulin (4 mg/mL, mixture of 1 rhodamine labeled/3 unlabeled tubulin units) in BRB80 buffer (80 mM potassium PIPES, pH 6.9, 1 mM EGTA, 1 mM  $MgCl_2$ ) with 4 mM  $MgCl_2$ , 1 mM  $Mg$ -GTP, and 5% DMSO at 37 °C. After 30 min, the microtubule polymers were stabilized and 100-fold diluted in room-temperature BRB80 containing 10  $\mu$ M taxol. Microtubules were sheared by passing them up and down three times through a 30-gauge needle.
- Although, using the presented method the fraction of the short microtubules would always contain a number of long ones, this could potentially be overcome by flowing the microtubules into the device at high concentration. Because of a higher diffusion coefficient, shorter microtubules would reach the active kinsein binding sites faster than the longer ones. Having bound to the surface at high density, the short microtubules would then prevent the binding of the longer ones because of steric hindrance (note that microtubules are stiff polymers with a persistence length of about 1  $\mu$ m in solution and that they have to land rather parallel to the surface in order to attach to the kinsein motors).

NL051235H

## Erklärung

Ich versichere, dass ich die vorliegende Arbeit selbstständig und nur unter Verwendung der angegebenen Hilfsmittel angefertigt habe.

Die Arbeit wurde bisher an keiner weiteren Hochschuleinrichtung eingereicht.